

nature

CATCHING THE RAYS

Neutrino detector secures evidence of the Sun's secondary fusion cycle

Coronavirus

How Iceland subdued COVID-19 with science

Family planning

Research and invest in contraceptives that meet women's needs

Environment

The effect of noise and light pollution on US bird populations

Nature

[Fri, 27 Nov 2020]

- [This Week](#)
- [News in Focus](#)
- [Books & Arts](#)
- [Opinion](#)
- [Work](#)
- [Research](#)

This Week

- **UNESCO must reform to stay relevant — and reconnect people through science** [25 November 2020]
Editorial • At 75, the UN agency with a focus on science cooperation is fighting for its future role.
- **The COVID vaccine challenges that lie ahead** [24 November 2020]
Editorial • As positive results emerge at last, researchers must help the world to address vaccine hesitancy, supply logistics and pricing.
- **University rankings need a rethink** [24 November 2020]
World View • World league tables for higher education are flawed, poorly used and entrench inequity.
- **A toxic metal contaminates the ocean's deepest trenches** [18 November 2020]
Research Highlight • Dead fish drifting into the Mariana and Kermadec trenches carry mercury pollution with them.
- **How the microbiome rouses the body's virus-fighting powers** [18 November 2020]
Research Highlight • A molecule on the surface of a common gut microbe helps to activate genes involved in the immune response.
- **For better health, don't sleep your age** [17 November 2020]
Research Highlight • Older people with 'young' sleep patterns have more robust cognition than those whose rest is typical for their age.
- **Technology for sterilizing medical instruments goes solar** [20 November 2020]
Research Highlight • A sunlight-powered device equipped with an a lightweight gel makes steam hot enough to kill dangerous microbes.

EDITORIAL

25 November 2020

UNESCO must reform to stay relevant — and reconnect people through science

At 75, the UN agency with a focus on science cooperation is fighting for its future role.



Member states should back reforms proposed by Audrey Azoulay, UNESCO's director-general since 2017. Credit: Chesnot/Getty

UNESCO was born on 16 November 1945, just a few weeks after the end of the Second World War. Its founders had been persuaded that science —

along with culture and education — could help to cement peace between countries, protect human rights and improve living standards. Now, as the United Nations and UNESCO turn 75, the Paris-based agency is struggling to determine its future.

There's a lot to show for those 75 years. Today, UNESCO operates the system that has awarded World Heritage status to more than 1,100 important historical sites; the agency has also established a global network of more than 700 biosphere reserves. It holds nations to account on their commitments to get every child into school, and monitors threats to journalists around the world.

But among the UN's family of specialized agencies, UNESCO has never been properly funded — and it has been trying to recover from a funding crisis for the past decade. Data supplied by UNESCO show that the agency spent US\$1.1 billion in the 2-year period from 2010 to 2011, but in 2012–13, spending was down by 16% after the Palestinian Authority was granted full membership and the United States and Israel stopped their financial contributions in protest. Although its spending was back to \$1.1 billion by 2018–19, inflation has greatly reduced its spending power. UNESCO is now in the middle of a transformation designed, in part, to enable it to live within its means.

When *Nature* spoke to UNESCO's current and former staff, as well as to researchers who study and collaborate with it, we found immense affection for the organization and respect for its past achievements. However, there was also a sense of frustration over its future. UNESCO needs to put these concerns to rest once and for all.

Pulling together

UNESCO's history is a stellar example of science's power to advance both knowledge and diplomacy. In the wake of two world wars, and especially during the cold war, the agency helped to unlock the doors to international scientific cooperation, particularly in the physical sciences.

In 1951, it hosted the meeting that led to the creation of CERN, Europe's particle-physics laboratory. Since then, CERN has mushroomed from a project intended to reunite and stimulate Europe's physicists to a place where scientists from all over the world can collaborate. It has spawned a number of technological spin-offs and has maintained its commitment to global knowledge-sharing.



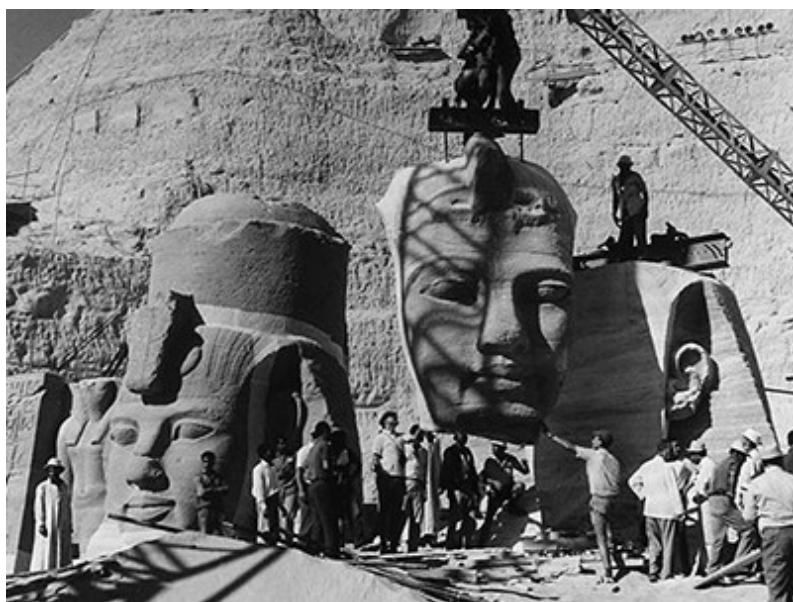
Some of UNESCO's founding nations, seen here meeting in London in 1945, have since treated the organization like a revolving door.Credit: UNESCO

When nations were reluctant to share their oceans data, UNESCO hosted the first meeting of the International Oceanographic Commission in 1961. The commission still has a role in international efforts to sustainably manage ocean resources. And UNESCO's efforts to connect scientists from countries with difficult relationships continued with SESAME, the Middle East's first synchrotron light source. That project was launched in 1999 and provides an essential tool to researchers in a range of fields, from medicine to materials

science. Getting scientists from Iran and Israel, or Cyprus and Turkey — all SESAME member countries — to work together is no small achievement.

That same year, UNESCO co-organized the World Conference on Science in Budapest. One of the outcomes was the creation of SciDev.Net, one of the first open-access platforms for sharing the results of scientific research, on which *Science* and *Nature* worked together to share some of their content with low- and middle-income countries.

And all of this happened in an organization that might never have had an ‘S’ in its title. UNESCO was originally conceived to protect and promote education and culture. It made room for science after leading scientists and science media (including *Nature*) helped to persuade the UN’s founding nations that their vision of a world at peace could not be a world without science.



UNESCO's troubled drive for peace through science and culture

And yet, for all its external successes, UNESCO has faced difficulties in how it is treated by some of its larger member states. That, in turn, has

affected the ability of its staff to get things done. It hasn't helped that some countries have treated their membership of UNESCO like a revolving door, joining and leaving as they wish, with little regard for the consequences for the agency's work when their funding stops. The United States has left twice, and the United Kingdom and Singapore have also withdrawn in the past, then returned some years later.

When richer countries stop paying, projects on the ground suffer, but so does trust in those nations' commitment to UNESCO's goals. It means officials at UNESCO's headquarters are forced to spend time and energy raising funds from other sources, and reorganizing staff and management structures to fit changing priorities — and end up spreading themselves too thinly. Time spent fire-fighting is time taken away from other priorities.

In 2013, UNESCO's leadership responded to its loss of income with a proposal that would probably have led to most of its work in its communication and information sector being abolished. But this was seen as a step too far and rejected by member states. Now, the director-general Audrey Azoulay is trying a different approach — intended, in part, to take some of the political heat out of UNESCO's work by focusing on things more countries can agree on, and playing to the agency's strengths as cultural guardian, ethical compass and laboratory of ideas.

Azoulay and her team have initiated a "strategic transformation" to spearhead internal reform and programme change — the latter requiring approval by member states late next year. Meanwhile, she is prioritizing five areas: rebuilding and reviving the devastated Iraqi city of Mosul; promoting open science; working on much-needed common standards on the ethics of artificial intelligence; a long-term vision for education; and biodiversity. The last of these is a belated, but much-needed recognition of UNESCO's long-standing experience in the study of Indigenous and local knowledge across research fields. Its importance is bolstered by the results of a UNESCO survey that asked 15,000 people what they saw as the biggest threats to peace — two-thirds of respondents said biodiversity and climate change were their greatest concern.

There's also a strong argument for reviving UNESCO's earlier science mission. In today's fractured world, fundamental and applied science could

once again be used to help bring people and societies together. In the Middle East, for example, UNESCO could help to reconnect scientists in Qatar with those in neighbouring countries. At present, researchers are unable to collaborate because of a regional dispute. The agency could have a greater role in South Asia's science, which is affected by the strained relations between India and Pakistan. And UNESCO could do more for researchers in Europe, where fractures are developing between members of the European Union.

UNESCO should seek to reconnect people through science, as it has done before. But there can be no illusions about how hard the task will be. After 75 years, UNESCO is facing one of its toughest tests. Member states must make every effort to pull together with the agency's headquarters and its field staff. UNESCO's potential in a crisis-ridden world should not be underestimated. If UNESCO ceased to exist, the world would need to recreate it.

Nature 587, 521-522 (2020)

doi: <https://doi.org/10.1038/d41586-020-03311-3>

Jobs from Nature Careers

- - - [All jobs](#)
 - - [Part-time Laboratory Assistant](#)
 - [Oklahoma Medical Research Foundation \(OMRF\)](#)
 - [Oklahoma City, United States](#)
 - [JOB POST](#)
 - [Assistant Professor of Teaching \(Tenure Track\)](#)

The University of British Columbia (UBC)

Vancouver, Canada

JOB POST

▪ **Principal Researcher / Senior Researcher**

Korea Brain Research Institute (KBRI)

Daegu, Korea, South

JOB POST

▪ **PhD Scholarship within Phosphorus Turnover in Lakes and Wetlands**

University of Southern Denmark (SDU)

Odense M, Denmark

JOB POST

This article was downloaded by **calibre** from <https://www.nature.com/articles/d41586-020-03311-3>

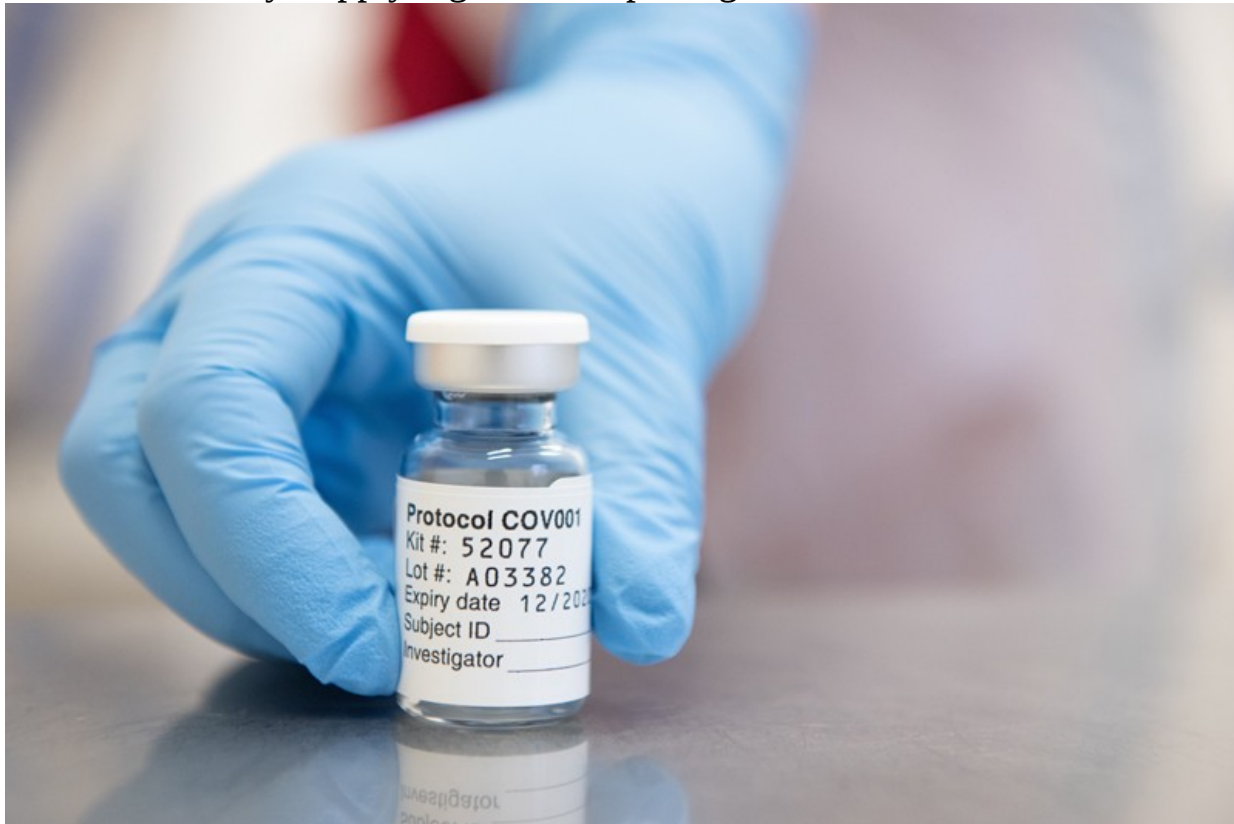
| [Section menu](#) | [Main menu](#) |

EDITORIAL

24 November 2020

The COVID vaccine challenges that lie ahead

As positive results emerge at last, researchers must help the world to address vaccine hesitancy, supply logistics and pricing.



The University of Oxford and Astra Zeneca have pledged that their COVID vaccine (pictured) will always be available at cost to low and middle income countries. Other developers must make the same commitment. Credit: Oxford Univ./John Cairns/EPA-EFE/Shutterstock

A year on from the first known case of COVID-19, the world has been hungry for good news. This month, vaccine makers have provided welcome

nourishment.

Large clinical trials of four vaccine candidates are showing remarkable promise, with three exceeding 90% efficacy — an unexpectedly high rate — according to results released so far. None reported worrying safety signals and one has shown promise in older adults, a demographic that is particularly vulnerable to SARS-CoV-2 but which sometimes responds less well to vaccines.

Early studies had shown that these candidate vaccines could stimulate an immune response. The latest trials show that this immune response can protect people against COVID-19 — a major achievement. Vaccine development is fraught with possibilities for failure, and even the most ardent optimist might not have expected to have a highly effective vaccine against a new virus less than a year after its genome was sequenced.

But there is still a vast amount of work for researchers and clinicians to do. First, they need to determine how well the vaccines work in people who are at high risk of COVID-19, including older individuals, people with obesity and those with diabetes. Second, it isn't clear how well some of the vaccines protect against severe COVID-19. Third, it is also not clear to what extent the vaccines prevent those who have been vaccinated from passing the virus on to others.



COVID vaccine confidence requires radical transparency

At the same time, researchers and policymakers must consider how to deal with challenges not related to the vaccine candidates themselves. These include vaccine hesitancy; weariness with current public-health restrictions; and the staggering logistics of vaccinating the world population. Although the finishing line seems to be in sight, there is still much difficult terrain to cross.

Some people are understandably concerned that the speed of both scientific review and vaccine regulation could compromise safety — despite vaccine developers' and regulators' assurances to the contrary. To build confidence in vaccination, it's important that regulators, companies and their research partners keep promises they have made to ensure transparency, publish data and engage with open discussion of those data as they arrive.

The US Food and Drug Administration, for example, has pledged to hold a public meeting of its external advisers in early December to discuss the data before issuing an emergency use authorization to distribute a vaccine. This kind of transparency — and the option for open airing of concerns about data, should there be any — is much needed. It stands in contrast to the agency's earlier, opaque granting of authorizations for COVID-19 treatments.



Why emergency COVID-19 vaccine approvals pose a dilemma for scientists:

Most vaccine teams and drug regulators have stated their commitment to data transparency. But much of what we know about the latest vaccine trials has been communicated through press releases and media interviews, rather than through research papers that have been subject to independent peer review.

Such speed of communication is necessary in an emergency. But more-complete data should not be held back, and the teams involved must be prepared to provide access to all relevant data as soon as this is practically possible, to allow others to scrutinize their findings and test their claims. It is important that companies continue to release their data as analyses are completed, and release preprint papers of completed studies, so that the work can be discussed quickly.

Regulators should also share their data and analyses with regulatory bodies in other countries, to speed up approval decisions around the world. And

regulators and vaccine makers must remember that vaccines will be less effective if people refuse inoculation because of vaccine hesitancy.

It's also crucial that the current public-health measures are not relaxed. The coming holiday season in some countries could trigger outbreaks as people rush to see long-missed family and friends. Vigilance is still important — perhaps even more so — as people see a welcome light at the end of the pandemic tunnel.

Vaccine distribution poses another daunting challenge, and is accompanied by questions such as how much it will cost and who will pay for it. One of the vaccines that has shown success in late-stage trials was developed by researchers at the University of Oxford, UK, and the pharmaceutical firm AstraZeneca in Cambridge, UK. This vaccine can be stored in a normal refrigerator, which makes rapid distribution more feasible than it would be for the vaccine developed by Pfizer in New York City and BioNTech in Mainz, Germany — which might be more effective than the Oxford vaccine, but needs to be stored at temperatures below -70°C .

Importantly, AstraZeneca and Oxford have also pledged to provide their vaccine at cost price to all during the pandemic, and to maintain this price for low- and middle-income countries after the pandemic, when a vaccine will still be needed in case of future outbreaks. But, as *Nature* went to press, neither Pfizer nor Moderna, a drug company in Cambridge, Massachusetts, which has a similarly promising vaccine candidate, had committed to keeping prices down once the current pandemic is over. They need to change this stance.

A number of countries — most of them wealthy — have already pre-ordered nearly four billion vaccine doses and have options for a further 5 billion, at the current prices. COVAX, a global alliance seeking to ensure that low- and middle-income countries get adequate vaccine provision, has been able to secure vaccines for only around 250 million people — far below what is needed. Once prices start to increase, the poorest countries will be even less able to pay than they are now.

Not making the vaccine affordable for these nations would be morally wrong. It would also be short-sighted, because, as infectious-disease

researchers often say, an outbreak anywhere is an outbreak everywhere.

Nature **587**, 522 (2020)

doi: <https://doi.org/10.1038/d41586-020-03334-w>

Jobs from Nature Careers

- - - [All jobs](#)
 - - [Part-time Laboratory Assistant](#)
 - [Oklahoma Medical Research Foundation \(OMRF\)](#)
 - [Oklahoma City, United States](#)
 - [JOB POST](#)
 - [Assistant Professor of Teaching \(Tenure Track\)](#)
 - [The University of British Columbia \(UBC\)](#)
 - [Vancouver, Canada](#)
 - [JOB POST](#)
 - [Principal Researcher / Senior Researcher](#)
 - [Korea Brain Research Institute \(KBRI\)](#)
 - [Daegu, Korea, South](#)
 - [JOB POST](#)

PhD Scholarship within Phosphorus Turnover in Lakes and Wetlands

University of Southern Denmark (SDU)

Odense M, Denmark

JOB POST

This article was downloaded by **calibre** from <https://www.nature.com/articles/d41586-020-03334-w>

| [Section menu](#) | [Main menu](#) |

WORLD VIEW
24 November 2020

University rankings need a rethink



World league tables for higher education are flawed, poorly used and entrench inequity.

Elizabeth Gadd

Elizabeth Gadd is a research-policy manager at Loughborough University, UK, and chair of the Research Evaluation Working Group for the International Network of Research Management Societies.

[Contact](#)

Search for this author in:

- [Pub Med](#)
- [Nature.com](#)
- [Google Scholar](#)

Researchers often complain about the indicators that hiring and grant committees use to judge them. In the past ten years, initiatives such as the San Francisco Declaration on Research Assessment and the Leiden Manifesto have pushed universities to rethink how and when to use publications and citations to assess research and researchers.

The use of rankings to assess universities also needs a rethink. These league tables, produced by the Academic Ranking of World Universities (ARWU) and the Times Higher Education World University Ranking (THE WUR) and others, determine eligibility for scholarships and other income, and sway where scholars decide to work and study. Governments devise policies and divert funds to help institutions in their countries claw up these rankings. Researchers at many institutions, such as mine, miss out on opportunities owing to their placing.

Two years ago, the International Network of Research Management Societies (INORMS), a collective of research-management organizations, invited me to chair a new working group on research evaluation with members from a dozen countries. From our first meeting, we were unanimous about our top concern: the need for fairer and more responsible university rankings. When we drew up criteria on what those would entail and rated the rankers, their shortcomings became clear.

This week, the Global Research Council, which includes heads of science- and engineering-funding agencies, is gathering experts online to discuss how assessments can improve research culture. This should include how university rankings are constructed and used.

The literature on research management is full of critiques of rankings. Rankings are methodologically challenged — often using inappropriate indicators such as counting Nobel-prizewinning alumni as a proxy for offering a quality education. They favour publications in English, and institutions that did well in past rankings. So, older, wealthier organizations in Europe and North America consistently top the charts. Rankings apply a combination of indicators that might not represent universities' particular missions, and often overlook societal impact or teaching quality.

Nonetheless, they have become entrenched, with new rankers cropping up each year. As with the journal impact factor, students, faculty members and funders turn to rankings as a lazy proxy for quality, no matter the flaws. The consequences are all too real: talent deterred, income affected. And inequities quickly become embedded.

Our working group combed the literature to develop our criteria, and asked for feedback through various community discussion lists open to academics, research-support professionals and related groups. We synthesized feedback into 20 principles involving good governance (such as the declaration of financial conflicts of interest), transparency (of aims, methods and data), measuring what matters (in line with a university's mission) and rigour (the indicators are a good proxy for what they claim to measure).

Then we converted these principles into a tool to assess rankings, qualitatively and quantitatively (see go.nature.com/2ioxhhq). We recruited international specialists to assess six of the world's highest-profile rankers, and invited rankers to self-assess. (Only one, CWTS Leiden, did so.) Richard Holmes, editor of the University Ranking Watch blog, calibrated the results, which we presented as profiles, not rankings.

The rankings with the largest audiences (ARWU, QS World University Ranking, THE WUR and US News & World Report global ranking) were found most wanting, particularly in terms of 'measuring what matters' and 'rigour'. None of these 'flagship' rankings considered open access, equality, diversity, sustainability or other society-focused agendas. None allows users to weigh indicators to reflect a university's mission. Yet all claim to identify the world's best universities.

Rankers might argue that our principles were unrealistic — that it's impossible to be completely fair in such evaluations, and that simple, overarching metrics have their place. I counter that we derived the principles from community best-practice expectations, and if rankers cannot meet them, perhaps they should stop ranking, or at least be honest about the inherent uncertainty in their conclusions (in our assessment, only CWTS Leiden attempted this).

Ultimately, rankers need to be made more accountable. I take heart from new expectations about how researchers are evaluated. From January 2021, UK research funder Wellcome will fund only organizations that present evidence that they conduct fair output assessments for researchers. Similarly, the European Commission's 'Towards 2030' vision statement calls for higher education to move beyond current ranking systems for assessing university performance because they are limited and "overly simplistic".

We hope that drawing attention to their weaknesses will draw in allies to push for change, such as neutral, independent oversight and standards for ethics and rigour as applied to other aspects of academia.

Such pressure could lead to greater alignment between the world rankers' approaches and the higher-education community's expectations for fair and responsible rankings. It might also help users to wise up to rankings' limitations, and to exercise due caution when using them for decision-making. Either would be progress.

Nature 587, 523 (2020)

doi: <https://doi.org/10.1038/d41586-020-03312-2>

Jobs from Nature Careers

- - - [All jobs](#)
 - - [Part-time Laboratory Assistant](#)
 - [Oklahoma Medical Research Foundation \(OMRF\)](#)
 - [Oklahoma City, United States](#)

[JOB POST](#)

- **Assistant Professor of Teaching (Tenure Track)**

The University of British Columbia (UBC)

Vancouver, Canada

JOB POST

- **Principal Researcher / Senior Researcher**

Korea Brain Research Institute (KBRI)

Daegu, Korea, South

JOB POST

- **PhD Scholarship within Phosphorus Turnover in Lakes and Wetlands**

University of Southern Denmark (SDU)

Odense M, Denmark

JOB POST

This article was downloaded by **calibre** from <https://www.nature.com/articles/d41586-020-03312-2>



A snailfish from the Kermadec Trench in the southwestern Pacific Ocean. Some of these snailfish have high levels of mercury in their tissues. Credit: Paul Yancey

Ocean sciences

18 November 2020

A toxic metal contaminates the ocean's deepest trenches

Dead fish drifting into the Mariana and Kermadec trenches carry mercury pollution with them.

At more than 10 kilometres deep, the Mariana Trench in the Pacific Ocean might seem remote enough to be pristine. But explorers have discovered plastic waste there — and now they've found mercury pollution, as well.

Mercury particles spread easily in the atmosphere, where they contaminate even the Arctic and Antarctic. Joel Blum at the University of Michigan in Ann Arbor and his colleagues wanted to see how much mercury has infiltrated the deep oceans.

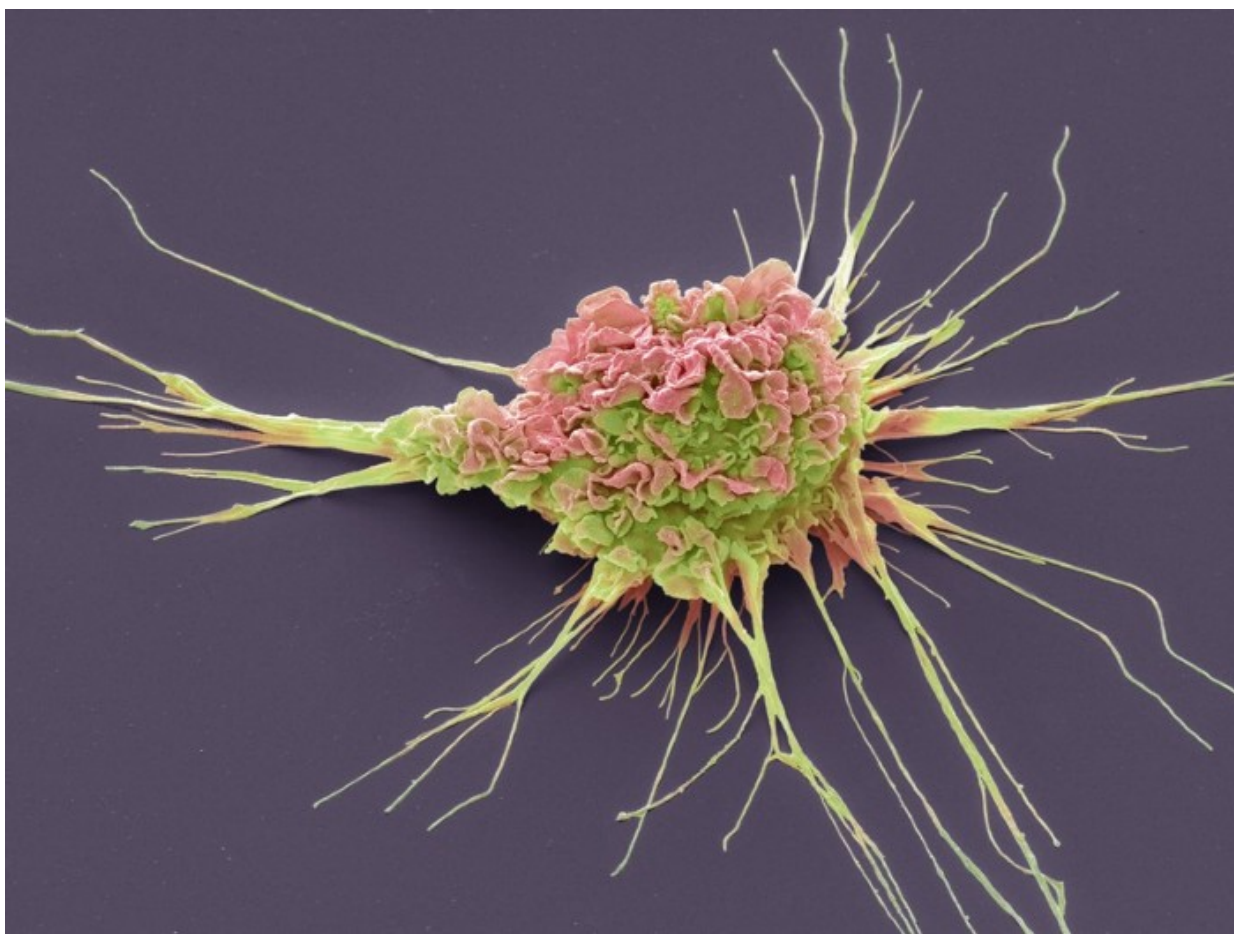
The scientists collected snailfish (*Notoliparis kermadecensis* and *Pseudoliparis swirei*) and small marine creatures known as amphipods at the bottoms of the Mariana trench and the Kermadec trench near New Zealand, at depths ranging from 6,000 to 10,250 metres. The researchers measured the amount and chemical composition of mercury in the animals. The results turned out to be similar to those in creatures living just 500 metres from the surface.

Mercury pollution from human activities permeates the near-surface waters. Fish consume that mercury; when they die, they sink into deep-sea trenches, carrying it with them, the authors say.

[Proc. Natl Acad. Sci. USA \(2020\)](#)

- [Ocean sciences](#)

This article was downloaded by **calibre** from <https://www.nature.com/articles/d41586-020-03261-w>



A dendritic cell (pictured; artificially coloured). Bacteria abundant in the gut wield molecules that activate these cells, which help the body to resist viruses. Credit: Steve Gschmeissner/SPL

Microbiome

18 November 2020

How the microbiome rouses the body's virus-fighting powers

A molecule on the surface of a common gut microbe helps to activate genes involved in the immune response.

Bacteria that thrive in the guts of humans and other mammals make a molecule that goads crucial immune cells into action, thus helping to repel invasive viruses.

The mammalian gut is occupied by trillions of harmless bacteria, including the abundant species *Bacteroides fragilis*. To investigate the microbiome–host relationship, Dennis Kasper at Harvard Medical School in Boston, Massachusetts, and his colleagues analysed how a molecule in *B. fragilis*'s outer membrane affects the immune system of mice. The team looked in particular at the rodents' dendritic cells, which act as the scouts of the immune system.

The researchers found that when dendritic cells were exposed to the membrane molecule, they secreted a powerful signalling chemical called interferon- β . That chemical in turn switched on a battery of genes that affect the immune response. Dendritic cells that were combined with the bacterial molecule in a laboratory dish largely fended off infection by influenza A virus, but almost half of the cells in a control group became infected.

Many relatives of *B. fragilis* have membrane molecules that stir a similar response, the authors say.

[Cell \(2020\)](#)

- [Microbiome](#)

This article was downloaded by **calibre** from <https://www.nature.com/articles/d41586-020-03269-2>



Youthful sleep in ageing people is linked to a lower prevalence of diabetes and other health conditions. Credit: Raquel Maria Carbonell Pagola/LightRocket/Getty

Ageing

17 November 2020

For better health, don't sleep your age

Older people with 'young' sleep patterns have more robust cognition than those whose rest is typical for their age.

Older people with sleep patterns like those of younger people tend to be in better physical and cognitive health than those with disrupted sleep.

Shaun Purcell at Harvard Medical School in Boston, Massachusetts, and his colleagues tracked the sleep of 3,819 people between 54 and 96 years old by recording their brain waves through electroencephalogram sensors that the participants wore throughout the night. The researchers then scored each person's sleep for more than 150 sleep characteristics and brain-activity patterns. These included factors such as sleep disturbance, the length of the sleep cycles in which dreams occur and preference for mornings or evenings.

The team found that older people with 'young' sleep patterns tend to have stronger cognitive abilities and a lower incidence of some health problems than do older people whose sleep patterns more closely reflect their age. Although it is unclear whether the better sleep improves health or vice versa, the researchers say that techniques such as electrical stimulation of the brain might modify sleep patterns in older people and improve their health.

[Nature Hum. Behav. \(2020\)](#)

- [Ageing](#)
-

This article was downloaded by **calibre** from <https://www.nature.com/articles/d41586-020-03244-x>



A copper collecting plate (long central structure) paired with a transparent, heat-trapping material (white strip, top) harvests enough solar heat to make steam. Credit: Lin Zhao

Renewable energy

20 November 2020

Technology for sterilizing medical instruments goes solar

A sunlight-powered device equipped with an a lightweight gel makes steam hot enough to kill dangerous microbes.

An airy insulating material doubles the efficiency of a device that converts sunshine to heat, enabling solar-powered production of steam suitable for sterilizing medical equipment.

Medical sterilization to prevent infections is routine in high-income nations, but less so in countries where people lack reliable access to energy. Existing solar absorbers can collect heat from sunlight but do not concentrate it well enough to create steam.

Evelyn Wang at the Massachusetts Institute of Technology in Cambridge and her colleagues modified an off-the-shelf solar absorber by adding a thin layer of foam tiles to the absorber's copper heat-collecting surface. The foam contains nanometre-scale silica particles that confer transparency, and is riddled with pores that help to trap heat, allowing light to pass through but preventing heat from leaving.

On a rooftop in Mumbai, India, water in a sealed chamber connected to the absorber began boiling within five minutes. For 30 minutes, the solar absorber produced steam at a temperature and pressure high enough to kill microorganisms.

The researchers hope their inexpensive device could help people in resource-poor regions to avoid infections acquired in medical settings.

[*Joule* \(2020\)](#)

- [Renewable energy](#)
-

This article was downloaded by **calibre** from <https://www.nature.com/articles/d41586-020-03278-1>

| [Section menu](#) | [Main menu](#) |

News in Focus

- **[Tiny swimming boat, AI summarizes research and COVID immunity](#)** [25 November 2020]
News Round-Up • The latest science news, in brief.
- **[Legendary Arecibo telescope will close forever — scientists are reeling](#)** [19 November 2020]
News • New satellite image reveals the damage that shut down the facility, ending an era in astronomical observation.
- **[Can dogs smell COVID? Here's what the science says](#)** [23 November 2020]
News • Canines seem to detect coronavirus infections with remarkable accuracy, but researchers say large-scale studies are needed before the approach is scaled up.
- **[Prospects for life on Venus fade — but aren't dead yet](#)** [17 November 2020]
News • Debate continues over controversial report of phosphine in the planet's atmosphere, as researchers reanalyse data and find a fainter signal.
- **[Simulating the pandemic: What COVID forecasters can learn from climate models](#)** [13 November 2020]
News • Methods that are routine in computation-heavy fields could lead to more reliable pandemic predictions.
- **[What the data say about asymptomatic COVID infections](#)** [18 November 2020]
News • People without symptoms can pass on the virus, but estimating their contribution to outbreaks is challenging.
- **[California's vote to revive controversial stem-cell institute sparks debate](#)** [16 November 2020]
News • The California Institute for Regenerative Medicine will receive billions in state funding — but some scientists oppose the plan.
- **[How Iceland hammered COVID with science](#)** [25 November 2020]
News Feature • The tiny island nation brought huge scientific heft to its attempts to contain and study the coronavirus. Here's what it learnt.

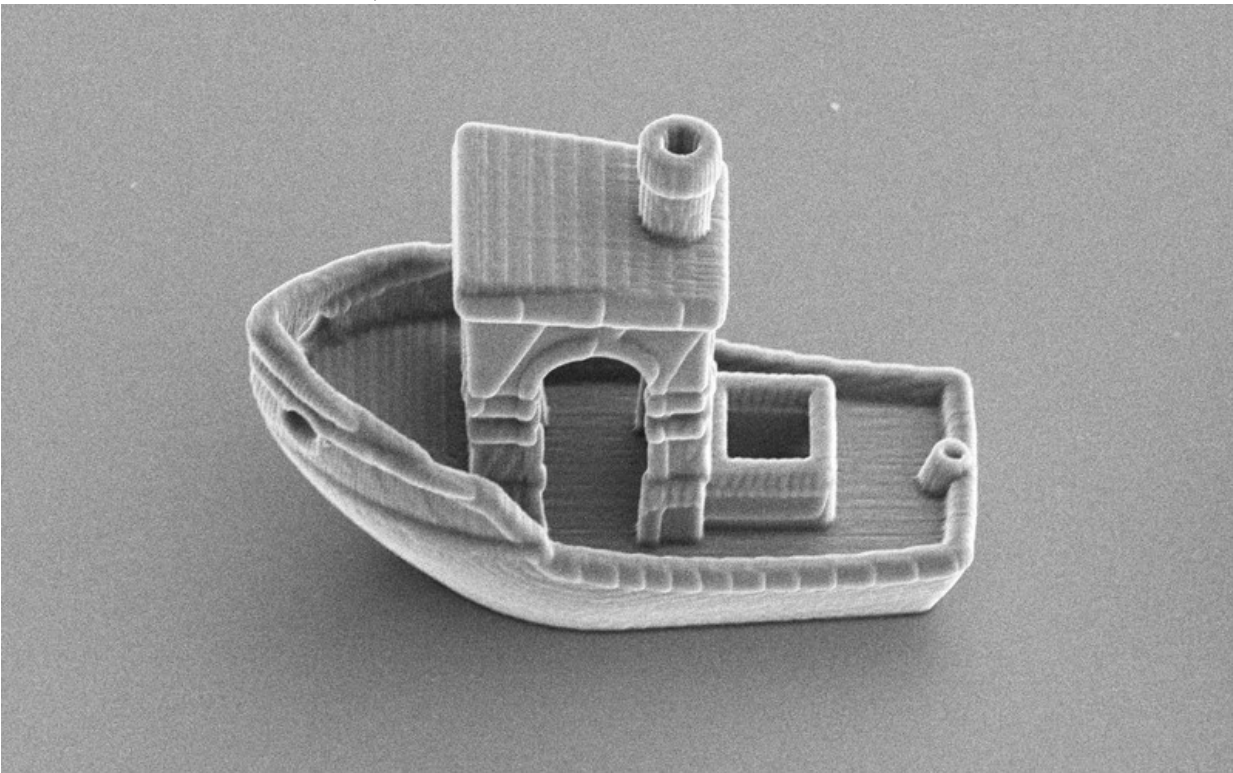
| [Next section](#) | [Main menu](#) | [Previous section](#) |

NEWS ROUND-UP

25 November 2020

Tiny swimming boat, AI summarizes research and COVID immunity

The latest science news, in brief.



Credit: R. P. Doherty *et al./Soft Matter*

3D-printed microboat

This boat-shaped particle measures just 30 micrometres in length, but is fully equipped with a cabin, chimney and flag post, and is able to propel itself

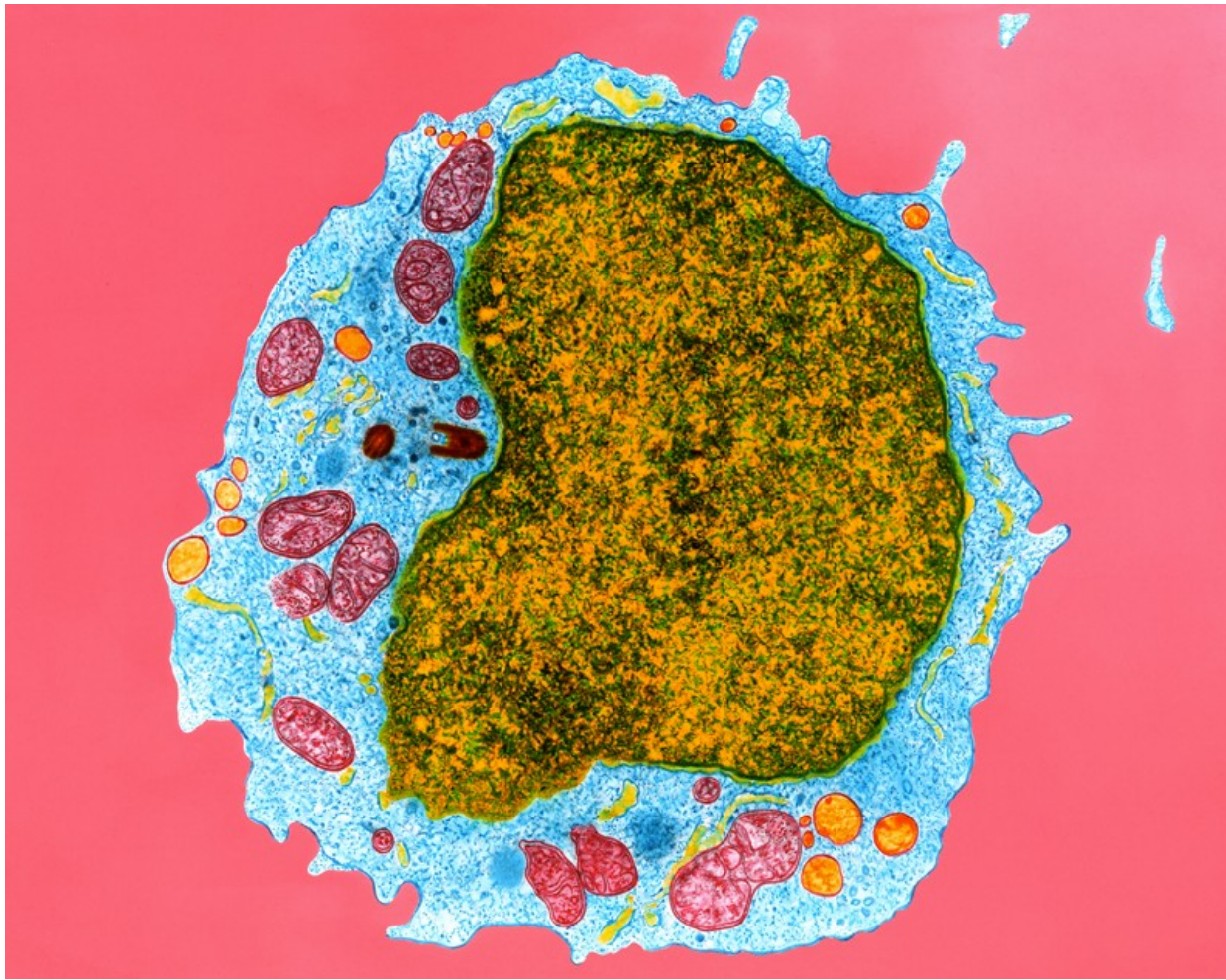
through a solution of 10% hydrogen peroxide. It was 3D printed using a technique called two-photon polymerization, and was then coated with a mixture of platinum and palladium, which catalyses the breakdown of the hydrogen peroxide. This reaction produces bubbles of gas that propel the particle along. Daniela Kraft's team at Leiden University in the Netherlands made many swimming shapes using the same method — including spheres, spirals, triangles and even a miniature starship (R. P. Doherty *et al.* *Soft Matter* <https://doi.org/fjrf>; 2020). They hope that this work will help them to study the effect of shape in microorganisms that swim, such as bacteria.

AI sums up TL;DR research in a sentence

The creators of a scientific search engine have unveiled [software that automatically generates one-sentence summaries](#) of research papers, which they say could help scientists to skim-read papers faster.

The free tool, called TLDR (the common Internet acronym for ‘Too long; didn’t read’), was activated this week for search results at Semantic Scholar, a search engine created by the non-profit Allen Institute for Artificial Intelligence (AI2) in Seattle, Washington. For the moment, TLDR generates sentences only for the ten million computer-science papers covered by Semantic Scholar, but the researchers say that papers from other disciplines should be getting summaries in the next month or so, once the software has been fine-tuned.

A preprint describing the tool was first published on the arXiv preprint server in April (I. Cachola *et al.* Preprint at <https://arxiv.org/abs/2004.15011>; 2020), and was accepted for publication after peer review by a natural-language-processing conference taking place this month. The authors have made their code freely available, along with a working demo website where anyone can try the tool (see go.nature.com/3psfs3t).



A cross section of a human B cell (artificially coloured). Credit: Dr Gopal Murti/SPL

Immune responses to coronavirus last six months

The immune system's memory of the new coronavirus lingers for at least six months in most people.

Sporadic accounts of coronavirus reinfection and reports of rapidly declining antibody levels have raised concerns that immunity to SARS-CoV-2 could dwindle within weeks of recovery from infection. Shane Crotty at the La Jolla Institute for Immunology in California and his colleagues analysed markers of the immune response in blood samples from 185 people who had a range of COVID-19 symptoms; 41 study participants were followed for at

least 6 months (J. M. Dan *et al.* Preprint at bioRxiv <https://doi.org/ghkc5k>; 2020).

The team found that participants' immune responses varied widely. But several components of immune memory for SARS-CoV-2 tended to persist for at least 6 months. Among the persistent immune defenders were memory B cells (pictured), which jump-start antibody production when a pathogen is re-encountered, and two important classes of T cell: memory CD4+ and memory CD8+ T cells. The results have not yet been peer reviewed.

Nature 587, 527 (2020)

doi: <https://doi.org/10.1038/d41586-020-03283-4>

Jobs from Nature Careers

- - - [All jobs](#)
 -
 - [Part-time Laboratory Assistant](#)

[Oklahoma Medical Research Foundation \(OMRF\)](#)

[Oklahoma City, United States](#)

[JOB POST](#)

- [Assistant Professor of Teaching \(Tenure Track\)](#)

[The University of British Columbia \(UBC\)](#)

[Vancouver, Canada](#)

[JOB POST](#)

- [Principal Researcher / Senior Researcher](#)

[Korea Brain Research Institute \(KBRI\)](#)

[Daegu, Korea, South](#)

[JOB POST](#)

- [PhD Scholarship within Phosphorus Turnover in Lakes and Wetlands](#)

[University of Southern Denmark \(SDU\)](#)

[Odense M, Denmark](#)

[JOB POST](#)

This article was downloaded by **calibre** from <https://www.nature.com/articles/d41586-020-03283-4>

| [Section menu](#) | [Main menu](#) |

NEWS

19 November 2020

- Update [19 November 2020](#)
- Correction [20 November 2020](#)

Legendary Arecibo telescope will close forever — scientists are reeling

New satellite image reveals the damage that shut down the facility, ending an era in astronomical observation.

Alexandra Witze

Search for this author in:

- [Pub Med](#)
- [Nature.com](#)
- [Google Scholar](#)

 Wide aerial shot showing a hole in the main collecting dish of the Arecibo Observatory radio telescope.

Damage to the Arecibo telescope from a 6 November cable break is too extensive to repair, the US National Science Foundation says. Credit: University of Central Florida/Arecibo Observatory

One of astronomy's most renowned telescopes — the 305-metre-wide radio telescope at Arecibo, Puerto Rico — is closing permanently. Engineers cannot find a safe way to repair it after two cables supporting the structure broke suddenly and catastrophically, one in August and one in early November.

It is the end of one of the most iconic and scientifically productive telescopes in the history of astronomy — and scientists are mourning its loss.

“I don’t know what to say,” says Robert Kerr, a former director of the observatory. “It’s just unbelievable.”



Arecibo telescope wins reprieve from US government

“I am totally devastated,” says Abel Méndez, an astrobiologist at the University of Puerto Rico at Arecibo who uses the observatory.

The Arecibo telescope, which was built in 1963, was the world’s largest radio telescope for decades and has historical and modern importance in astronomy. It was the site from which astronomers sent an interstellar radio message in 1974, in the hope that any extraterrestrials might hear it, and where the first confirmed extrasolar planet was discovered, in 1992.

It has also done pioneering work in exploring many phenomena, including near-Earth asteroids and the puzzling celestial blasts known as fast radio

bursts. All those lines of investigation have now been shut down for good, although limited science will continue at some smaller facilities on the Arecibo site.

Assessing the damage

The cables that broke helped to support a 900-tonne platform of scientific instruments, which hangs above the main telescope dish. The first cable slipped out of its socket and smashed panels at the edge of the dish, but the second broke in half and tore huge gashes in a central portion of the dish.

A high-resolution satellite image, produced at *Nature*'s request by Planet, an Earth-observation company based in San Francisco, California, shows the extent of the damage wrought by the second cable: the green of the vegetation below shows through large holes in the dish. A second photograph, released this week by observatory officials, also reveals the destruction. These are some of the only public glimpses of the damage so far.



A high-resolution satellite image of the Arecibo dish shows gashes in the main dish through which green vegetation below is visible. Credit: Planet

Labs, Inc.

If any more cables fail — which could happen at any time — the entire platform could crash into the dish below. The US National Science Foundation (NSF), which owns the Arecibo Observatory, is working on plans to lower the platform in a safe, controlled fashion.

But those plans will take weeks to develop, and there's no telling whether the platform might crash down uncontrollably in the meantime. "Even attempts at stabilization or at testing the cables could result in accelerating the catastrophic failure," said Ralph Gaume, director of the NSF's astronomy division, at a 19 November media briefing.

Why ultra-powerful radio bursts are the most perplexing mystery in astronomy

So the NSF decided to close the Arecibo dish permanently. "This decision is not an easy one to make, but safety is the number-one priority," said Sean Jones, head of the NSF's mathematical and physical sciences directorate.

The closure comes as a shock to the wider astronomical community. A social-media campaign with the hashtag #WhatAreciboMeansToMe sprung up almost immediately, with astronomers, engineers and other scientists — many from Puerto Rico — sharing stories of how the observatory had shaped their careers. "Losing the Arecibo Observatory would be a big loss for science, for planetary defence and for Puerto Rico," said Desireé Cotto-Figueroa, an astronomer at the University of Puerto Rico Humacao, in an e-mail before the closure was announced.

NSF officials insist that the cable failures came as a surprise. After the first, engineering teams spotted a handful of broken wires on the second cable, which was more crucial to holding up the platform, but they did not see it as a major problem because the weight it was carrying was well within its

design capacity. “It was not seen as an immediate threat,” says Ashley Zauderer, programme director for Arecibo at the NSF.



The main cable that failed experienced wire breaks (shown) before its sudden and unexpected collapse.Credit: University of Central Florida/Arecibo Observatory

But that main cable, which was installed in the early 1960s, had apparently degraded over time. Over the years, external review committees have highlighted the ongoing need to maintain the ageing cables. Zauderer said that maintenance in recent years had been completed according to schedule.

Before this year, the last major cable problems at the observatory were in January 2014, when a magnitude-6.4 earthquake caused damage to another of the main cables, which engineers repaired. The ageing structure has suffered other shocks in recent years, including damage to an antenna and the dish caused by Hurricane Maria in 2017.

There is no estimate yet for the cost of decommissioning the telescope.

A legendary site

The science that has ground to a halt includes Arecibo's world-leading asteroid studies. The telescope pinged radio waves at near-Earth asteroids to reveal the shape and spin of these threatening space rocks. Not having it "will be a big loss", says Alan Harris, an asteroid scientist in La Canada, California. (China's 500-meter Aperture Spherical Telescope (FAST), which opened in 2016, does not currently have the ability to do such radar studies.)

Some of the observatory's scientific projects could be transferred to other facilities, Gaume said — and he expects scientists to propose where to move their research. Much of the work conducted at Arecibo, however, could be done only with its unique array of astronomical instrumentation. "The Arecibo Telescope is irreplaceable," said a statement from two major US radio-astronomy organizations, the National Radio Astronomy Observatory in Charlottesville, Virginia, and the Green Bank Observatory in West Virginia.

Small amounts of science will continue at other portions of the Arecibo observatory, which encompasses more than the 305-metre dish. For instance, two lidar facilities shoot lasers into the atmosphere to study atmospheric phenomena.



Gigantic Chinese telescope opens to astronomers worldwide

The Arecibo telescope had been upgraded regularly, with several new instruments slated for installation in the coming years. “The telescope is in no way obsolete,” says Christopher Salter, an astronomer at the Green Bank Observatory, who worked at Arecibo for years.

Planned upgrades are now presumably on hold, including a US\$5.8-million antenna that was being developed for the telescope’s platform and would have massively increased its sensitivity. Brian Jeffs, an engineer at Brigham Young University in Provo, Utah, who heads the project, says his team expects to discuss options for its future with the NSF eventually. “Our greatest concerns are for the wonderful scientific, technical, management and support staff” of the observatory, he says.

The observatory is a major centre for science education in Puerto Rico, where it has fostered the careers of many astronomers and engineers. And it has become a part of the pop-culture lexicon, featuring in major movies such as *Contact* (1997), which was based on a novel by astronomer Carl Sagan, and the 1995 James Bond film *GoldenEye*.

The most recent major radio-telescope disaster happened in 1988, when a 300-foot-wide antenna at the Green Bank Observatory collapsed one night, owing to structural failure.

Nature 587, 529-530 (2020)

doi: <https://doi.org/10.1038/d41586-020-03270-9>

Updates & Corrections

- **Update 19 November 2020:** This story was updated to include more reactions from the scientific community and to add details about ongoing research and upgrades at the observatory.

- **Correction 20 November 2020:** This story was updated to correct the spelling of astronomer Abel Méndez's name, the full name of the National Radio Astronomy Observatory, and Christopher Salter's affiliation.

Jobs from Nature Careers

- - - [All jobs](#)
 - - [Part-time Laboratory Assistant](#)
[Oklahoma Medical Research Foundation \(OMRF\)](#)
[Oklahoma City, United States](#)
[JOB POST](#)
 - [Assistant Professor of Teaching \(Tenure Track\)](#)
[The University of British Columbia \(UBC\)](#)
[Vancouver, Canada](#)
[JOB POST](#)
 - [Principal Researcher / Senior Researcher](#)
[Korea Brain Research Institute \(KBRI\)](#)
[Daegu, Korea, South](#)
[JOB POST](#)
 -

PhD Scholarship within Phosphorus Turnover in Lakes and Wetlands

University of Southern Denmark (SDU)

Odense M, Denmark

JOB POST

This article was downloaded by **calibre** from <https://www.nature.com/articles/d41586-020-03270-9>

| [Section menu](#) | [Main menu](#) |

NEWS

23 November 2020

Can dogs smell COVID? Here's what the science says

Canines seem to detect coronavirus infections with remarkable accuracy, but researchers say large-scale studies are needed before the approach is scaled up.

Holly Else

Search for this author in:

- [Pub Med](#)
- [Nature.com](#)
- [Google Scholar](#)



Research groups around the world are testing whether dogs can detect COVID-19 by smell. Credit: Fatemeh Bahrami/Anadolu Agency/Getty

Asher is an eccentric, Storm likes sunbathing and Maple loves to use her brain. All three could play a part in controlling the COVID-19 pandemic, but they are not scientists or politicians. They are dogs.

And they are not alone. Around the world, canines are being trained to detect the whiff of COVID-19 infections. Dog trainers are claiming extraordinary results — in some cases, they say that dogs can detect the virus with almost perfect accuracy. Scientists involved with the efforts suggest that canines could help to control the pandemic because they can screen hundreds of people an hour in busy places such as airports or sports stadiums, and are cheaper to run than conventional testing methods such as the RNA-amplification technique PCR.

But most of these findings have not yet been peer reviewed or published, making it hard for the wider scientific community to evaluate the claims.

Researchers working on more conventional viral tests say that initial results from dog groups are intriguing and show promise. But some question whether the process can be scaled up to a level that would allow the animals to make a meaningful impact.

On 3 November, groups working with the animals met in an online workshop called International K9 Team to share preliminary results from experiments and to improve how their research is coordinated.

“No one is saying they can replace a PCR machine, but they could be very promising,” says veterinary neurologist Holger Volk at the University of Veterinary Medicine Hanover in Germany, who is leading an effort to train and study COVID-sniffing dogs and did not speak at the event.

Sense of wonder

Humans have taken advantage of canines’ superior sense of smell for decades. Dogs’ noses bear 300 million scent receptors, compared with humans’ 5 million or 6 million. That enables them to detect tiny concentrations of odour that people can’t. Sniffer dogs are already a familiar sight in airports, where they detect firearms, explosives and drugs. Scientists have also trained dogs to detect some cancers and malaria, but the animals are not routinely used for this purpose. Researchers don’t know for sure what the dogs are smelling, but many suspect that these illnesses cause the human body to let off a distinct pattern of volatile organic compounds (VOCs). These molecules readily evaporate to create scent that dogs can pick up. Previous work with non-COVID viruses has suggested that viral infections might also cause the body to do this.

Many sniffer-dog scientists turned their attention to COVID-19 early in the pandemic. They have trained their canines to smell samples, most often of sweat, in sterile containers, and to sit or paw the floor when they detect signs of infection. Trials at airports in the United Arab Emirates, Finland and Lebanon are using dogs to detect COVID-19 in sweat samples from passengers; these are then checked against conventional tests. According to data presented at the K9 meeting, dogs in Finland and Lebanon have

identified cases days before conventional tests picked up the virus, suggesting that they can spot infection before symptoms start.

Riad Sarkis, a surgeon and researcher at Saint Joseph University in Beirut, is part of a French–Lebanese project that has trained 18 dogs. Sarkis used the best two performers for the airport trial in Lebanon. The dogs screened 1,680 passengers and found 158 COVID-19 cases that were confirmed by PCR tests. The animals correctly identified negative results with 100% accuracy, and correctly detected 92% of positive cases, according to unpublished results. “This is very accurate, feasible, cheap and reproducible,” says Sarkis, who has been approached about using the dogs in schools, banks and prisons, and is working with a shopping mall to offer COVID-19 testing using the animals.

Low-income countries with limited lab space could particularly benefit from the approach, says Isabella Eckerle, a virologist at the University Hospitals of Geneva in Switzerland.

Sample sizes

But there is just one published journal article on dogs’ efficacy at sniffing out COVID-19, by Volk’s group; he describes it as a pilot study¹. The researchers trained eight dogs on samples taken from the mouths and windpipes of seven people hospitalized with COVID-19 and seven uninfected people. The dogs identified 83% of positive cases and 96% of negative ones.

The false positive and negative rates of the standard PCR lab test vary depending on the brand of test used and the timing of the test. A systematic review published as a preprint² on medRxiv found the false-negative rate of RT-PCR tests to be 2–33% if the same sample is tested repeated times. Up to 4% of UK PCR test results could be false positives, according to government documents.

Critics say the German dog study used samples from too few patients. The dogs could be learning to identify the specific scent of the samples rather than of COVID-19, says Cynthia Otto, who leads the Penn Vet Working Dog

Centre at the University of Pennsylvania in Philadelphia and is also working with COVID-19 sniffer dogs.

In her work, which is also unpublished, she has found that the dogs can tell the difference between samples of either urine or sweat from people with COVID-19 and those from people without the disease. She is working with chemists to understand which VOCs the dogs are picking up; a paper describing this is under review. “The dogs can do it. The challenge is the ignorance that we have as humans as to what can confuse the dogs,” she says. And in an effort to gather a large data set, her team is collecting sweat samples from 1,000 T-shirts worn overnight by people who have tested positive and negative for COVID-19.

A group in France, led by veterinary scientist Dominique Grandjean at the National Veterinary School of Alfort near Paris, posted its work³ on the preprint server bioRxiv in June. The researchers, who included Sarkis, trained 8 dogs to detect COVID-19 in 198 sweat samples, around half of which were from people with the disease. When these were hidden in a row of negative samples, the dogs identified the positive samples 83–100% of the time. The paper does not say how well the dogs identified negative test results. The research is now under review at a journal, but Grandjean says the process has not been easy. “To publish papers on detection dogs is very difficult because most reviewers do not know anything about working dogs,” he says.

The data in that study look promising, says Fyodor Urnov, a gene-editing scientist who is working on COVID testing at the University of California, Berkeley. But he would like to see larger data sets on how well dogs identify positive and negative samples. He also notes that there is variation in how well individual dogs perform. In Grandjean’s study, for example, 2 dogs identified 68 out of 68 positive samples, whereas one missed 10 out of 57 cases.

Groups need to boost their sample sizes before the wider scientific community can evaluate how useful the dogs might be, agrees James Logan, an infectious-disease researcher at the London School of Hygiene & Tropical Medicine who is training and studying COVID-19 dogs, including

Storm, Maple and Asher. “It’s important not to go out too early with grand claims and small data sets,” he says.

Nature **587**, 530-531 (2020)

doi: <https://doi.org/10.1038/d41586-020-03149-9>

References

1. 1.

Jendrny, P. *et al.* BMC Infect. Dis. **20**, 536 (2020).

2. 2.

Arevalo-Rodriguez, I. *et al.* Preprint at medRxiv
<https://doi.org/10.1101/2020.04.16.20066787> (2020).

3. 3.

Grandjean, D. *et al.* Preprint at bioRxiv
<https://doi.org/10.1101/2020.06.03.132134> (2020).

Jobs from Nature Careers

- - - [All jobs](#)
 -
 - [**Part-time Laboratory Assistant**](#)

[Oklahoma Medical Research Foundation \(OMRF\)](#)

[Oklahoma City, United States](#)

[JOB POST](#)

- **Assistant Professor of Teaching (Tenure Track)**

The University of British Columbia (UBC)

Vancouver, Canada

JOB POST

- **Principal Researcher / Senior Researcher**

Korea Brain Research Institute (KBRI)

Daegu, Korea, South

JOB POST

- **PhD Scholarship within Phosphorus Turnover in Lakes and Wetlands**

University of Southern Denmark (SDU)

Odense M, Denmark

JOB POST

This article was downloaded by **calibre** from <https://www.nature.com/articles/d41586-020-03149-9>

NEWS

17 November 2020

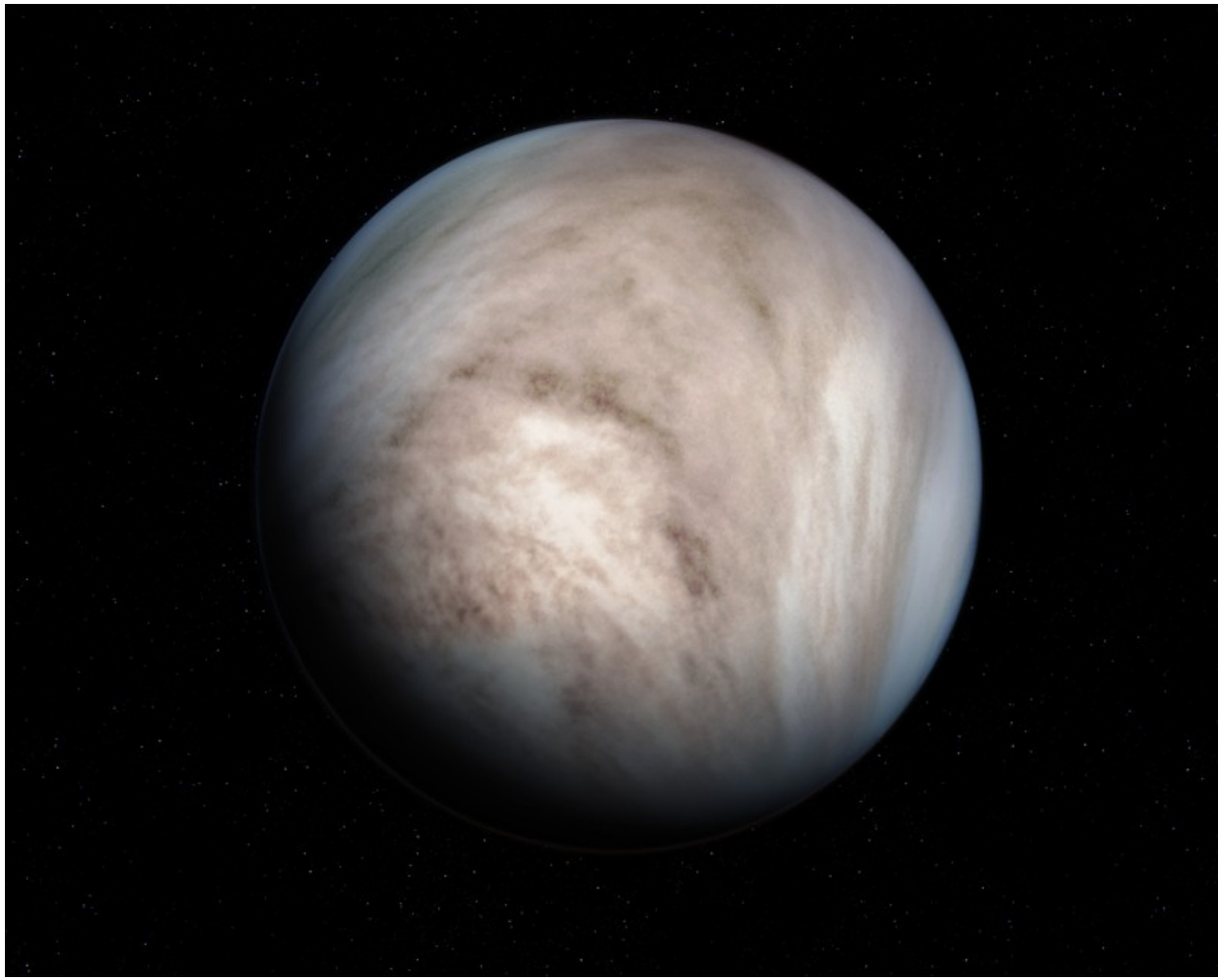
Prospects for life on Venus fade — but aren't dead yet

Debate continues over controversial report of phosphine in the planet's atmosphere, as researchers reanalyse data and find a fainter signal.

Alexandra Witze

Search for this author in:

- [Pub Med](#)
- [Nature.com](#)
- [Google Scholar](#)



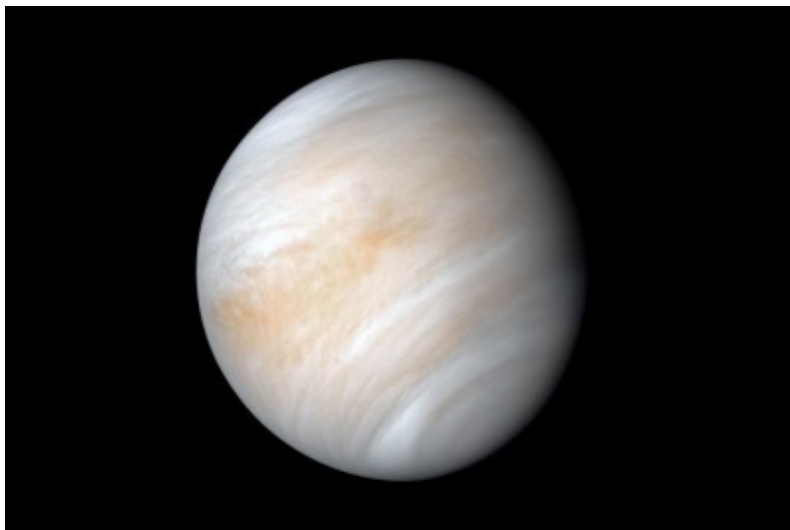
Scientists had long considered Venus, which has a thick, acidic atmosphere, unsuitable for life. Credit: Detlev Van Ravenswaay/Science Photo Library

Signs of the gas phosphine in Venus's atmosphere have faded — but they're still there, according to a new data analysis.

In September, an international team of astronomers made headlines when it reported finding phosphine — a potential marker of life — in the planet's atmosphere¹. Several studies [questioning the observations](#) and conclusions quickly followed. Now, the same team has reanalysed part of its data, citing a processing error in the original data set. The researchers confirmed the phosphine signal, but say that it's fainter than before.

The work is an important step forward in resolving the most exciting Venus debate in decades. "I've waited all my life for this," says Sanjay Limaye, a

planetary scientist at the University of Wisconsin–Madison, who says the debate has reinvigorated the field.



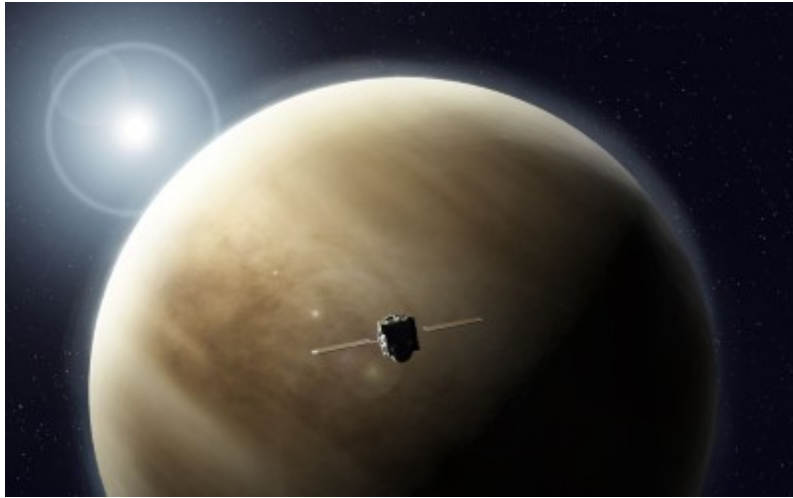
Life on Venus? Scientists hunt for the truth

The reanalysis, based on radio-telescope observations at the Atacama Large Millimeter/submillimeter Array (ALMA) in Chile, concludes that average phosphine levels across Venus are about one part per billion — approximately one-seventh of the earlier estimate. Unlike in their original report, the scientists now describe their discovery of phosphine on Venus as tentative².

It is the researchers' first public response to the criticisms that have been levelled against them in the past two months. "The scientific process is working," says Bob Grimm, a planetary scientist at the Southwest Research Institute in Boulder, Colorado, who is not involved with any of the phosphine studies. Researchers tend to respond to big claims with big efforts to gather evidence and either prove or disprove them.

Taking another look

In its September report, the team used data from ALMA and the James Clerk Maxwell Telescope (JCMT) in Hawaii to make its discovery. Team leader Jane Greaves, an astronomer at Cardiff University, UK, says she and her colleagues redid the work because they had learnt that the original ALMA data contained a spurious signal that could have affected the results. ALMA posted the corrected data on 16 November, and Greaves and her team ran a fresh analysis that night and posted it ahead of peer review on the preprint server arxiv.org. “We’ve been working like crazy,” she told a meeting of the Venus Exploration Analysis Group, a NASA community forum, on 17 November.



Venus is Earth’s evil twin — and space agencies can no longer resist its pull

According to Greaves and her colleagues, the ALMA data show the spectral signature of phosphine, a molecule made of one phosphorus and three hydrogen atoms. They say no other compound can explain the data. Finding phosphine on Venus would be tantalizing because microbes produce the gas on Earth. If the signal is real and indeed due to phosphine, it’s possible that microbes living in and drifting among the planet’s clouds could be producing the gas^{3,4} — but it’s also possible there might be a non-living source that

scientists have yet to identify. Before they can determine whether either of these scenarios is true, researchers first need to confirm phosphine's presence.

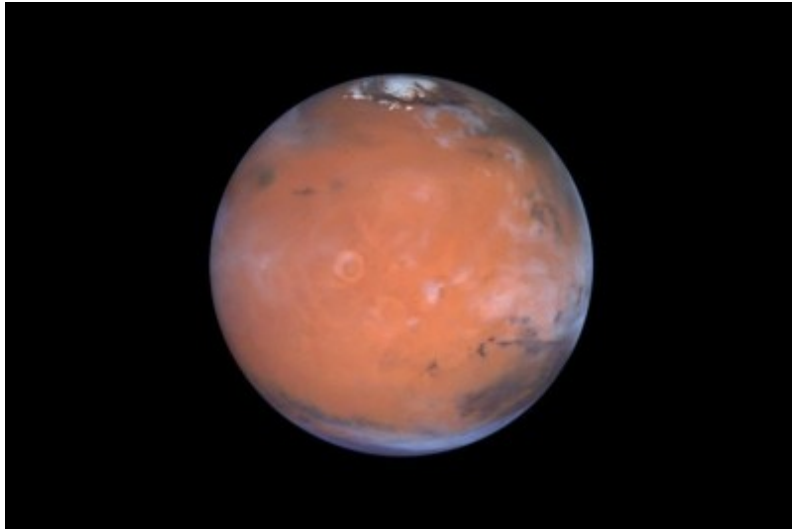
In one critique of the original study, researchers suggested⁵ that the signal reported as phosphine might really be coming from sulfur dioxide, a gas that is common in Venus's clouds but is not produced by life there. Greaves and her team fired back in their latest report that that can't be the case, because of how the phosphine fingerprint appears in data collected by the second telescope they used, the JCMT. Other critiques have focused on the difficulty of extracting a phosphine signal out of complicated data.

The reanalysis found that phosphine concentrations in Venus's atmosphere occasionally peak at five parts per billion. That means levels of the gas might wax and wane over time at different places on the planet, said Greaves — a situation similar to methane spikes appearing on Mars.

One other new strand of evidence supports phosphine on Venus. Inspired by Greaves's original report, a team led by Rakesh Mogul, a biochemist at California State Polytechnic University in Pomona, dug through decades-old data from NASA's 1978 Pioneer Venus mission. This spacecraft dropped a probe that measured the chemistry of clouds in the planet's atmosphere as it fell. It detected a phosphorus signal that could be attributed to phosphine or another phosphorus compound⁶. But “we believe the simplest gas that fits the data is phosphine”, Mogul said at the meeting on 17 November.

Work still ahead

Where the phosphine comes from remains a mystery. Even at the one-part-per-billion level, there's too much of it to be explained by volcanic eruptions at the planet's surface or by lightning strikes in the atmosphere, several scientists said at the meeting. But phosphorus-based compounds might be produced by geological processes and then transform into other chemicals, such as phosphine, as they rise into the clouds, said Mogul.



Water on Mars: discovery of three buried lakes intrigues scientists

The only spacecraft currently orbiting Venus, Japan's Akatsuki, does not carry instruments that could help settle the debate. The Indian Space Research Organisation is planning a Venus mission that would launch in 2025 and could potentially carry instruments capable of looking for phosphine. In the meantime, Greaves and other researchers are applying for more time on Earth-based telescopes, including ALMA.

Researchers are investigating many other aspects of Venus, says David Grinspoon, an astrobiologist at the Planetary Science Institute who is based in Washington DC. "There are 1,001 reasons to go back to Venus, and if the phosphine 'goes away' through further observations and analysis, there will still be 1,000 reasons to go."

Nature 587, 532 (2020)

doi: <https://doi.org/10.1038/d41586-020-03258-5>

References

1. 1.

Greaves, J. S. *et al.* *Nature Astron.* <https://doi.org/10.1038/s41550-020-1174-4> (2020).

2. 2.

Greaves, J. S. *et al.* Preprint at <https://arxiv.org/abs/2011.08176> (2020).

3. 3.

Bains, W. *et al.* Preprint at <https://arxiv.org/abs/2009.06499> (2020).

4. 4.

Seager, S. *et al.* *Astrobiology* <https://doi.org/10.1089/ast.2020.2244> (2020).

5. 5.

Villanueva, G. *et al.* Preprint at <https://arxiv.org/abs/2010.14305> (2020).

6. 6.

Mogul, R., Limaye, S. S., Way, M. J. & Cordova, J. A. Jr Preprint at <https://arxiv.org/abs/2009.12758> (2020).

Jobs from Nature Careers

- - - [All jobs](#)
 - - [Part-time Laboratory Assistant](#)
 - [Oklahoma Medical Research Foundation \(OMRF\)](#)
 - [Oklahoma City, United States](#)

JOB POST

- **Assistant Professor of Teaching.(Tenure Track)**

The University of British Columbia (UBC)

Vancouver, Canada

JOB POST

- **Principal Researcher / Senior Researcher**

Korea Brain Research Institute (KBRI)

Daegu, Korea, South

JOB POST

- **PhD Scholarship within Phosphorus Turnover in Lakes and Wetlands**

University of Southern Denmark (SDU)

Odense M, Denmark

JOB POST

This article was downloaded by **calibre** from <https://www.nature.com/articles/d41586-020-03258-5>

NEWS

13 November 2020

Simulating the pandemic: What COVID forecasters can learn from climate models

Methods that are routine in computation-heavy fields could lead to more reliable pandemic predictions.

David Adam

Search for this author in:

- [Pub Med](#)
- [Nature.com](#)
- [Google Scholar](#)



A second national lockdown began in England on 5 November.Credit: Hollie Adams/AFP/Getty

Epidemiologists predicting the spread of COVID-19 should adopt climate-modelling methods to make forecasts more reliable, say computer scientists who have spent months auditing one of the most influential models of the pandemic.

In a study that was uploaded to the preprint platform *Research Square* on 6 November¹, researchers commissioned by London’s Royal Society used a powerful supercomputer to re-examine CovidSim, a model developed by a group at Imperial College London. In March, that simulation helped convince British and US politicians to introduce lockdowns to prevent projected deaths, but it has since been scrutinized by researchers who doubt the reliability of its results.

The analysis, which has not yet been peer-reviewed, shows that because researchers didn’t appreciate how sensitive CovidSim was to small changes in its inputs, their results overestimated the extent to which a lockdown was

likely to reduce deaths, says Peter Coveney, a chemist and computer scientist at University College London, who led the study.



Special report: The simulations driving the world's response to COVID-19

Coveney is reluctant to criticize the Imperial group, led by epidemiologist Neil Ferguson, which he says did the best job possible under the circumstances. And the model correctly showed that “doing nothing at all would have disastrous consequences”, he says. But he argues that epidemiologists should stress-test their simulations by running ‘ensemble’ models, in which thousands of versions of the model are run with a range of assumptions and inputs, to provide a spread of scenarios with different probabilities. These ‘probabilistic’ methods are routine in computation-heavy fields, from weather forecasting to molecular dynamics. Coveney’s team has now done this for CovidSim: the findings suggest that if the model had been run as an ensemble, it would have forecast a range of probable death tolls under lockdown, with an average twice as high as the original prediction, and closer to the actual figures.

“CovidSim may be vaunted as the most complicated epidemiological model, but it’s almost like a toy compared with the really high-end supercomputing applications,” says Coveney, who was asked to check the model’s performance as part of the Royal Society’s Rapid Assistance in Modelling the Pandemic (RAMP) initiative.

Ensembles of calculations

Coveney’s team used the Eagle supercomputer at the Poznan Supercomputing and Networking Center in Poland to perform 6,000 separate runs of CovidSim, each with a unique set of input parameters. These represent features of the pandemic including the infectiousness and lethality of the virus, the probable number of contacts people make in various settings and the estimated success of measures such as telling people to work from home. Back in March, inputs for many of these parameters were educated guesses, with some drawn from preliminary data on the virus, and others based on experience with diseases such as influenza.

Models that predict the spread of disease often rely on hundreds of parameters — but this can introduce uncertainty. “There was a concern among the circles who set up the RAMP initiative that these models the epidemiologists work with have an absurd number of parameters in them and they can’t possibly be right,” Coveney says.

His team found 940 parameters in the CovidSim code, but whittled these down to the 19 that most affected the output. And up to two-thirds of the differences in the model’s results could be put down to changes in just three key variables: the length of the latent period during which an infected person has no symptoms and can’t pass the virus on; the effectiveness of social distancing; and how long after getting infected a person goes into isolation.



Why COVID outbreaks look set to worsen this winter

The study suggests that small variations in these parameters could have an outsized, non-linear impact on the model's output. For example, the majority of the team's thousands of runs suggested that the UK death toll under lockdown would be much higher than the Imperial team's initial projections — 5–6 times higher in some cases. Averaging the figures still suggested twice as many deaths as the Imperial group had forecast.

In one modelled scenario, which assumed that the United Kingdom would lock down when 60 people per week needed to be admitted to hospital for intensive care, the March report forecast a total of 8,700 deaths in the country. The probabilistic results produced by Coveney's group put this figure at around 15,000 on average, but said that death tolls of more than 40,000 were possible, depending on what parameters were used. It is hard to compare these projections with the actual figures for COVID-19 deaths in the United Kingdom, because the lockdown started a week later than the results of any of the models assume, by which time significantly higher amounts of the disease were already circulating.

“They didn't get it right,” says Coveney. “They ran the simulation correctly: it's just that they didn't know how to extract the correct probabilistic

description from it. That would mean having to run ensembles of calculations.” Coveney said he couldn’t comment on whether running an ensemble model would have altered policy, but Rowland Kao, an epidemiologist and data scientist at the University of Edinburgh, UK, points out that the government compares and synthesizes the results of several different COVID-19 models. “It would be overly simplified to consider that decision-making is based on a single model,” he says.

Improved models

Ferguson accepts most of Coveney’s points about the benefits of performing probabilistic forecasts, but says that “we just weren’t in a position to do that in March”. The Imperial group has significantly improved its models since then, he adds, and can now produce probabilistic results. For example, it now presents the uncertainty in CovidSim inputs using Bayesian statistical tools — already common in some epidemiological models of illnesses such as the livestock disease foot-and-mouth. And a simpler model, he adds, was used to inform the UK government’s decision to reintroduce lockdown measures in England this month. This model is more agile than CovidSim: “Because we can run it several times a week, it’s much easier to fit the data in real time, allowing for uncertainty,” Ferguson says.

“This sounds like a step in the right direction, and is aligned with the conclusions of our paper,” says Coveney.



Why schools probably aren't COVID hotspots

The choice of technique often comes down to a computational trade-off, Ferguson says. “If you want to routinely properly characterize all the uncertainty, then that is much easier with a less computationally intensive model.”

Bayesian tools are an improvement, says Tim Palmer, a climate physicist at the University of Oxford, UK, who pioneered the use of ensemble modelling in weather forecasting. But only ensemble modelling techniques that are run on the most powerful computers will deliver the most reliable pandemic projections, he says. Such techniques transformed the reliability of climate models, he adds, helped by the coordination of the Intergovernmental Panel on Climate Change (IPCC).

“We need something like the IPCC for these pandemic models. We need some kind of international facilities where these models can be developed properly,” Palmer says. “It has been rushed because of the urgency of the situation. But to take this forward, we need some kind of international organization that can work on synthesizing epidemiological models from around the world.”

Nature 587, 533-534 (2020)

doi: <https://doi.org/10.1038/d41586-020-03208-1>

References

1. 1.

Edeling, W. *et al.* Preprint at Research Square
<https://doi.org/10.21203/rs.3.rs-82122/v3> (2020).

Jobs from Nature Careers

- - - [All jobs](#)
 - - **[Part-time Laboratory Assistant](#)**
[Oklahoma Medical Research Foundation \(OMRF\)](#)
[Oklahoma City, United States](#)
[JOB POST](#)
 - **[Assistant Professor of Teaching \(Tenure Track\)](#)**
[The University of British Columbia \(UBC\)](#)
[Vancouver, Canada](#)
[JOB POST](#)
 - **[Principal Researcher / Senior Researcher](#)**
[Korea Brain Research Institute \(KBRI\)](#)
[Daegu, Korea, South](#)
[JOB POST](#)
 - **[PhD Scholarship within Phosphorus Turnover in Lakes and Wetlands](#)**
[University of Southern Denmark \(SDU\)](#)
[Odense M, Denmark](#)
[JOB POST](#)

This article was downloaded by **calibre** from <https://www.nature.com/articles/d41586-020-03208-1>

| [Section menu](#) | [Main menu](#) |

NEWS

18 November 2020

- Correction [20 November 2020](#)
- Correction [23 November 2020](#)

What the data say about asymptomatic COVID infections

People without symptoms can pass on the virus, but estimating their contribution to outbreaks is challenging.

Bianca Nogradiy

Search for this author in:

- [Pub Med](#)
- [Nature.com](#)
- [Google Scholar](#)



Roughly one in five people with COVID-19 don't experience symptoms.Credit: Ezra Acayan/Getty

How many people don't experience any symptoms after becoming infected with SARS-CoV-2? And what is their role in spreading COVID-19? These have been key questions since the beginning of the pandemic.

Now, evidence suggests that about one in five infected people will experience no symptoms, and they will transmit the virus to significantly fewer people than someone with symptoms. But researchers are divided about whether asymptomatic infections are acting as a 'silent driver' of the pandemic.

Although there is a growing understanding of asymptomatic infections, researchers say that people should continue to use measures to reduce viral spread, including social distancing and wearing masks, regardless of whether they have symptoms.

The issue with putting a reliable figure on the rate of asymptomatic COVID-19 is distinguishing between people who are asymptomatic and pre-symptomatic, says Krutika Kuppalli, an infectious-disease researcher at the Medical University of South Carolina in Charleston. “Asymptomatic is someone who never developed symptoms ever throughout the course of their disease, and pre-symptomatic is somebody who has mild symptoms before they do go on to develop symptoms,” Kuppalli says. There is also no standardized accepted definition of that, she says.

Research early in the pandemic suggested that the rate of asymptomatic infections could be as [high as 81%](#). But a meta-analysis published last month¹, which included 13 studies involving 21,708 people, calculated the rate of asymptomatic presentation to be 17%. The analysis defined asymptomatic people as those who showed none of the key COVID-19 symptoms during the entire follow-up period, and the authors included only studies that followed participants for at least seven days. Evidence suggests that most people develop symptoms in 7–13 days, says lead author Oyungerel Byambasuren, a biomedical researcher at the Institute for Evidence-Based Healthcare at Bond University in Gold Coast, Australia.

Silent reservoir

Byambasuren’s review also found that asymptomatic individuals were 42% less likely to transmit the virus than symptomatic people.

One reason that scientists want to know how frequently people without symptoms transmit the virus is because these infections largely go undetected. Testing in most countries is targeted at those with symptoms.

As part of a large population study in Geneva, Switzerland, researchers modelled viral spread among people living together. In a manuscript posted on medRxiv this month², they report that the risk of an asymptomatic person passing the virus to others in their home is about one-quarter of the risk of transmission from a symptomatic person.

Although there is a lower risk of transmission from asymptomatic people, they might still present a significant public-health risk because they are more

likely to be out in the community than isolated at home, says Andrew Azman, an infectious-disease epidemiologist at the Johns Hopkins Bloomberg School of Public Health in Baltimore, Maryland, who is based in Switzerland and was a co-author on the study. “The actual public-health burden of this massive pool of interacting ‘asymptomatics’ in the community probably suggests that a sizeable portion of transmission events are from asymptomatic transmissions,” he says.

But other researchers disagree about the extent to which asymptomatic infections are contributing to community transmission. If the studies are correct in finding that asymptomatic people are a low transmission risk, “these people are not the secret drivers of this pandemic”, says Byambasuren. They “are not coughing or sneezing as much, they’re probably not contaminating as much surfaces as other people”.

Muge Cevik, an infectious-disease researcher at the University of St Andrews, UK, points out that because most people are symptomatic, concentrating on identifying them will probably eliminate most transmission events.

Viral dynamics

To understand what is happening in people with no symptoms, Cevik and colleagues conducted a systematic review and meta-analysis³ of 79 studies on the viral dynamics and transmissibility of SARS-CoV-2, which is posted on social-sciences preprint server SSRN. Some studies showed that those without symptoms had similar initial viral loads — the number of viral particles present in a throat swab — when compared with people with symptoms. But asymptomatic people seem to clear the virus faster and are infectious for a shorter period.

The immune systems of asymptomatic individuals might be able to neutralize the virus more rapidly, says Cevik. But that doesn’t mean these people have a stronger or more durable immune response — and there is evidence that people with severe COVID-19 have a more substantial and long-lasting neutralizing antibody response, she says.

Although there is now a better understanding of asymptomatic infections and transmission of COVID-19, Cevik says that asymptomatic people should continue to use measures that reduce viral spread, such as social distancing, hand hygiene and wearing a mask.

Nature **587**, 534-535 (2020)

doi: <https://doi.org/10.1038/d41586-020-03141-3>

Updates & Corrections

- **Correction 20 November 2020:** A previous version of this story incorrectly stated that studies analyzed in the Cevik, M. *et al* meta-analysis had measured viral particles in the blood. Particle numbers were measured in throat swabs.
- **Correction 23 November 2020:** This article has been updated with the correct affiliation for Krutika Kuppalli.

References

1. 1.

Byambasuren, O. *et al.* *J. Assoc. Med. Microbiol. Infect. Dis. Can.* <https://doi.org/10.3138/jammi-2020-0030> (2020).

2. 2.

Bi, Q. *et al.* Preprint at medRxiv
<https://doi.org/10.1101/2020.11.04.20225573> (2020).

3. 3.

Cevik, M. *et al.* Preprint at SSRN <https://doi.org/10.2139/ssrn.3677918> (2020).

Jobs from Nature Careers

- - - [All jobs](#)
 - - **[Part-time Laboratory Assistant](#)**
[Oklahoma Medical Research Foundation \(OMRF\)](#)
[Oklahoma City, United States](#)
[JOB POST](#)
 - **[Assistant Professor of Teaching \(Tenure Track\)](#)**
[The University of British Columbia \(UBC\)](#)
[Vancouver, Canada](#)
[JOB POST](#)
 - **[Principal Researcher / Senior Researcher](#)**
[Korea Brain Research Institute \(KBRI\)](#)
[Daegu, Korea, South](#)
[JOB POST](#)
 - **[PhD Scholarship within Phosphorus Turnover in Lakes and Wetlands](#)**
[University of Southern Denmark \(SDU\)](#)
[Odense M, Denmark](#)
[JOB POST](#)

This article was downloaded by **calibre** from <https://www.nature.com/articles/d41586-020-03141-3>

| [Section menu](#) | [Main menu](#) |

NEWS

16 November 2020

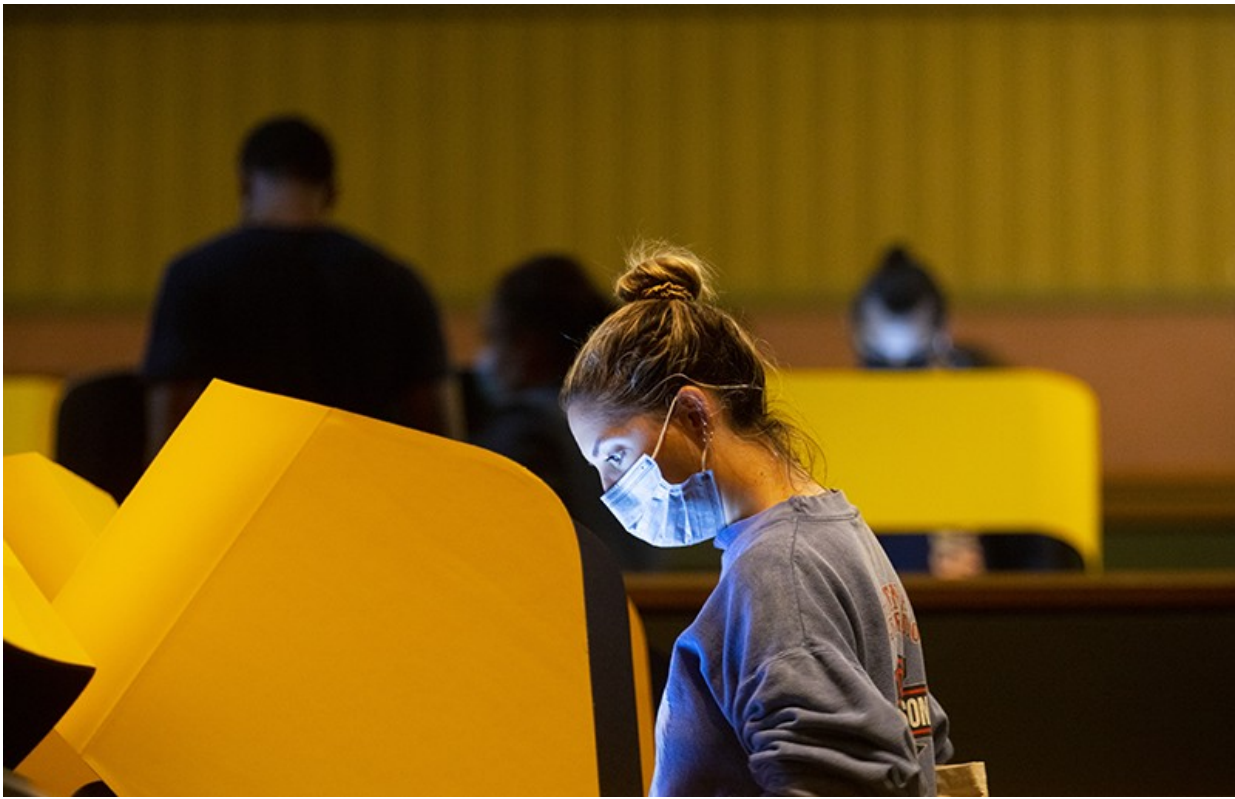
California's vote to revive controversial stem-cell institute sparks debate

The California Institute for Regenerative Medicine will receive billions in state funding — but some scientists oppose the plan.

Nidhi Subbaraman

Search for this author in:

- [Pub Med](#)
- [Nature.com](#)
- [Google Scholar](#)



Voters in the Golden State passed Proposition 14, which will fund stem cell research over 30 years. Credit: Francine Orr/Los Angeles Times/Getty

Voters in California have approved US\$5.5 billion in funding for stem-cell and other medical research, granting a lifeline to a controversial state agency. But scientists are split over whether the California Institute for Regenerative Medicine (CIRM) in Oakland is a worthwhile investment for the US state — or for the field of stem-cell research.

A measure to authorize new funds for CIRM, called Proposition 14, appeared on California ballots in the recent US election. After more than a week of vote counting, on 12 November the [Associated Press announced](#) that California had passed the proposal, which will be paid for with a state bond sale.

But critics of CIRM are concerned about oversight at the state agency, which has faced complaints about potential conflicts of interest among its board members for years. They also point out that the field has grown and now receives federal support, making state funding hard to justify — especially amid a pandemic that has imperilled California's economy.

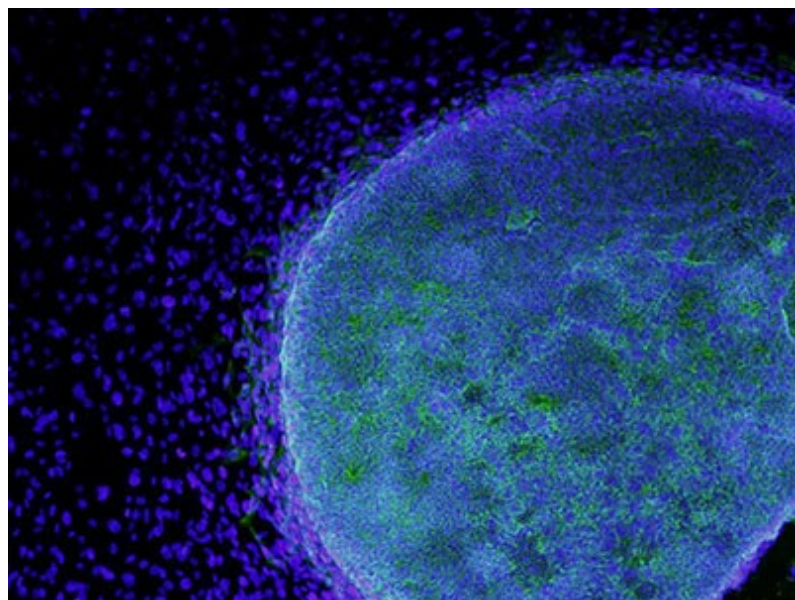
“Unfortunately, Proposition 14 sets a bad example for the use of public money for the advancement of science,” says Zach Hall, a neurobiologist who led CIRM as its first president between 2005 and 2007.

“As scientists, everybody always welcomes additional funding,” says Arlene Chiu, former director of scientific activities at CIRM. “But as a Californian, one wonders if there are better ways to do this.”

Votes for science

Launched 16 years ago, CIRM [drew top researchers to the state](#), and put California on the map as a hub for regenerative-medicine research. With CIRM’s original \$3 billion in state money running out last year, California property developer Robert Klein — an advocate for stem-cell research after his son was diagnosed with type 1 diabetes, and the agency’s original backer — [began canvassing support](#) for new funding. His efforts landed Proposition 14 on this year’s ballot.

“It is extraordinary that the patient-advocacy groups and the medical societies and the scientific societies have been able to act as a single coalition to reach millions of California voters,” says Klein, who co-wrote the 2004 ballot measure creating the agency and served as the institute’s founding chair until 2011.



California stem-cell agency's supporters reveal plan for \$5.5-billion ballot initiative

Some scientists are proponents of the agency, and say that the financial boost could push the field of regenerative medicine forwards. “It is very exciting that Prop. 14 passed and that CIRM will continue its funding,” says Cato Laurencin, a biomedical engineer at the University of Connecticut in Farmington, who is not funded by the institute. “This field is at a bit of an inflection point in terms of our understanding of stem-cell science.”

The approved proposition will cost Californians \$260 million annually for the next 30 years. Some of the money will go towards training scientists and building new facilities; \$1.5 billion of the total funds has been earmarked for research on brain disorders such as Parkinson’s disease and Alzheimer’s disease, for which treatments have been elusive.

A worthwhile investment?

CIRM emerged in 2004, when stem-cell research was a nascent field. Stem cells’ ability to renew themselves and to transform into a variety of other cell types offered the promise of treatments for challenging conditions such as heart disease and stroke, in which cells are irreversibly damaged. Much work at the time relied on stem cells obtained from human embryos donated by fertility clinics. Citing ethical concerns about the destruction of fertilized embryos, in 2001, US president George W. Bush severely restricted research in this area, and the science hit a wall.

So, three years later, CIRM’s launch was a boon. “It gave a tremendous boost to the field at a time when things looked very bad,” says Hall, who joined the agency in its earliest months.

California's \$3-billion bet on stem cells faces final test

CIRM has since handed out (as of June 2020) \$2.7 billion in grants to California scientists studying a variety of diseases, including diabetes, AIDS and leukaemia. It has built a dozen research facilities, funded more than 60 clinical trials and, according to [an independent, agency-funded report](#), helped create more than 56,500 jobs in the state.

But the agency has also drawn criticism for poor management of its public funds. [A 2012 Institute of Medicine report](#) pointed out that CIRM's policy of allowing board members to vote on grants or issues benefiting their institutions posed a potential conflict of interest. Unusually for a public agency, it is not overseen by any state bodies.



The potent effects of Japan's stem-cell policies

“There were too many cases in which the ethics were strained to the limit,” says Jeanne Loring, a geneticist at Scripps Research in La Jolla, who has received more than \$22 million as a principal investigator on CIRM projects.

Spokesperson Kevin McCormack says that although CIRM is not overseen by any other agency, the organization submits reports about its activities to the State Controller “several times a year”, and faces a financial audit annually.

A proposition for improvement

CIRM attempted to address some of the criticism in 2013, when it asked board members from agency-funded universities to abstain from voting on grants, among other changes.

Loring thinks Proposition 14 presented an opportunity to instate stronger safeguards against bias in grant review, but fell short. “It didn’t fix any of those things,” she says.

Doubts over heart stem-cell therapy

And former CIRM president Hall says that Proposition 14 doesn’t describe a clear scientific vision or take into account how the field has been transformed since 2004. For one thing, in 2009, president Barack Obama [removed restrictions](#) on federal funding for stem-cell research. In 2019, the US National Institutes of Health handed out more than \$2 billion for stem-cell research. “You could argue that California would do better, economically and scientifically, to have a CRISPR institute,” Hall says, arguing that the revolutionary precision gene-editing tool is better placed to benefit from such a huge infusion of cash.

Responding to the criticisms, Klein says he crafted the proposal with the guidance of multiple groups of experts, and kept the mandate deliberately broad to allow for flexibility as the field grows. “There’s an intent here,” he says, “to have the agency be responsive to the development of science.”

Nature 587, 535 (2020)

doi: <https://doi.org/10.1038/d41586-020-03147-x>

Jobs from Nature Careers

- - - [All jobs](#)
 - - [Part-time Laboratory Assistant](#)

[Oklahoma Medical Research Foundation \(OMRF\)](#)
[Oklahoma City, United States](#)
[JOB POST](#)
 - [Assistant Professor of Teaching \(Tenure Track\)](#)

[The University of British Columbia \(UBC\)](#)
[Vancouver, Canada](#)
[JOB POST](#)
 - [Principal Researcher / Senior Researcher](#)

[Korea Brain Research Institute \(KBRI\)](#)
[Daegu, Korea, South](#)
[JOB POST](#)
 - [PhD Scholarship within Phosphorus Turnover in Lakes and Wetlands](#)

University of Southern Denmark (SDU)

Odense M, Denmark

JOB POST

This article was downloaded by **calibre** from <https://www.nature.com/articles/d41586-020-03147-x>

| [Section menu](#) | [Main menu](#) |

NEWS FEATURE
25 November 2020

How Iceland hammered COVID with science

The tiny island nation brought huge scientific heft to its attempts to contain and study the coronavirus. Here's what it learnt.

Megan Scudellari

Megan Scudellari is a science journalist in Boston, Massachusetts.

Search for this author in:

- [Pub Med](#)
- [Nature.com](#)
- [Google Scholar](#)



Iceland's science has been pivotal in understanding the COVID-19 pandemic. Credit: Jon E. Gustafsson

Driving along Reykjavik's windswept roads on a cold March morning, Kári Stefánsson turned up the radio. The World Health Organization had just announced that an estimated 3.4% of people infected with SARS-CoV-2 would die — a shockingly high fatality rate, some 30 times larger than that for seasonal influenza.

There was a problem with that estimate, however: it was based on reported cases of COVID-19, rather than all cases, including mild and asymptomatic infections. "I couldn't figure out how they could calculate it out without knowing the spread of the virus," recalls Stefánsson, who is the founder and

chief executive of deCODE genetics, a human-genomics company in Reykjavik. He became convinced that making sense of the epidemic, and protecting the people of Iceland from it, would require a sweeping scientific response.

When Stefánsson arrived at work, he phoned the leadership of Amgen, the US pharmaceutical company that owns deCODE, and asked whether he could offer deCODE's resources to track the spread of the virus, which had landed on Icelandic shores only six days earlier. "The response I got from them was, 'For heaven's sake, do that,'" says Stefánsson.

Over the ensuing nine months, deCODE and Iceland's Directorate of Health, the government agency that oversees health-care services, worked hand-in-hand, sharing ideas, data, laboratory space and staff. The high-powered partnership, coupled with Iceland's diminutive size, has put the country in the enviable position of knowing practically every move the virus has made. The teams have tracked the health of every person who has tested positive for SARS-CoV-2, sequenced the genetic material of each viral isolate and screened more than half of the island's 368,000 residents for infection.



Why do COVID death rates seem to be falling?

Late nights analysing the resulting data trove led to some of the earliest insights about how the coronavirus spreads through a population. The data showed, for example, that almost half of infected people are asymptomatic, that children are much less likely to become sick than adults and that the most common symptoms of mild COVID-19 are muscle aches, headaches and a cough — not fever. “Scientific activities have been a huge part of the entire process,” says Runolfur Palsson, director of internal-medicine services at Landspítali — The National University Hospital of Iceland. Researchers at deCODE and the hospital worked day in and day out to gather and interpret the data.

Their achievements aren’t merely academic. Iceland’s science has been credited with preventing deaths — the country reports fewer than 7 per 100,000 people, compared with around 80 per 100,000 in the United States and the United Kingdom. It has also managed to prevent outbreaks while keeping its borders open, welcoming tourists from 45 countries since mid-June. The partnership again kicked into high gear in September, when a second large wave of infections threatened the nation.

Careful steps

COVID-19 is not the first pandemic to reach Iceland’s shores: in October 1918, two ships carrying pandemic influenza docked in Reykjavik’s downtown harbour. Within six weeks, two-thirds of the capital city’s inhabitants were infected¹.

A century later, the Icelandic government was better prepared, enacting a national pandemic preparedness plan at the beginning of January, two months before COVID-19 arrived. “We decided from the beginning we would use isolation, quarantine and contact tracing,” says Þórólfur Guðnason, chief epidemiologist at the Directorate of Health. As part of that

plan, the microbiology laboratory at the university hospital began testing citizens in early February.

On 28 February, a man returning from a skiing holiday in northeastern Italy tested positive for the virus. Within a week, the number of cases had climbed from 1 to 47, the opening notes of a coming crescendo. As health-care workers began ordering hundreds of tests per day, one of the hospital's machines for isolating and purifying RNA broke from overuse. "We were not able to cope with all the specimens coming in," recalls Karl Kristinsson, the university hospital's chief of microbiology.

By 13 March, deCODE had begun screening the general public and was able to quickly take over much of the hospital's testing. The company repurposed a large phenotyping centre that it had been using to study the genetics of Icelanders for more than two decades into a COVID-19 testing centre. "It almost looked like these 24 years preceding COVID-19 had just been a training session," says Stefánsson. "We dove into this full force."



One of the first families in Iceland to be screened with deCODE's COVID-19 test.Credit: Jon E. Gustafsson

The company has the staff and machinery to sequence 4,000 whole human genomes per week as part of its regular research activities, says Stefánsson. Throughout the spring, it would set that aside to devote its analytical and sequencing heft to the pandemic response.

deCODE's main activity has been COVID-19 screening, including open invitations to the general population. Today, any resident with even the mildest symptom can sign up to be tested. Residents sign up online using dedicated COVID software built by deCODE programmers. At a testing centre, they show a barcode from their phone to automatically print a label for a swab sample. Once taken, the sample is sent to a laboratory at deCODE's headquarters that is run jointly by the university hospital and deCODE and operates from 6 a.m. to 10 p.m. Results are always available within 24 hours, but are often ready in just 4 to 6. "We now have the capacity for about 5,000 samples per day," says Kristinsson. As a whole, the collaborators have so far screened 55% of the country's population.

If the test is negative, the person receives an all-clear text. If the test is positive, it triggers two chains of action: one at the hospital and one at the lab.

At the hospital, the individual is registered in a centralized database and enrolled in a tele-health monitoring service at a COVID outpatient clinic for a 14-day isolation period. They will receive frequent phone calls from a nurse or physician who documents their medical and social history, and runs through a standardized checklist of 19 symptoms. All the data are logged in a national electronic medical record system. A team of clinician-scientists at the hospital created the collection system in mid-March with science in mind. "We decided to document clinical findings in a structured way that would be useful for research purposes," says Palsson.



How many people has the coronavirus killed?

In the lab, each sample is tested for the amount of virus it contains, which has been used as an indicator for contagiousness and severity of illness. And the full RNA genome of the virus is sequenced to determine the strain of the virus and track its origin.

The same approach could work in other countries that have suitable resources, such as the United States, where all the methods deCODE is currently using were developed, says Stefánsson. In fact, early in the pandemic, many US labs pivoted to offer coronavirus testing, but were stymied by regulatory and administrative obstacles, which [critics attribute to a lack of federal leadership](#). “This was a wonderful opportunity for academia in the United States to show its worth, and it didn’t,” Stefánsson says. “I was surprised.”

Viral fingerprints

Researchers at deCODE, the university hospital and the Directorate of Health began analysing the wealth of data in early March, and quickly published several early results. “Once we started to generate data, we

couldn't resist the temptation to begin to try to pull something cohesive out of it," says Stefánsson.

Iceland's COVID-19 results are limited by the fact that cases are occurring in a small and genetically homogeneous population compared with other countries, notes Palsson. But in some cases, that small sample size is also a strength, because it has led to detailed, population-wide data.

In early spring, most of the world's COVID-19 studies focused on individuals with moderate or severe disease. By testing the general population in Iceland, deCODE was able to track the virus in people with mild or no symptoms. Of 9,199 people recruited for population screening between 13 March and 4 April, 13.3% tested positive for coronavirus. Of that infected group, 43% reported no symptoms at the time of testing². "This study was the first to provide high-quality evidence that COVID-19 infections are frequently asymptomatic," says Jade Benjamin-Chung, an epidemiologist at the University of California, Berkeley, who used the Iceland data to estimate rates of SARS-CoV-2 infection in the United States³. "It was the only study we were aware of at the time that conducted population-based testing in a large sample."



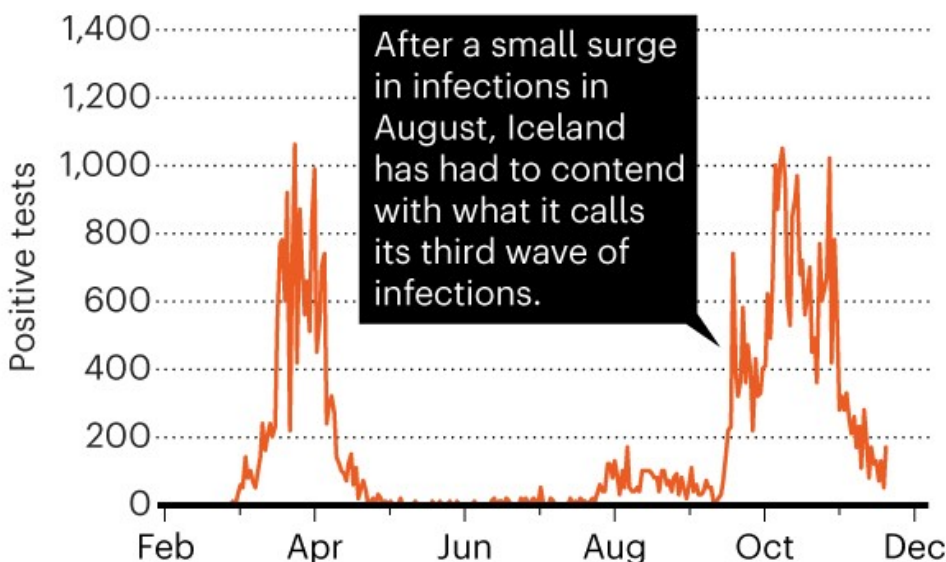
Two decades of pandemic war games failed to account for Donald Trump

A smaller population study, carried out in an Italian town, came to similar results on asymptomatic infection months later. When a 78-year-old man died in the northern Italian town of Vo', Italy's first COVID-19 death, the region's governor locked the town down and ordered that its 3,300 citizens be tested. After the initial round of government testing, Andrea Crisanti, head of microbiology at the University of Padua in Italy, asked the local government whether his team could run a second round of testing. "Then we could measure the effect of the lockdown and the efficiency of contact tracing," says Crisanti, who is currently on leave from Imperial College London. The local government agreed. On the basis of the results of the two rounds of testing, the researchers found that lockdown and isolation reduced transmission by 98%, and — in line with Iceland's results — that 43% of the infections across the two tests were asymptomatic⁴.

In addition to tracking asymptomatic infections, the researchers in Iceland concluded that children under 10 were about half as likely to test positive as people aged 10 and older — a finding confirmed in Crisanti's study of Vo', as well as studies in the United Kingdom⁵ and United States⁶. Additionally, the deCODE team analysed the viral genetic material of every positive case, and used that fingerprint to track where each strain of the virus came from and how it spread. Most of the initial cases, the researchers found, were imported from popular skiing destinations, whereas later transmission occurred mainly locally, within families (see 'Iceland's three COVID waves').

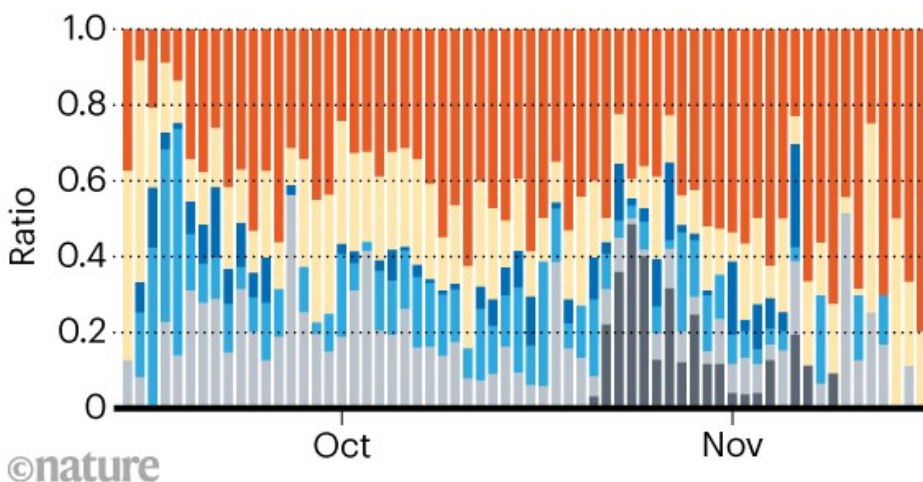
ICELAND'S THREE COVID WAVES

The island nation has identified about 5,250 positive cases of COVID-19 through testing, including random screening and double-testing of individuals who come to the country from abroad.



Contact-tracing data from the current COVID-19 surge reveals where domestic infections are coming from. Transmission within households is a key driver.

- Household transmission ■ No source identified
- School ■ Social outings ■ Work
- Health-care settings



Source: <http://www.covid.is/data>; deCODE genetics

That genetic-tracing approach, called molecular epidemiology, was similarly applied in New Zealand to good effect. In March, New Zealand's government implemented a stringent countrywide lockdown aimed at eliminating the virus. "Essentially, the New Zealand population more or less stayed at home for 7 weeks. After that, we emerged into a virus-free country," says Michael Baker, a public-health researcher at the University of Otago in Wellington. That's a feat for a country of 5 million people, more than 13 times larger than Iceland.

Genetic analysis of the first New Zealand wave, from March to May, showed that the strict lockdown began working right away. The rate of transmission — the number of people infected by each person with the virus — dropped from 7 to 0.2 in the first week in the largest cluster⁷. Sequencing data also showed that an August outbreak in Auckland, the source of which remains unknown, was from a single lineage, reassuring public-health authorities that there had only been one breach. "Genomics has played a vital role in tracking the re-emergence of COVID-19 in New Zealand," says Jemma Geoghegan, a microbiologist at Otago who co-led the project with Joep de Ligt at the Institute of Environmental Science and Research in Porirua.

Getting the full picture

This summer at the university hospital, Palsson's team used the clinical data to investigate⁸ the full spectrum of disease caused by SARS-CoV-2. The most common symptoms among the 1,797 people who tested positive between 31 January and 30 April were muscle aches, headache and a non-productive cough — not fever, a symptom listed in both the US Centers for Disease Control and the World Health Organization case definitions for COVID-19. When used to guide testing, those definitions are likely to miss some symptomatic people, says Palsson. "Hopefully others will come to a similar conclusion and that will result in changes in the criteria," he says.

The results from Palsson's team led to direct medical intervention in Iceland: individuals showing any sign of a common cold or aches are now encouraged to get tested, and the hospital categorizes new patients into one

of three stages according to their symptoms, which dictates their level of care.



How the pandemic might play out in 2021 and beyond

The most recent study from Iceland focused on a major COVID-19 question: how long does immunity to SARS-CoV-2 last? deCODE's team found that anti-SARS-CoV-2 antibodies remained high in the blood of 91% of infected people for 4 months after diagnosis⁹, running counter to earlier results suggesting that antibodies decline quickly after infection^{10,11}. It is possible that the conflicting results represent two waves of antibodies. In an editorial accompanying the paper¹², Galit Alter at Harvard Medical School in Boston, Massachusetts, and Robert Seder at the US National Institutes of Health's Vaccine Research Center in Bethesda, Maryland, suggest that a first wave is generated by short-lived plasma cells in response to acute infection, then a second wave, produced by longer-lived cells, bestows lasting immunity.

And finally, Stefánsson was able to pin down the elusive statistic that first intrigued him — the infection fatality ratio (IFR), or the proportion of infected people who die from the disease. Since the beginning of the

pandemic, IFR estimates have ranged from less than 0.1% to a whopping 25%, depending on the size of the study and the age of the population. A growing number of studies are converging at about 0.5 to 1%. In Iceland, where the median age is 37 — relatively young compared with other wealthy nations — and patients have access to good health care, Stefánsson's team found it to be 0.3%.

New wave

On 15 June, Iceland opened its borders to non-essential visitors from 31 European nations. A month later, on 16 July, the country also lifted restrictions on visitors from 12 more countries, including Canada, New Zealand and South Korea. The opening gave a boost to the struggling tourism industry, although numbers of visitors remained low, with about 75–80% fewer summer tourists than in 2019, according to the Icelandic Tourist Board.



Bars in Reykjavik reopened on 31 May, after a two-month closure.Credit: Haraldur Gudjonsson/AFP via Getty

Then, on 10 August, a pair of tourists at Reykjavik airport tested positive for SARS-CoV-2, ignored regulations and went into town. That incursion led to a small bump of cases in August centred on two pubs and a fitness centre visited by the tourists. Then, in mid-September, the number of infections increased abruptly, from 1 to 55 in a week. “This one clone of virus was able to spread around and cause lurking infections all over, especially in Reykjavik, and all of a sudden, we saw this increase,” says Guðnason. “It’s evidence of how difficult the virus is to contain.”

By October, coronavirus was more widespread in the community than it had been in the first wave, peaking at 291 infections per day. On 17 October, the number of active infections finally began to decline, which researchers attribute to widespread testing, tracing and quarantine procedures, as well as fresh government restrictions and emphasis on mask wearing. “Hopefully we can start relaxing our restrictions soon,” says Guðnason.

Despite the outbreak, the country continues to keep its borders open to tourists from some countries, although entry requirements are now stricter. Travellers must either self-quarantine for 14 days after arrival or participate in two screening tests: one on arrival, followed by five days of quarantine, then a second test. This method has led to the discovery that 20% of people who test negative in the first round will test positive in the second, notes Guðnason. That is a high number, but seems consistent with other analyses¹³. The new requirement is likely to have caught many strains of virus that would have otherwise entered the country.

Unlike New Zealand, which closed its borders, elimination was never supported in Iceland for fears that the country would go bankrupt without tourism. So it is possible that new cases will continue to arise, says Guðnason. Furthermore, he and others think the current outbreak might be in large part due to pandemic fatigue, as people disregard health precautions after months of being careful. “I think we’re going to be dealing with the virus, trying to suppress it as much as possible, until we get the vaccine,” he says.

And research continues in any and every spare hour. Palsson's team is planning to analyse the effect of viral loads on patient outcomes and viral transmission, and to use contact-tracing data to tease out the risk factors for a super-spreading event. "We've had households where almost everybody gets infected, then other places where people carry the infection and stay in the workplace and nobody gets infected," says Palsson. "It's very difficult to understand."

At deCODE, Stefánsson and his colleagues are investigating cellular immune responses and whether people with COVID-19 who are very sick produce antibodies directed against their own tissues. And together, the deCODE and university-hospital teams are collaborating on the long-term effects of COVID and how genetics affects susceptibility and responses to the disease.

"We've been committed for a long time to take everything we learn about human disease and publish it," says Stefánsson. "There is no way in which we would have not utilized the opportunity."

Nature **587**, 536–539 (2020)

doi: <https://doi.org/10.1038/d41586-020-03284-3>

References

1. 1.

Gottfredsson, M. *et al.* *Proc. Natl Acad. Sci. USA* **105**, 1303–1308 (2008).

2. 2.

Gudbjartsson, D. F. *et al.* *N. Engl. J. Med.* **382**, 2302–2315 (2020).

3. 3.

Wu, S. L. *et al.* *Nature Commun.* **11**, 4507 (2020).

4. 4.

Lavezzo, E. *et al.* *Nature* **584**, 425–429 (2020).

5. 5.

Docherty, A. B. *et al.* *Br. Med. J.* **369**, m1985 (2020).

6. 6.

Rosenberg, E. S. *et al.* *Clin. Infect. Dis.* **71**, 1953–1959 (2020).

7. 7.

Geoghegan, J. L. *et al.* Preprint at medRxiv
<https://doi.org/10.1101/2020.08.05.20168930> (2020).

8. 8.

Eythorsson, E. *et al.* Preprint at medRxiv
<https://doi.org/10.1101/2020.08.09.20171249> (2020).

9. 9.

Gudbjartsson, D. F. *et al.* *N. Engl. J. Med.* **383**, 1724–1734 (2020).

10. 10.

Long, Q.-X. *et al.* *Nature Med.* **26**, 1200–1204 (2020).

11. 11.

Ibarrondo, F. J. *et al.* *N. Engl. J. Med.* **383**, 1085–1087 (2020).

12. 12.

Alter, G. & Seder, R. N. *Engl. J. Med.* **383**, 1782–1784 (2020).

13. 13.

Kucirka, L. M., Lauer, S. A., Laeyendecker, O., Boon, D. & Lessler, J. *Ann. Intern. Med.* **173**, 262–267 (2020).

Jobs from Nature Careers

- - - [All jobs](#)
 - - [Part-time Laboratory Assistant](#)

[Oklahoma Medical Research Foundation \(OMRF\)](#)

[Oklahoma City, United States](#)

[JOB POST](#)
 - [Assistant Professor of Teaching \(Tenure Track\)](#)

[The University of British Columbia \(UBC\)](#)

[Vancouver, Canada](#)

[JOB POST](#)
 - [Principal Researcher / Senior Researcher](#)

[Korea Brain Research Institute \(KBRI\)](#)

[Daegu, Korea, South](#)

[JOB POST](#)
 - [PhD Scholarship within Phosphorus Turnover in Lakes and Wetlands](#)

University of Southern Denmark (SDU)

Odense M, Denmark

JOB POST

This article was downloaded by **calibre** from <https://www.nature.com/articles/d41586-020-03284-3>

| [Section menu](#) | [Main menu](#) |

Books & Arts

- **[When is sorrow sickness? A history of depression](#)** [23 November 2020]
Book Review • A book traces the shifting lines between sadness and illness, but not who gets to draw them.
- **[Book-burning through the ages, the Arctic laid bare, and capitalism under scrutiny: Books in brief](#)** [24 November 2020]
Book Review • Andrew Robinson reviews five of the week's best science picks.

BOOK REVIEW
23 November 2020

When is sorrow sickness? A history of depression

A book traces the shifting lines between sadness and illness, but not who gets to draw them.

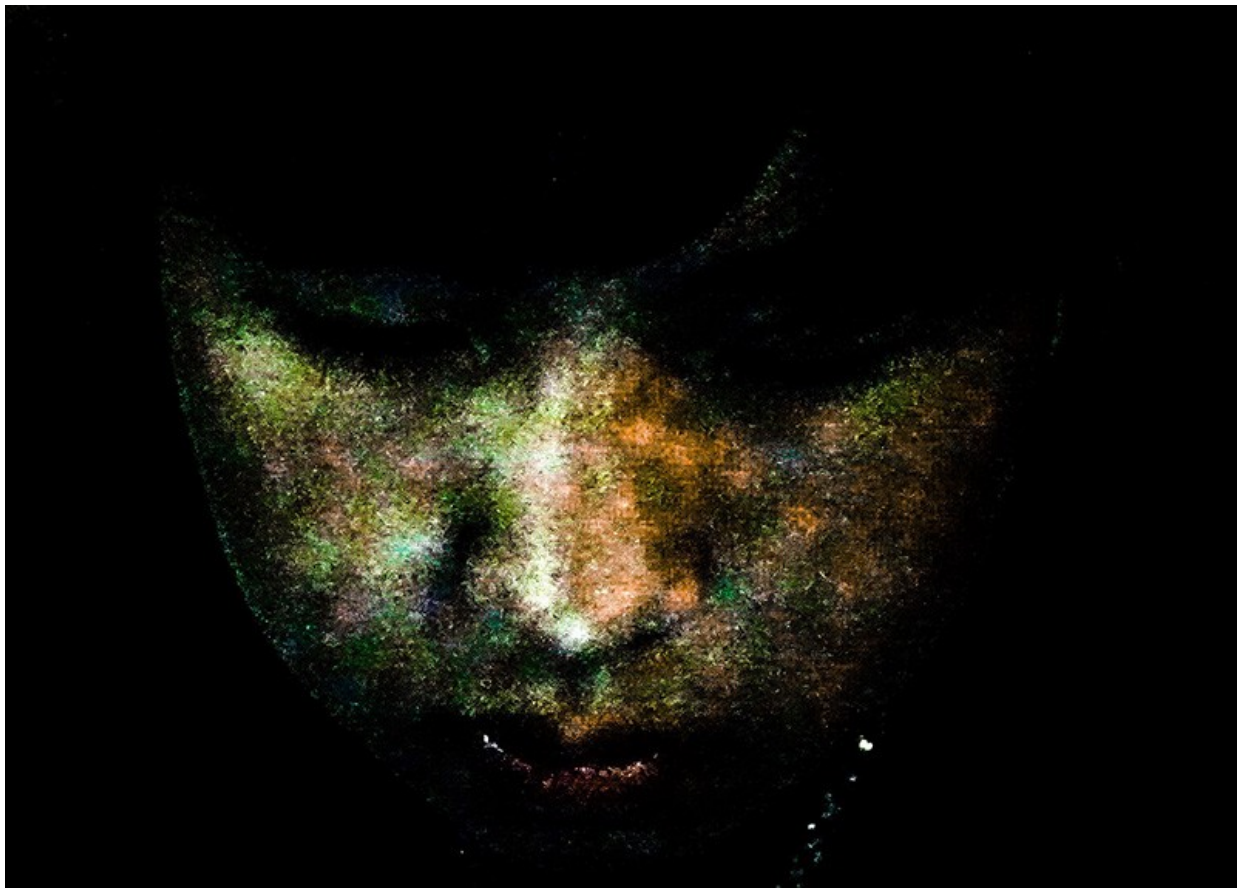
China Mills

China Mills is a senior lecturer in public health at City, University of London, and author of *Decolonizing Global Mental Health*.

[Contact](#)

Search for this author in:

- [Pub Med](#)
- [Nature.com](#)
- [Google Scholar](#)



Thoughts, a photograph portrait by Lisa Saltzman.Credit: Lisa Saltzman

The Empire of Depression: A New History Jonathan Sadowsky Polity (2020)

When is sorrow sickness? So begins Jonathan Sadowsky's *The Empire of Depression*, a history riven with professional turf wars around where to draw the line between normal sadness and something more serious — now, across much of the world, called depression. He argues against reductionism and dogma. Instead of getting stuck in old disagreements about whether depression is caused by a chemical imbalance or by social inequality, Sadowsky urges that depression can be psychological, biological and social, just as it can be a real illness even if it is cultural.

Given that the World Health Organization names depression as a major contributor to the global burden of disease, tracing its history is a significant task. And it is an important one, given the mental-health crisis attending the COVID-19 pandemic. It is no mean feat to characterize something that has

ever-shifting and contested boundaries dependent on time and place. Sadowsky, a historian of medicine, offers three possible reasons for the current boom in diagnoses: that there really is more depression; that the amount is the same but we're better at detecting it; or that emotional states not previously seen as illness are now being labelled as such.

This is no lament on over-diagnosis. Rather, Sadowsky offers a review of how psychiatry has helped people. His tale spans the 'melancholia' of Renaissance Europe (said to be caused by too much black bile, and treated by purging) and today's research on imbalances in neurotransmitters, treated by drugs. It takes us through the Christian Middle Ages and the emergence of questions about whether ill people were to be blamed for their suffering; Sigmund Freud's psychoanalytic ideas about anger turned inwards; and the 1980s cultural sensation of Prozac (fluoxetine), quantification and globalization.

In this positive take, the vast majority of people with depression are being treated voluntarily, and treatment helps them feel better. He makes no claims that people are being duped en masse into chemical cures. But this breezy approach doesn't reckon with power: a lot goes on between the lines of being forced to take medication and choosing to.

Cultural condition

Depression has a cultural life, as, others have argued, do panic disorder, bipolar disorder and suicide (see Jackie Orr's book *Panic Diaries* (2006); Emily Martin's *Bipolar Expeditions* (2007); and Ian Marsh's 2010 *Suicide*). A diagnosis can give validity to feelings, help people find others who share similar experiences and provide hope. But it can also stigmatize, embroil people in coercive treatment regimes and overlook context. That is why it is important to ask: what does depression 'do', personally and politically? Individual explanations can divert attention from wider societal factors and how they make some lives unliveable.

In other words, the history of depression is also about who decides what is normal and what is not. If life presents many reasons to be depressed — poverty, discrimination, precarious living situations — then should all

depression be seen as an illness? This is more than theoretical, as increasing prescriptions of antidepressants in austerity Britain and opioids in rural North America testify. To be fair, this idea is key to Sadowsky's history. He explains that choices about where to draw the line risk both medicalizing everyday suffering and disqualifying many people's suffering from being seen as clinical depression.

Depression, then, can't be separated from unequal power relations — between doctor and patient, and between countries and corporations with unequal power to globalize their ways of viewing distress and its treatments. The power to say who's rational and who isn't, and to detain people or treat them without consent, is perhaps the starker reminder of why treating depression is not just like administering insulin for diabetes, and of why stigma looms large despite (or because of) the understandable appeals to biochemistry. This concept is behind anti-psychiatry, the movement that protests against harmful practices, especially those founded on power differentials. Yet antipsychiatry makes only brief appearances in the book, like a pantomime villain.

False dichotomies

Sadowsky points out that era after era grapples with false choices — between a political understanding of depression and a medical one, or between physical and psychological understandings. He is right to call for a move beyond these crude binaries. In my view, to do so, we must face the central roles of racism, sexism and ableism in delineating diagnostic boundaries over the years — not dismiss them as unfortunate. For example, psychiatry has a history of labelling some people as too uncivilized to be mentally ill, yet also diagnosing anticolonialism as mental illness.

In fact, many forms of resistance have been deemed symptoms of mental illness, from enslaved Africans fleeing brutality in the nineteenth-century United States to the Black Power movement of the 1960s. It is alarming, then, that apart from using "empire" as an analogy for the global dominance of Western psychiatry in interpreting distress, Sadowsky devotes little attention here to power and politics — especially given his previous work on colonialism (in the 1999 book *Imperial Bedlam*).

The book ends with the wise injunction: “listen to patients”. Yet, apart from illness memoirs, the voices (and research) of people who experience depression, those who become patients, those who refuse to become patients, and service users or psychiatric survivors are almost completely absent from the book. These people (and the collectives they have formed) contribute to production of knowledge about depression by leading research and global movements fighting for their rights. A history of depression without these voices will always be one-sided.

Nature 587, 541-542 (2020)

doi: <https://doi.org/10.1038/d41586-020-03286-1>

Jobs from Nature Careers

- - - [All jobs](#)
 - - **Part-time Laboratory Assistant**
[Oklahoma Medical Research Foundation \(OMRF\)](#)
[Oklahoma City, United States](#)
[JOB POST](#)
 - **Assistant Professor of Teaching (Tenure Track)**
[The University of British Columbia \(UBC\)](#)
[Vancouver, Canada](#)
[JOB POST](#)
 - **Principal Researcher / Senior Researcher**

[Korea Brain Research Institute \(KBRI\)](#)

[Daegu, Korea, South](#)

[JOB POST](#)

- [PhD Scholarship within Phosphorus Turnover in Lakes and Wetlands](#)

[University of Southern Denmark \(SDU\)](#)

[Odense M, Denmark](#)

[JOB POST](#)

This article was downloaded by **calibre** from <https://www.nature.com/articles/d41586-020-03286-1>

| [Section menu](#) | [Main menu](#) |

BOOK REVIEW
24 November 2020

Book-burning through the ages, the Arctic laid bare, and capitalism under scrutiny: Books in brief

Andrew Robinson reviews five of the week's best science picks.

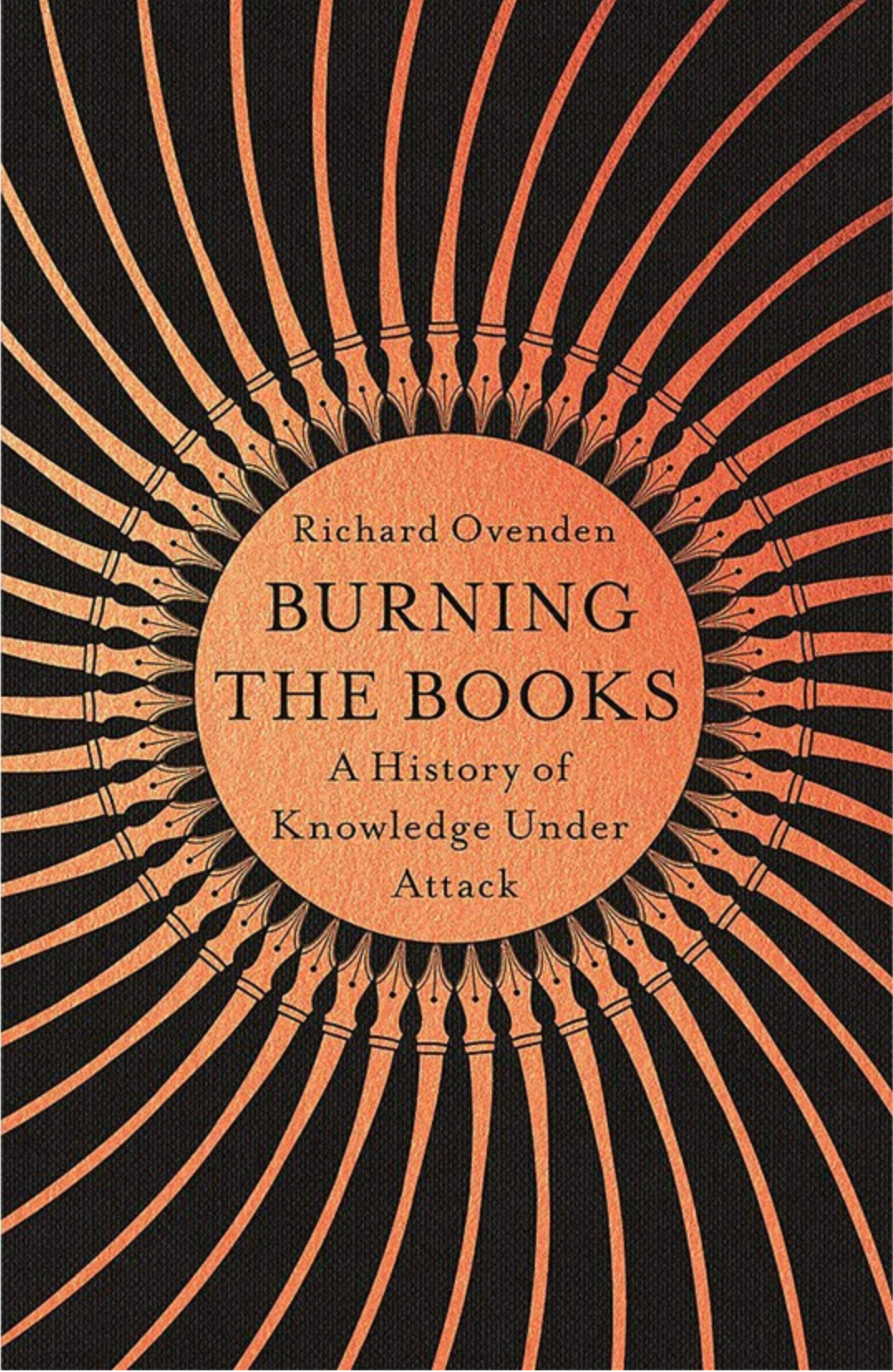
Andrew Robinson

Andrew Robinson's many books include *Lost Languages: The Enigma of the World's Undeciphered Scripts* and *Einstein on the Run: How Britain Saved the World's Greatest Scientist*. He is based in London.

[Contact](#)

Search for this author in:

- [Pub Med](#)
- [Nature.com](#)
- [Google Scholar](#)



Richard Ovenden

BURNING THE BOOKS

A History of
Knowledge Under
Attack

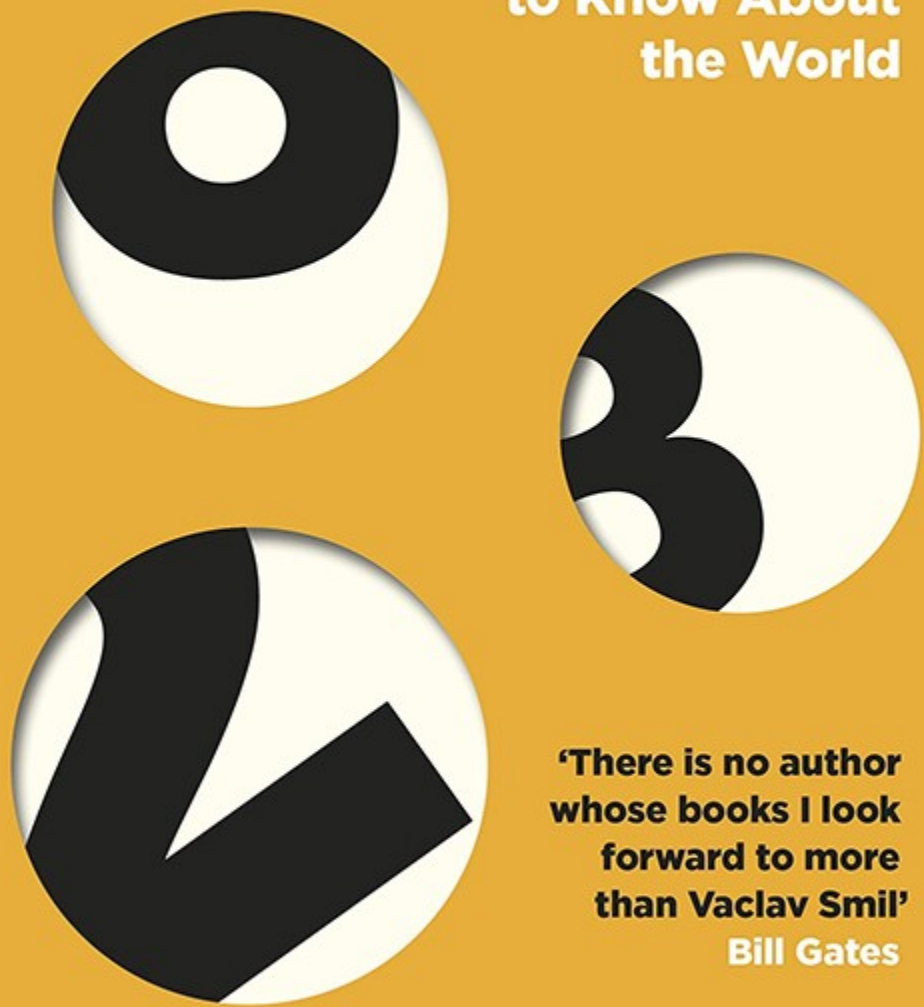
Burning the Books

Richard Ovenden *John Murray* (2020)

In 1660, when the British monarchy was restored, the University of Oxford ordered the burning of books by anti-royalist, pro-free-speech poet John Milton. This is one of many graphic examples inspired by the collections at the institution's Bodleian Library, cited in Bodleian librarian Richard Ovenden's powerful history, which ranges from ancient Mesopotamia and Egypt's Library of Alexandria to Nazi Germany and the Iraq wars. Attacks on books and archives are, he concludes, a "signal that attacks on humans cannot be far behind".

Numbers Don't Lie

**71 Things You Need
to Know About
the World**



**'There is no author
whose books I look
forward to more
than Vaclav Smil'**

Bill Gates

Vaclav Smil

Numbers Don't Lie

Vaclav Smil *Viking* (2020)

Vaclav Smil's publisher claims: "No other living scientist has had more books (on a wide variety of topics) reviewed in *Nature*." Smil might regard this as almost unprovable, but certainly Bill Gates calls him a impressive polymath. His latest book, an appraisal of statistics, offers 71 short, thoughtful essays on psychology, globalization, inventions, fuels and electricity, transport, diets and the environment. Discussing the annual World Happiness Report, he notes a "remarkable lack of correlation" between national happiness rankings and suicide rates.

The Citi exhibition

ARCTIC

CULTURE AND CLIMATE

Edited by Amber Lincoln, Jago Cooper and Jan Peter Laurens Loovers



Thames & Hudson

The British
Museum

Arctic

Eds Amber Lincoln *et al.* *Thames & Hudson/British Museum* (2020)

Humans have “the right to be cold”, says an Inuit political activist in this accompaniment to a British Museum exhibition. Arctic cultures encompass 4 million people across 8 nations, whose way of life is threatened: 75% of Arctic sea ice has melted over 40 years. Superb illustrations and many essays reveal fascinating accoutrements, such as Russian snow spectacles from 1850–80, crafted from reindeer skin, multicoloured glass beads and uranium beads, with minute metal slits protecting against blindness induced by Arctic spring sunlight.

YANIS

VAROUFAKIS

ARTHUR

BROOKS

KATRINA VANDEN

HEUVEL

DAVID

BROOKS

IS

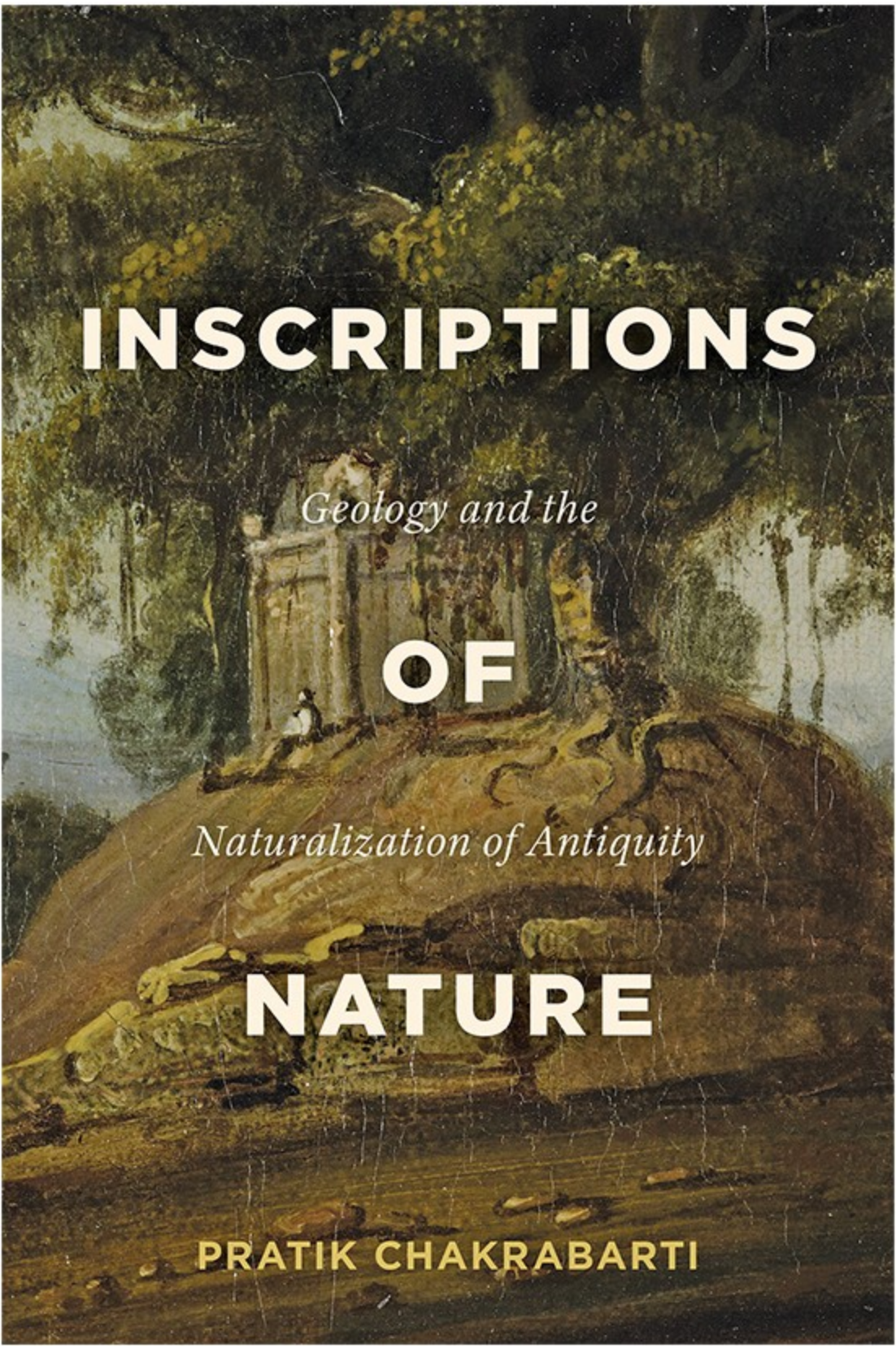
CAPITALISM

BROKEN?

Is Capitalism Broken?

Yanis Varoufakis *et al.* *Oneworld* (2020)

Two models of capitalism — US democratic and Chinese authoritarian — underlie this record of a 2019 debate. Former Greek finance minister Yanis Varoufakis and US publisher Katrina vanden Heuvel proposed that capitalism is broken. They were opposed by social scientist Arthur Brooks and journalist David Brooks, the narrow winners. But Varoufakis wins on eloquence: he says capitalism liberated us from prejudice and feudalism, but entangled us in “unbearable inequality, unsustainable debt, brazen authoritarianism, and, yes, catastrophic climate change”.



INSCRIPTIONS

Geology and the

OF

Naturalization of Antiquity

NATURE

PRATIK CHAKRABARTI

Inscriptions of Nature

Pratik Chakrabarti *Johns Hopkins Univ. Press* (2020)

Science historian Pratik Chakrabarti's idiosyncratic book ponders an 1820s excavation of the Yamuna Canal in India's Indo-Gangetic Plain, which revealed ancient canal networks, vanished river beds, traces of mythological rivers and prehistoric fossils. Simultaneously, geologists, ethnologists, archaeologists and missionaries dug into ancient texts and legends. From both perspectives, the plain seemed to be the bedrock of Indian civilization — a view complicated by the 1920s discovery of the Indus civilization.

Nature **587**, 542 (2020)

doi: <https://doi.org/10.1038/d41586-020-03285-2>

Jobs from Nature Careers

- - - [All jobs](#)
 - - [**Part-time Laboratory Assistant**](#)
[Oklahoma Medical Research Foundation \(OMRF\)](#)
[Oklahoma City, United States](#)
[JOB POST](#)
 - [**Assistant Professor of Teaching \(Tenure Track\)**](#)
[The University of British Columbia \(UBC\)](#)
[Vancouver, Canada](#)
[JOB POST](#)

▪ **Principal Researcher / Senior Researcher**

Korea Brain Research Institute (KBRI)

Daegu, Korea, South

JOB POST

▪ **PhD Scholarship within Phosphorus Turnover in Lakes and Wetlands**

University of Southern Denmark (SDU)

Odense M, Denmark

JOB POST

This article was downloaded by **calibre** from <https://www.nature.com/articles/d41586-020-03285-2>

| [Section menu](#) | [Main menu](#) |

Opinion

- **[Reboot contraceptives research — it has been stuck for decades](#)** [25 November 2020]
Comment • There is a huge global market, and exciting tools are ready to help develop what women want.
- **[Memo for President Biden: Five steps to getting more from science](#)** [08 November 2020]
Comment • Going back to normal is not enough. A revamp is required.
- **[COVID-19: students caught in Pakistan's digital divide](#)** [24 November 2020]
Correspondence •
- **[Giant tortoises make a comeback in Madagascar](#)** [24 November 2020]
Correspondence •
- **[COVID-19: Panama stockpiles unproven drugs](#)** [24 November 2020]
Correspondence •
- **[Explain ESA's last-minute ditching of new space telescope](#)** [24 November 2020]
Correspondence •

COMMENT

25 November 2020

Reboot contraceptives research — it has been stuck for decades

There is a huge global market, and exciting tools are ready to help develop what women want.

Sarah G. Chamberlain,

Sarah G. Chamberlain is a partner at Boston Consulting Group, Seattle, Washington, USA.

Search for this author in:

- [Pub Med](#)
- [Nature.com](#)
- [Google Scholar](#)

Kirsten M. Vogelsong,

Kirsten M. Vogelsong is a senior program officer at the Bill & Melinda Gates Foundation, Seattle, Washington, USA.

Search for this author in:

- [Pub Med](#)
- [Nature.com](#)
- [Google Scholar](#)

Michelle Weinberger,

Michelle Weinberger is a senior associate at Avenir Health, Washington DC, USA.

Search for this author in:

- [Pub Med](#)
- [Nature.com](#)
- [Google Scholar](#)

Emily Serazin,

Emily Serazin is a partner and managing director at Boston Consulting Group, Washington DC, USA.

Search for this author in:

- [Pub Med](#)
- [Nature.com](#)
- [Google Scholar](#)

Sarah Cairns-Smith &

Sarah Cairns-Smith is a senior adviser at Boston Consulting Group, Boston, Massachusetts, USA.

Search for this author in:

- [Pub Med](#)
- [Nature.com](#)
- [Google Scholar](#)

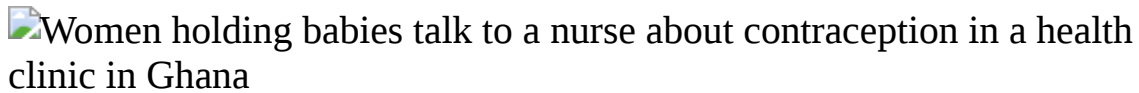
Stephen E. Gerrard

Stephen E. Gerrard co-authored this article while a program officer at the Bill & Melinda Gates Foundation, Seattle, Washington, USA.

[Contact](#)

Search for this author in:

- [Pub Med](#)
- [Nature.com](#)
- [Google Scholar](#)



A nurse at a health centre in Cape Coast, Ghana, talks to women about family planning. Credit Kate Holt/eyevine

Worldwide, almost half of women who are of reproductive age use contraception¹. Another 171 million women — around 1 in 11 aged between 15 and 49 — do not use it, yet want to avoid pregnancy¹. Several factors contribute to this unmet need. New, effective and more-desirable contraceptive options are urgently needed. Family planning is a key aspect to meeting United Nations Sustainable Development Goals 3 and 5.

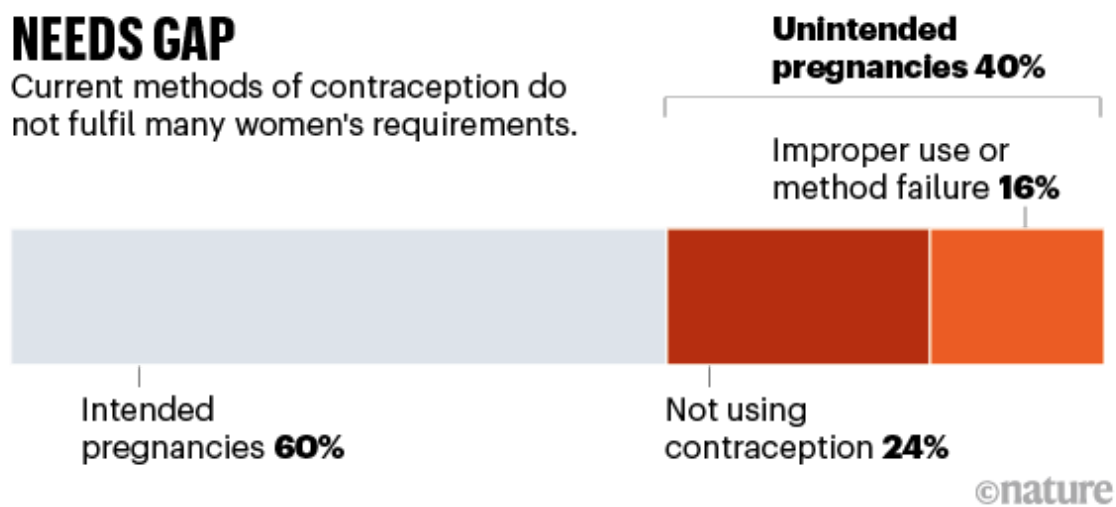
Many women and men are highly dissatisfied with the contraceptives available². Male condoms fail too often — in the first year of condom use, about 13% of women become pregnant³ — and women must rely on men. Implants and intra-uterine devices (IUDs) require medical procedures and can be invasive; pills have to be taken every day. Hormonal methods and non-hormonal IUDs can have side effects, including irregular or unpredictable menstrual bleeding, headaches, acne and weight gain, as well as depression and other mood changes⁴. For many women worldwide, contraception has been difficult to obtain or afford, even before the COVID-19 pandemic.

All of this has serious consequences. Around 40% of pregnancies globally are unintended, and about half of those end in induced abortion⁵. A high proportion of unintended pregnancies occur even where contraception is relatively accessible and cultural stigma against it is generally low, for example in North America (48%) and Europe (43%)⁵. Those pregnancies can happen because women aren't using contraception, because their method failed or because it was used incorrectly. Nearly 25% of unintended

pregnancies in low- and middle-income countries (LMICs) occur in women who were using modern forms of contraception⁶, and globally it's an even higher share (see 'Needs gap').

NEEDS GAP

Current methods of contraception do not fulfil many women's requirements.



©nature

Source: Internal analysis by Avenir Health using multiple sources of global pregnancy data; funded by the Bill & Melinda Gates Foundation.

Unintended pregnancies can have lasting effects on women, children, families and society. The direct health-care costs in LMICs amounted to US\$10 billion⁶ in 2019 alone; the indirect, longer-term economic costs could be 40 times that⁷. Estimates suggest that US unplanned births resulted in \$21 billion in publicly funded medical costs in 2010⁸. Progress in contraceptives research and development (R&D) has been slow in recent decades. Pharmaceutical companies typically spend around 20% of their sales revenue on R&D for new products⁹. For contraception, that figure is just 2%. We estimate that most of this spending has focused on incremental improvements to classes of hormonal contraceptive compound that have been in use for decades.

Encouragingly, there are now more opportunities than ever for innovation. Many scientific advances of the past decade can now be applied to developing non-hormonal drugs that target the egg, sperm or processes along the journey to conception. Such products could have fewer and less-severe side effects than current ones. And alongside daily oral pills, to meet the needs of women who want contraception for different lengths of time,

various non-hormonal products with months or years of action could be delivered — through injections, implants, IUDs and other user-responsive systems that are currently in development.

At the same time, the COVID-19 pandemic is changing health-care services, possibly forever. Many of today's contraceptives, such as implants and IUDs, require an in-person appointment¹⁰. New methods could be delivered remotely, directly to users.

A coalition of innovators, researchers, biopharmaceutical firms, donors and investors needs to come together now to produce better contraception for women. Many of the steps needed might catalyse innovation in male contraception, too.

Lack of satisfaction

The contraceptives available do not fully meet many women's changing needs and preferences through their reproductive lives. Among women in LMICs who do not want to get pregnant but are not using modern contraceptives, more than one-quarter cite side effects as the main reason¹¹. And the same types of side effect accompany many different products. Globally, about one-third of women discontinue their hormonal method of contraception in the first year of use, many citing side effects or health concerns as the main reason⁴.

Large-scale, detailed data are extremely sparse, especially from women who continue to use a method of contraception despite being dissatisfied with it. More than 100,000 women from nearly 200 countries completed a survey on contraceptive preferences within 1 month of its opening. (The survey was released through the reproductive-health app Clue and online at <http://shapefuturect.org>; it was developed by Avenir Health, where M.W. works, and funded by the Bill & Melinda Gates Foundation in Seattle, Washington, with S.E.G. as program officer). Early analysis suggests that a range of side effects would lead respondents to stop using a method, especially changes to mood, physical changes such as acne, weight gains of 2–4.5 kilograms, loss of hair and lowered sex drive. These findings echo others (go.nature.com/35hgqsm). A 2018 review showed that changes to

heaviness or frequency of menstrual bleeding have all been associated with reported dissatisfaction with contraceptives¹².

All of this probably helps to explain the enthusiastic responses to product launches over the past decade. For example, the Mirena family of products, a hormone-releasing intra-uterine system made by Bayer in Leverkusen, Germany, has maintained blockbuster sales of more than \$1 billion for each of the past 5 years. An oral contraceptive introduced in 2011, Lo Loestrin, which offers the lowest amount of daily oestrogen available (with the potential for fewer side effects than for those of related products), captured a significant share of the market⁹ and net revenues have seen double-digit growth over time. In 2018, an app called Natural Cycles was approved as a contraceptive, and relies on body temperature to inform users when they are fertile. Earlier this year, Evofem launched Phexxi — a first-in-class vaginal pH modulator that works as a non-hormonal contraceptive. The impact of these two latest products will become clear over the next few years.



A women's clinic in Cairo.Credit: Tara Todras-Whitehill/NYT/Redux/eyevine

Yet there are few truly innovative and highly effective contraceptive products in development. According to ClinicalTrials.gov, there have been 20–25 industry-funded clinical trials between 2017 and 2020. The majority focus on incremental revisions to existing hormonal products. By comparison, in 2019 there were about 3,100 trials for cancer drugs, 600 for cardiovascular drugs and 140 for treatments for eye disorders^{[13](#)}.

Funding of R&D for female contraception comes from just a handful of players. These include the Eunice Kennedy Shriver National Institute of Child Health and Human Development in Rockville, Maryland, the Bill & Melinda Gates Foundation (where K.M.V. works and S.E.G. recently worked) and the US Agency for International Development. Over the past few years, other organizations have funded or invested in specific non-hormonal technologies, including the BioInnovation Institute in Copenhagen and US-based RHIA Ventures and Adjuvant Capital. There's room for many more.

Cycle of neglect

Why are funding and R&D so limited for female contraceptives? One reason is that they are given to healthy women of reproductive age, so the safety requirements for regulatory approval are (appropriately) very high: serious or severe adverse effects are not acceptable. Efficacy requirements are also extremely stringent. These regulations act as commercial disincentives for trying something new.

In addition, there are unique liability concerns for new products in reproductive health — especially in the United States, which is a litigious market. There have been a number of high-profile cases against leading contraceptive manufacturers, resulting in multimillion-dollar settlements (see go.nature.com/3ncb7jy). Vaccines are one of the only other product classes that are administered to a healthy population. However, in the United States, vaccine manufacturers are protected from liability under the National Childhood Vaccine Injury Act, established by an Act of Congress in 1986. This is unlikely to happen for contraception.

Another problem is that, from a business perspective, the contraceptive market seems to be healthy and growing. It was valued at \$24 billion in 2018¹⁴. Yet the demand from women for transformational change is not reflected as a reduction in sales. Furthermore, women's health issues, and their preferences, are simply under-studied and under-funded, and unmet needs are ignored and misunderstood by those who could work to address these issues.



Six decades of struggle over the pill

These barriers — tight regulations, high liability risk and the lack of a strong market signal — fuel a false perception of low return on investment in contraceptive R&D. So, over the past 20 years, many global biopharma companies have sold off, reduced or closed divisions that were developing non-hormonal contraceptives and other women's health products, such as those to support menopause. Companies have instead focused on therapeutic areas that are evidently fast-growing, such as oncology.

When drug firms step away from a field, it can start a cycle of neglect. Venture capitalists become wary of supporting technologies with unclear opportunities for exit strategies. Academics become cautious about pursuing an area with reduced commercial outlets and financial support. Private

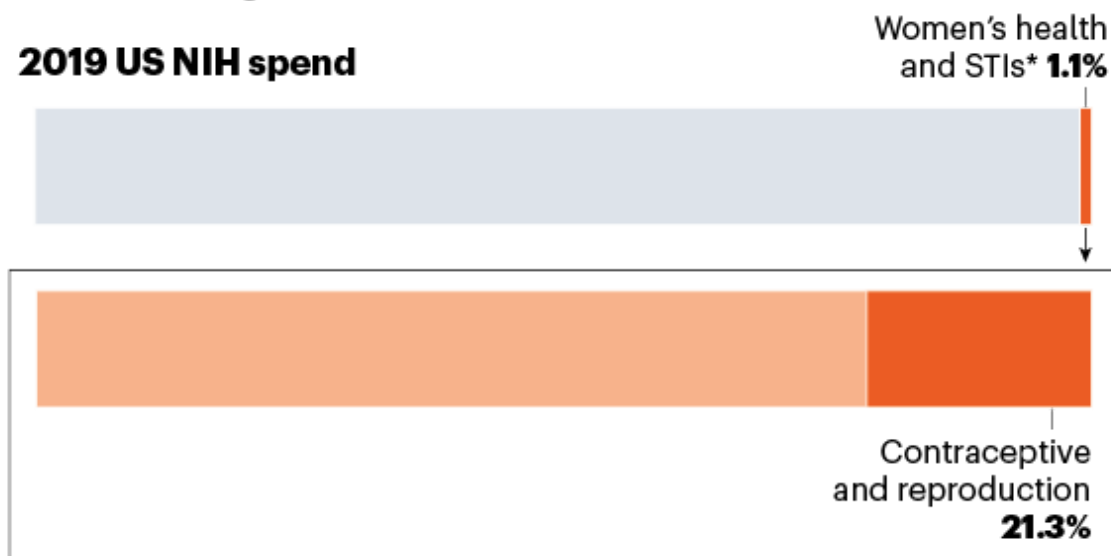
companies have few promising avenues to explore, and potential funders cannot easily identify where to invest.

For contraception, this has led to missed opportunities, because the scientific tools for R&D have mushroomed. Public-sector funding has been one of the key reasons the field has dodged dormancy (see ‘Funding gap’).

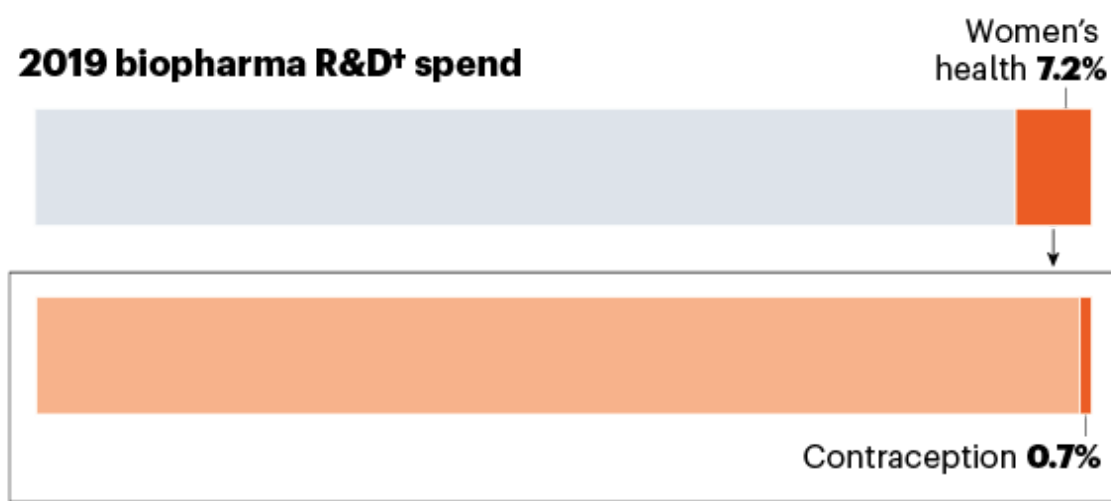
FUNDING GAP

Contraceptives research needs more investment globally. Private firms and public sources such as the US National Institutes of Health are key to future funding.

2019 US NIH spend



2019 biopharma R&D† spend



*STIs, sexually transmitted infections; †R&D, research and development.

Sources: NIH/EvaluatePharma/BCG Analysis

Prime time

For the first time in a generation, a coalition of stakeholders could revolutionize the sector. For example, it is now possible to use genomics tools in a way that was not available 20 years ago. Operating costs have plummeted, and analytical methods and data sets have rapidly expanded in sophistication and size. Biostatisticians can comb for genes or proteins key to egg or follicle maturation, fertilization or gamete function. This can isolate targets for non-hormonal pharmaceutical interventions in a way that is much more efficient than previous, failed approaches.

The neighbouring fields of gynaecological oncology and infertility have seen industry funding increase over the past decade. Advances in those fields could help contraceptive R&D. For example, progress in understanding the mechanisms underpinning ovulation could help to identify potential drugs that could temporarily affect the same biological pathways.

Online tools also offer opportunities. Between 2015 and 2018, investors ploughed more than \$1 billion into digital and diagnostic products and services that aid family planning, including menstruation and fertility-tracking apps (go.nature.com/2toj2vp). The sector is expected to be worth \$50 billion by 2025 (go.nature.com/3pcswpt). Other apps and social media could help to create large-scale data sets articulating women's needs, as long as privacy can be protected.

Key collaborations

Public–private partnerships will be key. The best innovation models in oncology, immunology and applied genomics, for example, engage industry in early stages. Such collaboration focuses research on saleable products targeted at consumer need. It also increases reproducibility of results, breaks down silos and brings in diverse perspectives to improve robustness. Without early buy-in, innovation efforts typically fall outside biopharma's tolerance for risk.

Fresh thinking will also be needed to ensure that the latest contraceptive products get to those who need them most. For example, new non-hormonal contraceptives might require new manufacturing processes and are therefore likely to be priced higher than existing products. Revenue from high-income markets could subsidize affordable prices in LMICs^{[15](#)}.



Women are most affected by pandemics — lessons from past outbreaks

Vaccine development is a good example of collaboration on product development that enables access by LMICs. Research communities such as the Collaboration for AIDS Vaccine Discovery focus on discovery. These bring the best scientists together, prioritize high-impact research and support the development of assays and model systems. To aggregate public, private and philanthropic funding, product-development partnerships have come together, such as the International AIDS Vaccine Initiative, the International Vaccine Institute and PATH Center for Vaccine Innovation and Access. These mechanisms drive innovation and significantly reduce the financial risk of early-stage investment. This type of infrastructure and collaboration

has been crucial to the fast pace of innovation and development for COVID-19 vaccines and therapeutics.

Regulators, too, can help to lower the barriers to innovation. For example, once contraceptive drugs are well studied for safety and efficacy, developers might be allowed to use modelling, alongside clinical-trial data, in support of future products using the same drug¹⁶. Regulators might also need to consider how they assess effectiveness. A new non-hormonal product might have lower efficacy in clinical settings but have fewer side effects than some existing products, leading to higher acceptance and use, for example.

New funding is crucial to catalyse innovation in any sector. Venture funds, biopharma, biotechnology firms and universities should assess opportunities to apply their technologies and expertise to contraception, which could accelerate and increase innovations in R&D across multiple fields.

The public needs to speak up about its desires and demands, so that we can move from methods that women tolerate to those that actually satisfy their needs.

Success stories of new, reliable contraceptives with fewer side effects will create a virtuous cycle, spurring more funding and research and better options for consumers. A thriving contraceptive R&D ecosystem might also catalyse innovation in other sectors of women's health: infertility, endometriosis and sexually transmitted infections, to name a few. What are we waiting for?

Nature 587, 543-545 (2020)

doi: <https://doi.org/10.1038/d41586-020-03287-0>

References

1. 1.

United Nations Population Division. *Estimates and Projections of Family Planning Indicators 2020: Regions* (UN, 2020).

2. 2.

Moreau, C., Cleland, K. & Trussell, J. *Contraception* **76**, 267–272 (2007).

3. 3.

Trussell, J., Aiken, A. R. A., Micks, E. & Guthrie, K. A. in *Contraceptive Technology* 21st edn (eds Hatcher, R. A. *et al.*) (Ayer, 2018).

4. 4.

Ali, M. M., Cleland, J. G., Shah, I. H. & World Health Organization. *Causes and Consequences of Contraceptive Discontinuation* (WHO, 2012).

5. 5.

Bearak, J., Popinchalk, A., Alkema, L. & Sedgh, G. *Lancet Glob. Health* **6**, e380–e389 (2018).

6. 6.

Sully, E. *et al. Adding It Up: Investing in Sexual and Reproductive Health* (Guttmacher Inst., 2019).

7. 7.

Kohler, H. & Behrman, J. *Benefits and Costs of the Population and Demography Targets for the Post-2015 Development Agenda* (Copenhagen Consensus Center/Univ. Pennsylvania, 2014).

8. 8.

Sonfield, A. & Kost, K. *Public Costs from Unintended Pregnancies and the Role of Public Insurance Programs in Paying for Pregnancy-Related Care: National and State Estimates for 2010* (Guttmacher Inst., 2015).

9. 9.

EvaluatePharma Database; available at <https://go.nature.com/2khvqot> (Evaluate, 2019).

10. 10.

Weinberger, M., Hayes, B., White, J. & Skibiak, J. *Glob. Health Sci. Practice* **8**, 169–175 (2020).

11. 11.

Guttmacher Institute. *Reasons for Unmet Need For Contraception in Developing Countries: Fact Sheet* (Guttmacher Inst., 2016).

12. 12.

Polis, C. B., Hussain, R. & Berry, A. *Reprod. Health* **15**, 114 (2018).

13. 13.

Shin, D. *Clinical Trials 2019 Round-up* (PharmaIntelligence Informa, 2019).

14. 14.

Ugalmugle, S. & Swain, R. *Contraceptives Market Size By Product* (Global Market Insights, 2019).

15. 15.

Kaslow, D. C. in *Global Innovation Index 2019. Creating Healthy Lives — the Future of Medical Innovation* Ch. 11 (WIPO, 2019).

16. 16.

Li, L. *et al. Annu. Rev. Pharmacol. Toxicol.*
<https://doi.org/10.1146/annurev-pharmtox-031120-015212> (2020).

Supplementary Information

1. Further reading and acknowledgements

Competing Financial Interests

Sarah G. Chamberlain and Emily Serazin are employees of, and Sarah Cairns-Smith is an adviser to, The Boston Consulting Group (BCG), a management consultancy that works with non-profit, government and for-profit organizations in the women's health sector. The research for this article was funded by The Bill & Melinda Gates Foundation and BCG's Social Impact Practice. Stephen E. Gerrard is an adviser to Women's Health Innovation Summit, run by Kisaco Research. Sarah Cairns-Smith is a board member of Engender Health, an international non-governmental organization working in the field of women's health.

Jobs from Nature Careers

- - - [All jobs](#)
 - - [Part-time Laboratory Assistant](#)
 - [Oklahoma Medical Research Foundation \(OMRF\)](#)
 - [Oklahoma City, United States](#)
 - [JOB POST](#)
 - [Assistant Professor of Teaching \(Tenure Track\)](#)
 - [The University of British Columbia \(UBC\)](#)
 - [Vancouver, Canada](#)

JOB POST

- **Principal Researcher / Senior Researcher**

Korea Brain Research Institute (KBRI)

Daegu, Korea, South

JOB POST

- **PhD Scholarship within Phosphorus Turnover in Lakes and Wetlands**

University of Southern Denmark (SDU)

Odense M, Denmark

JOB POST

This article was downloaded by **calibre** from <https://www.nature.com/articles/d41586-020-03287-0>

COMMENT

08 November 2020

Memo for President Biden: Five steps to getting more from science

Going back to normal is not enough. A revamp is required.

Roger Pielke Jr &

Roger Pielke Jr is a professor of environmental studies at the University of Colorado Boulder, USA. His books include *The Honest Broker: Making Sense of Science in Policy and Politics*.

[Contact](#)

Search for this author in:

- [Pub Med](#)
- [Nature.com](#)
- [Google Scholar](#)

Neal Lane

Neal Lane is a senior fellow in science and technology policy at Rice University's Baker Institute in Houston, Texas, and former director of the White House Office of Science and Technology Policy and the National Science Foundation.

[Contact](#)

Search for this author in:

- [Pub Med](#)
- [Nature.com](#)

- [Google Scholar](#)



President-elect Joe Biden has a very different approach from that of his electoral opponent. Credit: Kevin Lamarque/Reuters

As things look now, the US presidency of Donald Trump will soon be in the rear-view mirror, but the damage his administration leaves behind will require a sustained effort to repair. That's especially true when it comes to restoring competency and trust in federal research agencies. President-elect Joe Biden needs to do this as soon as possible, not least to quell a pandemic that is setting records for the numbers of new cases and is on track to kill more Americans than died in the Second World War. The country cannot continue to bear the ad hoc, ineffective and incoherent pandemic response it has endured under Trump.

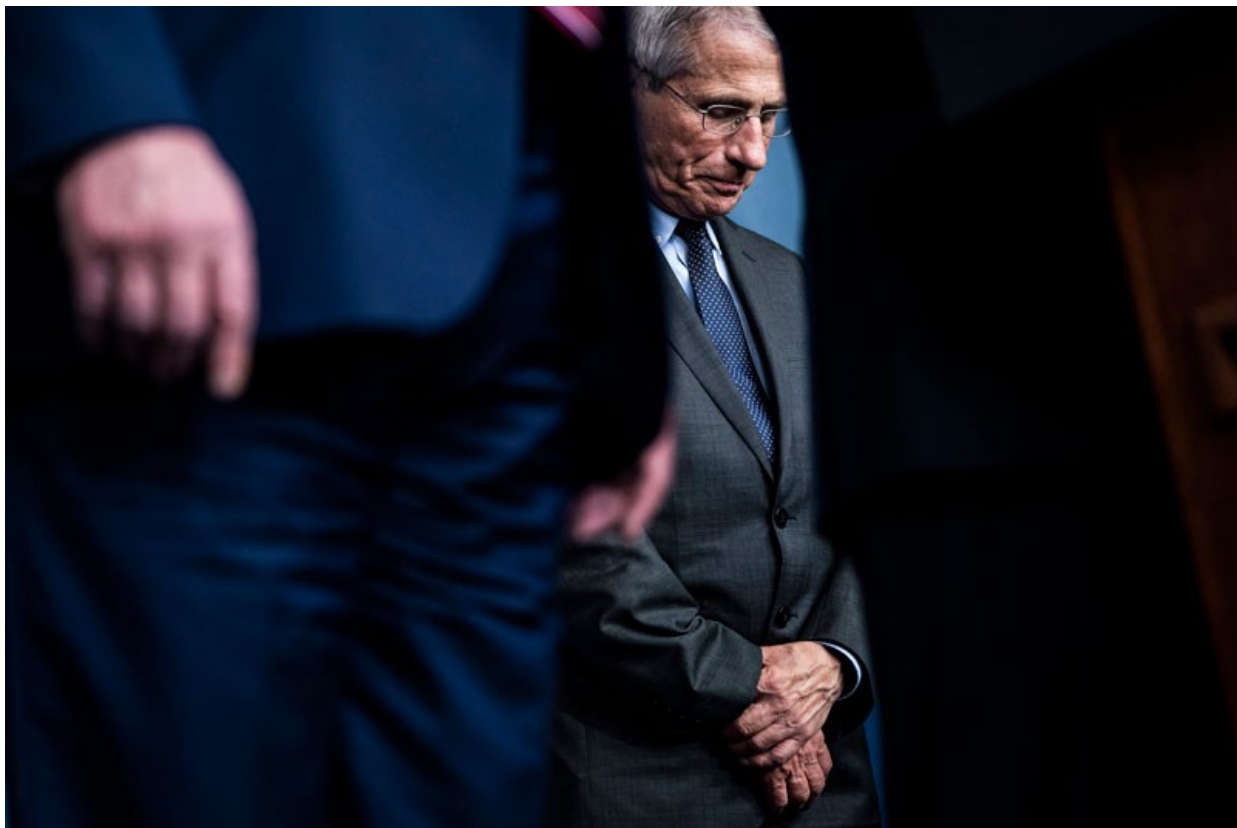
The list of needed actions is long, but here we highlight five that the Biden administration should take swiftly. We call not for a return to business as usual but for fundamental, sometimes counter-intuitive changes that will strengthen the use of science in US policy and by the research community more broadly.

Let an oft-overlooked White House office lead the pandemic response

Trump's coronavirus task force, which ostensibly guided the administration's response to the pandemic, had little authority and no accountability, had to fight for attention against other priorities, and was deliberately politicized. The task force usurped the leading role of the Department of Health and Human Services, and sidelined its Centers for Disease Control and Prevention, damaging public trust in both.

A better, albeit less-obvious, option to lead the pandemic response under Biden is the White House Office of Science and Technology Policy (OSTP, which one of us, N.L., led from 1998 to 2001). It was established in 1976 to

advise the president and coordinate federal science agencies. Although the OSTP has predominantly focused on deciding priorities for research funding, its history and mandate make it ideally poised to coordinate a national effort for responding to COVID-19.



Anthony Fauci, director of the US National Institute of Allergy and Infectious Diseases and a member of Donald Trump's coronavirus task force, has clashed with Trump over the handling of the pandemic. Credit: Jabin Botsford/The Washington Post/Getty

In February, as the pandemic was just beginning to spread in the United States, the Government Accountability Office warned that the nation's biodefence strategy needed "to move away from traditional mission stovepipes toward a strategic enterprise-wide approach". The OSTP has the perspective needed to work across agencies, and it has coordinated policy before. Former president Ronald Reagan relied on it to advance his 'Star Wars' ballistic-missile defence programme.

What's more, the OSTP would offer a fresh start to the pandemic response. Under Trump, it had little visible role and so, unlike the federal public-health agencies, has been less politicized.



Three secrets of survival in science advice

Finally, the OSTP sits in the White House but is also accountable to Congress, with a director confirmed by the Senate. That keeps it both close to the president and subject to congressional oversight, unlike Trump's coronavirus task force. Leadership will require working across branches of government, and having the OSTP in charge would boost legitimacy, because the Democrat-led office may be working with a Republican-led Senate. At the same time, the head of the OSTP — the White House science adviser — should also be elevated to the president's cabinet. This guarantees a seat at the table when the most important, consequential decisions are made. It will also signify the importance of the role to federal agencies, to Congress and to the public.

Make advisory processes more independent

A tenet of effective advisory bodies is that advisers advise and decision makers decide. Advice might take the form of narrow technical guidance on scientific matters (does a particular drug improve COVID-19 health outcomes?), presentation of policy alternatives (what are the risk-reduction options for reopening schools?), or recommendation of a specific action (should masks be mandatory indoors?). Under Trump, scientific advice was typically ignored or, worse, manipulated for political expediency. That is easier to do when responses are managed by ad hoc groups. For example, radiologist Scott Atlas was selected as Trump's top pandemic adviser to counter government staff scientists and support the political agenda of the president.



Four principles to make evidence synthesis more useful for policy

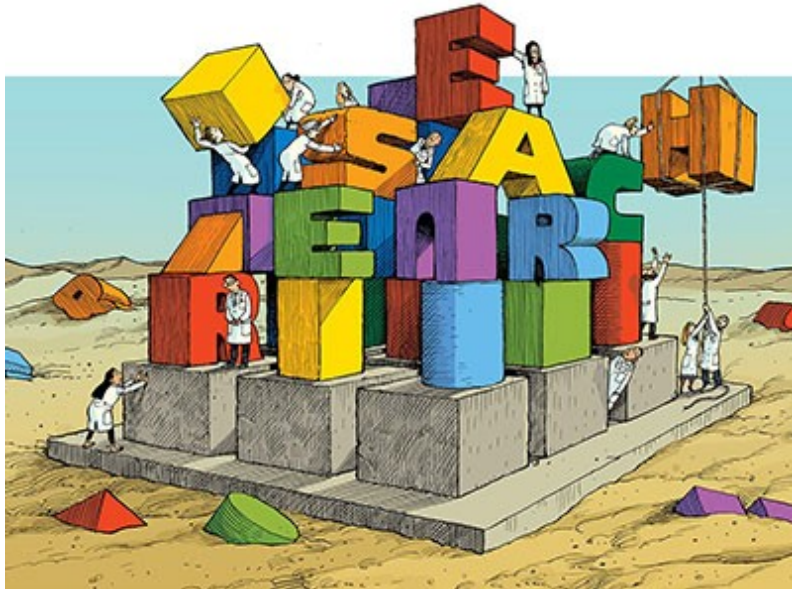
The advisory mechanisms available to draw on are broad and deep. The US government lists more than 1,000 bodies currently active under the Federal Advisory Committee Act. Biden and the OSTP must ensure that advisory committees consist of independent experts selected for competency, that their role is clear, and that their advice reaches decision makers in the field — from public health to environmental protection.

The White House will also need to reject Trump-era policies that keep the government from drawing on competent expertise. First in line should be reversal of an executive order signed last month that removed civil-service protections from positions usually filled by career employees, making them easier to fire for political reasons. Advisory committees, such as those leading the US National Climate Assessment, should comprise independent experts, selected by bipartisan panels (as is typically done for committees linked to politicized issues), and not political appointees. And political appointees should never alter or edit science advisory-committee reports or recommendations.

The main criticism of such reforms might be that they would empower independent experts over administration officials. Indeed — we see that as a feature, not a flaw. Also, having independent advice doesn't mean decision makers will always heed it; the administration of former president Barack Obama decided, contrary to recommendations of its expert advisers, to limit distribution of the morning- after pill in 2011; it similarly rejected expert advice in 2016 to strengthen ozone regulations. Still, as Biden has said, decision makers have an obligation to “listen to the scientists”.

Expedite scientific-integrity legislation

The Obama administration instigated an effort to implement scientific-integrity policies across federal agencies; some 24 agencies developed relevant administrative policies in response.



Research integrity: nine ways to move from talk to walk

But several subsequent reviews, including one by the Government Accountability Office, found these scientific-integrity policies to be unevenly interpreted and applied. Some agencies, such as the Department of Defense, were not included under the mandate. Others, including the National Institutes of Health and the Department of Labor, did not develop policies. Agencies that did develop policies defined ‘scientific integrity’ in different ways, and created conflicting guidelines for topics such as media relations and how to handle disparate scientific perspectives. And the Trump administration rode roughshod over these rules anyway, for instance by barring a Department of State analyst from including information about climate change in written testimony to a congressional committee.

Harmonized legislation that allows congressional oversight would be more difficult to ignore or evade. Several proposals exist that would promote scientific integrity, protect agency officials and strengthen the ability of Congress to keep the executive branch in check. Presidents rarely advocate restricting their own power, but Biden should. One relevant bill was

introduced in the House of Representatives in 2019 and has more than 200 co-sponsors.

Give public universities tough love and lots of support

The US public-university system has suffered deep budget cuts during the pandemic, with no relief in sight. And state governments had been cutting support in the decades before that. On average, according to the American Academy of Arts and Sciences, states cut funding per student by 30% between 2000 and 2014 — leading to tuition and fee hikes, a greater reliance on out-of-state tuition to replace those state funds, and drastically increased student debt. Some students are particularly disadvantaged: a recent report from the Education Trust gave failing grades to more than 75% of the nation's top 101 universities for their accessibility to Black students, with about 50% receiving failing grades for accessibility to Latino students (see go.nature.com/2i7pidk).



Boosting research without supporting universities is wrong-

headed

The federal government should help public universities with long-term financial sustainability, and perhaps even provide temporary recovery funding. Strings attached should include plans to boost diversity among students, faculty members and researchers.

Critics might argue that such issues are not the concern of the federal government. However, the data indicate that these issues are a systemic, national concern. There is ample precedent for a federal role in higher-education policy, dating back to the 1965 Higher Education Act.

Refocus science funding

In spite of the Trump administration's efforts to slash investment, Congress ensured that federal funding of research and development increased by more than 20% between 2017 and 2020. Still, the United States ranks tenth among member nations of the Organisation for Economic Co-operation and Development in national investment (public and private, as a percentage of gross domestic product) in research and development, and the federal government's share of that has fallen steadily over recent decades.



Scientists relieved as Joe Biden wins tight US presidential election

Policy proposals from Biden's team, and several bipartisan bills in Congress, suggest that federal research and development funding will grow substantially. That growth must come with shifts in priorities. It should no longer be based on incremental changes to legacy budgets, as presidents often put forward. Instead, it must give higher priority to achieving national policy goals, beyond fundamental scientific knowledge.

For instance, achieving net-zero carbon dioxide emissions from electricity generation will require a new era of federal–industry partnerships supporting sustained energy-technology innovation. Other priorities should include research and development to help Americans recover from the pandemic, the economic catastrophe, the ‘infodemic’ and the ravages of systemic inequality.

The academic research community conventionally emphasizes basic research over science directed at solving societal challenges, because the former occurs mainly in academia and the latter in federal laboratories. To gain researchers' support for 'mission science', the Biden administration will need to assure them of its continuing support for basic research.

The challenges the Biden administration faces are daunting. Yet they create opportunities to make 'build back better' a reality, not just a bumper sticker.

Nature 587, 546-547 (2020)

doi: <https://doi.org/10.1038/d41586-020-03148-w>

Jobs from Nature Careers

- - - [All jobs](#)
 -

- **Part-time Laboratory Assistant**

Oklahoma Medical Research Foundation (OMRF)

Oklahoma City, United States

JOB POST

- **Assistant Professor of Teaching (Tenure Track)**

The University of British Columbia (UBC)

Vancouver, Canada

JOB POST

- **Principal Researcher / Senior Researcher**

Korea Brain Research Institute (KBRI)

Daegu, Korea, South

JOB POST

- **PhD Scholarship within Phosphorus Turnover in Lakes and Wetlands**

University of Southern Denmark (SDU)

Odense M, Denmark

JOB POST

CORRESPONDENCE

24 November 2020

COVID-19: students caught in Pakistan's digital divide

Aziz Khan

Aziz Khan Stanford University, California, USA.

[Contact](#)

Search for this author in:

- [Pub Med](#)
- [Nature.com](#)
- [Google Scholar](#)

Education in developing countries with patchy Internet coverage is particularly hard-hit by the COVID-19 pandemic (see [*Nature* 585, 482; 2020](#)), compromising the future of students unable to access online teaching. A United Nations' resolution emphasizes access to the Internet as a means of bridging the digital divide and facilitating the fundamental human right to education (see go.nature.com/2kcjp1p). In Pakistan, for example, nationwide Internet availability must be accelerated if the country's potential is not to be irreversibly compromised.

Take the remote mountainous Gilgit-Baltistan region, which has a record of high literacy. This will plummet without proper Internet connectivity because local schools can no longer teach. University students returning home in lockdown cannot access their institutional online classes.

In December 2019, the government started the Digital Pakistan initiative (DPI) to prioritize “access and connectivity”. After a year, an unacceptable

proportion of the population is still without electricity, let alone broadband. A further blow to Pakistan's education and research has been dealt by the government's continual axing of the country's Higher Education Commission (HEC) budget.

As a researcher from Pakistan, I urge the government and the leadership of the DPI and the HEC to speed up plans to rectify this digital divide so that education can flourish again (see also [*Nature* 582, 162–164; 2020](#)).

Nature 587, 548 (2020)

doi: <https://doi.org/10.1038/d41586-020-03291-4>

Jobs from Nature Careers

- - - [All jobs](#)
 - - [Part-time Laboratory Assistant](#)
[Oklahoma Medical Research Foundation \(OMRF\)](#)
[Oklahoma City, United States](#)
[JOB POST](#)
 - [Assistant Professor of Teaching \(Tenure Track\)](#)
[The University of British Columbia \(UBC\)](#)
[Vancouver, Canada](#)
[JOB POST](#)
 - [Principal Researcher / Senior Researcher](#)

[Korea Brain Research Institute \(KBRI\)](#)

[Daegu, Korea, South](#)

[JOB POST](#)

- [PhD Scholarship within Phosphorus Turnover in Lakes and Wetlands](#)

[University of Southern Denmark \(SDU\)](#)

[Odense M, Denmark](#)

[JOB POST](#)

This article was downloaded by **calibre** from <https://www.nature.com/articles/d41586-020-03291-4>

| [Section menu](#) | [Main menu](#) |

CORRESPONDENCE

24 November 2020

Giant tortoises make a comeback in Madagascar

Miguel Pedrono,

CIRAD, University of Montpellier, France.

[Contact](#)

Search for this author in:

- [Pub Med](#)
- [Nature.com](#)
- [Google Scholar](#)

Elodi Rambeloson &

Anjajavy Nature Reserve, Madagascar.

Search for this author in:

- [Pub Med](#)
- [Nature.com](#)
- [Google Scholar](#)

Alison Clausen

UNESCO, Paris, France.

Search for this author in:

- [Pub Med](#)
- [Nature.com](#)
- [Google Scholar](#)

Just two years after their reintroduction as part of a bold conservation strategy, giant tortoises (*Aldabrachelys gigantea*) have hatched in the wild in Madagascar for the first time in around 600 years. This milestone in rewilding could provide insight into the structure and dynamics of Madagascar's unique ecosystems, which were shaped by megafauna extirpated centuries ago. For us, some of the conservation biologists involved, it feels like a time-travel bonanza.

Overexploited and driven to extinction in Madagascar after humans arrived on the island 1,500 years or so ago (see [B. E. Crowley *Quat. Sci. Rev.* **29**, 2591–2603; 2010](#)), giant tortoises survived because they colonized remote islands in the Seychelles. With the support of the Madagascan government, 12 were released in 2018 into a secure nature reserve. Two hatchlings appeared there in 2019, followed by another 25 in October this year. Now in a nursery, these juveniles will be returned to the wild once their carapaces can protect them from predators.

This type of innovative approach could help stop the catastrophic decline in the island's biodiversity, particularly in a changing climate (see also [B. B. N. Strassburg *et al. Nature* **586**, 724–729; 2020](#)).

Nature **587**, 548 (2020)

doi: <https://doi.org/10.1038/d41586-020-03290-5>

[Jobs from Nature Careers](#)

- - - [All jobs](#)
 -
 - [Part-time Laboratory Assistant](#)

Oklahoma Medical Research Foundation (OMRF)

Oklahoma City, United States

JOB POST

▪ **Assistant Professor of Teaching (Tenure Track)**

The University of British Columbia (UBC)

Vancouver, Canada

JOB POST

▪ **Principal Researcher / Senior Researcher**

Korea Brain Research Institute (KBRI)

Daegu, Korea, South

JOB POST

▪ **PhD Scholarship within Phosphorus Turnover in Lakes and Wetlands**

University of Southern Denmark (SDU)

Odense M, Denmark

JOB POST

This article was downloaded by **calibre** from <https://www.nature.com/articles/d41586-020-03290-5>

CORRESPONDENCE

24 November 2020

COVID-19: Panama stockpiles unproven drugs

Ivonne Torres-Atencio,

University of Panama, Panama.

Search for this author in:

- [Pub Med](#)
- [Nature.com](#)
- [Google Scholar](#)

Amador Goodridge &

INDICASAT-AIP, City of Knowledge, Panama.

[Contact](#)

Search for this author in:

- [Pub Med](#)
- [Nature.com](#)
- [Google Scholar](#)

Silvio Vega

Hospital Doctor Arnulfo Arias Madrid, Panama.

Search for this author in:

- [Pub Med](#)
- [Nature.com](#)
- [Google Scholar](#)

Panama has gone one step further than other Latin American countries that use the unproven drug ivermectin against COVID-19 (see [Nature 586, 481–482; 2020](#)). The government has approved this drug and hydroxychloroquine — despite the lack of efficacy data for either — and is stockpiling both. We find this alarming because the drugs' side effects could be toxic in a significant proportion of the population.

In March 2020, hydroxychloroquine was prescribed only to people with COVID-19 who were taking part in a clinical-trial protocol. Panama's ministry of health followed the advice of its Scientific Advisory Committee and two months later suspended the trial on the basis of growing evidence of the drug's ineffectiveness (see [M. R. Mehra *et al. Lancet* 395, 1820; 2020](#)). The World Health Organization subsequently declared that, according to the available data, hydroxychloroquine does not reduce fatality in people hospitalized with COVID-19, nor does it ameliorate symptoms of mild or moderate illness.

Despite these developments, Panama has since purchased 2,900,000 doses of hydroxychloroquine and 450,000 doses of ivermectin, to be distributed as part of a self-treatment kit to people self-isolating with the virus.

Nature 587, 548 (2020)

doi: <https://doi.org/10.1038/d41586-020-03289-y>

[Jobs from Nature Careers](#)

- - - [All jobs](#)
 -
 - [Part-time Laboratory Assistant](#)

Oklahoma Medical Research Foundation (OMRF)

Oklahoma City, United States

JOB POST

▪ **Assistant Professor of Teaching (Tenure Track)**

The University of British Columbia (UBC)

Vancouver, Canada

JOB POST

▪ **Principal Researcher / Senior Researcher**

Korea Brain Research Institute (KBRI)

Daegu, Korea, South

JOB POST

▪ **PhD Scholarship within Phosphorus Turnover in Lakes and Wetlands**

University of Southern Denmark (SDU)

Odense M, Denmark

JOB POST

This article was downloaded by **calibre** from <https://www.nature.com/articles/d41586-020-03289-y>.

CORRESPONDENCE

24 November 2020

Explain ESA's last-minute ditching of new space telescope

David L. Clements,

Imperial College London, UK.

[Contact](#)

Search for this author in:

- [Pub Med](#)
- [Nature.com](#)
- [Google Scholar](#)

Stephen Serjeant &

The Open University, UK.

Search for this author in:

- [Pub Med](#)
- [Nature.com](#)
- [Google Scholar](#)

Shoko Jin

SRON Netherlands Institute for Space Research, the Netherlands.

Search for this author in:

- [Pub Med](#)
- [Nature.com](#)
- [Google Scholar](#)

The European Space Agency (ESA) has cancelled its proposed Space Infrared Telescope for Cosmology and Astrophysics (SPICA; go.nature.com/2jfp8fw) just months before the final mission-selection review. The decision — made by the executive on the grounds of undisclosed costs, not by the Science Programme Committee on the basis of peer review — has left many in the astronomy community with no confidence in the decision-making processes at the agency's highest levels (see public letter to ESA's director of science signed by almost 300 scientists, at <https://spicarebelalliance.com>).

ESA member states and collaborating countries have invested heavily in developing SPICA and expected a fair, transparent process for all competing projects. This cancellation was imposed without negotiation or communication with the SPICA team, and no details were given about the underlying costings. Why these suddenly became a problem after the completion of several comprehensive reviews is a mystery. The project team was given no opportunity to find a solution.

Without transparency and accountability in the making of such decisions, nothing will prevent other ESA projects from experiencing a similar fate.

Nature 587, 548 (2020)

doi: <https://doi.org/10.1038/d41586-020-03288-z>

Jobs from Nature Careers

- - - [All jobs](#)
 - - [**Part-time Laboratory Assistant**](#)

Oklahoma Medical Research Foundation (OMRF)

Oklahoma City, United States

JOB POST

▪ **Assistant Professor of Teaching (Tenure Track)**

The University of British Columbia (UBC)

Vancouver, Canada

JOB POST

▪ **Principal Researcher / Senior Researcher**

Korea Brain Research Institute (KBRI)

Daegu, Korea, South

JOB POST

▪ **PhD Scholarship within Phosphorus Turnover in Lakes and Wetlands**

University of Southern Denmark (SDU)

Odense M, Denmark

JOB POST

This article was downloaded by **calibre** from <https://www.nature.com/articles/d41586-020-03288-z>

Work

- **Postdocs under pressure: ‘Can I even do this any more?’**

[23 November 2020]

Career Feature • Long hours and a lack of job security, combined with workplace bullying and discrimination, are forcing many to consider leaving science, finds Nature’s inaugural survey of postdoctoral researchers.

- **Flame thrower** [23 November 2020]

Where I Work • Fire-safety researcher Luke Bisby investigates which materials can take the heat.

CAREER FEATURE

23 November 2020

Postdocs under pressure: ‘Can I even do this any more?’

Long hours and a lack of job security, combined with workplace bullying and discrimination, are forcing many to consider leaving science, finds *Nature*’s inaugural survey of postdoctoral researchers.

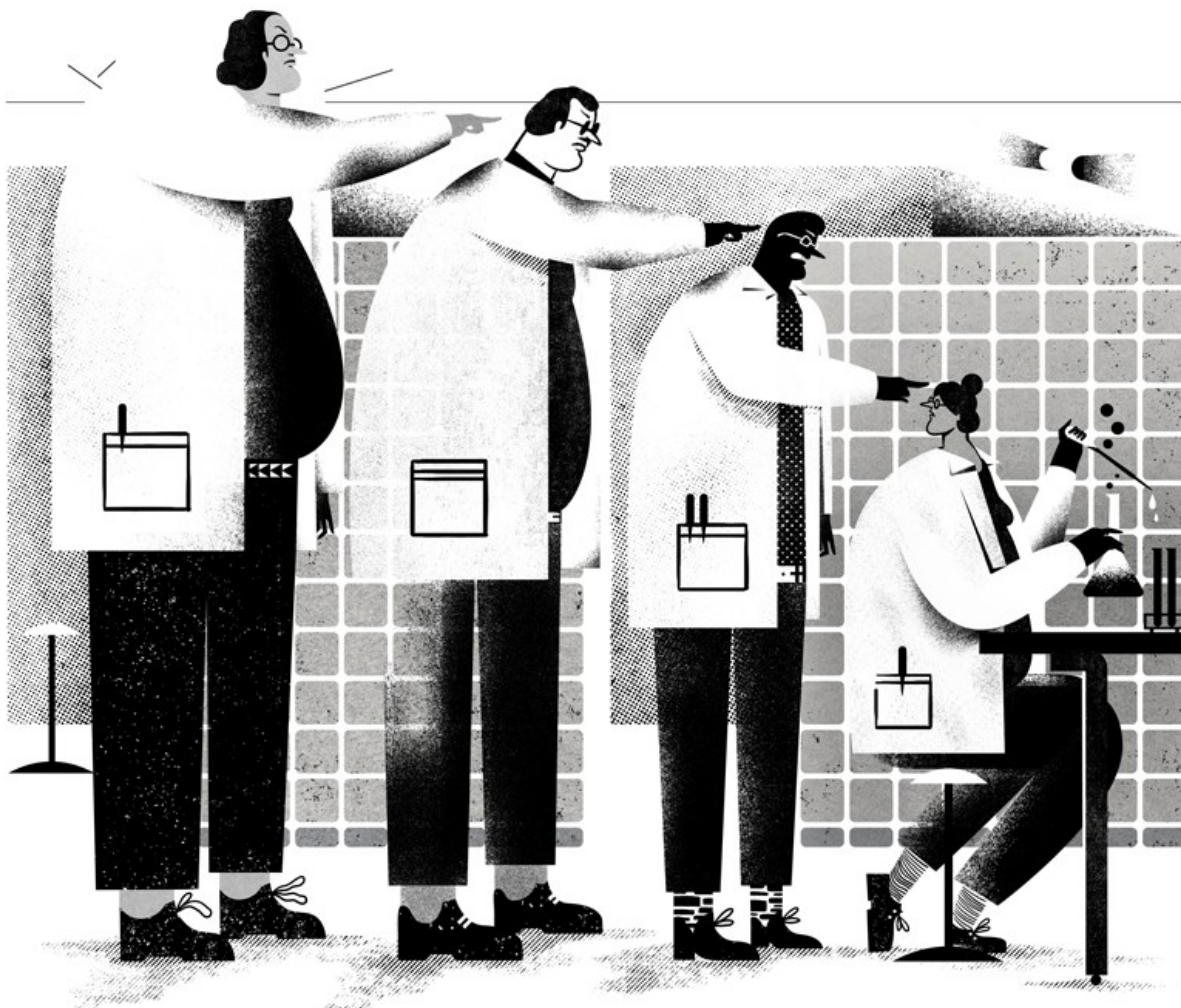
Chris Woolston

Chris Woolston is a freelance writer in Billings, Montana.

Search for this author in:

- [Pub Med](#)
- [Nature.com](#)
- [Google Scholar](#)

[Find a new job](#)



Credit: Miguel Monk

During a two-year stint as a postdoctoral researcher in computational microbiology at the University of Liverpool, UK, Adrian Cazares suffered despite his successes. “I published papers but I wasn’t happy,” he says. “[Postdocs] are under so much pressure all the time. We take it to every part of our lives. It really started to affect my mental health.”

Cazares, who in February started his second postdoc — this one at the European Bioinformatics Institute on the Wellcome Genome Campus near Cambridge, UK — was one of more than 7,600 researchers in 93 countries who responded to *Nature*’s first-ever survey of postdoctoral scientists. The self-selecting survey, which ran in June and July, included a series of

questions designed to illuminate postdocs' quality-of-life issues, including - mental health, working hours and experiences of discrimination and harassment (see '*Nature's* postdoc survey').

Nature's postdoc survey

In September, *Nature* reported survey results about [how COVID-19 has affected postdocs](#) and their views of the future. The second article in the series offers an overview of their circumstances worldwide. The third explores postdocs' quality of life, including mental health and experiences of discrimination and harassment. The final article examines respondents' sense of their career prospects, a crucial issue for postdocs as they look ahead. The survey, created together with Shift Learning, a market-research company in London, was advertised on nature.com, in Springer Nature digital products and through e-mail campaigns. It was offered in English, Mandarin Chinese, Spanish, French and Portuguese. The full survey data sets are available at go.nature.com/3tmckuq.

'Tipping point'

Through survey answers, free-text comments and follow-up interviews, respondents shared the day-to-day realities of a pivotal, and often precarious, stage of a scientific life. Responses uncovered a list of issues — including high pressure, long hours, relatively low wages compared with those for analogous research positions outside academia, and pervasive job insecurity — that can threaten to derail a scientific career. "A postdoc can be a tipping point," says Renate Ysseldyk, a health psychologist at Carleton University in Ottawa, Canada. Ysseldyk was the lead author of a study published last year that used interviews and a survey to explore challenges facing female postdocs in academia ([R. Ysseldyk et al. *Front. Psychol.* **10**, 1297; 2019](#)). "It's a time when career uncertainty collides with the stress of personal life," she adds. "You reach that point and you have to ask yourself: Is it worth it? Can I even do this any more?"

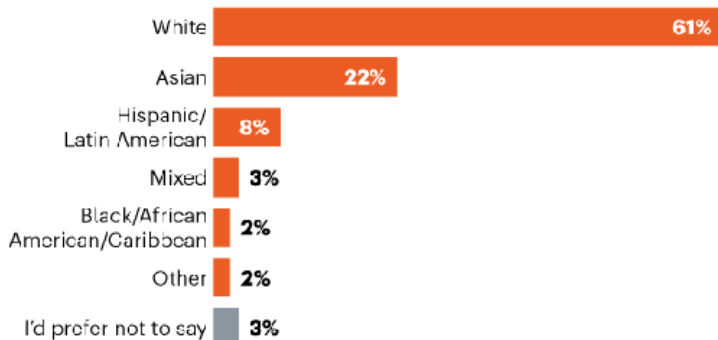
Many postdocs are asking themselves just that: 51% of respondents said that they had considered leaving science because of mental-health concerns related to their work (see 'Existential doubts'). Some groups are especially

likely to have such doubts. Fifty-five per cent of female respondents said that they had considered quitting science, compared with 46% of male respondents. And two-thirds of those who reported disabilities said that they had considered leaving because of mental-health concerns.

EXISTENTIAL DOUBTS

Postdoctoral researchers are a diverse, resilient group, but mental and emotional strain has made many question their ability to remain in science. Some have received help for anxiety and depression, but even more have never sought assistance, despite wanting to — a sign that postdocs don't always have clear access to needed services.

What is your ethnicity?*



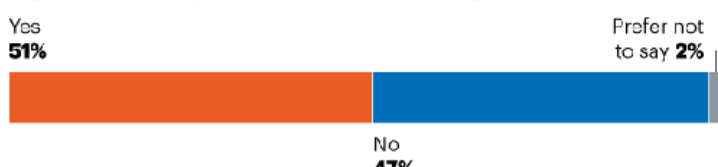
Do you consider yourself part of a minority ethnic and/or racial group?



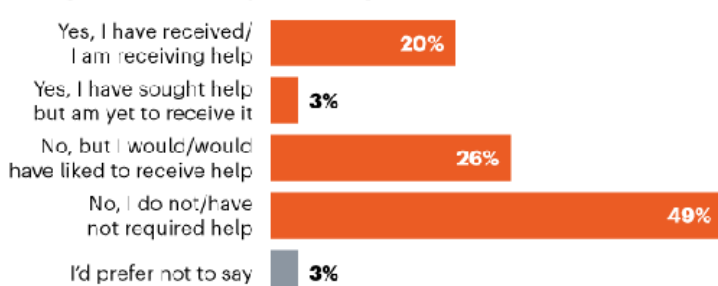
Do you experience any long-term health problems or a disability?



Have you considered leaving science because of depression, anxiety or similar issues related to your work?



Have you sought or received professional help for depression or anxiety related to your work?*



Ysseldyk is not surprised that so many postdocs doubt their ability to carry on. “That’s certainly how I felt,” she says, citing her own experience that postdoctoral work can seem incompatible with motherhood. “I felt like a professional failure and a negligent mother at the same time,” she says. In their 2019 study, Ysseldyk and colleagues found that concerns about parenthood were common among female postdocs. Some worried about ‘falling behind’ as they started families. “It’s such a tenuous time for women, in particular when they go on maternity leave,” Ysseldyk says. “They can’t put in those hours any more. And yet they are going to be compared to their colleagues.”



Kathryn Cutts, a geologist at Rio de Janeiro State University in Brazil, is on her fourth postdoctorate and yearns for the stability of a permanent position. Credit: Kathryn Cutts

Even for those who are not parents, postdoctoral positions can greatly complicate life plans. Kathryn Cutts, a geologist at Rio de Janeiro State University in Brazil, started her two-year placement in May. It’s her second in Brazil and her fourth overall. “I’ve really enjoyed doing postdocs,” says

Cutts, who is from Australia. “I’ve been able to travel the world.” But after so many years without a stable, permanent post, her life still feels precarious. When you’re a postdoc, she says, “you’re at the point where you want to start a family and settle down. But you have to have an amazing track record to get a permanent position at a university. There’s a pressure to produce.”

Natalie Sirisaengtaksin, a postdoctoral cancer researcher at the University of Texas Health Sciences Center at Houston, says that she understands why so many postdocs think about quitting. “It all comes down to the mentor,” she says. “Without my mentor, I don’t think I’d still be in science.” She has observed that some postdocs get pushed too far for too long, often at the expense of other parts of their lives. “We have a support group of postdocs who get together monthly to talk about the issues that we have,” she says. Some former members of the group, she adds, have left academia in the hope of improving their mental health.

Balancing act

Achieving a good work–life balance is an elusive dream for many postdocs. In the survey, just four out of ten respondents said that they were satisfied with the balance in their lives. For many, long hours at work leave little room for other concerns. Thirty-one per cent of respondents said their contracts called for at least 40 hours per week, but contracts are often little more than a piece of paper. Thirty-one per cent of respondents reported putting in at least 10 hours a week beyond their contracts, and 8% said they put in 20 or more extra hours. Almost all (97%) reported working at weekends and on days off, and 49% said they had done so at least 20 times in their career.



How failure benefits science

Those extra hours are often not compensated, says Anna Coussens, an immunologist at WEHI (formerly known as the Walter and Eliza Hall Institute of Medical Research) in Parkville, Australia, and a former member of the executive committee of the Global Young Academy, a science-advocacy group based in Halle, Germany. One of her previous postdoctoral positions was in the United Kingdom, where she had to sign a waiver stating that she would work extra hours beyond her contract. Even postdocs who didn't sign such contracts tended to live by the same rule, she says.

"Everyone knows that you work beyond the hours that you get paid for."

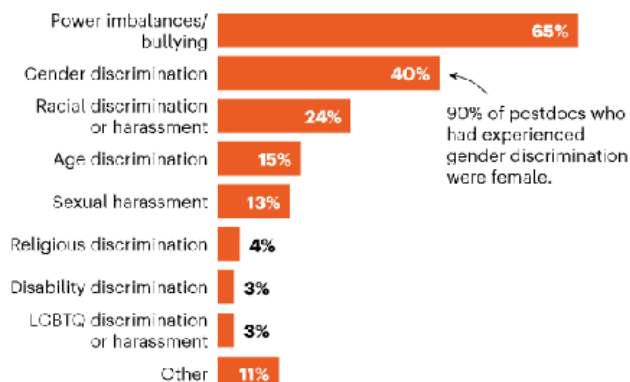
Mental-health toll

The combination of long hours, stress and uncertainty can pose a serious threat to mental health (see 'Academia has truly ruined my life'). Nearly half (49%) of respondents wanted help for depression or anxiety caused by their work. About one-quarter (23%) had received support, and even more (26%) said that they hadn't sought help but had wanted to do so.

HARASSMENT AND DISCRIMINATION

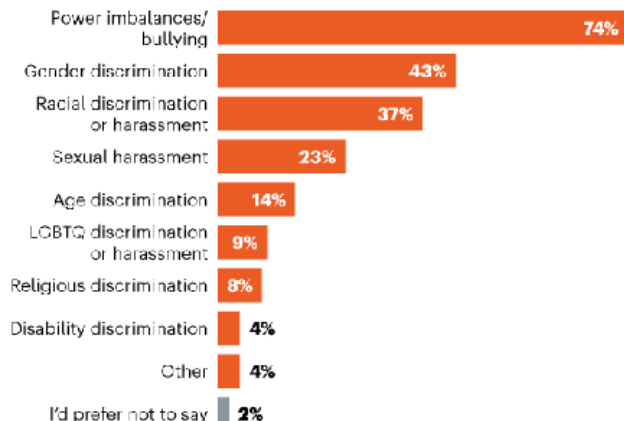
Nearly one in four postdocs reported experiencing harassment and/or discrimination in their current positions, much of it coming from the top. Principal Investigators are frequent perpetrators, a sign of power imbalances and abuses. Many of these postdocs feel that their institutions aren't doing enough to promote equality.

Which of the following have you experienced directly?

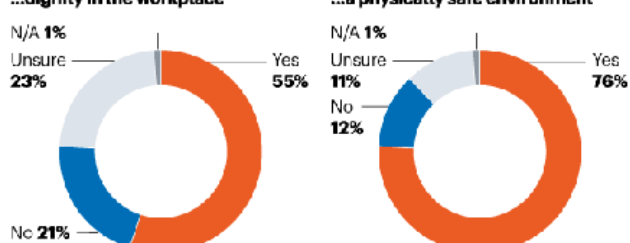


90% of postdocs who had experienced gender discrimination were female.

Which of the following have you observed?

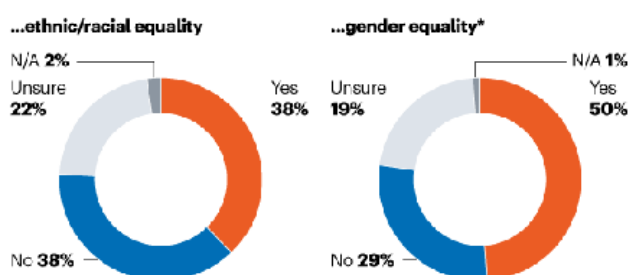


Do you believe that your postdoc workplace is doing enough to promote...



...dignity in the workplace

...a physically safe environment



...gender equality*

©nature

*Figures have been rounded and so do not add up to 100%.

Some groups experience greater distress than do others. Female respondents were more likely than male respondents to have sought help (27% compared with 16%). Field of study matters, too. Twenty-three per cent of researchers in ecology and evolution and 20% of researchers in biomedical sciences said they were already receiving mental-health help. By contrast, only 13% of respondents in chemistry and 11% of respondents in engineering were getting help.

Compared with some groups in other surveys, postdoctoral researchers seem reluctant to seek help for mental-health concerns. In [Nature's 2019 survey of PhD students](#), 36% of respondents said they had sought help for depression or anxiety caused by their PhD studies. In a [survey of more than 13,000 researchers](#) at various career stages, conducted this year by Cactus Communications, a scholarly-communications company with offices around the world, 37% of respondents said they had sought help for their mental health.

‘Academia has truly ruined my life’

In free-text comments, respondents to Nature’s inaugural survey of postdoctoral researchers disclosed discontent and disillusionment.

- In Brazil, PhD students need to sell food on the street in order to support themselves financially, as most of them are unable to obtain scholarships or jobs to sustain themselves. *Bioinformatician, Brazil*
- I was told to go out to dinner and drinks with an older male collaborator each time he was in town, but my male colleagues were not required to do the same thing. This man pressured me to tell him where I lived and kept trying to drive me home. *Biomedical researcher, United Kingdom*
- As a Latina postdoc in the United States, I heard racist comments from my principal investigator. My work was never recognized. It was the worst experience. *Biotechnology researcher now working in Europe*
- The lack of stability in a postdoc position is a huge source of anxiety and depression in this group. You cannot plan your life more than for the next

two or three years and you are always looking for a new place to live.

Physicist, Denmark

- There is little support for gay postdoc groups in China. *Healthcare researcher, China*
- I'm facing more gender discrimination than I have at any other stage of training. I fear that this puts me at a significant disadvantage relative to the male postdocs in my lab who started around the same time. We will likely go on the job market at a similar time and I will look less productive.
Biomedical researcher, United States
- I'm very unhappy about the lack of support from my supervisor and the constant pressure to work ridiculously long hours for a small salary. I'm heavily involved in our local postdoc association to change the conditions for future postdocs. *Biomedical researcher, Canada*
- Academia has truly ruined my life. All of my peers are either married with kids or they're making six figures at their job with only a Bachelor's degree. I am still single, no kids, have depression and extreme anxiety, and I'm still poor. *Biomedical researcher, United States*

One possible reason for this reluctance is that, for postdocs struggling with mental-health issues, assistance isn't necessarily easy to find. In this year's survey, just over one-quarter (27%) of respondents agreed with the statement that "my university/institution offers adequate mental health support". Less than one-fifth (18%) agreed with the statement that "mental health and wellbeing services in my university are tailored and appropriate to the needs of postdocs".

Because postdocs often fall into a grey zone between staff and students, they might not be eligible for mental-health services that are available to others at their institutions, Ysseldyk says, describing it as "another issue where postdocs are falling through the cracks in the system".



Computational microbiologist Adrian Cazares at the European Bioinformatics Institute near Cambridge, UK, says the pressures of being a postdoc have affected his mental health. Credit: Adrian Cazares

Cazares says that his mental health has suffered in the competitive atmosphere of postdoctoral research, especially during his first postdoctoral stint, at the University of Liverpool. (The university did not respond to requests for comment.) For him, Twitter was a particular source of anxiety. The non-stop chatter about grants, publications and awards has given him an uneasy feeling that he might be falling behind. “Everyone is keen to share success but very few [postdocs] talk about competition and failures, which are actually way more common,” he says. “We have to think about the impact of our words on others.”

As noted in a [previous article](#), respondents to the survey are a diverse, globally mobile group. Sixty-one per cent are currently working outside their home country, and nearly 20% consider themselves to be members of a minority ethnic group. The global reach of postdocs helps to drive scientific innovation, but it also creates opportunities for friction. A geneticist from

Africa who is a postdoc at a prestigious research university in the US Midwest wrote in the comment section that it's "difficult to navigate academia as a minority. People assume you are lazy, not intelligent or a diversity hire at all times."



Career resources for postdoctoral researchers

One-quarter (24%) of respondents said they had experienced discrimination or harassment during their current postdoctoral stint (see 'Harrassment and discrimination'), a slightly higher proportion than the 21% of PhD students who reported such mistreatment in our [survey of graduate students last year](#). International postdocs (25%) were rather more likely than their peers working in their home countries (21%) to report harassment or discrimination. Thirty-four per cent of respondents who identified as members of an ethnic minority (and 22% of those who don't identify as such) said they had experienced discrimination or harassment. Female respondents (30%) were more likely than male respondents (18%) to report experiencing -discrimination and harassment.

Power imbalance

When asked to identify the type or types of mistreatment they had experienced, most (65%) pointed to power imbalances or bully-ing, 40% reported gender discrimination and 24% reported racial discrimination. Consistent with previous *Nature* surveys, one in ten respondents who reported gender-based discrimination were male.



Nature special: Young scientists

Less than half of female respondents (47%) agreed that their institution is doing enough to promote gender equality. One postdoc wrote in the comment section that she had suggested workplace changes that were not implemented, only to see a male colleague praised later for making those same suggestions. Another respondent underscored in her comments how women are often judged harshly for reasons that have nothing to do with the quality of their work. “Age and body size”, the commenter wrote, “are implicated in the inability to get a promotion.”

Troubling behaviours often come from the top. Asked to identify the perpetrator, 57% of respondents who had experienced harassment or discrimination pointed to their supervisor or principal investigator (PI). “There is a real lack of protection against discrimination and harassment from PIs,” wrote a cell biologist from France who is a postdoc at a university

on the US East Coast. “And it needs to change.” One-quarter implicated another postdoc in their group. Just half (50%) of respondents said that their institution is doing enough to support gender equality; slightly more than one-third (38%) said that their institutions were adequately addressing racial and ethnic equality.



Philip Scholten, a chemistry postdoc at the Adolphe Merkle Institute in Fribourg, Switzerland, says European institutions must do more to tackle inherent racism.Credit: AMI/Scott Capper

Some postdocs who participated in the *Nature* survey are also helping to lead the way to change. Philip Scholten, a chemist at the Adolphe Merkle Institute in Fribourg, Switzerland, is part of a postdoctoral group putting together a survey to assess issues of racism and sexism at their institution. The Merkle Institute, which is affiliated with the University of Fribourg, has a small but diverse community. “This institute has a lot of nationalities that bring a lot of richness,” Scholten says. “But there is racism and racial inequality in Europe, and it’s often overlooked in academia.” We should do more to combat those obstacles, he adds.

For his part, Cazares, who is from Mexico, says that he has never sensed any racial discrimination or bias during his time in the United Kingdom.

“Liverpool and Cambridge have been very welcoming,” he says, adding that he is also trying to do his part to help other postdocs feel comfortable in their positions. “If I see someone who is falling behind or is stressed about their achievements, and if they are working on similar things, I try to reach out to them and propose collaboration instead of competition,” he says.

As the survey underscores, many postdocs are struggling. Acknowledging those challenges and hardships can be an important step forward. “People feel better if you tell them that you also fail,” Cazares says.

Nature 587, 689-692 (2020)

doi: <https://doi.org/10.1038/d41586-020-03235-y>

Jobs from Nature Careers

- - - [All jobs](#)
 -
 - [Part-time Laboratory Assistant](#)

[Oklahoma Medical Research Foundation \(OMRF\)](#)

[Oklahoma City, United States](#)

[JOB POST](#)

- [Assistant Professor of Teaching \(Tenure Track\)](#)

[The University of British Columbia \(UBC\)](#)

[Vancouver, Canada](#)

[JOB POST](#)

▪ **Principal Researcher / Senior Researcher**

Korea Brain Research Institute (KBRI)

Daegu, Korea, South

JOB POST

▪ **PhD Scholarship within Phosphorus Turnover in Lakes and Wetlands**

University of Southern Denmark (SDU)

Odense M, Denmark

JOB POST

This article was downloaded by **calibre** from <https://www.nature.com/articles/d41586-020-03235-y>.

| [Section menu](#) | [Main menu](#) |

WHERE I WORK
23 November 2020

Flame thrower

Fire-safety researcher Luke Bisby investigates which materials can take the heat.

Kendall Powell

Kendall Powell is a science journalist in Boulder, Colorado.

Search for this author in:

- [Pub Med](#)
- [Nature.com](#)
- [Google Scholar](#)



Luke Bisby stands in his lab at University of Edinburgh.

Luke Bisby is a structural engineer and fire-safety researcher at the University of Edinburgh, UK. Credit: Kieran Dodds for *Nature*

As chair of fire and structures at the University of Edinburgh, UK, I work in three laboratory spaces. We do everything from small-scale experiments on various building materials to see how easily they ignite or spread fire, to large-scale analyses of the load-bearing systems of skyscrapers using complex computer simulations. Around 2008, my group moved into fire science — the study of how things burn, from ignition to growth of the fire and all of the underlying physics.

There's a trend towards using engineered timber for buildings because, as a material, it is considered more sustainable, and it takes less carbon to produce than does concrete, steel or masonry. But, unlike those materials,

timber burns. This is a total change of philosophy in modern construction, because the building itself is made out of fuel.

Here, I'm standing where we set stuff on fire beneath a large steel ventilation hood. We might burn sofas or Christmas trees to understand their combustion. We measure how much energy is produced (fires have a wattage, like a light bulb), the heat-release rate, the toxicity of gases coming off and the opacity of the smoke. It's important to know the amount and rate of heat energy that is released because that tells you whether the fire's likely to spread: how much heat does it take to ignite a nearby object?

I'm behind a 'fire sword' — a stainless-steel pipe with holes to vent propane gas. It allows us to expose objects to impinging flames while controlling the flames' direction and magnitude, and we can measure the amount of energy we are putting into the system. Then, we can calculate how dangerous the burning object is.

Ultimately, we're studying fire to prevent tragedy. That image of a kid holding a stick in a campfire until it catches, pulling it out until it stops burning and then plunging it in again? That's fundamentally the question we're studying in timber buildings: how much heat is too much?

Nature 587, 694 (2020)

doi: <https://doi.org/10.1038/d41586-020-03292-3>

Jobs from Nature Careers

- - - [All jobs](#)
 - - [Part-time Laboratory Assistant](#)

[Oklahoma Medical Research Foundation \(OMRF\)](#)

[Oklahoma City, United States](#)

JOB POST

- **Assistant Professor of Teaching (Tenure Track)**

The University of British Columbia (UBC)

Vancouver, Canada

JOB POST

- **Principal Researcher / Senior Researcher**

Korea Brain Research Institute (KBRI)

Daegu, Korea, South

JOB POST

- **PhD Scholarship within Phosphorus Turnover in Lakes and Wetlands**

University of Southern Denmark (SDU)

Odense M, Denmark

JOB POST

This article was downloaded by **calibre** from <https://www.nature.com/articles/d41586-020-03292-3>

Research

- **Genetic variability of memory performance is explained by differences in the brain's thalamus** [16 November 2020]
News & Views • An innovative approach has been used to link genetics to behaviour in mice. The analysis reveals that the gene Gpr12 underpins the role of the brain's thalamus region in maintaining short-term memory.
- **Neutrino detection gets to the core of the Sun** [25 November 2020]
News & Views • The first detection of neutrinos produced by the Sun's secondary solar-fusion cycle paves the way for a detailed understanding of the structure of the Sun and of the formation of massive stars.
- **Neanderthal DNA highlights complexity of COVID risk factors** [26 October 2020]
News & Views • A genetic analysis reveals that some people who have severe reactions to the SARS-CoV-2 virus inherited certain sections of their DNA from Neanderthals. However, our ancestors can't take all the blame for how someone responds to the virus.
- **Isoforms of GPCR proteins combine for diverse signalling** [04 November 2020]
News & Views • Many receptor proteins of the GPCR family exist in multiple isoforms. A comprehensive analysis of different combinations of GPCR isoforms that produce diverse signalling patterns in cells has implications for drug development.
- **Fibrosis: from mechanisms to medicines** [25 November 2020]
Review Article • This review discusses how single-cell profiling and other technological advances are increasing our understanding of the mechanisms of fibrosis, thereby accelerating the discovery, development and testing of new treatments.
- **Discoveries in structure and physiology of mechanically activated ion channels** [25 November 2020]
Review Article • This Review summarizes developments in the field of mechanically activated ion channels, which have been driven by the increasing breadth of structural studies.
- **Experimental evidence of neutrinos produced in the CNO fusion cycle in the Sun** [25 November 2020]
Article • Direct experimental evidence of the carbon–nitrogen–oxygen fusion cycle in the Sun is provided by the detection of neutrinos emitted during this process.

- **Observing the emergence of a quantum phase transition shell by shell** [25 November 2020]
Article • An atomic simulator formed of a few ultracold fermionic atoms trapped in a two-dimensional harmonic potential exhibits precursors of a quantum phase transition, revealing the onset of collective quantum many-body phenomena in a few-body system.
- **Spin-enhanced nanodiamond biosensing for ultrasensitive diagnostics** [25 November 2020]
Article • Lateral-flow in vitro diagnostic assays based on fluorescent nanodiamonds, in which microwave-based spin manipulation is used to increase sensitivity, are demonstrated using the biotin–avidin model and by the single-copy detection of HIV-1 RNA.
- **Lanthanide-doped inorganic nanoparticles turn molecular triplet excitons bright** [25 November 2020]
Article • Optically dark (non-emitting) triplet excitons on organic molecules may be rendered bright by coupling the molecules to lanthanide-doped nanoparticles, providing a way to control such excitons in optoelectronic systems.
- **Antarctic ice dynamics amplified by Northern Hemisphere sea-level forcing** [25 November 2020]
Article • Changes in Northern Hemisphere ice-sheet size during ice-age cycles enhance the advance and retreat of the grounding line of the Antarctic Ice Sheet, owing to interhemispheric sea-level forcing.
- **Sensory pollutants alter bird phenology and fitness across a continent** [11 November 2020]
Article • Human-generated noise and night lighting affect breeding habits and fitness in birds, implying that sensory pollutants must be considered alongside other environmental factors in assessing biodiversity conservation.
- **The major genetic risk factor for severe COVID-19 is inherited from Neanderthals** [30 September 2020]
Article • Risk of severe COVID-19 is conferred by a genomic segment that is inherited from Neanderthals and is carried by around 50% and 16% of people in south Asia and Europe, respectively.
- **Microglia-organized scar-free spinal cord repair in neonatal mice** [07 October 2020]
Article • In neonatal mice, scar-free healing after spinal cord injury is organized by microglia, and transplantation of neonatal microglia or peptidase-inhibitor-treated adult microglia into adult mice after injury improves healing and axon regrowth.
- **A molecular cell atlas of the human lung from single-cell RNA sequencing** [18 November 2020]

Article • Expression profiling on 75,000 single cells creates a comprehensive cell atlas of the human lung that includes 41 out of 45 previously known cell types and 14 new ones.

- **Macrophage-derived glutamine boosts satellite cells and muscle regeneration** [28 October 2020]

Article • Mouse models of muscle injuries and ageing characterized by low levels of intra-tissue glutamine are ameliorated by macrophage-specific deletion or systemic pharmacological inhibition of glutamate dehydrogenase 1, which results in constitutively high activity of glutamine synthetase.

- **DNA targeting and interference by a bacterial Argonaute nuclease** [30 July 2020]

Article • Argonaute protein from the bacterium *C. butyricum* targets multicopy genetic elements and functions in the suppression of plasmid and phage propagation, and there appears to be a DNA-mediated immunity pathway in prokaryotes.

- **Host ANP32A mediates the assembly of the influenza virus replicase** [18 November 2020]

Article • Structural and biochemical studies of influenza virus RNA polymerase in complex with host acidic nuclear phosphoprotein 32 (ANP32) show how ANP32-mediated polymerase dimerization enables the replication of influenza viral RNA in a host-dependent manner.

- **Cell-type-specific 3D epigenomes in the developing human cortex** [14 October 2020]

Article • Analysis of cis-regulatory chromatin interactions, open chromatin and transcriptomes for different cell types isolated from mid-gestational human cortex samples provides insights into gene regulation during development.

- **Combinatorial expression of GPCR isoforms affects signalling and drug responses** [04 November 2020]

Article • Transcriptomics, proteomics, single-cell RNA sequencing, population-wide genetic association studies and structure–function analyses provide a picture of how the differential expression of G-protein-coupled receptor isoforms can diversify signalling in different tissues.

- **Papain-like protease regulates SARS-CoV-2 viral spread and innate immunity** [29 July 2020]

Article • Biochemical, structural and functional studies on the severe acute respiratory syndrome coronavirus 2 (SARS-CoV-2) papain-like protease PLpro reveal that it regulates host antiviral responses by preferentially cleaving the ubiquitin-like interferon-stimulated gene 15 protein (ISG15) and identify this protease as a potential therapeutic target for coronavirus disease 2019 (COVID-19).

- **Site-specific RNA methylation by a methyltransferase ribozyme** [28 October 2020]

Article • A methyltransferase ribozyme, along with the small-molecule cofactor O6-methylguanine, is shown to catalyse the site-specific installation of 1-methyladenosine in various RNAs, providing insights into the catalytic abilities of RNA.

- **Structural mechanism of cGAS inhibition by the nucleosome** [10 September 2020]

Article • Using cryo-electron microscopy, the authors determine the structure of cGAS bound to nucleosomes and present evidence for the mechanism by which nucleosome binding to cGAS prevents cGAS dimerization and its binding to free double-stranded DNA.

- **The molecular basis of tight nuclear tethering and inactivation of cGAS** [10 September 2020]

Article • Structural studies show that cyclic GMP–AMP synthase binds to nucleosomes through its DNA-binding site, which maintains it in an inactive conformation and prevents self-DNA binding.

- **Structural basis for sequestration and autoinhibition of cGAS by chromatin** [10 September 2020]

Article • Biochemical and structural analyses show how tethering of the nucleotidyltransferase cGAS to chromatin prevents autoimmune recognition of nuclear DNA.

- **Structural basis for the final steps of human 40S ribosome maturation** [18 November 2020]

Article • Studies of five cryo-electron microscopy structures reveal the composition and conformational progression in the final maturation events of human 40S ribosomal subunit assembly.

NEWS AND VIEWS

16 November 2020

Genetic variability of memory performance is explained by differences in the brain's thalamus

An innovative approach has been used to link genetics to behaviour in mice. The analysis reveals that the gene *Gpr12* underpins the role of the brain's thalamus region in maintaining short-term memory.

Michael M. Halassa

Michael M. Halassa is at the McGovern Institute and in the Department of Brain and Cognitive Sciences, Massachusetts Institute of Technology, Cambridge, Massachusetts 02139, USA.

[Contact](#)

Search for this author in:

- [Pub Med](#)
- [Nature.com](#)
- [Google Scholar](#)

The brain's thalamus has historically been thought of as a relay centre that transmits sensory and motor inputs to the cortex for processing, or that transmits information from one part of the cortex to another. In 2017, three groups made the unexpected discovery that the thalamus also has a key role in short-term memory — specifically, in maintaining the recurrent patterns of cortical activity that underlie memory^{1–3}. However, the genetic basis of this role for the thalamus remained unexplored. [Writing in Cell](#), Hsiao *et al.*⁴ reveal that the gene *Gpr12* is key to thalamic maintenance of short-term

memory. Their findings will have relevance for many fields, from cognitive therapeutics to artificial intelligence.

[Read the paper: A Thalamic Orphan Receptor Drives Variability in Short-Term Memory](#)

Perhaps one of the biggest scientific challenges of our time is explaining how intelligent behaviour arises in both natural and artificial systems. Resolving this question will have practical applications. For natural systems, it could allow us to describe and correct behavioural disorders with unprecedented precision. For artificial systems, it would enable safe distribution of agents that will enhance many aspects of our lives, from controlling self-driving cars to fighting misinformation.

Many parallels can be drawn between the two system types, but there are also many differences. For instance, unlike a typical artificial system, the mammalian brain contains organized networks of tight reciprocal connections between two distinct components — the thalamus and the cortex. These two components have different internal structures: neurons in the cortex are highly interconnected, whereas thalamic neurons are not.

In artificial systems, recurrent neural networks can produce short-term memory patterns⁵. The cortex, at some level of abstraction, can be considered as a collection of recurrent networks that handles different types of short-term memory. So the question arises: why is a thalamus needed in the midst of all of this?

An understanding of the molecular mechanisms that regulate thalamocortical circuits might help us to tackle this question. But identifying genes associated with cognitive processes is hard, because genetic mapping requires many repeated measurements, which can be difficult to obtain from behavioural studies. Hsiao *et al.* used an innovative

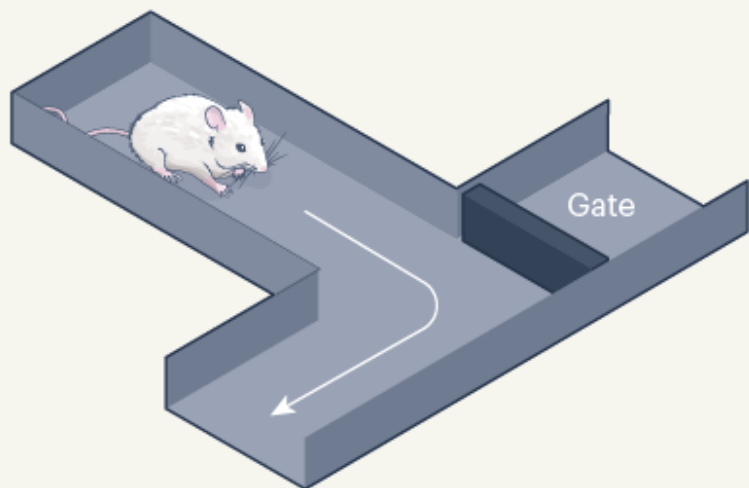
approach to overcome this obstacle, making use of a method called quantitative trait locus (QTL) analysis that can link traits (such as eye colour, height or propensity to develop a given disease) to specific locations in the genome, or even to specific genes⁶.

The team tested the working memory of mice using a simple behavioural task — a maze test, in which the animals explored arms of a T-shaped maze at will. If they chose to explore arms they had not previously visited, they passed the test, whereas if they returned to familiar arms, they failed. The authors found that performance varied between mouse strains, which they reasoned might be partly explained by the ability of individual animals to keep previous actions in mind as short-term memory patterns.

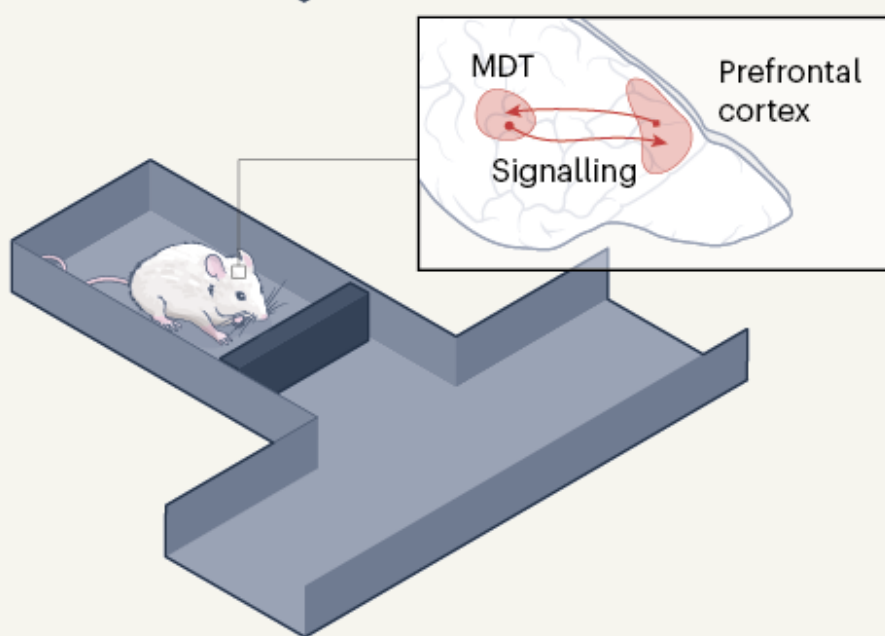
The researchers performed QTL analysis, and found one genetic region that stood out as different between the various strains of mice; they named this region *Smart1* (short for spontaneous T-maze alternation QTL 1). In particular, animals that had one particular DNA sequence at *Smart1* (dubbed *Smart1*^{CAST}) were especially good at the exploratory task, and those with another (*Smart1*^{B6}) were especially poor.

Having identified this region, Hsiao and colleagues confirmed their findings from the high-throughput behavioural test using a similar but more-complex maze assay designed to test spatial working memory. In this assay, which used fewer animals, mice had to remember which arm of a maze they had visited on a first visit, and choose to visit the other arm to get a reward on a second visit (Fig. 1). Again, *Smart1*^{CAST} and *Smart1*^{B6} animals performed better or worse, respectively, than the group as a whole.

a Sample



b Delay



c Choice

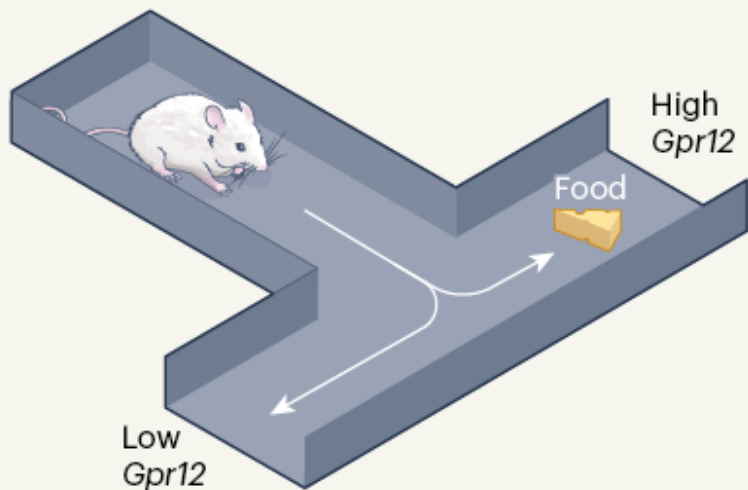


Figure 1 | A gene involved in short-term memory. Hsiao *et al.*⁴ report that variability in expression of the gene *Gpr12* in the thalamus of the mouse brain leads to variability in how well animals can keep short-term memory patterns in mind. The authors verified this finding using a working-memory task. **a**, Animals were placed in a T-shaped maze. In the initial sample phase of the test, one arm was gated off at random, allowing the animals to enter the other arm. **b**, During the delay between the first and second parts of the task, reciprocal signalling between the brain's prefrontal cortex and mediolateral thalamus (MDT) becomes synchronized. **c**, The animals had been trained to know that, in the second part of the task, they could retrieve a food reward by visiting the previously unexplored arm. Those that expressed high levels of the gene *Gpr12* in the MDT were good at remembering which arm they had visited, and so choosing the arm that contained the reward. By contrast, those with low *Gpr12* expression performed poorly.

Next, Hsiao *et al.* examined gene-expression patterns across several brain regions in these two mouse strains. The most significant differences between the two were in the mediiodorsal thalamus, in expression of a gene called *Gpr12* that is located in *Smart1*. This brain region is strongly connected to the prefrontal cortex, which is involved in higher-level cognitive functions such as working memory. The authors found that reducing expression of *Gpr12* led to poorer task performance in *Smart1^{CAST}* mice, whereas overexpressing the gene improved the performance of *Smart1^{B6}* animals.

Gpr12 encodes a protein belonging to a family known as orphan receptors, in which no ligand molecule that binds to and activates each receptor has been identified. *Gpr12* probably enhances the activity of mediiodorsal thalamus neurons once they are engaged by external inputs (such as those from the prefrontal cortex). Indeed, Hsiao *et al.* found that patterns of neuronal activity in the mediiodorsal thalamus became much more in-sync with those in the prefrontal cortex during those parts of the maze test when animals were presumably remembering where they had been on the previous maze run.

Hsiao and colleagues' work provides key evidence to reinforce the conclusions of the 2017 papers^{1–3}. Their findings also indicate that coordinated thalamocortical activity patterns depend on the version of *Smart1* present: the more *Gpr12* is expressed from this region, the more thalamocortical coordination occurs and the better the performance of spatial working memory.

The discovery of this role for *Gpr12* could lead to the development of pharmacological agents that boost working-memory performance. However, it would be important to first determine the types of cortical activity pattern that are enhanced by thalamic *Gpr12*. For example, in tasks in which animals have to withhold actions while remembering a task-relevant piece of information^{2,7,8}, would we see the same type of effect?

It is also intriguing to speculate on what other types of cognitive function could be linked to genetic underpinnings using a QTL approach. The mediodorsal thalamus is known to be involved in switching between tasks^{9,10}; could one find a simple and scalable behavioural test that could be used to assess this process and probe its genetic underpinnings?

Finally, to return to the comparison between natural and artificial systems, is the lack of a thalamus-like architecture in most artificial models of intelligence a missed opportunity? On the one hand, artificial recurrent neural networks require no such structure to maintain memory patterns or switch them across tasks. On the other, perhaps incorporating this biological inspiration into artificial-intelligence systems would enable us to expand their computational capabilities, power efficiency or both. It is exciting to think about the many possibilities ahead as we continue to draw biological inspiration from innovative work such as that of Hsiao and colleagues.

Nature 587, 549-550 (2020)

doi: <https://doi.org/10.1038/d41586-020-03195-3>

References

1. 1.

Bolkan, S. S. *et al.* *Nature Neurosci.* **20**, 987–996 (2017).

2. 2.

Guo, Z. V. *et al.* *Nature* **545**, 181–186 (2017).

3. 3.

Schmitt, L. I. *et al.* *Nature* **545**, 219–223 (2017).

4. 4.

Hsiao, K. *et al.* *Cell* **183**, 522–536 (2020).

5. 5.

Barak, O. *Curr. Opin. Neurobiol.* **46**, 1–6 (2017).

6. 6.

Miles, C. M. & Wayne, M. *Nature Educ.* **1**, 208 (2008).

7. 7.

Akrami, A., Kopec, C. D., Diamond, M. E. & Brody, C. D. *Nature* **554**, 368–372 (2018).

8. 8.

Wimmer, R. *et al.* *Nature* **526**, 705–709 (2015).

9. 9.

Chakraborty, S., Kolling, N., Walton, M. E. & Mitchell, A. S. *eLife* **5**, e13588 (2016).

10. 10.

Rikhye, R. V., Gilra, A. & Halassa, M. M. *Nature Neurosci.* **21**, 1753–1763 (2018).

Jobs from Nature Careers

- - - [All jobs](#)
 - - [Part-time Laboratory Assistant](#)

[Oklahoma Medical Research Foundation \(OMRF\)](#)

[Oklahoma City, United States](#)

[JOB POST](#)
 - [Assistant Professor of Teaching \(Tenure Track\)](#)

[The University of British Columbia \(UBC\)](#)

[Vancouver, Canada](#)

[JOB POST](#)
 - [Principal Researcher / Senior Researcher](#)

[Korea Brain Research Institute \(KBRI\)](#)

[Daegu, Korea, South](#)

[JOB POST](#)
 - [PhD Scholarship within Phosphorus Turnover in Lakes and Wetlands](#)

University of Southern Denmark (SDU)

Odense M, Denmark

JOB POST

This article was downloaded by **calibre** from <https://www.nature.com/articles/d41586-020-03195-3>

| [Section menu](#) | [Main menu](#) |

NEWS AND VIEWS

25 November 2020

Neutrino detection gets to the core of the Sun

The first detection of neutrinos produced by the Sun's secondary solar-fusion cycle paves the way for a detailed understanding of the structure of the Sun and of the formation of massive stars.

Gabriel D. Orebi Gann

Gabriel D. Orebi Gann is in the Department of Physics, University of California, Berkeley, Berkeley, California 94720, USA, and at the Lawrence Berkeley National Laboratory.

[Contact](#)

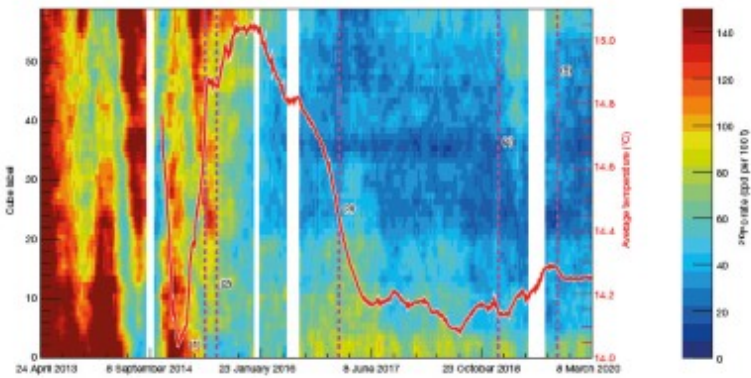
Search for this author in:

- [Pub Med](#)
- [Nature.com](#)
- [Google Scholar](#)

[Writing in Nature](#), the Borexino Collaboration¹ reports results that blast past a milestone in neutrino physics. They have detected solar neutrinos produced by a cycle of nuclear-fusion reactions known as the carbon–nitrogen–oxygen (CNO) cycle. Measurements of these neutrinos have the potential to resolve uncertainties about the composition of the solar core, and offer crucial insights into the formation of heavy stars.

Neutrinos are tiny, subatomic particles. They were first postulated to exist by Wolfgang Pauli in 1930, to account for the energy that was apparently missing during β -decay, a process in which energetic electrons are emitted

from an atomic nucleus. The presence of a massless particle that could carry any fraction of the energy from the decay would explain why the spectrum of emitted electron energies is continuous. Pauli's explanation for why neutrinos had never been observed was that they interact incredibly weakly with matter. Subsequent decades of research have yielded a wealth of information about Pauli's 'ghost particle', including the Nobel-prizewinning discovery that neutrinos do, in fact, have a mass^{2–4}, albeit one so small as to be beyond the reach of current measurements.



Read the paper: Experimental evidence of neutrinos produced in the CNO fusion cycle in the Sun

Fusion reactions in the Sun produce an astonishing number of neutrinos: roughly 100 billion solar neutrinos pass through each of your thumbnails every second. Because of the weakness of their interactions, they are barely deterred from their path even when they have to pass through the entire body of the Earth: cutting-edge experiments⁵ (see also go.nature.com/36sktyj) have struggled to observe a difference in the measured neutrino flux between daytime and night-time, owing to the vanishingly small scale of this effect.

Neutrinos are therefore both challenging to observe and yet able to offer insights into other-wise unreachable regions of the Universe, such as distant supernovae or the interiors of stars. Energy produced in the centre of the Sun in the form of photons takes tens of thousands of years to escape, but a solar neutrino can escape the Sun and reach Earth in just eight minutes. This gives us a unique window into the core of this blazing star.

The Sun is powered by fusion reactions that occur in its core: in the intense heat of this highly pressurized environment, protons fuse together to form helium. This occurs in two distinct cycles of nuclear reactions. The first is called the proton–proton chain (or *pp* chain), and dominates energy production in stars the size of our Sun. The second is the CNO cycle, which accounts for roughly 1% of solar power, but dominates energy production in heavier stars⁶.

The first experiment to detect solar neutrinos was carried out using a detector in Homestake Mine, South Dakota. This used measurements of *pp*-chain solar neutrinos to probe the Standard Solar Model (SSM), which describes nuclear fusion in the Sun. The surprising result from this experiment was that only approximately one-third as many neutrinos of the expected type (flavour) were detected⁷.

A decades-long campaign of experiments followed, seeking to resolve this ‘solar neutrino problem’. Nobel-prizewinning results from the Sudbury Neutrino Observatory in Ontario, Canada, eventually explained the deficit: the neutrinos were changing flavour between their production and detection³. The Borexino experiment at the Gran Sasso National Laboratory in Italy followed up this result with a full spectral analysis of neutrinos from many stages of the *pp* chain⁸. This analysis finally allowed the field to come full circle, re-opening the possibility of using solar neutrinos as a means of probing the Sun’s interior.

The Borexino Collaboration now reports another groundbreaking achievement from its experiment: the first detection of neutrinos from the CNO cycle. This result is a huge leap forward, offering the chance to resolve the mystery of the elemental composition of the Sun’s core. In astrophysics, any element heavier than helium is termed a metal. The exact metal content (the metallicity) of a star’s core affects the rate of the CNO cycle. This, in

turn, influences the temperature and density profile — and thus the evolution — of the star, as well as the opacity of its outer layers.

The metallicity and opacity of the Sun affect the speed of sound waves propagating through its volume. For decades, helio-seismological measurements were in agreement with SSM predictions for the speed of sound in the Sun, giving confidence in that model. However, more-recent spectroscopic measurements of solar opacity produced results that were significantly lower than previously thought, leading to discrepancies with the helio-seismological data⁹. Precise measurements of CNO-cycle neutrinos offer the only independent handle by which to investigate this difference. Such measurements would also shed further light on stellar evolution.

The chief obstacles to making these measurements are the low energy and flux of CNO neutrinos, and the difficulty of separating the neutrino signal from sources of background signals, such as radioactive-decay processes. The Borexino experiment detects light produced when solar neutrinos scatter off electrons in a large vat of liquid scintillator — a medium that produces light in response to the passage of charged particles. A precise measurement of the energy and time profile of the detected light allows the scintillation caused by solar neutrinos to be differentiated from light resulting from other sources, such as radio-active contamination in the scintillator itself and in surrounding detector components.

The Borexino Collaboration carried out a multi-year purification campaign to ensure unprecedentedly low levels of radioactive contaminants in the scintillator. Even so, minor convection currents caused by temperature variations allowed radioactive contaminants to diffuse from the outer edges of the detector. The researchers mitigated this effect by establishing exquisitely fine control of thermal variations in the detector (Fig. 1), thus allowing them to achieve the extremely challenging feat of detecting CNO neutrinos. The resulting measurements are not yet precise enough to resolve the question of solar metallicity, but they offer a path towards this objective.



Figure 1 | The Borexino neutrino detector. The Borexino experiment detects light produced when solar neutrinos scatter off electrons in a large vat of liquid scintillator — a medium that produces light in response to the passage of charged particles. The Borexino Collaboration wrapped the detector in thermal insulation to control temperature variations in the detector. This helped the team to take the highly precise measurements needed to detect solar neutrinos produced by the Sun’s secondary solar-fusion cycle¹. Source: Ref. 1

Future experiments will seek to improve on the precision achieved by Borexino, by developing innovative methods to identify and reject background noise caused by radioactive contamination. In the meantime, the Borexino Collaboration’s tremendous accomplishment moves us closer to a complete understanding of our Sun, and of the formation of massive stars, and is likely to define the goal in this field for years to come.

Nature 587, 550-552 (2020)

doi: <https://doi.org/10.1038/d41586-020-03238-9>

References

1. 1.

The Borexino Collaboration. *Nature* **587**, 577–582 (2020).

2. 2.

Ahmad, Q. R. *Phys. Rev. Lett.* **87**, 071301 (2001).

3. 3.

Ahmad, Q. R. *Phys. Rev. Lett.* **89**, 011301 (2002).

4. 4.

Ashie, Y. *et al.* *Phys. Rev. D* **71**, 112005 (2005).

5. 5.

Aharmim, B. *et al.* *Phys. Rev. C* **72**, 055502 (2005).

6. 6.

Adelberger, E. G. *et al.* *Rev. Mod. Phys.* **83**, 195 (2011).

7. 7.

Davis, R. Jr, Harmer, D. S. & Hoffman, K. C. *Phys. Rev. Lett.* **20**, 1205 (1968).

8. 8.

Agostini, M. *et al.* *Nature* **562**, 505–510 (2018).

9. 9.

Asplund, M., Grevesse, N., Sauval, A. J. & Scott, P. *Annu. Rev. Astron. Astrophys.* **47**, 481–522 (2009).

Jobs from Nature Careers

- - - [All jobs](#)
 - - [Part-time Laboratory Assistant](#)

[Oklahoma Medical Research Foundation \(OMRF\)](#)

[Oklahoma City, United States](#)

[JOB POST](#)
 - [Assistant Professor of Teaching \(Tenure Track\)](#)

[The University of British Columbia \(UBC\)](#)

[Vancouver, Canada](#)

[JOB POST](#)
 - [Principal Researcher / Senior Researcher](#)

[Korea Brain Research Institute \(KBRI\)](#)

[Daegu, Korea, South](#)

[JOB POST](#)
 - [PhD Scholarship within Phosphorus Turnover in Lakes and Wetlands](#)

[University of Southern Denmark \(SDU\)](#)

[Odense M, Denmark](#)

JOB POST

This article was downloaded by **calibre** from <https://www.nature.com/articles/d41586-020-03238-9>

| [Section menu](#) | [Main menu](#) |

NEWS AND VIEWS

26 October 2020

Neanderthal DNA highlights complexity of COVID risk factors

A genetic analysis reveals that some people who have severe reactions to the SARS-CoV-2 virus inherited certain sections of their DNA from Neanderthals. However, our ancestors can't take all the blame for how someone responds to the virus.

Yang Luo

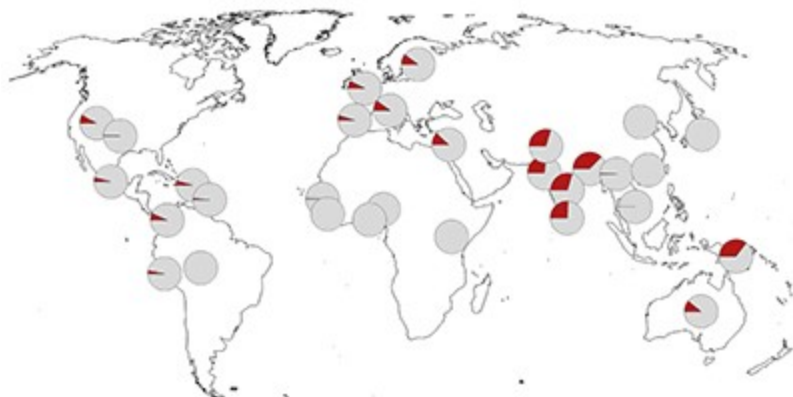
Yang Luo is in the Department of Genetics, Harvard Medical School, Boston, Massachusetts 02115, USA.

[Contact](#)

Search for this author in:

- [Pub Med](#)
- [Nature.com](#)
- [Google Scholar](#)

A key part of tackling COVID-19 is understanding why some people experience more-severe symptoms than do others. Earlier this year, a segment of DNA 50,000 nucleotides long (corresponding to 0.002% of the human genome) was found to have a strong association with severe COVID-19 infection and hospitalization¹. Writing in *Nature*, Zeberg and Pääbo² report that this region is inherited from Neanderthals. Their results not only shed light on one reason that some people are more susceptible to severe disease, but also provide insights into human evolutionary biology.



Read the paper: The major genetic risk factor for severe COVID-19 is inherited from Neanderthals

DNA sequences that are physically close to one other in the genome are often inherited (linked) together. These blocks of DNA, known as haplotypes, therefore contain tightly linked variants — DNA sequences or nucleotides that vary between individuals in a population. For example, the COVID-19 risk haplotype described earlier this year¹ harbours variants across its entire 50,000-nucleotide span that are inherited together more than 98% of the time. Long haplotypes such as this could be a result of positive selection, maintained in our genomes because they contributed to our species' chances of survival and reproductive success. They could also be introduced as a result of interbreeding with archaic hominin species such as the Denisovans and Neanderthals.

Some 1–4% of the modern human genome comes from these ancient relatives³. Many of the surviving archaic genes are harmful to modern humans, and are associated with infertility and an increased risk of disease⁴.

But a few are beneficial. Examples include the Denisovan-like version of a gene called *EPAS1* that helps modern Tibetans to cope with life at extremely high altitudes⁵, a Neanderthal gene that increases our sensitivity to pain⁶ and others that help us fend off viruses⁷.

To investigate whether the COVID-19 risk haplotype might have been introduced from our ancient relatives, Zeberg and Pääbo compared the region with an online database of archaic genomes from around the world. They found the region to be closely related to that in the genome of a Neanderthal individual that lived in modern-day Croatia around 50,000 years ago, but it was not related to any known Denisovan genomes.

The authors next checked the prevalence of the Neanderthal-derived haplotype in the modern human population. They report that it is rare or completely absent in east Asians and Africans. Among Latin Americans and Europeans, the risk haplotype is maintained at a modest frequency (4% and 8%, respectively). By contrast, the haplotype occurs at a frequency of 30% in individuals who have south Asian ancestry, reaching as high as 37% in those with Bangladeshi heritage (Fig. 1).

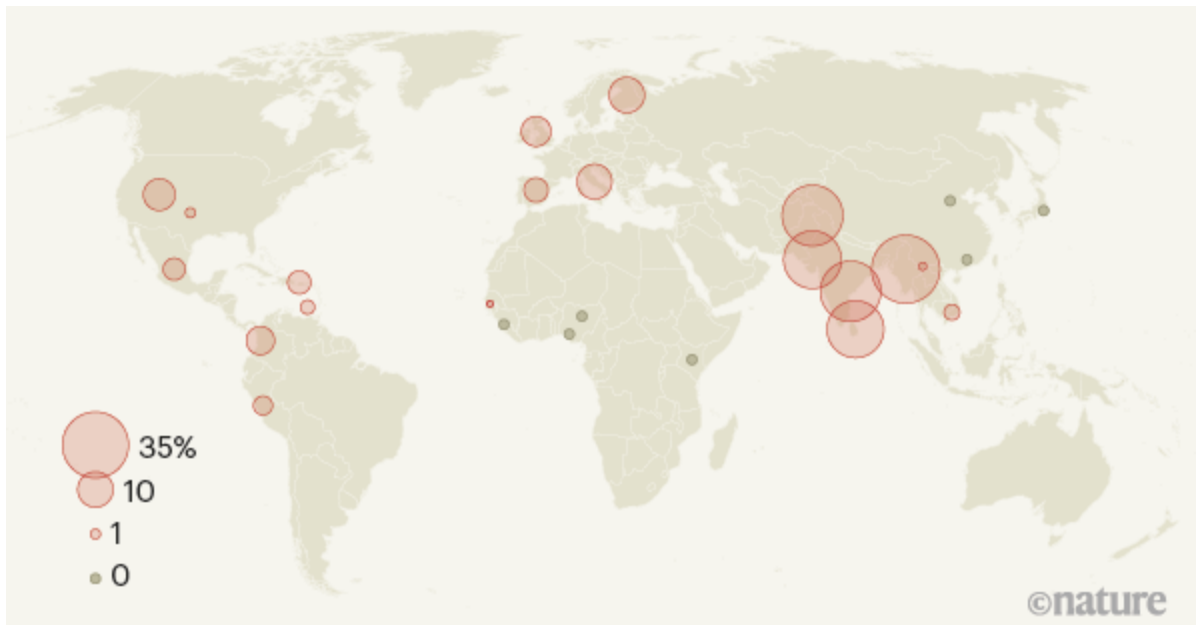
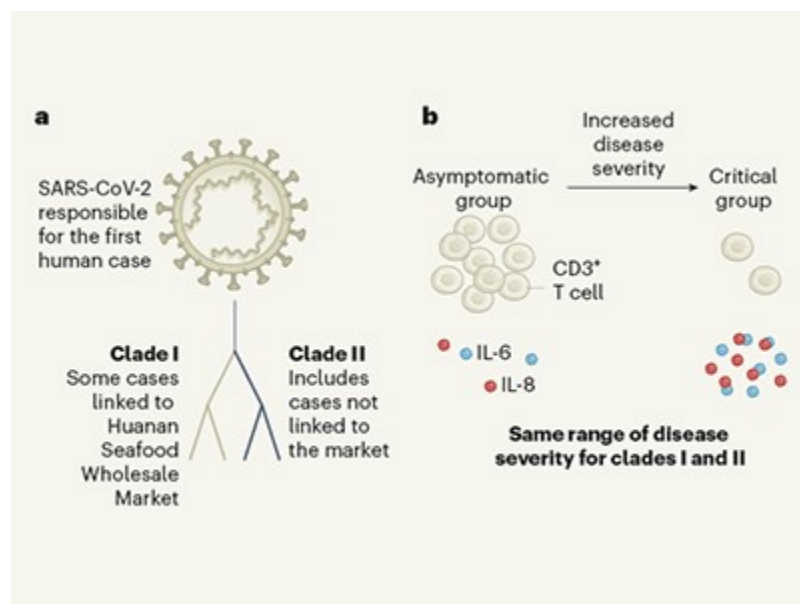


Figure 1 | Uneven global spread of a genetic risk factor for COVID-19. Zeberg and Pääbo² report that a long sequence of DNA that is associated with severe COVID-19 infection and hospitalization is derived from

Neanderthals. The sequence is unevenly distributed across modern human populations. This map shows the frequency at which the risk factor is found in various populations from around the world. The sequencing data for these populations were gathered by the 1000 Genomes Project¹⁰. (Adapted from Fig. 3 of ref. 2.)

The researchers therefore speculate that the Neanderthal-derived haplotype is a substantial contributor to COVID-19 risk in specific groups. Their hypothesis is supported by hospital data⁸ from the Office for National Statistics in the United Kingdom, which indicates that individuals of Bangladeshi origin in the country are twice as likely to die from COVID-19 as are members of the general population (although other risk factors will, of course, contribute to these statistics).

Why has this haplotype been retained in some populations? The authors posit that it might be protective against other ancient pathogens, and therefore positively selected for in certain populations around the world⁹. But when individuals are infected with the SARS-CoV-2 coronavirus, the protective immune response mediated by these ancient genes might be overly aggressive, leading to the potentially fatal immune response observed in people who develop severe COVID-19 symptoms. As a result, a haplotype that at times in our past might have been beneficial for survival could now be having an adverse effect.



A race to determine what drives COVID-19 severity

Despite the correlation between this risk haplotype and clinical outcomes, genetics alone do not determine a person's risk of developing severe COVID-19. Our genes and their origins clearly influence the development and progression of COVID-19 (and other infectious diseases), but environmental factors also have key roles in disease outcomes.

For example, although the Neanderthal-derived risk haplotype is almost completely absent in people with African ancestry, this population has a higher COVID-19 mortality rate than do people of other ethnic backgrounds, even after adjusting for geography and socio-economic factors (see go.nature.com/3jcxezx ('Demographics' tab) and go.nature.com/2h4qfqu, for example). Social inequality and its repercussions seem likely to account for a larger proportion of the risk of COVID-19 death than does Neanderthal-derived DNA.

It is fascinating to think that our ancestor's genetic legacy might be playing a part in the current pandemic. However, the underlying impact of the inherited DNA on the body's response to the virus is unclear. Ongoing global efforts to study associations between our genetics and COVID-19 by analysing more individuals from diverse populations, such as that being undertaken by the COVID-19 Host Genetics Initiative (www.covid19hg.org), will help us to develop a better understanding of the disease's aetiology. It is important to acknowledge that, although genes involved in the COVID-19 response might be inherited, social factors and behaviours (such as social distancing and mask wearing) are in our control, and can effectively reduce the risk of infection.

Nature 587, 552-553 (2020)

doi: <https://doi.org/10.1038/d41586-020-02957-3>

References

1. 1.
The Severe Covid-19 GWAS Group. *N. Engl. J. Med.* **383**, 1522–1534 (2020).
2. 2.
Zeberg, H. & Pääbo, S. *Nature* **587**, 610–612 (2020).
3. 3.
Green, R. E. *et al.* *Science* **328**, 710–722 (2010).
4. 4.
Sankararaman, S. *et al.* *Nature* **507**, 354–357 (2014).
5. 5.
Huerta-Sánchez, E. *et al.* *Nature* **512**, 194–197 (2014).
6. 6.
Zeberg, H. *et al.* *Curr. Biol.* **30**, 3465–3469 (2020).
7. 7.
Enard, D. & Petrov, D. A. *Cell* **175**, 360–371 (2018).
8. 8.
Public Health England. *Disparities in the Risk and Outcomes of COVID-19* (PHE Publs, 2020).
9. 9.
Browning, S. R., Browning, B. L., Zhou, Y., Tucci, S. & Akey, J. M. *Cell* **173**, 53–61 (2018).

10. 10.

The 1000 Genomes Project Consortium. *Nature* **526**, 68–74 (2015).

Jobs from Nature Careers

- - - [All jobs](#)
 -
 - [Part-time Laboratory Assistant](#)
 - [Oklahoma Medical Research Foundation \(OMRF\)](#)
 - [Oklahoma City, United States](#)
 - [JOB POST](#)
 - [Assistant Professor of Teaching \(Tenure Track\)](#)
 - [The University of British Columbia \(UBC\)](#)
 - [Vancouver, Canada](#)
 - [JOB POST](#)
 - [Principal Researcher / Senior Researcher](#)
 - [Korea Brain Research Institute \(KBRI\)](#)
 - [Daegu, Korea, South](#)
 - [JOB POST](#)
 - [PhD Scholarship within Phosphorus Turnover in Lakes and Wetlands](#)

University of Southern Denmark (SDU)

Odense M, Denmark

JOB POST

This article was downloaded by **calibre** from <https://www.nature.com/articles/d41586-020-02957-3>

| [Section menu](#) | [Main menu](#) |

NEWS AND VIEWS

04 November 2020

Isoforms of GPCR proteins combine for diverse signalling

Many receptor proteins of the GPCR family exist in multiple isoforms. A comprehensive analysis of different combinations of GPCR isoforms that produce diverse signalling patterns in cells has implications for drug development.

Joshua C. Snyder &

Joshua C. Snyder is in the Departments of Surgery and Cell Biology, Duke University School of Medicine, Durham, North Carolina 27710, USA.

Search for this author in:

- [Pub Med](#)
- [Nature.com](#)
- [Google Scholar](#)

Sudarshan Rajagopal

Sudarshan Rajagopal is in the Departments of Medicine and Biochemistry, Duke University School of Medicine.

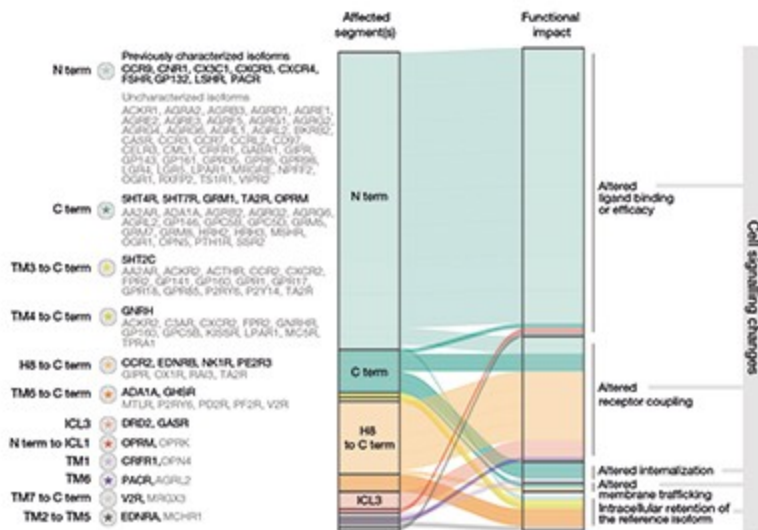
[Contact](#)

Search for this author in:

- [Pub Med](#)
- [Nature.com](#)

- Google Scholar

With more than 800 members¹, the G-protein-coupled receptor (GPCR) superfamily is the largest family of cell-surface receptor proteins in humans. GPCRs trigger intracellular signalling pathways in response to activation by extracellular factors. In doing so, they determine how a cell responds to and interacts with its environment, thereby influencing nearly every aspect of physiology. As such, they are excellent drug targets — at least 475 drugs approved by the US Food and Drug Administration (FDA) are aimed at GPCRs². But many GPCRs exist in multiple isoforms, or variants, complicating attempts to find drugs that can bind to them. [Writing in Nature](#), Marti-Solano *et al.*³ describe a catalogue of the structure and expression of GPCR isoforms in humans. This resource has been added to a GPCR database, called GPCRdb, and is already openly available to the scientific community⁴ (<https://gpcrdb.org/protein/isoforms>).



Read the paper: Combinatorial expression of GPCR isoforms

affects signalling and drug responses

One common hurdle when attempting to design drugs that control GPCR signalling is that the same GPCR can activate multiple intracellular signalling pathways⁵. Pharmacologically altering the receptor's activity can therefore lead to unforeseen side effects. Drugs called biased agonists that target just one pathway downstream of GPCRs have shown great promise^{6,7}. However, they are effective in only some cases — perhaps because the genes that encode GPCRs can be processed in different ways during transcription, producing multiple versions of the final messenger RNA, called splice variants. Through this splicing mechanism, specific domains can be excluded from a GPCR or atypical ones added, producing a range of isoforms. Each one might preferentially activate alternative downstream signalling pathways. So far, our understanding of this key aspect of GPCR biology has been limited to studies of a few isoforms in unnatural settings^{8,9}.

Marti-Solano and colleagues set out to determine how the presence of various isoforms affects the signalling of around 350 GPCRs across tissues of the human body. First, they made use of information about GPCR structures and DNA sequences from GPCRdb to help them identify candidate GPCRs in a database called GTex — a catalogue of gene expression in human tissues. This produced a list of 625 GPCR isoforms, with 38% of GPCRs having more than one.

The group then systematically organized these GPCR isoforms according to their topology. They developed a set of ‘structural fingerprints’ for GPCR isoforms, based on the specific extracellular, intracellular and transmembrane domains present in each one (Fig. 1a). The most common structural fingerprints preserved GPCR topology, and the most frequent changes were seen only in the protein’s extracellular amino terminus or intracellular carboxy terminus. The N-terminal alterations typically caused changes in the binding of ligand molecules or efficacy. By contrast, C-terminal alterations led to changes in the ability of the receptor to couple

with other receptor monomers, or in alterations in the internalization or transport of receptors through the cell inside vesicles — all of which are key to downstream signalling.

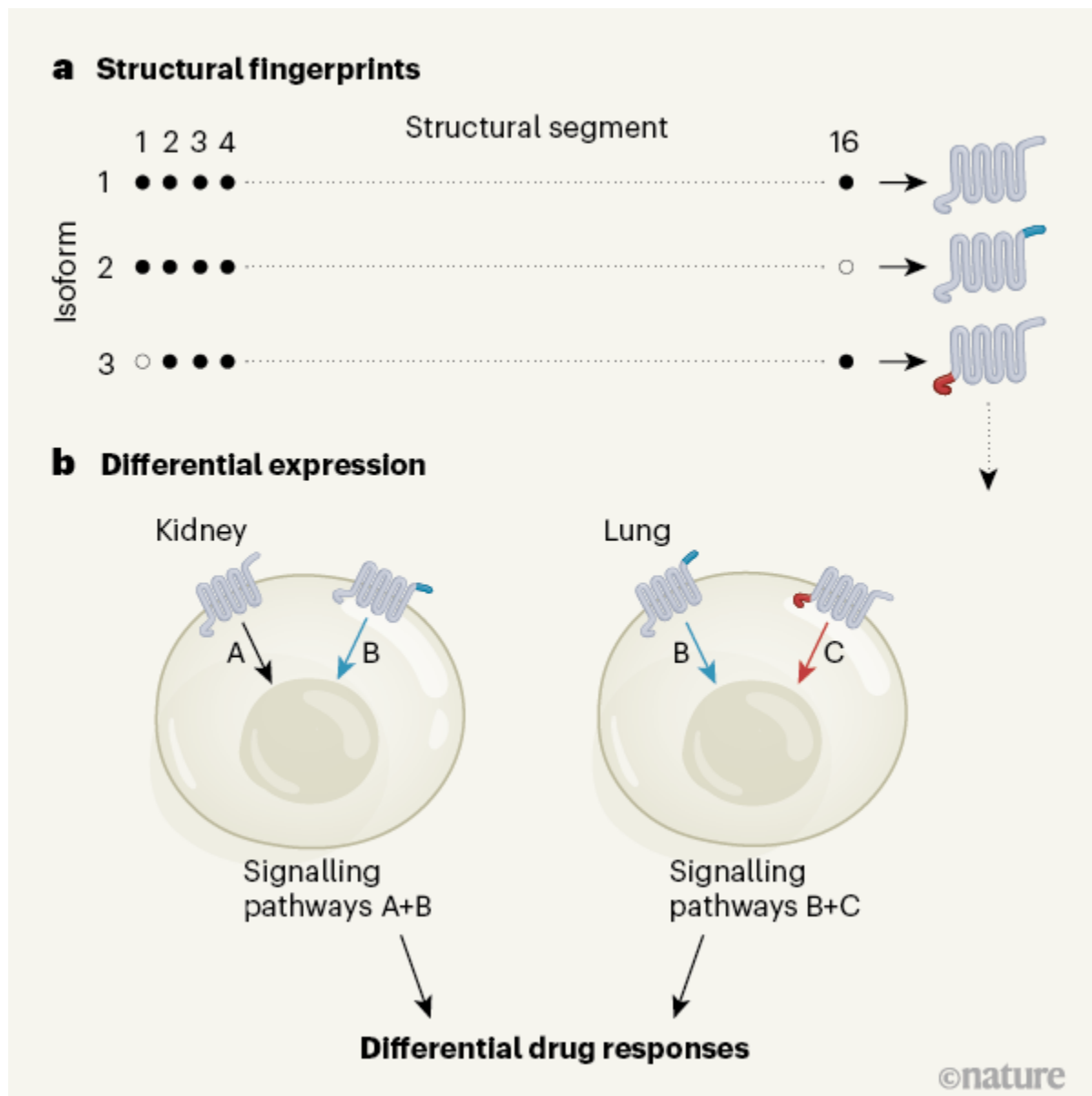


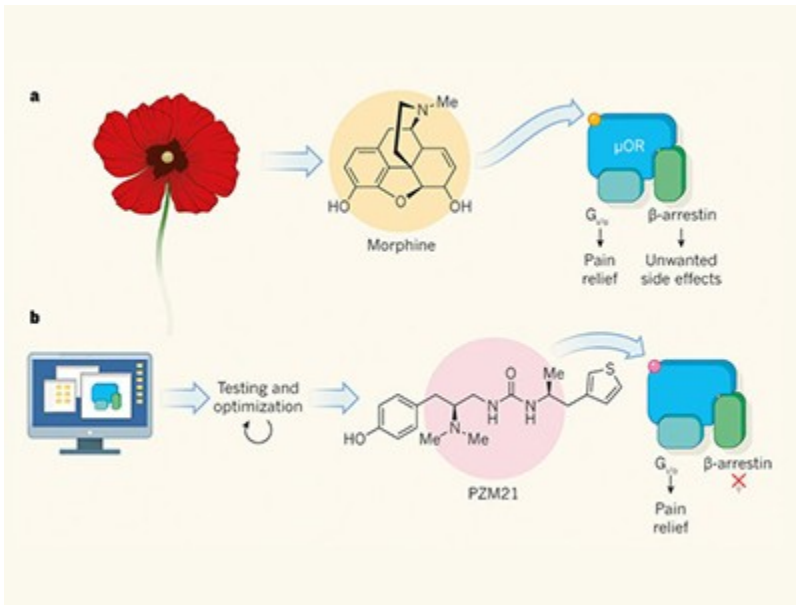
Figure 1 | Cataloguing G-protein coupled receptor (GPCR) isoforms. Martí-Solano *et al.*³ analysed 625 GPCR isoforms expressed across 30 human tissues, and show that there is often more than one isoform of the same receptor in a tissue. **a**, The authors catalogued structural variation between GPCR isoforms by generating structural fingerprints — descriptions of the structural segments included in each isoform (dark

circles indicate segments that are part of a given isoform; empty circles indicate segments that are missing). This simplified schematic shows three isoforms for one imagined GPCR; many more are possible (dashed arrow). **b**, The group shows that these isoforms are expressed in different combinations across tissues. Each combination might activate different downstream signalling pathways, and so respond differently to drugs.

The authors also found a few truncated isoforms, in which transmembrane domains were eliminated. They propose that these decrease receptor signalling. The truncated isoforms might be expressed only inside the cell, where they bind to more-complete versions — isoforms internalized in this way are unable to signal.

Next, to model the potential tissue-specific effects of different isoforms, Marti-Solano *et al.* generated tissue-expression signatures — maps of the expression of each isoform for each receptor across 30 tissues. This revealed different combinations across tissues. The authors confirmed that co-expressing various combinations of isoforms of a given receptor in cells in culture resulted in different patterns of downstream signalling (Fig. 1b). It is not surprising that isoforms have different signalling properties. Nonetheless, the demonstration that co-expression of different isoforms alters signalling suggests a broad mechanism for generating ‘systems bias’¹⁰, in which various tissue-expression signatures promote differential activation of intracellular signalling pathways.

The authors next checked that the tissue-expression signatures they observed truly reflected co-expression of multiple isoforms of a receptor, rather than expression of different isoforms in different cell types within a tissue. They analysed isoform-level expression in various cell lines, as well as data from single-cell RNA sequencing. These assays confirmed that single cells expressed multiple receptor isoforms.



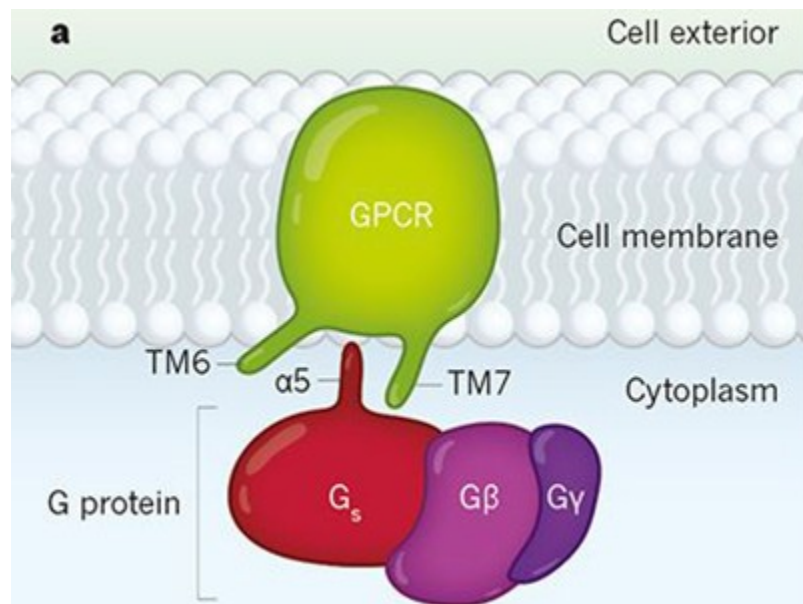
Designing the ideal opioid

Lastly, Marti-Solano *et al.* showed that 42% of the 111 GPCRs that are targets of FDA-approved drugs had more than one isoform — and that in many cases each of the isoforms for a given receptor has a different tissue distribution. The authors also found that specific single-nucleotide DNA mutations in some were associated with disease. This finding suggests that isoform-selective drugs might be useful for treating human diseases. The search for these drugs recalls the long and continuing process of developing subtype-selective drugs for many GPCRs¹¹ (drugs that modulate just one of the 13 GPCRs activated by the chemical serotonin, for instance). The current finding indicates that drugs might need to be both subtype- and isoform-selective. Time will tell whether thoughtful design of isoform-selective drugs will lead to increased specificity and fewer off-target effects than occur with current drugs.

It is important to note the limitations inherent in this study. Isoform expression could be assessed only at the level of gene expression, whereas the gold standard in receptor biology is to measure protein expression using an approach called radioligand binding. However, radioligands might not differentiate between receptor isoforms. Furthermore, Marti-Solano *et al.*

did analyse mass spectrometry data to confirm protein expression for some isoforms.

Another caveat is that the authors' experiments on how isoforms act in combination involved expressing the proteins in an atypical setting, in cells in culture. However, the biology of these isoforms is complex and cell-specific. Their behaviour might depend on spatial localization of receptors, on cell-specific cofactors, or on the isoforms' ability to control cell-intrinsic responses to an external microenvironment. As such, an *in vitro* setting might not fully reveal how each isoform would act *in vivo*.



How the ubiquitous GPCR receptor family selectively activates signalling pathways

It will also be of interest to determine whether plasticity in isoform expression serves as a mechanism by which to dynamically regulate system-level responses. Could tissue-expression signatures change over time or in response to signals from other regions of the body, enabling a

tissue to respond to the same signal in different ways under different conditions?

A related avenue for future research will be to systematically determine how splicing affects the expression and activity of the protein ligands that bind to GPCRs. New ligand isoforms can arise in cancer, as a result of gene fusions¹². For example, the expression of these ‘oncogenic fusion ligands’ leads to changes in the stem-cell microenvironment of the colon that enable the spread of precancerous stem cells¹³. It seems likely that splice isoforms of GPCRs could alter system-level responses in disease, separate from or together with ligand fusions. Going forward, the same possibility could be investigated for all transmembrane receptors, because biased signalling has also been described for receptor tyrosine kinases¹⁴ — these receptors also have a range of isoforms that have roles in health and disease. For example, splice isoforms of the tyrosine kinase ERBB2 are drivers of breast and lung cancers^{15,16}.

Finally, we need to consider whether we should update our approach to GPCR drug development. The current study clearly indicates that tissue-specific expression of receptor isoforms could complicate attempts to target a given GPCR. This is especially true when trying to design a biased agonist that blocks only one downstream signalling pathway — such drugs might have different effects in different tissues. A better understanding of the system bias induced by different isoform combinations will be needed to overcome this obstacle. Experiments should move beyond cell lines to analyse systems bias in cells taken directly from tissues, or *in vivo*. Martí-Solano and colleagues’ valuable resource will be essential for informing such studies.

Nature 587, 553-554 (2020)

doi: <https://doi.org/10.1038/d41586-020-03001-0>

References

1. 1.

Fredriksson, R., Lagerström, M. C., Lundin, L.-G. & Schiöth, H. B. *Mol. Pharmacol.* **63**, 1256–1272 (2003).

2. 2.

Hauser, A. S., Attwood, M. M., Rask-Andersen, M., Schiöth, H. B. & Gloriam, D. E. *Nature Rev. Drug Discov.* **16**, 829–842 (2017).

3. 3.

Marti-Solano, M. *et al.* *Nature* **587**, 650–656 (2020).

4. 4.

Munk, C. *et al.* *Br. J. Pharmacol.* **173**, 2195–2207 (2016).

5. 5.

Galandrin, S. & Bouvier, M. *Mol. Pharmacol.* **70**, 1575–1584 (2006).

6. 6.

Slosky, L. M. *et al.* *Cell* **181**, 1364–1379 (2020).

7. 7.

Smith, J. S., Lefkowitz, R. J. & Rajagopal, S. *Nature Rev. Drug Discov.* **17**, 243–260 (2018).

8. 8.

Kendall, R. T. & Senogles, S. E. *Neuropharmacology* **60**, 336–342 (2011).

9. 9.

Smith, J. S. *et al.* *Mol. Pharmacol.* **92**, 136–150 (2017).

10. 10.

Kenakin, T. & Christopoulos, A. *Nature Rev. Drug Discov.* **12**, 205–216 (2013).

11. 11.

Lindsley, C. W. *et al.* *Chem. Rev.* **116**, 6707–6741 (2016).

12. 12.

Seshagiri, S. *et al.* *Nature* **488**, 660–664 (2012).

13. 13.

Boone, P. G. *et al.* *Nature Commun.* **10**, 5490 (2019).

14. 14.

Ho, C. C. M. *et al.* *Cell* **168**, 1041–1052 (2017).

15. 15.

Turpin, J. *et al.* *Oncogene* **35**, 6053–6064 (2016).

16. 16.

Smith, H. W. *et al.* *Proc. Natl Acad. Sci. USA* **117**, 20139–20148 (2020).

Jobs from Nature Careers

- - - [All jobs](#)
 - - [Part-time Laboratory Assistant](#)

[Oklahoma Medical Research Foundation \(OMRF\)](#)

[Oklahoma City, United States](#)

[JOB POST](#)

▪ [**Assistant Professor of Teaching \(Tenure Track\)**](#)

[The University of British Columbia \(UBC\)](#)

[Vancouver, Canada](#)

[JOB POST](#)

▪ [**Principal Researcher / Senior Researcher**](#)

[Korea Brain Research Institute \(KBRI\)](#)

[Daegu, Korea, South](#)

[JOB POST](#)

▪ [**PhD Scholarship within Phosphorus Turnover in Lakes and Wetlands**](#)

[University of Southern Denmark \(SDU\)](#)

[Odense M, Denmark](#)

[JOB POST](#)

This article was downloaded by **calibre** from <https://www.nature.com/articles/d41586-020-03001-0>

- Review
- [Published: 25 November 2020](#)

Fibrosis: from mechanisms to medicines

- [Neil C. Henderson](#) ORCID: [orcid.org/0000-0002-2273-4094^{1,2}](https://orcid.org/0000-0002-2273-4094),
- [Florian Rieder^{3,4}](#) &
- [Thomas A. Wynn](#) ORCID: [orcid.org/0000-0002-7244-8731⁵](https://orcid.org/0000-0002-7244-8731)

[Nature](#) volume 587, pages555–566(2020) [Cite this article](#)

- 159 Altmetric
- [Metrics details](#)

Subjects

- [Crohn's disease](#)
- [Immunology](#)

Abstract

Fibrosis can affect any organ and is responsible for up to 45% of all deaths in the industrialized world. It has long been thought to be relentlessly progressive and irreversible, but both preclinical models and clinical trials in various organ systems have shown that fibrosis is a highly dynamic process. This has clear implications for therapeutic interventions that are designed to capitalize on this inherent plasticity. However, despite substantial progress in our understanding of the pathobiology of fibrosis, a translational gap remains between the identification of putative antifibrotic targets and conversion of this knowledge into effective treatments in

humans. Here we discuss the transformative experimental strategies that are being leveraged to dissect the key cellular and molecular mechanisms that regulate fibrosis, and the translational approaches that are enabling the emergence of precision medicine-based therapies for patients with fibrosis.

[Access through your institution](#)

[Change institution](#)

[Buy or subscribe](#)

Access options

Subscription info for Chinese customers

We have a dedicated website for our Chinese customers. Please go to [naturechina.com](#) to subscribe to this journal.

[Go to naturechina.com](#)

Rent or Buy article

Get time limited or full article access on ReadCube.

from \$8.99

[Rent or Buy](#)

All prices are NET prices.

Additional access options:

- [Log in](#)
- [Access through your institution](#)
- [Learn about institutional subscriptions](#)

Fig. 1: Deconvolving fibrosis using multi-modal single-cell approaches.



Fig. 2: Functional heterogeneity and plasticity of fibroblasts.



Fig. 3: Metabolomic reprogramming of activated fibroblasts.



Fig. 4: Divergent cytokine pathways drive fibrosis.



Fig. 5: Challenges and solutions in the translation of antifibrotic mechanisms into drugs.



References

1. 1.

Eming, S. A., Martin, P. & Tomic-Canic, M. Wound repair and regeneration: mechanisms, signaling, and translation. *Sci. Transl. Med.* **6**, 265sr6 (2014).

[PubMed](#) [PubMed Central](#) [Google Scholar](#)

2. 2.

Allen, R. J. et al. Genetic variants associated with susceptibility to idiopathic pulmonary fibrosis in people of European ancestry: a genome-wide association study. *Lancet Respir. Med.* **5**, 869–880 (2017).

[CAS](#) [PubMed](#) [PubMed Central](#) [Google Scholar](#)

3. 3.

Kim, H. Y. et al. Genotype-related clinical characteristics and myocardial fibrosis and their association with prognosis in hypertrophic cardiomyopathy. *J. Clin. Med.* **9**, E1671 (2020).

[PubMed](#) [Google Scholar](#)

4. 4.

Young, C. N. J. et al. Total absence of dystrophin expression exacerbates ectopic myofiber calcification and fibrosis and alters macrophage infiltration patterns. *Am. J. Pathol.* **190**, 190–205 (2020).

[CAS](#) [PubMed](#) [Google Scholar](#)

5. 5.

Schiller, H. B. et al. The Human Lung Cell Atlas: a high-resolution reference map of the human lung in health and disease. *Am. J. Respir. Cell Mol. Biol.* **61**, 31–41 (2019).

[CAS](#) [PubMed](#) [PubMed Central](#) [Google Scholar](#)

6. 6.

Zepp, J. A. et al. Distinct mesenchymal lineages and niches promote epithelial self-renewal and myofibrogenesis in the lung. *Cell* **170**, 1134–1148 (2017).

[CAS](#) [PubMed](#) [PubMed Central](#) [Google Scholar](#)

7. 7.

Xie, T. et al. Single-cell deconvolution of fibroblast heterogeneity in mouse pulmonary fibrosis. *Cell Rep.* **22**, 3625–3640 (2018).

[CAS](#) [PubMed](#) [PubMed Central](#) [Google Scholar](#)

8. 8.

Peyser, R. et al. Defining the activated fibroblast population in lung fibrosis using single-cell sequencing. *Am. J. Respir. Cell Mol. Biol.* **61**, 74–85 (2019).

[CAS](#) [PubMed](#) [Google Scholar](#)

9. 9.

Tsukui, T. et al. Collagen-producing lung cell atlas identifies multiple subsets with distinct localization and relevance to fibrosis. *Nat. Commun.* **11**, 1920 (2020).

[ADS](#) [CAS](#) [PubMed](#) [PubMed Central](#) [Google Scholar](#)

10. 10.

Reyfman, P. A. et al. Single-cell transcriptomic analysis of human lung provides insights into the pathobiology of pulmonary fibrosis. *Am. J. Respir. Crit. Care Med.* **199**, 1517–1536 (2019).

[CAS](#) [PubMed](#) [PubMed Central](#) [Google Scholar](#)

11. 11.

Misharin, A. V. et al. Monocyte-derived alveolar macrophages drive lung fibrosis and persist in the lung over the life span. *J. Exp. Med.* **214**, 2387–2404 (2017).

[CAS](#) [PubMed](#) [PubMed Central](#) [Google Scholar](#)

12. 12.

Xu, Y. et al. Single-cell RNA sequencing identifies diverse roles of epithelial cells in idiopathic pulmonary fibrosis. *JCI Insight* **1**, e90558 (2016).

[PubMed](#) [PubMed Central](#) [Google Scholar](#)

13. 13.

Wu, H. et al. Progressive pulmonary fibrosis is caused by elevated mechanical tension on alveolar stem cells. *Cell* **180**, 107–121 (2020).

[CAS](#) [PubMed](#) [Google Scholar](#)

14. 14.

Adams, T. S. et al. Single cell RNA-seq reveals ectopic and aberrant lung resident cell populations in idiopathic pulmonary fibrosis. *Sci. Adv.* **6**, eaba1983 (2019).

[Google Scholar](#)

15. 15.

Halpern, K. B. et al. Single-cell spatial reconstruction reveals global division of labour in the mammalian liver. *Nature* **542**, 352–356 (2017).

[ADS](#) [CAS](#) [PubMed](#) [PubMed Central](#) [Google Scholar](#)

16. 16.

MacParland, S. A. et al. Single cell RNA sequencing of human liver reveals distinct intrahepatic macrophage populations. *Nat. Commun.* **9**, 4383 (2018).

[ADS](#) [PubMed](#) [PubMed Central](#) [Google Scholar](#)

17. 17.

Aizarani, N. et al. A human liver cell atlas reveals heterogeneity and epithelial progenitors. *Nature* **572**, 199–204 (2019).

[CAS](#) [PubMed](#) [PubMed Central](#) [Google Scholar](#)

18. 18.

Halpern, K. B. et al. Paired-cell sequencing enables spatial gene expression mapping of liver endothelial cells. *Nat. Biotechnol.* **36**, 962–970 (2018).

[CAS](#) [PubMed](#) [PubMed Central](#) [Google Scholar](#)

19. 19.

Friedman, S. L., Roll, F. J., Boyles, J. & Bissell, D. M. Hepatic lipocytes: the principal collagen-producing cells of normal rat liver. *Proc. Natl Acad. Sci. USA* **82**, 8681–8685 (1985).

[ADS](#) [CAS](#) [PubMed](#) [Google Scholar](#)

20. 20.

Dobie, R. et al. Single-cell transcriptomics uncovers zonation of function in the mesenchyme during liver fibrosis. *Cell Rep.* **29**, 1832–1847 (2019).

[CAS](#) [PubMed](#) [PubMed Central](#) [Google Scholar](#)

21. 21.

Krenkel, O., Hundertmark, J., Ritz, T. P., Weiskirchen, R. & Tacke, F. Single cell RNA sequencing identifies subsets of hepatic stellate cells and myofibroblasts in liver fibrosis. *Cells* **8**, E503 (2019).

[PubMed](#) [Google Scholar](#)

22. 22.

Ramachandran, P. et al. Resolving the fibrotic niche of human liver cirrhosis at single-cell level. *Nature* **575**, 512–518 (2019). **This study dissected unanticipated aspects of the cellular and molecular basis of human liver fibrosis at a single-cell level, providing a framework for the discovery of rational therapeutic targets in liver cirrhosis.**

[ADS](#) [CAS](#) [PubMed](#) [PubMed Central](#) [Google Scholar](#)

23. 23.

Vento-Tormo, R. et al. Single-cell reconstruction of the early maternal–fetal interface in humans. *Nature* **563**, 347–353 (2018).

[ADS](#) [CAS](#) [PubMed](#) [Google Scholar](#)

24. 24.

Efremova, M. & Teichmann, S. A. Computational methods for single-cell omics across modalities. *Nat. Methods* **17**, 14–17 (2020).

[CAS](#) [PubMed](#) [Google Scholar](#)

25. 25.

Butler, A., Hoffman, P., Smibert, P., Papalexis, E. & Satija, R. Integrating single-cell transcriptomic data across different conditions, technologies, and species. *Nat. Biotechnol.* **36**, 411–420 (2018).

[CAS](#) [PubMed](#) [PubMed Central](#) [Google Scholar](#)

26. 26.

Ratziu, V. & Friedman, S. L. Why do so many NASH trials fail? *Gastroenterology* <https://doi.org/10.1053/j.gastro.2020.05.046> (2020).

27. 27.

Kinchen, J. et al. Structural remodeling of the human colonic mesenchyme in inflammatory bowel disease. *Cell* **175**, 372–386 (2018).

[CAS](#) [PubMed](#) [PubMed Central](#) [Google Scholar](#)

28. 28.

Croft, A. P. et al. Distinct fibroblast subsets drive inflammation and damage in arthritis. *Nature* **570**, 246–251 (2019). **This study uncovered anatomically discrete, functionally distinct subsets of fibroblasts in the context of arthritis.**

[ADS](#) [CAS](#) [PubMed](#) [PubMed Central](#) [Google Scholar](#)

29. 29.

Kirita, Y., Wu, H., Uchimura, K., Wilson, P. C. & Humphreys, B. D. Cell profiling of mouse acute kidney injury reveals conserved cellular responses to injury. *Proc. Natl Acad. Sci. USA* **117**, 15874–15883 (2020).

[CAS](#) [PubMed](#) [Google Scholar](#)

30. 30.

Kuppe, C. et al. Decoding myofibroblast origins in human kidney fibrosis. *Nature* (in the press, 2020).

31. 31.

Der, E. et al. Tubular cell and keratinocyte single-cell transcriptomics applied to lupus nephritis reveal type I IFN and fibrosis relevant pathways. *Nat. Immunol.* **20**, 915–927 (2019).

[CAS](#) [PubMed](#) [PubMed Central](#) [Google Scholar](#)

32. 32.

Driskell, R. R. et al. Distinct fibroblast lineages determine dermal architecture in skin development and repair. *Nature* **504**, 277–281 (2013).

[ADS](#) [CAS](#) [PubMed](#) [PubMed Central](#) [Google Scholar](#)

33. 33.

Rinkevich, Y. et al. Skin fibrosis. Identification and isolation of a dermal lineage with intrinsic fibrogenic potential. *Science* **348**, aaa2151 (2015).

[PubMed](#) [PubMed Central](#) [Google Scholar](#)

34. 34.

Guerrero-Juarez, C. F. et al. Single-cell analysis reveals fibroblast heterogeneity and myeloid-derived adipocyte progenitors in murine skin wounds. *Nat. Commun.* **10**, 650 (2019).

[ADS](#) [CAS](#) [PubMed](#) [PubMed Central](#) [Google Scholar](#)

35. 35.

Bergmeier, V. et al. Identification of a myofibroblast-specific expression signature in skin wounds. *Matrix Biol.* **65**, 59–74 (2018).

[CAS](#) [PubMed](#) [Google Scholar](#)

36. 36.

Correa-Gallegos, D. et al. Patch repair of deep wounds by mobilized fascia. *Nature* **576**, 287–292 (2019). **This work identified a specialized subset of fibroblasts, fascia fibroblasts, which gather the surrounding ECM and then rise to the surface of the skin after wounding.**

[CAS](#) [PubMed](#) [Google Scholar](#)

37. 37.

Shook, B. A. et al. Myofibroblast proliferation and heterogeneity are supported by macrophages during skin repair. *Science* **362**, eaar2971 (2018).

[PubMed](#) [PubMed Central](#) [Google Scholar](#)

38. 38.

Montero-Melendez, T. et al. Therapeutic senescence via GPCR activation in synovial fibroblasts facilitates resolution of arthritis. *Nat. Commun.* **11**, 745 (2020).

[ADS](#) [CAS](#) [PubMed](#) [PubMed Central](#) [Google Scholar](#)

39. 39.

Schafer, M. J., Haak, A. J., Tschumperlin, D. J. & LeBrasseur, N. K. Targeting senescent cells in fibrosis: pathology, paradox, and practical considerations. *Curr. Rheumatol. Rep.* **20**, 3 (2018).

[PubMed](#) [Google Scholar](#)

40. 40.

Amor, C. et al. Senolytic CAR T cells reverse senescence-associated pathologies. *Nature* **583**, 127–132 (2020).

[ADS](#) [CAS](#) [PubMed](#) [Google Scholar](#)

41. 41.

Hickson, L. J. et al. Senolytics decrease senescent cells in humans: preliminary report from a clinical trial of Dasatinib plus Quercetin in individuals with diabetic kidney disease. *EBioMedicine* **47**, 446–456 (2019).

[PubMed](#) [PubMed Central](#) [Google Scholar](#)

42. 42.

Schneider, R. K. et al. Gli 1^+ mesenchymal stromal cells are a key driver of bone marrow fibrosis and an important cellular therapeutic target. *Cell Stem Cell* **23**, 308–309 (2018).

[CAS](#) [PubMed](#) [Google Scholar](#)

43. 43.

El Agha, E. et al. Two-way conversion between lipogenic and myogenic fibroblastic phenotypes marks the progression and resolution of lung fibrosis. *Cell Stem Cell* **20**, 261–273 (2017).

[CAS](#) [PubMed](#) [Google Scholar](#)

44. 44.

Scott, R. W., Arostegui, M., Schweitzer, R., Rossi, F. M. V. & Underhill, T. M. Hic1 defines quiescent mesenchymal progenitor subpopulations with distinct functions and fates in skeletal muscle regeneration. *Cell Stem Cell* **25**, 797–813 (2019).

[CAS](#) [PubMed](#) [Google Scholar](#)

45. 45.

Soliman, H. et al. Pathogenic potential of Hic1-expressing cardiac stromal progenitors. *Cell Stem Cell* **26**, 459–461 (2020).

[CAS](#) [PubMed](#) [Google Scholar](#)

46. 46.

Mahmoudi, S. et al. Heterogeneity in old fibroblasts is linked to variability in reprogramming and wound healing. *Nature* **574**, 553–558 (2019).

[ADS](#) [CAS](#) [PubMed](#) [PubMed Central](#) [Google Scholar](#)

47. 47.

Kisseleva, T. et al. Myofibroblasts revert to an inactive phenotype during regression of liver fibrosis. *Proc. Natl Acad. Sci. USA* **109**, 9448–9453 (2012).

[ADS](#) [CAS](#) [PubMed](#) [Google Scholar](#)

48. 48.

Troeger, J. S. et al. Deactivation of hepatic stellate cells during liver fibrosis resolution in mice. *Gastroenterology* **143**, 1073–1083 (2012).

[CAS](#) [PubMed](#) [Google Scholar](#)

49. 49.

Wohlfahrt, T. et al. PU.1 controls fibroblast polarization and tissue fibrosis. *Nature* **566**, 344–349 (2019).

[ADS](#) [CAS](#) [PubMed](#) [PubMed Central](#) [Google Scholar](#)

50. 50.

Plikus, M. V. et al. Regeneration of fat cells from myofibroblasts during wound healing. *Science* **355**, 748–752 (2017).

[ADS](#) [CAS](#) [PubMed](#) [PubMed Central](#) [Google Scholar](#)

51. 51.

Song, G. et al. Direct reprogramming of hepatic myofibroblasts into hepatocytes in vivo attenuates liver fibrosis. *Cell Stem Cell* **18**, 797–808 (2016).

[CAS](#) [PubMed](#) [Google Scholar](#)

52. 52.

Rezvani, M. et al. In vivo hepatic reprogramming of myofibroblasts with AAV vectors as a therapeutic strategy for liver fibrosis. *Cell Stem Cell* **18**, 809–816 (2016).

[CAS](#) [PubMed](#) [PubMed Central](#) [Google Scholar](#)

53. 53.

Aghajanian, H. et al. Targeting cardiac fibrosis with engineered T cells. *Nature* **573**, 430–433 (2019).

[ADS](#) [CAS](#) [PubMed](#) [PubMed Central](#) [Google Scholar](#)

54. 54.

Pereira, B. I. et al. Senescent cells evade immune clearance via HLA-E-mediated NK and CD8⁺ T cell inhibition. *Nat. Commun.* **10**, 2387 (2019).

[ADS](#) [PubMed](#) [PubMed Central](#) [Google Scholar](#)

55. 55.

Pakshir, P. & Hinz, B. The big five in fibrosis: macrophages, myofibroblasts, matrix, mechanics, and miscommunication. *Matrix Biol.* **68-69**, 81–93 (2018).

[CAS](#) [PubMed](#) [Google Scholar](#)

56. 56.

Januszyk, M. et al. Mechanical offloading of incisional wounds is associated with transcriptional downregulation of inflammatory pathways in a large animal model. *Organogenesis* **10**, 186–193 (2014).

[PubMed](#) [PubMed Central](#) [Google Scholar](#)

57. 57.

Froese, A. R. et al. Stretch-induced activation of transforming growth factor- β 1 in pulmonary fibrosis. *Am. J. Respir. Crit. Care Med.* **194**, 84–96 (2016).

[CAS](#) [PubMed](#) [Google Scholar](#)

58. 58.

Lindsey, M. L., Iyer, R. P., Jung, M., DeLeon-Pennell, K. Y. & Ma, Y. Matrix metalloproteinases as input and output signals for post-myocardial infarction remodeling. *J. Mol. Cell. Cardiol.* **91**, 134–140 (2016).

[CAS](#) [PubMed](#) [Google Scholar](#)

59. 59.

Craig, V. J., Zhang, L., Hagood, J. S. & Owen, C. A. Matrix metalloproteinases as therapeutic targets for idiopathic pulmonary fibrosis. *Am. J. Respir. Cell Mol. Biol.* **53**, 585–600 (2015).

[CAS](#) [PubMed](#) [PubMed Central](#) [Google Scholar](#)

60. 60.

Lundberg, E. & Borner, G. H. H. Spatial proteomics: a powerful discovery tool for cell biology. *Nat. Rev. Mol. Cell Biol.* **20**, 285–302 (2019).

[CAS](#) [PubMed](#) [Google Scholar](#)

61. 61.

Schwabe, R. F., Tabas, I. & Pajvani, U. B. Mechanisms of fibrosis development in nonalcoholic steatohepatitis. *Gastroenterology* **158**, 1913–1928 (2020).

[CAS](#) [PubMed](#) [Google Scholar](#)

62. 62.

Xie, N. et al. Glycolytic reprogramming in myofibroblast differentiation and lung fibrosis. *Am. J. Respir. Crit. Care Med.* **192**, 1462–1474 (2015).

[CAS](#) [PubMed](#) [PubMed Central](#) [Google Scholar](#)

63. 63.

Faubert, B. et al. Lactate metabolism in human lung tumors. *Cell* **171**, 358–371 (2017).

[CAS](#) [PubMed](#) [PubMed Central](#) [Google Scholar](#)

64. 64.

Kottmann, R. M. et al. Lactic acid is elevated in idiopathic pulmonary fibrosis and induces myofibroblast differentiation via pH-dependent activation of transforming growth factor- β . *Am. J. Respir. Crit. Care Med.* **186**, 740–751 (2012).

[CAS](#) [PubMed](#) [PubMed Central](#) [Google Scholar](#)

65. 65.

Liu, G. & Summer, R. Cellular metabolism in lung health and disease. *Annu. Rev. Physiol.* **81**, 403–428 (2019).

[CAS](#) [PubMed](#) [Google Scholar](#)

66. 66.

Nigdelioglu, R. et al. Transforming growth factor (TGF)- β promotes de novo serine synthesis for collagen production. *J. Biol. Chem.* **291**, 27239–27251 (2016).

[CAS](#) [PubMed](#) [PubMed Central](#) [Google Scholar](#)

67. 67.

Park, S. Y., Le, C. T., Sung, K. Y., Choi, D. H. & Cho, E. H. Succinate induces hepatic fibrogenesis by promoting activation, proliferation, and migration, and inhibiting apoptosis of hepatic stellate cells. *Biochem. Biophys. Res. Commun.* **496**, 673–678 (2018).

[CAS](#) [PubMed](#) [Google Scholar](#)

68. 68.

Lian, N. et al. Curcumin regulates cell fate and metabolism by inhibiting hedgehog signaling in hepatic stellate cells. *Lab. Invest.* **95**, 790–803 (2015).

[CAS](#) [PubMed](#) [Google Scholar](#)

69. 69.

Ding, H. et al. Inhibiting aerobic glycolysis suppresses renal interstitial fibroblast activation and renal fibrosis. *Am. J. Physiol. Renal Physiol.* **313**, F561–F575 (2017).

[CAS](#) [PubMed](#) [Google Scholar](#)

70. 70.

Wei, Q. et al. Glycolysis inhibitors suppress renal interstitial fibrosis via divergent effects on fibroblasts and tubular cells. *Am. J. Physiol. Renal Physiol.* **316**, F1162–F1172 (2019).

[CAS](#) [PubMed](#) [PubMed Central](#) [Google Scholar](#)

71. 71.

Ge, J. et al. Glutaminolysis promotes collagen translation and stability via α -ketoglutarate-mediated mTOR activation and proline hydroxylation. *Am. J. Respir. Cell Mol. Biol.* **58**, 378–390 (2018).

[CAS](#) [PubMed](#) [PubMed Central](#) [Google Scholar](#)

72. 72.

Bai, L. et al. Glutaminolysis epigenetically regulates antiapoptotic gene expression in idiopathic pulmonary fibrosis fibroblasts. *Am. J. Respir. Cell Mol. Biol.* **60**, 49–57 (2019).

[CAS](#) [PubMed](#) [PubMed Central](#) [Google Scholar](#)

73. 73.

Cui, H. et al. Inhibition of glutaminase 1 attenuates experimental pulmonary fibrosis. *Am. J. Respir. Cell Mol. Biol.* **61**, 492–500 (2019).

[CAS](#) [PubMed](#) [PubMed Central](#) [Google Scholar](#)

74. 74.

Kang, H. M. et al. Defective fatty acid oxidation in renal tubular epithelial cells has a key role in kidney fibrosis development. *Nat. Med.* **21**, 37–46 (2015). **This study elegantly links abnormal fatty acid oxidation to fibrogenesis.**

[CAS](#) [PubMed](#) [Google Scholar](#)

75. 75.

Luengo, A., Gui, D. Y. & Vander Heiden, M. G. Targeting metabolism for cancer therapy. *Cell Chem. Biol.* **24**, 1161–1180 (2017).

[CAS](#) [PubMed](#) [PubMed Central](#) [Google Scholar](#)

76. 76.

Wynn, T. A. & Vannella, K. M. Macrophages in tissue repair, regeneration, and fibrosis. *Immunity* **44**, 450–462 (2016).

[CAS](#) [PubMed](#) [PubMed Central](#) [Google Scholar](#)

77. 77.

Vannella, K. M. & Wynn, T. A. Mechanisms of organ injury and repair by macrophages. *Annu. Rev. Physiol.* **79**, 593–617 (2017).

[CAS](#) [PubMed](#) [Google Scholar](#)

78. 78.

Krenkel, O. & Tacke, F. Liver macrophages in tissue homeostasis and disease. *Nat. Rev. Immunol.* **17**, 306–321 (2017).

[CAS](#) [PubMed](#) [Google Scholar](#)

79. 79.

Chakarov, S. et al. Two distinct interstitial macrophage populations coexist across tissues in specific subtissular niches. *Science* **363**, eaau0964 (2019).

[CAS](#) [PubMed](#) [Google Scholar](#)

80. 80.

Guilliams, M., Thierry, G. R., Bonnardel, J. & Bajenoff, M. Establishment and maintenance of the macrophage niche. *Immunity* **52**, 434–451 (2020).

[CAS](#) [PubMed](#) [Google Scholar](#)

81. 81.

Lavine, K. J. et al. Distinct macrophage lineages contribute to disparate patterns of cardiac recovery and remodeling in the neonatal and adult heart. *Proc. Natl Acad. Sci. USA* **111**, 16029–16034 (2014).

[ADS](#) [CAS](#) [PubMed](#) [Google Scholar](#)

82. 82.

Duffield, J. S. et al. Selective depletion of macrophages reveals distinct, opposing roles during liver injury and repair. *J. Clin. Invest.* **115**, 56–65 (2005).

[CAS](#) [PubMed](#) [PubMed Central](#) [Google Scholar](#)

83. 83.

Borthwick, L. A. et al. Macrophages are critical to the maintenance of IL-13-dependent lung inflammation and fibrosis. *Mucosal Immunol.* **9**, 38–55 (2016).

[CAS](#) [PubMed](#) [Google Scholar](#)

84. 84.

Satoh, T. et al. Identification of an atypical monocyte and committed progenitor involved in fibrosis. *Nature* **541**, 96–101 (2017).

[ADS](#) [CAS](#) [PubMed](#) [Google Scholar](#)

85. 85.

Bajpai, G. et al. The human heart contains distinct macrophage subsets with divergent origins and functions. *Nat. Med.* **24**, 1234–1245 (2018).

[CAS](#) [PubMed](#) [PubMed Central](#) [Google Scholar](#)

86. 86.

Aran, D. et al. Reference-based analysis of lung single-cell sequencing reveals a transitional profibrotic macrophage. *Nat. Immunol.* **20**, 163–172 (2019).

[CAS](#) [PubMed](#) [PubMed Central](#) [Google Scholar](#)

87. 87.

Dick, S. A. et al. Self-renewing resident cardiac macrophages limit adverse remodeling following myocardial infarction. *Nat. Immunol.* **20**, 29–39 (2019).

[CAS](#) [PubMed](#) [Google Scholar](#)

88. 88.

Wang, J. & Kubes, P. A reservoir of mature cavity macrophages that can rapidly invade visceral organs to affect tissue repair. *Cell* **165**, 668–678 (2016).

[CAS](#) [PubMed](#) [Google Scholar](#)

89. 89.

Deniset, J. F. et al. Gata6⁺ pericardial cavity macrophages relocate to the injured heart and prevent cardiac fibrosis. *Immunity* **51**, 131–140 (2019).

[CAS](#) [PubMed](#) [PubMed Central](#) [Google Scholar](#)

90. 90.

Adler, M. et al. Principles of cell circuits for tissue repair and fibrosis. *iScience* **23**, 100841 (2020).

[ADS](#) [CAS](#) [PubMed](#) [PubMed Central](#) [Google Scholar](#)

91. 91.

Henderson, N. C. et al. Galectin-3 expression and secretion links macrophages to the promotion of renal fibrosis. *Am. J. Pathol.* **172**, 288–298 (2008).

[CAS](#) [PubMed](#) [PubMed Central](#) [Google Scholar](#)

92. 92.

Zhou, X. et al. Circuit design features of a stable two-cell system. *Cell* **172**, 744–757 (2018).

[CAS](#) [PubMed](#) [PubMed Central](#) [Google Scholar](#)

93. 93.

Lodyga, M. et al. Cadherin-11-mediated adhesion of macrophages to myofibroblasts establishes a profibrotic niche of active TGF β . *Sci. Signal.* **12**, eaao3469 (2019).

[CAS](#) [PubMed](#) [Google Scholar](#)

94. 94.

Minutti, C. M. et al. A macrophage-pericyte axis directs tissue restoration via amphiregulin-induced transforming growth factor beta activation. *Immunity* **50**, 645–654 (2019).

[CAS](#) [PubMed](#) [PubMed Central](#) [Google Scholar](#)

95. 95.

Pakshir, P. et al. Dynamic fibroblast contractions attract remote macrophages in fibrillar collagen matrix. *Nat. Commun.* **10**, 1850 (2019).

[ADS](#) [PubMed](#) [PubMed Central](#) [Google Scholar](#)

96. 96.

Diebold, R. J. et al. Early-onset multifocal inflammation in the transforming growth factor beta 1-null mouse is lymphocyte mediated. *Proc. Natl Acad. Sci. USA* **92**, 12215–12219 (1995).

[ADS](#) [CAS](#) [PubMed](#) [Google Scholar](#)

97. 97.

McEntee, C. P., Gunaltay, S. & Travis, M. A. Regulation of barrier immunity and homeostasis by integrin-mediated transforming growth factor β activation. *Immunology* **160**, 139–148 (2020).

[CAS](#) [PubMed](#) [Google Scholar](#)

98. 98.

Kelly, A. et al. Human monocytes and macrophages regulate immune tolerance via integrin $\alpha v\beta 8$ -mediated TGF β activation. *J. Exp. Med.* **215**, 2725–2736 (2018).

1. [CAS](#) [PubMed](#) [PubMed Central](#) [Google Scholar](#)

2. 99.

Barczyk, M., Carracedo, S. & Gullberg, D. Integrins. *Cell Tissue Res.* **339**, 269–280 (2010).

[CAS](#) [PubMed](#) [Google Scholar](#)

3. 100.

Hynes, R. O. Integrins: bidirectional, allosteric signaling machines. *Cell* **110**, 673–687 (2002).

[CAS](#) [PubMed](#) [Google Scholar](#)

4. 101.

Robertson, I. B. & Rifkin, D. B. Regulation of the bioavailability of TGF β and TGF β -related proteins. *Cold Spring Harb. Perspect. Biol.* **8**, a021907 (2016).

[PubMed](#) [PubMed Central](#) [Google Scholar](#)

5. 102.

Reed, N. I. et al. The $\alpha v \beta 1$ integrin plays a critical in vivo role in tissue fibrosis. *Sci. Transl. Med.* **7**, 288ra79 (2015).

[PubMed](#) [PubMed Central](#) [Google Scholar](#)

6. 103.

Munger, J. S. et al. A mechanism for regulating pulmonary inflammation and fibrosis: the integrin $\alpha v \beta 6$ binds and activates latent TGF β 1. *Cell* **96**, 319–328 (1999).

[CAS](#) [PubMed](#) [Google Scholar](#)

7. 104.

Wipff, P. J., Rifkin, D. B., Meister, J. J. & Hinz, B. Myofibroblast contraction activates latent TGF β 1 from the extracellular matrix. *J. Cell Biol.* **179**, 1311–1323 (2007).

[CAS](#) [PubMed](#) [PubMed Central](#) [Google Scholar](#)

8. 105.

Shi, M. et al. Latent TGF β structure and activation. *Nature* **474**, 343–349 (2011).

[CAS](#) [PubMed](#) [PubMed Central](#) [Google Scholar](#)

9. 106.

Dong, X. et al. Force interacts with macromolecular structure in activation of TGF β . *Nature* **542**, 55–59 (2017).

[ADS](#) [CAS](#) [PubMed](#) [PubMed Central](#) [Google Scholar](#)

10. 107.

Dong, X., Hudson, N. E., Lu, C. & Springer, T. A. Structural determinants of integrin β -subunit specificity for latent TGF β . *Nat. Struct. Mol. Biol.* **21**, 1091–1096 (2014).

[CAS](#) [PubMed](#) [PubMed Central](#) [Google Scholar](#)

11. 108.

Campbell, M. G. et al. Cryo-EM reveals integrin-mediated TGF β activation without release from latent TGF β . *Cell* **180**, 490–501 (2020).

[CAS](#) [PubMed](#) [Google Scholar](#)

12. 109.

Hahm, K. et al. $\alpha v\beta 6$ integrin regulates renal fibrosis and inflammation in Alport mouse. *Am. J. Pathol.* **170**, 110–125 (2007).

[CAS](#) [PubMed](#) [PubMed Central](#) [Google Scholar](#)

13. 110.

Wang, B. et al. Role of $\alpha v\beta 6$ integrin in acute biliary fibrosis. *Hepatology* **46**, 1404–1412 (2007).

[CAS](#) [PubMed](#) [PubMed Central](#) [Google Scholar](#)

14. 111.

Peng, Z. W. et al. Integrin $\alpha v\beta 6$ critically regulates hepatic progenitor cell function and promotes ductular reaction, fibrosis, and tumorigenesis. *Hepatology* **63**, 217–232 (2016).

[CAS](#) [PubMed](#) [Google Scholar](#)

15. 112.

Horan, G. S. et al. Partial inhibition of integrin $\alpha v\beta 6$ prevents pulmonary fibrosis without exacerbating inflammation. *Am. J. Respir. Crit. Care Med.* **177**, 56–65 (2008).

[CAS](#) [PubMed](#) [Google Scholar](#)

16. 113.

Puthawala, K. et al. Inhibition of integrin $\alpha v\beta 6$, an activator of latent transforming growth factor- β , prevents radiation-induced lung fibrosis. *Am. J. Respir. Crit. Care Med.* **177**, 82–90 (2008).

[CAS](#) [PubMed](#) [Google Scholar](#)

17. 114.

Araya, J. et al. Squamous metaplasia amplifies pathologic epithelial-mesenchymal interactions in COPD patients. *J. Clin. Invest.* **117**, 3551–3562 (2007).

[CAS](#) [PubMed](#) [PubMed Central](#) [Google Scholar](#)

18. 115.

Kitamura, H. et al. Mouse and human lung fibroblasts regulate dendritic cell trafficking, airway inflammation, and fibrosis through integrin $\alpha v\beta 8$ -mediated activation of TGF β . *J. Clin. Invest.* **121**, 2863–2875 (2011).

[CAS](#) [PubMed](#) [PubMed Central](#) [Google Scholar](#)

19. 116.

Minagawa, S. et al. Selective targeting of TGF β activation to treat fibroinflammatory airway disease. *Sci. Transl. Med.* **6**, 241ra79 (2014).

[PubMed](#) [PubMed Central](#) [Google Scholar](#)

20. 117.

Henderson, N. C. et al. Targeting of αv integrin identifies a core molecular pathway that regulates fibrosis in several organs. *Nat. Med.* **19**, 1617–1624 (2013).

[CAS](#) [PubMed](#) [Google Scholar](#)

21. 118.

Barron, L. & Wynn, T. A. Fibrosis is regulated by Th2 and Th17 responses and by dynamic interactions between fibroblasts and macrophages. *Am. J. Physiol. Gastrointest. Liver Physiol.* **300**, G723–G728 (2011).

[CAS](#) [PubMed](#) [PubMed Central](#) [Google Scholar](#)

22. 119.

Park, M. J. et al. IL-1–IL-17 signaling axis contributes to fibrosis and inflammation in two different murine models of systemic sclerosis. *Front. Immunol.* **9**, 1611 (2018).

[PubMed](#) [PubMed Central](#) [Google Scholar](#)

23. 120.

Wilson, M. S. et al. Bleomycin and IL-1 β -mediated pulmonary fibrosis is IL-17A dependent. *J. Exp. Med.* **207**, 535–552 (2010).

[ADS](#) [CAS](#) [PubMed](#) [PubMed Central](#) [Google Scholar](#)

24. 121.

Wang, B. Z. et al. Interleukin-17A antagonist attenuates radiation-induced lung injuries in mice. *Exp. Lung Res.* **40**, 77–85 (2014).

[ADS](#) [CAS](#) [PubMed](#) [Google Scholar](#)

25. 122.

Meng, F. et al. Interleukin-17 signaling in inflammatory, Kupffer cells, and hepatic stellate cells exacerbates liver fibrosis in mice. *Gastroenterology* **143**, 765–776 (2012).

[CAS](#) [PubMed](#) [PubMed Central](#) [Google Scholar](#)

26. 123.

Sun, B. et al. Role of interleukin 17 in TGF β signaling-mediated renal interstitial fibrosis. *Cytokine* **106**, 80–88 (2018).

[CAS](#) [PubMed](#) [Google Scholar](#)

27. 124.

Feng, W. et al. IL-17 induces myocardial fibrosis and enhances RANKL/OPG and MMP/TIMP signaling in isoproterenol-induced heart failure. *Exp. Mol. Pathol.* **87**, 212–218 (2009).

[CAS](#) [PubMed](#) [Google Scholar](#)

28. 125.

Fabre, T. et al. Type 3 cytokines IL-17A and IL-22 drive TGF β -dependent liver fibrosis. *Sci. Immunol.* **3**, eaar7754 (2018).

[PubMed](#) [Google Scholar](#)

29. 126.

Tan, Z. et al. IL-17A plays a critical role in the pathogenesis of liver fibrosis through hepatic stellate cell activation. *J. Immunol.* **191**, 1835–1844 (2013).

[CAS](#) [PubMed](#) [Google Scholar](#)

30. 127.

Zhang, S. et al. Neutralization of interleukin-17 attenuates cholestatic liver fibrosis in mice. *Scand. J. Immunol.* **83**, 102–108 (2016).

[CAS](#) [PubMed](#) [Google Scholar](#)

31. 128.

Zhang, X. W. et al. Antagonism of interleukin-17A ameliorates experimental hepatic fibrosis by restoring the IL-10/STAT3-suppressed autophagy in hepatocytes. *Oncotarget* **8**, 9922–9934 (2017).

[PubMed](#) [Google Scholar](#)

32. 129.

Fabre, T., Kared, H., Friedman, S. L. & Shoukry, N. H. IL-17A enhances the expression of profibrotic genes through upregulation of the TGF β receptor on hepatic stellate cells in a JNK-dependent manner. *J. Immunol.* **193**, 3925–3933 (2014).

[CAS](#) [PubMed](#) [PubMed Central](#) [Google Scholar](#)

33. 130.

Oh, K. et al. Epithelial transglutaminase 2 is needed for T cell interleukin-17 production and subsequent pulmonary inflammation and fibrosis in bleomycin-treated mice. *J. Exp. Med.* **208**, 1707–1719 (2011).

[CAS](#) [PubMed](#) [PubMed Central](#) [Google Scholar](#)

34. 131.

Wree, A. et al. NLRP3 inflammasome driven liver injury and fibrosis: roles of IL-17 and TNF in mice. *Hepatology* **67**, 736–749 (2018).

[CAS](#) [PubMed](#) [Google Scholar](#)

35. 132.

Gasse, P. et al. IL-1 and IL-23 mediate early IL-17A production in pulmonary inflammation leading to late fibrosis. *PLoS One* **6**, e23185 (2011).

[ADS](#) [CAS](#) [PubMed](#) [PubMed Central](#) [Google Scholar](#)

36. 133.

Lemmers, A. et al. The interleukin-17 pathway is involved in human alcoholic liver disease. *Hepatology* **49**, 646–657 (2009).

[CAS](#) [PubMed](#) [Google Scholar](#)

37. 134.

Macek Jilkova, Z. et al. Progression of fibrosis in patients with chronic viral hepatitis is associated with IL-17⁺ neutrophils. *Liver Int.* **36**, 1116–1124 (2016).

[CAS](#) [PubMed](#) [Google Scholar](#)

38. 135.

Yang, D. et al. Dysregulated lung commensal bacteria drive interleukin-17b production to promote pulmonary fibrosis through their outer membrane vesicles. *Immunity* **50**, 692–706 (2019).

[CAS](#) [PubMed](#) [Google Scholar](#)

39. 136.

Seki, E. et al. TLR4 enhances TGFβ signaling and hepatic fibrosis. *Nat. Med.* **13**, 1324–1332 (2007).

[CAS](#) [PubMed](#) [Google Scholar](#)

40. 137.

de Kretser, D. M. et al. Serum activin A and B levels predict outcome in patients with acute respiratory failure: a prospective cohort study. *Crit. Care* **17**, R263 (2013).

[PubMed](#) [PubMed Central](#) [Google Scholar](#)

41. 138.

Gieseck, R. L., III, Wilson, M. S. & Wynn, T. A. Type 2 immunity in tissue repair and fibrosis. *Nat. Rev. Immunol.* **18**, 62–76 (2018).

[CAS](#) [PubMed](#) [Google Scholar](#)

42. 139.

Hams, E. et al. IL-25 and type 2 innate lymphoid cells induce pulmonary fibrosis. *Proc. Natl Acad. Sci. USA* **111**, 367–372 (2014).

[ADS](#) [CAS](#) [PubMed](#) [Google Scholar](#)

43. 140.

Jessup, H. K. et al. Intradermal administration of thymic stromal lymphopoietin induces a T cell- and eosinophil-dependent systemic Th2 inflammatory response. *J. Immunol.* **181**, 4311–4319 (2008).

[CAS](#) [PubMed](#) [Google Scholar](#)

44. 141.

McHedlidze, T. et al. Interleukin-33-dependent innate lymphoid cells mediate hepatic fibrosis. *Immunity* **39**, 357–371 (2013).

[CAS](#) [PubMed](#) [PubMed Central](#) [Google Scholar](#)

45. 142.

Vannella, K. M. et al. Combinatorial targeting of TSLP, IL-25, and IL-33 in type 2 cytokine-driven inflammation and fibrosis. *Sci. Transl. Med.* **8**, 337ra65 (2016).

[PubMed](#) [Google Scholar](#)

46. 143.

Lee, C. G. et al. Interleukin-13 induces tissue fibrosis by selectively stimulating and activating transforming growth factor β_1 . *J. Exp. Med.* **194**, 809–821 (2001).

[CAS](#) [PubMed](#) [PubMed Central](#) [Google Scholar](#)

47. 144.

Kaviratne, M. et al. IL-13 activates a mechanism of tissue fibrosis that is completely TGF β independent. *J. Immunol.* **173**, 4020–4029 (2004).

[CAS](#) [PubMed](#) [Google Scholar](#)

48. 145.

Gieseck, R. L. III et al. Interleukin-13 activates distinct cellular pathways leading to ductular reaction, steatosis, and fibrosis. *Immunity* **45**, 145–158 (2016).

[CAS](#) [PubMed](#) [PubMed Central](#) [Google Scholar](#)

49. 146.

Hart, K. M. et al. Type 2 immunity is protective in metabolic disease but exacerbates NAFLD collaboratively with TGF β . *Sci. Transl. Med.* **9**, eaal3694 (2017). **This study identified opposing roles for type 2 immunity in metabolic syndrome and liver fibrosis in an experimental model of NASH.**

[PubMed](#) [Google Scholar](#)

50. 147.

Chiaramonte, M. G., Donaldson, D. D., Cheever, A. W. & Wynn, T. A. An IL-13 inhibitor blocks the development of hepatic fibrosis during a T-helper type 2-dominated inflammatory response. *J. Clin. Invest.* **104**, 777–785 (1999).

[CAS](#) [PubMed](#) [PubMed Central](#) [Google Scholar](#)

51. 148.

Xue, J. et al. Alternatively activated macrophages promote pancreatic fibrosis in chronic pancreatitis. *Nat. Commun.* **6**, 7158 (2015).

[ADS](#) [CAS](#) [PubMed](#) [PubMed Central](#) [Google Scholar](#)

52. 149.

Liu, L. et al. CD4⁺ T lymphocytes, especially Th2 cells, contribute to the progress of renal fibrosis. *Am. J. Nephrol.* **36**, 386–396 (2012).

[CAS](#) [PubMed](#) [Google Scholar](#)

53. 150.

Chung, S. I. et al. IL-13 is a therapeutic target in radiation lung injury. *Sci. Rep.* **6**, 39714 (2016).

[ADS](#) [CAS](#) [PubMed](#) [PubMed Central](#) [Google Scholar](#)

54. 151.

Singh, B., Kasam, R. K., Sontake, V., Wynn, T. A. & Madala, S. K. Repetitive intradermal bleomycin injections evoke T-helper cell 2 cytokine-driven pulmonary fibrosis. *Am. J. Physiol. Lung Cell. Mol. Physiol.* **313**, L796–L806 (2017).

[PubMed](#) [PubMed Central](#) [Google Scholar](#)

55. 152.

Sciurba, J. C. et al. Fibroblast-specific integrin-alpha V differentially regulates type 17 and type 2 driven inflammation and fibrosis. *J. Pathol.* **248**, 16–29 (2019).

[CAS](#) [PubMed](#) [Google Scholar](#)

56. 153.

Wang, M. et al. Cross-talk between T_H2 and T_H17 pathways in patients with chronic rhinosinusitis with nasal polyps. *J. Allergy Clin. Immunol.* **144**, 1254–1264 (2019).

[CAS](#) [PubMed](#) [Google Scholar](#)

57. 154.

Choy, D. F. et al. T_H2 and T_H17 inflammatory pathways are reciprocally regulated in asthma. *Sci. Transl. Med.* **7**, 301ra129 (2015).

[PubMed](#) [Google Scholar](#)

58. 155.

Ramalingam, T. R. et al. Enhanced protection from fibrosis and inflammation in the combined absence of IL-13 and IFN- γ . *J. Pathol.* **239**, 344–354 (2016).

[CAS](#) [PubMed](#) [PubMed Central](#) [Google Scholar](#)

59. 156.

Tang, W. et al. Targeted expression of IL-11 in the murine airway causes lymphocytic inflammation, bronchial remodeling, and airways obstruction. *J. Clin. Invest.* **98**, 2845–2853 (1996). **This paper identified autocrine IL-11–IL-11R signaling in fibroblasts as a key mechanism driving cardiovascular fibrosis in response to a variety of stimuli.**

[CAS](#) [PubMed](#) [PubMed Central](#) [Google Scholar](#)

60. 157.

Schafer, S. et al. IL-11 is a crucial determinant of cardiovascular fibrosis. *Nature* **552**, 110–115 (2017).

[ADS](#) [CAS](#) [PubMed](#) [PubMed Central](#) [Google Scholar](#)

61. 158.

Ng, B. et al. Interleukin-11 is a therapeutic target in idiopathic pulmonary fibrosis. *Sci. Transl. Med.* **11**, eaaw1237 (2019).

[CAS](#) [PubMed](#) [Google Scholar](#)

62. 159.

Abreu, M. T. et al. Mutations in NOD2 are associated with fibrostenosing disease in patients with Crohn's disease. *Gastroenterology* **123**, 679–688 (2002).

[CAS](#) [PubMed](#) [Google Scholar](#)

63. 160.

Rieder, F. et al. Association of the novel serologic anti-glycan antibodies anti-laminarin and anti-chitin with complicated Crohn's disease behavior. *Inflamm. Bowel Dis.* **16**, 263–274 (2010).

[PubMed](#) [Google Scholar](#)

64. 161.

Rieder, F. et al. Serum anti-glycan antibodies predict complicated Crohn's disease behavior: a cohort study. *Inflamm. Bowel Dis.* **16**, 1367–1375 (2010).

[PubMed](#) [Google Scholar](#)

65. 162.

Rieder, F., Kessler, S., Sans, M. & Fiocchi, C. Animal models of intestinal fibrosis: new tools for the understanding of pathogenesis and therapy of human disease. *Am. J. Physiol. Gastrointest. Liver Physiol.* **303**, G786–G801 (2012).

[CAS](#) [PubMed](#) [PubMed Central](#) [Google Scholar](#)

66. 163.

Moresco, E. M., LaVine, D. & Beutler, B. Toll-like receptors. *Curr. Biol.* **21**, R488–R493 (2011).

[CAS](#) [PubMed](#) [Google Scholar](#)

67. 164.

Månsson, L. E. et al. MyD88 signaling promotes both mucosal homeostatic and fibrotic responses during *Salmonella*-induced colitis. *Am. J. Physiol. Gastrointest. Liver Physiol.* **303**, G311–G323 (2012).

[PubMed](#) [Google Scholar](#)

68. 165.

Imai, J. et al. Flagellin-mediated activation of IL-33-ST2 signaling by a pathobiont promotes intestinal fibrosis. *Mucosal Immunol.* **12**, 632–643 (2019).

[CAS](#) [PubMed](#) [PubMed Central](#) [Google Scholar](#)

69. 166.

Jacob, N. et al. Inflammation-independent TL1A-mediated intestinal fibrosis is dependent on the gut microbiome. *Mucosal Immunol.* **11**, 1466–1476 (2018).

[CAS](#) [PubMed](#) [PubMed Central](#) [Google Scholar](#)

70. 167.

Otte, J. M., Rosenberg, I. M. & Podolsky, D. K. Intestinal myofibroblasts in innate immune responses of the intestine. *Gastroenterology* **124**, 1866–1878 (2003).

[CAS](#) [PubMed](#) [Google Scholar](#)

71. 168.

Zhao, S. et al. Selective deletion of MyD88 signaling in α-SMA positive cells ameliorates experimental intestinal fibrosis via post-transcriptional regulation. *Mucosal Immunol.* **13**, 665–678 (2020). **This study highlights a selective mechanism by which bacteria activate myofibroblasts through flagellin.**

[PubMed](#) [PubMed Central](#) [Google Scholar](#)

72. 169.

Chan, C. C. et al. Prognostic value of plasma endotoxin levels in patients with cirrhosis. *Scand. J. Gastroenterol.* **32**, 942–946 (1997).

[CAS](#) [PubMed](#) [Google Scholar](#)

73. 170.

Seki, E. & Brenner, D. A. Toll-like receptors and adaptor molecules in liver disease: update. *Hepatology* **48**, 322–335 (2008).

[CAS](#) [PubMed](#) [Google Scholar](#)

74. 171.

Sun, L. et al. Lipopolysaccharide enhances TGF β 1 signalling pathway and rat pancreatic fibrosis. *J. Cell. Mol. Med.* **22**, 2346–2356 (2018).

[CAS](#) [PubMed](#) [PubMed Central](#) [Google Scholar](#)

75. 172.

Yang, L. et al. TRIF differentially regulates hepatic steatosis and inflammation/fibrosis in mice. *Cell. Mol. Gastroenterol. Hepatol.* **3**, 469–483 (2017).

[PubMed](#) [PubMed Central](#) [Google Scholar](#)

76. 173.

Mazagova, M. et al. Commensal microbiota is hepatoprotective and prevents liver fibrosis in mice. *FASEB J.* **29**, 1043–1055 (2015).

[CAS](#) [PubMed](#) [Google Scholar](#)

77. 174.

Leaf, I. A. et al. Pericyte MyD88 and IRAK4 control inflammatory and fibrotic responses to tissue injury. *J. Clin. Invest.* **127**, 321–334 (2017).

[PubMed](#) [Google Scholar](#)

78. 175.

Jialal, I., Major, A. M. & Devaraj, S. Global Toll-like receptor 4 knockout results in decreased renal inflammation, fibrosis and podocytopathy. *J. Diabetes Complications* **28**, 755–761 (2014).

[PubMed](#) [Google Scholar](#)

79. 176.

Liu, J. H. et al. A novel inhibitor of homodimerization targeting MyD88 ameliorates renal interstitial fibrosis by counteracting TGF β 1-induced EMT in vivo and in vitro. *Kidney Blood Press. Res.* **43**, 1677–1687 (2018).

[CAS](#) [PubMed](#) [Google Scholar](#)

80. 177.

Stifano, G. et al. Chronic Toll-like receptor 4 stimulation in skin induces inflammation, macrophage activation, transforming growth factor beta signature gene expression, and fibrosis. *Arthritis Res. Ther.* **16**, R136 (2014).

[PubMed](#) [PubMed Central](#) [Google Scholar](#)

81. 178.

Liang, J. et al. Hyaluronan and TLR4 promote surfactant-protein-C-positive alveolar progenitor cell renewal and prevent severe pulmonary fibrosis in mice. *Nat. Med.* **22**, 1285–1293 (2016). **This work discovered an anti-fibrotic mechanism for hyaluronan in pulmonary fibrosis, revealing a novel function for TLR4.**

[CAS](#) [PubMed](#) [PubMed Central](#) [Google Scholar](#)

82. 179.

Pilling, D. et al. Reduction of bleomycin-induced pulmonary fibrosis by serum amyloid P. *J. Immunol.* **179**, 4035–4044 (2007).

[CAS](#) [PubMed](#) [PubMed Central](#) [Google Scholar](#)

83. 180.

Nakagawa, N. et al. Pentraxin-2 suppresses c-Jun/AP-1 signaling to inhibit progressive fibrotic disease. *JCI Insight* **1**, e87446 (2016).

[PubMed](#) [PubMed Central](#) [Google Scholar](#)

84. 181.

Rogliani, P., Calzetta, L., Cavalli, F., Matera, M. G. & Cazzola, M. Pirfenidone, nintedanib and N-acetylcysteine for the treatment of idiopathic pulmonary fibrosis: a systematic review and meta-analysis. *Pulm. Pharmacol. Ther.* **40**, 95–103 (2016).

[CAS](#) [PubMed](#) [Google Scholar](#)

85. 182.

Cao, J. et al. Joint profiling of chromatin accessibility and gene expression in thousands of single cells. *Science* **361**, 1380–1385 (2018).

[ADS](#) [CAS](#) [PubMed](#) [PubMed Central](#) [Google Scholar](#)

86. 183.

Peterson, V. M. et al. Multiplexed quantification of proteins and transcripts in single cells. *Nat. Biotechnol.* **35**, 936–939 (2017).

[CAS](#) [PubMed](#) [Google Scholar](#)

87. 184.

Stoeckius, M. et al. Simultaneous epitope and transcriptome measurement in single cells. *Nat. Methods* **14**, 865–868 (2017).

[CAS](#) [PubMed](#) [PubMed Central](#) [Google Scholar](#)

88. 185.

Rodrigues, S. G. et al. Slide-seq: a scalable technology for measuring genome-wide expression at high spatial resolution. *Science* **363**, 1463–1467 (2019).

[ADS](#) [CAS](#) [PubMed](#) [PubMed Central](#) [Google Scholar](#)

89. 186.

Vickovic, S. et al. High-definition spatial transcriptomics for in situ tissue profiling. *Nat. Methods* **16**, 987–990 (2019).

[CAS](#) [PubMed](#) [PubMed Central](#) [Google Scholar](#)

90. 187.

Eng, C. L. et al. Transcriptome-scale super-resolved imaging in tissues by RNA seqFISH+. *Nature* **568**, 235–239 (2019).

[ADS](#) [CAS](#) [PubMed](#) [PubMed Central](#) [Google Scholar](#)

91. 188.

Stuart, T. et al. Comprehensive integration of single-cell data. *Cell* **177**, 1888–1902 (2019).

[CAS](#) [PubMed](#) [PubMed Central](#) [Google Scholar](#)

92. 189.

Regev, A. et al. The Human Cell Atlas. *eLife* **6**, e27041 (2017).

[PubMed](#) [PubMed Central](#) [Google Scholar](#)

93. 190.

Dudley, J. T. et al. Computational repositioning of the anticonvulsant topiramate for inflammatory bowel disease. *Sci. Transl. Med.* **3**, 96ra76 (2011).

[CAS](#) [PubMed](#) [PubMed Central](#) [Google Scholar](#)

94. 191.

Torok, N. J., Dranoff, J. A., Schuppan, D. & Friedman, S. L. Strategies and endpoints of antifibrotic drug trials: summary and recommendations from the AASLD Emerging Trends Conference, Chicago, June 2014. *Hepatology* **62**, 627–634 (2015).

[PubMed](#) [PubMed Central](#) [Google Scholar](#)

95. 192.

Rieder, F. et al. An expert consensus to standardise definitions, diagnosis and treatment targets for anti-fibrotic stricture therapies in Crohn's disease. *Aliment. Pharmacol. Ther.* **48**, 347–357 (2018).

[CAS](#) [PubMed](#) [PubMed Central](#) [Google Scholar](#)

96. 193.

Montesi, S. B., Désogère, P., Fuchs, B. C. & Caravan, P. Molecular imaging of fibrosis: recent advances and future directions. *J. Clin. Invest.* **129**, 24–33 (2019).

[PubMed](#) [PubMed Central](#) [Google Scholar](#)

97. 194.

Montesi, S. B. et al. Type I collagen-targeted positron emission tomography imaging in idiopathic pulmonary fibrosis: first-in-human

studies. *Am. J. Respir. Crit. Care Med.* **200**, 258–261 (2019).

[CAS](#) [PubMed](#) [PubMed Central](#) [Google Scholar](#)

[Download references](#)

Acknowledgements

N.C.H. is supported by a Wellcome Trust Senior Research Fellowship in Clinical Science (ref. 219542/Z/19/Z), the Medical Research Council, a Chan Zuckerberg Initiative Seed Network Grant, the British Heart Foundation and Tenovus Scotland. F.R. is supported by grants from the National Institutes of Health (T32DK083251, P30DK097948 Pilot, K08DK110415 and R01DK123233), the Crohn's and Colitis Foundation, the Cleveland Clinic, the Rainin Foundation and the Helmsley Charitable Trust through the Stenosis Therapy and Anti-Fibrotic Research (STAR) Consortium.

Author information

Affiliations

1. University of Edinburgh Centre for Inflammation Research, The Queen's Medical Research Institute, Edinburgh BioQuarter, Edinburgh, UK

Neil C. Henderson

2. MRC Human Genetics Unit, Institute of Genetics and Molecular Medicine, University of Edinburgh, Edinburgh, UK

Neil C. Henderson

3. Department of Inflammation and Immunity, Lerner Research Institute, Cleveland Clinic Foundation, Cleveland, USA

Florian Rieder

4. Department of Gastroenterology, Hepatology and Nutrition, Digestive Diseases and Surgery Institute, Cleveland Clinic Foundation, Cleveland, Ohio, USA

Florian Rieder

5. Inflammation & Immunology Research Unit, Pfizer Worldwide Research, Development & Medical, Cambridge, MA, USA

Thomas A. Wynn

Authors

1. Neil C. Henderson

[View author publications](#)

You can also search for this author in [PubMed](#) [Google Scholar](#)

2. Florian Rieder

[View author publications](#)

You can also search for this author in [PubMed](#) [Google Scholar](#)

3. Thomas A. Wynn

[View author publications](#)

You can also search for this author in [PubMed](#) [Google Scholar](#)

Contributions

N.C.H., F.R. and T.A.W contributed equally to the writing and editing of all aspects of this review.

Corresponding author

Correspondence to [Thomas A. Wynn](#).

Ethics declarations

Competing interests

N.C.H. has received research funding from AbbVie, Pfizer, Gilead and Galeto, and is an advisor or consultant for Galeto, Indalo Therapeutics, Pliant Therapeutics, GSK and Boehringer-Ingelheim. F.R. is an advisor or consultant for AbbVie, Allergan, BMS, Boehringer-Ingelheim, Celgene, Falk Pharma, Gilead, Genentech, Gossamer, GSK, Receptos, Thetis, UCB, Samsung, Koutif, Pliant Therapeutics, Metacrine, Takeda, Theravance, Pfizer, Agomab, Helmsley, RedX and Roche. T.A.W. is employed by Pfizer.

Additional information

Peer review information *Nature* thanks Christopher Buckley and the other, anonymous, reviewer(s) for their contribution to the peer review of this work.

Publisher's note Springer Nature remains neutral with regard to jurisdictional claims in published maps and institutional affiliations.

Supplementary information

[Supplementary Information](#)

This file contains Supplementary Tables 1-2.

Rights and permissions

[Reprints and Permissions](#)

About this article



Check for
updates

Cite this article

Henderson, N.C., Rieder, F. & Wynn, T.A. Fibrosis: from mechanisms to medicines. *Nature* **587**, 555–566 (2020). <https://doi.org/10.1038/s41586-020-2938-9>

[Download citation](#)

- Received: 04 May 2020
- Accepted: 14 September 2020
- Published: 25 November 2020
- Issue Date: 26 November 2020
- DOI: <https://doi.org/10.1038/s41586-020-2938-9>

Comments

By submitting a comment you agree to abide by our [Terms](#) and [Community Guidelines](#). If you find something abusive or that does not comply with our terms or guidelines please flag it as inappropriate.

[Access through your institution](#)

[Change institution](#)

[Buy or subscribe](#)

| [Section menu](#) | [Main menu](#) |

- Review
- [Published: 25 November 2020](#)

Discoveries in structure and physiology of mechanically activated ion channels

- [J. M. Kefauver^{1,2} nAff3](#),
- [A. B. Ward](#) [ORCID: orcid.org/0000-0001-7153-3769²](#) &
- [A. Patapoutian](#) [ORCID: orcid.org/0000-0003-0726-7034¹](#)

[Nature](#) volume 587, pages567–576(2020) [Cite this article](#)

- 9 Altmetric
- [Metrics details](#)

Subjects

- [Cryoelectron microscopy](#)
- [Ion transport](#)

Abstract

The ability to sense physical forces is conserved across all organisms. Cells convert mechanical stimuli into electrical or chemical signals via mechanically activated ion channels. In recent years, the identification of new families of mechanosensitive ion channels—such as PIEZO and OSCA/TMEM63 channels—along with surprising insights into well-studied mechanosensitive channels have driven further developments in the mechanotransduction field. Several well-characterized mechanosensory

roles such as touch, blood-pressure sensing and hearing are now linked with primary mechanotransducers. Unanticipated roles of mechanical force sensing continue to be uncovered. Furthermore, high-resolution structures representative of nearly every family of mechanically activated channel described so far have underscored their diversity while advancing our understanding of the biophysical mechanisms of pressure sensing. Here we summarize recent discoveries in the physiology and structures of known mechanically activated ion channel families and discuss their implications for understanding the mechanisms of mechanical force sensing.

[Access through your institution](#)

[Change institution](#)

[Buy or subscribe](#)

Access options

Subscription info for Chinese customers

We have a dedicated website for our Chinese customers. Please go to [naturechina.com](#) to subscribe to this journal.

[Go to naturechina.com](#)

Rent or Buy article

Get time limited or full article access on ReadCube.

from \$8.99

[Rent or Buy](#)

All prices are NET prices.

Additional access options:

- [Log in](#)
- [Access through your institution](#)
- [Learn about institutional subscriptions](#)

Fig. 1: Structures of mechanically activated ion channels.

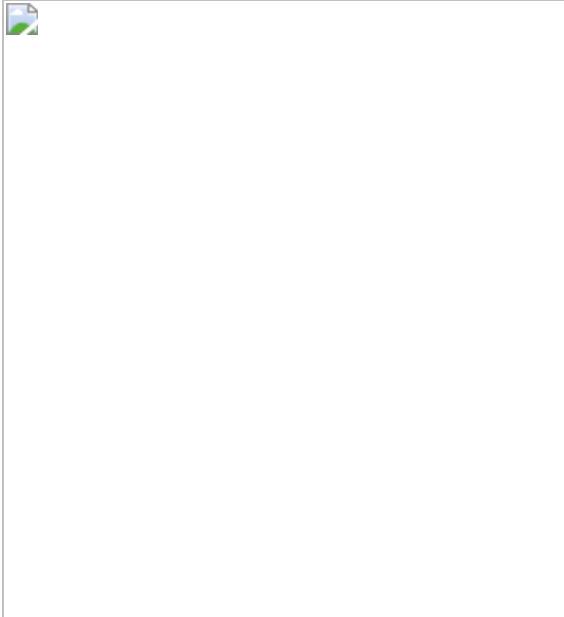


Fig. 2: Mechanistic models of mechanically activated ion channel gating.

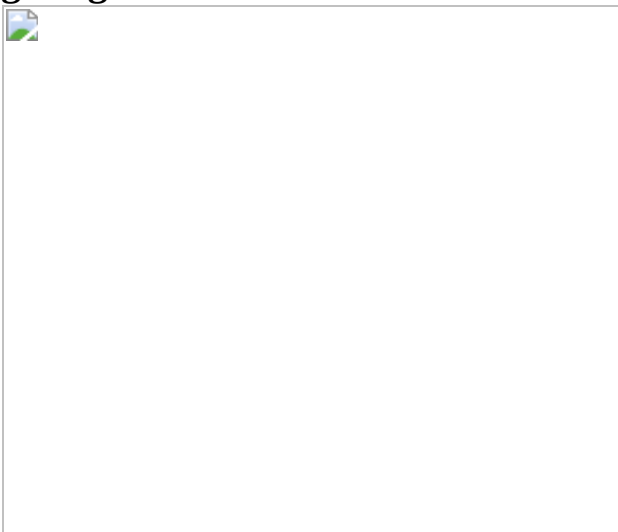
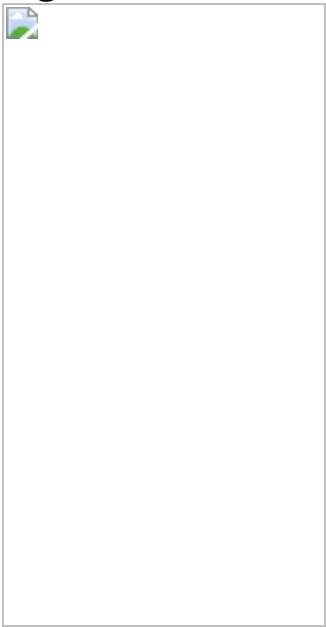


Fig. 3: Lipids observed in structures of mechanosensitive ion channels.



Fig. 4: The MET channel complex.



References

1. 1.

Anishkin, A., Loukin, S. H., Teng, J. & Kung, C. Feeling the hidden mechanical forces in lipid bilayer is an original sense. *Proc. Natl Acad. Sci. USA* **111**, 7898–7905 (2014).

[ADS](#) [CAS](#) [PubMed](#) [Google Scholar](#)

2. 2.

Arnadóttir, J. & Chalfie, M. Eukaryotic mechanosensitive channels. *Annu. Rev. Biophys.* **39**, 111–137 (2010).

[PubMed](#) [Google Scholar](#)

3. 3.

Ranade, S. S., Syeda, R. & Patapoutian, A. Mechanically activated ion channels. *Neuron* **87**, 1162–1179 (2015).

[CAS](#) [PubMed](#) [PubMed Central](#) [Google Scholar](#)

4. 4.

Cox, C. D., Bavi, N. & Martinac, B. Bacterial mechanosensors. *Annu. Rev. Physiol.* **80**, 71–93 (2018).

[CAS](#) [PubMed](#) [Google Scholar](#)

5. 5.

Chalfie, M. Neurosensory mechanotransduction. *Nat. Rev. Mol. Cell Biol.* **10**, 44–52 (2009).

[CAS](#) [PubMed](#) [Google Scholar](#)

6. 6.

Douguet, D. & Honoré, E. Mammalian mechanoelectrical transduction: structure and function of force-gated ion channels. *Cell* **179**, 340–354 (2019).

[CAS](#) [PubMed](#) [Google Scholar](#)

7. 7.

Jin, P., Jan, L. Y. & Jan, Y.-N. Mechanosensitive ion channels: structural features relevant to mechanotransduction mechanisms. *Annu. Rev. Neurosci.* **43**, 207–229 (2020).

[CAS](#) [PubMed](#) [Google Scholar](#)

8. 8.

Coste, B. et al. Piezo1 and Piezo2 are essential components of distinct mechanically activated cation channels. *Science* **330**, 55–60 (2010).
This study uses an RNA interference screen to identify PIEZOs as essential components of a mechanically activated ion channel.

[ADS](#) [CAS](#) [PubMed](#) [PubMed Central](#) [Google Scholar](#)

9. 9.

Murthy, S. E., Dubin, A. E. & Patapoutian, A. Piezos thrive under pressure: mechanically activated ion channels in health and disease. *Nat. Rev. Mol. Cell Biol.* **18**, 771–783 (2017).

[CAS](#) [PubMed](#) [Google Scholar](#)

10. 10.

Brohawn, S. G., Su, Z. & MacKinnon, R. Mechanosensitivity is mediated directly by the lipid membrane in TRAAK and TREK1 K⁺ channels. *Proc. Natl Acad. Sci. USA* **111**, 3614–3619 (2014). **This**

study demonstrates that the mechanically activated K2P channels, TRAAK and TREK1, are inherently mechanosensitive.

[ADS](#) [CAS](#) [PubMed](#) [Google Scholar](#)

11. 11.

Murthy, S. E. et al. OSCA/TMEM63 are an evolutionarily conserved family of mechanically activated ion channels. *eLife* 7, 1–17 (2018). **Several OSCA genes and their mammalian homologues, the TMEM63 family, are shown to be inherently mechanosensitive ion channels.**

[CAS](#) [Google Scholar](#)

12. 12.

Rasmussen, T., Flegler, V. J., Rasmussen, A. & Böttcher, B. Structure of the mechanosensitive channel MscS embedded in the membrane bilayer. *J. Mol. Biol.* 431, 3081–3090 (2019).

[CAS](#) [PubMed](#) [Google Scholar](#)

13. 13.

Reddy, B., Bavi, N., Lu, A., Park, Y. & Perozo, E. Molecular basis of force-from-lipids gating in the mechanosensitive channel MscS. *eLife* 8, e50486 (2019). **These two articles present cryo-EM structures of the bacterial MscS channel in a lipidic nanodisc, substantially updating our understanding of how it is embedded within the membrane.**

[CAS](#) [PubMed](#) [PubMed Central](#) [Google Scholar](#)

14. 14.

Jin, P. et al. Electron cryo-microscopy structure of the mechanotransduction channel NOMPC. *Nature* 547, 118–122 (2017). **This study presents the cryo-EM structure of NOMPC, revealing**

that the large ankyrin repeat domain is arranged with a large spring-like architecture.

[ADS](#) [CAS](#) [PubMed](#) [PubMed Central](#) [Google Scholar](#)

15. 15.

Deng, Z. et al. Cryo-EM and X-ray structures of TRPV4 reveal insight into ion permeation and gating mechanisms. *Nat. Struct. Mol. Biol.* **25**, 252–260 (2018).

[CAS](#) [PubMed](#) [PubMed Central](#) [Google Scholar](#)

16. 16.

Ge, J. et al. Structure of mouse protocadherin 15 of the stereocilia tip link in complex with LHFPL5. *eLife* **7**, e38770 (2018). **Co-expression and purification of the MET complex components PCDH15 and LHFPL5 reveal that a TM helix of the PCDH15 subunit interacts extensively with the TM helices of each LHFPL5 subunit.**

[PubMed](#) [PubMed Central](#) [Google Scholar](#)

17. 17.

Noreng, S., Bharadwaj, A., Posert, R., Yoshioka, C. & Baconguis, I. Structure of the human epithelial sodium channel by cryo-electron microscopy. *eLife* **7**, e39340 (2018).

[PubMed](#) [PubMed Central](#) [Google Scholar](#)

18. 18.

Guo, Y. R. & MacKinnon, R. Structure-based membrane dome mechanism for Piezo mechanosensitivity. *eLife* **6**, e33660 (2017).

[PubMed](#) [PubMed Central](#) [Google Scholar](#)

19. 19.

Saotome, K. et al. Structure of the mechanically activated ion channel Piezo1. *Nature* **554**, 481–486 (2018).

[ADS](#) [CAS](#) [PubMed](#) [Google Scholar](#)

20. 20.

Zhao, Q. et al. Structure and mechanogating mechanism of the Piezo1 channel. *Nature* **554**, 487–492 (2018).

[ADS](#) [CAS](#) [PubMed](#) [Google Scholar](#)

21. 21.

Wang, L. et al. Structure and mechanogating of the mammalian tactile channel PIEZO2. *Nature* **573**, 225–229 (2019). **These four studies present cryo-EM structures of PIEZO1 and PIEZO2, revealing that its curved shape probably resides within the membrane, and providing a near-atomic-resolution view of several features that may be involved in gating by mechanical force.**

[ADS](#) [CAS](#) [PubMed](#) [Google Scholar](#)

22. 22.

Zhang, M. et al. Structure of the mechanosensitive OSCA channels. *Nat. Struct. Mol. Biol.* **25**, 850–858 (2018).

[CAS](#) [PubMed](#) [Google Scholar](#)

23. 23.

Jojoa-Cruz, S. et al. Cryo-EM structure of the mechanically activated ion channel OSCA1.2. *eLife* **7**, e41845 (2018).

[PubMed](#) [PubMed Central](#) [Google Scholar](#)

24. 24.

Liu, X., Wang, J. & Sun, L. Structure of the hyperosmolality-gated calcium-permeable channel OSCA1.2. *Nat. Commun.* **9**, 5060 (2018).

[ADS](#) [PubMed](#) [PubMed Central](#) [Google Scholar](#)

25. 25.

Maity, K. et al. Cryo-EM structure of OSCA1.2 from *Oryza sativa* elucidates the mechanical basis of potential membrane hyperosmolality gating. *Proc. Natl Acad. Sci. USA* **116**, 14309–14318 (2019). **These four studies present cryo-EM structures of OSCA1.2 and other OSCA family members, revealing their structural homology to TMEM16 and highlighting features that may be involved in mechanical gating.**

[CAS](#) [PubMed](#) [Google Scholar](#)

26. 26.

Bavi, N., Cox, C. D., Perozo, E. & Martinac, B. Toward a structural blueprint for bilayer-mediated channel mechanosensitivity. *Channels* **11**, 91–93 (2017). **This study proposed the dragging mechanism of mechanotransduction.**

[PubMed](#) [Google Scholar](#)

27. 27.

Dong, Y. Y. et al. K2P channel gating mechanisms revealed by structures of TREK-2 and a complex with Prozac. *Science* **347**, 1256–1259 (2015).

[ADS](#) [CAS](#) [PubMed](#) [PubMed Central](#) [Google Scholar](#)

28. 28.

Argudo, D., Capponi, S., Bethel, N. P. & Grabe, M. A multiscale model of mechanotransduction by the ankyrin chains of the NOMPC channel. *J. Gen. Physiol.* **151**, 316–327 (2019).

[CAS](#) [PubMed](#) [PubMed Central](#) [Google Scholar](#)

29. 29.

Sukharev, S. I., Martinac, B., Arshavsky, V. Y. & Kung, C. Two types of mechanosensitive channels in the *Escherichia coli* cell envelope: solubilization and functional reconstitution. *Biophys. J.* **65**, 177–183 (1993).

[ADS](#) [CAS](#) [PubMed](#) [PubMed Central](#) [Google Scholar](#)

30. 30.

Haswell, E. S. & Meyerowitz, E. M. MscS-like proteins control plastid size and shape in *Arabidopsis thaliana*. *Curr. Biol.* **16**, 1–11 (2006).

[CAS](#) [PubMed](#) [Google Scholar](#)

31. 31.

Kloda, A. & Martinac, B. Common evolutionary origins of mechanosensitive ion channels in Archaea, Bacteria and cell-walled Eukarya. *Archaea* **1**, 35–44 (2002).

[CAS](#) [PubMed](#) [Google Scholar](#)

32. 32.

Perozo, E., Kloda, A., Cortes, D. M. & Martinac, B. Physical principles underlying the transduction of bilayer deformation forces during mechanosensitive channel gating. *Nat. Struct. Biol.* **9**, 696–703 (2002).

[CAS](#) [PubMed](#) [Google Scholar](#)

33. 33.

Betanzos, M., Chiang, C. S., Guy, H. R. & Sukharev, S. A large iris-like expansion of a mechanosensitive channel protein induced by

membrane tension. *Nat. Struct. Biol.* **9**, 704–710 (2002). **Disulfide cross-linking between the first TM helices on adjacent subunits of MscL in the resting state and in osmotically shocked cells provides the first evidence for the area-expansion model of mechanotransduction.**

[CAS](#) [PubMed](#) [Google Scholar](#)

34. 34.

Chang, G., Spencer, R. H., Lee, A. T., Barclay, M. T. & Rees, D. C. Structure of the MscL homolog from *Mycobacterium tuberculosis*: a gated mechanosensitive ion channel. *Science* **282**, 2220–2226 (1998).

[ADS](#) [CAS](#) [PubMed](#) [Google Scholar](#)

35. 35.

Anishkin, A. et al. On the conformation of the COOH-terminal domain of the large mechanosensitive channel MscL. *J. Gen. Physiol.* **121**, 227–244 (2003).

[CAS](#) [PubMed](#) [PubMed Central](#) [Google Scholar](#)

36. 36.

Isla, I., Wray, R. & Blount, P. The dynamics of protein–protein interactions between domains of MscL at the cytoplasmic–lipid interface. *Channels* **6**, 255–261 (2012).

[CAS](#) [PubMed](#) [PubMed Central](#) [Google Scholar](#)

37. 37.

Li, J. et al. Mechanical coupling of the multiple structural elements of the large-conductance mechanosensitive channel during expansion. *Proc. Natl Acad. Sci. USA* **112**, 10726–10731 (2015).

[ADS](#) [CAS](#) [PubMed](#) [Google Scholar](#)

38. 38.

Bavi, N. et al. The role of MscL amphipathic N terminus indicates a blueprint for bilayer-mediated gating of mechanosensitive channels. *Nat. Commun.* **7**, 11984 (2016).

[ADS](#) [CAS](#) [PubMed](#) [PubMed Central](#) [Google Scholar](#)

39. 39.

Wang, Y. et al. Single molecule FRET reveals pore size and opening mechanism of a mechano-sensitive ion channel. *eLife* **3**, e01834 (2014).

[PubMed](#) [PubMed Central](#) [Google Scholar](#)

40. 40.

Chiang, C. S., Anishkin, A. & Sukharev, S. Gating of the large mechanosensitive channel *in situ*: estimation of the spatial scale of the transition from channel population responses. *Biophys. J.* **86**, 2846–2861 (2004).

[ADS](#) [CAS](#) [PubMed](#) [PubMed Central](#) [Google Scholar](#)

41. 41.

Wiggins, P. & Phillips, R. Membrane–protein interactions in mechanosensitive channels. *Biophys. J.* **88**, 880–902 (2005).

[ADS](#) [CAS](#) [PubMed](#) [Google Scholar](#)

42. 42.

Bass, R. B., Strop, P., Barclay, M. & Rees, D. C. Crystal structure of *Escherichia coli* MscS, a voltage-modulated and mechanosensitive channel. *Science* **298**, 1582–1587 (2002).

[ADS](#) [CAS](#) [PubMed](#) [Google Scholar](#)

43. 43.

Wang, W. et al. The structure of an open form of an *E. coli* mechanosensitive channel at 3.45 Å resolution. *Science* **321**, 1179–1183 (2008).

[ADS](#) [CAS](#) [PubMed](#) [PubMed Central](#) [Google Scholar](#)

44. 44.

Anishkin, A., Kamaraju, K. & Sukharev, S. Mechanosensitive channel MscS in the open state: modeling of the transition, explicit simulations, and experimental measurements of conductance. *J. Gen. Physiol.* **132**, 67–83 (2008).

[CAS](#) [PubMed](#) [PubMed Central](#) [Google Scholar](#)

45. 45.

Vásquez, V., Sotomayor, M., Cordero-Morales, J., Schulten, K. & Perozo, E. A structural mechanism for MscS gating in lipid bilayers. *Science* **321**, 1210–1214 (2008).

[ADS](#) [PubMed](#) [PubMed Central](#) [Google Scholar](#)

46. 46.

Rasmussen, T. et al. Interaction of the mechanosensitive channel, MscS, with the membrane bilayer through lipid intercalation into grooves and pockets. *J. Mol. Biol.* **431**, 3339–3352 (2019).

[CAS](#) [PubMed](#) [PubMed Central](#) [Google Scholar](#)

47. 47.

Edwards, M. D., Bartlett, W. & Booth, I. R. Pore mutations of the *Escherichia coli* MscS channel affect desensitization but not ionic preference. *Biophys. J.* **94**, 3003–3013 (2008).

[ADS](#) [CAS](#) [PubMed](#) [Google Scholar](#)

48. 48.

Cox, C. D. et al. Selectivity mechanism of the mechanosensitive channel MscS revealed by probing channel subconducting states. *Nat. Commun.* **4**, 2137 (2013).

[ADS](#) [CAS](#) [PubMed](#) [Google Scholar](#)

49. 49.

Rowe, I., Anishkin, A., Kamaraju, K., Yoshimura, K. & Sukharev, S. The cytoplasmic cage domain of the mechanosensitive channel MscS is a sensor of macromolecular crowding. *J. Gen. Physiol.* **143**, 543–557 (2014).

[CAS](#) [PubMed](#) [PubMed Central](#) [Google Scholar](#)

50. 50.

Hamilton, E. S., Schlegel, A. M. & Haswell, E. S. United in diversity: mechanosensitive ion channels in plants. *Annu. Rev. Plant Biol.* **66**, 113–137 (2015).

[CAS](#) [PubMed](#) [Google Scholar](#)

51. 51.

Lee, J. S., Wilson, M. E., Richardson, R. A. & Haswell, E. S. Genetic and physical interactions between the organellar mechanosensitive ion channel homologs MSL1, MSL2, and MSL3 reveal a role for inter-organellar communication in plant development. *Plant Direct* **3**, e00124 (2019).

[PubMed](#) [PubMed Central](#) [Google Scholar](#)

52. 52.

Hamilton, E. S. & Haswell, E. S. The tension-sensitive ion transport activity of MSL8 is critical for its function in pollen hydration and germination. *Plant Cell Physiol.* **58**, 1222–1237 (2017).

[CAS](#) [PubMed](#) [Google Scholar](#)

53. 53.

Basu, D., Shoots, J. M. & Haswell, E. S. Interactions between the N- and C-termini of the mechanosensitive ion channel AtMSL10 are consistent with a three-step mechanism for activation. *J. Exp. Bot.* **71**, 4020–4032 (2020).

[PubMed](#) [Google Scholar](#)

54. 54.

Basu, D. & Haswell, E. S. The mechanosensitive ion channel MSL10 potentiates responses to cell swelling in *Arabidopsis* seedlings. *Curr. Biol.* **30**, 2716–2728.e6 (2020).

[CAS](#) [PubMed](#) [Google Scholar](#)

55. 55.

Li, Y. et al. Structural insights into a plant mechanosensitive ion channel MSL1. *Cell Rep.* **30**, 4518–4527.e3 (2020). **This study presents the open and closed structures of MSL1, providing insights into the gating of this plant mechanosensitive channel.**

[CAS](#) [PubMed](#) [Google Scholar](#)

56. 56.

Deng, Z. et al. Structural mechanism for gating of a eukaryotic mechanosensitive channel of small conductance. *Nat. Commun.* **11**, 3690 (2020).

[ADS](#) [CAS](#) [PubMed](#) [PubMed Central](#) [Google Scholar](#)

57. 57.

Brohawn, S. G. How ion channels sense mechanical force: insights from mechanosensitive K₂P channels TRAAK, TREK1, and TREK2. *Ann. NY Acad. Sci.* **1352**, 20–32 (2015).

[ADS](#) [CAS](#) [PubMed](#) [Google Scholar](#)

58. 58.

Brohawn, S. G. et al. The mechanosensitive ion channel TRAAK is localized to the mammalian node of Ranvier. *eLife* **8**, 713990 (2019).

[Google Scholar](#)

59. 59.

Brohawn, S. G., Campbell, E. B. & MacKinnon, R. Domain-swapped chain connectivity and gated membrane access in a Fab-mediated crystal of the human TRAAK K⁺ channel. *Proc. Natl Acad. Sci. USA* **110**, 2129–2134 (2013).

[ADS](#) [CAS](#) [PubMed](#) [Google Scholar](#)

60. 60.

Schewe, M. et al. A non-canonical voltage-sensing mechanism controls gating in K₂P K⁺ channels. *Cell* **164**, 937–949 (2016).

[CAS](#) [PubMed](#) [PubMed Central](#) [Google Scholar](#)

61. 61.

Brohawn, S. G., del Mármo, J. & MacKinnon, R. Crystal structure of the human K₂P TRAAK, a lipid- and mechano-sensitive K⁺ ion channel. *Science* **335**, 436–441 (2012).

[ADS](#) [CAS](#) [PubMed](#) [PubMed Central](#) [Google Scholar](#)

62. 62.

Brohawn, S. G., Campbell, E. B. & MacKinnon, R. Physical mechanism for gating and mechanosensitivity of the human TRAAK K⁺ channel. *Nature* **516**, 126–130 (2014).

[ADS](#) [CAS](#) [PubMed](#) [PubMed Central](#) [Google Scholar](#)

63. 63.

Lolicato, M., Riegelhaupt, P. M., Arrigoni, C., Clark, K. A. & Minor, D. L., Jr. Transmembrane helix straightening and buckling underlies activation of mechanosensitive and thermosensitive K(2P) channels. *Neuron* **84**, 1198–1212 (2014). **These two articles present crystal structures of mechanosenstive K2P channels with opposing interpretations of the activity state of the channel; Brohawn et al. observe lipid density that extends into the channel pore.**

[CAS](#) [PubMed](#) [PubMed Central](#) [Google Scholar](#)

64. 64.

McClenaghan, C. et al. Polymodal activation of the TREK-2 K2P channel produces structurally distinct open states. *J. Gen. Physiol.* **147**, 497–505 (2016).

[CAS](#) [PubMed](#) [PubMed Central](#) [Google Scholar](#)

65. 65.

Aryal, P. et al. Bilayer-mediated structural transitions control mechanosensitivity of the TREK-2 K2P channel. *Structure* **25**, 708–718.e2 (2017). **Molecular dynamics modelling of TREK-2 elucidates the gating transition upon membrane tension.**

[CAS](#) [PubMed](#) [PubMed Central](#) [Google Scholar](#)

66. 66.

Clausen, M. V., Jarerattanachat, V., Carpenter, E. P., Sansom, M. S. P. & Tucker, S. J. Asymmetric mechanosensitivity in a eukaryotic ion channel. *Proc. Natl Acad. Sci. USA* **114**, E8343–E8351 (2017).

[CAS](#) [PubMed](#) [Google Scholar](#)

67. 67.

Lolicato, M. et al. K₂P2.1 (TREK-1)-activator complexes reveal a cryptic selectivity filter binding site. *Nature* **547**, 364–368 (2017).

[ADS](#) [CAS](#) [PubMed](#) [PubMed Central](#) [Google Scholar](#)

68. 68.

Murthy, S. E. et al. The mechanosensitive ion channel Piezo2 mediates sensitivity to mechanical pain in mice. *Sci. Transl. Med.* **10**, eaat9897 (2018).

[PubMed](#) [PubMed Central](#) [Google Scholar](#)

69. 69.

Szczot, M. et al. PIEZO2 mediates injury-induced tactile pain in mice and humans. *Sci. Transl. Med.* **10**, eaat9892 (2018).

[PubMed](#) [PubMed Central](#) [Google Scholar](#)

70. 70.

Zeng, W. Z. et al. PIEZOs mediate neuronal sensing of blood pressure and the baroreceptor reflex. *Science* **362**, 464–467 (2018).

[ADS](#) [CAS](#) [PubMed](#) [PubMed Central](#) [Google Scholar](#)

71. 71.

Nonomura, K. et al. Mechanically activated ion channel PIEZO1 is required for lymphatic valve formation. *Proc. Natl Acad. Sci. USA*

115, 12817–12822 (2018).

[CAS](#) [PubMed](#) [Google Scholar](#)

72. 72.

Choi, D. et al. Piezo1 incorporates mechanical force signals into the genetic program that governs lymphatic valve development and maintenance. *JCI Insight* **4**, e125068 (2019).

[PubMed Central](#) [Google Scholar](#)

73. 73.

Faucherre, A. et al. Piezo1 is required for outflow tract and aortic valve development. *J. Mol. Cell. Cardiol.* **143**, 51–62 (2020).

[CAS](#) [PubMed](#) [Google Scholar](#)

74. 74.

Duchemin, A. L., Vignes, H. & Vermot, J. Mechanically activated piezo channels modulate outflow tract valve development through the Yap1 and Klf2–Notch signaling axis. *eLife* **8**, e44706 (2019).

[CAS](#) [PubMed](#) [PubMed Central](#) [Google Scholar](#)

75. 75.

1. Kang, H. et al. Piezo1 mediates angiogenesis through activation of MT1-MMP signaling. *Am. J. Physiol. Cell Physiol.* **316**, C92–C103 (2019).

[CAS](#) [PubMed](#) [Google Scholar](#)

2. 76.

He, L., Si, G., Huang, J., Samuel, A. D. T. & Perrimon, N. Mechanical regulation of stem-cell differentiation by the stretch-activated Piezo channel. *Nature* **555**, 103–106 (2018).

[ADS](#) [CAS](#) [PubMed](#) [PubMed Central](#) [Google Scholar](#)

3. 77.

Sun, W. et al. The mechanosensitive Piezo1 channel is required for bone formation. *eLife* **8**, e47454 (2019).

[CAS](#) [PubMed](#) [PubMed Central](#) [Google Scholar](#)

4. 78.

Li, X. et al. Stimulation of Piezo1 by mechanical signals promotes bone anabolism. *eLife* **8**, e49631 (2019).

[PubMed](#) [PubMed Central](#) [Google Scholar](#)

5. 79.

Ellefsen, K. L. et al. Myosin-II mediated traction forces evoke localized Piezo1-dependent Ca^{2+} flickers. *Commun. Biol.* **2**, 298 (2019).

[PubMed](#) [PubMed Central](#) [Google Scholar](#)

6. 80.

Song, Y. et al. The mechanosensitive ion channel Piezo inhibits axon regeneration. *Neuron* **102**, 373–389 (2019).

[CAS](#) [PubMed](#) [PubMed Central](#) [Google Scholar](#)

7. 81.

Solis, A. G. et al. Mechanosensation of cyclical force by PIEZO1 is essential for innate immunity. *Nature* **573**, 69–74 (2019).

[ADS](#) [CAS](#) [PubMed](#) [PubMed Central](#) [Google Scholar](#)

8. 82.

Ma, S. et al. Common PIEZO1 allele in African populations causes RBC dehydration and attenuates *Plasmodium* infection. *Cell* **173**, 443–455 (2018).

[CAS](#) [PubMed](#) [PubMed Central](#) [Google Scholar](#)

9. 83.

Nguetse, C. N. et al. A common polymorphism in the druggable ion channel *PIEZO1* is associated with protection from severe malaria. *Proc. Natl Acad. Sci. USA* **117**, 9074–9081 (2020).

[CAS](#) [PubMed](#) [Google Scholar](#)

10. 84.

Ge, J. et al. Architecture of the mammalian mechanosensitive Piezo1 channel. *Nature* **527**, 64–69 (2015).

[ADS](#) [CAS](#) [PubMed](#) [Google Scholar](#)

11. 85.

Wu, J., Goyal, R. & Grandl, J. Localized force application reveals mechanically sensitive domains of Piezo1. *Nat. Commun.* **7**, 12939

(2016).

[ADS](#) [CAS](#) [PubMed](#) [PubMed Central](#) [Google Scholar](#)

12. 86.

Wu, J. et al. Inactivation of mechanically activated Piezo1 ion channels is determined by the C-terminal extracellular domain and the inner pore helix. *Cell Rep.* **21**, 2357–2366 (2017).

[CAS](#) [PubMed](#) [PubMed Central](#) [Google Scholar](#)

13. 87.

Lewis, A. H. & Grandl, J. Inactivation kinetics and mechanical gating of Piezo1 ion channels depend on subdomains within the cap. *Cell Rep.* **30**, 870–880 (2020).

[CAS](#) [PubMed](#) [PubMed Central](#) [Google Scholar](#)

14. 88.

Coste, B. et al. Piezo1 ion channel pore properties are dictated by C-terminal region. *Nat. Commun.* **6**, 7223 (2015).

[ADS](#) [PubMed](#) [PubMed Central](#) [Google Scholar](#)

15. 89.

Drin, G. & Antonny, B. Amphipathic helices and membrane curvature. *FEBS Lett.* **584**, 1840–1847 (2010).

[CAS](#) [PubMed](#) [Google Scholar](#)

16. 90.

Geng, J. et al. A plug-and-latch mechanism for gating the mechanosensitive Piezo channel. *Neuron* **106**, 438–451 (2020).

[CAS](#) [PubMed](#) [Google Scholar](#)

17. 91.

Wang, Y. et al. A lever-like transduction pathway for long-distance chemical- and mechano-gating of the mechanosensitive Piezo1 channel. *Nat. Commun.* **9**, 1300 (2018).

[ADS](#) [PubMed](#) [PubMed Central](#) [Google Scholar](#)

18. 92.

Taberner, F. J. et al. Structure-guided examination of the mechanogating mechanism of PIEZO2. *Proc. Natl Acad. Sci. USA* **116**, 14260–14269 (2019).

[CAS](#) [PubMed](#) [Google Scholar](#)

19. 93.

Bae, C., Sachs, F. & Gottlieb, P. A. The mechanosensitive ion channel Piezo1 is inhibited by the peptide GsMTx4. *Biochemistry* **50**, 6295–6300 (2011).

[CAS](#) [PubMed](#) [PubMed Central](#) [Google Scholar](#)

20. 94.

Alcaino, C., Knutson, K., Gottlieb, P. A., Farrugia, G. & Beyder, A. Mechanosensitive ion channel Piezo2 is inhibited by D-GsMTx4. *Channels* **11**, 245–253 (2017).

[PubMed](#) [PubMed Central](#) [Google Scholar](#)

21. 95.

Suchyna, T. M. Piezo channels and GsMTx4: two milestones in our understanding of excitatory mechanosensitive channels and their role in pathology. *Prog. Biophys. Mol. Biol.* **130**, 244–253 (2017).

[CAS](#) [PubMed](#) [PubMed Central](#) [Google Scholar](#)

22. 96.

Syeda, R. et al. Chemical activation of the mechanotransduction channel Piezo1. *eLife* **4**, e07369 (2015).

[PubMed Central](#) [Google Scholar](#)

23. 97.

Evans, E. L. et al. Yoda1 analogue (Dooku1) which antagonizes Yoda1-evoked activation of Piezo1 and aortic relaxation. *Br. J. Pharmacol.* **175**, 1744–1759 (2018).

[CAS](#) [PubMed](#) [PubMed Central](#) [Google Scholar](#)

24. 98.

Lacroix, J. J., Botello-Smith, W. M. & Luo, Y. Probing the gating mechanism of the mechanosensitive channel Piezo1 with the small molecule Yoda1. *Nat. Commun.* **9**, 2029 (2018).

[ADS](#) [PubMed](#) [PubMed Central](#) [Google Scholar](#)

25. 99.

Hou, C. et al. DUF221 proteins are a family of osmosensitive calcium-permeable cation channels conserved across eukaryotes. *Cell Res.* **24**, 632–635 (2014).

[CAS](#) [PubMed](#) [PubMed Central](#) [Google Scholar](#)

26. 100.

Yuan, F. et al. OSCA1 mediates osmotic-stress-evoked Ca^{2+} increases vital for osmosensing in *Arabidopsis*. *Nature* **514**, 367–371 (2014).

[ADS](#) [CAS](#) [PubMed](#) [Google Scholar](#)

27. 101.

Yan, H. et al. Heterozygous variants in the mechanosensitive ion channel TMEM63A result in transient hypomyelination during infancy. *Am. J. Hum. Genet.* **105**, 996–1004 (2019).

[CAS](#) [PubMed](#) [PubMed Central](#) [Google Scholar](#)

28. 102.

Pan, B. et al. TMC1 forms the pore of mechanosensory transduction channels in vertebrate inner ear hair cells. *Neuron* **99**, 736–753 (2018).

[CAS](#) [PubMed](#) [PubMed Central](#) [Google Scholar](#)

29. 103.

Ballesteros, A., Fenollar-Ferrer, C. & Swartz, K. J. Structural relationship between the putative hair cell mechanotransduction channel TMC1 and TMEM16 proteins. *eLife* **7**, e38433 (2018).

[PubMed](#) [PubMed Central](#) [Google Scholar](#)

30. 104.

Startek, J. B., Boonen, B., Talavera, K. & Meseguer, V. TRP channels as sensors of chemically-induced changes in cell membrane mechanical properties. *Int. J. Mol. Sci.* **20**, 371 (2019).

[PubMed Central](#) [Google Scholar](#)

31. 105.

Walker, R. G., Willingham, A. T. & Zuker, C. S. A. *A Drosophila* mechanosensory transduction channel. *Science* **287**, 2229–2234 (2000). **This study identifies the *nompC* gene via a genetic screen with a readout of transduction currents upon mechanical stimulus of mechanoreceptor bristles in *D. melanogaster*.**

[ADS](#) [CAS](#) [PubMed](#) [Google Scholar](#)

32. 106.

Cheng, L. E., Song, W., Looger, L. L., Jan, L. Y. & Jan, Y. N. The role of the TRP channel NompC in *Drosophila* larval and adult locomotion. *Neuron* **67**, 373–380 (2010).

[CAS](#) [PubMed](#) [PubMed Central](#) [Google Scholar](#)

33. 107.

Sidi, S., Friedrich, R. W. & Nicolson, T. NompC TRP channel required for vertebrate sensory hair cell mechanotransduction. *Science* **301**, 96–99 (2003).

[ADS](#) [CAS](#) [PubMed](#) [Google Scholar](#)

34. 108.

Lee, J., Moon, S., Cha, Y. & Chung, Y. D. *Drosophila* TRPN(=NOMPC) channel localizes to the distal end of mechanosensory cilia. *PLoS ONE* **5**, e11012 (2010).

[ADS](#) [PubMed](#) [PubMed Central](#) [Google Scholar](#)

35. 109.

Yan, Z. et al. *Drosophila* NOMPC is a mechanotransduction channel subunit for gentle-touch sensation. *Nature* **493**, 221–225 (2013).

[ADS](#) [CAS](#) [PubMed](#) [Google Scholar](#)

36. 110.

Sun, L. et al. Ultrastructural organization of NompC in the mechanoreceptive organelle of *Drosophila* campaniform mechanoreceptors. *Proc. Natl Acad. Sci. USA* **116**, 7343–7352 (2019).

[CAS](#) [PubMed](#) [Google Scholar](#)

37. 111.

Lee, G. et al. Nanospring behaviour of ankyrin repeats. *Nature* **440**, 246–249 (2006).

[ADS](#) [CAS](#) [PubMed](#) [Google Scholar](#)

38. 112.

Wang, Y. et al. Push-to-open: The gating mechanism of the tethered mechanosensitive ion channel NompC. Preprint at <https://doi.org/10.1101/853721> (2019).

39. 113.

Servin-Vences, M. R., Moroni, M., Lewin, G. R. & Poole, K. Direct measurement of TRPV4 and PIEZO1 activity reveals multiple mechanotransduction pathways in chondrocytes. *eLife* **6**, e21074 (2017).

[PubMed](#) [Google Scholar](#)

40. 114.

Nikolaev, Y. A. et al. Mammalian TRP ion channels are insensitive to membrane stretch. *J. Cell Sci.* **132**, 238360 (2019).

[Google Scholar](#)

41. 115.

Corey, D. P. & Hudspeth, A. J. Kinetics of the receptor current in bullfrog saccular hair cells. *J. Neurosci.* **3**, 962–976 (1983). **This study provided one of the first confirmations of the existence of a channel directly activated by mechanical stimuli, measured in hair cells from the vestibular system of a bullfrog.**

[CAS](#) [PubMed](#) [PubMed Central](#) [Google Scholar](#)

42. 116.

Cunningham, C. L. & Müller, U. Molecular structure of the hair cell mechanoelectrical transduction complex. *Cold Spring Harb. Perspect. Med.* **9**, a033167 (2019).

[CAS](#) [PubMed](#) [Google Scholar](#)

43. 117.

Jia, Y. et al. TMC1 and TMC2 proteins are pore-forming subunits of mechanosensitive ion channels. *Neuron* **105**, 310–321 (2020). **A study showing that TMC1 and TMC2 proteins, putative pore-forming components of the MET channel complex, form mechanically activated channels when reconstituted in liposomes.**

[CAS](#) [PubMed](#) [Google Scholar](#)

44. 118.

Xiong, W. et al. TMHS is an integral component of the mechanotransduction machinery of cochlear hair cells. *Cell* **151**, 1283–1295 (2012).

[CAS](#) [PubMed](#) [PubMed Central](#) [Google Scholar](#)

45. 119.

Cunningham, C. L. et al. TMIE defines pore and gating properties of the mechanotransduction channel of mammalian cochlear hair cells. *Neuron* **107**, 126–143 (2020).

[CAS](#) [PubMed](#) [Google Scholar](#)

46. 120.

Driscoll, M. & Chalfie, M. The *mec-4* gene is a member of a family of *Caenorhabditis elegans* genes that can mutate to induce neuronal degeneration. *Nature* **349**, 588–593 (1991). **In this study, *mec-4*, the founding member of the DEG gene family of mechanoreceptors in *C. elegans* was cloned.**

[ADS](#) [CAS](#) [PubMed](#) [Google Scholar](#)

47. 121.

Chen, Y., Bharill, S., Isacoff, E. Y. & Chalfie, M. Subunit composition of a DEG/ENaC mechanosensory channel of *Caenorhabditis elegans*. *Proc. Natl Acad. Sci. USA* **112**, 11690–11695 (2015).

[ADS](#) [CAS](#) [PubMed](#) [Google Scholar](#)

48. 122.

Ben-Shahar, Y. Sensory functions for degenerin/epithelial sodium channels (DEG/ENaC). *Adv. Genet.* **76**, 1–26 (2011).

[CAS](#) [PubMed](#) [PubMed Central](#) [Google Scholar](#)

49. 123.

Lin, S. H. et al. Evidence for the involvement of ASIC3 in sensory mechanotransduction in proprioceptors. *Nat. Commun.* **7**, 11460 (2016).

[ADS](#) [CAS](#) [PubMed](#) [PubMed Central](#) [Google Scholar](#)

50. 124.

Knoepp, F. et al. Shear force sensing of epithelial Na⁺ channel (ENaC) relies on N-glycosylated asparagines in the palm and knuckle domains of αENaC. *Proc. Natl Acad. Sci. USA* **117**, 717–726 (2020).

[CAS](#) [PubMed](#) [Google Scholar](#)

51. 125.

Martinac, B., Adler, J. & Kung, C. Mechanosensitive ion channels of *E. coli* activated by amphipaths. *Nature* **348**, 261–263 (1990).

[ADS](#) [CAS](#) [PubMed](#) [Google Scholar](#)

52. 126.

Martinac, B. et al. Tuning ion channel mechanosensitivity by asymmetry of the transbilayer pressure profile. *Biophys. Rev.* **10**, 1377–1384 (2018).

[CAS](#) [PubMed](#) [PubMed Central](#) [Google Scholar](#)

53. 127.

Nomura, T. et al. Differential effects of lipids and lyso-lipids on the mechanosensitivity of the mechanosensitive channels MscL and MscS. *Proc. Natl Acad. Sci. USA* **109**, 8770–8775 (2012).

[ADS](#) [CAS](#) [PubMed](#) [Google Scholar](#)

54. 128.

Syeda, R. et al. Piezo1 channels are inherently mechanosensitive. *Cell Rep.* **17**, 1739–1746 (2016).

[CAS](#) [PubMed](#) [PubMed Central](#) [Google Scholar](#)

55. 129.

Cantor, R. S. The influence of membrane lateral pressures on simple geometric models of protein conformational equilibria. *Chem. Phys. Lipids* **101**, 45–56 (1999).

[CAS](#) [PubMed](#) [Google Scholar](#)

56. 130.

Ridone, P. et al. “Force-from-lipids” gating of mechanosensitive channels modulated by PUFAs. *J. Mech. Behav. Biomed. Mater.* **79**, 158–167 (2018).

[CAS](#) [PubMed](#) [Google Scholar](#)

57. 131.

Pliotas, C. et al. The role of lipids in mechanosensation. *Nat. Struct. Mol. Biol.* **22**, 991–998 (2015).

[CAS](#) [PubMed](#) [PubMed Central](#) [Google Scholar](#)

58. 132.

Pliotas, C. & Naismith, J. H. Spectator no more, the role of the membrane in regulating ion channel function. *Curr. Opin. Struct. Biol.* **45**, 59–66 (2017). **This review discusses an entropy-based mechanism of mechanotransduction in which lipids dissociate from hydrophobic pockets, inducing conformational changes in mechanically-activated channels.**

[CAS](#) [PubMed](#) [Google Scholar](#)

59. 133.

Haselwandter, C. A. & MacKinnon, R. Piezo’s membrane footprint and its contribution to mechanosensitivity. *eLife* **7**, e41968 (2018).

[PubMed](#) [PubMed Central](#) [Google Scholar](#)

60. 134.

Lin, Y.-C. C. et al. Force-induced conformational changes in PIEZO1. *Nature* **573**, 230–234 (2019). **This study uses atomic force microscopy to both induce membrane tension and measure its effects on reconstituted PIEZO1, providing evidence that PIEZO1 expands under tension.**

[ADS](#) [CAS](#) [PubMed](#) [PubMed Central](#) [Google Scholar](#)

61. 135.

Hu, J., Chiang, L. Y., Koch, M. & Lewin, G. R. Evidence for a protein tether involved in somatic touch. *EMBO J.* **29**, 855–867 (2010).

[CAS](#) [PubMed](#) [PubMed Central](#) [Google Scholar](#)

62. 136.

Cox, C. D., Bavi, N. & Martinac, B. Biophysical principles of ion-channel-mediated mechanosensory transduction. *Cell Rep.* **29**, 1–12 (2019).

[CAS](#) [PubMed](#) [Google Scholar](#)

63. 137.

Li Fraine, S., Patel, A., Duprat, F. & Sharif-Naeini, R. Dynamic regulation of TREK1 gating by polycystin 2 via a filamin A-mediated cytoskeletal mechanism. *Sci. Rep.* **7**, 17403 (2017).

[ADS](#) [PubMed](#) [PubMed Central](#) [Google Scholar](#)

64. 138.

Lopes, C. M. B. et al. PIP2 hydrolysis underlies agonist-induced inhibition and regulates voltage gating of two-pore domain K⁺ channels. *J. Physiol.* **564**, 117–129 (2005).

[CAS](#) [PubMed](#) [PubMed Central](#) [Google Scholar](#)

65. 139.

Borbiro, I., Badheka, D. & Rohacs, T. Activation of TRPV1 channels inhibits mechanosensitive Piezo channel activity by depleting membrane phosphoinositides. *Sci. Signal.* **8**, ra15 (2015).

[PubMed](#) [PubMed Central](#) [Google Scholar](#)

66. 140.

Anishkin, A. & Kung, C. Stiffened lipid platforms at molecular force foci. *Proc. Natl Acad. Sci. USA* **110**, 4886–4892 (2013). **This article proposes an innovative model for mechanotransduction in which cholesterol-rich platforms, maintained by cholesterol-binding scaffold proteins and localized to focal adhesions or adherens junctions, provide specialized force-sensing domains.**

[ADS](#) [CAS](#) [PubMed](#) [Google Scholar](#)

67. 141.

Petersen, E. N., Chung, H. W., Nayebosadri, A. & Hansen, S. B. Kinetic disruption of lipid rafts is a mechanosensor for phospholipase D. *Nat. Commun.* **7**, 13873 (2016).

[ADS](#) [CAS](#) [PubMed](#) [PubMed Central](#) [Google Scholar](#)

68. 142.

Chen, X. et al. A feedforward mechanism mediated by mechanosensitive ion channel PIEZO1 and tissue mechanics promotes glioma aggression. *Neuron* **100**, 799–815 (2018).

[CAS](#) [PubMed](#) [Google Scholar](#)

69. 143.

Poole, K., Herget, R., Lapatsina, L., Ngo, H. D. & Lewin, G. R. Tuning Piezo ion channels to detect molecular-scale movements relevant for fine touch. *Nat. Commun.* **5**, 3520 (2014).

[ADS](#) [PubMed](#) [PubMed Central](#) [Google Scholar](#)

70. 144.

Qi, Y. et al. Membrane stiffening by STOML3 facilitates mechanosensation in sensory neurons. *Nat. Commun.* **6**, 8512 (2015).

[ADS](#) [CAS](#) [PubMed](#) [PubMed Central](#) [Google Scholar](#)

71. 145.

Beaulieu-Laroche, L. et al. TACAN is an ion channel involved in sensing mechanical pain. *Cell* **180**, 956–967 (2020).

[CAS](#) [PubMed](#) [Google Scholar](#)

72. 146.

Patkunarajah, A. et al. TMEM87a/Elkin1, a component of a novel mechanoelectrical transduction pathway, modulates melanoma adhesion and migration. *eLife* **9**, e53308 (2020).

[PubMed](#) [PubMed Central](#) [Google Scholar](#)

73. 147.

Xu, J. et al. GPR68 senses flow and is essential for vascular physiology. *Cell* **173**, 762–775 (2018).

[CAS](#) [PubMed](#) [PubMed Central](#) [Google Scholar](#)

74. 148.

Bavi, O., Vossoughi, M., Naghdabadi, R. & Jamali, Y. The combined effect of hydrophobic mismatch and bilayer local bending on the regulation of mechanosensitive ion channels. *PLoS ONE* **11**, e0150578 (2016).

[PubMed](#) [PubMed Central](#) [Google Scholar](#)

[Download references](#)

Acknowledgements

This work was supported by NIH grants R01 HL143297. A.P. is an investigator of the Howard Hughes Medical Institute. We thank J. Grandl, S. Murthy, S. Jojoa-Cruz and A. Gharpure for critical reading of the manuscript.

Author information

Author notes

1. J. M. Kefauver

Present address: Department of Molecular Biology, University of Geneva, Geneva, Switzerland

Affiliations

1. Howard Hughes Medical Institute, Department of Neuroscience, The Scripps Research Institute, La Jolla, CA, USA

J. M. Kefauver & A. Patapoutian

2. Department of Integrative Structural and Computational Biology, The Scripps Research Institute, La Jolla, CA, USA

J. M. Kefauver & A. B. Ward

Authors

1. J. M. Kefauver

[View author publications](#)

You can also search for this author in [PubMed](#) [Google Scholar](#)

2. A. B. Ward

[View author publications](#)

You can also search for this author in [PubMed](#) [Google Scholar](#)

3. A. Patapoutian

[View author publications](#)

You can also search for this author in [PubMed](#) [Google Scholar](#)

Contributions

J.M.K, A.B.W. and A.P. conceptualized the content of this work. J.M.K. reviewed the literature and drafted the manuscript and figures. J.M.K., A.B.W. and A.P. discussed, wrote and edited the Review.

Corresponding authors

Correspondence to [A. B. Ward](#) or [A. Patapoutian](#).

Ethics declarations

Competing interests

The authors declare no competing interests.

Additional information

Peer review information *Nature* thanks Boris Martinac and the other, anonymous, reviewer(s) for their contribution to the peer review of this work.

Publisher's note Springer Nature remains neutral with regard to jurisdictional claims in published maps and institutional affiliations.

Rights and permissions

[Reprints and Permissions](#)

About this article



Check for
updates

Cite this article

Kefauver, J.M., Ward, A.B. & Patapoutian, A. Discoveries in structure and physiology of mechanically activated ion channels. *Nature* **587**, 567–576 (2020). <https://doi.org/10.1038/s41586-020-2933-1>

[Download citation](#)

- Received: 01 April 2020
- Accepted: 19 August 2020
- Published: 25 November 2020
- Issue Date: 26 November 2020
- DOI: <https://doi.org/10.1038/s41586-020-2933-1>

Comments

By submitting a comment you agree to abide by our [Terms](#) and [Community Guidelines](#). If you find something abusive or that does not comply with our terms or guidelines please flag it as inappropriate.

[Access through your institution](#)

[Change institution](#)

[Buy or subscribe](#)

This article was downloaded by **calibre** from <https://www.nature.com/articles/s41586-020-2933-1>

- Article
- [Published: 25 November 2020](#)

Experimental evidence of neutrinos produced in the CNO fusion cycle in the Sun

- [The Borexino Collaboration](#)

Nature volume 587, pages577–582(2020) [Cite this article](#)

- 531 Altmetric
- [Metrics details](#)

Subjects

- [Experimental particle physics](#)
- [Stars](#)
- [Stellar evolution](#)

Abstract

For most of their existence, stars are fuelled by the fusion of hydrogen into helium. Fusion proceeds via two processes that are well understood theoretically: the proton–proton (*pp*) chain and the carbon–nitrogen–oxygen (CNO) cycle^{1,2}. Neutrinos that are emitted along such fusion processes in the solar core are the only direct probe of the deep interior of the Sun. A complete spectroscopic study of neutrinos from the *pp* chain, which produces about 99 per cent of the solar energy, has been performed previously³; however, there has been no reported experimental evidence of

the CNO cycle. Here we report the direct observation, with a high statistical significance, of neutrinos produced in the CNO cycle in the Sun. This experimental evidence was obtained using the highly radiopure, large-volume, liquid-scintillator detector of Borexino, an experiment located at the underground Laboratori Nazionali del Gran Sasso in Italy. The main experimental challenge was to identify the excess signal—only a few counts per day above the background per 100 tonnes of target—that is attributed to interactions of the CNO neutrinos. Advances in the thermal stabilization of the detector over the last five years enabled us to develop a method to constrain the rate of bismuth-210 contaminating the scintillator. In the CNO cycle, the fusion of hydrogen is catalysed by carbon, nitrogen and oxygen, and so its rate—as well as the flux of emitted CNO neutrinos—depends directly on the abundance of these elements in the solar core. This result therefore paves the way towards a direct measurement of the solar metallicity using CNO neutrinos. Our findings quantify the relative contribution of CNO fusion in the Sun to be of the order of 1 per cent; however, in massive stars, this is the dominant process of energy production. This work provides experimental evidence of the primary mechanism for the stellar conversion of hydrogen into helium in the Universe.

[Access through your institution](#)

[Change institution](#)

[Buy or subscribe](#)

Access options

Subscription info for Chinese customers

We have a dedicated website for our Chinese customers. Please go to [naturechina.com](#) to subscribe to this journal.

[Go to naturechina.com](#)

Rent or Buy article

Get time limited or full article access on ReadCube.

from \$8.99

[Rent or Buy](#)

All prices are NET prices.

Additional access options:

- [Log in](#)
- [Access through your institution](#)
- [Learn about institutional subscriptions](#)

Fig. 1: CNO nuclear fusion sequences and the energy spectra of solar neutrinos.

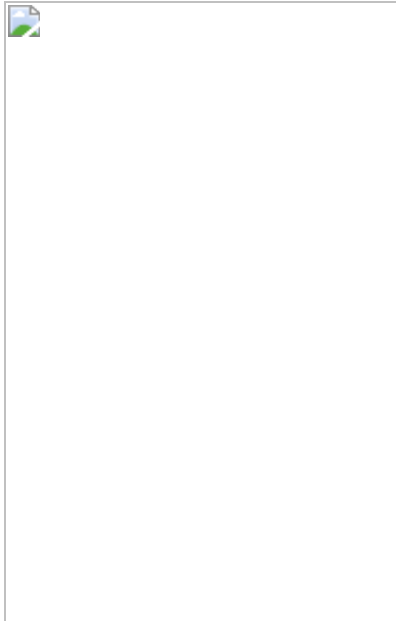


Fig. 2: Spectral fit of the Borexino data.

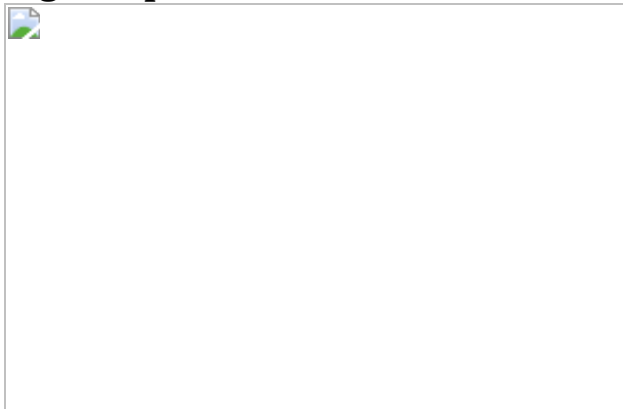
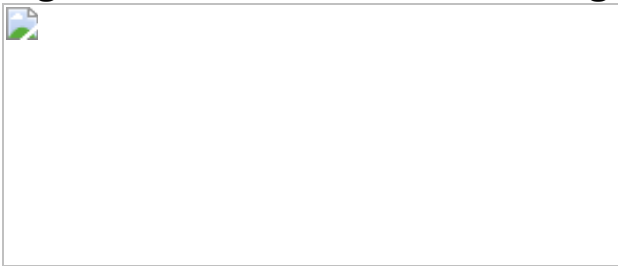


Fig. 3: Spatial and temporal distribution of ^{210}Po activity.



Fig. 4: Results of the CNO counting and spectral analyses.



Data availability

The datasets generated during the current study are freely available from the repository <https://bxopen.lngs.infn.it/>. Additional information is available from the Borexino Collaboration spokesperson (spokesperson-borex@lngs.infn.it) upon reasonable request.

References

1. 1.

Bahcall, J. N. *Neutrino Astrophysics* (Cambridge Univ. Press, 1989).

2. 2.

Vinyoles, N. et al. A new generation of standard solar models. *Astrophys. J.* **835**, 202 (2017).

[ADS](#) [Google Scholar](#)

3. 3.

The Borexino Collaboration. Comprehensive measurement of pp -chain solar neutrinos. *Nature* **562**, 505–510 (2018).

[ADS](#) [CAS](#) [Google Scholar](#)

4. 4.

Salaris, M. & Cassisi, S. *Evolution of Stars and Stellar Populations* (John Wiley & Sons, 2005).

5. 5.

Angulo, C. et al. A compilation of charged-particle induced thermonuclear reaction rates. *Nucl. Phys. A* **656**, 3–183 (1999).

[ADS](#) [Google Scholar](#)

6. 6.

Davis, R. Jr *A Half-Century with Solar Neutrinos*. Nobel Prize Lecture <https://www.nobelprize.org/prizes/physics/2002/davis/lecture/> (2002).

7. 7.

GALLEX collaboration. Solar neutrinos observed by GALLEX at Gran Sasso. *Phys. Lett. B* **285**, 376 (1992).

[Google Scholar](#)

8. 8.

SAGE collaboration. Results from SAGE (The Russian–American Gallium solar neutrino experiment). *Phys. Lett. B* **328**, 234 (1994).

[Google Scholar](#)

9. 9.

McDonald, A. B. *The Sudbury Neutrino Observatory: Observation of Flavor Change for Solar Neutrinos*. Nobel Prize Lecture
<https://www.nobelprize.org/prizes/physics/2015/mcdonald/lecture/>
(2015).

10. 10.

Hirata, K. et al. Observation of ${}^8\text{B}$ solar neutrinos in the Kamiokande-II detector. *Phys. Rev. Lett.* **63**, 16 (1989).

[ADS](#) [CAS](#) [PubMed](#) [Google Scholar](#)

11. 11.

Ahmad, Q. et al. Direct evidence for neutrino flavor transformation from neutral-current interactions in the Sudbury Neutrino Observatory. *Phys. Rev. Lett.* **89**, 011301 (2002).

[ADS](#) [CAS](#) [PubMed](#) [Google Scholar](#)

12. 12.

Araki, T. et al. Measurement of neutrino oscillation with KamLAND: evidence of spectral distortion. *Phys. Rev. Lett.* **94**, 081801 (2005).

[ADS](#) [CAS](#) [PubMed](#) [Google Scholar](#)

13. 13.

Borexino Collaboration. Neutrinos from the primary proton–proton fusion process in the Sun. *Nature* **512**, 383–386 (2014).

[ADS](#) [Google Scholar](#)

14. 14.

Bellini, G. et al. Precision measurement of the ${}^7\text{Be}$ solar neutrino interaction rate in Borexino. *Phys. Rev. Lett.* **107**, 141302 (2011).

[ADS](#) [CAS](#) [PubMed](#) [Google Scholar](#)

15. 15.

Bethe, H. A. Energy production in stars. *Phys. Rev.* **55**, 434–456 (1939).

[ADS](#) [CAS](#) [MATH](#) [Google Scholar](#)

16. 16.

von Weizsäcker, C. F. Über Elementumwandlungen im Innern der Sterne I. *Phys. Z.* **38**, 176 (1937).

[MATH](#) [Google Scholar](#)

17. 17.

Serenelli, A. M., Haxton, W. C. & Peña-Garay, C. Solar models with accretion. I. application to the solar abundance problem. *Astrophys. J.* **743**, 24 (2011).

[ADS](#) [Google Scholar](#)

18. 18.

Alimonti, G. et al. The Borexino detector at the Laboratori Nazionali del Gran Sasso. *Nucl. Instrum. Methods Phys. Res. A* **600**, 568–593 (2009).

[ADS](#) [CAS](#) [Google Scholar](#)

19. 19.

Bellini, G. et al. Final results of Borexino Phase-I on low-energy solar neutrino spectroscopy. *Phys. Rev. D* **89**, 112007 (2014).

[ADS](#) [Google Scholar](#)

20. 20.

Agostini, M. et al. Simultaneous precision spectroscopy of $p\bar{p}$, ^7Be and $pe\bar{p}$ solar neutrinos with Borexino Phase-II. *Phys. Rev. D* **100**, 082004 (2019).

[ADS](#) [CAS](#) [Google Scholar](#)

21. 21.

Alimonti, G. et al. Science and technology of BOREXINO: a real-time detector for low energy solar neutrinos. *Astropart. Phys.* **16**, 205–234 (2002).

[ADS](#) [Google Scholar](#)

22. 22.

Agostini, M. et al. Comprehensive geoneutrino analysis with Borexino. *Phys. Rev. D* **101**, 012009 (2020).

[ADS](#) [CAS](#) [Google Scholar](#)

23. 23.

Ding, X. F. GooStats: A GPU-based framework for multi-variate analysis in particle physics. *J. Instrum.* **13**, P12018 (2018).

[CAS](#) [Google Scholar](#)

24. 24.

Agostini, M. et al. Sensitivity to neutrinos from the solar CNO cycle in Borexino. *Eur. Phys. J. C* <https://doi.org/10.1140/epjc/s10052-020-08534-2> (2020).

25. 25.

Vissani, F. Luminosity constraint and entangled solar neutrino signals. In *Solar Neutrinos, Proc. 5th International Solar Neutrino Conference* (eds Meyer, M. & Zuber, K.) 121–141 (World Scientific, 2019).

26. 26.

Bergström, J., Gonzalez-Garcia, M. C., Maltoni, M., Peña-Garay, C., Serenelli, A. M. & Song, N. Updated determination of the solar neutrino fluxes from solar neutrino data. *J. High Energy Phys.* **2016**, 132 (2016).

[Google Scholar](#)

27. 27.

Capozzi, F., Lisi, E., Marrone, A. & Palazzo, A. Global analysis of oscillation parameters. *J. Phys. Conf. Ser.* **1312**, 012005 (2019).

[CAS](#) [Google Scholar](#)

28. 28.

Villante, F. L., Ianni, A., Lombardi, F., Pagliaroli, G. & Vissani, F. A step toward CNO solar neutrino detection in liquid scintillators. *Phys. Lett. B* **701**, 336–341 (2011).

[ADS](#) [CAS](#) [Google Scholar](#)

29. 29.

Bravo-Berguño, D. et al. The Borexino Thermal Monitoring & Management System and simulations of the fluid-dynamics of the Borexino detector under asymmetrical, changing boundary conditions. *Nucl. Instrum. Methods Phys. Res. A* **885**, 38–53 (2018).

[ADS](#) [Google Scholar](#)

30. 30.

Di Marcello, V. et al. Fluid-dynamics and transport of ^{210}Po in the scintillator Borexino detector: a numerical analysis. *Nucl. Instrum. Methods Phys. Res. A* **964**, 163801 (2020).

[Google Scholar](#)

31. 31.

Agostini, M. et al. The Monte Carlo simulation of the Borexino detector. *Astropart. Phys.* **97**, 136–159 (2018).

[ADS](#) [Google Scholar](#)

32. 32.

Daniel, H. Das β -spektrum des RaE. *Nucl. Phys.* **31**, 293–307 (1962).

[CAS](#) [Google Scholar](#)

33. 33.

Grau Carles, A. & Grau Malonda, A. Precision measurement of the RaE shape factor. *Nucl. Phys. A* **596**, 83–90 (1996).

[ADS](#) [Google Scholar](#)

34. 34.

Alekseev, I. E. et al. Precision measurement of ^{210}Bi β -spectrum. Preprint at <https://arxiv.org/abs/2005.08481> (2020).

35. 35.

Back, H. et al. Borexino calibrations: hardware, methods, and results. *J. Instrum.* **7**, P10018 (2012).

[Google Scholar](#)

36. 36.

de Holanda, P. C., Liao, W. & Smirnov, A. Yu. Toward precision measurements in solar neutrinos. *Nucl. Phys. B* **702**, 307–332 (2004).

[ADS](#) [Google Scholar](#)

37. 37.

Capozzi, F., Lisi, E., Marrone, A. & Palazzo, A. Current unknowns in the three neutrino framework. *Prog. Part. Nucl. Phys.* **102**, 48–72 (2018).

[ADS](#) [CAS](#) [Google Scholar](#)

38. 38.

Cowan, G., Cranmer, K., Gross, E. & Vitells, O. Asymptotic formulae for likelihood-based tests of new physics. *Eur. Phys. J. C* **71**, 1554 (2011).

[ADS](#) [Google Scholar](#)

39. 39.

Bahcall, J. N. Line versus continuum solar neutrinos. *Phys. Rev. D* **41**, 2964–2966 (1990).

[ADS](#) [CAS](#) [Google Scholar](#)

40. 40.

Stonehill, L. C., Formaggio, J. A. & Robertson, R. G. H. Solar neutrinos from CNO electron capture. *Phys. Rev. C* **69**, 015801 (2004).

[ADS](#) [Google Scholar](#)

41. 41.

Villante, F. L. ecCNO solar neutrinos: a challenge for gigantic ultra-pure liquid scintillator detectors. *Phys. Lett. B* **742**, 279–284 (2015).

[ADS](#) [CAS](#) [Google Scholar](#)

42. 42.

Birks, J. B. *The Theory and Practice of Scintillation Counting* (Pergamon, 1964).

43. 43.

Benziger, J. et al. The scintillator purification system for the Borexino solar neutrino detector. *Nucl. Instrum. Methods Phys. Res. A* **587**, 277–291 (2008).

[ADS](#) [CAS](#) [Google Scholar](#)

44. 44.

Alimonti, G. et al. The liquid handling systems for the Borexino solar neutrino detector. *Nucl. Instrum. Methods Phys. Res. A* **609**, 58–78 (2009).

[ADS](#) [CAS](#) [Google Scholar](#)

45. 45.

Bellini, G. et al. Cosmic-muon flux and annual modulation in Borexino at 3800 m water-equivalent depth. *J. Cosmol. Astropart. Phys.* **2012**, 015 (2012).

[Google Scholar](#)

46. 46.

Bellini, G. et al. Cosmogenic backgrounds in Borexino at 3800 m water-equivalent depth. *J. Cosmol. Astropart. Phys.* **2013**, 049 (2013).

[Google Scholar](#)

47. 47.

Bellini, G. et al. Muon and cosmogenic neutron detection in Borexino. *J. Instrum.* **6**, P05005 (2011).

[Google Scholar](#)

48. 48.

Cruickshank Miller, C. The Stokes–Einstein law for diffusion in solution. *Proc. R. Soc. Lond. A* **106**, 724–729 (1924).

[ADS](#) [Google Scholar](#)

49. 49.

Wójcik, M., Wlazlo, W., Zuzel, G. & Heusser, G. Radon diffusion through polymer membranes used in the solar neutrino experiment Borexino. *Nucl. Instrum. Methods Phys. Res. A* **449**, 158–171 (2000).

[ADS](#) [Google Scholar](#)

50. 50.

Hoecker, A., Speckmayer, P., Stelzer, J., Therhaag, J., von Toerne, H. & Voss, E. TMVA - toolkit for multivariate data analysis. Preprint at <https://arxiv.org/abs/physics/0703039> (2007).

51. 51.

Feroz, F., Hobson, M. P., Cameron, E. & Pettitt, A. N. Importance nested sampling and the MultiNest algorithm. *Open J. Astrophys.* **2**, 10 (2019).

[Google Scholar](#)

52. 52.

Feroz, F., Hobson, M. P. & Bridges, M. MultiNest: an efficient and robust Bayesian inference tool for cosmology and particle physics. *Mon. Not. R. Astron. Soc.* **398**, 1601–1614 (2009).

[ADS](#) [Google Scholar](#)

53. 53.

Feroz, F. & Hobson, M. P. Multimodal nested sampling: an efficient and robust alternative to Markov Chain Monte Carlo methods for astronomical data analyses. *Mon. Not. R. Astron. Soc.* **384**, 449–463 (2008).

[ADS](#) [Google Scholar](#)

54. 54.

Fick, A. Ueber Diffusion. *Ann. Phys.* **170**, 59–86 (1855).

[Google Scholar](#)

55. 55.

Gorski, K. M., Wandelt, B. D., Hansen, F. K., Hivon, E. & Banday, A. J. The HEALPix Primer. Preprint at <https://arxiv.org/abs/astro-ph/9905275> (1999).

56. 56.

Agostini, M. et al. Seasonal modulation of the ${}^7\text{Be}$ solar neutrino rate in Borexino. *Astropart. Phys.* **92**, 21–29 (2017).

[ADS](#) [Google Scholar](#)

57. 57.

Bellini, G. et al. First evidence of *pep* solar neutrinos by direct detection in Borexino. *Phys. Rev. Lett.* **108**, 051302 (2012).

[ADS](#) [CAS](#) [PubMed](#) [Google Scholar](#)

58. 58.

Cousins, R. D. & Highland, V. L. Incorporating systematic uncertainties into an upper limit. *Nucl. Instrum. Methods Phys. Res. A* **320**, 331–335 (1992).

[ADS](#) [Google Scholar](#)

59. 59.

Brown, L. D., Cai, T. T. & Das Gupta, A. Interval estimation for a binomial proportion. *Stat. Sci.* **16**, 101–133 (2001).

[MathSciNet](#) [Google Scholar](#)

[Download references](#)

Acknowledgements

We acknowledge the hospitality and support of the Laboratori Nazionali del Gran Sasso (Italy). The Borexino program is made possible by funding from Istituto Nazionale di Fisica Nucleare (INFN) (Italy), National Science Foundation (NSF) (USA), Deutsche Forschungsgemeinschaft (DFG) and Helmholtz-Gemeinschaft (HGF) (Germany), Russian Foundation for Basic Research (RFBR) (grant numbers 16-29-13014ofi-m, 17-02-00305A and 19-02-00097A), Russian Science Foundation (RSF) (grant number 17-12-01009) and Ministry of Science and Higher Education of the Russian Federation (contract number 075-15-2020-778) (Russia), and Narodowe Centrum Nauki (NCN) (grant number UMO 2017/26/M/ST2/00915) (Poland). We acknowledge the computing services of Bologna INFN-CNAF data centre and U-Lite Computing Center and Network Service at LNGS (Italy), and the computing time granted through JARA on the supercomputer JURECA at Forschungszentrum Jülich (Germany). This research was supported in part by PLGrid Infrastructure (Poland).

Author information

Author notes

1. Z. Bagdasarian

Present address: Department of Physics, University of California,
Berkeley, Berkeley, CA, USA

2. D. Bravo

Present address: Departamento de Física Teórica, Universidad
Autónoma de Madrid, Madrid, Spain

3. P. Cavalcante & A. Goretti

Present address: INFN Laboratori Nazionali del Gran Sasso, Assergi,
Italy

4. Y. Suvorov

Present address: Dipartimento di Fisica, Università degli Studi
Federico II e INFN, Naples, Italy

Affiliations

**1. Department of Physics and Astronomy, University College London,
London, UK**

M. Agostini

**2. Physik-Department E15, Technische Universität München, Garching,
Germany**

M. Agostini, K. Altenmüller, S. Appel, D. Jeschke, B. Neumair, L.
Oberauer, L. Papp, S. Schönert & F. von Feilitzsch

3. National Research Centre Kurchatov Institute, Moscow, Russia

V. Atroshchenko, E. Litvinovich, G. Lukyanchenko, L.
Lukyanchenko, I. Machulin, R. Nugmanov, G. Raikov, M.
Skorokhvatov & Y. Suvorov

4. Institut für Kernphysik, Forschungszentrum Jülich, Jülich, Germany

Z. Bagdasarian, A. S. Göttel, S. Kumaran, L. Ludhova, Ö. Penek, M. Redchuk, G. Settanta & A. Singhal

5. Dipartimento di Fisica, Università degli Studi and INFN, Milan, Italy

D. Basilico, G. Bellini, D. Bravo, B. Caccianiga, D. D'Angelo, A. Formozov, M. Giannarchi, P. Lombardi, E. Meroni, L. Miramonti, L. Pelicci, G. Ranucci & A. Re

6. Chemical Engineering Department, Princeton University, Princeton, NJ, USA

J. Benziger

7. INFN Laboratori Nazionali del Gran Sasso, Assergi, Italy

R. Biondi, A. Di Giacinto, V. Di Marcello, C. Ghiano, Aldo Ianni, M. Laubenstein, M. T. Ranalli, A. Razeto, N. Rossi, Y. Suvorov, R. Tartaglia & F. L. Villante

8. Physics Department, Princeton University, Princeton, NJ, USA

F. Calaprice, X. F. Ding, A. Di Ludovico, C. Galbiati, A. Goretti, Andrea Ianni & L. Pietrofaccia

9. Dipartimento di Fisica, Università degli Studi and INFN, Genoa, Italy

A. Caminata, S. Davini, L. Di Noto, M. Pallavicini, G. Testera & S. Zavatarelli

10. Physics Department, Virginia Polytechnic Institute and State University, Blacksburg, VA, USA

P. Cavalcante & R. B. Vogelaar

11. Lomonosov Moscow State University Skobeltsyn Institute of Nuclear Physics, Moscow, Russia

A. Chepurnov & M. Gromov

12. St Petersburg Nuclear Physics Institute, NRC Kurchatov Institute,
Gatchina, Russia

A. Derbin, I. Drachnev, I. Lomskaya, V. Muratova, N. Pilipenko, D.
Semenov & E. Unzhakov

13. Joint Institute for Nuclear Research, Dubna, Russia

A. Formozov, M. Gromov, O. Smirnov, A. Sotnikov & A. Vishneva

14. Astroparticule et Cosmologie, Université de Paris, CNRS, Paris,
France

D. Franco

15. Gran Sasso Science Institute, L'Aquila, Italy

C. Galbiati

16. III. Physikalisches Institut B, RWTH Aachen University, Aachen,
Germany

A. S. Göttel, S. Kumaran, L. Ludhova, Ö. Penek, M. Redchuk & A.
Singhal

17. Institute of Physics and Excellence Cluster PRISMA+, Johannes
Gutenberg-Universität Mainz, Mainz, Germany

D. Guffanti, J. Martyn, M. Nieslony, V. Orekhov & M. Wurm

18. M. Smoluchowski Institute of Physics, Jagiellonian University,
Krakow, Poland

A. Jany, M. Misiaszek, M. Wojcik & G. Zuzel

19. Institute for Nuclear Research of NAS Ukraine, Kyiv, Ukraine

V. Kobychev

20. Department of Physics, School of Engineering, Physical and Mathematical Sciences, Royal Holloway, University of London, Egham, UK

G. Korga

21. Institute of Nuclear Research (Atomki), Debrecen, Hungary

G. Korga

22. National Research Nuclear University MEPhI (Moscow Engineering Physics Institute), Moscow, Russia

E. Litvinovich, I. Machulin, R. Nugmanov & M. Skorokhvatov

23. Department of Physics, Technische Universität Dresden, Dresden, Germany

M. Meyer, J. Thurn & K. Zuber

24. Dipartimento di Chimica, Biologia e Biotecnologie, Università degli Studi e INFN, Perugia, Italy

F. Ortica & A. Romani

25. Amherst Center for Fundamental Interactions and Physics Department, University of Massachusetts, Amherst, MA, USA

A. Pocar

26. Dipartimento di Scienze Fisiche e Chimiche, Università dell'Aquila, L'Aquila, Italy

F. L. Villante

Consortia

The Borexino Collaboration

- , M. Agostini
- , K. Altenmüller
- , S. Appel
- , V. Atroshchenko
- , Z. Bagdasarian
- , D. Basilico
- , G. Bellini
- , J. Benziger
- , R. Biondi
- , D. Bravo
- , B. Caccianiga
- , F. Calaprice
- , A. Caminata
- , P. Cavalcante
- , A. Chepurnov
- , D. D'Angelo
- , S. Davini
- , A. Derbin
- , A. Di Giacinto
- , V. Di Marcello
- , X. F. Ding
- , A. Di Ludovico
- , L. Di Noto
- , I. Drachnev
- , A. Formozov
- , D. Franco
- , C. Galbiati
- , C. Ghiano
- , M. Giammarchi
- , A. Goretti
- , A. S. Göttel
- , M. Gromov
- , D. Guffanti
- , Aldo Ianni
- , Andrea Ianni

- , A. Jany
- , D. Jeschke
- , V. Kobychev
- , G. Korga
- , S. Kumaran
- , M. Laubenstein
- , E. Litvinovich
- , P. Lombardi
- , I. Lomskaya
- , L. Ludhova
- , G. Lukyanchenko
- , L. Lukyanchenko
- , I. Machulin
- , J. Martyn
- , E. Meroni
- , M. Meyer
- , L. Miramonti
- , M. Misiaszek
- , V. Muratova
- , B. Neumair
- , M. Nieslony
- , R. Nugmanov
- , L. Oberauer
- , V. Orekhov
- , F. Ortica
- , M. Pallavicini
- , L. Papp
- , L. Pelicci
- , Ö. Penek
- , L. Pietrofaccia
- , N. Pilipenko
- , A. Pocar
- , G. Raikov
- , M. T. Ranalli
- , G. Ranucci
- , A. Razeto
- , A. Re

- , M. Redchuk
- , A. Romani
- , N. Rossi
- , S. Schönert
- , D. Semenov
- , G. Settanta
- , M. Skorokhvatov
- , A. Singhal
- , O. Smirnov
- , A. Sotnikov
- , Y. Suvorov
- , R. Tartaglia
- , G. Testera
- , J. Thurn
- , E. Unzhakov
- , F. L. Villante
- , A. Vishneva
- , R. B. Vogelaar
- , F. von Feilitzsch
- , M. Wojcik
- , M. Wurm
- , S. Zavatarelli
- , K. Zuber
- & G. Zuzel

Contributions

The Borexino detector was designed, constructed and commissioned by the Borexino Collaboration over the span of more than 30 years. The Borexino Collaboration sets the science goals. Scintillator purification and handling, material radiopurity assay, source calibration campaigns, photomultiplier tube and electronics operations, signal processing and data acquisition, Monte Carlo simulations of the detector, and data analyses were performed by Borexino members, who also discussed and approved the scientific results. This Article was prepared by a subgroup of authors that was appointed by the Collaboration and was subjected to an internal

collaboration-wide review process. All authors reviewed and approved the final version of the manuscript.

Corresponding author

Correspondence to [G. Ranucci](#).

Ethics declarations

Competing interests

The authors declare no competing interests.

Additional information

Peer review information *Nature* thanks Marc Pinsonneault, Gabriel Orebí Gann and David Wark for their contribution to the peer review of this work. Peer reviewer reports are available.

Publisher's note Springer Nature remains neutral with regard to jurisdictional claims in published maps and institutional affiliations.

Extended data figures and tables

[Extended Data Fig. 1 The Borexino detector.](#)

Schematic view of the structure of the Borexino apparatus. From inside to outside: the liquid scintillator, the buffer liquid, the stainless steel sphere with the photomultipliers, and the water tank.

[Extended Data Fig. 2 The Borexino detector after the thermal stabilization.](#)

The Borexino water tank after completion of the thermal insulation and deployment of the active temperature control system.

Extended Data Fig. 3 Temperature probes of the Borexino detector.

Distribution of temperature probes around and inside the Borexino detector. For simplicity, the probes on the water tank (WT) dome and in the pit below the detector are not shown.

Extended Data Fig. 4 Temperature evolution over time in the Borexino detector.

Graph depicting the temperature as a function of time in different volumes of the Borexino detector. The vertical dashed lines show the beginning of the thermal insulation installation (1), the turning off of the water loop inside the water tank (2), the completing of the thermal insulation installation (3), the activation of the temperature control system on the dome of the water tank (4), the set-point change (5) and the activation of the air control system in experimental hall C (6).

Extended Data Fig. 5 The low polonium field in the Borexino scintillator.

Three-dimensional view of the ^{210}Po activity inside the entire nylon vessel (see colour code). The innermost blue region contains the LPoF (black grid). The white grid is the software-defined fiducial volume. a.u., arbitrary units.

Extended Data Fig. 6 Analysis of the low polonium field.

Top, the rate of ^{210}Po in cylinders of 3-m radius and 10-cm height located along the z axis from -2 m to 2 m, as a function of time with 1-month binning. The dashed lines indicate the z coordinate of the fiducial volume. The markers show the positions of the centre of the LPoF obtained with two fit methods: paraboloid (red) and spline (white). Both fit methods follow the dark-blue minimum of the ^{210}Po activity well. The structure visible in mid-2019 is due to a local instability produced by a tuning of the active temperature control system. This transient has no effect on the final result.

Bottom, distribution of ^{210}Po events after the blind alignment of data using the z_0 from the paraboloidal fit (red markers in the top graph). The red solid lines indicate the paraboloidal fit within 20 t with equation (4).

Extended Data Fig. 7 Angular and radial uniformity of the β events in the optimized energy window.

Top, angular power spectrum as a function of the multipole moment l of observed β events (black points) compared with 10^4 uniformly distributed events from Monte Carlo simulations at 1σ (dark pink) and 2σ (pink) confidence levels (C.L.). Data are compatible with a uniform distribution within the uncertainty of 0.59 cpd per 100 t. Inset, angular distribution of the β events. Bottom, normalized radial distribution of β events r/r_0 (black points), where $r_0 = 2.5$ m is the radius of the sphere surrounding the analysis fiducial volume. The linear fit of the data (red solid line) is shown along with the 1σ (yellow) and 2σ (green) confidence level bands. The data are compatible with a uniform distribution within 0.52 cpd per 100 t.

Extended Data Fig. 8 Energy distributions from a multivariate fit of the Borexino data.

Full multivariate fit results for the TFC-subtracted (left) and the TFC-tagged (right) energy spectra with corresponding residuals. In both graphs the magenta lines represent the resulting fit function, the red line is the CNO neutrino electron recoil spectrum, the green dotted line is the *pep* neutrino electron recoil spectrum, the dashed blue line is the ^{210}Bi β spectrum, and in grey we report the remaining background (bkgs) contributions.

Extended Data Fig. 9 Radial distribution from a multivariate fit of the Borexino data.

Radial distribution of events in the multivariate fit. The red line is the resulting fit, the green line represents the internal uniform contribution and

the blue line shows the non-uniform contribution from the external background. NDF, the number of degrees of freedom in the fit.

[Extended Data Fig. 10 Frequentist hypothesis test for the CNO observation.](#)

Distribution of the test statistics q (equation (5) from Monte Carlo pseudo-datasets). The grey distribution q_0 is obtained with no CNO simulated data and includes the systematic uncertainty. The black vertical line represents $q_{\text{data}} = 30.05$. The corresponding P value of q_0 with respect to q_{data} gives the significance of the CNO discovery ($>5.0\sigma$ at 99% confidence level). For comparison, in blue is the q_0 without the systematics. The red histogram represents the expected test statistics distribution for an injected CNO rate equal to 7.2 cpd per 100 t—that is, our best fit value.

Supplementary information

[Peer Review File](#)

Rights and permissions

[Reprints and Permissions](#)

About this article



Check for
updates

Cite this article

The Borexino Collaboration., Agostini, M., Altenmüller, K. *et al.*
Experimental evidence of neutrinos produced in the CNO fusion cycle in

the Sun. *Nature* **587**, 577–582 (2020). <https://doi.org/10.1038/s41586-020-2934-0>

[Download citation](#)

- Received: 26 June 2020
- Accepted: 02 October 2020
- Published: 25 November 2020
- Issue Date: 26 November 2020
- DOI: <https://doi.org/10.1038/s41586-020-2934-0>

Comments

By submitting a comment you agree to abide by our [Terms](#) and [Community Guidelines](#). If you find something abusive or that does not comply with our terms or guidelines please flag it as inappropriate.

[Access through your institution](#)

[Change institution](#)

[Buy or subscribe](#)

This article was downloaded by **calibre** from <https://www.nature.com/articles/s41586-020-2934-0>

- Article
- [Published: 25 November 2020](#)

Observing the emergence of a quantum phase transition shell by shell

- [Luca Bayha](#) [ORCID: orcid.org/0000-0001-8835-437X^{1 na1}](#),
- [Marvin Holten](#) [ORCID: orcid.org/0000-0002-0652-4484^{1 na1}](#),
- [Ralf Klemt¹](#),
- [Keerthan Subramanian¹](#),
- [Johannes Bjerlin^{2,3,4}](#),
- [Stephanie M. Reimann²](#),
- [Georg M. Bruun^{5,6}](#),
- [Philipp M. Preiss](#) [ORCID: orcid.org/0000-0002-5677-617X¹](#) &
- [Selim Jochim](#) [ORCID: orcid.org/0000-0001-6049-2658¹](#)

[Nature](#) volume 587, pages583–587(2020)[Cite this article](#)

- 200 Accesses
- 22 Altmetric
- [Metrics details](#)

Subjects

- [Phase transitions and critical phenomena](#)
- [Quantum simulation](#)
- [Ultracold gases](#)

Abstract

Many-body physics describes phenomena that cannot be understood by looking only at the constituents of a system¹. Striking examples are broken symmetry, phase transitions and collective excitations². To understand how such collective behaviour emerges as a system is gradually assembled from individual particles has been a goal in atomic, nuclear and solid-state physics for decades^{3,4,5,6}. Here we observe the few-body precursor of a quantum phase transition from a normal to a superfluid phase. The transition is signalled by the softening of the mode associated with amplitude vibrations of the order parameter, usually referred to as a Higgs mode⁷. We achieve fine control over ultracold fermions confined to two-dimensional harmonic potentials and prepare closed-shell configurations of 2, 6 and 12 fermionic atoms in the ground state with high fidelity.

Spectroscopy is then performed on our mesoscopic system while tuning the pair energy from zero to a value larger than the shell spacing. Using full atom counting statistics, we find the lowest resonance to consist of coherently excited pairs only. The distinct non-monotonic interaction dependence of this many-body excitation, combined with comparison with numerical calculations allows us to identify it as the precursor of the Higgs mode. Our atomic simulator provides a way to study the emergence of collective phenomena and the thermodynamic limit, particle by particle.

[Access through your institution](#)

[Change institution](#)

[Buy or subscribe](#)

Access options

Subscription info for Chinese customers

We have a dedicated website for our Chinese customers. Please go to naturechina.com to subscribe to this journal.

[Go to naturechina.com](#)

Rent or Buy article

Get time limited or full article access on ReadCube.

from \$8.99

[Rent or Buy](#)

All prices are NET prices.

Additional access options:

- [Log in](#)
- [Access through your institution](#)
- [Learn about institutional subscriptions](#)

Fig. 1: Deterministic preparation of two-dimensional closed-shell configurations.



Fig. 2: Excitation spectrum for 6 particles.



Fig. 3: Excitation spectra as function of interaction strength for 6 and 12 particles.



Fig. 4: Coherent driving of the lower pair excitation mode.



Data availability

The data that support the findings of this study are available from the corresponding authors upon reasonable request. [Source data](#) are provided

with this paper.

References

1. 1.

Anderson, P. W. More is different. *Science* **177**, 393–396 (1972).

[ADS](#) [CAS](#) [Article](#) [Google Scholar](#)

2. 2.

Sachdev, S. *Quantum Phase Transitions* 2nd edn (Cambridge Univ. Press, 2011).

3. 3.

Bohr, A. & Mottelson, B. R. *Nuclear Structure* Vols. I, II (Benjamin, 1975).

4. 4.

Grebenev, S., Toennies, J. P. & Vilesov, A. F. Superfluidity within a small helium-4 cluster: the microscopic Andronikashvili experiment. *Science* **279**, 2083–2086 (1998).

[ADS](#) [CAS](#) [Article](#) [Google Scholar](#)

5. 5.

Wenz, A. N. et al. From few to many: observing the formation of a Fermi sea one atom at a time. *Science* **342**, 457–460 (2013).

[ADS](#) [CAS](#) [Article](#) [Google Scholar](#)

6. 6.

Launey, K. D. *Emergent Phenomena in Atomic Nuclei from Large-Scale Modeling* (World Scientific, 2017).

7. 7.

Bruun, G. M. Long-lived Higgs mode in a two-dimensional confined Fermi system. *Phys. Rev. A* **90**, 023621 (2014).

[ADS](#) [Article](#) [Google Scholar](#)

8. 8.

Bloch, I., Dalibard, J. & Zwerger, W. Many-body physics with ultracold gases. *Rev. Mod. Phys.* **80**, 885–964 (2008).

[ADS](#) [CAS](#) [Article](#) [Google Scholar](#)

9. 9.

Bjerlin, J., Reimann, S. M. & Bruun, G. M. Few-body precursor of the Higgs mode in a Fermi gas. *Phys. Rev. Lett.* **116**, 155302 (2016).

[ADS](#) [CAS](#) [Article](#) [Google Scholar](#)

10. 10.

Sooryakumar, R. & Klein, M. V. Raman scattering by superconducting-gap excitations and their coupling to charge-density waves. *Phys. Rev. Lett.* **45**, 660–662 (1980).

[ADS](#) [CAS](#) [Article](#) [Google Scholar](#)

11. 11.

Rüegg, C. et al. Quantum magnets under pressure: controlling elementary excitations in TlCuCl₃. *Phys. Rev. Lett.* **100**, 205701 (2008).

[ADS](#) [Article](#) [Google Scholar](#)

12. 12.

Bissbort, U. et al. Detecting the amplitude mode of strongly interacting lattice bosons by Bragg scattering. *Phys. Rev. Lett.* **106**, 205303 (2011).

[ADS](#) [Article](#) [Google Scholar](#)

13. 13.

Endres, M. et al. The ‘Higgs’ amplitude mode at the two-dimensional superfluid/Mott insulator transition. *Nature* **487**, 454–458 (2012).

[ADS](#) [CAS](#) [Article](#) [Google Scholar](#)

14. 14.

Matsunaga, R. et al. Higgs amplitude mode in the BCS superconductors $\text{Nb}_{1-x}\text{Ti}_x\text{N}$ induced by terahertz pulse excitation. *Phys. Rev. Lett.* **111**, 057002 (2013).

[ADS](#) [Article](#) [Google Scholar](#)

15. 15.

Léonard, J., Morales, A., Zupancic, P., Donner, T. & Esslinger, T. Monitoring and manipulating Higgs and Goldstone modes in a supersolid quantum gas. *Science* **358**, 1415–1418 (2017).

[ADS](#) [Article](#) [Google Scholar](#)

16. 16.

Katsumi, K. et al. Higgs mode in the d -wave superconductor $\text{Bi}_2\text{Sr}_2\text{CaCu}_2\text{O}_{8+x}$ driven by an intense terahertz pulse. *Phys. Rev. Lett.* **120**, 117001 (2018).

[ADS](#) [CAS](#) [Article](#) [Google Scholar](#)

17. 17.

Behrle, A. et al. Higgs mode in a strongly interacting fermionic superfluid. *Nat. Phys.* **14**, 781–785 (2018).

[CAS](#) [Article](#) [Google Scholar](#)

18. 18.

Serwane, F. et al. Deterministic preparation of a tunable few-fermion system. *Science* **332**, 336–338 (2011).

[ADS](#) [CAS](#) [Article](#) [Google Scholar](#)

19. 19.

Kohmoto, M. & Takada, Y. Superconductivity from an insulator. *J. Phys. Soc. Jpn* **59**, 1541–1544 (1990).

[ADS](#) [Article](#) [Google Scholar](#)

20. 20.

Nozières, P. & Pistolesi, F. From semiconductors to superconductors: a simple model for pseudogaps. *Eur. Phys. J. B* **10**, 649–662 (1999).

[ADS](#) [Article](#) [Google Scholar](#)

21. 21.

Heiselberg, H. & Mottelson, B. Shell structure and pairing for interacting fermions in a trap. *Phys. Rev. Lett.* **88**, 190401 (2002).

[ADS](#) [Article](#) [Google Scholar](#)

22. 22.

Bruun, G. M. Low-energy monopole modes of a trapped atomic Fermi gas. *Phys. Rev. Lett.* **89**, 263002 (2002).

[ADS](#) [CAS](#) [Article](#) [Google Scholar](#)

23. 23.

Rontani, M., Eriksson, G., Åberg, S. & Reimann, S. M. On the renormalization of contact interactions for the configuration-interaction method in two-dimensions. *J. Phys. At. Mol. Opt. Phys.* **50**, 065301 (2017).

[ADS](#) [Article](#) [Google Scholar](#)

24. 24.

Zürn, G. et al. Precise characterization of ${}^6\text{Li}$ Feshbach resonances using trap-sideband-resolved RF spectroscopy of weakly bound molecules. *Phys. Rev. Lett.* **110**, 135301 (2013).

[ADS](#) [Article](#) [Google Scholar](#)

25. 25.

Randeria, M., Duan, J. M. & Shieh, L. Y. Superconductivity in a two-dimensional Fermi gas: evolution from Cooper pairing to Bose condensation. *Phys. Rev. B* **41**, 327–343 (1990).

[ADS](#) [CAS](#) [Article](#) [Google Scholar](#)

26. 26.

Idziaszek, Z. & Calarco, T. Analytical solutions for the dynamics of two trapped interacting ultracold atoms. *Phys. Rev. A* **74**, 022712 (2006).

[ADS](#) [Article](#) [Google Scholar](#)

27. 27.

Bruun, G. M. & Mottelson, B. R. Low energy collective modes of a superfluid trapped atomic Fermi gas. *Phys. Rev. Lett.* **87**, 270403

(2001).

[CAS](#) [Article](#) [Google Scholar](#)

28. 28.

D'Alessio, L., Kafri, Y., Polkovnikov, A. & Rigol, M. From quantum chaos and eigenstate thermalization to statistical mechanics and thermodynamics. *Adv. Phys.* **65**, 239–362 (2016).

[ADS](#) [Article](#) [Google Scholar](#)

29. 29.

Cremon, J. *Quantum Few-Body Physics with the Configuration Interaction Approach: Method Development and Application to Physical Systems*. Ph.D. thesis, Lund University (2010).

30. 30.

Hu, H., Mulkerin, B. C., Toniolo, U., He, L. & Liu, X.-J. Reduced quantum anomaly in a quasi-two-dimensional fermi superfluid: significance of the confinement-induced effective range of interactions. *Phys. Rev. Lett.* **122**, 070401 (2019).

[ADS](#) [CAS](#) [Article](#) [Google Scholar](#)

[Download references](#)

Acknowledgements

The experimental work has been supported by the ERC consolidator grant 725636, the Heidelberg Center for Quantum Dynamics, the DFG Collaborative Research Centre SFB 1225 (ISOQUANT) and the European Union's Horizon 2020 research and innovation programme under grant agreement number 817482 PASQuanS. K.S. acknowledges support by the Landesgraduiertenförderung Baden-Württemberg. P.M.P. acknowledges funding from the Daimler and Benz Foundation. S.M.R. and J.B.

acknowledge financial support by the Swedish Research Council, the Knut and Alice Wallenberg Foundation and NanoLund. G.M.B. acknowledges financial support from the Independent Research Fund Denmark—Natural Sciences via grant number DFF-8021-00233B and the Danish National Research Foundation through the Center of Excellence “CCQ” (grant agreement number DNRF156).

Author information

Author notes

1. These authors contributed equally: Luca Bayha, Marvin Holten

Affiliations

1. Physikalisches Institut der Universität Heidelberg, Heidelberg, Germany

Luca Bayha, Marvin Holten, Ralf Klemt, Keerthan Subramanian, Philipp M. Preiss & Selim Jochim

2. Mathematical Physics and NanoLund, LTH, Lund University, Lund, Sweden

Johannes Bjerlin & Stephanie M. Reimann

3. The Niels Bohr Institute, University of Copenhagen, Copenhagen, Denmark

Johannes Bjerlin

4. Department of Physics and Astronomy, University of Southern California, Los Angeles, CA, USA

Johannes Bjerlin

5. Center for Complex Quantum Systems, Department of Physics and Astronomy, Aarhus University, Aarhus, Denmark

Georg M. Bruun

6. Shenzhen Institute for Quantum Science and Engineering and Department of Physics, Southern University of Science and Technology, Shenzhen, China

Georg M. Bruun

Authors

1. Luca Bayha

[View author publications](#)

You can also search for this author in [PubMed](#) [Google Scholar](#)

2. Marvin Holten

[View author publications](#)

You can also search for this author in [PubMed](#) [Google Scholar](#)

3. Ralf Klemt

[View author publications](#)

You can also search for this author in [PubMed](#) [Google Scholar](#)

4. Keerthan Subramanian

[View author publications](#)

You can also search for this author in [PubMed](#) [Google Scholar](#)

5. Johannes Bjerlin

[View author publications](#)

You can also search for this author in [PubMed](#) [Google Scholar](#)

6. Stephanie M. Reimann

[View author publications](#)

You can also search for this author in [PubMed](#) [Google Scholar](#)

7. Georg M. Bruun

[View author publications](#)

You can also search for this author in [PubMed](#) [Google Scholar](#)

8. Philipp M. Preiss

[View author publications](#)

You can also search for this author in [PubMed](#) [Google Scholar](#)

9. Selim Jochim

[View author publications](#)

You can also search for this author in [PubMed](#) [Google Scholar](#)

Contributions

L.B. and M.H. contributed equally to this work. L.B., M.H. and K.S. performed the measurements and analysed the data. J.B., S.M.R. and G.M.B. developed the theoretical framework. J.B. performed the numerical calculations. P.M.P. and S.J. supervised the experimental part of the project. All authors contributed to the discussion of the results and the writing of the manuscript.

Corresponding authors

Correspondence to [Luca Bayha](#) or [Marvin Holten](#).

Ethics declarations

Competing interests

The authors declare no competing interests.

Additional information

Peer review information *Nature* thanks Hui Hu and the other, anonymous, reviewer(s) for their contribution to the peer review of this work. Peer reviewer reports are available.

Publisher's note Springer Nature remains neutral with regard to jurisdictional claims in published maps and institutional affiliations.

Extended data figures and tables

[Extended Data Fig. 1 Experimental protocol.](#)

The sequence can be separated into three parts. First, several evaporation and spilling stages are combined with a transfer from a quasi-1D to a quasi-2D trap geometry. This is needed to prepare closed-shell ground state configurations of up to 12 atoms. Second, we excite the system at some defined frequency f_{exc} and magnetic offset field B using a sinusoidal modulation of either the radial or axial confinement. Third, detection is implemented by spilling to the ground state a second time and a transfer of all remaining atoms to the magneto-optical trap, where we count them.

[Extended Data Fig. 2 Excitation spectrum for two particles.](#)

We define the two-body excitation energy E_{exc} as the energy difference between the ground state and the lowest monopole excitation of the two atom system. It is measured using the same modulation scheme as for the Higgs mode. The system is initialized with one filled shell, that is, two particles. The analytical solution of the two-body problem (solid line) shows good agreement with the measurement (blue points). The systematic uncertainty of around 2% on the measured radial and axial trap frequencies that enters into the analytical solution is indicated by the grey error band. Residual systematic deviations can be explained by the trap anharmonicity. For the measurement (blue points) error bars are extracted from the fit to the spectrum and are smaller than the data points.

[Extended Data Fig. 3 Comparison of different modulation schemes.](#)

A modulation of the radial trap frequency leads to similar transition probabilities for the pair excitation mode and the higher excited states (top). In contrast, a modulation of the axial confinement effectively only modulates the interaction strength and couples predominantly to the pair excitation mode. Excitations to higher states are suppressed by this modulation scheme (bottom). This qualitative observation agrees with the coupling elements that were predicted in ref. ⁹. The two modulation amplitudes have been chosen such that they lead to a similar response of the pair excitation mode. The data are taken for $E_B = 0.09hf_r$. For this measurement the radial trap frequency was $2f_r = 1,660$ Hz. Error bars show the standard error of the mean. Each data point is the average of at least 24 measurements.

Extended Data Fig. 4 Probabilities of different atom numbers remaining in the lowest two shells for the $N = 6$ initial state.

a–f, The probabilities for different remaining atom numbers after modulating the 6-atom ground state with a defined frequency given on the y axis and subsequent removal of excited atoms. All possible excitations manifest themselves by a reduced probability of remaining in the ground state of 6 atoms (**a**). We find that the lowest excitation, or Higgs mode, mostly consists of excitations to four atoms (**c**), while the higher excited peaks are predominantly generated by the loss of a single atom (**b**). For each setting the experiment is repeated between 42 and 47 times.

Extended Data Fig. 5 Probabilities of different atom numbers remaining in the lowest three shells for the $N = 12$ initial state.

a–f, The probabilities for different remaining atom numbers after modulating the 12-atom ground state with a defined frequency given on the y axis and subsequent removal of excited atoms. All possible excitations manifest themselves by a reduced probability of remaining in the ground state of 12 atoms (**a**). We find that lowest excitation, or Higgs mode, mainly consists of excitations to ten atoms (**c**), while the higher excited peaks are predominantly generated by the loss of even more atoms (**d–f**). For each setting the experiment is repeated between 19 and 63 times.

Extended Data Fig. 6 Numerically calculated excitation spectrum for 6 particles.

a, The level spectrum obtained by exact diagonalization with parameters $A = 20$ and $\gamma = 0.99$ for the potential as well as the experimental results. The calculation includes states up to $(\{E\}_{\{\{\rm{sp}\}\}}^{\{\{\rm{cut}\}\}}=10\hbar\omega_r)$ and up to a many-body energy of $28\hbar\omega_r$. For comparison the experimental data are shown by green diamonds. Values and errors bars are obtained as in Fig. 3c. **b**, The numerically calculated excitation spectrum for a modulation of the interaction strength. As in the experiment we observe that this modulation couples to two non-monotonous modes. We note that the calculations performed for **b** employ a smaller cut-off ($(\{E\}_{\{\{\rm{sp}\}\}}^{\{\{\rm{cut}\}\}}=6\hbar\omega_r)$) and a maximal many-body energy of $24\hbar\omega_r$) than in **a** owing to the computational demand in calculating the matrix element (equation (4)).

Supplementary information

[Peer Review File](#)

Source data

[Source Data Fig. 1](#)

[Source Data Fig. 3c](#)

[Source Data Fig. 4](#)

Rights and permissions

[Reprints and Permissions](#)

About this article



Check for
updates

Cite this article

Bayha, L., Holten, M., Klemt, R. *et al.* Observing the emergence of a quantum phase transition shell by shell. *Nature* **587**, 583–587 (2020). <https://doi.org/10.1038/s41586-020-2936-y>

[Download citation](#)

- Received: 24 April 2020
- Accepted: 03 September 2020
- Published: 25 November 2020
- Issue Date: 26 November 2020
- DOI: <https://doi.org/10.1038/s41586-020-2936-y>

Comments

By submitting a comment you agree to abide by our [Terms](#) and [Community Guidelines](#). If you find something abusive or that does not comply with our terms or guidelines please flag it as inappropriate.

[Access through your institution](#)

[Change institution](#)

[Buy or subscribe](#)

This article was downloaded by **calibre** from <https://www.nature.com/articles/s41586-020-2936-y>

- Article
- [Published: 25 November 2020](#)

Spin-enhanced nanodiamond biosensing for ultrasensitive diagnostics

- [Benjamin S. Miller](#) ORCID: [orcid.org/0000-0003-3032-018X^{1,2}](https://orcid.org/0000-0003-3032-018X),
- [Léonard Bezingé](#) ORCID: [orcid.org/0000-0002-9733-9697¹](https://orcid.org/0000-0002-9733-9697),
- [Harriet D. Gliddon¹](#),
- [Da Huang¹](#),
- [Gavin Dold](#) ORCID: [orcid.org/0000-0002-6155-3800^{1,3}](https://orcid.org/0000-0002-6155-3800),
- [Eleanor R. Gray](#) ORCID: [orcid.org/0000-0002-6515-839X¹](https://orcid.org/0000-0002-6515-839X),
- [Judith Heaney⁴](#),
- [Peter J. Dobson⁵](#),
- [Eleni Nastouli⁶](#),
- [John J. L. Morton](#) ORCID: [orcid.org/0000-0002-0891-1111^{1,3}](https://orcid.org/0000-0002-0891-1111) &
- [Rachel A. McKendry](#) ORCID: [orcid.org/0000-0003-2018-6829^{1,2}](https://orcid.org/0000-0003-2018-6829)

[Nature](#) volume 587, pages588–593(2020) [Cite this article](#)

- 63 Altmetric
- [Metrics details](#)

Subjects

- [Biomedical engineering](#)
- [Biosensors](#)
- [Diagnostic devices](#)
- [Nanoparticles](#)

Abstract

The quantum spin properties of nitrogen-vacancy defects in diamond enable diverse applications in quantum computing and communications¹. However, fluorescent nanodiamonds also have attractive properties for in vitro biosensing, including brightness², low cost³ and selective manipulation of their emission⁴. Nanoparticle-based biosensors are essential for the early detection of disease, but they often lack the required sensitivity. Here we investigate fluorescent nanodiamonds as an ultrasensitive label for in vitro diagnostics, using a microwave field to modulate emission intensity⁵ and frequency-domain analysis⁶ to separate the signal from background autofluorescence⁷, which typically limits sensitivity. Focusing on the widely used, low-cost lateral flow format as an exemplar, we achieve a detection limit of 8.2×10^{-19} molar for a biotin–avidin model, 10^5 times more sensitive than that obtained using gold nanoparticles. Single-copy detection of HIV-1 RNA can be achieved with the addition of a 10-minute isothermal amplification step, and is further demonstrated using a clinical plasma sample with an extraction step. This ultrasensitive quantum diagnostics platform is applicable to numerous diagnostic test formats and diseases, and has the potential to transform early diagnosis of disease for the benefit of patients and populations.

[Access through your institution](#)

[Change institution](#)

[Buy or subscribe](#)

Access options

Subscription info for Chinese customers

We have a dedicated website for our Chinese customers. Please go to [naturechina.com](#) to subscribe to this journal.

[Go to naturechina.com](#)

Rent or Buy article

Get time limited or full article access on ReadCube.

from \$8.99

[Rent or Buy](#)

All prices are NET prices.

Additional access options:

- [Log in](#)
- [Access through your institution](#)
- [Learn about institutional subscriptions](#)

Fig. 1: Schematic illustration of the use of FNDs in LFAs.

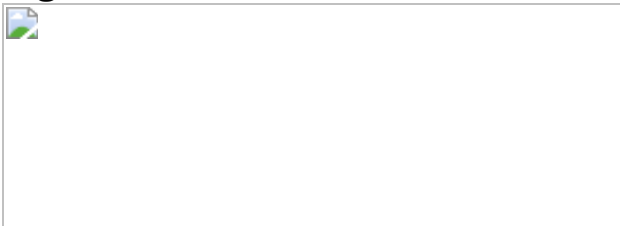


Fig. 2: Microwave modulation of FNDs on paper.

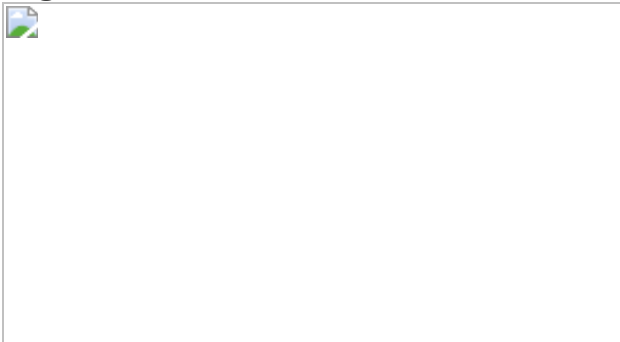


Fig. 3: Characterizing the fundamental limit of detection using biotin–avidin binding of FNDs on LFAs.

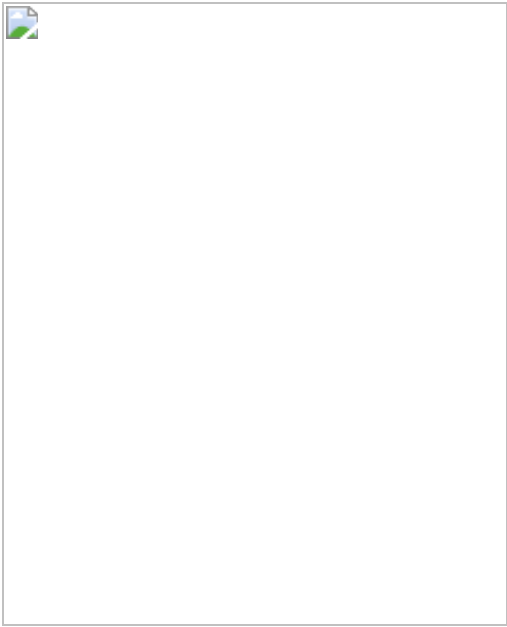
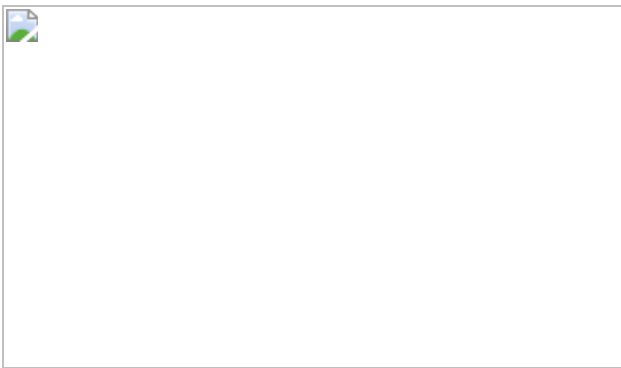


Fig. 4: Single-copy detection of HIV-1 RNA on LFAs using RT-RPA and FNDs.



Data availability

The datasets generated during and/or analysed during the current study, and the computer code used are available from the corresponding author on reasonable request, in line with the requirements of UCL and the funder (EPSRC policy framework on research data).

References

1. 1.

Childress, L. & Hanson, R. Diamond NV centers for quantum computing and quantum networks. *MRS Bull.* **38**, 134–138 (2013).

[CAS](#) [Google Scholar](#)

2. 2.

Mochalin, V. N., Shenderova, O., Ho, D. & Gogotsi, Y. The properties and applications of nanodiamonds. *Nat. Nanotechnol.* **7**, 11–23 (2012).

[ADS](#) [CAS](#) [Google Scholar](#)

3. 3.

Boudou, J.-P. et al. High yield fabrication of fluorescent nanodiamonds. *Nanotechnology* **20**, 235602 (2009).

[ADS](#) [PubMed](#) [PubMed Central](#) [Google Scholar](#)

4. 4.

Schirhagl, R., Chang, K., Loretz, M. & Degen, C. L. Nitrogen-vacancy centers in diamond: nanoscale sensors for physics and biology. *Annu. Rev. Phys. Chem.* **65**, 83–105 (2014).

[ADS](#) [CAS](#) [PubMed](#) [Google Scholar](#)

5. 5.

Igarashi, R. et al. Real-time background-free selective imaging of fluorescent nanodiamonds *in vivo*. *Nano Lett.* **12**, 5726–5732 (2012).

[ADS](#) [CAS](#) [PubMed](#) [Google Scholar](#)

6. 6.

Leis, J., Martin, P. & Buttsworth, D. Simplified digital lock-in amplifier algorithm. *Electron. Lett.* **48**, 259 (2012).

[ADS](#) [Google Scholar](#)

7. 7.

Shah, K. G. & Yager, P. Wavelengths and lifetimes of paper autofluorescence: a simple substrate screening process to enhance the sensitivity of fluorescence-based assays in paper. *Anal. Chem.* **89**, 12023–12029 (2017).

[CAS](#) [PubMed](#) [Google Scholar](#)

8. 8.

Childress, L. et al. Coherent dynamics of coupled electron and nuclear spin qubits in diamond. *Science* **314**, 281–285 (2006).

[ADS](#) [CAS](#) [PubMed](#) [Google Scholar](#)

9. 9.

Chang, H.-C., Hsiao, W. W.-W. & Su, M.-C. *Fluorescent Nanodiamonds* Ch. 11 (Wiley, 2018).

10. 10.

Yu, S. J., Kang, M. W., Chang, H. C., Chen, K. M. & Yu, Y. C. Bright fluorescent nanodiamonds: no photobleaching and low cytotoxicity. *J. Am. Chem. Soc.* **127**, 17604–17605 (2005).

[CAS](#) [PubMed](#) [Google Scholar](#)

11. 11.

Shenderova, O. A. & McGuire, G. E. Science and engineering of nanodiamond particle surfaces for biological applications (review). *Biointerphases* **10**, 030802 (2015).

[PubMed](#) [Google Scholar](#)

12. 12.

Chang, Y. R. et al. Mass production and dynamic imaging of fluorescent nanodiamonds. *Nat. Nanotechnol.* **3**, 284–288 (2008).

[CAS](#) [PubMed](#) [Google Scholar](#)

13. 13.

Maze, J. R. et al. Nanoscale magnetic sensing with an individual electronic spin in diamond. *Nature* **455**, 644–647 (2008).

[ADS](#) [CAS](#) [PubMed](#) [Google Scholar](#)

14. 14.

Balasubramanian, G. et al. Nanoscale imaging magnetometry with diamond spins under ambient conditions. *Nature* **455**, 648–651 (2008).

[ADS](#) [CAS](#) [PubMed](#) [Google Scholar](#)

15. 15.

Tetienne, J. P. et al. Magnetic-field-dependent photodynamics of single NV defects in diamond: An application to qualitative all-optical magnetic imaging. *New J. Phys.* **14**, 103033 (2012).

[Google Scholar](#)

16. 16.

Acosta, V. M. et al. Temperature dependence of the nitrogen-vacancy magnetic resonance in diamond. *Phys. Rev. Lett.* **104**, 070801 (2010).

[ADS](#) [CAS](#) [PubMed](#) [Google Scholar](#)

17. 17.

Hsiao, W. W. W., Hui, Y. Y., Tsai, P. C. & Chang, H. C. Fluorescent nanodiamond: a versatile tool for long-term cell tracking, super-resolution imaging, and nanoscale temperature sensing. *Acc. Chem. Res.* **49**, 400–407 (2016).

[CAS](#) [PubMed](#) [Google Scholar](#)

18. 18.

Vaijayanthimala, V. & Chang, H.-C. Functionalized fluorescent nanodiamonds for biomedical applications. *Nanomedicine* **4**, 47–55 (2009).

[CAS](#) [PubMed](#) [Google Scholar](#)

19. 19.

Fu, C.-C. et al. Characterization and application of single fluorescent nanodiamonds as cellular biomarkers. *Proc. Natl Acad. Sci. USA* **104**, 727–732 (2007).

[ADS](#) [CAS](#) [PubMed](#) [Google Scholar](#)

20. 20.

Chang, B. M. et al. Highly fluorescent nanodiamonds protein-functionalized for cell labeling and targeting. *Adv. Funct. Mater.* **23**, 5737–5745 (2013).

[CAS](#) [Google Scholar](#)

21. 21.

Waddington, D. E. et al. Nanodiamond-enhanced MRI via in situ hyperpolarization. *Nat. Commun.* **8**, 15118 (2017).

[ADS](#) [PubMed](#) [PubMed Central](#) [Google Scholar](#)

22. 22.

Hegyi, A. & Yablonovitch, E. Molecular imaging by optically detected electron spin resonance of nitrogen-vacancies in nanodiamonds. *Nano Lett.* **13**, 1173–1178 (2013).

[ADS](#) [CAS](#) [PubMed](#) [Google Scholar](#)

23. 23.

Sarkar, S. K. et al. Wide-field in vivo background free imaging by selective magnetic modulation of nanodiamond fluorescence. *Biomed. Opt. Express* **5**, 1190 (2014).

[PubMed](#) [PubMed Central](#) [Google Scholar](#)

24. 24.

Chapman, R. & Plakhotnik, T. Background-free imaging of luminescent nanodiamonds using external magnetic field for contrast enhancement. *Opt. Lett.* **38**, 1847 (2013).

[ADS](#) [CAS](#) [PubMed](#) [Google Scholar](#)

25. 25.

Doronina-Amitonova, L., Fedotov, I. & Zheltikov, A. Ultrahigh-contrast imaging by temporally modulated stimulated emission depletion. *Opt. Lett.* **40**, 725 (2015).

[ADS](#) [CAS](#) [PubMed](#) [Google Scholar](#)

26. 26.

Bhutta, Z. A., Sommerfeld, J., Lassi, Z. S., Salam, R. A. & Das, J. K. Global burden, distribution, and interventions for infectious diseases of poverty. *Infect. Dis. Poverty* **3**, 21 (2014).

[PubMed](#) [PubMed Central](#) [Google Scholar](#)

27. 27.

Global HIV & AIDS statistics — 2018 fact sheet.
<https://www.unaids.org/en/resources/fact-sheet> (UNAIDS, 2018).

28. 28.

May, M. et al. Impact of late diagnosis and treatment on life expectancy in people with HIV-1: UK Collaborative HIV Cohort (UK CHIC) Study. *Br. Med. J.* **343**, d6016 (2011).

[Google Scholar](#)

29. 29.

Gray, E. R. et al. p24 revisited: a landscape review of antigen detection for early HIV diagnosis. *AIDS* **32**, 2089–2102 (2018).

[CAS](#) [PubMed](#) [PubMed Central](#) [Google Scholar](#)

30. 30.

Price, C. P. Point of care testing. *Br. Med. J.* **322**, 1285–1288 (2001).

[CAS](#) [Google Scholar](#)

31. 31.

World Malaria Report.
<https://www.who.int/malaria/publications/world-malaria-report-2018/en/> (WHO, 2018).

32. 32.

Land, K. J., Boeras, D. I., Chen, X. S., Ramsay, A. R. & Peeling, R. W. REASSURED diagnostics to inform disease control strategies, strengthen health systems and improve patient outcomes. *Nat. Microbiol.* **4**, 46–54 (2019).

[CAS](#) [PubMed](#) [Google Scholar](#)

33. 33.

Walter, J. G. et al. Protein microarrays: reduced autofluorescence and improved LOD. *Eng. Life Sci.* **10**, 103–108 (2010).

[CAS](#) [Google Scholar](#)

34. 34.

Kim, J. et al. Rapid and background-free detection of avian influenza virus in opaque sample using NIR-to-NIR upconversion nanoparticle-based lateral flow immunoassay platform. *Biosens. Bioelectron.* **112**, 209–215 (2018).

[CAS](#) [PubMed](#) [Google Scholar](#)

35. 35.

Paterson, A. S. et al. A low-cost smartphone-based platform for highly sensitive point-of-care testing with persistent luminescent phosphors. *Lab Chip* **17**, 1051–1059 (2017).

[CAS](#) [PubMed](#) [PubMed Central](#) [Google Scholar](#)

36. 36.

Boudou, J. P., David, M. O., Joshi, V., Eidi, H. & Curmi, P. A. Hyperbranched polyglycerol modified fluorescent nanodiamond for biomedical research. *Diamond Relat. Mater.* **38**, 131–138 (2013).

[ADS](#) [CAS](#) [Google Scholar](#)

37. 37.

Hermanson, G. T. Zero-length crosslinkers. In *Bioconjugate Techniques* 3rd edn (ed. Hermanson, G. T.) Ch. 4 (Academic, 2013).

38. 38.

González Flecha, F. L. & Levi, V. Determination of the molecular size of BSA by fluorescence anisotropy. *Biochem. Mol. Biol. Educ.* **31**, 319–322 (2003).

[Google Scholar](#)

39. 39.

Reth, M. Matching cellular dimensions with molecular sizes. *Nat. Immunol.* **14**, 765–767 (2013).

[CAS](#) [PubMed](#) [Google Scholar](#)

40. 40.

Ngom, B., Guo, Y., Wang, X. & Bi, D. Development and application of lateral flow test strip technology for detection of infectious agents and chemical contaminants: a review. *Anal. Bioanal. Chem.* **397**, 1113–1135 (2010).

[CAS](#) [PubMed](#) [Google Scholar](#)

41. 41.

Armbruster, D. A. & Pry, T. Limit of blank, limit of detection and limit of quantitation. *Clin. Biochem. Rev.* **29**, S49–S52 (2008).

[PubMed](#) [PubMed Central](#) [Google Scholar](#)

42. 42.

Daher, R. K., Stewart, G., Boissinot, M. & Bergeron, M. G. Recombinase polymerase amplification for diagnostic applications. *Clin. Chem.* **62**, 947–958 (2016).

[CAS](#) [PubMed](#) [PubMed Central](#) [Google Scholar](#)

43. 43.

Lillis, L. et al. Cross-subtype detection of HIV-1 using reverse transcription and recombinase polymerase amplification. *J. Virol. Methods* **230**, 28–35 (2016).

[CAS](#) [PubMed](#) [PubMed Central](#) [Google Scholar](#)

44. 44.

Crannell, Z. A., Rohrman, B. & Richards-Kortum, R. Equipment-free incubation of recombinase polymerase amplification reactions using body heat. *PLoS ONE* **9**, e112146 (2014).

[ADS](#) [PubMed](#) [PubMed Central](#) [Google Scholar](#)

45. 45.

Rohrman, B. A. & Richards-Kortum, R. R. A paper and plastic device for performing recombinase polymerase amplification of HIV DNA. *Lab Chip* **12**, 3082 (2012).

[CAS](#) [PubMed](#) [PubMed Central](#) [Google Scholar](#)

46. 46.

Boyle, D. S., Lehman, D. A. & Lillis, L. Rapid detection of HIV-1 proviral DNA for early infant diagnosis using rapid detection of HIV-1 proviral DNA for early infant diagnosis. *MBio* **4**, e00135-13 (2013).

[PubMed](#) [PubMed Central](#) [Google Scholar](#)

47. 47.

Dineva, M. A., Mahilum-Tapay, L. & Lee, H. Sample preparation: a challenge in the development of point-of-care nucleic acid-based assays for resource-limited settings. *Analyst* **132**, 1193 (2007).

[ADS](#) [CAS](#) [PubMed](#) [Google Scholar](#)

48. 48.

Jauset-Rubio, M. et al. Ultrasensitive, rapid and inexpensive detection of DNA using paper based lateral flow assay. *Sci. Rep.* **6**, 37732 (2016).

[ADS](#) [CAS](#) [PubMed](#) [PubMed Central](#) [Google Scholar](#)

49. 49.

Phillips, A. et al. Sustainable HIV treatment in Africa through viral-load-informed differentiated care. *Nature* **528**, S68–S76 (2015).

[PubMed](#) [PubMed Central](#) [Google Scholar](#)

50. 50.

Kuo, Y., Hsu, T.-Y., Wu, Y.-C., Hsu, J.-H. & Chang, H.-C. Fluorescence lifetime imaging microscopy of nanodiamonds in vivo. In *Proc. Advances in Photonics of Quantum Computing, Memory, and Communication VI* Vol. 8635, 863503 (SPIE, 2013).

51. 51.

Kim, E. Y. et al. A real-time PCR-based method for determining the surface coverage of thiol-capped oligonucleotides bound onto gold nanoparticles. *Nucleic Acids Res.* **34**, e54 (2006).

[PubMed](#) [PubMed Central](#) [Google Scholar](#)

52. 52.

Besnier, C., Takeuchi, Y. & Towers, G. Restriction of lentivirus in monkeys. *Proc. Natl Acad. Sci. USA* **99**, 11920–11925 (2002).

[ADS](#) [CAS](#) [PubMed](#) [Google Scholar](#)

53. 53.

Bainbridge, J. W. et al. In vivo gene transfer to the mouse eye using an HIV-based lentiviral vector; efficient long-term transduction of

corneal endothelium and retinal pigment epithelium. *Gene Ther.* **8**, 1665–1668 (2001).

[CAS](#) [PubMed](#) [Google Scholar](#)

54. 54.

Foley, B. et al. HIV Sequence Compendium 2017. LA-UR-18-25673 (Los Alamos National Laboratory, 2018).

55. 55.

Kong, J. & Yu, S. Fourier transform infrared spectroscopic analysis of protein secondary structures. *Acta Biochim. Biophys. Sin. (Shanghai)* **39**, 549–559 (2007).

[CAS](#) [Google Scholar](#)

56. 56.

Zadeh, J. N. et al. NUPACK: Analysis and design of nucleic acid systems. *J. Comput. Chem.* **32**, 170–173 (2011).

[CAS](#) [PubMed](#) [Google Scholar](#)

57. 57.

SantaLucia, J. A unified view of polymer, dumbbell, and oligonucleotide DNA nearest-neighbor thermodynamics. *Proc. Natl Acad. Sci. USA* **95**, 1460–1465 (1998).

[ADS](#) [CAS](#) [PubMed](#) [Google Scholar](#)

58. 58.

Laitinen, M. P. & Vuento, M. Affinity immunosensor for milk progesterone: Identification of critical parameters. *Biosens. Bioelectron.* **11**, 1207–1214 (1996).

[CAS](#) [PubMed](#) [Google Scholar](#)

[Download references](#)

Acknowledgements

We thank M. Schormans for help with circuit design, M. Thomas for assistance with dynamic light scattering measurements and M. Towner for assistance with FTIR measurements. This work was funded by the i-sense EPSRC IRC in Early Warning Sensing Systems for Infectious Diseases (EP/K031953/1); i-sense EPSRC IRC in Agile Early Warning Sensing Systems in Infectious Diseases and Antimicrobial Resistance (EP/R00529X/1); the National Institute for Health Research University College London Hospitals Biomedical Research Centre; Royal Society Wolfson Research Merit Award to R.A.M. (WM130111); LCN Departmental Studentship to B.S.M.; EPSRC Centre for Doctoral Training in Delivering Quantum Technologies to G.D. (EP/L015242/1); H2020 European Research Council Local quantum operations achieved through the motion of spins to J.J.L.M. (771493); and the UCLH NHS Foundation Trust to J.H. and E.N.

Author information

Affiliations

1. London Centre for Nanotechnology, University College London, London, UK

Benjamin S. Miller, Léonard Bezinge, Harriet D. Gliddon, Da Huang, Gavin Dold, Eleanor R. Gray, John J. L. Morton & Rachel A. McKendry

2. Division of Medicine, University College London, London, UK

Benjamin S. Miller & Rachel A. McKendry

3. Department of Electronic and Electrical Engineering, University College London, London, UK

Gavin Dold & John J. L. Morton

4. Advanced Pathogens Diagnostic Unit, University College London Hospitals, London, UK

Judith Heaney

5. The Queens College, University of Oxford, Oxford, UK

Peter J. Dobson

6. Department of Virology, University College London Hospitals, London, UK

Eleni Nastouli

Authors

1. Benjamin S. Miller

[View author publications](#)

You can also search for this author in [PubMed](#) [Google Scholar](#)

2. Léonard Bezinge

[View author publications](#)

You can also search for this author in [PubMed](#) [Google Scholar](#)

3. Harriet D. Gliddon

[View author publications](#)

You can also search for this author in [PubMed](#) [Google Scholar](#)

4. Da Huang

[View author publications](#)

You can also search for this author in [PubMed](#) [Google Scholar](#)

5. Gavin Dold

[View author publications](#)

You can also search for this author in [PubMed](#) [Google Scholar](#)

6. Eleanor R. Gray

[View author publications](#)

You can also search for this author in [PubMed](#) [Google Scholar](#)

7. Judith Heaney

[View author publications](#)

You can also search for this author in [PubMed](#) [Google Scholar](#)

8. Peter J. Dobson

[View author publications](#)

You can also search for this author in [PubMed](#) [Google Scholar](#)

9. Eleni Nastouli

[View author publications](#)

You can also search for this author in [PubMed](#) [Google Scholar](#)

10. John J. L. Morton

[View author publications](#)

You can also search for this author in [PubMed](#) [Google Scholar](#)

11. Rachel A. McKendry

[View author publications](#)

You can also search for this author in [PubMed](#) [Google Scholar](#)

Contributions

B.S.M. and R.A.M. conceived the research and led the study; P.J.D. advised on nanodiamonds and J.J.L.M. on microwave modulation. B.S.M. demonstrated the initial proof-of-concept; B.S.M. and L.B. designed and optimized the lock-in analysis, functionalization and LFA design; B.S.M., L.B. and D.H. performed all the FND LFA experiments; H.D.G. designed, optimized and performed RT-RPA assays including primer design and template generation; D.H. adapted and performed RT-RPA assays and purification; J.J.L.M. and G.D. designed the microwave delivery including resonators; E.R.G. performed clinical RNA extraction, and advised on virology including primer design; J.H. performed qPCR on the seroconversion panel; E.N. provided clinical expertise; B.S.M. and E.R.G. designed and performed binding-site quantification experiments; B.S.M., L.B. and R.A.M. drafted the manuscript; and all authors reviewed and revised the manuscript.

Corresponding authors

Correspondence to [Benjamin S. Miller](#) or [Rachel A. McKendry](#).

Ethics declarations

Competing interests

B.S.M., L.B., G.D., P.J.D., J.J.L.M. and R.A.M. are inventors on the UK patent application number 1814532.6 filed by University College London Business.

Additional information

Peer review information *Nature* thanks Takuya Segawa and the other, anonymous, reviewer(s) for their contribution to the peer review of this work.

Publisher's note Springer Nature remains neutral with regard to jurisdictional claims in published maps and institutional affiliations.

Extended data figures and tables

Extended Data Fig. 1 Optimization of microwave modulation.

a–f, A linear resonator was designed to have a wideband response over the range 1–4 GHz, and an omega narrowband resonator was designed to have a stronger, narrower resonance at 2.87 GHz with quality factor $Q = 100$. The schematic printed circuit board layouts for the two resonators are shown in **a** and **d**, respectively. The resulting simulated fields are shown in **b** and **e**, respectively. The reflected power (S_{11}) is plotted against frequency in **c** and **f**. The narrowband resonator shows 5–6 orders of magnitude greater absorption than the wideband resonator at 2.87 GHz, indicating resonant coupling giving strong absorption. Panel **f** also shows the corresponding FND intensity dip. **g**, Emission spectra of FNDs acted on by a 2.87 GHz microwave field. The powers listed in decibel-milliwatts are the output power of the microwave generator (before the 17 dB amplifier). **h**, Each spectrum is integrated over the whole wavelength range to give a total intensity, which is plotted against preamplifier power. This shows a linear relationship between fluorescence intensity and microwave power (in dBm) above a threshold power, and up to 7 dBm, where the amplifier reaches its 1 dB compression power. At this point, the fluorescence starts to increase again owing to a loss in the quality of the sinusoid leading to power lost in harmonics. Dots show means and error bars show the s.d., with $n = 3$ measurement repeats.

Extended Data Fig. 2 Optimization of lock-in analysis.

a, Schematic of the computational lock-in algorithm used to extract the microwave modulated FND signal from the background. The input signal is high-pass filtered using a moving average filter to remove low-frequency drift. It is subsequently multiplied by cosine and sine functions with frequency F_m , and the resulting signals are low-pass filtered to generate the in phase and quadrature components, respectively, of the vector representation of the signal. The magnitude of this vector is calculated to remove the effect of phase, giving the output magnitude. **b**, The variation of lock-in amplitude with modulation rate (F_m) at various sampling rates (F_s).

A single strip with very high intensity was modulated at F_m values between 1–450 Hz, and sampled at various F_s values between 3.89–996 Hz. The resulting plot shows that lock-in amplitude is independent of F_s when $F_s > 2F_m$. **c, d**, The relationships between lock-in amplitude, exposure time (T_e) and modulation frequency (F_m). An identical LFA strip was measured with exposure times between 10–50 ms, using the maximum possible F_s for each T_e , and F_m values between 1–15 Hz. **d** shows F_m against lock-in amplitude at various exposure times. It is shown that the lock-in amplitude has its maximum at around 5 Hz for all frequencies, and reduces when F_m is close to $F_s/2$, its maximum possible value. This is evident in the raw signal plots in **c** for each F_m at a fixed exposure time of 30 ms. As F_m approaches $F_s/2$, the sampling effects obscure the square wave, decreasing lock-in amplitude. For maximum lock-in amplitude, the highest possible T_e should be used. Here, we are limited to 50 ms by the background autofluorescence of the nitrocellulose, which saturates the camera above this value. A corresponding F_m of 4 Hz was chosen as it is in the optimal range and is a power of 2, so can be achieved by simply dividing the temperature compensation crystal oscillator (TCXO) frequency. **e**, The variation of lock-in amplitude with total measurement time at $F_m = 4$ Hz and $F_s = 20$ Hz for five different concentrations of FNDs and a negative control, immobilized with a biotin–avidin interaction. The positive amplitudes stabilize quickly, reaching 5% of their 15 s value in 3.9 s for positive results. The negative results take longer to stabilize, reaching 5% of their 15 s value in 13 s. A measurement time of 15 s (300 frames) was used for subsequent measurements. **f**, Schematic circuit design of temperature compensation crystal oscillator (TCXO)-based modulated microwave source. It is powered by a 5 V source which powers a TCXO, which outputs a 32.768 kHz square wave. This is converted to a 4 Hz signal by a 4060 counter chip. This square wave controls two transistors which deliver 12 V stepped up power (d.c. converter) to the microwave VCO. The bias voltage is regulated from 12 V to 8.15 V by a voltage regulator. The VCO microwave output is amplified by the MW amplifier and transmitted to the omega resonator. **g**, Printed circuit board layout of the prototype (65 mm × 38 mm). Outputs for the microwave amplifier and microwave VCO are at

the top right and bottom right, respectively. A photo of the printed circuit board with a £1 coin (GBP) for scale is shown below.

Extended Data Fig. 3 FND characterization and functionalization.

a, Comparison of the non-specific binding of various commercial FNDs with various surface functionalizations on LFAs. The lock-in amplitude at the test line was measured to quantify non-specific binding. The LFAs were also pre-blocked with a polyvinylpyrrolidone-sucrose solution (proprietary method, Mologic). The lowest non-specific binding was from the PG-functionalized particles (FND–PG), as the PG adds a hydrophilic layer. **b**, Dynamic light scattering of three different FND particle core diameters: 120, 200 and 600 nm. **c**, A schematic of antibody functionalization of FND–PG. DSC activates hydroxyl surface groups to form succinimidyl carbonates, which can then react with antibodies to form stable carbamate or urethane bonds. **d–f**, Scanning electron microscope images of FNDs with particle core diameters of 120, 200 and 600 nm, respectively. **g**, Dynamic light scattering was also used to measure the size and aggregated fraction after functionalization of 120 nm FND–PG before and after functionalization with BSA-biotin or antibodies. Dots show the means of $n = 3$ measurement replicates. Fitting the number plots to skew exponentials (equation (3), plotted as lines) gave peak particle hydrodynamic diameters of 106, 121 and 128 nm. **h**, The fitted peak diameters are plotted with error bars denoting their 95% confidence intervals ($n = 3$ measurement replicates), showing no significant difference between the bio-functionalized diameters (FND–biotin, FND–antibody), but both are significantly different from the pre-functionalization diameter (FND–PG): * $P \leq 0.05$; ** $P \leq 0.01$, ANOVA with Tukey HSD post hoc test. **i**, FTIR spectroscopy of FND–PG and antibody-functionalized FND–PG. Lines show means of $n = 6$ measurement replicates for FND samples and $n = 2$ measurement replicates for the blank. C–O and C–H peaks, indicative of the PG layer, can be seen in both FND–PG and FND–PG–antibody at around $1,100\text{ cm}^{-1}$ and at around $2,900\text{ cm}^{-1}$, respectively. The FND–PG–antibody spectrum displays additional peaks at around $1,640\text{ cm}^{-1}$ and at around $1,540\text{ cm}^{-1}$, suggesting protein amide I and amide II bonds, respectively⁵⁵, showing that protein functionalization was successful.

Extended Data Fig. 4 Quantification of the number of available binding sites per FND.

a, Initially, binding constants of the anti-DIG antibody binding to DIG were measured using interferometry. Full experimental details are shown in Supplementary Information [section 1](#). Binding at different concentrations was measured and the resulting curves were fitted to exponentials. To find the equilibrium dissociation constant (K_D), equilibrium binding values, B , were plotted here against concentration, C . A Langmuir adsorption isotherm was fitted $\frac{B}{(K_D + C)} = \frac{a \times C}{C}$ giving a K_D value of $5.1 \times 10^{-10} \text{ M}$.

b, In order to find the on- and off-rates, k_{on} and k_{off} , the observed reaction rates, k_{obs} , at each concentration were plotted and fitted to the linear relationship:

$$k_{\text{obs}} = k_{\text{off}} + C \times k_{\text{on}}$$

The resulting fitted values are $k_{\text{on}} = 1.6 \times 10^5 \text{ M}^{-1} \text{ s}^{-1}$ and $k_{\text{off}} = 9.1 \times 10^{-5} \text{ s}^{-1}$.

c, A schematic of the assay to quantify the number of available binding sites per FND. After functionalization of FNDs with anti-DIG antibodies, an approximately 50-fold excess of DIG-modified DNA was added and left to bind for 2 h. The negative DNA control used the same sequence, but with no DIG modification to compensate for non-specific binding and adequate washing. After multiple washes by centrifugation to remove the excess DNA, the remaining DNA (bound to FNDs) was quantified by qPCR. See Extended Data Fig. [8d](#) for template, primer and probe sequences, and Methods for full experimental details.

d, A kinetic binding simulation was performed to verify that all available sites would be occupied after 2 h with the above excess. The graph shows the fraction of sites on the FNDs which are occupied, with this approximately 50-fold excess, over a range of K_D , k_{on} and k_{off} values. The red cross in circle marks the location of the anti-DIG antibody used in this paper (using the values measured in **a** and **b**), indicating that more than 99.9% of available sites will be occupied after 2 h. This means that quantifying the DNA gives a true measure of available binding sites.

e, Amplification plot showing the normalized fluorescence intensity against the number of cycles. A standard curve of each decade from 40 copies to 4×10^8 copies is plotted, along with the sample and negative control FND samples described above. The negative diluent controls are also plotted along with the C_q

threshold. The lines show means and shaded areas show the s.d. of repeats ($n = 3$ technical replicates for standard curve, and $n = 6$ for samples). **f**, The resulting C_q values are plotted against copy number per reaction. Dots show means and error bars show s.d. ($n = 3$ technical replicates for standard curve and $n = 6$ for samples). The standard curve was fitted to a logarithmic curve ($C_q = -3.2\log_{10}$ copies + 39), enabling calculation of the number of copies in the DIG–DNA sample and negative DNA control. Dividing by the particle concentration (measured as shown in Extended Data Fig. [5c](#)) and subtracting the negative DNA control value gives the number of available binding sites per particle as 4,300 sites. This is within what is geometrically plausible, giving an area per antibody of at least 200 nm^2 (assuming at least 1 paratope available of at least 75% of the bound antibodies). The corresponding calculated values for 120 and 200 nm particles are 172 and 477 available binding sites per FND respectively, assuming the same loading density.

Extended Data Fig. 5 Lateral flow and FND benchmarking.

a, Measurement of flow rate of lateral flow strips. During wetting, the flow follows the Washburn equation, where $\sqrt{V} \approx t^{1/2}$ (inset), and during fully-wetted flow, Darcy's law for capillary flow is followed ($V \approx t$), with a constant flow rate of $6.9 \mu\text{l min}^{-1}$. **b**, Using a one-to-one receptor–ligand binding approximation, the binding of biotinylated FNDs to streptavidin was modelled kinetically, indicating that all the FNDs bind with a residency time of more than about 10^{-3} s . Here, the residency time is measured as 4 s, using the flow rate from **a**, so all the FNDs should bind. **c**, An example of the measurement of FND concentration. FND fluorescence is unaffected by surface chemistry, so is used to quantify concentration. A serial dilution of FND suspensions from a known stock concentration was performed (dots showing means with error bars showing s.d., $n = 6$ measurement replicates). This was then fitted with a linear regression (lines) to find a relationship between fluorescence intensity and concentration. After each FND functionalization, the fluorescence intensities of the final suspensions were measured, and the linear fit was used to estimate concentration (crosses). **d**, Fundamental LODs for different sized FNDs on LFAs, using a model biotin–avidin interaction. Suspensions

(55 µl) of BSA–biotin-functionalized FNDs were run at different concentrations on poly-streptavidin strips. Concentrations were chosen to span the dynamic range of the camera, limited by over-exposure, as seen with the top concentration of 200 and 600 nm FNDs. Dots show means and error bars show s.d. ($n = 3$ technical replicates, $n = 3$ measurement replicates). Each series is fitted to a simple linear regression, shown as the solid line, with 95% confidence intervals shown shaded. LODs for 120, 200 and 600 nm diameter FNDs are 200 aM, 46 aM, and 820 zM respectively, defined by the intersection of the lower 95% confidence intervals of the linear fit with the upper 95% confidence intervals of the blanks for each particle size.

Extended Data Fig. 6 Assay optimization by buffer selection.

Sensitivity is limited by the non-specific binding of FNDs at the LFA test line. LFA strip blocking, running buffer and washing step are, therefore, key factors in improving LOD. In this section 120 nm FNDs were used for optimization. **a**, Signal-to-background comparison for the FNDs in different running buffers. There is no wash step. Error bars show s.d. ($n = 3$ measurement replicates). Milk was selected as the basis for the running buffer. **b**, Subsequently, a sweep of different surfactants was performed ($n = 1$ measurement replicate). The best signal-to-background ratio came from adding 0.05 vol% Empigen, showing a significant increase in the signal-to-background. There is no wash step. **c–e**, The best running buffer was then used for a washing buffer pH sweep ($n = 1$ measurement replicate) (**c**). All washing buffers were run at a volume of 75 µl, chosen because preliminary experiments showed it to be a good compromise between assay time and washing success. Although results were similar, pH 5 gave the best signal-to-background ratio, so acetate buffer at 10 mM pH 5 was used as the basis for a second washing buffer sweep, shown in (**d**), testing a number of detergents and adding casein at 0.2 wt% as a blocking protein ($n = 1$ measurement replicate). As a final test, the three best running buffers were tested, each with the three best washing conditions, displayed as a grid in (**e**). Each square is the average of three measurements ($n = 3$ measurement replicates). The results were consistent with previous sweeps, the combination of the best running buffer and best washing buffer giving

the best signal-to-background. Milk and protein percentages are by weight and detergent percentages are by volume.

Extended Data Fig. 7 Optimization of FND concentration.

The background was reduced by optimising the particle concentration, shown here for 120-nm FNDs. **a**, A positive LFA strip (500 pM of ssDNA) and a negative control (deionized water) were run at varying FND concentrations between 3.88 fM and 496 fM, plotted against FND concentration, and fitted to simple linear regressions. The dots show means and error bars show the s.d. of repeat measurements ($n = 3$ measurement replicates). Linear regressions are shown by solid lines, and shaded areas show the 95% confidence intervals of the fits. **b**, Signal-to-background ratio, found by dividing the fitted linear regressions in **a**, is plotted against FND concentration. At higher concentrations, where the gradient term of the linear regression dominates, the positive and negative lock-in values tend to a constant separation on the log–log plot, so the signal-to-background ratio tends to a constant value of around 27. At low concentrations, the positive and negative curves converge as the negative lock-in amplitude levels off at the noise threshold, and the signal-to-background ratio tends to 1. **c**, The fitted linear regressions in **a** were used, along with the antibody equilibrium dissociation constant measured in Extended Data Fig. 4, to estimate the variation of lock-in amplitude with analyte concentration at different FND concentrations. The principles and equations are described in full in Supplementary Information section 2. The LOD for each FND concentration is defined as the intersection of this plot with the value of the blank plus two times the 95% confidence interval at that value, assuming a low concentration positive would have a similar confidence interval. **d**, The estimated LODs and dynamic ranges from **c**, plotted against FND concentration, to determine the optimum.

Extended Data Fig. 8 Primer optimization.

a, List of forward primers (F1–F5) and reverse primers (R1–R5) tested for the initial primer screen. **b**, An initial primer screen was performed to achieve the highest amplification efficiency ($n = 3$ technical replicates) using the TwistAmp Exo Reverse Transcription Kit (TwistDx). The yield of

each primer combination was measured by the fluorescence of the exo probe with a fluorescence microplate reader (SpectraMax i3, Molecular Devices LLC). Primers F5 and R3 gave the highest yield, although all the yields were above 63% of this value. **c**, Interactions between forward primers and reverse primers to predict the minimum free energy structures for the ten primer combinations that gave the largest yield of RPA product in the primer screen. The table shows the results of simulations in NUPACK⁵⁶, using an input of 10 µM for each oligonucleotide. The minimum free energy secondary structures are the most energetically favourable secondary structures that can be assumed for oligonucleotides of a given primary sequence, calculated using the nearest-neighbour method⁵⁷. Primers F1 and R4 were selected for future work since the energetics of their hybridization are much less favourable than that of F3 and R5, yet they still gave a high RPA yield in the primer screen (93% of the highest yield pair). **d**, A list of oligonucleotides used for PCR, RPA and qPCR assays. The PCR reverse primer included a T7 promoter for RNA transcription (underlined) and a spacer (bold). **e**, Gel electrophoresis of 1,503 bp template sequence produced by PCR using a 1% agarose gel. **f**, Gel electrophoresis of 181 bp double-stranded RT–RPA products using a 1% agarose gel.

Extended Data Fig. 9 Comparison of LODs of model ssDNA with real RPA amplicons and gold nanoparticles.

a, The dilution series of the real RPA amplicons and the model ssDNA ‘amplicons’ were plotted against concentration for 600 nm FNDs (dots showing means with error bars showing s.d., $n = 3\text{--}9$ technical replicates, $n = 3$ measurement replicates) with their respective linear fits (solid lines with 95% confidence intervals of the fit shown shaded). The curves are similar, with fitted K_D values of 29 and 22 fM for model and real amplicons, respectively, and similar dynamic ranges. The real amplicons showed increased variation in the blanks, leading to a higher blank cutoff giving a higher LOD, and slightly reduced signal-to-blank ratio. **b**, The dilution series of model ssDNA ‘amplicons’ were plotted against concentration for 120, 200 and 600 nm FNDs (dots showing means with error bars showing s.d., $n = 3$ technical replicates, $n = 3$ measurement

replicates) with their respective linear fits (solid lines with 95% confidence intervals of the fit shown shaded). The LODs are 3.7, 3.6 and 0.8 fM respectively. **c**, Comparison of 600 nm FNDs with 40 nm gold nanoparticles on LFAs, often used in LFAs owing to a good compromise between stability (and therefore ease of functionalization), and sensitivity⁵⁸. Serial dilutions are plotted (dots showing means with error bars showing s.d., $n = 3$ technical replicates, $n = 3$ measurement replicates for the FNDs; and dots with error bars showing the s.d. across the test line, $n = 1$ technical replicate, $n = 1$ measurement replicate for the gold nanoparticles). LODs are calculated as previously, giving 800 aM and 6.0 pM, respectively. **d, e**, A Monte Carlo simulation of the signal variation that can be explained by the FND size distribution (from DLS measurements in Extended Data Fig. 3b) was performed ($n = 200,000$). The violin plots (**d**) show the normalized simulated random variation in lock-in amplitudes due to the 600-nm FND size distribution in the clinical sample assays in Fig. 4d (negative plasma control and clinical standard). The experimental data are overlaid, showing that FND size distribution explains approximately 8–9% of the total experimental signal variance. Full details of the simulation are given in Supplementary Information [section 3](#). A further approximately 0.1–2% of the variance is explained by periodic drift in modulation amplitude, shown over 45 min in **e**, normalized to the mean. **f**, A plot of the variation in lock-in amplitude due to small changes in the modulation frequency, F_m . The variance of the frequency is $3 \times 10^{-8}\%$ over the same period, giving negligible differences in lock-in amplitude.

Extended Data Fig. 10 Further analysis of RT-RPA samples.

a, ANOVA analysis was performed on the measured lock-in amplitudes of the FND LFAs, giving a P value of 7.4×10^{-29} and F value of 95.6, with 71 total degrees of freedom. Box plots of the data groups are shown (grouped by RNA concentration). The horizontal red lines represent the medians, the horizontal blue lines represent the 25th and 75th percentiles and the notches represent the 95% confidence intervals of the medians. The black dashed lines represent the range for each group. **b**, A graphical comparison of the means of the groups (grouped by RNA concentration). The circles represent the means, and the horizontal lines represent the comparison intervals of the means from Tukey HSD post hoc test (overlap of these intervals denotes

statistical similarity). The negative control, highlighted in blue, is shown to be not significantly different from the 10^{-2} and 10^{-1} RNA copy number samples (P values >0.999 , shown in grey), but it is significantly different from the 1, 10^1 and 10^2 RNA copy number samples (P values $\approx 10^{-8}$, shown in red). **c**, A table of ANOVA P values. The P value for the null hypothesis that the difference between the means of the two groups is zero. **d**, Comparison of amplification time for a low copy number RT–RPA sample (average of 1.26 RNA copies). Multiple RPA reactions were run and stopped after different times, before adding to FND LFAs, as described in Methods. A negative control is shown for comparison, and the dashed line represents the upper 95% confidence interval of the negative control. Dots show the mean of $n = 3$ measurement replicates, crosses show the individual measurements, and error bars represent the s.d. **e**, Early disease detection using FND LFAs was demonstrated by a seroconversion panel (ZeptoMetrix Corporation, Panel Donor No. 73698), taken from a single donor over a period of six weeks spanning the early stages of an HIV-1 infection. The thirteen samples of the panel were measured on FND LFAs ($n = 1\text{--}2$ experimental replicates, $n = 3$ measurement replicates). The measured values are plotted along with positive and negative non-amplification controls. They are colour-coded for RT–PCR results, and labelled with sample numbers, dates, and copy numbers in brackets. The blank cutoff is defined as the upper 95% interval of the negative control. The results show that the RNA was detectable on FND LFAs as early as RT–PCR, and six out of seven RT–PCR-positive samples were detected on FND LFAs, while six out of six RT–PCR-negative samples were negative.

[Extended Data Fig. 11 Detection of HIV-1 capsid protein on using 600 nm FNDs.](#)

A serial dilution of the capsid protein was detected on streptavidin-modified LFAs using a sandwich of a biotinylated capture nanobody and antibody-modified FNDs. The results are plotted ($n = 3\text{--}4$ experimental replicates, $n = 3$ measurement replicates), normalized to the blanks for each sample set with dots showing means and error bars showing s.d. These data were then fitted to a Langmuir curve (equation (6), shown as a line with shaded area denoting the 95% confidence interval of the fit). This gives a LOD of 120 fM, and a lowest concentration that is significantly different from the blank

(at the 95% confidence level) of 3 pM, marked with *. Full experimental details are shown in Supplementary Information section 4.

Extended Data Fig. 12 Effect of lateral flow test strip drying on lock-in amplitude of FND assay.

a, Positive and negative lateral flow test strips were measured over time after running was complete (time = 0), showing a small increase in the positive strip lock-in amplitude as the strip dries (the initial lock-in amplitude is around 70% of the final value); however, no increase is seen in the negative control. The shaded areas show the standard deviation between repeats ($n = 3$ technical replicates). **b**, The resulting signal-to-blank ratio variation over time. The shaded areas show the standard deviation between repeats ($n = 3$ technical replicates), showing that the effect of drying is quite small compared to strip-to-strip variation.

Supplementary information

Supplementary Information

This file contains Supplementary Methods for Extended Data Figures: quantification of antibody binding constants, modelling of FND concentration, simulation of FND size distributions, antigen detection, qRT-PCR; and three Supplementary Tables summarizing estimated costs; comparing FNDs with other fluorescent reporters; and total assay time taken and outlook towards a point-of-care test.

Rights and permissions

Reprints and Permissions

About this article



Check for
updates

Cite this article

Miller, B.S., Bezinge, L., Gliddon, H.D. *et al.* Spin-enhanced nanodiamond biosensing for ultrasensitive diagnostics. *Nature* **587**, 588–593 (2020).
<https://doi.org/10.1038/s41586-020-2917-1>

[Download citation](#)

- Received: 24 May 2019
- Accepted: 16 September 2020
- Published: 25 November 2020
- Issue Date: 26 November 2020
- DOI: <https://doi.org/10.1038/s41586-020-2917-1>

Comments

By submitting a comment you agree to abide by our [Terms](#) and [Community Guidelines](#). If you find something abusive or that does not comply with our terms or guidelines please flag it as inappropriate.

[Access through your institution](#)

[Change institution](#)

[Buy or subscribe](#)

This article was downloaded by **calibre** from <https://www.nature.com/articles/s41586-020-2917-1>

- Article
- [Published: 25 November 2020](#)

Lanthanide-doped inorganic nanoparticles turn molecular triplet excitons bright

- [Sanyang Han](#) ORCID: [orcid.org/0000-0001-7414-7193^{1 na1}](https://orcid.org/0000-0001-7414-7193),
- [Renren Deng](#) ORCID: [orcid.org/0000-0001-8213-6304^{1,2 na1}](https://orcid.org/0000-0001-8213-6304),
- [Qifei Gu¹](#),
- [Limeng Ni](#) ORCID: [orcid.org/0000-0001-6604-7336¹](https://orcid.org/0000-0001-6604-7336),
- [Uyen Huynh¹](#),
- [Jiangbin Zhang](#) ORCID: [orcid.org/0000-0001-6565-5962^{1,3,4}](https://orcid.org/0000-0001-6565-5962),
- [Zhigao Yi](#) ORCID: [orcid.org/0000-0003-0853-2055⁵](https://orcid.org/0000-0003-0853-2055),
- [Baodan Zhao^{1,6}](#),
- [Hiroyuki Tamura](#) ORCID: [orcid.org/0000-0002-1345-0647⁷](https://orcid.org/0000-0002-1345-0647),
- [Anton Pershin⁸](#),
- [Hui Xu](#) ORCID: [orcid.org/0000-0002-2687-5388⁹](https://orcid.org/0000-0002-2687-5388),
- [Zhiyuan Huang¹⁰](#),
- [Shahab Ahmad](#) ORCID: [orcid.org/0000-0002-7846-4804¹¹](https://orcid.org/0000-0002-7846-4804),
- [Mojtaba Abdi-Jalebi](#) ORCID: [orcid.org/0000-0002-9430-6371^{1,12}](https://orcid.org/0000-0002-9430-6371),
- [Aditya Sadhanala](#) ORCID: [orcid.org/0000-0003-2832-4894¹](https://orcid.org/0000-0003-2832-4894),
- [Ming Lee Tang¹⁰](#),
- [Artem Bakulin](#) ORCID: [orcid.org/0000-0002-3998-2000³](https://orcid.org/0000-0002-3998-2000),
- [David Beljonne⁸](#),
- [Xiaogang Liu](#) ORCID: [orcid.org/0000-0003-2517-5790^{5,13,14}](https://orcid.org/0000-0003-2517-5790) &
- [Akshay Rao](#) ORCID: [orcid.org/0000-0003-0320-2962¹](https://orcid.org/0000-0003-0320-2962)

- 231 Accesses
- 26 Altmetric
- [Metrics details](#)

Subjects

- [Organic–inorganic nanostructures](#)
- [Optical spectroscopy](#)
- [Ultrafast photonics](#)

Abstract

The generation, control and transfer of triplet excitons in molecular and hybrid systems is of great interest owing to their long lifetime and diffusion length in both solid-state and solution phase systems, and to their applications in light emission¹, optoelectronics^{2,3}, photon frequency conversion^{4,5} and photocatalysis^{6,7}. Molecular triplet excitons (bound electron–hole pairs) are ‘dark states’ because of the forbidden nature of the direct optical transition between the spin-zero ground state and the spin-one triplet levels⁸. Hence, triplet dynamics are conventionally controlled through heavy-metal-based spin–orbit coupling^{9,10,11} or tuning of the singlet–triplet energy splitting^{12,13} via molecular design. Both these methods place constraints on the range of properties that can be modified and the molecular structures that can be used. Here we demonstrate that it is possible to control triplet dynamics by coupling organic molecules to lanthanide-doped inorganic insulating nanoparticles. This allows the classically forbidden transitions from the ground-state singlet to excited-state triplets to gain oscillator strength, enabling triplets to be directly generated on molecules via photon absorption. Photogenerated singlet excitons can be converted to triplet excitons on sub-10-picosecond timescales with unity efficiency by intersystem crossing. Triplet exciton states of the molecules can undergo energy transfer to the lanthanide ions with unity efficiency, which allows us to achieve luminescent harvesting of the dark triplet excitons. Furthermore, we demonstrate that the triplet

excitons generated in the lanthanide nanoparticle–molecule hybrid systems by near-infrared photoexcitation can undergo efficient upconversion via a lanthanide–triplet excitation fusion process: this process enables endothermic upconversion and allows efficient upconversion from near-infrared to visible frequencies in the solid state. These results provide a new way to control triplet excitons, which is essential for many fields of optoelectronic and biomedical research.

[Access through your institution](#)

[Change institution](#)

[Buy or subscribe](#)

Access options

Subscription info for Chinese customers

We have a dedicated website for our Chinese customers. Please go to [naturechina.com](#) to subscribe to this journal.

[Go to naturechina.com](#)

Rent or Buy article

Get time limited or full article access on ReadCube.

from \$8.99

[Rent or Buy](#)

All prices are NET prices.

Additional access options:

- [Log in](#)
- [Access through your institution](#)
- [Learn about institutional subscriptions](#)

Fig. 1: Lanthanide-nanocrystal-coupled triplet excitation.



Fig. 2: Ultrafast intersystem crossing in organic molecules coupled to lanthanide-doped nanoparticles.



Fig. 3: Triplet energy transfer from molecules to nanoparticles.



Fig. 4: Lanthanide–triplet excitation fusion upconversion in nanoparticle–molecule blends.



Data availability

The data underlying all figures in the main text and [Supplementary Information](#) are publicly available from the University of Cambridge repository at <https://doi.org/10.17863/CAM.59063>.

References

1. 1.

Bolton, O., Lee, K., Kim, H. J., Lin, K. Y. & Kim, J. Activating efficient phosphorescence from purely organic materials by crystal design. *Nat. Chem.* **3**, 205–210 (2011); correction **3**, 415 (2011).

[CAS Article](#) [Google Scholar](#)

2. 2.

Baldo, M. A. et al. Highly efficient phosphorescent emission from organic electroluminescent devices. *Nature* **395**, 151–154 (1998).

[ADS](#) [CAS Article](#) [Google Scholar](#)

3. 3.

Uoyama, H., Goushi, K., Shizu, K., Nomura, H. & Adachi, C. Highly efficient organic light-emitting diodes from delayed fluorescence. *Nature* **492**, 234–238 (2012).

[ADS](#) [CAS Article](#) [Google Scholar](#)

4. 4.

Yanai, N. & Kimizuka, N. New triplet sensitization routes for photon upconversion: thermally activated delayed fluorescence molecules, inorganic nanocrystals, and singlet-to-triplet absorption. *Acc. Chem. Res.* **50**, 2487–2495 (2017).

[CAS Article](#) [Google Scholar](#)

5. 5.

Schulze, T. F. & Schmidt, T. W. Photochemical upconversion: present status and prospects for its application to solar energy conversion. *Energy Environ. Sci.* **8**, 103–125 (2015).

[CAS](#) [Article](#) [Google Scholar](#)

6. 6.

Ravetz, B. D. et al. Photoredox catalysis using infrared light via triplet fusion upconversion. *Nature* **565**, 343–346 (2019); correction **570**, E24 (2019).

[ADS](#) [CAS](#) [Article](#) [Google Scholar](#)

7. 7.

Mongin, C., Garakyaraghi, S., Razgoniaeva, N., Zamkov, M. & Castellano, F. N. Direct observation of triplet energy transfer from semiconductor nanocrystals. *Science* **351**, 369–372 (2016).

[ADS](#) [CAS](#) [Article](#) [Google Scholar](#)

8. 8.

Köhler, A. & Bassler, H. Triplet states in organic semiconductors. *Mater. Sci. Eng. Rep.* **66**, 71–109 (2009).

[Article](#) [Google Scholar](#)

9. 9.

Lamansky, S. et al. Highly phosphorescent bis-cyclometalated iridium complexes: synthesis, photophysical characterization, and use in organic light emitting diodes. *J. Am. Chem. Soc.* **123**, 4304–4312 (2001).

[CAS](#) [Article](#) [Google Scholar](#)

10. 10.

Bünzli, J.-C. G. On the design of highly luminescent lanthanide complexes. *Coord. Chem. Rev.* **293–294**, 19–47 (2015).

[Article](#) [Google Scholar](#)

11. 11.

Klink, S. I., Kerizer, H. & van Veggel, F. C. J. M. Transition metal complexes as photosensitizers for near-infrared lanthanide luminescence. *Angew. Chem. Int. Ed.* **39**, 4319–4321 (2000).

[CAS](#) [Article](#) [Google Scholar](#)

12. 12.

Penfold, T. J., Gindensperger, E., Daniel, C. & Marian, C. M. Spin-vibronic mechanism for intersystem crossing. *Chem. Rev.* **118**, 6975–7025 (2018).

[CAS](#) [Article](#) [Google Scholar](#)

13. 13.

Smith, M. B. & Michl, J. Singlet fission. *Chem. Rev.* **110**, 6891–6936 (2010).

[CAS](#) [Article](#) [Google Scholar](#)

14. 14.

Wykes, M., Parambil, R., Beljonne, D. & Gierschner, J. Vibronic coupling in molecular crystals: a Franck-Condon Herzberg-Teller model of H-aggregate fluorescence based on quantum chemical cluster calculations. *J. Chem. Phys.* **143**, 114116 (2015).

[ADS](#) [CAS](#) [Article](#) [Google Scholar](#)

15. 15.

Auzel, F. Upconversion and anti-Stokes processes with f and d ions in solids. *Chem. Rev.* **104**, 139–174 (2004).

[CAS](#) [Article](#) [Google Scholar](#)

16. 16.

Tobita, S., Arakawa, M. & Tanaka, I. The paramagnetic metal effect on the ligand localized $S_1 \rightarrow T_1$ intersystem crossing in the rare-earth-metal complexes with methyl salicylate. *J. Phys. Chem.* **89**, 5649–5654 (1985).

[CAS](#) [Article](#) [Google Scholar](#)

17. 17.

Tiberghien, A. & Delacote, G. Evaluation of the crystalline tetracene triplet Davydov splitting. *Chem. Phys. Lett.* **8**, 88–90 (1971).

[ADS](#) [CAS](#) [Article](#) [Google Scholar](#)

18. 18.

Tao, S. et al. Optical pump-probe spectroscopy of photocarriers in rubrene single crystals. *Phys. Rev. B* **83**, 075204 (2011).

[ADS](#) [Article](#) [Google Scholar](#)

19. 19.

Thompson, N. J. et al. Energy harvesting of non-emissive triplet excitons in tetracene by emissive PbS nanocrystals. *Nat. Mater.* **13**, 1039–1043 (2014).

[ADS](#) [CAS](#) [Article](#) [Google Scholar](#)

20. 20.

Tabachnyk, M. et al. Resonant energy transfer of triplet excitons from pentacene to PbSe nanocrystals. *Nat. Mater.* **13**, 1033–1038 (2014).

[ADS](#) [CAS](#) [Article](#) [Google Scholar](#)

21. 21.

Wu, M. et al. Solid-state infrared-to-visible upconversion sensitized by colloidal nanocrystals. *Nat. Photon.* **10**, 31–34 (2016).

[ADS](#) [CAS](#) [Article](#) [Google Scholar](#)

22. 22.

Zhao, J., Ji, S. & Guo, H. Triplet–triplet annihilation based upconversion: from triplet sensitizers and triplet acceptors to upconversion quantum yields. *RSC Adv.* **1**, 937–950 (2011).

[CAS](#) [Article](#) [Google Scholar](#)

23. 23.

Singh-Rachford, T. N. & Castellano, F. N. Photon upconversion based on sensitized triplet–triplet annihilation. *Coord. Chem. Rev.* **254**, 2560–2573 (2010).

[CAS](#) [Article](#) [Google Scholar](#)

24. 24.

Burdett, J. J., Müller, A. M., Gosztola, D. & Bardeen, C. J. Excited state dynamics in solid and monomeric tetracene: the roles of superradiance and exciton fission. *J. Chem. Phys.* **133**, 144506 (2010).

[ADS](#) [Article](#) [Google Scholar](#)

25. 25.

Zhao, J. et al. Single-nanocrystal sensitivity achieved by enhanced upconversion luminescence. *Nat. Nanotechnol.* **8**, 729–734 (2013).

[ADS](#) [CAS](#) [Article](#) [Google Scholar](#)

26. 26.

Haase, M. & Schäfer, H. Upconverting nanoparticles. *Angew. Chem. Int. Ed.* **50**, 5808–5829 (2011).

[CAS](#) [Article](#) [Google Scholar](#)

27. 27.

Garfield, D. J. et al. Enrichment of molecular antenna triplets amplifies upconverting nanoparticle emission. *Nat. Photon.* **12**, 402–407 (2018).

[ADS](#) [CAS](#) [Article](#) [Google Scholar](#)

28. 28.

Pollnau, M., Gamelin, D. R., Lüthi, S. R., Güdel, H. U. & Hehlen, M. P. Power dependence of upconversion luminescence in lanthanide and transition-metal-ion systems. *Phys. Rev. B* **61**, 3337–3346 (2000).

[ADS](#) [CAS](#) [Article](#) [Google Scholar](#)

29. 29.

Nienhaus, L., Wu, M., Bulović, V., Baldo, M. A. & Bawendi, M. G. Using lead chalcogenide nanocrystals as spin mixers: a perspective on near-infrared-to-visible upconversion. *Dalton Trans.* **47**, 8509–8516 (2018).

[CAS](#) [Article](#) [Google Scholar](#)

30. 30.

Nienhaus, L. et al. Speed limit for triplet-exciton transfer in solid-state PbS nanocrystal-sensitized photon upconversion. *ACS Nano* **11**, 7848–7857 (2017).

[CAS Article](#) [Google Scholar](#)

31. 31.

Huang, Z. et al. Hybrid molecule–nanocrystal photon upconversion across the visible and near-infrared. *Nano Lett.* **15**, 5552–5557 (2015).

[ADS](#) [CAS Article](#) [Google Scholar](#)

32. 32.

Wang, F., Deng, R. & Liu, X. Preparation of core-shell NaGdF₄ nanoparticles doped with luminescent lanthanide ions to be used as upconversion-based probes. *Nat. Protoc.* **9**, 1634–1644 (2014).

[CAS Article](#) [Google Scholar](#)

33. 33.

Bogdan, N., Vetrone, F., Ozin, G. A. & Capobianco, J. A. Synthesis of ligand-free colloidally stable water dispersible brightly luminescent lanthanide-doped upconverting nanoparticles. *Nano Lett.* **11**, 835–840 (2011).

[ADS](#) [CAS Article](#) [Google Scholar](#)

34. 34.

de Mello, J. C., Wittmann, H. F. & Friend, R. H. An improved experimental determination of external photoluminescence quantum efficiency. *Adv. Mater.* **9**, 230–232 (1997).

[Article](#) [Google Scholar](#)

[Download references](#)

Acknowledgements

This project received funding from the European Research Council (ERC) under the European Union's Horizon 2020 research and innovation programme (grant agreement no. 758826) and from Marie Skłodowska-Curie grant agreements nos 797619 (TET-Lanthanide project), 748042 (MILORD project) and 646176 (EXTMOS project). We acknowledge support from the Engineering and Physical Sciences Research Council (EPSRC) and the Winton Programme for the Physics of Sustainability, the Singapore Ministry of Education (grant MOE2017-T2-2-110), the Singapore Agency for Science, Technology and Research (grant A1883c0011), and the National Research Foundation, Prime Minister's Office, Singapore under the NRF Investigatorship programme (award no. NRF-NRFI05-2019-0003). R.D. acknowledges support from the National Natural Science Foundation of China (grant 51872256) and the Zhejiang Provincial Natural Science Foundation of China (grant LR19B010002). Computational resources were provided by the Consortium des Équipements de Calcul Intensif (CÉCI), funded by the Fonds de la Recherche Scientifique de Belgique (FRS-FNRS) under grant no. 2.5020.11, and by the Tier-1 supercomputer of the Fédération Wallonie-Bruxelles, which is infrastructure funded by the Walloon Region under grant agreement no. 1117545. L.N. acknowledges support from the Jardine Foundation. J.Z. thanks the China Scholarship Council for a PhD scholarship (no. 201503170255). S.A. acknowledges financial support from DST-UKIERI (DST/INT/UK/P-167/2017) and SERB-ECRA (ECR/2018/002056).

Author information

Author notes

1. These authors contributed equally: Sanyang Han, Renren Deng

Affiliations

1. Cavendish Laboratory, University of Cambridge, Cambridge, UK

Sanyang Han, Renren Deng, Qifei Gu, Limeng Ni, Uyen Huynh, Jiangbin Zhang, Baodan Zhao, Mojtaba Abdi-Jalebi, Aditya Sadhanala & Akshay Rao

2. Institute for Composites Science Innovation, School of Materials Science and Engineering, Zhejiang University, Hangzhou, China

Renren Deng

3. Department of Chemistry, Imperial College London, London, UK

Jiangbin Zhang & Artem Bakulin

4. College of Advanced Interdisciplinary Studies, National University of Defense Technology, Changsha, China

Jiangbin Zhang

5. Department of Chemistry, National University of Singapore, Singapore, Singapore

Zhilao Yi & Xiaogang Liu

6. State Key Laboratory of Modern Optical Instrumentation, College of Optical Science and Engineering, International Research Center for Advanced Photonics, Zhejiang University, Hangzhou, China

Baodan Zhao

7. Department of Chemical System Engineering, The University of Tokyo, Tokyo, Japan

Hiroyuki Tamura

8. Laboratory for Chemistry of Novel Materials, University of Mons, Mons, Belgium

Anton Pershin & David Beljonne

9. School of Chemistry and Material Science, Heilongjiang University,
Harbin, China

Hui Xu

10. Department of Chemistry, University of California, Riverside,
Riverside, CA, USA

Zhiyuan Huang & Ming Lee Tang

11. Advanced Energy Materials Group, Department of Physics, Indian
Institute of Technology Jodhpur, Jodhpur, India

Shahab Ahmad

12. Institute for Materials Discovery, University College London, London,
UK

Mojtaba Abdi-Jalebi

13. The N.1 Institute for Health, National University of Singapore,
Singapore, Singapore

Xiaogang Liu

14. Joint School of National University of Singapore and Tianjin
University, International Campus of Tianjin University, Fuzhou, China

Xiaogang Liu

Authors

1. Sanyang Han
[View author publications](#)

You can also search for this author in [PubMed](#) [Google Scholar](#)

2. Renren Deng
[View author publications](#)

You can also search for this author in [PubMed](#) [Google Scholar](#)

3. Qifei Gu

[View author publications](#)

You can also search for this author in [PubMed](#) [Google Scholar](#)

4. Limeng Ni

[View author publications](#)

You can also search for this author in [PubMed](#) [Google Scholar](#)

5. Uyen Huynh

[View author publications](#)

You can also search for this author in [PubMed](#) [Google Scholar](#)

6. Jiangbin Zhang

[View author publications](#)

You can also search for this author in [PubMed](#) [Google Scholar](#)

7. Zhigao Yi

[View author publications](#)

You can also search for this author in [PubMed](#) [Google Scholar](#)

8. Baodan Zhao

[View author publications](#)

You can also search for this author in [PubMed](#) [Google Scholar](#)

9. Hiroyuki Tamura

[View author publications](#)

You can also search for this author in [PubMed](#) [Google Scholar](#)

10. Anton Pershin

[View author publications](#)

You can also search for this author in [PubMed](#) [Google Scholar](#)

11. Hui Xu

[View author publications](#)

You can also search for this author in [PubMed](#) [Google Scholar](#)

12. Zhiyuan Huang

[View author publications](#)

You can also search for this author in [PubMed](#) [Google Scholar](#)

13. Shahab Ahmad

[View author publications](#)

You can also search for this author in [PubMed](#) [Google Scholar](#)

14. Mojtaba Abdi-Jalebi

[View author publications](#)

You can also search for this author in [PubMed](#) [Google Scholar](#)

15. Aditya Sadhanala

[View author publications](#)

You can also search for this author in [PubMed](#) [Google Scholar](#)

16. Ming Lee Tang

[View author publications](#)

You can also search for this author in [PubMed](#) [Google Scholar](#)

17. Artem Bakulin

[View author publications](#)

You can also search for this author in [PubMed](#) [Google Scholar](#)

18. David Beljonne

[View author publications](#)

You can also search for this author in [PubMed](#) [Google Scholar](#)

19. Xiaogang Liu

[View author publications](#)

You can also search for this author in [PubMed](#) [Google Scholar](#)

20. Akshay Rao

[View author publications](#)

You can also search for this author in [PubMed](#) [Google Scholar](#)

Contributions

S.H., R.D. and A.R. designed the experiments. S.H., R.D., Z.Y. and B.Z. performed nanocrystal synthesis and film preparation. S.H., R.D., L.N., U.H., A.S. and S.A. carried out spectroscopic measurements. S.H., Q.G. and J.Z. contributed to transient absorption experiments and data analysis under the supervision of A.B. and A.R. H.T., A.P. and D.B. carried out theoretical calculations. H.X. prepared organic molecules. Z.H. prepared tetracene derivatives under the supervision of M.L.T. M.A.-J. and A.S. performed PDS measurements. S.H., R.D., X.L. and A.R. wrote the manuscript. X.L. and A.R. supervised the project. All authors discussed the results and commented on the manuscript.

Corresponding authors

Correspondence to [Renren Deng](#) or [Xiaogang Liu](#) or [Akshay Rao](#).

Ethics declarations

Competing interests

The authors declare no competing interests.

Additional information

Peer review information *Nature* thanks Jiajia Zhou and the other, anonymous, reviewer(s) for their contribution to the peer review of this work.

Publisher's note Springer Nature remains neutral with regard to jurisdictional claims in published maps and institutional affiliations.

Supplementary information

Supplementary Information

This file contains Supplementary Figures 1-54 and Supplementary Tables 1-3.

Rights and permissions

Reprints and Permissions

About this article



Check for
updates

Cite this article

Han, S., Deng, R., Gu, Q. *et al.* Lanthanide-doped inorganic nanoparticles turn molecular triplet excitons bright. *Nature* **587**, 594–599 (2020).
<https://doi.org/10.1038/s41586-020-2932-2>

Download citation

- Received: 24 April 2019
- Accepted: 23 September 2020

- Published: 25 November 2020
- Issue Date: 26 November 2020
- DOI: <https://doi.org/10.1038/s41586-020-2932-2>

Comments

By submitting a comment you agree to abide by our [Terms](#) and [Community Guidelines](#). If you find something abusive or that does not comply with our terms or guidelines please flag it as inappropriate.

[Access through your institution](#)

[Change institution](#)

[Buy or subscribe](#)

This article was downloaded by **calibre** from <https://www.nature.com/articles/s41586-020-2932-2>

| [Section menu](#) | [Main menu](#) |

- Article
- [Published: 25 November 2020](#)

Antarctic ice dynamics amplified by Northern Hemisphere sea-level forcing

- [Natalya Gomez](#) ORCID: orcid.org/0000-0002-2463-7917¹,
- [Michael E. Weber](#) ORCID: orcid.org/0000-0003-2175-8980²,
- [Peter U. Clark](#)^{3,4},
- [Jerry X. Mitrovica](#)⁵ &
- [Holly K. Han](#) ORCID: orcid.org/0000-0002-3819-5275¹

Nature volume 587, pages600–604(2020) [Cite this article](#)

- 370 Accesses
- 255 Altmetric
- [Metrics details](#)

Subjects

- [Climate and Earth system modelling](#)
- [Cryospheric science](#)
- [Geodynamics](#)
- [Palaeoceanography](#)
- [Palaeoclimate](#)

Abstract

Sea-level rise due to ice loss in the Northern Hemisphere in response to insolation and greenhouse gas forcing is thought to have caused grounding-line retreat of marine-based sectors of the Antarctic Ice Sheet (AIS)^{1,2,3}. Such interhemispheric sea-level forcing may explain the synchronous evolution of global ice sheets over ice-age cycles. Recent studies that indicate that the AIS experienced substantial millennial-scale variability during and after the last deglaciation^{4,5,6,7} (roughly 20,000 to 9,000 years ago) provide further evidence of this sea-level forcing. However, global sea-level change as a result of mass loss from ice sheets is strongly nonuniform, owing to gravitational, deformational and Earth rotational effects⁸, suggesting that the response of AIS grounding lines to Northern Hemisphere sea-level forcing is more complicated than previously modelled^{1,2,6}. Here, using an ice-sheet model coupled to a global sea-level model, we show that AIS dynamics are amplified by Northern Hemisphere sea-level forcing. As a result of this interhemispheric interaction, a large or rapid Northern Hemisphere sea-level forcing enhances grounding-line advance and associated mass gain of the AIS during glaciation, and grounding-line retreat and mass loss during deglaciation. Relative to models without these interactions, the inclusion of Northern Hemisphere sea-level forcing in our model increases the volume of the AIS during the Last Glacial Maximum (about 26,000 to 20,000 years ago), triggers an earlier retreat of the grounding line and leads to millennial-scale variability throughout the last deglaciation. These findings are consistent with geologic reconstructions of the extent of the AIS during the Last Glacial Maximum and subsequent ice-sheet retreat, and with relative sea-level change in Antarctica^{3,4,5,6,7,9,10}.

[Access through your institution](#)

[Change institution](#)

[Buy or subscribe](#)

Access options

Subscription info for Chinese customers

We have a dedicated website for our Chinese customers. Please go to naturechina.com to subscribe to this journal.

[Go to naturechina.com](#)

Rent or Buy article

Get time limited or full article access on ReadCube.

from \$8.99

[Rent or Buy](#)

All prices are NET prices.

Additional access options:

- [Log in](#)
- [Access through your institution](#)
- [Learn about institutional subscriptions](#)

Fig. 1: Contributions to deglacial sea-level changes in Antarctica.

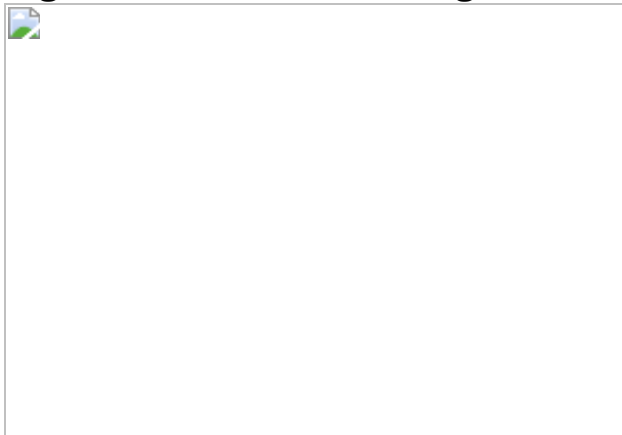


Fig. 2: Timing of Northern Hemisphere sea-level forcing and its influence on Antarctic ice volume changes.



Fig. 3: Enhanced Antarctic ice loss during MWP-1A and the early Holocene.



Fig. 4: Agreement of predicted sea-level and ice-cover changes with geological records in the Ross Sea sector.



Data availability

The datasets generated for this publication are available in the PANGAEA database (<https://doi.org/10.1594/PANGAEA.919498>) and as source data for Extended Data Fig. 9. The modelling results are available in the OSF database (https://osf.io/g5ur2/?view_only=8acbf1e38c184d9c8f09811c8bbef036). [Source data](#) are provided with this paper.

Code availability

The coupled ice-sheet–sea-level model used is reported in refs. [26,28](#); the PSU 3D ice-sheet model is reported in ref. [37](#). Ice-sheet and sea-level models are available on request from the authors of the references listed.

References

1. 1.

Denton, G. H. & Hughes, T. J. Milankovitch theory of ice ages: hypothesis of ice-sheet linkage between regional insolation and global climate. *Quat. Res.* **20**, 125–144 (1983).

[Google Scholar](#)

2. 2.

Huybrechts, P. J. Sea-level changes at the LGM from ice-dynamic reconstructions of the Greenland and Antarctic ice sheets during the glacial cycles. *Quat. Sci. Rev.* **21**, 203–231 (2002).

[ADS](#) [Google Scholar](#)

3. 3.

Weber, M. E. et al. Interhemispheric ice-sheet synchronicity during the Last Glacial Maximum. *Science* **334**, 1265–1269 (2011).

[ADS](#) [CAS](#) [PubMed](#) [Google Scholar](#)

4. 4.

Weber, M. E. et al. Millennial-scale variability in Antarctic ice-sheet discharge during the last deglaciation. *Nature* **510**, 134–138 (2014).

[ADS](#) [CAS](#) [PubMed](#) [Google Scholar](#)

5. 5.

Golledge, N. R. et al. Antarctic contribution to meltwater pulse 1A from reduced Southern Ocean overturning. *Nat. Commun.* **5**, 5107 (2014).

[ADS](#) [CAS](#) [PubMed](#) [Google Scholar](#)

6. 6.

Fogwill, C. J. et al. Antarctic ice sheet discharge driven by atmosphere–ocean feedbacks at the Last Glacial Termination. *Sci. Rep.* **7**, 39979 (2017).

[ADS](#) [CAS](#) [PubMed](#) [PubMed Central](#) [Google Scholar](#)

7. 7.

Bart, P. J., DeCesare, M., Rosenheim, B. E., Majewski, W. & McGlannan, A. A centuries-long delay between a paleo-ice-shelf collapse and grounding-line retreat in the Whales Deep Basin, eastern Ross Sea, Antarctica. *Sci. Rep.* **8**, 12392 (2018).

[ADS](#) [PubMed](#) [PubMed Central](#) [Google Scholar](#)

8. 8.

Milne, G. A. & Mitrovica, J. X. Searching for eustasy in deglacial sea-level histories. *Quat. Sci. Rev.* **27**, 2292–2302 (2008).

[ADS](#) [Google Scholar](#)

9. 9.

Hall, B. L. & Denton, G. H. New relative sea-level curves for the southern Scott Coast, Antarctica: evidence for Holocene deglaciation of the western Ross Sea. *J. Quat. Sci.* **14**, 641–650 (1999).

[Google Scholar](#)

10. 10.

Fogwill, C. J. et al. Southern Ocean carbon sink enhanced by sea-ice feedbacks at the Antarctic Cold Reversal. *Nat. Geosci.* **13**, 489–497 (2020).

[ADS](#) [CAS](#) [Google Scholar](#)

11. 11.

Kawamura, K. et al. Northern Hemisphere forcing of climatic cycles in Antarctica over the past 360,000 years. *Nature* **448**, 912–916 (2007).

[ADS](#) [CAS](#) [PubMed](#) [Google Scholar](#)

12. 12.

Huybers, P. & Denton, G. Antarctic temperature at orbital timescales controlled by local summer duration. *Nat. Geosci.* **1**, 787–792 (2008).

[ADS](#) [CAS](#) [Google Scholar](#)

13. 13.

Clark, P. U. et al. The last glacial maximum. *Science* **325**, 710–714 (2009).

[ADS](#) [CAS](#) [PubMed](#) [Google Scholar](#)

14. 14.

Pollard, D., Chang, W., Haran, M., Applegate, P. & DeConto, R. Large ensemble modeling of the last deglacial retreat of the West Antarctic Ice Sheet: comparison of simple and advanced statistical techniques. *Geosci. Model Dev.* **9**, 1697–1723 (2016).

[ADS](#) [Google Scholar](#)

15. 15.

Clark, P. U. et al. Oceanic forcing of penultimate deglacial and last interglacial sea-level rise. *Nature* **577**, 660–664 (2020).

[ADS](#) [CAS](#) [PubMed](#) [Google Scholar](#)

16. 16.

Weertman, J. Stability of the junction of an ice sheet and an ice shelf. *J. Glaciol.* **13**, 3–11 (1974).

[ADS](#) [Google Scholar](#)

17. 17.

Schoof, C. Ice sheet grounding line dynamics: steady states, stability, and hysteresis. *J. Geophys. Res.* **112**, F03S28 (2007).

[ADS](#) [Google Scholar](#)

18. 18.

Denton, G. H., Hughes, T. J. & Karlén, W. Global ice-sheet system interlocked by sea level. *Quat. Res.* **26**, 3–26 (1986).

[CAS](#) [Google Scholar](#)

19. 19.

Tigchelaar, M., Timmermann, A., Friedrich, T., Heinemann, M. & Pollard, D. Nonlinear response of the Antarctic Ice Sheet to late Quaternary sea level and climate forcing. *Cryosphere* **13**, 2615–2631 (2019).

[ADS](#) [Google Scholar](#)

20. 20.

Yokoyama, Y., Lambeck, K., De Deckker, P., Johnston, P. & Fifield, L. K. Timing of the Last Glacial Maximum from observed sea-level minima. *Nature* **406**, 713–716 (2000); corrigendum **412**, 99 (2001).

[ADS](#) [CAS](#) [PubMed](#) [Google Scholar](#)

21. 21.

Deschamps, P. et al. Ice-sheet collapse and sea-level rise at the Bølling warming 14,600 years ago. *Nature* **483**, 559–564 (2012).

[ADS](#) [CAS](#) [PubMed](#) [Google Scholar](#)

22. 22.

Bard, E., Hamelin, B. & Delanghe-Sabatier, D. Deglacial meltwater pulse 1B and Younger Dryas sea levels revisited with boreholes at Tahiti. *Science* **327**, 1235–1237 (2010).

[ADS](#) [CAS](#) [PubMed](#) [Google Scholar](#)

23. 23.

Abdul, N. A., Mortlock, R. A., Wright, J. D. & Fairbanks, R. G. Younger Dryas sea level and meltwater pulse 1B recorded in Barbados reef crest coral *Acropora palmata*. *Paleoceanography* **31**, 330–344 (2016).

[ADS](#) [Google Scholar](#)

24. 24.

Bakker, P., Clark, P. U., Golledge, N. R., Schmittner, A. & Weber, M. E. Centennial-scale Holocene climate variations amplified by Antarctic Ice Sheet discharge. *Nature* **541**, 72–76 (2017).

[ADS](#) [CAS](#) [PubMed](#) [Google Scholar](#)

25. 25.

Hallmann, N. et al. Ice volume and climate changes from a 6000 year sea-level record in French Polynesia. *Nat. Commun.* **9**, 285 (2018).

[ADS](#) [CAS](#) [PubMed](#) [PubMed Central](#) [Google Scholar](#)

26. 26.

Gomez, N., Pollard, D. & Mitrovica, J. X. A 3-D coupled ice sheet – sea level model applied to Antarctica through the last 40 ky. *Earth Planet. Sci. Lett.* **384**, 88–99 (2013).

[ADS](#) [CAS](#) [Google Scholar](#)

27. 27.

Peltier, W. R. Global glacial isostasy and the surface of the ice-age Earth: the ICE-5G (VM2) model and GRACE. *Annu. Rev. Earth Planet. Sci.* **32**, 111–149 (2004).

[ADS](#) [CAS](#) [Google Scholar](#)

28. 28.

Pollard, D., Gomez, N. & DeConto, R. M. Variations of the Antarctic Ice Sheet in a coupled ice sheet-Earth-sea level model: sensitivity to viscoelastic Earth properties. *J. Geophys. Res. Earth Surf.* **122**, 2124–2138 (2017).

[ADS](#) [Google Scholar](#)

29. 29.

Tarasov, L., Dyke, A. S., Neal, R. M. & Peltier, W. R. A data-calibrated distribution of deglacial chronologies for the North American ice complex from glaciological modeling. *Earth Planet. Sci. Lett.* **315–316**, 30–40 (2012).

[ADS](#) [Google Scholar](#)

30. 30.

Lambeck, K., Rouby, H., Purcell, A., Sun, Y. & Sambridge, M. Sea level and global ice volumes from the Last Glacial Maximum to the Holocene. *Proc. Natl Acad. Sci. USA* **111**, 15296–15303 (2014).

[ADS](#) [CAS](#) [PubMed](#) [Google Scholar](#)

31. 31.

Peltier, W. R., Argus, D. F. & Drummond, R. Space geodesy constrains ice age terminal deglaciation: the global ICE-6G_C (VM5a) model. *J. Geophys. Res. Solid Earth* **120**, 450–487 (2015).

[ADS](#) [Google Scholar](#)

32. 32.

Fretwell, P. et al. Bedmap2: improved ice bed, surface and thickness datasets for Antarctica. *Cryosphere* **7**, 375–393 (2013).

[ADS](#) [Google Scholar](#)

33. 33.

Bard, E., Hamelin, B., Deschamps, P. & Camoin, G. Comment on “Younger Dryas sea level and meltwater pulse 1B recorded in

Barbados reefal crest coral *Acropora palmata*" by N. A. Abdul et al. *Paleoceanography* **31**, 1603–1608 (2016).

[ADS](#) [Google Scholar](#)

34. 34.

Briggs, R. D. & Tarasov, L. How to evaluate model-derived deglaciation chronologies: a case study using Antarctica. *Quat. Sci. Rev.* **63**, 109–127 (2013).

[ADS](#) [Google Scholar](#)

35. 35.

Jones, R., Whitehouse, P., Bentley, M., Small, D. & Dalton, A. Impact of glacial isostatic adjustment on cosmogenic surface-exposure dating. *Quat. Sci. Rev.* **212**, 206–212 (2019).

[ADS](#) [Google Scholar](#)

36. 36.

Gomez, N., Pollard, D. & Holland, D. Sea-level feedback lowers projections of future Antarctic Ice Sheet mass loss. *Nat. Commun.* **6**, 8798 (2015).

[ADS](#) [CAS](#) [PubMed](#) [PubMed Central](#) [Google Scholar](#)

37. 37.

Pollard, D. & DeConto, R. M. Description of a hybrid ice sheet-shelf model, and application to Antarctica. *Geosci. Model Dev.* **5**, 1273–1295 (2012).

[ADS](#) [Google Scholar](#)

38. 38.

Kendall, R. A., Mitrovica, J. X. & Milne, G. A. On post-glacial sea level – II. Numerical formulation and comparative results on spherically symmetric models. *Geophys. J. Int.* **161**, 679–706 (2005).

[ADS](#) [Google Scholar](#)

39. 39.

Gomez, N., Mitrovica, J. X., Tamisiea, M. E. & Clark, P. U. A new projection of sea level change in response to collapse of marine sectors of the Antarctic Ice Sheet. *Geophys. J. Int.* **180**, 623–634 (2010).

[ADS](#) [Google Scholar](#)

40. 40.

MacAyeal, D. R. Large-scale ice flow over a viscous basal sediment: theory and application to ice stream B, Antarctica. *J. Geophys. Res. Solid Earth* **94**, 4071–4087 (1989).

[Google Scholar](#)

41. 41.

Andrews, J. T. & Mahaffy, M. A. W. Growth rate of the Laurentide Ice Sheet and sea level lowering (with emphasis on the 115 000 BP sea level low). *Quat. Res.*, **6**, 167–183 (1976).

[Google Scholar](#)

42. 42.

Pattyn, F. et al. Grounding-line migration in plan-view marine ice-sheet models: results of the ice2sea MISMIP3d intercomparison. *J. Glaciol.* **59**, 410–422 (2013).

[ADS](#) [Google Scholar](#)

43. 43.

Pollard, D. & DeConto, R. M. A simple inverse method for the distribution of basal sliding coefficients under ice sheets, applied to Antarctica. *Cryosphere* **6**, 953–971 (2012).

[ADS](#) [Google Scholar](#)

44. 44.

Pattyn, F. Sea-level response to melting of Antarctic ice shelves on multi-centennial time scales with the fast elementary thermomechanical ice sheet model (f.ETISh v1.0). *Cryosphere* **11**, 1851–1878 (2017).

[ADS](#) [Google Scholar](#)

45. 45.

Tsai, V. C., Stewart, A. L. & Thompson, A. F. Marine ice-sheet profiles and stability under Coulomb basal conditions. *J. Glaciol.* **61**, 205–215 (2015).

[ADS](#) [Google Scholar](#)

46. 46.

Le Brocq, A. M., Payne, A. J. & Vieli, A. An improved Antarctic dataset for high resolution numerical ice sheet models (ALBMAP v1). *Earth Syst. Sci. Data* **2**, 247–260 (2010).

[ADS](#) [Google Scholar](#)

47. 47.

Lisiecki, L. E. & Raymo, M. E. A Pliocene-Pleistocene stack of 57 globally distributed benthic $\delta^{18}\text{O}$ records. *Paleoceanography* **20**, PA1003 (2005); correction **20**, PA2007 (2005).

[ADS](#) [Google Scholar](#)

48. 48.

Liu, Z. et al. Transient simulation of last deglaciation with a new mechanism for Bolling-Allerod warming. *Science* **325**, 310–314 (2009).

[ADS](#) [CAS](#) [PubMed](#) [Google Scholar](#)

49. 49.

Dziewonski, A. M. & Anderson, D. L. Preliminary reference Earth model. *Phys. Earth Planet. Inter.* **25**, 297–356 (1981).

[ADS](#) [Google Scholar](#)

50. 50.

Mitrovica, J. X. & Forte, A. M. A new inference of mantle viscosity based upon joint inversion of convection and glacial isostatic adjustment data. *Earth Planet. Sci. Lett.* **225**, 177–189 (2004).

[ADS](#) [CAS](#) [Google Scholar](#)

51. 51.

Huybrechts, P. & de Wolde, J. The dynamic response of the Greenland and Antarctic ice sheets to multiple-century climatic warming. *J. Clim.* **12**, 2169–2188 (1999).

[ADS](#) [Google Scholar](#)

52. 52.

National Geophysical Data Center. *2-minute Gridded Global Relief Data (ETOPO2) v2* (NOAA, 2006); <https://data.nodc.noaa.gov/cgi-bin/iso?id=gov.noaa.ngdc.mgg.dem:301>.

53. 53.

Weber, M. E. et al. Dust transport from Patagonia to Antarctica – a new stratigraphic approach from the Scotia Sea and its implications for the last glacial cycle. *Quat. Sci. Rev.* **36**, 177–188 (2012).

[ADS](#) [Google Scholar](#)

54. 54.

Ruth, U. et al. “EDML1”: a chronology for the EPICA deep ice core from Dronning Maud Land, Antarctica, over the last 150 000 years. *Clim. Past* **3**, 475–484 (2007).

[Google Scholar](#)

55. 55.

Veres, D. et al. The Antarctic ice core chronology (AICC2012): an optimized multi-parameter and multi-site dating approach for the last 120 thousand years. *Clim. Past* **9**, 1733–1748 (2013).

[Google Scholar](#)

56. 56.

Bazin, L. et al. An optimized multi-proxy, multi-site Antarctic ice and gas orbital chronology (AICC2012): 120–800 ka. *Clim. Past* **9**, 1715–1731 (2013).

[Google Scholar](#)

57. 57.

Lamy, F. et al. Increased dust deposition in the Pacific Southern Ocean during glacial periods. *Science* **343**, 403–407 (2014).

[ADS](#) [CAS](#) [PubMed](#) [Google Scholar](#)

58. 58.

Martínez-García, A. et al. Iron fertilization of the subantarctic ocean during the last ice age. *Science* **343**, 1347–1350 (2014).

[ADS](#) [PubMed](#) [Google Scholar](#)

59. 59.

Small, D., Bentley, M. J., Jones, R. S., Pittard, M. L. & Whitehouse, P. L. Antarctic ice sheet palaeo-thinning rates from vertical transects of cosmogenic exposure ages. *Quat. Sci. Rev.* **206**, 65–80 (2019).

[ADS](#) [Google Scholar](#)

[Download references](#)

Acknowledgements

N.G. and H.K.H. were supported by the Natural Sciences and Engineering Research Council (NSERC), the Canada Research Chair's programme and the Canadian Foundation for Innovation, M.E.W. by the Deutsche Forschungsgemeinschaft (DFG; grant numbers We2039/8-1 and We 2039/17-1), and J.X.M. by NASA grant NNX17AE17G and Harvard University. We thank G. Tseng for assistance with exploratory research that informed this study, and D. Pollard for insight on and use of the PSU ice-sheet model.

Author information

Affiliations

1. Department of Earth and Planetary Sciences, McGill University, Montreal, Quebec, Canada

Natalya Gomez & Holly K. Han

2. Department of Geochemistry and Petrology, Institute for Geosciences, University of Bonn, Bonn, Germany

Michael E. Weber

3. College of Earth, Ocean, and Atmospheric Sciences, Oregon State University, Corvallis, OR, USA

Peter U. Clark

4. School of Geography and Environmental Sciences, University of Ulster, Coleraine, UK

Peter U. Clark

5. Department of Earth and Planetary Sciences, Harvard University, Cambridge, MA, USA

Jerry X. Mitrovica

Authors

1. Natalya Gomez

[View author publications](#)

You can also search for this author in [PubMed](#) [Google Scholar](#)

2. Michael E. Weber

[View author publications](#)

You can also search for this author in [PubMed](#) [Google Scholar](#)

3. Peter U. Clark

[View author publications](#)

You can also search for this author in [PubMed](#) [Google Scholar](#)

4. Jerry X. Mitrovica

[View author publications](#)

You can also search for this author in [PubMed](#) [Google Scholar](#)

5. Holly K. Han

[View author publications](#)

You can also search for this author in [PubMed](#) [Google Scholar](#)

Contributions

N.G. contributed the numerical modelling and analysis; H.K.H. prepared model input; M.E.W. contributed iceberg-rafted debris records and, together with P.U.C. and J.X.M., other published data and related discussion. All authors contributed to developing the idea and to writing and refining the manuscript.

Corresponding author

Correspondence to [Natalya Gomez](#).

Ethics declarations

Competing interests

The authors declare no competing interests.

Additional information

Peer review information *Nature* thanks Frank Pattyn and the other, anonymous, reviewer(s) for their contribution to the peer review of this work.

Publisher's note Springer Nature remains neutral with regard to jurisdictional claims in published maps and institutional affiliations.

Extended data figures and tables

Extended Data Fig. 1 Sensitivity of results to ice and Earth model parameters.

a, Changes in Antarctic ice volume predicted in simulations with evolving (solid lines) and fixed (dashed lines) Northern Hemisphere ice mass, and adopting the LVZ Earth model (Methods). Blue lines are identical to those in Fig. 2b, corresponding to a basal sliding coefficient of $b = 10^{-5} \text{ m yr}^{-1} \text{ Pa}^{-2}$; red lines correspond to a basal sliding coefficient of $b = 10^{-6} \text{ m yr}^{-1} \text{ Pa}^{-2}$. The black dotted line shows changes in Northern Hemisphere ice volume (right axis; in metres of global-mean sea level (gmsl) equivalent) prescribed in the ICE5G²⁷ ice history. **b**, As in **a**, but adopting the HV Earth model (Methods). Blue (**a**) and red (**b**) vertical bands represent the timing of MWP and AID events, as in Fig. 2a,c, respectively.

Extended Data Fig. 2 Evolution of Antarctic ice cover with and without Northern Hemisphere sea-level forcing.

a, b, Thickness of grounded ice (in metres) and extent of ice shelves, at 30 ka, 20 ka, 10 ka and the present day, predicted from simulations that include variations in the Northern Hemisphere ice sheets represented by the ICE5G²⁷ ice history (**a**) and from simulations in which ice cover in the Northern Hemisphere remains fixed (**b**). Black lines show the grounding lines. **c**, The difference in grounded ice thickness between simulations in **a** and **b**, representing the effect of sea-level changes associated with Northern Hemisphere ice sheets on the evolution of the AIS. Green and black lines represent the positions of the grounding lines with (**a**) and without (**b**) the Northern Hemisphere sea-level forcing included.

Extended Data Fig. 3 Influence of Northern Hemisphere sea-level forcing on Antarctic ice cover during the deglaciation.

The colour scale indicates the difference in the thickness (in metres) of grounded ice, at the indicated times, between simulations that include variations in the Northern Hemisphere ice sheets from ICE5G²⁷ ice history and in which ice cover in the Northern Hemisphere remains fixed

throughout the simulation. Differences are displayed as in Fig. 3c, but every 1 kyr for the past 19 kyr. Green and black lines represent the positions of the grounding lines with and without the Northern Hemisphere sea-level forcing included, respectively.

Extended Data Fig. 4 Antarctic ice-volume changes in the Ross Sea and Weddell Sea sectors.

a, Changes in ice volume in the Weddell Sea sector predicted in simulations with fixed (red) and evolving (black) Northern Hemisphere ice from the ICE5G²⁷ ice history. **b**, As in **a**, but for the Ross Sea sector. **c**, Blue lines outline the areas included in the calculations in **a** and **b**; colour scale indicates the change in ice thickness (in metres) from 20 ka to the present day in the simulations that include Northern Hemisphere ice-cover changes from ICE5G²⁷.

Extended Data Fig. 5 Influence of Northern Hemisphere sea-level forcing on the rate of Antarctic ice loss.

a–e, Rate of change of Antarctic ice volume, including grounded and floating ice, calculated with a 100-year running mean, predicted from simulations including (black) and excluding (red) Northern Hemisphere ice-cover changes, using the ice histories indicated in the legend (Methods). The mean and standard deviation of these five panels are shown in Fig. 3a.

Extended Data Fig. 6 Patterns of sea-level change for Antarctic ice loss during MWP-1A and the early Holocene.

a, b, Predicted sea-level change, normalized by the global-mean sea-level-equivalent associated with Antarctic ice loss during MWP-1A (**a**) and the early Holocene (including MWP-1B; **b**). Calculations are associated with simulations that include Northern Hemisphere ice cover changes given by ICE5G²⁷. The patterns of sea-level change and the global mean sea-level equivalent used in the normalization are calculated over the time windows indicated by the green vertical bands in Fig. 2b. Green and

magenta asterisks indicate the locations of the far-field relative sea-level records in Tahiti and Barbados.

Extended Data Fig. 7 Sensitivity of the Weddell Sea sector to geographic variability in sea-level forcing.

a, Same as Fig. 3b, but zoomed in on the Weddell Sea region, where geographically variable sea-level changes associated with Northern Hemisphere ice loss are largest (Fig. 1c). The colour scale shows the change in ice thickness predicted from a simulation adopting the ICE5G²⁷ ice history in the Northern Hemisphere, which includes geographically variable sea-level changes associated with gravitational, deformational and Earth rotational effects activated by ice-cover changes globally, during MWP-1A (14.5–13.5 ka). Grey and black lines indicate the grounding-line position at the start and end of the time interval, respectively. **b**, The difference between **a** and the same calculation but adopting the simulation with globally uniform sea-level change from the Northern Hemisphere. The black line is as in **a**; the blue line indicates the grounding-line position at the end of the time interval for the uniform sea-level simulation. **c**, Antarctic ice-volume variations from simulations with geographically variable (black) and uniform (red) sea-level changes associated with Northern Hemisphere ice loss over the MWP-1A interval. **d–f**, As in **a–c**, but for the early Holocene interval (11.5–9 ka). In this case, **d** is the same as Fig. 3d, but zoomed in on the Weddell Sea region. The uniform sea-level change is calculated relative to modern topography and scaled such that the total contribution to global sea-level change from the Northern Hemisphere over the last deglaciation (since 21 ka) is 95.5 m, in agreement with ref. ²⁷.

Extended Data Fig. 8 Predicted Antarctic ice-volume changes and global-mean sea-level contributions.

a, Changes in AIS volume predicted in a simulation with Northern Hemisphere ice cover fixed at the 40 ka configuration within ICE5G²⁷ (solid red line) and in simulations with evolving Northern Hemisphere ice adopting the ICE5G²⁷ (solid black line),

ICE6GC³¹ (dashed black line) and ANU³⁰ (cyan line) ice histories, as well as two composite ice histories in which ice cover over North America and Greenland in ICE5G has been replaced by regional GLAC1D²⁹ models (blue lines). The dashed red line represents a simulation in which the Northern Hemisphere ice sheets are fixed at the modern configuration rather than at the 40 ka configuration throughout the simulation. In this case, marine-based sectors of the AIS start on even shallower bedrock, and hence the predicted ice-sheet growth is larger at the LGM, while the ice loss during the deglaciation occurs later and is of even smaller magnitude than in the original simulation. Note that this is not a realistic starting configuration. **b**, As in **a**, but expressed as a global-mean sea-level-equivalent (GMSLE) relative to the modern state. This is calculated by taking the ice above floatation thickness in Antarctica relative to the palaeo bedrock topography at each time step in the model, and dividing by the area of the modern ocean. Note that **a** and **b** are not directly proportional because as the bedrock topography in Antarctica evolves the volume of ice above floatation in marine sectors also changes. Blue (**a**) and red (**b**) vertical bands represent the timing of MWP and AID events, as in Fig. [2a](#), [c](#), respectively.

Extended Data Fig. 9 Age model comparison and uncertainty for IBRD flux record from Iceberg Alley.

a, Age difference between the AICC 2012^{55,56} and EDML1⁵⁴ age models. **b**, Age uncertainty in the AICC 2012 age model. **c**, IBRD flux time series adopting the AICC 2012 (black line, as in Figs. [2c](#), [4b](#)) and EDML1/EDC3 (blue dotted line) age scales. The IBRD stack is composed of records from sites MD07-3133 and MD07-3134. It is presented here for 20–0 ka and was combined with previous data for 27–7 ka⁴ and 8–0 ka²⁴. Vertical brown bars indicate AID events 1–7⁴ on the AICC 2012 age scale. Blue vertical bars indicate MWP-1A²¹ and MWP-1B²². Horizontal black error bars show propagated uncertainties for the upper and lower bounds of each AID event for errors in tie-point correlation to EDML⁴ and uncertainties of the AICC 2012 age model. [Source data](#).

Extended Data Fig. 10 Comparison of predicted and observed ice-thickness changes in the Weddell Sea region.

a, b, Predicted (lines) and observed (error bars) ice thickness (in metres) above the modern thickness at sites 11–13 (**a**) and 14, 15 (**b**) from ref. [35](#). Predictions are from simulations in which Northern Hemisphere ice cover is evolving according to ICE5G²⁷ (black lines) or is fixed (blue lines). Error bars show cosmogenic exposure age data with 2σ uncertainty from ref. [35](#). **c**, Map of predicted ice thickness at 12 ka, in the simulation with ICE5G²⁷. The locations of the relevant sites in the Weddell Sea and Ross Sea (see Extended Data Fig. [11](#)) regions are indicated. See [Methods](#) for further discussion of these results.

Extended Data Fig. 11 Comparison of predicted and observed ice-thickness changes in the Ross Sea region.

a, Predicted (lines) and observed (2σ error bars) ice thickness (in metres) above the modern thickness at Scott Coast site S (black) and sites 1 (red) and 3–5 (shades of blue) from ref. [35](#). The locations of the sites are indicated in **b–e**. Predictions are from simulations in which Northern Hemisphere ice cover is evolving according to ICE5G²⁷ (solid lines) or is fixed (dashed lines). Observations are cosmogenic exposure age data from ref. [35](#). Red vertical bands represent the timing of AID events 1 and 2, as in Fig. [2c](#). **b**, Map of predicted ice thickness 12 ka in the Ross Sea, in the simulation with evolving Northern Hemisphere ice. **c–e**, The difference in ice thickness between 12 ka (**b**) and 11 ka (**c**), 10 ka (**d**) and 9 ka (**e**). See [Methods](#) for further discussion of these results.

Source data

[Source Data Extended Data Fig. 9](#)

Rights and permissions

[Reprints and Permissions](#)

About this article



Check for
updates

Cite this article

Gomez, N., Weber, M.E., Clark, P.U. *et al.* Antarctic ice dynamics amplified by Northern Hemisphere sea-level forcing. *Nature* **587**, 600–604 (2020). <https://doi.org/10.1038/s41586-020-2916-2>

[Download citation](#)

- Received: 20 September 2019
- Accepted: 16 September 2020
- Published: 25 November 2020
- Issue Date: 26 November 2020
- DOI: <https://doi.org/10.1038/s41586-020-2916-2>

Comments

By submitting a comment you agree to abide by our [Terms](#) and [Community Guidelines](#). If you find something abusive or that does not comply with our terms or guidelines please flag it as inappropriate.

[Access through your institution](#)

[Change institution](#)

[Buy or subscribe](#)

| [Section menu](#) | [Main menu](#) |

- Article
- [Published: 11 November 2020](#)

Sensory pollutants alter bird phenology and fitness across a continent

- [Masayuki Senzaki](#)^{1,2 na1},
- [Jesse R. Barber](#)³,
- [Jennifer N. Phillips](#) [ORCID: orcid.org/0000-0002-0014-2995](#)^{1,4},
- [Neil H. Carter](#)⁵,
- [Caren B. Cooper](#)^{6,7},
- [Mark A. Ditmer](#) [ORCID: orcid.org/0000-0003-4311-3331](#)⁵,
- [Kurt M. Fristrup](#)⁸,
- [Christopher J. W. McClure](#) [ORCID: orcid.org/0000-0003-1216-7425](#)^{3,9},
- [Daniel J. Mennitt](#)¹⁰,
- [Luke P. Tyrrell](#) [ORCID: orcid.org/0000-0001-8322-1930](#)¹¹,
- [Jelena Vukomanovic](#)^{12,13},
- [Ashley A. Wilson](#)¹ &
- [Clinton D. Francis](#) [ORCID: orcid.org/0000-0003-2018-4954](#)^{1 na1}

[Nature](#) volume 587, pages605–609(2020) [Cite this article](#)

- 3387 Accesses
- 456 Altmetric
- [Metrics details](#)

Subjects

- [Conservation biology](#)
- [Macroecology](#)
- [Urban ecology](#)

Abstract

Expansion of anthropogenic noise and night lighting across our planet^{1,2} is of increasing conservation concern^{3,4,5,6}. Despite growing knowledge of physiological and behavioural responses to these stimuli from single-species and local-scale studies, whether these pollutants affect fitness is less clear, as is how and why species vary in their sensitivity to these anthropic stressors. Here we leverage a large citizen science dataset paired with high-resolution noise and light data from across the contiguous United States to assess how these stimuli affect reproductive success in 142 bird species. We find responses to both sensory pollutants linked to the functional traits and habitat affiliations of species. For example, overall nest success was negatively correlated with noise among birds in closed environments. Species-specific changes in reproductive timing and hatching success in response to noise exposure were explained by vocalization frequency, nesting location and diet. Additionally, increased light-gathering ability of species' eyes was associated with stronger advancements in reproductive timing in response to light exposure, potentially creating phenological mismatches⁷. Unexpectedly, better light-gathering ability was linked to reduced clutch failure and increased overall nest success in response to light exposure, raising important questions about how responses to sensory pollutants counteract or exacerbate responses to other aspects of global change, such as climate warming. These findings demonstrate that anthropogenic noise and light can substantially affect breeding bird phenology and fitness, and underscore the need to consider sensory pollutants alongside traditional dimensions of the environment that typically inform biodiversity conservation.

[Access through your institution](#)

[Change institution](#)

[Buy or subscribe](#)

Access options

Subscription info for Chinese customers

We have a dedicated website for our Chinese customers. Please go to naturechina.com to subscribe to this journal.

[Go to naturechina.com](http://naturechina.com)

Rent or Buy article

Get time limited or full article access on ReadCube.

from \$8.99

[Rent or Buy](#)

All prices are NET prices.

Additional access options:

- [Log in](#)
- [Access through your institution](#)
- [Learn about institutional subscriptions](#)

Fig. 1: Anthropogenic noise and night lighting are widespread and affect a variety of species.



Fig. 2: Responses to light and noise by birds in open and closed habitats.



Fig. 3: Relationships between species-specific responses to noise or light (model estimate \pm s.e.) and functional traits.



Data availability

The datasets analysed during this study are available at <https://doi.org/10.5061/dryad.dbry15dzc>; Additional publicly available data used in this study include: Anthropogenic noise levels from the National Park Service Data Store (<https://irma.nps.gov/DataStore/Reference/Profile/2217356>); New World Atlas of Artificial Night Sky Brightness (<https://dataservices.gfz-potsdam.de/contact/showshort.php?id=escidoc:1541893&contactform>); the 2011 US National Land Cover Database (<https://www.mrlc.gov/data/nlcd-2011-land-cover-conus-0>); US Human population density data (<https://data.census.gov/cedsci/>); EltonTraits 1.0 database (<http://www.esapubs.org/archive/ecol/E095/178/>), *Birds of North America Online* (recently changed to *Birds of the World*, <https://birdsoftheworld.org/bow/home>) and vocal frequency (<https://doi.org/10.5061/dryad.75nn1932>) and body morphology data (<https://doi.org/10.6084/m9.figshare.3527864.v1>). **Source data** are provided with this paper.

References

1. 1.

Buxton, R. T. et al. Noise pollution is pervasive in U.S. protected areas. *Science* **356**, 531–533 (2017).

[ADS](#) [CAS](#) [PubMed](#) [Google Scholar](#)

2. 2.

Kyba, C. C. M. et al. Artificially lit surface of Earth at night increasing in radiance and extent. *Sci. Adv.* **3**, e1701528 (2017).

[ADS](#) [PubMed](#) [PubMed Central](#) [Google Scholar](#)

3. 3.

Barber, J. R., Crooks, K. R. & Fistrup, K. M. The costs of chronic noise exposure for terrestrial organisms. *Trends Ecol. Evol.* **25**, 180–189 (2010).

[PubMed](#) [Google Scholar](#)

4. 4.

Swaddle, J. P. et al. A framework to assess evolutionary responses to anthropogenic light and sound. *Trends Ecol. Evol.* **30**, 550–560 (2015).

[PubMed](#) [Google Scholar](#)

5. 5.

Gaston, K. J., Davies, T. W., Nedelec, S. L. & Holt, L. A. Impacts of artificial light at night on biological timings. *Annu. Rev. Ecol. Evol. Syst.* **48**, 49–68 (2017).

[Google Scholar](#)

6. 6.

Dominoni, D. M. et al. Why conservation biology can benefit from sensory ecology. *Nat. Ecol. Evol.* **4**, 502–511 (2020).

[PubMed](#) [Google Scholar](#)

7. 7.

Visser, M. E. & Gienapp, P. Evolutionary and demographic consequences of phenological mismatches. *Nat. Ecol. Evol.* **3**, 879–885 (2019).

[PubMed](#) [PubMed Central](#) [Google Scholar](#)

8. 8.

Francis, C. D. & Barber, J. R. A framework for understanding noise impacts on wildlife: an urgent conservation priority. *Front. Ecol. Environ.* **11**, 305–313 (2013).

[Google Scholar](#)

9. 9.

Shannon, G. et al. A synthesis of two decades of research documenting the effects of noise on wildlife. *Biol. Rev. Camb. Philos. Soc.* **91**, 982–1005 (2016).

[PubMed](#) [Google Scholar](#)

10. 10.

van Langevelde, F., Ettema, J. A., Donners, M., WallisDeVries, M. F. & Groenendijk, D. Effect of spectral composition of artificial light on the attraction of moths. *Biol. Conserv.* **144**, 2274–2281 (2011).

[Google Scholar](#)

11. 11.

Hale, J. D., Fairbrass, A. J., Matthews, T. J., Davies, G. & Sadler, J. P. The ecological impact of city lighting scenarios: exploring gap

crossing thresholds for urban bats. *Glob. Chang. Biol.* **21**, 2467–2478 (2015).

[ADS](#) [PubMed](#) [PubMed Central](#) [Google Scholar](#)

12. 12.

Halfwerk, W., Holleman, L. J. M., Lessells, C. M. & Slabbekoorn, H. Negative impact of traffic noise on avian reproductive success. *J. Appl. Ecol.* **48**, 210–219 (2011).

[Google Scholar](#)

13. 13.

Kight, C. R., Saha, M. S. & Swaddle, J. P. Anthropogenic noise is associated with reductions in the productivity of breeding Eastern Bluebirds (*Sialia sialis*). *Ecol. Appl.* **22**, 1989–1996 (2012).

[PubMed](#) [Google Scholar](#)

14. 14.

Injaian, A. S., Poon, L. Y. & Patricelli, G. L. Effects of experimental anthropogenic noise on avian settlement patterns and reproductive success. *Behav. Ecol.* **29**, 1181–1189 (2018).

[Google Scholar](#)

15. 15.

Kempenaers, B., Borgström, P., Loës, P., Schlicht, E. & Valcu, M. Artificial night lighting affects dawn song, extra-pair siring success, and lay date in songbirds. *Curr. Biol.* **20**, 1735–1739 (2010).

[CAS](#) [PubMed](#) [Google Scholar](#)

16. 16.

Cooper, C. B., Hochachka, W. M., Butcher, G. & Dhondt, A. A. Seasonal and latitudinal trends in clutch size: thermal constraints during laying and incubation. *Ecology* **86**, 2018–2031 (2005).

[Google Scholar](#)

17. 17.

Van Renterghem, T., Botteldooren, D. & Verheyen, K. Road traffic noise shielding by vegetation belts of limited depth. *J. Sound Vibrat.* **331**, 2404–2425 (2012).

[ADS](#) [Google Scholar](#)

18. 18.

Luginbuhl, C. B. et al. From the ground up II: sky glow and near-ground artificial light propagation in Flagstaff, Arizona. *Publ. Astron. Soc. Pacif.* **121**, 204–212 (2009).

[ADS](#) [Google Scholar](#)

19. 19.

Boncoraglio, G. & Saino, N. Habitat structure and the evolution of bird song: a meta-analysis of the evidence for the acoustic adaptation hypothesis. *Funct. Ecol.* **21**, 134–142 (2007).

[Google Scholar](#)

20. 20.

Francis, C. D. Vocal traits and diet explain avian sensitivities to anthropogenic noise. *Glob. Chang. Biol.* **21**, 1809–1820 (2015).

[ADS](#) [PubMed](#) [Google Scholar](#)

21. 21.

Huet des Aunay, G. et al. Negative impact of urban noise on sexual receptivity and clutch size in female domestic canaries. *Ethology* **123**, 843–853 (2017).

[Google Scholar](#)

22. 22.

Proppe, D. S., Sturdy, C. B. & St Clair, C. C. Anthropogenic noise decreases urban songbird diversity and may contribute to homogenization. *Glob. Chang. Biol.* **19**, 1075–1084 (2013).

[ADS](#) [PubMed](#) [Google Scholar](#)

23. 23.

Kleist, N. J., Guralnick, R. P., Cruz, A., Lowry, C. A. & Francis, C. D. Chronic anthropogenic noise disrupts glucocorticoid signaling and has multiple effects on fitness in an avian community. *Proc. Natl Acad. Sci. USA* **115**, E648–E657 (2018).

[CAS](#) [PubMed](#) [Google Scholar](#)

24. 24.

Dominoni, D., Quetting, M. & Partecke, J. Artificial light at night advances avian reproductive physiology. *Proc. Biol. Sci. B* **280**, 20123017 (2013).

[Google Scholar](#)

25. 25.

Visser, M. E., Both, C. & Lambrechts, M. M. Global climate change leads to mistimed avian reproduction. *Adv. Ecol. Res.* **35**, 89–110 (2004).

[Google Scholar](#)

26. 26.

Winkler, D. W., Dunn, P. O. & McCulloch, C. E. Predicting the effects of climate change on avian life-history traits. *Proc. Natl Acad. Sci. USA* **99**, 13595–13599 (2002).

[ADS](#) [CAS](#) [PubMed](#) [Google Scholar](#)

27. 27.

Dunn, P. O. & Winkler, D. W. Climate change has affected the breeding date of tree swallows throughout North America. *Proc. Biol. Sci.* **266**, 2487–2490 (1999).

[CAS](#) [PubMed Central](#) [Google Scholar](#)

28. 28.

Both, C. & Visser, M. E. Adjustment to climate change is constrained by arrival date in a long-distance migrant bird. *Nature* **411**, 296–298 (2001).

[ADS](#) [CAS](#) [PubMed](#) [Google Scholar](#)

29. 29.

Burgess, M. D. et al. Tritrophic phenological match-mismatch in space and time. *Nat. Ecol. Evol.* **2**, 970–975 (2018).

[PubMed](#) [Google Scholar](#)

30. 30.

van de Pol, M. & Wright, J. A simple method for distinguishing within- versus between-subject effects using mixed models. *Anim. Behav.* **77**, 753–758 (2009).

[Google Scholar](#)

31. 31.

Cornell Laboratory of Ornithology. *The Birds of North America Online* (Cornell Laboratory of Ornithology, 2015).

32. 32.

Falchi, F. et al. The new world atlas of artificial night sky brightness. *Sci. Adv.* **2**, e1600377 (2016).

[ADS](#) [PubMed](#) [PubMed Central](#) [Google Scholar](#)

33. 33.

Mennitt, D. J. & Fristrup, K. M. Influence factors and spatiotemporal patterns of environmental sound levels in the contiguous United States. *Noise Control Eng. J.* **64**, 342–353 (2016).

[Google Scholar](#)

34. 34.

Dooling, R. J., Lohr, B. & Dent, M. L. in *Comparative Hearing: Birds and Reptiles* (eds. Dooling, R. J. et al.) 308–359 (Springer, 2000).

35. 35.

Arnold, C. L. & Gibbons, C. J. Impervious surface coverage: the emergence of a key environmental indicator. *J. Am. Plann. Assoc.* **62**, 243–258 (1996).

[Google Scholar](#)

36. 36.

McKinney, M. L. Urbanization as a major cause of biotic homogenization. *Biol. Conserv.* **127**, 247–260 (2006).

[Google Scholar](#)

37. 37.

Xian, G. *et al.* Change of impervious surface area between 2001 and 2006 in the conterminous United States. *Photogramm. Eng. Remote Sensing* **77**, 758–762 (2012).

[Google Scholar](#)

38. 38.

United States Census Bureau. *2010 Census* <https://data.census.gov/cedsci/> (US Census Bureau, 2011).

39. 39.

Hall, M. I. & Ross, C. F. Eye shape and activity pattern in birds. *J. Zool. (Lond.)* **271**, 437–444 (2007).

[Google Scholar](#)

40. 40.

Kirk, E. C. Comparative morphology of the eye in primates. *Anat. Rec. A Discov. Mol. Cell. Evol. Biol.* **281**, 1095–1103 (2004).

[PubMed](#) [Google Scholar](#)

41. 41.

Martin, G. R. in *Perception and Motor Control in Birds: An Ecological Approach* (eds. Davies, M. & Green, P.) 5–34 (Springer, 1994).

42. 42.

Blackwell, B. F., Fernández-Juricic, E., Seamans, T. W. & Dolan, T. Avian visual system configuration and behavioural response to object approach. *Anim. Behav.* **77**, 673–684 (2009).

[Google Scholar](#)

43. 43.

Hall, M. I., Iwaniuk, A. N. & Gutiérrez-Ibáñez, C. Optic foramen morphology and activity pattern in birds. *Anat. Rec. (Hoboken)* **292**, 1827–1845 (2009).

[Google Scholar](#)

44. 44.

Moore, B. A., Doppler, M., Young, J. E. & Fernández-Juricic, E. Interspecific differences in the visual system and scanning behavior of three forest passerines that form heterospecific flocks. *J. Comp. Physiol. A Neuroethol. Sens. Neural Behav. Physiol.* **199**, 263–277 (2013).

[PubMed](#) [Google Scholar](#)

45. 45.

Ritland, S. M. *The Allometry of the Vertebrate Eye* (Univ. of Chicago, 1983).

46. 46.

Tyrrell, L. P. & Fernández-Juricic, E. The hawk-eyed songbird: retinal morphology, eye shape, and visual fields of an aerial insectivore. *Am. Nat.* **189**, 709–717 (2017).

[PubMed](#) [Google Scholar](#)

47. 47.

Goolsby, E. W., Bruggeman, J. & Ané, C. Rphylopars: fast multivariate phylogenetic comparative methods for missing data and within-species variation. *Methods Ecol. Evol.* **8**, 22–27 (2017).

[Google Scholar](#)

48. 48.

Uyeda, J. C., Pennell, M. W., Miller, E. T., Maia, R. & McClain, C. R. The evolution of energetic scaling across the vertebrate tree of life. *Am. Nat.* **190**, 185–199 (2017).

[PubMed](#) [Google Scholar](#)

49. 49.

Vitousek, M. N. et al. Macroevolutionary patterning in glucocorticoids suggests different selective pressures shape baseline and stress-induced levels. *Am. Nat.* **193**, 866–880 (2019).

[PubMed](#) [Google Scholar](#)

50. 50.

Jetz, W., Thomas, G. H., Joy, J. B., Hartmann, K. & Mooers, A. O. The global diversity of birds in space and time. *Nature* **491**, 444–448 (2012).

[ADS](#) [CAS](#) [PubMed](#) [Google Scholar](#)

51. 51.

Wilman, H. et al. EltonTraits 1.0: species-level foraging attributes of the world's birds and mammals. *Ecology* **95**, 1717–2032 (2014).

[Google Scholar](#)

52. 52.

Lislevand, T., Figuerola, J. & Székely, T. Avian body sizes in relation to fecundity, mating system, display behavior, and resource sharing. *Ecology* **88**, 1605 (2007).

[Google Scholar](#)

53. 53.

Cornell Laboratory of Ornithology. *All About Birds* <https://www.allaboutbirds.org> (Cornell Laboratory of Ornithology, 2018).

54. 54.

Rousset, F. & Ferdy, J.-B. Testing environmental and genetic effects in the presence of spatial autocorrelation. *Ecography* **37**, 781–790 (2014).

[Google Scholar](#)

55. 55.

Smith, R. J. & Moore, F. R. Arrival timing and seasonal reproductive performance in a long-distance migratory landbird. *Behav. Ecol. Sociobiol.* **57**, 231–239 (2005).

[Google Scholar](#)

56. 56.

Pinheiro, J., Bates, D., DebRoy, S. & Sarkar, D. nlme: linear and nonlinear mixed effects models (R package version 3.1-104, 2012).

57. 57.

Revell, L. J. Phylogenetic signal and linear regression on species data. *Methods Ecol. Evol.* **1**, 319–329 (2010).

[Google Scholar](#)

58. 58.

Ives, A. R., Midford, P. E. & Garland, T. Jr. Within-species variation and measurement error in phylogenetic comparative methods. *Syst. Biol.* **56**, 252–270 (2007).

[PubMed](#) [Google Scholar](#)

59. 59.

Garamszegi, L. Z. in *Modern Phylogenetic Comparative Methods and Their Application in Evolutionary Biology* (ed. Garamszegi, L. Z.) 157–199 (Springer, 2014).

60. 60.

Jones, K. E. & Purvis, A. An optimum body size for mammals? Comparative evidence from bats. *Funct. Ecol.* **11**, 751–756 (1997).

[Google Scholar](#)

61. 61.

Hurlbert, S. H., Levine, R. A. & Utts, J. Coup de grâce for a tough old bull: “statistically significant” expires. *Am. Stat.* **73**, 352–357 (2019).

[Google Scholar](#)

62. 62.

Amrhein, V., Greenland, S. & McShane, B. Scientists rise up against statistical significance. *Nature* **567**, 305–307 (2019).

[ADS](#) [CAS](#) [PubMed](#) [Google Scholar](#)

63. 63.

Halsey, L. G. The reign of the p-value is over: what alternative analyses could we employ to fill the power vacuum? *Biol. Lett.* **15**, 20190174 (2019).

[PubMed](#) [PubMed Central](#) [Google Scholar](#)

64. 64.

Ware, H. E., McClure, C. J. W., Carlisle, J. D. & Barber, J. R. A phantom road experiment reveals traffic noise is an invisible source of habitat degradation. *Proc. Natl Acad. Sci. USA* **112**, 12105–12109 (2015).

[ADS](#) [CAS](#) [PubMed](#) [Google Scholar](#)

65. 65.

R Core Team. R: a language and environment for statistical computing (R Foundation for Statistical Computing, 2019).

66. 66.

Brooks, M. E. et al. glmmTMB balances speed and flexibility among packages for zero-inflated generalized linear mixed modeling. *R J.* **9**, 378–400 (2017).

[Google Scholar](#)

67. 67.

Lüdecke, D., Makowski, D. & Waggoner, P. *Performance: Assessment of Regression Models Performance* (2019).

68. 68.

Dormann, C. F. et al. Methods to account for spatial autocorrelation in the analysis of species distributional data: a review. *Ecography* **30**, 609–628 (2007).

[Google Scholar](#)

69. 69.

Yu, G. & Ekstrøm, C. T. emojifont: emoji and font awesome in graphics (R package version 0.5.3, 2019).

[Download references](#)

Acknowledgements

We thank the NestWatch Program for use of their nesting database, the volunteers who monitored the nests and F. Rousset for advice in using the spaMM package. Supported by US National Science Foundation grants 1414171 to C.D.F. and J.R.B., 1556177 to J.R.B., 1556192 to C.D.F. and 1812280 to J.N.P.; NASA Ecological Forecasting grant NNX17AG36G to N.H.C., C.D.F. and J.R.B.; and Japanese Society for the Promotion of Science KAKENHI grant 17J00646 to M.S.

Author information

Author notes

1. These authors contributed equally: Masayuki Senzaki, Clinton D. Francis

Affiliations

1. Biological Sciences, California Polytechnic State University, San Luis Obispo, CA, USA

Masayuki Senzaki, Jennifer N. Phillips, Ashley A. Wilson & Clinton D. Francis

2. Faculty of Environmental Earth Science, Hokkaido University, Sapporo, Japan

Masayuki Senzaki

3. Biological Sciences, Boise State University, Boise, ID, USA

Jesse R. Barber & Christopher J. W. McClure

4. Department of Science and Mathematics, Texas A&M San Antonio, San Antonio, TX, USA

Jennifer N. Phillips

5. School for Environment and Sustainability, University of Michigan,
Ann Arbor, MI, USA

Neil H. Carter & Mark A. Ditmer

6. Department of Forestry and Environmental Resources, North Carolina
State University, Raleigh, NC, USA

Caren B. Cooper

7. Leadership in Public Science, North Carolina State University,
Raleigh, NC, USA

Caren B. Cooper

8. National Park Service Natural Sounds and Night Skies Division, Fort
Collins, CO, USA

Kurt M. Fristrup

9. The Peregrine Fund, Boise, ID, USA

Christopher J. W. McClure

10. Exponent, Denver, CO, USA

Daniel J. Mennitt

11. Department of Biological Sciences, State University of New York
Plattsburgh, Plattsburgh, NY, USA

Luke P. Tyrrell

12. Department of Parks, Recreation and Tourism Management, North
Carolina State University, Raleigh, NC, USA

Jelena Vukomanovic

13. Center for Geospatial Analytics, North Carolina State University,
Raleigh, NC, USA

Jelena Vukomanovic

Authors

1. Masayuki Senzaki

[View author publications](#)

You can also search for this author in [PubMed](#) [Google Scholar](#)

2. Jesse R. Barber

[View author publications](#)

You can also search for this author in [PubMed](#) [Google Scholar](#)

3. Jennifer N. Phillips

[View author publications](#)

You can also search for this author in [PubMed](#) [Google Scholar](#)

4. Neil H. Carter

[View author publications](#)

You can also search for this author in [PubMed](#) [Google Scholar](#)

5. Caren B. Cooper

[View author publications](#)

You can also search for this author in [PubMed](#) [Google Scholar](#)

6. Mark A. Ditmer

[View author publications](#)

You can also search for this author in [PubMed](#) [Google Scholar](#)

7. Kurt M. Fristrup

[View author publications](#)

You can also search for this author in [PubMed](#) [Google Scholar](#)

8. Christopher J. W. McClure
[View author publications](#)

You can also search for this author in [PubMed](#) [Google Scholar](#)

9. Daniel J. Mennitt
[View author publications](#)

You can also search for this author in [PubMed](#) [Google Scholar](#)

10. Luke P. Tyrrell
[View author publications](#)

You can also search for this author in [PubMed](#) [Google Scholar](#)

11. Jelena Vukomanovic
[View author publications](#)

You can also search for this author in [PubMed](#) [Google Scholar](#)

12. Ashley A. Wilson
[View author publications](#)

You can also search for this author in [PubMed](#) [Google Scholar](#)

13. Clinton D. Francis
[View author publications](#)

You can also search for this author in [PubMed](#) [Google Scholar](#)

Contributions

C.D.F., J.R.B. and C.J.W.M. conceived the project. C.B.C. and J.V. contributed geospatial NestWatch data and data validation, D.J.M and K.M.F. provided key data on noise and night lighting and L.P.T. provided key trait data. M.S., A.A.W., J.N.P. and C.D.F. performed analyses with

advice from M.A.D. and N.H.C. All authors contributed to the writing of the manuscript.

Corresponding author

Correspondence to [Clinton D. Francis](#).

Ethics declarations

Competing interests

The authors declare no competing interests.

Additional information

Peer review information *Nature* thanks Albert Phillimore and Andrew Radford for their contribution to the peer review of this work.

Publisher's note Springer Nature remains neutral with regard to jurisdictional claims in published maps and institutional affiliations.

Extended data figures and tables

[Extended Data Fig. 1 Natural log of zenith artificial sky brightness as a ratio to the natural background sky brightness.](#)

Brighter colours indicate higher light levels.

[Extended Data Fig. 2 Anthropogenic component of sound levels \(\$L_{50}\$, A-weighted dB\) across the contiguous United States.](#)

Brighter colours indicate higher sound levels. Sound levels used in analyses were exceedance values, calculated by the logarithmic subtraction of the natural from the existing sound projections.

Extended Data Fig. 3 Exposure to noise and light.

Reproduction or breeding phenology was influenced by noise or light for most species, and mean exposure to noise and to light per species were positively correlated (solid black line, Spearman's correlation test; $n = 27$, rho = 0.830, $P < 0.001$). Points and error bars denote mean \pm s.d. Twenty-four of the 27 species had apparent responses warranting consideration with 85% CIs that did not overlap zero. Red squares denote species affected by both noise and light, red triangles and circles indicate those affected by either noise or light, respectively, and blue diamonds denote species that appear uninfluenced by either stimulus. Thick horizontal and vertical yellow lines represent mean exposure levels to light and noise, respectively, across all nests in the dataset.

Extended Data Fig. 4 Forest plot illustrating estimated effect sizes and 95% CI of noise (red) and light (blue) on clutch initiation date.

Spatially explicit linear mixed-effect model parameter estimates are centred and scaled for direct comparison. Diamonds for 'Overall' reflect means for listed species, where the diamond centre denotes the mean effect (vertical dashed lines) and the width of the diamond reflects the 95% CI. See Supplementary Table 7 for more model results for each species.

Extended Data Fig. 5 Forest plot illustrating estimated effect sizes and 95% CI of noise (red) and light (blue) on clutch size.

Spatially explicit generalized linear mixed-effect model parameter estimates are centred and scaled for direct comparison. Diamonds for 'Overall' reflect means for listed species, where the diamond centre denotes the mean effect (vertical dashed lines) and the width of the diamond reflects the 95% CI. See Supplementary Table 7 for more model results for each species.

Extended Data Fig. 6 Forest plot illustrating estimated effect sizes and 95% CI of noise (red) and light (blue) on clutch failure.

Spatially explicit generalized linear mixed-effect model parameter estimates are centred and scaled for direct comparison. Diamonds for ‘Overall’ reflect means for listed species, where the diamond centre denotes the mean effect (vertical dashed lines) and the width of the diamond reflects the 95% CI. See Supplementary Table [7](#) for more model results for each species.

Extended Data Fig. 7 Forest plot illustrating estimated effect sizes and 95% CI of noise (red) and light (blue) on incidence of partial hatch.

Spatially explicit generalized linear mixed-effect model parameter estimates are centred and scaled for direct comparison. Diamonds for ‘Overall’ reflect means for listed species, where the diamond centre denotes the mean effect (vertical dashed lines) and the width of the diamond reflects the 95% CI. See Supplementary Table [7](#) for more model results for each species.

Extended Data Fig. 8 Forest plot illustrating estimated effect sizes and 95% CI of noise (red) and light (blue) on overall nest success.

Spatially explicit generalized linear mixed-effect model parameter estimates are centred and scaled for direct comparison. Diamonds for ‘Overall’ reflect means for above-listed species. where the diamond centre denotes the mean effect (vertical dashed lines) and the width of the diamond reflects the 95% CI. House sparrow (*Passer domesticus*) not included here because of management actions on nests of this species during the nestling period. See Supplementary Table [7](#) for more model results for each species.

Extended Data Fig. 9 Multiple traits linked to responses to noise and light exposure.

Light bulbs reflect responses to light, and speakers reflect responses to noise. Red symbols reflect a decline in fitness, or delay in timing for clutch initiation, and blue symbols reflect an improvement in fitness, or advancement in timing for clutch initiation. Symbol shading reflects the strength of the observed effect. See Supplementary Table [8](#) for individual

model results. Light bulb and speaker symbols are from the R package emojifont^{[69](#)}.

Supplementary information

Supplementary Information

This file contains Supplementary Text and Supplementary Tables S1-S3, S9, S10. Supplementary Tables S4-S8, S11 are included as separate spreadsheets due to their large sizes.

Reporting Summary

Supplementary Table

This file contains Supplementary Table S4.

Supplementary Table

This file contains Supplementary Table S5.

Supplementary Table

This file contains Supplementary Table S6.

Supplementary Table

This file contains Supplementary Table S7.

Supplementary Table

This file contains Supplementary Table S8.

Supplementary Table

This file contains Supplementary Table S11.

Source data

[Source Data Fig. 2](#)

[Source Data Fig. 3](#)

Rights and permissions

[Reprints and Permissions](#)

About this article



Check for
updates

Cite this article

Senzaki, M., Barber, J.R., Phillips, J.N. *et al.* Sensory pollutants alter bird phenology and fitness across a continent. *Nature* **587**, 605–609 (2020).
<https://doi.org/10.1038/s41586-020-2903-7>

[Download citation](#)

- Received: 30 January 2019
- Accepted: 12 August 2020
- Published: 11 November 2020
- Issue Date: 26 November 2020
- DOI: <https://doi.org/10.1038/s41586-020-2903-7>

Comments

By submitting a comment you agree to abide by our [Terms](#) and [Community Guidelines](#). If you find something abusive or that does not comply with our terms or guidelines please flag it as inappropriate.

[Access through your institution](#)

[Change institution](#)

[Buy or subscribe](#)

This article was downloaded by **calibre** from <https://www.nature.com/articles/s41586-020-2903-7>

| [Section menu](#) | [Main menu](#) |

The major genetic risk factor for severe COVID-19 is inherited from Neanderthals
[Download PDF](#)

- Article
- [Published: 30 September 2020](#)

The major genetic risk factor for severe COVID-19 is inherited from Neanderthals

- [Hugo Zeberg](#) ORCID: [orcid.org/0000-0001-7118-1249^{1,2}](https://orcid.org/0000-0001-7118-1249) &
- [Svante Pääbo](#) ORCID: [orcid.org/0000-0002-4670-6311^{1,3}](https://orcid.org/0000-0002-4670-6311)

[Nature](#) volume 587, pages610–612(2020)[Cite this article](#)

- 376k Accesses
- 6 Citations
- 4318 Altmetric
- [Metrics details](#)

Subjects

- [Evolutionary genetics](#)
- [Infectious diseases](#)
- [SARS-CoV-2](#)

Abstract

A recent genetic association study¹ identified a gene cluster on chromosome 3 as a risk locus for respiratory failure after infection with severe acute respiratory syndrome coronavirus 2 (SARS-CoV-2). A separate study (COVID-19 Host Genetics Initiative)² comprising 3,199 hospitalized patients with coronavirus disease 2019 (COVID-19) and control individuals showed that this cluster is the major

genetic risk factor for severe symptoms after SARS-CoV-2 infection and hospitalization. Here we show that the risk is conferred by a genomic segment of around 50 kilobases in size that is inherited from Neanderthals and is carried by around 50% of people in south Asia and around 16% of people in Europe.

[Download PDF](#)

Main

The COVID-19 pandemic has caused considerable morbidity and mortality, and has resulted in the death of over a million people to date³. The clinical manifestations of the disease caused by the virus, SARS-CoV-2, vary widely in severity, ranging from no or mild symptoms to rapid progression to respiratory failure⁴. Early in the pandemic, it became clear that advanced age is a major risk factor, as well as being male and some co-morbidities⁵. These risk factors, however, do not fully explain why some people have no or mild symptoms whereas others have severe symptoms. Thus, genetic risk factors may have a role in disease progression. A previous study¹ identified two genomic regions that are associated with severe COVID-19: one region on chromosome 3, which contains six genes, and one region on chromosome 9 that determines ABO blood groups. Recently, a dataset was released by the COVID-19 Host Genetics Initiative in which the region on chromosome 3 is the only region that is significantly associated with severe COVID-19 at the genome-wide level (Fig. 1a). The risk variant in this region confers an odds ratio for requiring hospitalization of 1.6 (95% confidence interval, 1.42–1.79) (Extended Data Fig. 1).

Fig. 1: Genetic variants associated with severe COVID-19.

 **figure1**

a, Manhattan plot of a genome-wide association study of 3,199 hospitalized patients with COVID-19 and 897,488 population controls. The dashed line indicates genome-wide significance ($P = 5 \times 10^{-8}$). Data were modified from the COVID-19 Host Genetics Initiative² (<https://www.covid19hg.org/>). **b**, Linkage disequilibrium between the index risk variant (rs35044562) and genetic variants in the 1000 Genomes Project. Red circles indicate genetic variants for which the alleles are correlated to the risk variant ($r^2 > 0.1$) and the risk alleles match the Vindija 33.19 Neanderthal genome. The core Neanderthal haplotype ($r^2 > 0.98$) is indicated by a black bar. Some individuals carry longer Neanderthal-like haplotypes. The location of the genes in the region are indicated below using standard gene symbols. The x axis shows hg19 coordinates.

[Full size image](#)

The genetic variants that are most associated with severe COVID-19 on chromosome 3 (45,859,651–45,909,024 (hg19)) are all in high linkage disequilibrium (LD)—that is, they are all strongly associated with each other in the population ($r^2 > 0.98$)—and span 49.4 thousand bases (kb) (Fig. 1b). This ‘core’ haplotype is furthermore in weaker linkage disequilibrium with longer haplotypes of up to 333.8 kb ($r^2 > 0.32$) (Extended Data Fig. 2). Some such long haplotypes have entered the human population by gene flow from Neanderthals or Denisovans, extinct hominins that contributed genetic variants to the ancestors of present-day humans around 40,000–60,000 years ago^{6,7}. We therefore investigated whether the haplotype may have come from Neanderthals or Denisovans.

The index variants of the two studies^{1,2} are in high linkage disequilibrium ($r^2 > 0.98$) in non-African populations (Extended Data Fig. 3). We found that the risk alleles of both of these variants are present in a homozygous form in the genome of the Vindija 33.19 Neanderthal, an approximately 50,000-year-old Neanderthal from Croatia in southern Europe⁸. Of the 13 single nucleotides polymorphisms constituting the core haplotype, 11 occur in a homozygous form in the Vindija 33.19 Neanderthal (Fig. 1b). Three of these variants occur in the Altai⁹ and Chagyrskaya 8¹⁰ Neanderthals, both of whom come from the Altai Mountains in southern Siberia and are around 120,000 and about 60,000 years old, respectively (Extended Data Table 1), whereas none of the variants occurs in the Denisovan genome¹¹. In the 333.8-kb haplotype, the alleles associated with risk of severe COVID-19 similarly match alleles in the genome of the Vindija 33.19 Neanderthal (Fig. 1b). Thus, the risk haplotype is similar to the corresponding genomic region in the Neanderthal from Croatia and less similar to the Neanderthals from Siberia.

We next investigated whether the core 49.4-kb haplotype might be inherited by both Neanderthals and present-day people from the common ancestors of the two groups that lived about 0.5 million years ago⁹. The longer a present-day human haplotype shared with Neanderthals is, the less likely it is to originate from the common ancestor, because recombination in each generation will tend to break up haplotypes into smaller segments. Assuming a generational time of 29 years¹², the local recombination rate¹³ (0.53 cM per Mb), a split between Neanderthals and modern humans of 550,000 years⁹ and interbreeding between the two groups around 50,000 years ago, and using a published equation¹⁴, we exclude that the Neanderthal-like haplotype derives from the common ancestor ($P = 0.0009$). For the 333.8-kb-long Neanderthal-like haplotype, the probability of an origin from the common ancestral population is even lower ($P = 1.6 \times 10^{-26}$). The risk haplotype thus entered the modern human population from Neanderthals. This is in agreement with several previous studies, which have identified gene flow from Neanderthals in this chromosomal region^{15,16,17,18,19,20,21} (Extended Data Table 2). The close relationship of the risk haplotype to the Vindija 33.19 Neanderthal is compatible with this Neanderthal being closer to the majority of the Neanderthals who contributed DNA to present-day people than the other two Neanderthals¹⁰.

A Neanderthal haplotype that is found in the genomes of the present human population is expected to be more similar to a Neanderthal genome than to other haplotypes in the current human population. To investigate the relationships of the 49.4-kb haplotype to Neanderthal and other human haplotypes, we analysed all 5,008 haplotypes in the 1000 Genomes Project²² for this genomic region. We included all positions that are called in the Neanderthal genomes and excluded

variants found on only one chromosome and haplotypes seen only once in the 1000 Genomes Project data. This resulted in 253 present-day haplotypes that contained 450 variable positions. Figure 2 shows a phylogeny relating the haplotypes that were found more than 10 times (see Extended Data Fig. 4 for all haplotypes). We find that all risk haplotypes associated with severe COVID-19 form a clade with the three high-coverage Neanderthal genomes. Within this clade, they are most closely related to the Vindija 33.19 Neanderthal.

Fig. 2: Phylogeny relating the DNA sequences that cover the core Neanderthal haplotype in individuals from the 1000 Genomes Project and Neanderthals.

 figure2

The coloured area highlights the haplotypes that carry the risk allele at rs35044562—that is, the risk haplotypes for severe COVID-19. Arabic numbers indicate bootstrap support (100 replicates). The phylogeny is rooted with the inferred ancestral sequence of present-day humans. The three Neanderthal genomes carry no

heterozygous positions in this region. Scale bar, number of substitutions per nucleotide position.

[Full size image](#)

Among the individuals in the 1000 Genomes Project, the Neanderthal-derived haplotypes are almost completely absent from Africa, consistent with the idea that gene flow from Neanderthals into African populations was limited and probably indirect²⁰. The Neanderthal core haplotype occurs in south Asia at an allele frequency of 30%, in Europe at an allele frequency of 8%, among admixed Americans with an allele frequency of 4% and at lower allele frequencies in east Asia²³ (Fig. 3). In terms of carrier frequencies, we find that 50% of people in South Asia carry at least one copy of the risk haplotype, whereas 16% of people in Europe and 9% of admixed American individuals carry at least one copy of the risk haplotype. The highest carrier frequency occurs in Bangladesh, where more than half the population (63%) carries at least one copy of the Neanderthal risk haplotype and 13% is homozygous for the haplotype. The Neanderthal haplotype may thus be a substantial contributor to COVID-19 risk in some populations in addition to other risk factors, including advanced age. In apparent agreement with this, individuals of Bangladeshi origin in the UK have an about two times higher risk of dying from COVID-19 than the general population²⁴ (hazard ratio of 2.0, 95% confidence interval, 1.7–2.4).

Fig. 3: Geographical distribution of the Neanderthal core haplotype that confers risk for severe COVID-19.

 [figure3](#)

Pie charts show the minor allele frequency at rs35044562. Frequency data were obtained from the 1000 Genomes Project²². Map source data were obtained from OpenStreetMap²³.

[Full size image](#)

It is notable that the Neanderthal risk haplotype occurs at a frequency of 30% in south Asia whereas it is almost absent in east Asia (Fig. 3). This extent of difference in allele frequencies between south and east Asia is unusual ($P = 0.006$, Extended Data Fig. 5) and indicates that it may have been affected by selection in the past. Indeed, previous studies have suggested that the Neanderthal haplotype has been positively selected in Bangladesh²⁵. At this point, we can only speculate about the reason for this—one possibility is protection against other pathogens. It is also possible that the haplotype has decreased in frequency in east Asia owing to negative selection, perhaps because of coronaviruses or other pathogens. In any case, the COVID-19 risk haplotype on chromosome 3 is similar to some other Neanderthal and Denisovan genetic variants that have reached high frequencies in some populations owing to positive selection or drift^{14,26,27,28}, but it is now under negative selection owing to the COVID-19 pandemic.

It is currently not known what feature in the Neanderthal-derived region confers risk for severe COVID-19 and whether the effects of any such feature are specific to SARS-CoV-2, to other coronaviruses or to other pathogens. Once the functional feature is elucidated, it may be possible to speculate about the susceptibility of Neanderthals to relevant pathogens. However, with respect to the current pandemic, it is clear that gene flow from Neanderthals has tragic consequences.

Methods

Linkage disequilibrium was calculated using LDlink 4.1²⁹ and alleles were compared to the archaic genomes^{8,9,10,11} using tabix³⁰ (HTSlib 1.10). Haplotypes were constructed from the phase 3 release of the 1000 Genomes Project²² as described. Phylogenies were estimated with phyML 3.3³¹ using the Hasegawa–Kishino–Yano-85³² substitution model with a gamma shape parameter and the proportion of invariant sites estimated from the data. The probability of observing a haplotype of a particular length or longer owing to incomplete lineage sorting was calculated as previously described¹⁴. The inferred ancestral states at variable positions among present-day humans were taken from Ensembl³³. The distribution of frequency differences of Neanderthal haplotypes between east and south Asia was computed by filtering diagnostic Neanderthal variants (fixed positions in the

three high-coverage Neanderthal genomes and the Neanderthal allele missing in 108 Yoruba individuals) using a published introgression map²⁰, followed by pruning using PLINK1.90³⁴ (r^2 cut-off of 0.5 in a sliding window of 100 variants) and allele frequency assessment in the 1000 Genomes Project. Maps displaying allele frequencies and linkage disequilibrium in different populations were made using Mathematica 11.0 (Wolfram Research) and OpenStreetMap data.

For the meta-analysis carried out by the COVID-19 Host Genetics Initiative², participants consented and ethical approvals were obtained (<https://www.covid19hg.org/partners/>). The following eight studies contributed to the meta-analysis of hospitalization versus population controls: Genetic modifiers for COVID-19-related disease ‘BelCovid’ (Université Libre de Bruxelles, Belgium), Genetic determinants of COVID-19 complications in the Brazilian population ‘BRACOVID’ (University of São Paulo, Brazil), deCODE (deCODE Genetics, Iceland), FinnGen (Institute for Molecular Medicine Finland, Finland), GEN-COVID (University of Siena, Italy), Genes & Health (Queen Mary University of London, UK), COVID-19-Host(age) (Kiel University and University Hospitals of Oslo and Schleswig-Holstein, Germany and Norway) and the UK Biobank (UK).

Reporting summary

Further information on research design is available in the [Nature Research Reporting Summary](#) linked to this paper.

Data availability

The summary statistics of the genome-wide association study that support the finding of this study are available from the COVID-19 Host Genetics Initiative (round 3, ANA_B2_V2: hospitalized patients with COVID-19 compared with population controls; <https://www.covid19hg.org/>). The genomes used are available from the 1000 Genomes Project (phase 3 release, <https://www.internationalgenome.org/>) and the Max Planck Institute for Evolutionary Anthropology (Chagyrskaya, Altai and Vindija 33.19, <http://cdna.eva.mpg.de/neandertal/>). The ancestral alleles are available at Ensembl (release 100, <https://www.ensembl.org/>). Map data are from OpenStreetMap and available from <https://www.openstreetmap.org>.

References

1. 1.

Ellinghaus, D. et al. Genomewide association study of severe COVID-19 with respiratory failure. *N. Engl. J. Med.* <https://doi.org/10.1056/NEJMoa2020283> (2020).

2. 2.

COVID-19 Host Genetics Initiative. The COVID-19 Host Genetics Initiative, a global initiative to elucidate the role of host genetic factors in susceptibility and severity of the SARS-CoV-2 virus pandemic. *Eur. J. Hum. Genet.* **28**, 715–718 (2020).

[Article](#) [Google Scholar](#)

3. 3.

WHO. *Coronavirus disease (COVID-19) Weekly Epidemiological Update and Weekly Operational Update: Weekly Epidemiological Update 14 September 2020* <https://www.who.int/emergencies/diseases/novel-coronavirus-2019/situation-reports> (2020).

4. 4.

Vetter, P. et al. Clinical features of COVID-19. *Br. Med. J.* **369**, m1470 (2020).

[Article](#) [Google Scholar](#)

5. 5.

Zhou, F. et al. Clinical course and risk factors for mortality of adult inpatients with COVID-19 in Wuhan, China: a retrospective cohort study. *Lancet* **395**, 1054–1062 (2020).

[CAS](#) [Article](#) [Google Scholar](#)

6. 6.

Green, R. E. et al. A draft sequence of the Neandertal genome. *Science* **328**, 710–722 (2010).

[CAS](#) [Article](#) [ADS](#) [Google Scholar](#)

7. 7.

Sankararaman, S., Patterson, N., Li, H., Pääbo, S. & Reich, D. The date of interbreeding between Neandertals and modern humans. *PLoS Genet.* **8**, e1002947 (2012).

[CAS](#) [Article](#) [ADS](#) [Google Scholar](#)

8. 8.

Prüfer, K. et al. A high-coverage Neandertal genome from Vindija Cave in Croatia. *Science* **358**, 655–658 (2017).

[Article](#) [ADS](#) [Google Scholar](#)

9. 9.

Prüfer, K. et al. The complete genome sequence of a Neanderthal from the Altai Mountains. *Nature* **505**, 43–49 (2014).

[Article](#) [ADS](#) [Google Scholar](#)

10. 10.

Mafessoni, F. et al. A high-coverage Neandertal genome from Chagyrskaya Cave. *Proc. Natl Acad. Sci. USA* **117**, 15132–15136 (2020).

[Article](#) [Google Scholar](#)

11. 11.

Meyer, M. et al. A high-coverage genome sequence from an archaic Denisovan individual. *Science* **338**, 222–226 (2012).

[CAS](#) [Article](#) [ADS](#) [Google Scholar](#)

12. 12.

Langergraber, K. E. et al. Generation times in wild chimpanzees and gorillas suggest earlier divergence times in great ape and human evolution. *Proc. Natl Acad. Sci. USA* **109**, 15716–15721 (2012).

[CAS](#) [Article](#) [ADS](#) [Google Scholar](#)

13. 13.

Kong, A. et al. A high-resolution recombination map of the human genome. *Nat. Genet.* **31**, 241–247 (2002).

[CAS](#) [Article](#) [Google Scholar](#)

14. 14.

Huerta-Sánchez, E. et al. Altitude adaptation in Tibetans caused by introgression of Denisovan-like DNA. *Nature* **512**, 194–197 (2014).

[Article](#) [ADS](#) [Google Scholar](#)

15. 15.

Sankararaman, S. et al. The genomic landscape of Neanderthal ancestry in present-day humans. *Nature* **507**, 354–357 (2014).

[CAS](#) [Article](#) [ADS](#) [Google Scholar](#)

16. 16.

Vernot, B. & Akey, J. M. Resurrecting surviving Neandertal lineages from modern human genomes. *Science* **343**, 1017–1021 (2014).

[CAS](#) [Article](#) [ADS](#) [Google Scholar](#)

17. 17.

Vernot, B. et al. Excavating Neandertal and Denisovan DNA from the genomes of Melanesian individuals. *Science* **352**, 235–239 (2016).

[CAS](#) [Article](#) [ADS](#) [Google Scholar](#)

18. 18.

Steinrücken, M., Spence, J. P., Kamm, J. A., Wieczorek, E. & Song, Y. S. Model-based detection and analysis of introgressed Neanderthal ancestry in modern humans. *Mol. Ecol.* **27**, 3873–3888 (2018).

[Article](#) [Google Scholar](#)

19. 19.

Gittelman, R. M. et al. Archaic hominin admixture facilitated adaptation to out-of-Africa environments. *Curr. Biol.* **26**, 3375–3382 (2016).

[CAS](#) [Article](#) [Google Scholar](#)

20. 20.

Chen, L., Wolf, A. B., Fu, W., Li, L. & Akey, J. M. Identifying and interpreting apparent Neanderthal ancestry in African individuals. *Cell* **180**, 677–687 (2020).

[CAS](#) [Article](#) [Google Scholar](#)

21. 21.

Skov, L. et al. The nature of Neanderthal introgression revealed by 27,566 Icelandic genomes. *Nature* **582**, 78–83 (2020).

[CAS](#) [Article](#) [ADS](#) [Google Scholar](#)

22. 22.

The 1000 Genomes Project Consortium. A global reference for human genetic variation. *Nature* **526**, 68–74 (2015).

[Article](#) [Google Scholar](#)

23. 23.

OpenStreetMap. *Planet OSM*. <https://planet.osm.org/> (2017).

24. 24.

Public Health England. *COVID-19: Review of Disparities in Risks and Outcomes*. <https://www.gov.uk/government/publications/covid-19-review-of-disparities-in-risks-and-outcomes> (2020).

25. 25.

Browning, S. R., Browning, B. L., Zhou, Y., Tucci, S. & Akey, J. M. Analysis of human sequence data reveals two pulses of archaic Denisovan admixture. *Cell* **173**, 53–61 (2018).

[CAS](#) [Article](#) [Google Scholar](#)

26. 26.

Dannemann, M., Andrés, A. M. & Kelso, J. Introgression of Neandertal- and Denisovan-like haplotypes contributes to adaptive variation in human Toll-like receptors. *Am. J. Hum. Genet.* **98**, 22–33 (2016).

[CAS](#) [Article](#) [Google Scholar](#)

27. 27.

Zeberg, H., Kelso, J. & Pääbo, S. The Neandertal progesterone receptor. *Mol. Biol. Evol.* **37**, 2655–2660 (2020).

[Article](#) [Google Scholar](#)

28. 28.

Zeberg, H. et al. A Neanderthal sodium channel increases pain sensitivity in present-day humans. *Curr. Biol.* **30**, 3465–3469 (2020).

[CAS](#) [Article](#) [Google Scholar](#)

29. 29.

Machiela, M. J. & Chanock, S. J. LDlink: a web-based application for exploring population-specific haplotype structure and linking correlated alleles of possible functional variants. *Bioinformatics* **31**, 3555–3557 (2015).

[CAS](#) [Article](#) [Google Scholar](#)

30. 30.

Li, H. Tabix: fast retrieval of sequence features from generic TAB-delimited files. *Bioinformatics* **27**, 718–719 (2011).

[Article](#) [Google Scholar](#)

31. 31.

Guindon, S. et al. New algorithms and methods to estimate maximum-likelihood phylogenies: assessing the performance of PhyML 3.0. *Syst. Biol.*

59, 307–321 (2010).

[CAS](#) [Article](#) [Google Scholar](#)

32. 32.

Hasegawa, M., Kishino, H. & Yano, T. Dating of the human–ape splitting by a molecular clock of mitochondrial DNA. *J. Mol. Evol.* **22**, 160–174 (1985).

[CAS](#) [Article](#) [Google Scholar](#)

33. 33.

Yates, A. D. et al. Ensembl 2020. *Nucleic Acids Res.* **48**, D682–D688 (2020).

[CAS](#) [Article](#) [Google Scholar](#)

34. 34.

Chang, C. C. et al. Second-generation PLINK: rising to the challenge of larger and richer datasets. *Gigascience* **4**, 7 (2015).

[Article](#) [Google Scholar](#)

[Download references](#)

Acknowledgements

We thank the COVID-19 Host Genetics Initiative for making the data from the genome-wide association study available, and the Max Planck Society and the NOMIS Foundation for funding.

Author information

Affiliations

1. Max Planck Institute for Evolutionary Anthropology, Leipzig, Germany

Hugo Zeberg & Svante Pääbo

2. Department of Neuroscience, Karolinska Institutet, Stockholm, Sweden

Hugo Zeberg

3. Okinawa Institute of Science and Technology, Onna-son, Japan

Svante Pääbo

Authors

1. Hugo Zeberg

[View author publications](#)

You can also search for this author in [PubMed](#) [Google Scholar](#)

2. Svante Pääbo

[View author publications](#)

You can also search for this author in [PubMed](#) [Google Scholar](#)

Contributions

H.Z. performed the haplotype analysis. H.Z. and S.P. jointly wrote the manuscript.

Corresponding authors

Correspondence to [Hugo Zeberg](#) or [Svante Pääbo](#).

Ethics declarations

Competing interests

The authors declare no competing interests.

Additional information

Peer review information *Nature* thanks Tobias Lenz, Yang Luo and the other, anonymous, reviewer(s) for their contribution to the peer review of this work. Peer reviewer reports are available.

Publisher's note Springer Nature remains neutral with regard to jurisdictional claims in published maps and institutional affiliations.

Extended data figures and tables

Extended Data Fig. 1 Odds ratios for hospitalization owing to COVID-19 for cohorts contributing to the meta-analysis (round 3) of the COVID-19 Host Genetics Initiative (rs35044562).

The odds ratio and the P value for the summary effect are odds ratio = 1.60 (95% confidence interval, 1.42–1.79) and $P = 3.1 \times 10^{-15}$ (two-sided z-test, $n = 3,199$ patients with COVID-19 and 897,488 controls over 8 independent studies). Data are the odds ratios and 95% confidence intervals. HOST(age), UK Biobank European (EUR), GENCOVID, deCODE and BelCovid use European population controls. BRACOVID, Genes & Health and FinnGen use American, south Asian and Finnish population controls, respectively.

Extended Data Fig. 2 Pairwise linkage disequilibrium between diagnostic Neanderthal variants.

Heat map of linkage disequilibrium between genetic variants in which one allele is shared with three Neanderthal genomes and missing in 108 Yoruba individuals. The black box highlights a haplotype of 333.8 kb between rs17763537 and rs13068572 (chromosome 3: 45,843,315–46,177,096). Red, r^2 correlation; blue, D' correlation.

Extended Data Fig. 3 Linkage disequilibrium between index variant rs11385942 and the index variant of the COVID-19 Host Genetics Initiative (rs35044562).

Shades of red indicate the extent of linkage disequilibrium (r^2) in the populations included in the 1000 Genomes Project. Populations labelled ‘n/a’ are monomorphic for the protective allele of rs35044562. The previously described index variant (rs11385942)¹ does not have any genetic variants in linkage disequilibrium ($r^2 > 0.8$) in populations from Africa. Map source data from OpenStreetMap²³.

Extended Data Fig. 4 Phylogeny of haplotypes in individuals included in the 1000 Genomes Project and Neanderthals covering the genomic region of the core risk haplotype.

The shaded area highlights a monophyletic group that contains all present-day haplotypes carrying the risk allele at rs35044562 and the haplotypes of the three

high-coverage Neanderthals. Arabic numbers show bootstrap support (100 replicates). The tree is rooted with the inferred ancestral human sequence. Scale bar, number of substitutions per nucleotide position.

Extended Data Fig. 5 Frequency differences between south and east Asia for haplotypes introgressed from Neanderthals.

The dashed line indicates the frequency difference for the Neanderthal haplotype that confers risk of severe COVID-19.

Extended Data Table 1 Genetic variants in LD ($r^2 > 0.98$) with rs35044562 and the corresponding Neanderthal variants

[Full size table](#)

Extended Data Table 2 Previous studies that identified gene flow from Neanderthals at the core haplotype

[Full size table](#)

Supplementary information

[**Reporting Summary**](#)

[**Peer Review File**](#)

Rights and permissions

[Reprints and Permissions](#)

About this article



Check for
updates

Cite this article

Zeberg, H., Pääbo, S. The major genetic risk factor for severe COVID-19 is inherited from Neanderthals. *Nature* **587**, 610–612 (2020).
<https://doi.org/10.1038/s41586-020-2818-3>

[Download citation](#)

- Received: 03 July 2020
- Accepted: 22 September 2020
- Published: 30 September 2020
- Issue Date: 26 November 2020
- DOI: <https://doi.org/10.1038/s41586-020-2818-3>

Further reading

- [<p>Flattening the Risk: Pre-Exposure Prophylaxis for COVID-19</p>](#)

- Raphael B Stricker
 - & Melissa C Fesler

Infection and Drug Resistance (2020)

- [Human genetic factors associated with susceptibility to SARS-CoV-2 infection and COVID-19 disease severity](#)

- Cleo Anastassopoulou
 - , Zoi Gkizarioti
 - , George P. Patrinos
 - & Athanasios Tsakris

Human Genomics (2020)

- [Neanderthal DNA highlights complexity of COVID risk factors](#)

- Yang Luo

Nature (2020)

- [COVID-19 and geographical area of origin](#)

- Norman FF

- , C. Crespillo-Andújar
- , J.A. Pérez-Molina
- , Comeche B
- , Chamorro S
- , B. Monge-Maillo
- , S. Moreno-Guillén
- , R. López-Vélez
- , Pilar Vizcarra
- , Francesca Norman
- , Clara Crespillo
- , José Pérez-Molina
- , Belén Comeche
- , Sandra Chamorro
- , Begoña Monge
- , Santiago Moreno
- , Rogelio López-Vélez
- , María Jesús Pérez-Eliás
- , Jesús Fortún
- , Enrique Navas
- , Carmen Quereda
- , Fernando Dronda
- , Santos Del Campo
- , Javier Cobo Reinoso
- , José Luis Casado
- , Ana Moreno
- , Pilar Martín-Dávila
- , José Manuel Hermida
- , Vicente Pintado
- , Sergio Serrano-Villar
- , Matilde Sánchez-Conde
- , Rosa Escudero
- , Francesca Gioia
- , Sabina Herrera
- , Raquel Ron
- , Javier Martínez-Sanz
- , Mario Pons-Guillén
- & María Jesús Vivancos

Clinical Microbiology and Infection (2020)

Comments

By submitting a comment you agree to abide by our [Terms](#) and [Community Guidelines](#). If you find something abusive or that does not comply with our terms or guidelines please flag it as inappropriate.

[Download PDF](#)

Associated Content

Nature | News & Views

[Neanderthal DNA highlights complexity of COVID risk factors](#)

- Yang Luo

This article was downloaded by **calibre** from <https://www.nature.com/articles/s41586-020-2818-3>

| [Section menu](#) | [Main menu](#) |

- Article
- [Published: 07 October 2020](#)

Microglia-organized scar-free spinal cord repair in neonatal mice

- [Yi Li^{1,2 na1}](#),
- [Xuelian He^{1,2 na1}](#),
- [Riki Kawaguchi^{3,4 na1}](#),
- [Yu Zhang^{1,2}](#),
- [Qing Wang^{3,4}](#),
- [Aboozar Monavarfeshani^{1,2}](#),
- [Zhiyun Yang^{1,2}](#),
- [Bo Chen^{1,2}](#),
- [Zhongju Shi^{1,2}](#),
- [Huyan Meng^{1,2}](#),
- [Songlin Zhou^{1,2}](#),
- [Junjie Zhu ORCID: orcid.org/0000-0002-3827-1741^{1,2}](#),
- [Anne Jacobi^{1,2}](#),
- [Vivek Swarup ORCID: orcid.org/0000-0003-3762-2746⁵](#),
- [Phillip G. Popovich ORCID: orcid.org/0000-0003-1329-7395^{6,7}](#),
- [Daniel H. Geschwind ORCID: orcid.org/0000-0003-2896-3450^{3,4,8}](#) &
- [Zhigang He ORCID: orcid.org/0000-0001-6080-6880^{1,2,9}](#)

[Nature](#) volume 587, pages613–618(2020) [Cite this article](#)

- 9606 Accesses
- 2 Citations
- 170 Altmetric

- [Metrics details](#)

Subjects

- [Microglia](#)
- [Spinal cord injury](#)

Abstract

Spinal cord injury in mammals is thought to trigger scar formation with little regeneration of axons^{1,2,3,4}. Here we show that a crush injury to the spinal cord in neonatal mice leads to scar-free healing that permits the growth of long projecting axons through the lesion. Depletion of microglia in neonatal mice disrupts this healing process and stalls the regrowth of axons, suggesting that microglia are critical for orchestrating the injury response. Using single-cell RNA sequencing and functional analyses, we find that neonatal microglia are transiently activated and have at least two key roles in scar-free healing. First, they transiently secrete fibronectin and its binding proteins to form bridges of extracellular matrix that ligate the severed ends of the spinal cord. Second, neonatal—but not adult—microglia express several extracellular and intracellular peptidase inhibitors, as well as other molecules that are involved in resolving inflammation. We transplanted either neonatal microglia or adult microglia treated with peptidase inhibitors into spinal cord lesions of adult mice, and found that both types of microglia significantly improved healing and axon regrowth. Together, our results reveal the cellular and molecular basis of the nearly complete recovery of neonatal mice after spinal cord injury, and suggest strategies that could be used to facilitate scar-free healing in the adult mammalian nervous system.

[Access through your institution](#)

[Change institution](#)

[Buy or subscribe](#)

Access options

Subscription info for Chinese customers

We have a dedicated website for our Chinese customers. Please go to naturechina.com to subscribe to this journal.

[Go to naturechina.com](#)

Rent or Buy article

Get time limited or full article access on ReadCube.

from \$8.99

[Rent or Buy](#)

All prices are NET prices.

Additional access options:

- [Log in](#)
- [Access through your institution](#)
- [Learn about institutional subscriptions](#)

Fig. 1: Scar-free wound healing after crush injury to the spinal cord in neonatal mice.



Fig. 2: Microglia are required for bridge formation and rapid healing after neonatal injury.



Fig. 3: scRNA-seq analysis of microglia isolated from lesion sites after P2 injury.



Fig. 4: Loss of fibronectin in microglia impairs wound healing and axon regrowth after P2 injury.



Fig. 5: Transplanted neonatal microglia or proteinase-inhibitor-treated adult microglia improve wound healing and axon regeneration in adult mice.



Data availability

RNA-seq data have been deposited in the Gene Expression Omnibus (GEO) (www.ncbi.nlm.nih.gov/geo) under the accession number [GSE150871](#). [Source data](#) are provided with this paper.

References

1. 1.

O’Shea, T. M., Burda, J. E. & Sofroniew, M. V. Cell biology of spinal cord injury and repair. *J. Clin. Invest.* **127**, 3259–3270 (2017).

[PubMed](#) [PubMed Central](#) [Google Scholar](#)

2. 2.

Tran, A. P., Warren, P. M. & Silver, J. The biology of regeneration failure and success after spinal cord injury. *Physiol. Rev.* **98**, 881–917 (2018).

[CAS](#) [PubMed](#) [PubMed Central](#) [Google Scholar](#)

3. 3.

Hilton, B. J. & Bradke, F. Can injured adult CNS axons regenerate by recapitulating development? *Development* **144**, 3417–3429 (2017).

[CAS](#) [PubMed](#) [Google Scholar](#)

4. 4.

Stenudd, M., Sabelström, H. & Frisén, J. Role of endogenous neural stem cells in spinal cord injury and repair. *JAMA Neurol.* **72**, 235–237 (2015).

[PubMed](#) [Google Scholar](#)

5. 5.

Mokalled, M. H. et al. Injury-induced *ctgfa* directs glial bridging and spinal cord regeneration in zebrafish. *Science* **354**, 630–634 (2016).

[ADS](#) [CAS](#) [PubMed](#) [PubMed Central](#) [Google Scholar](#)

6. 6.

Zukor, K. A., Kent, D. T. & Odelberg, S. J. Meningeal cells and glia establish a permissive environment for axon regeneration after spinal cord injury in newts. *Neural Dev.* **6**, 1 (2011).

[PubMed](#) [PubMed Central](#) [Google Scholar](#)

7. 7.

Jin, Y. & Zheng, B. Multitasking: dual leucine zipper-bearing kinases in neuronal development and stress management. *Annu. Rev. Cell Dev. Biol.* **35**, 501–521 (2019).

[CAS](#) [PubMed](#) [PubMed Central](#) [Google Scholar](#)

8. 8.

He, Z. & Jin, Y. Intrinsic control of axon regeneration. *Neuron* **90**, 437–451 (2016).

[CAS](#) [PubMed](#) [Google Scholar](#)

9. 9.

Bregman, B. S. Spinal cord transplants permit the growth of serotonergic axons across the site of neonatal spinal cord transection. *Brain Res.* **34**, 265–279 (1987).

[Google Scholar](#)

10. 10.

Fry, E. J., Stolp, H. B., Lane, M. A., Dziegielewska, K. M. & Saunders, N. R. Regeneration of supraspinal axons after complete transection of the thoracic spinal cord in neonatal opossums (*Monodelphis domestica*). *J. Comp. Neurol.* **466**, 422–444 (2003).

[PubMed](#) [Google Scholar](#)

11. 11.

Schafer, D. P. et al. Microglia sculpt postnatal neural circuits in an activity and complement-dependent manner. *Neuron* **74**, 691–705 (2012).

[CAS](#) [PubMed](#) [PubMed Central](#) [Google Scholar](#)

12. 12.

Butovsky, O. et al. Identification of a unique TGF- β -dependent molecular and functional signature in microglia. *Nat. Neurosci.* **17**, 131–143 (2014).

[CAS](#) [Google Scholar](#)

13. 13.

Hammond, T. R. et al. Single-cell RNA sequencing of microglia throughout the mouse lifespan and in the injured brain reveals complex cell-state changes. *Immunity* **50**, 253–271 (2019).

[CAS](#) [PubMed](#) [Google Scholar](#)

14. 14.

Popovich, P. G. & Hickey, W. F. Bone marrow chimeric rats reveal the unique distribution of resident and recruited macrophages in the contused rat spinal cord. *J. Neuropathol. Exp. Neurol.* **60**, 676–685 (2001).

[CAS](#) [PubMed](#) [Google Scholar](#)

15. 15.

Elmore, M. R. et al. Colony-stimulating factor 1 receptor signaling is necessary for microglia viability, unmasking a microglia progenitor cell in the adult brain. *Neuron* **82**, 380–397 (2014).

[CAS](#) [PubMed](#) [PubMed Central](#) [Google Scholar](#)

16. 16.

Rudge, J. S. & Silver, J. Inhibition of neurite outgrowth on astroglial scars in vitro. *J. Neurosci.* **10**, 3594–3603 (1990).

[CAS](#) [PubMed](#) [PubMed Central](#) [Google Scholar](#)

17. 17.

McKeon, R. J., Schreiber, R. C., Rudge, J. S. & Silver, J. Reduction of neurite outgrowth in a model of glial scarring following CNS injury is correlated with the expression of inhibitory molecules on reactive astrocytes. *J. Neurosci.* **11**, 3398–3411 (1991).

[CAS](#) [PubMed](#) [PubMed Central](#) [Google Scholar](#)

18. 18.

Buettner, F. et al. Computational analysis of cell-to-cell heterogeneity in single-cell RNA-sequencing data reveals hidden subpopulations of cells. *Nat. Biotechnol.* **33**, 155–160 (2015).

[CAS](#) [PubMed](#) [Google Scholar](#)

19. 19.

Li, Q. et al. Developmental heterogeneity of microglia and brain myeloid cells revealed by deep single-cell RNA sequencing. *Neuron* **101**, 207–223.e10 (2019).

[CAS](#) [PubMed](#) [Google Scholar](#)

20. 20.

Mrdjen, D. et al. High-dimensional single-cell mapping of central nervous system immune cells reveals distinct myeloid subsets in health, aging, and disease. *Immunity* **48**, 380–395 (2018).

[CAS](#) [PubMed](#) [Google Scholar](#)

21. 21.

Jordão, M. J. C. et al. Single-cell profiling identifies myeloid cell subsets with distinct fates during neuroinflammation. *Science* **363**, eaat7554 (2019).

[PubMed](#) [Google Scholar](#)

22. 22.

Keren-Shaul, H. et al. A unique microglia type associated with restricting development of Alzheimer’s disease. *Cell* **169**, 1276–1290 (2017).

[CAS](#) [Google Scholar](#)

23. 23.

Tan, K. & Lawler, J. The interaction of thrombospondins with extracellular matrix proteins. *J. Cell Commun. Signal.* **3**, 177–187 (2009).

[PubMed](#) [PubMed Central](#) [Google Scholar](#)

24. 24.

Jaffe, E. A. & Mosher, D. F. Synthesis of fibronectin by cultured human endothelial cells. *J. Exp. Med.* **147**, 1779–1791 (1978).

[CAS](#) [PubMed](#) [PubMed Central](#) [Google Scholar](#)

25. 25.

Zhou, X. et al. Microglia and macrophages promote corralling, wound compaction and recovery after spinal cord injury via Plexin-B2. *Nat. Neurosci.* **23**, 337–350 (2020).

[CAS](#) [PubMed](#) [PubMed Central](#) [Google Scholar](#)

26. 26.

Miya, D. et al. Fetal transplants alter the development of function after spinal cord transection in newborn rats. *J. Neurosci.* **17**, 4856–4872 (1997).

[CAS](#) [PubMed](#) [PubMed Central](#) [Google Scholar](#)

27. 27.

Conrad, S., Schluesener, H. J., Adibzahdeh, M. & Schwab, J. M. Spinal cord injury induction of lesional expression of profibrotic and angiogenic connective tissue growth factor confined to reactive astrocytes, invading fibroblasts and endothelial cells. *J. Neurosurg. Spine* **2**, 319–326 (2005).

[PubMed](#) [Google Scholar](#)

28. 28.

Stevens, B. & Schafer, D. P. Roles of microglia in nervous system development, plasticity, and disease. *Dev. Neurobiol.* **78**, 559–560 (2018).

[PubMed](#) [Google Scholar](#)

29. 29.

Pluvinage, J. V. et al. CD22 blockade restores homeostatic microglial phagocytosis in ageing brains. *Nature* **568**, 187–192 (2019).

[ADS](#) [CAS](#) [PubMed](#) [PubMed Central](#) [Google Scholar](#)

30. 30.

Yona, S. et al. Fate mapping reveals origins and dynamics of monocytes and tissue macrophages under homeostasis. *Immunity* **38**, 79–91 (2013).

[CAS](#) [PubMed](#) [Google Scholar](#)

31. 31.

Kisanuki, Y. Y. et al. *Tie2-Cre* transgenic mice: a new model for endothelial cell-lineage analysis in vivo. *Dev. Biol.* **230**, 230–242 (2001).

[CAS](#) [PubMed](#) [Google Scholar](#)

32. 32.

Postic, C. et al. Dual roles for glucokinase in glucose homeostasis as determined by liver and pancreatic beta cell-specific gene knock-outs using Cre recombinase. *J. Biol. Chem.* **274**, 305–315 (1999).

[CAS](#) [PubMed](#) [Google Scholar](#)

33. 33.

Sakai, T. et al. Plasma fibronectin supports neuronal survival and reduces brain injury following transient focal cerebral ischemia but is not essential for skin-wound healing and hemostasis. *Nat. Med.* **7**, 324–330 (2001).

[CAS](#) [PubMed](#) [Google Scholar](#)

34. 34.

Li, J., Chen, K., Zhu, L. & Pollard, J. W. Conditional deletion of the colony stimulating factor-1 receptor (*c-fms* proto-oncogene) in mice. *Genesis* **44**, 328–335 (2006).

[CAS](#) [PubMed](#) [Google Scholar](#)

35. 35.

Saederup, N. et al. Selective chemokine receptor usage by central nervous system myeloid cells in CCR2-red fluorescent protein knock-in mice. *PLoS One* **5**, e13693 (2010).

[ADS](#) [PubMed](#) [PubMed Central](#) [Google Scholar](#)

36. 36.

Jung, S. et al. Analysis of fractalkine receptor CX₃CR1 function by targeted deletion and green fluorescent protein reporter gene insertion. *Mol. Cell. Biol.* **20**, 4106–4114 (2000).

[CAS](#) [PubMed](#) [PubMed Central](#) [Google Scholar](#)

37. 37.

Liu, K. et al. PTEN deletion enhances the regenerative ability of adult corticospinal neurons. *Nat. Neurosci.* **13**, 1075–1081 (2010).

[CAS](#) [PubMed](#) [PubMed Central](#) [Google Scholar](#)

38. 38.

Zukor, K. et al. Short hairpin RNA against PTEN enhances regenerative growth of corticospinal tract axons after spinal cord injury. *J. Neurosci.* **33**, 15350–15361 (2013).

[CAS](#) [PubMed](#) [PubMed Central](#) [Google Scholar](#)

39. 39.

Chen, B. et al. Reactivation of dormant relay pathways in injured spinal cord by KCC2 manipulations. *Cell* **174**, 521–535 (2018).

[CAS](#) [PubMed](#) [PubMed Central](#) [Google Scholar](#)

40. 40.

Liu, Y. et al. A sensitized IGF1 treatment restores corticospinal axon-dependent functions. *Neuron* **95**, 817–833 (2017).

[CAS](#) [PubMed](#) [PubMed Central](#) [Google Scholar](#)

41. 41.

Hanada, K. et al. Isolation and characterization of E-64, a new thiol protease inhibitor. *Agric. Biol. Chem.* **42**, 523–528 (1978).

[CAS](#) [Google Scholar](#)

42. 42.

Vicuña, L. et al. The serine protease inhibitor serpinA3N attenuates neuropathic pain by inhibiting T cell-derived leukocyte elastase. *Nat. Med.* **21**, 518–523 (2015).

[PubMed](#) [PubMed Central](#) [Google Scholar](#)

43. 43.

Ou, J. et al. iPSCs from a hibernator provide a platform for studying cold adaptation and its potential medical applications. *Cell* **173**, 851–863 (2018).

[CAS](#) [PubMed](#) [PubMed Central](#) [Google Scholar](#)

[Download references](#)

Acknowledgements

We thank J. Sanes and I. Benhar for discussion and S. Hegarty, J. Sanes, B. Stevens, F. Wang, K. H. Wang, C. Winter and C. Woolf for critically reading the manuscript. This study was supported by NIH R01 grants NS096294 and NS110850 (to Z.H.); NIH-NINDS R35NS111582 and a Ray W. Poppleton endowment (to P.G.P.); grants from the Dr. Miriam and Sheldon G. Adelson Medical Research Foundation (to Z.H., R.K., V.S. and D.H.G.); the Craig H. Neilson Foundation (to Y.L.); and a NIH training grant T32NS007473 (to A.M.). The Intellectual and Developmental Disabilities Research Center (IDRRC) and viral cores supported by the grants NIH HD018655 and P30EY012196 were used for this study.

Author information

Author notes

1. These authors contributed equally: Yi Li, Xuelian He, Riki Kawaguchi

Affiliations

1. F.M. Kirby Neurobiology Center, Boston Children's Hospital, Boston, MA, USA

Yi Li, Xuelian He, Yu Zhang, Aboozar Monavarfeshani, Zhiyun Yang, Bo Chen, Zhongju Shi, Huyan Meng, Songlin Zhou, Junjie Zhu, Anne Jacobi & Zhigang He

2. Department of Neurology, Harvard Medical School, Boston, MA, USA

Yi Li, Xuelian He, Yu Zhang, Aboozar Monavarfeshani, Zhiyun Yang, Bo Chen, Zhongju Shi, Huyan Meng, Songlin Zhou, Junjie Zhu, Anne Jacobi & Zhigang He

3. Program in Neurogenetics, Department of Neurology, David Geffen School of Medicine, University of California Los Angeles, Los Angeles, CA, USA

Riki Kawaguchi, Qing Wang & Daniel H. Geschwind

4. Semel Institute for Neuroscience and Human Behavior, David Geffen School of Medicine, University of California Los Angeles, Los Angeles, CA, USA

Riki Kawaguchi, Qing Wang & Daniel H. Geschwind

5. Department of Neurobiology and Behavior, School of Biological Sciences, University of California Irvine, Irvine, CA, USA

Vivek Swarup

6. Department of Neuroscience, The Ohio State University, Columbus, OH, USA

Phillip G. Popovich

7. Center for Brain and Spinal Cord Repair and the Belford Center for Spinal Cord Injury, The Ohio State University, Columbus, OH, USA

Phillip G. Popovich

8. Department of Human Genetics, David Geffen School of Medicine, University of California Los Angeles, Los Angeles, CA, USA

Daniel H. Geschwind

9. Department of Ophthalmology, Harvard Medical School, Boston, MA,
USA

Zhigang He

Authors

1. Yi Li

[View author publications](#)

You can also search for this author in [PubMed](#) [Google Scholar](#)

2. Xuelian He

[View author publications](#)

You can also search for this author in [PubMed](#) [Google Scholar](#)

3. Riki Kawaguchi

[View author publications](#)

You can also search for this author in [PubMed](#) [Google Scholar](#)

4. Yu Zhang

[View author publications](#)

You can also search for this author in [PubMed](#) [Google Scholar](#)

5. Qing Wang

[View author publications](#)

You can also search for this author in [PubMed](#) [Google Scholar](#)

6. Aboozar Monavarfeshani

[View author publications](#)

You can also search for this author in [PubMed](#) [Google Scholar](#)

7. Zhiyun Yang

[View author publications](#)

You can also search for this author in [PubMed](#) [Google Scholar](#)

8. Bo Chen

[View author publications](#)

You can also search for this author in [PubMed](#) [Google Scholar](#)

9. Zhongju Shi

[View author publications](#)

You can also search for this author in [PubMed](#) [Google Scholar](#)

10. Huyan Meng

[View author publications](#)

You can also search for this author in [PubMed](#) [Google Scholar](#)

11. Songlin Zhou

[View author publications](#)

You can also search for this author in [PubMed](#) [Google Scholar](#)

12. Junjie Zhu

[View author publications](#)

You can also search for this author in [PubMed](#) [Google Scholar](#)

13. Anne Jacobi

[View author publications](#)

You can also search for this author in [PubMed](#) [Google Scholar](#)

14. Vivek Swarup

[View author publications](#)

You can also search for this author in [PubMed](#) [Google Scholar](#)

15. Phillip G. Popovich

[View author publications](#)

You can also search for this author in [PubMed](#) [Google Scholar](#)

16. Daniel H. Geschwind

[View author publications](#)

You can also search for this author in [PubMed](#) [Google Scholar](#)

17. Zhigang He

[View author publications](#)

You can also search for this author in [PubMed](#) [Google Scholar](#)

Contributions

Y.L., X.H., P.G.P. and Z.H. conceived the project; Y.L., X.H., Q.W., A.M., B.C., Z.S., H.M., S.Z., J.Z. and A.J. performed the experiments and discussed the results; R.K., Y.Z., Z.Y., V.S. and D.H.G. participated in data analysis; Y.L., X.H. and Z.H. prepared the manuscript with inputs from all authors.

Corresponding author

Correspondence to [Zhigang He](#).

Ethics declarations

Competing interests

Z.H. is an advisor of SpineX. The remaining authors declare no competing interests.

Additional information

Peer review information *Nature* thanks Elizabeth Bradbury, Jerry Silver and Binhai Zheng for their contribution to the peer review of this work. Peer reviewer reports are available.

Publisher's note Springer Nature remains neutral with regard to jurisdictional claims in published maps and institutional affiliations.

Extended data figures and tables

Extended Data Fig. 1 Age-dependent decline in serotonergic axon regrowth and wound healing.

a, Representative images of spinal cord sagittal sections showing 5HT-labelled axons from sham, P7 or P20 mice at two weeks after injury. Scale bar, 500 µm. **b**, Representative images of spinal cord sections from sham, P7 or P20 mice at two weeks after injury, stained with antibodies against collagen I, CD68, P2Y12 or CD31. Scale bar, 250 µm. **c**, Representative images of spinal sagittal sections at four weeks after sham control or P2 injury, with CST axons labelled with AAV-ChR2-mCherry. Red stars indicate the lesion site. Scale bar, 500 µm. **d**, Representative images of sagittal spinal cord sections at two weeks after injury, stained with antibodies against laminin, CSPG and GFAP. Scale bar, 250 µm. **e**, Representative images of sagittal spinal cord sections at two weeks after P20 injury, stained with antibodies against laminin, GFAP and 5-HT. Scale bar, 250 µm. All experiments shown were independently repeated three times with similar results.

Extended Data Fig. 2 Distinct microglia and macrophage responses after crush injury to neonatal or adult spinal cord.

a, Images of spinal cord sections stained with antibodies against CD68 and P2Y12 from mice at 3 dpi, 7 dpi or 14 dpi. Higher-magnification images showing P2Y12⁺ cells were co-labelled with CD68 at 3 dpi. Cells with highly ramified morphology at 7 dpi and 14 dpi can be seen around lesion sites. Scale bar, 100 µm. **b**, Higher-magnification images from Fig. 2a showing that CD68⁺ cells and fibronectin matrix form bridges between gaps at 3 dpi. Scale bar, 50 µm. **c**, Immunolabelling for CD68 and P2Y12 in adult mice at 3 dpi, 7 dpi or 14 dpi, showing CD68⁺ cells that lack P2Y12 expression. Scale bar, 200 µm. All experiments shown were independently repeated three times with similar results.

Extended Data Fig. 3 Histological assessments of bridges formed after neonatal spinal cord injury.

a, Higher-magnification images of sections of the spinal cord bridge area stained with antibodies against fibronectin, GFAP, P2Y12 and collagen I, or with DAPI (blue), at 3 dpi in P2 injury. Scale bar, 50 µm. **b**, Representative images of spinal sections of *Cx3cr1*^{GFP} mice immunolabelled with caspase-3 showing cells around the lesion sites at 3 dpi in P2 injury. Scale bar, 200 µm. All experiments shown were independently repeated three times with similar results.

Extended Data Fig. 4 Infiltrated CCR2⁺ monocytes and macrophages were eliminated after neonatal but not adult spinal cord injury.

a, b, Representative images of sagittal sections of injured spinal cord of *Ccr2*^{RFP} mice at 3 or 14 dpi in P2 injury (**a**) or adult injury (**b**). Sections were immunostained for CD68 and RFP (for *Ccr2*^{RFP}). Scale bar, 250 µm. All experiments shown were independently repeated three times with similar results.

Extended Data Fig. 5 Microglia depletion impairs wound healing and axon regrowth after neonatal spinal cord injury.

a, Left, representative P2Y12-stained spinal cord images showing PLX3397-mediated depletion of microglia cells. Right, quantification of microglia depletion in spinal cord treated with PLX3397 or vehicle at 0, 7 or 14 dpi ($n = 3, 5$ and 5 for 0, 7 and 14 dpi, respectively). Student's *t*-test (two-tailed, unpaired), *** $P < 0.0001$. Data are mean ± s.e.m. Scale bar, 250 µm. **b**, Representative images of P2Y12-stained spinal cord sections from control (*Csf1rl*^{f/f}) and *Csf1r*-knockout (*Cx3cr*^{cre}; *Csf1rl*^{f/f}) mice showing an approximately 70% reduction of microglia throughout the spinal cord in the mutant mice ($n = 5$ per group). Student's *t*-test (two-tailed, unpaired), *** $P = 0.0004$. Data are mean ± s.e.m. Scale bar, 250 µm. **c**, Representative images of sagittal spinal sections taken at 14 days after P2

injury and immunostained with antibodies against 5-HT, GFAP, laminin, CSPG or CD31. Scale bar, 200 μ m. **d**, Higher-magnification images from **c**, showing 5-HT $^{+}$ axons and GFAP $^{+}$ astrocytes in the lesion site. Scale bar, 50 μ m. [Source data](#)

Extended Data Fig. 6 Isolation and scRNA-seq results for immune cells after neonatal spinal cord injury.

a, FACS plots showing selection of CD11b $^{+}$ and CD45 $^{+}$ cells from dissociated cells from neonatal spinal cord. **b**, t-SNE plot showing 14 clusters and population annotations. **c**, **d**, Relative proportions of microglia among total cells (**c**) and dividing microglia among microglia cells (**d**). **e**, Left, table showing the percentage of each cluster and their signature genes. Right, heat map depicting the top 30 differentially expressed genes for each of the 14 clusters. [Source data](#)

Extended Data Fig. 7 Feature plots showing examples of differentially expressed genes in different clusters.

Gene expression of *P2ry12*, *Tmem119*, *Siglech*, *Fn1*, *Igf1*, *Spp1*, *Ms4a7*, *Thbs1*, *Anxa1*, *Cstb*, *Serpinb6a* and *Stfa1* in different microglia clusters.

Extended Data Fig. 8 Comparison of changes in gene expression in proliferative-region-associated microglia, disease-associated microglia and MG3.

Dot plots of gene expression correlation between proliferative-region-associated microglia (PAM) and disease-associated microglia (DAM) (normalized to homeostatic microglia) and MG3 (normalized to MG0), showing different sets of upregulated and downregulated genes ($n = 13,755$ and 14,423 genes for PAM and DAM, respectively).

Extended Data Fig. 9 Network analysis and further characterization of MG3 differentially expressed genes.

a, Diagram depicting correlated gene modules that underlie cluster identities of MG3 microglia. **b, c**, Expression of genes associated with endopeptidase inhibitor activity (**b**) and the ECM (**c**), in adult microglia at 0, 3 and 5 dpi, using bulk RNA-seq ($n = 3$ per group). One-way ANOVA followed by post-hoc Bonferroni correction. * $P = 0.03$ (*Lgals3*), 0.04 (*Lgals1*), 0.01 (*Ecm1*), 0.01(*Pf4*); ** $P = 0.003$ (*Fn1*), 0.0013 (*Pf4*). Data are mean \pm s.e.m. [Source data](#)

Extended Data Fig. 10 Microglia isolation and transplantation.

a, Representative images (left) and quantification (right) of isolated microglia (P2Y12^+) from neonatal or adult *Cx3cr1*^{GFP} mice (3 h after isolation, $n = 400$ cells examined over three independent experiments). Data are mean \pm s.e.m. Scale bar, 50 μm . **b**, Representative images of spinal cord sections showing the activation of transplanted microglia in the adult lesion at two days after grafting. Scale bar, 250 μm . All experiments shown in **b** were independently repeated three times with similar results. **c**, Representative images of spinal cord sections showing the GFAP and CSPG staining in the adult lesion at 14 days after grafting. Quantification results are shown in Fig. 5d. Scale bar, 250 μm . [Source data](#)

Supplementary information

Reporting Summary

Peer Review File

Source data

Source Data Fig. 1

Source Data Fig. 2

Source Data Fig. 3

[Source Data Fig. 4](#)

[Source Data Fig. 5](#)

[Source Data Extended Data Fig. 5](#)

[Source Data Extended Data Fig. 6](#)

[Source Data Extended Data Fig. 9](#)

[Source Data Extended Data Fig. 10](#)

Rights and permissions

[Reprints and Permissions](#)

About this article



Check for
updates

Cite this article

Li, Y., He, X., Kawaguchi, R. *et al.* Microglia-organized scar-free spinal cord repair in neonatal mice. *Nature* **587**, 613–618 (2020).

<https://doi.org/10.1038/s41586-020-2795-6>

[Download citation](#)

- Received: 06 March 2020
- Accepted: 10 July 2020
- Published: 07 October 2020

- Issue Date: 26 November 2020
- DOI: <https://doi.org/10.1038/s41586-020-2795-6>

Further reading

- [**Microglia coordinate repair**](#)

- Katherine Whalley

Nature Reviews Neuroscience (2020)

- [**The role of brain innate immune response in lysosomal storage disorders: fundamental process or evolutionary side effect?**](#)

- Einat B. Vitner

FEBS Letters (2020)

Comments

By submitting a comment you agree to abide by our [Terms](#) and [Community Guidelines](#). If you find something abusive or that does not comply with our terms or guidelines please flag it as inappropriate.

[Access through your institution](#)

[Change institution](#)

[Buy or subscribe](#)

This article was downloaded by **calibre** from <https://www.nature.com/articles/s41586-020-2795-6>

A molecular cell atlas of the human lung from single-cell RNA sequencing
[Download PDF](#)

- Article
- [Published: 18 November 2020](#)

A molecular cell atlas of the human lung from single-cell RNA sequencing

- [Kyle J. Travaglini](#) [ORCID: orcid.org/0000-0003-3164-6448](#)^{1,2 na1},
- [Ahmad N. Nabhan](#)^{1,2 na1 nAff12},
- [Lolita Penland](#)^{3 nAff13},
- [Rahul Sinha](#)^{4,5},
- [Astrid Gillich](#) [ORCID: orcid.org/0000-0002-7016-0494](#)^{1,2},
- [Rene V. Sit](#)³,
- [Stephen Chang](#) [ORCID: orcid.org/0000-0001-7385-075X](#)^{1,2},
- [Stephanie D. Conley](#)^{4,5},
- [Yasuo Mori](#)^{4,5 nAff14},
- [Jun Seita](#)^{4,5 nAff15},
- [Gerald J. Berry](#)⁵,
- [Joseph B. Shrager](#)⁶,
- [Ross J. Metzger](#) [ORCID: orcid.org/0000-0003-0069-4949](#)^{2,7},
- [Christin S. Kuo](#)⁸,
- [Norma Neff](#) [ORCID: orcid.org/0000-0001-7141-5420](#)³,
- [Irving L. Weissman](#) [ORCID: orcid.org/0000-0002-9077-7467](#)^{4,5,9,10},
- [Stephen R. Quake](#) [ORCID: orcid.org/0000-0002-1613-0809](#)^{3,11} &
- [Mark A. Krasnow](#) [ORCID: orcid.org/0000-0002-1976-5471](#)^{1,2}

[Nature](#) volume 587, pages619–625(2020)[Cite this article](#)

- 22k Accesses
- 101 Altmetric
- [Metrics details](#)

Subjects

- [Evolutionary genetics](#)
- [Gene expression](#)
- [Transcriptomics](#)

Abstract

Although single-cell RNA sequencing studies have begun to provide compendia of cell expression profiles^{1,2,3,4,5,6,7,8,9}, it has been difficult to systematically identify and localize all molecular cell types in individual organs to create a full molecular cell atlas. Here, using droplet- and plate-based single-cell RNA sequencing of approximately 75,000 human cells across all lung tissue compartments and circulating blood, combined with a multi-pronged cell annotation approach, we create an extensive cell atlas of the human lung. We define the gene expression profiles and anatomical locations of 58 cell populations in the human lung, including 41 out of 45 previously known cell types and 14 previously unknown ones. This comprehensive molecular atlas identifies the biochemical functions of lung cells and the transcription factors and markers for making and monitoring them; defines the cell targets of circulating hormones and predicts local signalling interactions and immune cell homing; and identifies cell types that are directly affected by lung disease genes and respiratory viruses. By comparing human and mouse data, we identified 17 molecular cell types that have been gained or lost during lung evolution and others with substantially altered expression profiles, revealing extensive plasticity of cell types and cell-type-specific gene expression during organ evolution including expression switches between cell types. This atlas provides the molecular foundation for investigating how lung cell identities, functions and interactions are achieved in development and tissue engineering and altered in disease and evolution.

[Download PDF](#)

Main

Since Malpighi¹⁰, dozens of lung cell types have been discovered by microscopy¹¹, creating histological atlases that are the cellular foundation for pulmonary medicine. More recently, cell-type-specific markers^{12,13} have been identified that provide molecular definitions and functions of the cell types¹⁴, reaching its apex in genome-wide expression profiling by single-cell RNA sequencing (scRNA-seq)^{15,16,17,18,19}. We sought to create a comprehensive molecular cell atlas of adult human lung using

scRNA-seq analysis, a substantial challenge because the 45 histological cell types have diverse structures, locations, and abundances that vary over five orders of magnitude ([Supplementary Table 1](#)).

Fifty-eight molecular cell types of the human lung

We acquired histologically normal lung tissue intraoperatively from bronchi (proximal), bronchiole (medial), and alveolar (distal) regions along with peripheral blood (Extended Data Fig. [1a, d](#)). Lung samples were dissociated into cell suspensions, and each suspension was sorted into epithelial (EPCAM⁺), endothelial/immune (CD31⁺CD45⁺) and stromal (EPCAM⁻CD31⁻CD45⁻) populations ([Supplementary Fig. 1a](#)). This allowed us to balance tissue compartment representation for sequencing. We also sorted blood cells to balance immune lineages ([Supplementary Fig. 1b](#)). Sequencing libraries were prepared using 10x Chromium (10x) or SmartSeq2 (SS2)^{[20](#)}. Higher throughput of 10x enabled discovery of rare cell types, whereas SS2 gave deeper transcriptomic information; there were also platform-specific idiosyncrasies in cell capture. We sequenced thousands of cells from each compartment for each subject ([Supplementary Table 2](#)) to directly compare cell types without batch correction, and did so for three subjects to address individual differences. High-quality transcriptomes were obtained from approximately 75,000 cells (65,662 10x; 9,404 SS2).

We grouped cells based on the expression of compartment-specific markers (Extended Data Fig. [1b](#)), then iteratively clustered^{[21](#)} them for each subject to identify transcriptionally distinct cell populations. Populations between subjects were merged using cluster-specific marker genes for downstream analyses. Our approach identified 58 transcriptionally distinct cell populations (mean 51 per subject) (Extended Data Fig. [1c](#), [Supplementary Table 2](#)), 37 more than a recent state-of-the-art study^{[19](#)}.

Transcriptomes of canonical cell types

The 58 molecular types included 15 epithelial, 9 endothelial, 9 stromal and 25 immune populations, greater than the number of classical cell types in each compartment ([Supplementary Table 2](#)). Using extant and newly identified (bronchial vessel) markers ([Supplementary Table 1](#)) and single-molecule fluorescence in situ hybridization (smFISH), we found clusters that represent all but one classical lung cell type in epithelial, endothelial and stromal compartments (Fig. [1a, b](#)).

Fig. 1: Identities and locations of lung epithelial, endothelial, and stromal cell types.

 figure1

a, Human lung molecular cell types identified after iterative clustering (each level of hierarchy is an iteration) of scRNA-seq profiles of cells in indicated tissue compartments. Black, canonical types; blue, proliferating or differentiating subpopulations; red, novel populations. Number of cells shown below cluster name. AdvF, adventitial fibroblast; AlvF, alveolar fibroblast; Art, artery; ASM, airway smooth muscle; AT2-s, AT2-signalling; Bas, basal; Bas-d, differentiating basal; Bas-p, proliferating basal; Bas-px, proximal basal; Bro1, bronchial vessel 1 cell; Bro2, bronchial vessel 2 cell; Cap, general capillary cell; Cap-a, capillary aerocyte; Cap-i1, capillary intermediate 1 cell; Cap-i2, capillary intermediate 2 cell; Cil, ciliated; Cil-px, proximal ciliated; FibM, fibromyocyte; Gob, goblet; Ion, ionocytes; LipF, lipofibroblast; Lym, lymphatic; Meso, mesothelial; MyoF, myofibroblast; Muc, mucous; NE, neuroendocrine; Peri, pericyte; Ser, serous; VSM, vascular smooth muscle. **b**, Diagrams showing localization and morphology of each type (cell type numbering or names in **a** and Fig. [2a](#)). **c**, Dot plot of AT2 marker expression (10x dataset). UP10K, unique molecular identifiers (UMIs) per 10,000. CPM, counts per million mapped reads. **d**, smFISH and quantification ($n = 203$ cells scored, staining repeated in two different participants from those profiled) for shared AT2 and AT2-signalling marker *SFTPC* (white) and specific AT2 marker *WIF1* (red puncta). Scale bar, 10 μm . AT2-signalling cells ($SFTPC^+ WIF1^-$; box, enlarged at right, yellow arrowhead) are intermingled among AT2 cells ($SFTPC^+ WIF1^+$, white arrowheads). **e**, Dot plot of stromal markers (10x dataset). FB, fibroblast. **f**, smFISH and quantification for general fibroblast marker *COL1A2* (white), alveolar fibroblast

marker *GPC3* (red, left) and adventitial fibroblast marker *SERPINF1* (red, right). Blue, DAPI; green, extracellular matrix (ECM; autofluorescence); prox., proximal. Adventitial fibroblasts (arrowheads, right) localize around vessels (ECM). Graph shows quantification of stromal cell type in alveolar and proximal vascular regions (n denotes number of cells scored in each region; staining repeated in two different participants from those profiled). Pericyte and lipofibroblast marker staining in Extended Data Fig. 4*h, i*. Scale bars, 10 μm . For more details on statistics and reproducibility, see [Methods](#).

[Source data](#)

[Full size image](#)

Immune cells were the most heterogeneous and included circulating, egressed and lung-resident cells. To aid identity assignment, we defined transcriptional profiles of circulating immune cells by bulk RNA sequencing of 21 sorted, functionally characterized classes of human blood cells (Extended Data Fig. 2*a*, [Supplementary Table 3](#)). We also obtained scRNA-seq profiles of around 5,000 blood cells from two patients whose lung cells we analysed. Canonical immune markers and the ascertained panels of differentially expressed genes were used to assign the identities to 25 immune clusters from our lung and blood scRNA-seq analysis, including all but one previously known lung immune cell type (Fig. 2*a*, Extended Data Fig. 2*b*).

Fig. 2: Identity and residency of lung immune cells.



a, Human lung immune molecular types clustered and annotated as in Fig. [1a](#). Clusters 45 (grey) and 56 (light red) were found only in one subject. Bar graphs show relative abundance of each immune type in lung (blue) and blood (red) samples. Lung ‘resident’ (Res) or ‘homing’ (Hom) immune types, more than 90% enrichment in lung samples; ‘intravascular’ (IV), more than 90% enrichment in blood; ‘egressed’ (Egr), all other types (assignments are provisional because cell harvesting influences enrichment values). Red lettering denotes cells not previously known to home to (be enriched in) lung or change expression (Δ) after egression from blood. Mono Cl., classical monocyte; CD4 M/E, CD8 $^+$ memory/effector T cell; CD4 Na, CD4 $^+$ naive T; CD8 M/E, CD8 $^+$ memory/effector T; CD8 Na, CD8 $^+$ naive T; DC, dendritic cell; Mono Int., intermediate monocyte; mDC, myeloid dendritic; pDC, plasmacytoid dendritic cell; MP, macrophage; MP-p, proliferating macrophage; Mono NC, non-classical monocyte; NK, natural killer cell; NKT, natural killer T cell; NK/T-p, proliferating natural killer/T cells. **b**, Dot plot showing expression (10x dataset) in dendritic cell clusters 50–54 of, from top row to bottom: two canonical dendritic markers, four myeloid dendritic (mDC1, mDC2) markers, and six markers for three novel dendritic populations (IGSF21 $^+$, EREG $^+$ and TREM2 $^+$). **c**, Box-and-whisker plots of general, lymphocyte-specific, and myeloid-specific lung residency (egression) signature scores (of cells in **a**) based on expression of indicated genes in 10x profiles of indicated immune types isolated from blood (intravascular, IV) or lung (L). Many previously known lymphocyte residency genes (for example, *S1PR1*, *RUNX3*, *RBPJ* and *HOBIT*) were lowly expressed and only uncovered in SS2 profiles. Grey shading denotes myeloid cells. *n* cells in each box-and-whisker (from left to right): 725; 187; 419; 771; 631; 1,411; 594; 2,419; 644; 288; 519; 4,250; 21; 116; 1,064; 1,013; 200; and 604. For more details on statistics and reproducibility, see [Methods](#).

[Full size image](#)

Our approach defined genome-wide expression profiles for nearly all classical lung cell types (41 out of 45, 91%), from the most abundant (capillaries, approximately 23% of lung cells) to exceedingly rare (ionocytes, 0.01%) ([Supplementary Table 1](#)). One-quarter (11 out of 45) previously lacked high-quality single-cell transcriptomes. The only classical types not captured are extremely rare (neurons, glia), primarily found in disease (tuft cells)²², or require special isolation methods (eosinophils).

New lung cell types, subtypes and states

Many canonical types were represented by more than one cluster, so the specific identities of 25 clusters remained uncertain. All but one were found in samples from

several participants so were unlikely to be subject-specific ([Supplementary Table 2](#)). This suggested that the distinct expression profiles uncovered represented discrete molecular states or novel cell types or subtypes. To distinguish these possibilities, we analysed the differentially expressed genes and examined cell structure and location.

We first identified clusters representing common cell states. Three clusters (proliferating basal cells, proliferating natural killer/T cells, and proliferating macrophages) were enriched in the expression of cell cycle genes, which indicates that they represent the proliferative states of basal cells, natural killer cells, T cells and macrophages, respectively, and are the most proliferative lung cell types (Extended Data Fig. [3a](#)). Another cluster (differentiating basal cells) had reduced expression of *KRT5* and increased expression of *HES1*, *KRT7* and *SCGB3A2*, indicating active differentiation to other epithelial fates^{[23,24](#)}, consistent with their transitional morphology (Extended Data Fig. b, c). Proliferating and differentiating basal cells derived mostly from proximal lung samples (Extended Data Fig. [3d,e](#)), suggesting one-third of proximal basal cells are active.

The other basal cell clusters were quiescent and localized to proximal (large, pseudostratified) airways, or both proximal and distal (small, simple) airways (Extended Data Fig. [3e,f](#)). The basal cell clusters are distinguished by hundreds of genes, which suggests that they are molecularly distinct cell types that differ in hormone production (*ALOX15*, *ADH7*, *SNCA*) and adhesion (*POSTN*, *ISLR*, *PCDH7*) (Extended Data Fig. [3b](#)). There were also distinct clusters of ciliated cells along the proximal–distal axis (Extended Data Fig. [3g,h](#)).

We uncovered two clusters of alveolar type 2 (AT2) cells (Fig. [1c](#)), which produce surfactant that prevents alveolar collapse. These are intermingled throughout the alveolar epithelium (Fig. [1d](#)). One cluster ($WIF1^+HHIP^+CA2^+$) expressed higher levels of some canonical AT2 markers (*SFTPA1*, *SFTPC* and *ETV5*) and selectively expressed inhibitors of Wnt (*WIF1*) and Hedgehog (*HHIP*) signalling and the cell cycle (*CDKN1A*), indicating that they are quiescent (Extended Data Fig. [3i](#), left). The other, tenfold less-abundant cluster (AT2-signalling cells) selectively expressed genes involved in Wnt signalling (*WNT5A*, *LRP5*, *CTNNBIP* and *TCF7L2* (also known as *TCF4*)) and detoxification (*CP*, *GSTA1* and *CYP4B1*) (Extended Data Fig. [3i](#), right). AT2-signalling cells could be alveolar stem cells, homologous to the rare, Wnt-active subpopulation of mouse AT2 cells (AT2^{stem})^{[25,26](#)}. However, homology between human AT2-signalling and mouse AT2^{stem} cells is provisional, because although both show increased Wnt signalling or components, the many other expression differences between human AT2-signalling and ‘bulk’ AT2 cells are not shared by mouse AT2^{stem} cells.

We found unexpected molecular diversity in the endothelial compartment (Extended Data Fig. 3j). Two populations were identified as bronchial by their localization around bronchi (Extended Data Fig. 3k). Thus, bronchial endothelial cells are distinct from their counterparts in the pulmonary circulation, distinguished by matrix (*VWA1* and *HSPG2*), fenestrated morphology²⁷ (*PLVAP*) and cell cycle-associated (*MYC* and *HBEGF*) genes. Four clusters of endothelial cells in the pulmonary circulation expressed capillary markers. Two (capillary aerocytes and general capillary cells) are intermingled alveolar capillary cell types²⁸; the others are rare capillary types showing features of both (capillary ‘intermediates’ 1 and 2).

We identified new types in the stroma, the least characterized compartment. Two clusters expressed classical fibroblast markers (*BSG* and *COL1A2*) (Fig. 1e) but one (*SPINT2*⁺*FGFR4*⁺*GPC3*⁺) localized to alveoli (‘alveolar fibroblasts’) and the other (*SFRP2*⁺*PI16*⁺*SERPINF1*⁺) to vascular adventitia and nearby airways (‘adventitial fibroblasts’) (Fig. 1f, Extended Data Fig. 4a–d). Both expressed genes involved in canonical fibroblast functions (matrix biosynthesis, adhesion and signalling regulators) but the specific genes often differed (Extended Data Fig. 4e). Each cluster also has distinct functions: expression of voltage-gated sodium channel *SCN7A* and glutamate receptor *GRIA1* suggest alveolar fibroblasts are excitable cells with glutamatergic input (Supplementary Table 4). Their profiles also suggest novel, shared functions including the recruitment of immune cells (*IL1RL1*, *IL32*, *CXCL2* and genes in the class II major histocompatibility complex locus) and the complement system (*C2*, *C3*, *C7*, *CFI*, *CFD*, *CFH* and *CFB*).

Two stromal clusters were enriched for *ACTA2*, a canonical marker of myofibroblasts (Fig. 1e), which help form and stabilize alveoli. One cluster (*WIF1*⁺*FGF18*⁺*ASPN*⁺) is classical myofibroblasts and localized to alveolar ducts (Extended Data Fig. 4f). The other (‘fibromyocytes’) showed higher expression of contractile genes (*MYH11*, *CNN1* and *TAGLN*), was preferentially isolated from samples of proximal lungs, and was found both intermingled with airway smooth muscle and in alveoli (Extended Data Figs. 3e, 4g). Both populations shared expression of genes for canonical fibroblast functions, although the specific genes differed from alveolar and adventitial fibroblasts (Supplementary Table 4).

Lung immune cell residency signatures

To distinguish between lung-resident, egressed and circulating immune cells, we compared the relative abundance of each immune population in lung and peripheral blood samples from the same subject (Fig. 2a). Eleven clusters (including alveolar macrophages, as expected²⁹) consisted of cells only from lung samples, with no or

rare exception, which indicates that they are lung-resident or greatly enriched. This included three novel lung dendritic populations: IGSF21⁺ and rare EREG⁺ dendritic cells express asthma genes (*CCL2*, *CCL13* and *IGSF21*) and developmental signals (*EREG*, *VEGFA*, *AREG*), respectively, and both localize to proximal vessels; TREM2⁺ dendritic cells localize to vessels and alveoli and express lipid machinery (*APOC1*, *APOE* and *CYP27A1*) (Fig. 2b, Extended Data Fig. 4k–n).

The other immune cell types were found in both lung and blood samples. For some types, every cell—whether from lung or blood—clustered together. However, for other types, cells from lung formed a separate cluster (Extended Data Fig. 4o). Some of the differentially expressed genes may be due to technical differences (for example, collagenase treatment of lung³⁰, circulating RNA in blood³¹), but others such as upregulation in lung cells of lymphocyte-residence gene *CD69* probably represent genes induced after egression³². We identified a core transcriptional signature for all human lung-resident lymphocytes (Fig. 2c), which overlaps a residence signature found by bulk RNA sequencing of CD8⁺ T cells in mouse spleen, gut and liver³³. We also found a residency signature for lung myeloid cells that overlaps the lymphocyte signature, supporting a core residency program for immune cells plus specific subprograms for myeloid cells and lymphocytes.

Cell markers, regulators and interactions

We identified optimal markers for each previously known and newly identified lung cell type (Extended Data Fig. 5a, [Supplementary Table 4](#)). Approximately 200 markers can distinguish virtually all types (Extended Data Fig. 5b), so could be used with multiplexed smFISH^{34,35,36} to simultaneously detect in clinical specimens alterations in their numbers and relationships. A similar compendium of membrane protein markers ([Supplementary Table 4](#)) could be used to purify or therapeutically target specific lung cell types. We also identified around 400 cell type-selective transcription factors (Extended Data Fig. 5e, [Supplementary Table 4](#)), putative ‘master regulators’ that could help create all lung cell types by cellular reprogramming. These include what may be long-sought master regulators of AT1 cells (for example, *MYRF*), which comprise the gas-exchange surface, and of pericytes (*TBX5*) (Extended Data Fig. 5c, d).

The atlas allowed us to map the cell targets of circulating hormones, based on expression of their cognate receptors. Receptors for some hormones are broadly expressed, indicating direct action throughout the lung (Extended Data Fig. 6a). Other hormones have specific and unexpected targets, such as somatostatin (*SSTR1*, arteries), melanocortin (*MC1R*, ionocytes), and oxytocin (*OXTR*, ciliated cells).

Pericytes are predicted targets of several hormones, which could affect their contractile machinery to regulate alveolar perfusion (Extended Data Fig. [6b](#)). Receptors for half the hormones were not detectably expressed so these hormones may not directly influence lung physiology. We also mapped local signalling interactions by examining expression of ligands and receptors, which predicts up to hundreds of interactions among neighbouring cell types (Extended Data Fig. [6c](#), [Supplementary Table 5](#)).

The expression of chemokine receptors illuminated immune cell homing (Fig. [3](#)). Our data confirmed canonical homing interactions such as CD4⁺ T cells to lymphatic vessels, and provides specificity for others such as plasma cell homing to epithelial mucosa through *CCL28* from serous cells. It also predicts new interactions such as *CX3CR1*-mediated homing of nonclassical monocytes to *CX3CL1*-expressing endothelial and airway epithelial cells. All three new dendritic populations express *CCR1*, which could mediate their attraction to veins (*CCL23*), bronchial vessels (*CCL14*), ciliated cells (*CCL15*), and lymphocytes (*CCL5*). Ionocytes are the only non-immune cell to express appreciable levels of any chemokine receptor (*CXCR4*).

Fig. 3: Chemokine signalling predicts immune cell homing in lung.



Dot plots showing expression of chemokine receptors (left) and ligands (right) in human lung cells (10x dataset); only cell types and chemokines with detected expression are shown. Colored lines connect ligand sources (target cells) with migrating immune cell types and ionocytes (ion, red) expressing cognate receptor; thicker lines indicate previously unknown interactions. For more details on statistics and reproducibility, see [Methods](#). Bas/Ma, basophil/mast cell; MK, megakaryocyte.

[Full size image](#)

Mapping cellular focus of lung diseases

We determined the expression of 233 extant lung disease genes (Extended Data Fig. 2). Disease genes with cell-type-specific expression (Extended Data Fig. 8a) and cell types expressing many genes associated with a specific disease (Extended Data Fig. 8b) are of special interest because they can pinpoint the cellular origin of disease. This supported known or suspected ‘culprit’ cells for 27 genes involved in 12 diseases, and identified potential culprits for 21 genes implicated in 15 diseases including pericytes in pulmonary hypertension, capillaries in atrioventricular dysplasia, and AT2 cells in chronic obstructive pulmonary disease (COPD). We confirmed pericyte, capillary and AT2 expression of disease genes by smFISH (Extended Data Fig. 8c–e).

We mapped expression of 80 genes encoding virus receptors, including 26 used by respiratory viruses (Extended Data Figs. 9a, 10). *NECTIN4* (measles virus receptor) was enriched in club, ciliated, differentiating basal, and goblet cells, and *CDHR3* ('common cold' rhinovirus C) was enriched in ciliated and neuroendocrine cells, indicating that infections initiate in those bronchial types. By contrast, *ACE2* (SARS, COVID-19 coronaviruses) and *DPP4* (MERS coronavirus) were both detected in AT2 cells (Extended Data Fig. 9b), consistent with severe alveolar pathology³⁷.

Evolution of cell types and expression

Construction of a mouse lung atlas² plus additional cells annotated as above for human ([Supplementary Table 6](#)) allowed analysis of evolutionary conservation of lung cell types and their transcriptomes. Homologous cell types were assigned by conserved expression of cell-type markers (Fig. 4a). Notably, mice seem to lack 17 (29%) of the 58 human lung cell types including 12 of the 14 (86%) newly identified types. Some missing mouse populations might be rare, transient, unstable, or too diverged to relate transcriptionally so may be uncovered by further studies. By contrast, just five mouse cell populations, all immune, were not found in human. This suggests substantial diversification of lung cell types during mammalian evolution.

Fig. 4: Evolutionary divergence of lung cell types and expression patterns.

 figure4

a, Mouse (top) lung molecular cell types (profiled and identified as for human, see [Methods](#)) aligned with homologous human types (bottom, Figs. [1a](#), [2a](#)) by expression of classical markers in [Supplementary Table 6](#). Thin lines, evolutionary expansions; dashed lines, potential expansions of functionally-related types. Red text, newly identified populations (light red, identified in only one subject); blue, cell states more abundant in human; grey, extant mouse cell types not captured in our data or found in only one patient in human. Asterisk denotes missing cell types. AlvMP, alveolar macrophages; AlvMP-p, proliferating alveolar macrophages. **b**, Scatter plot comparing average expression levels (dots) in AT2 cells of each expressed human gene and mouse orthologue (SS2 datasets; $n = 3,404$ human and 318 mouse AT2 cells). R denotes Pearson correlation coefficient. Red dots denote divergent genes (selected ones indicated) expressed 20-fold higher in either species. $P < 0.05$, ‘MAST’ differential gene expression test. Scale, $\ln(\text{CPM} + 1)$. **c**, Alveolar sections from mouse (top, *Mm*) and human (bottom, *Hs*) immunostained for HOPX (red) and AT2 marker MUC1 (green), and DAPI (blue). HOPX is expressed selectively in AT1 cells (arrowheads) in mouse but in human expression has expanded to AT2 and AT2-signalling cells (dashed circles). Scale bars, 10 μm . Staining repeated on three participants and mice. **d**, Alveolar sections from mouse (top) and human (bottom) probed by smFISH for *Hhip* and *HHIP* (red) and hydrazide staining for myofibroblast marker elastin (green) in mouse and smFISH for AT2 marker *SFTPC* (green) in human. Note *HHIP* expression switch from myofibroblast (mouse, arrowhead) to AT2 cells (human, dashed circles). Scale bars, 10 μm . Staining repeated on three human participants and mice. **e**, Dot plots of expression (SS2 data sets) of homologous genes indicated in mouse and human lung

cell types (ordered as in **a**) exemplifying the four observed scenarios (type 0, 1, 2, 3) for evolution of cellular expression pattern. Colours highlight cell types with conserved (blue) and diverged (red) expression. Endo, endothelial; Epi, epithelial. For more details on statistics and reproducibility, see [Methods](#).

[Full size image](#)

We compared expression levels of all active genes in each human cell type with those of the orthologous genes in the corresponding mouse type (Extended Data Fig. [11a](#), [Supplementary Table 7](#)). Most cell types correlated best with their counterparts across species, but surprisingly one human type (goblet) showed greater correlation with another mouse type (club, $R = 0.68$ versus 0.63) (Extended Data Fig. [11b](#))—despite conserved expression of canonical markers and master regulator *SPDEF* (Extended Data Fig. [11c](#)). Corresponding cell types in human and mouse diverged in expression (a greater than 20-fold change, $P < 0.05$) of hundreds of genes, such as *SERPINA1*, *PGC*, *WIF1* and *LYZ* in AT2 cells (Fig. [4b](#)). Lung as a whole had fewer diverged genes than any cell type, which suggests that expression lost in one type is gained in another (Extended Data Fig. [11d](#)). Diverged genes varied above age-related expression changes in mice (Extended Data Fig. [11e](#)) and included canonical cell-type markers, transcription factors, signalling molecules and disease genes.

Evolutionary changes in expression grouped into four types ([Supplementary Table 7](#)). Type 0 ('conserved') genes are expressed in the same cell types in mouse and human (Fig. [4e](#), Extended Data Fig. [12a](#)). Type 1 ('expression gain/loss') genes show simple gain (or loss) of expression between species, which involved a single cell type (type 1a, *PGC*) (Fig. [4e](#)), several types (type 1b, *RNASE1*) (Extended Data Fig. [12b](#)), or entire lung (type 1c, *TRIM38*) (Extended Data Fig. [12b](#)). Type 2 ('expression expansion/contraction') changes involved gain (or loss) of expression in additional lung cell types, expanding (or contracting) expression of the gene during evolution. For example, *HOPX*, the canonical AT1 transcription factor in mouse, is expressed in both AT1 and AT2 cells in human (Fig. [4c,e](#)), which indicates the existence of other AT1 transcription factors such as *MYRF*, which is AT1-selective in both species (Extended Data Fig. [12c](#)). Expanded expression of *RAMP3*, co-receptor for vasodilators CGRP and adrenomedullin, presumably alters pulmonary vascular response to these hormones (Extended Data Fig. [12d](#)).

Type 3 ('expression switch') changes involve a switch in expression from one cell type to another. Two medically important examples are COPD/emphysema genes *SERPINA1* and *HHIP*, both selectively expressed in AT2 cells in human but alveolar stromal cells in mice (Fig. [4d,e](#), Extended Data Fig. [12e](#)); other hedgehog pathway components were mostly conserved (Extended Data Fig. [12f](#)). Extreme examples occurred during evolution of species-specific cell types, such as consolidation in the

expression of anti-bacterial enzymes (*LTF*, *LYZ* and *BPIFB1*) from several mouse airway cells into human-specific serous cells, and consolidation of broadly expressed lipid-handling genes (*PLIN2* and *APOE*) from mouse alveolar fibroblasts (which can contain lipid droplets) and myofibroblasts to human-specific lipofibroblasts (Extended Data Fig. [12g](#)).

Despite general conservation of cell type expression patterns noted above, only 6% of expressed genes showed fully conserved patterns (type 0), most extremely specific or broadly expressed (Extended Data Fig. [12h](#), [Supplementary Table 8](#)). Thus, expression patterns of nearly all genes are evolutionarily labile, most undergoing broadening (55%, type 2) or simple gain or loss (29%, type 1) and rarely cell type switching (10%, type 3) ([Supplementary Table 9](#)).

Discussion

We constructed a comprehensive expression atlas of human lung comprising 58 molecular types and their locations (Fig. [1b](#)) including 41 out of 45 previously known cell types, all but the exceedingly rare. We identified 14 novel populations across all four compartments that are as distinct molecularly as the canonical cell types; each must be thoroughly characterized, as done for new capillary types^{[28](#)}. If there are other lung cell types, they must be exceedingly rare, fragile, region- or stage-specific, or so similar to the 58 that they are not resolved by current methods.

The atlas has broad implications for physiology and medicine, providing insight into the functions, regulation and interactions of the known and new cell types. It identifies those directly affected by hormones, viruses and extant lung disease genes, and distinguishes lung-resident and homing immune cell types and infers their expression changes after egression from circulation and the cellular sources of homing signals. The atlas defines type-selective transcription factors for creating cells to engineer a lung, and provides optimal markers and a benchmark for monitoring all types and how they change during development, ageing, disease and evolution.

Mice appear to lack 17 out of the 58 human molecular lung cell types, including most (12 out of 14) of the newly discovered ones. This suggests a considerable expansion of cell types in the human lineage, perhaps for new functions, durability, or regenerative capacity of our 6,000-fold larger lungs and 30-times longer lifespan^{[38,39](#)}. Even homologous cell types diverged in expression of hundreds of genes. Indeed, just 6% of expressed genes had fully conserved expression patterns across the lung, indicating widespread gain, loss or conversion of cell-type-specific transcriptional enhancers during mammalian evolution. It will be important to

unravel the genetic mechanisms and functional consequences of these changes, and to determine the selective forces operative for genes with fully conserved expression. The evolutionary cell type and expression changes predict where mouse will fail to model human lung physiology and disease.

The success of our atlas relied on: procuring fresh tissue across the organ plus matched blood; balancing tissue compartments to ensure broad cell representation; extensive profiling of each subject using broad cell capture and deep gene coverage scRNA-seq strategies; clustering subject and compartment data separately and iteratively; assigning cell identities using extant markers, functions of selectively expressed genes, and tissue localization. Applying the approach to other organs could create a comprehensive human molecular cell atlas.

Methods

Human lung tissue and peripheral blood

Freshly resected lung tissue was procured intraoperatively from patients undergoing lobectomy for focal lung tumours. Normal lung tissues (approximately 5 cm³) were obtained from uninvolved regions and annotated for the specific lung lobe and location along the airway or periphery. Pathological evaluation (by G.B.) confirmed normal histology of the profiled regions, except for areas of very mild emphysema in patient 1. Patient 1 was a 75-year-old male with a remote history of smoking, diagnosed with early stage adenocarcinoma who underwent left upper lobe (LUL) lobectomy; two blocks of normal tissue were obtained from lung periphery (distal 1a and 1b). Patient 2 was a 46-year-old male, non-smoker with a right middle lobe (RML) endobronchial carcinoid, who underwent surgical resection of the right upper and middle lobes; two blocks of tissue were selected from mid-bronchial region (medial 2) and periphery (distal 2) of right upper lobe (RUL). Patient 3 was a 51-year-old female, non-smoker with mild adult-onset asthma and a left lower lobe (LLL) endobronchial typical carcinoid, who underwent LLL lobectomy; three tissue blocks were resected from the bronchus (proximal 3), mid-bronchial (medial 2), and periphery (distal 3) of the LLL. All tissues were received and immediately placed in cold PBS and transported on ice directly to the research lab for single cell dissociation procedures. Peripheral blood was collected from patients 1 and 3 in EDTA tubes. For bulk RNA-seq of canonical immune populations, whole blood from healthy human donors was obtained commercially (AllCells) in EDTA tubes. Patient tissues were obtained under a protocol approved by Stanford University's Human Subjects Research Compliance Office (IRB 15166) and informed consent was obtained from each patient before surgery. All experiments followed applicable regulations and guidelines.

Mouse lung tissue

Lung tissue for Tabula Muris Senis⁴⁰ was obtained as previously described. We obtained additional tissue from two mice expressing Cre recombinase and two expressing oestrogen-inducible Cre recombinase (Cre-ERT2) for conditional cell-specific labelling in vivo with the gene-targeted alleles FVB-*Tbx4-LME-cre*^{41,42} (lung stroma) and B6.129-*Axin2-cre-ERT2*⁴¹, respectively. Cre-dependent reporter alleles *Rosa26ZsGreen1*, which expresses cytosolic ZsGreen1 following Cre-mediated recombination, and *Rosa26mTmG*, which expresses membrane-targeted green fluorescent protein (mGFP) after recombination and membrane-targeted tdTomato (mTomato) in all other tissues, were used to label cells expressing *Tbx4* and *Axin2*, respectively^{43,44}. Induction of the *Axin2-cre-ERT2* allele was done by intraperitoneal injection of tamoxifen (3 mg) once a day for three days as described²⁵. All mouse experiments followed applicable regulations and guidelines and were approved by the Institutional Animal Care and Use Committee at Stanford University (Protocol 9780).

Isolation of lung and blood cells

Individual human lung samples were dissected, minced, and placed in digestion media (400 µg ml⁻¹ liberase DL (Sigma 5466202001) and 100 µg ml⁻¹ elastase (Worthington LS006365) in RPMI (Gibco 72400120) in a gentleMACS c-tube (Miltenyi 130-096-334). Samples were partially dissociated by running ‘m_lung_01’ on a gentleMACS Dissociator (Miltenyi 130-093-235), incubated on a Nutator at 37 °C for 30 min, and then dispersed to a single cell suspension by running ‘m_lung_02’. Processing buffer (5% fetal bovine serum in PBS) and DNase I (100 µg ml⁻¹, Worthington LS006344) were then added and the samples rocked at 37 °C for 5 min. Samples were then placed at 4 °C for the remainder of the protocol. Cells were filtered through a 100-µm filter, pelleted (300g, 5 min, 4 °C), and resuspended in ACK red blood cell lysis buffer (Gibco A1049201) for 3 min, after which the buffer was inactivated by adding excess processing buffer. Cells were then filtered through a 70-µm strainer (Fisherbrand 22363548), pelleted again (300g, 5 min, 4 °C), and resuspended in magnetic activated cell sorting (MACS) buffer (0.5% BSA, 2 mM EDTA in PBS) with Human FcR Blocking Reagent (Miltenyi 130-059-901) to block non-specific binding of antibodies (see below).

Immune cells, including granulocytes, were isolated from peripheral blood using a high density ficoll gradient⁴⁵. In brief, peripheral blood was diluted tenfold with FACS buffer (2% FBS in PBS), carefully layered on an RT Ficoll gradient (Sigma HISTOPAQUE-1119), and centrifuged at 400g for 30 min at room temperature. The

buffy coat was carefully removed, diluted fivefold with FACS buffer, pelleted ($300g$, 5 min, $4\text{ }^{\circ}\text{C}$), and incubated in ice cold FACS buffer containing DNase I (Worthington LS006344) for 10 min at $4\text{ }^{\circ}\text{C}$. Clumps were separated by gentle pipetting to create a single-cell suspension.

Mouse lung samples were processed into single cell suspensions as previously described². In brief, each lung was dissected, minced, and placed in gentleMACS c-tubes (Miltenyi 130-096-334) with digestion buffer ($400\text{ }\mu\text{g ml}^{-1}$ liberase DL (Sigma 5466202001) in RPMI (Gibco 72400120)). The minced tissue was partially dissociated by running ‘m_lung_01’ on a gentleMACS Dissociator (Miltenyi 130-093-235), incubated at $37\text{ }^{\circ}\text{C}$ on a nutator for 30 min, completely dissociated on a gentleMACS by running ‘m_lung_02’, and kept at $4\text{ }^{\circ}\text{C}$ or on ice for the remainder of the protocol. Cells were washed with 5% FBS in PBS, centrifuged at $300g$ for 5 min, resuspended in 5% FBS in PBS, filtered through a 70- μm strainer (Fisherbrand 22363548), and centrifuged again and resuspended in FACS buffer (2% FBS in PBS).

Magnetic separation of lung tissue compartments

Immune and endothelial cells were overrepresented in our previous mouse single-cell suspensions. To partially deplete these populations in our human samples, we stained cells isolated from lung with MACS microbeads conjugated to CD31 and CD45 (Miltenyi 130-045-801, 130-091-935) then passed them through an LS MACS column (Miltenyi, 130-042-401) on a MidiMACS Separator magnet (Miltenyi, 130-042-302). Cells retained on the column were designated ‘immune and endothelial enriched’. The flowthrough cells were then split, with 80% immunostained for FACS (see below) and the remaining 20% stained with EPCAM microbeads (Miltenyi 130-061-101). EPCAM stained cells were passed through another LS column. Cells retained on the column were labelled ‘epithelial enriched’, and cells that flowed through were designated ‘stromal’.

Flow cytometry and cell sorting

Lysis plates for single-cell mRNA sequencing were prepared as previously described². 96-well lysis plates were used for cells from the blood and mouse samples and contained 4 μl of lysis buffer instead of 0.4 μl .

After negative selection against immune and endothelial cells by MACS, the remaining human lung cells were incubated with FcR Block (Becton Dickinson 564219) for 5 min and stained with directly conjugated anti-human CD45 (Biolegend 304006) and EPCAM (eBioscience 25-9326-42) antibodies on a Nutator

for 30 min at the manufacturer's recommended concentration. Cells were then pelleted ($300g$, 5 min, 4°C), washed with FACS buffer three times, then incubated with cell viability marker Sytox blue (1:3,000, ThermoFisher S34857) and loaded onto a Sony SH800S cell sorter. Living single cells (Sytox blue-negative) were sorted into lysis plates based on three gates: EPCAM $^{+}$ CD45 $^{-}$ (designated epithelial), EPCAM $^{-}$ CD45 $^{+}$ (designated immune), and EPCAM $^{-}$ CD45 $^{-}$ (designated endothelial or stromal).

Immune cells from subject matched blood were incubated with FcR Block and Brilliant Violet buffer (BD 563794) for 20 min and then stained with directly conjugated anti-human CD3 (BD 563548), CD4 (BD 340443), CD8 (BD 340692), CD14 (BD 557831), CD19 (Biolegend 302234), CD47 (BD 563761), CD56 (BD 555516), and CD235a (BD 559944) antibodies for 30 min at the manufacturer's recommended concentration. Cells were pelleted ($300g$, 5 min, 4°C), washed with FACS buffer twice, and then incubated with the viability marker propidium iodide and loaded onto a BD FACSAria II cell sorter. Living (propidium iodide-negative) single, non-red blood (CD235a $^{-}$) cells were sorted into lysis plates along with specific immune populations: B cells (CD19 $^{+}$ CD3 $^{-}$), CD8 $^{+}$ T cells (CD8 $^{+}$), CD4 $^{+}$ T cells (CD4 $^{+}$), natural killer cells (CD19 $^{-}$ CD3 $^{-}$ CD56 $^{+}$ CD14 $^{-}$), classical monocytes (CD19 $^{-}$ CD3 $^{-}$ CD56 $^{-}$ CD14 $^{+}$). After sorting, plates were quickly sealed, vortexed, spun down for 1 min at $1,000g$, snap frozen on dry ice, and stored at -80 until cDNA synthesis.

Mouse cells were incubated with the viability marker DAPI and loaded onto a BD Influx cell sorter. Living (DAPI-negative) single cells were sorted into lysis plates based on presence or absence of the fluorescent lineage label (mEGFP for *Axin2-cre-ERT2*, ZsGreen1 for *Tbx4-LME-cre*).

Immune cells for bulk mRNA sequencing were incubated with FcR Block for 20 min and then stained with one of six panels of directly conjugated antibodies for 30 min at the manufacturers recommended concentration: anti-human CD16 (BD 558122), CD123 (BD 560826), CCR3 (R&D FAB155F), ITGB7 (BD 551082), CD3 (BD 555341), CD14 (Invitrogen MHCD1406), CD19 (BD 555414), and CD56 (BD 555517) (basophils, neutrophils and eosinophils); anti-human CD16 (BD 558122), CD14 (BD 347497), CD4 (BD 340443), CD3 (BD 555341), CD8 (BD 555368), CD19 (BD 555414), and CD56 (BD 555517) (classical and nonclassical monocytes); anti-human CD16 (BD 558122), CD1c (Miltenyi Biotec 130-098-007), CD11c (BD 340544), CCR3 (R&D FAB155F), CD123 (BD 560826), HLA-DR (BD 335796), CD3 (BD 555341), CD4 (BD 555348), CD8 (BD 555368), CD14 (Invitrogen MHCD1406), CD19 (BD 555414), and CD56 (BD 555517) (pDCs, mDCs, CD16 $^{+}$ dendritic cells); anti-human IgM/IgD (BD 555778), CD19 (BD

557835), CD27 (BD 558664), CD20 (BD 335794), CD3 (BD 555341), CD4 (BD 555348), CD14 (Invitrogen MHCD1406), and CD56 (BD 555517) (B cells); anti-human CD16 (BD 558122), CD57 (BD 347393), CD56 (BD 557747), CD3 (BD 555341), CD4 (BD 555348), CD14 (Invitrogen MHCD1406), and CD19 (BD 555414) (natural killer cells); and anti-human CD45RA (Biolegend 304118), CCR7 (R&D FAB197F), CD62L (BD 555544), CD45RO (BD Pharmingen 560608), CD4 (BD 340443), CD8 (BD 340584), CD11b (BD 555389), CD14 (Invitrogen MHCD1406), CD19 (BD 555414), CD56 (BD 555517) (T cells). Cells were washed with FACS buffer twice, incubated with the viability marker propidium iodide and loaded onto a BD FACSAria II cell sorter. Approximately 40,000 cells from 21 canonical immune populations ([Supplementary Table 3](#)) were sorted in duplicate into Trizol LS (Invitrogen 10296010).

After sorting, all plates and samples were quickly sealed, vortexed, spun down for 1 min at 1,000*g* and then snap frozen on dry ice and stored at -80 °C until cDNA synthesis.

Single-cell mRNA sequencing

mRNA from single cells sorted from human and mouse lungs and human blood into lysis plates was reverse transcribed to cDNA and amplified as previously described². Illumina sequencing libraries for cDNA from single cells were prepared as previously described². In brief, cDNA libraries were prepared using the Nextera XT Library Sample Preparation kit (Illumina, FC-131-1096). Nextera tagmentation DNA buffer (Illumina) and Tn5 enzyme (Illumina) were added, and the sample was incubated at 55 °C for 10 min. The reaction was neutralized by adding Neutralize Tagment Buffer (Illumina) and centrifuging at room temperature at 3,220*g* for 5 min. Mouse samples were then indexed via PCR by adding i5 indexing primer, i7 indexing primer, and Nextera NPM mix (Illumina). Human samples were similarly indexed via PCR using custom, dual-unique indexing primers (IDT)².

Following library preparation, wells of each library plate were pooled using a Mosquito liquid handler (TTP Labtech), then purified twice using 0.7x AMPure beads (Fisher A63881). Library pool quality was assessed by capillary electrophoresis on a Tapestation system (Agilent) with either a high sensitivity or normal D5000 ScreenTape assay kit (Agilent) or Fragment analyser (AATI), and library cDNA concentrations were quantified by qPCR (Kapa Biosystems KK4923) on a CFX96 Touch Real-Time PCR Detection System (Biorad). Plate pools were normalized and combined equally to make each sequencing sample pool. A PhiX control library was spiked in at 1% before sequencing. Human libraries were

sequenced on a NovaSeq 6000 (Illumina) and mouse libraries on a NextSeq 500 (Illumina).

Cells isolated from each compartment (immune and endothelial enriched, epithelial enriched, stromal) and subject blood were captured in droplet emulsions using a Chromium Single-Cell instrument (10x Genomics) and libraries were prepared using the 10x Genomics 3' Single Cell V2 protocol as previously described². All 10x libraries were pooled and sequenced on a NovaSeq 6000 (Illumina).

Immune cell bulk mRNA sequencing

Total RNA from bulk-sorted canonical immune populations was reverse transcribed to cDNA, amplified, and prepared as sequencing libraries as previously described⁴⁵. Libraries were sequenced on a NextSeq 500 (Illumina).

Immunohistochemistry

Mouse and human lungs were collected as previously described^{25,46}. After inflation, lungs were removed en bloc, fixed in 4% paraformaldehyde (PFA) overnight at 4 °C with gentle rocking, then cryo-embedded in Optimal Cutting Temperature compound (OCT, Sakura) and sectioned using a cryostat (Leica) onto Superfrost Plus Microscope Slides (Fisherbrand). Immunohistochemistry was performed using primary antibodies raised against the following antigens and used at the indicated dilutions to stain slides overnight at 4 °C: anti-proSP-C (rabbit, Chemicon AB3786, 1:250 dilution), HES1 (rabbit, Cell Signaling 11988S clone D6P2U, 1:100), MUC-1 (hamster, Thermo Scientific HM1630, clone MH1, 1:250), Ki67 (rat, DAKO M7249 clone MIB-1, 1:100), and keratin-5 (chicken, Biolegend 905901, 1:100). Primary antibodies were detected with Alexa Fluor-conjugated secondary antibodies (Jackson ImmunoResearch) unless otherwise noted, then mounted in Vectashield containing DAPI (5 µg ml⁻¹, Vector labs). Images were acquired with a laser scanning confocal fluorescence microscope (Zeiss LSM780) and processed with Fiji (v.2.0) and Imaris (v.9.2.0, Oxford Instruments). Immunostaining experiments were performed on at least two human or mouse participants distinct from the donors used for sequencing, and quantifications were based on at least 10 fields of view in each.

Single molecule in situ hybridization

Samples were fixed in either 10% neutral buffered formalin, dehydrated with ethanol and embedded in paraffin wax or fixed in 4% paraformaldehyde and embedded in OCT compound. Sections from

paraffin (5 µm) and OCT (20 µm) blocks were processed using standard pre-treatment conditions for each per the RNAscope multiplex fluorescent reagent kit version 2 (Advanced Cell Diagnostics) assay protocol. TSA-plus fluorescein, Cy3 and Cy5 fluorophores were used at 1:500 dilution. Micrographs were acquired with a laser scanning confocal fluorescence microscope (Zeiss LSM780) and processed with ImageJ and Imaris (version 9.2.0, Oxford Instruments). smFISH experiments were performed on at least two human or mouse participants distinct from the donors used for sequencing, and quantifications were based on at least 10 fields of view in each. For smFISH, fields of view were scored manually, calling a cell positive for each gene probed if its nucleus had at least three associated expression puncta. Proprietary (Advanced Cell Diagnostics) probes used were: KRT5 (547901-C2), SERPINB3 (828601-C3), SFTPC (452561-C2), WIF1 (429391), CLDN5 (517141-C2, 517141-C3), MYC (311761-C3), ACKR1 (525131, 525131-C2), COL1A2 (432721), GPC3 (418091-C2), SERPINF1 (564391-C3), C20rf85 (560841-C3), DHRS9 (467261), GJA5 (471431), CCL21 (474371-C2), COX4I2 (570351-C3), APOE (433091-C2), ACGT2 (828611-C2), ASPN (404481), IGSF21 (572181-C3), GPR34 (521021), EREG (313081), GPR183 (458801-C2), TREM2 (420491-C3), CHI3L1 (408121), MYRF (499261), AGER (470121-C3), TBX5 (564041), KCNK3 (536851), ACVRL1 (559221), SERPINA1 (435441), HHIP (464811), SLC7A10 (497081-C2), FGFR4 (443511), PI16 (451311-C2), SERPINF1 (310731), HHIP (448441-C3), SFTPC (314101-C2), NKX2-1 (434721-C3), and MYRF (524061).

Sequencing read alignments and quality control

Reads from single cells isolated using 10x chromium were demultiplexed and then aligned to the GRCh38.p12 human reference (from 10x Genomics) using Cell Ranger (version 2.0, 10x Genomics). Cells with fewer than 500 genes detected or 1,000 UMIs were excluded from further analyses.

Reads from single cells isolated by flow cytometry were demultiplexed using bcl2fastq (v.2.19.0.316, Illumina), pruned for low nucleotide quality scores and adaptor sequences using skewer (v.0.2.2), and aligned to either (depending on organism) the GRCh38.p12 human reference genome with both the gencode-vH29 and NCBI-108 annotations or the GRCm38.p6

mouse reference genome with the NCBI-106 annotation (with fluorescent genes mEGFP, tdTomato, and ZsGreen1 supplemented) using STAR (v.2.6.1d) in two-pass mapping mode, in which the first pass identifies novel splice junctions and the second pass aligns reads after rebuilding the genome index with the novel junctions. The number of reads mapping to each annotated gene were calculated by STAR during the second pass alignment, and cells with fewer than 500 genes detected or 50,000 mapped reads were excluded from later analyses. Reads from mRNA sequencing of canonical immune populations were demultiplexed, aligned and quantified using the same pipeline.

Cell clustering, doublet calling, and annotation

Expression profiles of cells from different subjects and different capture approaches (10x and SS2) were clustered separately using the R software package Seurat (v.2.3)⁴⁷. In brief, counts (SS2) and UMIs (10x) were normalized across cells, scaled per million (SS2) or per 10,000 (10x), and converted to log scale using the ‘NormalizeData’ function. These values were converted to z-scores using the ‘ScaleData’ command and highly variable genes were selected with the ‘FindVariableGenes’ function with a dispersion cutoff of 0.5. Principle components were calculated for these selected genes and then projected onto all other genes with the ‘RunPCA’ and ‘ProjectPCA’ commands. Clusters of similar cells were detected using the Louvain method for community detection including only biologically meaningful principle components (see below) to construct the shared nearest neighbour map and an empirically set resolution, as implemented in the ‘FindClusters’ function.

When clustering all cells from a single subject at once, we found that the first principal components defining heterogeneity represented differences in tissue compartment, but some cell types within a compartment (for example, basal, goblet club, neuroendocrine and ionocyte) had a tendency to co-cluster. Clusters were therefore grouped based on expression of tissue compartment markers (for example, *EPCAM*, *CLDN5*, *COL1A2* and *PTPRC*) using the ‘SubsetData’ command and the same procedure (from ‘ScaleData’ onwards) was applied iteratively to each tissue compartment until the markers enriched in identified clusters, identified using the

‘MAST’ statistical framework⁴⁸ implemented in the ‘FindMarkers’ command, were no longer biologically meaningful (for example, clusters distinguished by dissociation-induced genes³⁰, ribosomal genes, mitochondrial genes, or ambient RNA released by abundant cells such as RBCs³¹). Doublets were identified by searching for cells with substantial and coherent expression profiles from two or more tissue compartments and/or cell types.

To assign clusters identities, we first compiled a list of all established lung cell types, their abundances, their classical markers, and any RNA markers (when available) ([Supplementary Table 1](#)). RNA markers for canonical immune populations ([Supplementary Table 3](#)) were obtained from bulk mRNA sequencing by correlating the average expression (each captured in duplicate) with a test vector where the target population position equaled 10 and all others equaled 0 (see GitHub for details). Clusters were assigned a canonical identity based on enriched expression of these marker genes. Pearson correlations were calculated between the average expression profiles from each immune cluster for all cells in the SS2 with the average bulk profiles using the ‘cor’ function in R. There were no clusters that lacked expression of canonical marker genes. When two or more clusters were assigned the same identity, we first determined whether their tissue locations differed substantially (for example, proximal versus distal, alveolar versus adventitial) and prepended these locations when applicable. When both clusters localized to the same tissue region (for example, capillary endothelial cells or AT2 cells), we next compared their differentially expressed genes head-to-head to identify differences in molecular functions. These functional differences were also prepended, when applicable (for example, signalling AT2 versus AT2, proliferating basal versus basal). If the clusters could not be resolved by location or function, we prepended a representative marker gene to their ‘canonical’ identity (for example, IGSF21⁺ dendritic, EREG⁺ dendritic, and TREM2⁺ dendritic). Cells from different subjects with the same annotation were merged into a single group for all downstream analyses.

Approximately 35,000 mouse lung and blood cell expression profiles by SS2 and 10x from Tabula Muris Senis² were combined with 522 cells isolated from *Axin2-Cre-ERT2> Rosa26mTmG* (A.N.N.) and *Tbx4-LME-*

Cre > Rosa26ZsGreen1 (K.J.T.) mice and amplified by SS2. Cells were stratified by technology (10x versus SS2), re-clustered and re-annotated using the strategy described above for human lung cells.

Re-annotation of existing human lung single cell RNA sequencing datasets

UMI tables were obtained from the Gene Expression Omnibus (GSE122960 for ref. [18](#), GSE130148 for ref. [19](#)), clustered, and annotated using the strategy described above. New annotations for each cell are available on GitHub (see below).

Cell type pairwise correlations

We obtained average expression profiles for each cell type from all cells in the 10x dataset, supplemented with the average expression profile from neutrophils in the SS2 dataset, and calculated pairwise Pearson correlation coefficients using the ‘cor’ function in R.

Identification of proliferation signature

Expression profiles from matched proliferating and quiescent cell types were compared head-to-head using the ‘MAST’ statistical framework implemented in the ‘FindMarkers’ command in Seurat. Differentially-expressed genes common in each proliferating cell type were converted to z-scores using the ‘ScaleData’ command in Seurat, and summed to create a proliferation score for each cell in the 10x dataset.

Identification of immune egression signatures

Blood and tissue expression profiles for each immune cell type were compared head-to-head using the ‘MAST’ statistical framework implemented in the ‘FindMarkers’ command in Seurat. Differentially-expressed genes common in each subject were screened for dissociation artefact and contamination by red blood cells. Genes specific to tissue immune cells were binned based on their breadth of expression

(lymphocyte, myeloid or both), converted to z-scores using the ‘ScaleData’ command in Seurat, and summed to create an egression score for each cell in the 10x dataset.

Identification of enriched marker genes, transcription factors, and disease genes

Differentially expressed genes for each annotated cell type relative to the other cells within its tissue compartment were identified using the ‘FindMarkers’ command in Seurat with the ‘MAST’ statistical framework after downsampling each cell type to 100 (SS2) or 500 (10x) cells. To obtain the most sensitive and specific markers for each cell type, we ranked enriched genes, with a *P* value less than 10^{-5} and a sensitivity greater than 0.4, by their Matthews correlation coefficients (MCCs) calculated for each cell type from all cells in the 10x data set (numbers available in [Supplementary Table 2](#)). To measure the utility of using multiple markers in assigning cell identities, we calculated MCC scores for all possible combinations of each cell type’s top five marker genes.

Enriched genes were annotated as transcription factors or genes associated with pulmonary pathology based on lists compiled from The Animal Transcription Factor Database (<http://bioinfo.life.hust.edu.cn/AnimalTFDB>), The Online Mendelian Inheritance in Man Catalog (OMIM)⁴⁹, and Genome Wide Association Studies (GWAS) obtained from the EMBL-EBI Catalog⁵⁰ (EFO IDs 0000270, 0000341, 0000464, 0000571, 0000702, 0000707, 0000708, 0000768, 0001071, 0003060, 0003106, 0004244, 0004312, 0004313, 0004314, 0004647, 0004713, 0004806, 0004829, 0005220, 0005297, 0006505, 0006953, 0007627, 0007744, 0007944, 0008431, 0009369, 0009370; GO IDs 0031427, 0097366; Orphanet IDs 586 182098; log(p-value) < -20, statistical tests vary in indicated studies). Viral entry genes were obtained from Gene Ontology (GO:0046718) and then curated and associated with their cognate virus(es) based on literature citations available in our GitHub repository.

Cellular interaction and hormone target mapping

Interactions between cell types were predicted using CellPhoneDB ('statistical_analysis' method) with all cells in the SS2 dataset, as previously described⁶. For our targeted analyses, we curated the chemokine receptor-ligand interaction map and list of hormone receptors from an extensive literature search (available on GitHub, see below).

Human and mouse gene alignment, cell type correlation, and gene expression comparisons

The gene expression matrices from our human SS2 cells and the Tabula Muris Senis SS2 cells, supplemented with the 522 mouse cells from *Axin2-creER > mTmG* and *Tbx4-Cre > ZsGreen1* described above, were collapsed to HomologyIDs obtained from the Mouse Genome Informatics database to enable direct comparison. We obtained mean expression profiles for each cell type from all cells in the SS2 dataset and calculated pairwise Pearson correlation coefficients using the 'cor' function in R. We defined species-specific gene expression as those enriched 20-fold in either direction (mouse > human or human > mouse) with a *P* value less than 10^{-5} (calculated by 'MAST' as above) from all cells for the indicated types in the SS2 dataset. Correlations and age-specific genes were obtained the same manner using all cells from 3-month and 24-month in the combined SS2 mouse dat set.

To compare the expression pattern of each gene across species we binarized genes as expressed (1) or not expressed (0) in each cell type's average expression profile calculated from all mouse and human SS2 cells of the types compared above. A cell type 'expressed' a gene if the median of that gene's non-zero expression values across the constituent cells was greater than the median of every non-zero expression value for all other genes plus or minus two standard deviations (varied in 0.25 increments) and if the percentage of cells within the cell type with non-zero expression values was greater than the median percent of non-zero expression values for all other genes plus or minus two standard decisions (varied in 0.25 increments). These cutoffs were varied independently to ensure genes were robustly categorized. We then ordered these gene vectors to match homologous cell types between species with at least five cells and combined them to a single vector for each gene ($V = (a - b) + 2ab$, in which a is the ordered human

vector and b is the ordered mouse vector) that indicated for each cell type whether: Both mouse and human expressed the gene (2), only human (1), only mouse (-1), or neither (0). We then classified genes by the following: conserved if any element of V equaled 2 and all other elements equaled 0; type 2 if any element equaled 2 and any other equaled 1 or -1; not expressed if all elements equaled 0; type 3 if elements were both positive and negative; and type 1 if elements were either positive or negative and 0.

Statistics and reproducibility

All heat maps and plots with single cell expression data include every cell from indicated types (numbers available in [Supplementary Table 2](#) for human and [Supplementary Table 6](#) for mouse) for sequencing technology specified (SS2 or 10x), unless otherwise stated. Scatter plots were generated with ggplot2's 'geom_point' function. Dot plots were generated using a modified version of Seurat's 'DotPlot' function (available on GitHub). Violin plots were created with Seurat's 'VlnPlot' function and show proportion of single cells at indicated expression levels. Box-and-whisker plots were generated with ggplot2's 'geom_boxplot' function; lower and upper hinges correspond to first and third quartiles, whiskers extend from hinge to the largest or smallest value no further than 1.5 times the interquartile range. Data beyond whiskers are shown as outlying points. Correlations use Pearson's coefficient. Differentially expressed genes were identified using the 'MAST' statistical framework⁴⁸ implemented in Seurat's 'FindMarkers' function. Immunostaining and smFISH experiments were performed on at least 2 human or mouse subjects distinct from the donors used for sequencing, and quantifications were based on at least 10 fields of view in each. For smFISH, fields of view were scored manually, calling a cell positive for each gene probed if its nucleus had at least three associated expression puncta. No statistical methods were used to predetermine sample size. The experiments were not randomized and investigators were not blinded to allocation during experiments and outcome assessment.

Reporting summary

Further information on research design is available in the [Nature Research Reporting Summary](#) linked to this paper.

Data availability

Counts/UMI tables, cellular metadata, Seurat objects, and scanpy objects are available on Synapse

(<https://www.synapse.org/#/Synapse:syn21041850>). The data can be explored in a browser using cellxgene at <https://hlca.ds.czbiohub.org/>. Human sequencing data are available by data access agreement on the European Genome-phenome Archive (EGA) under accession EGAS00001004344. Use of human sequencing data are restricted to not for profit research only and requires approval or a waiver from requesting investigator's institutional review board. Mouse sequencing data are available on the National Institute of Health's Sequence Read Archive (SRA) under BioProject accession PRJNA632939. [Source data](#) are provided with this paper.

Code availability

The code for demultiplexing counts/UMI tables, clustering, annotation, downstream analyses, and obtaining source data/generating figures that include single-cell expression data are available on GitHub (<https://github.com/krasnowlab/HLCA>).

References

1. 1.

Enge, M. et al. Single-cell analysis of human pancreas reveals transcriptional signatures of aging and somatic mutation patterns. *Cell* 171, 321–330.e14 (2017).

[CAS](#) [PubMed](#) [PubMed Central](#) [Google Scholar](#)

2. 2.

Tabula Muris Consortium. Single-cell transcriptomics of 20 mouse organs creates a Tabula Muris. *Nature* **562**, 367–372 (2018).

[ADS](#) [Google Scholar](#)

3. 3.

Han, X. et al. Mapping the mouse cell atlas by microwell-seq. *Cell* **173**, 1307 (2018).

[CAS](#) [PubMed](#) [Google Scholar](#)

4. 4.

Zeisel, A. et al. Molecular architecture of the mouse nervous system. *Cell* **174**, 999–1014.e22 (2018).

[CAS](#) [PubMed](#) [PubMed Central](#) [Google Scholar](#)

5. 5.

Saunders, A. et al. Molecular diversity and specializations among the cells of the adult mouse brain. *Cell* **174**, 1015–1030.e16 (2018).

[CAS](#) [PubMed](#) [PubMed Central](#) [Google Scholar](#)

6. 6.

Vento-Tormo, R. et al. Single-cell reconstruction of the early maternal-fetal interface in humans. *Nature* **563**, 347–353 (2018).

[ADS](#) [CAS](#) [PubMed](#) [Google Scholar](#)

7. 7.

Young, M. D. et al. Single-cell transcriptomes from human kidneys reveal the cellular identity of renal tumors. *Science* **361**, 594–599 (2018).

[ADS](#) [CAS](#) [PubMed](#) [PubMed Central](#) [Google Scholar](#)

8. 8.

Aizarani, N. et al. A human liver cell atlas reveals heterogeneity and epithelial progenitors. *Nature* **572**, 199–204 (2019).

[CAS](#) [PubMed](#) [PubMed Central](#) [Google Scholar](#)

9. 9.

Han, X. et al. Construction of a human cell landscape at single-cell level. *Nature* **581**, 303–309 (2020).

[ADS](#) [CAS](#) [PubMed](#) [PubMed Central](#) [Google Scholar](#)

10. 10.

Young, J. Malpighi’s “De pulmonibus.”. *Proc. R. Soc. Med.* **23**, 1–11 (1929).

[CAS](#) [PubMed](#) [PubMed Central](#) [Google Scholar](#)

11. 11.

Gehr, P., Bachofen, M. & Weibel, E. R. The normal human lung: ultrastructure and morphometric estimation of diffusion capacity. *Respir. Physiol.* **32**, 121–140 (1978).

[CAS](#) [PubMed](#) [Google Scholar](#)

12. 12.

Balis, J. U., Paterson, J. F., Paciga, J. E., Haller, E. M. & Shelley, S. A. Distribution and subcellular localization of surfactant-associated glycoproteins in human lung. *Lab. Invest.* **52**, 657–669 (1985).

[CAS](#) [PubMed](#) [Google Scholar](#)

13. 13.

Hermans, C. & Bernard, A. Lung epithelium-specific proteins: characteristics and potential applications as markers. *Am. J. Respir. Crit. Care Med.* **159**, 646–678 (1999).

[CAS](#) [PubMed](#) [Google Scholar](#)

14. 14.

Franks, T. J. et al. Resident cellular components of the human lung: current knowledge and goals for research on cell phenotyping and function. *Proc. Am. Thorac. Soc.* **5**, 763–766 (2008).

[PubMed](#) [Google Scholar](#)

15. 15.

Tang, F. et al. mRNA-Seq whole-transcriptome analysis of a single cell. *Nat. Methods* **6**, 377–382 (2009).

[CAS](#) [PubMed](#) [Google Scholar](#)

16. 16.

Gawad, C., Koh, W. & Quake, S. R. Single-cell genome sequencing: current state of the science. *Nat. Rev. Genet.* **17**, 175–188 (2016).

[CAS](#) [PubMed](#) [Google Scholar](#)

17. 17.

Treutlein, B. et al. Reconstructing lineage hierarchies of the distal lung epithelium using single-cell RNA-seq. *Nature* **509**, 371–375 (2014).

[ADS](#) [CAS](#) [PubMed](#) [PubMed Central](#) [Google Scholar](#)

18. 18.

Reyfman, P. A. et al. Single-cell transcriptomic analysis of human lung provides insights into the pathobiology of pulmonary fibrosis. *Am. J. Respir. Crit. Care Med.* **199**, 1517–1536 (2019).

[CAS](#) [PubMed](#) [PubMed Central](#) [Google Scholar](#)

19. 19.

Braga, F. A. V. et al. A cellular census of human lungs identifies novel cell states in health and in asthma. *Nat. Med.* **25**, 1153–1163 (2019).

[Google Scholar](#)

20. 20.

Picelli, S. et al. Full-length RNA-seq from single cells using Smart-seq2. *Nat. Protoc.* **9**, 171–181 (2014).

[CAS](#) [PubMed](#) [Google Scholar](#)

21. 21.

Blondel, V. D. et al. Fast unfolding of communities in large networks. *J. Stat. Mech.* **2008**, P10008 (2008).

[MATH](#) [Google Scholar](#)

22. 22.

Howitt, M. R. et al. Tuft cells, taste-chemosensory cells, orchestrate parasite type 2 immunity in the gut. *Science* **351**, 1329–1333 (2016).

[ADS](#) [CAS](#) [PubMed](#) [PubMed Central](#) [Google Scholar](#)

23. 23.

Rock, J. R. et al. Notch-dependent differentiation of adult airway basal stem cells. *Cell Stem Cell* **8**, 639–648 (2011).

[CAS](#) [PubMed](#) [PubMed Central](#) [Google Scholar](#)

24. 24.

Garcia, S. R. et al. Single-cell RNA sequencing reveals novel cell differentiation dynamics during human airway epithelium regeneration. Preprint at <https://doi.org/10.1101/451807> (2018).

25. 25.

Nabhan, A. N., Brownfield, D. G., Harbury, P. B., Krasnow, M. A. & Desai, T. J. Single-cell Wnt signaling niches maintain stemness of alveolar type 2 cells. *Science* **359**, 1118–1123 (2018).

[ADS](#) [CAS](#) [PubMed](#) [PubMed Central](#) [Google Scholar](#)

26. 26.

Zacharias, W. J. et al. Regeneration of the lung alveolus by an evolutionarily conserved epithelial progenitor. *Nature* **555**, 251–255 (2018).

[ADS](#) [CAS](#) [PubMed](#) [PubMed Central](#) [Google Scholar](#)

27. 27.

Stan, R. V. et al. The diaphragms of fenestrated endothelia: gatekeepers of vascular permeability and blood composition. *Dev. Cell* **23**, 1203–1218 (2012).

[CAS](#) [PubMed](#) [PubMed Central](#) [Google Scholar](#)

28. 28.

Gillich, A. et al. Capillary cell-type specialization in the alveolus. *Nature* **586**, 785–789 (2020).

[CAS](#) [PubMed](#) [Google Scholar](#)

29. 29.

Tan, S. Y. S. & Krasnow, M. A. Developmental origin of lung macrophage diversity. *Development* **143**, 1318–1327 (2016).

[CAS](#) [PubMed](#) [PubMed Central](#) [Google Scholar](#)

30. 30.

van den Brink, S. C. et al. Single-cell sequencing reveals dissociation-induced gene expression in tissue subpopulations. *Nat. Methods* **14**, 935–936 (2017).

[PubMed](#) [Google Scholar](#)

31. 31.

Zheng, G. X. Y. et al. Massively parallel digital transcriptional profiling of single cells. *Nat. Commun.* **8**, 14049 (2017).

[ADS](#) [CAS](#) [PubMed](#) [PubMed Central](#) [Google Scholar](#)

32. 32.

Shiow, L. R. et al. CD69 acts downstream of interferon- α/β to inhibit S1P1 and lymphocyte egress from lymphoid organs. *Nature* **440**, 540–544 (2006).

[ADS](#) [CAS](#) [PubMed](#) [Google Scholar](#)

33. 33.

Mackay, L. K. et al. Hobit and Blimp1 instruct a universal transcriptional program of tissue residency in lymphocytes. *Science* **352**, 459–463 (2016).

[ADS](#) [CAS](#) [PubMed](#) [Google Scholar](#)

34. 34.

Moffitt, J. R. & Zhuang, X. RNA imaging with multiplexed error-robust fluorescence *in situ* hybridization (MERFISH). *Methods Enzymol.* **572**, 1–49 (2016).

[CAS](#) [PubMed](#) [PubMed Central](#) [Google Scholar](#)

35. 35.

Wang, X. et al. Three-dimensional intact-tissue sequencing of single-cell transcriptional states. *Science* **361**, eaat5691 (2018).

[PubMed](#) [PubMed Central](#) [Google Scholar](#)

36. 36.

Eng, C. L. et al. Transcriptome-scale super-resolved imaging in tissues by RNA seqFISH. *Nature* **568**, 235–239 (2019).

[ADS](#) [CAS](#) [PubMed](#) [PubMed Central](#) [Google Scholar](#)

37. 37.

Huang, C. et al. Clinical features of patients infected with 2019 novel coronavirus in Wuhan, China. *Lancet* **395**, 497–506 (2020).

[CAS](#) [PubMed](#) [PubMed Central](#) [Google Scholar](#)

38. 38.

Limjunyawong, N., Fallica, J., Horton, M. R. & Mitzner, W. Measurement of the pressure-volume curve in mouse lungs. *J. Vis. Exp.* **52376**, 52376 (2015).

[Google Scholar](#)

39. 39.

Seeley, R. R., Stephens, T. D. & Tate, P. *Essentials of Anatomy and Physiology* 7th edn (2005).

40. 40.

Tabula Muris Consortium. A single cell transcriptomic atlas characterizes aging tissues in the mouse. *Nature* **583**, 590–595 (2019).

[Google Scholar](#)

41. 41.

van Amerongen, R., Bowman, A. N. & Nusse, R. Developmental stage and time dictate the fate of Wnt/β-catenin-responsive stem cells in the mammary gland. *Cell Stem Cell* **11**, 387–400 (2012).

[PubMed](#) [Google Scholar](#)

42. 42.

Greif, D. M. et al. Radial construction of an arterial wall. *Dev. Cell* **23**, 482–493 (2012).

[CAS](#) [PubMed](#) [PubMed Central](#) [Google Scholar](#)

43. 43.

Muzumdar, M. D., Tasic, B., Miyamichi, K., Li, L. & Luo, L. A global double-fluorescent Cre reporter mouse. *Genesis* **45**, 593–605 (2007).

[CAS](#) [PubMed](#) [Google Scholar](#)

44. 44.

Madisen, L. et al. A robust and high-throughput Cre reporting and characterization system for the whole mouse brain. *Nat. Neurosci.* **13**, 133–140 (2010).

[CAS](#) [PubMed](#) [PubMed Central](#) [Google Scholar](#)

45. 45.

Moraga, I. et al. Tuning cytokine receptor signaling by re-orienting dimer geometry with surrogate ligands. *Cell* **160**, 1196–1208 (2015).

[CAS](#) [PubMed](#) [PubMed Central](#) [Google Scholar](#)

46. 46.

Desai, T. J., Brownfield, D. G. & Krasnow, M. A. Alveolar progenitor and stem cells in lung development, renewal and cancer. *Nature* **507**, 190–194 (2014).

[ADS](#) [CAS](#) [PubMed](#) [PubMed Central](#) [Google Scholar](#)

47. 47.

Butler, A. et al. Integrating single-cell transcriptomic data across different conditions, technologies, and species. *Nat. Biotechnol.* **36**, 411–420 (2018).

[CAS](#) [PubMed](#) [PubMed Central](#) [Google Scholar](#)

48. 48.

Finak, G. et al. MAST: a flexible statistical framework for assessing transcriptional changes and characterizing heterogeneity in single-cell RNA sequencing data. *Genome Biol.* **16**, 278 (2015).

[PubMed](#) [PubMed Central](#) [Google Scholar](#)

49. 49.

Amberger, J. S. et al. OMIM.org: Online Mendelian Inheritance in Man (OMIM), an online catalog of human genes and genetic disorders. *Nucleic Acids Res.* **43**, D789–D798 (2014).

[PubMed](#) [PubMed Central](#) [Google Scholar](#)

50. 50.

Buniello, A. et al. The NHGRI-EBI GWAS Catalog of published genome-wide association studies, targeted arrays and summary statistics 2019. *Nucleic Acids Res.* **47** (D1), D1005–D1012 (2019).

[CAS](#) [PubMed](#) [Google Scholar](#)

[Download references](#)

Acknowledgements

We are grateful to the tissue donors and the clinical staff at Stanford Medical Center who made tissue collection possible, especially J. Benson and E. Chen. We are especially grateful to Jim Spudich who spurred this study. We also thank the Stanford Shared FACS Facility for their expertise and sorting services, especially L. Nichols and M. Weglarz; members of Chan Zuckerberg Biohub and Quake laboratory who supported this work, particularly A. McGeever, B. Yu, B. Jones and S. Kolluru; M. Kumar for discussions on annotation of stromal cells; and M. Petersen for illustrating the lung schematic (Fig. 1b) and C. Kao for help with figure formatting. Some computing for this project was performed on the Sherlock cluster; we thank Stanford University and the Stanford Research Computing Center for providing computational resources and support that contributed to the results. We thank J. Spudich and members of the Krasnow laboratory for discussions and comments on the manuscript, and A. Lozano for discussions on bioinformatic analyses. This work was supported by funding from the Chan Zuckerberg Biohub (S.R.Q.), the Howard Hughes Medical Institute, National Institutes of Health, and the Vera Moulton Wall Center for Pulmonary Vascular Disease (M.A.K.), and the Ludwig Cancer Center at Stanford (I.L.W.). K.J.T was supported by a Paul and Mildred Berg Stanford Graduate Fellowship. M.A.K. is an investigator of the Howard Hughes Medical Institute.

Author information

Author notes

1. Ahmad N. Nabhan

Present address: Genentech, South San Francisco, CA, USA

2. Lolita Penland

Present address: Calico Life Sciences, South San Francisco, CA, USA

3. Yasuo Mori

Present address: Department of Medicine and Biosystemic Science,
Kyushu University Graduate School of Medical Science, Fukuoka,
Japan

4. Jun Seita

Present address: Medical Sciences Innovation Hub Program, RIKEN,
Tokyo, Japan

5. These authors contributed equally: Kyle J. Travaglini, Ahmad N.
Nabhan

Affiliations

1. Department of Biochemistry, Howard Hughes Medical Institute, Stanford University School of Medicine, Stanford, CA, USA

Kyle J. Travaglini, Ahmad N. Nabhan, Astrid Gillich, Stephen Chang & Mark A. Krasnow

2. Vera Moulton Wall Center for Pulmonary Vascular Disease, Stanford University School of Medicine, Stanford, CA, USA

Kyle J. Travaglini, Ahmad N. Nabhan, Astrid Gillich, Stephen Chang, Ross J. Metzger & Mark A. Krasnow

3. Chan Zuckerberg Biohub, San Francisco, CA, USA

Lolita Penland, Rene V. Sit, Norma Neff & Stephen R. Quake

4. Institute for Stem Cell Biology and Regenerative Medicine, Stanford University School of Medicine, Stanford, CA, USA

Rahul Sinha, Stephanie D. Conley, Yasuo Mori, Jun Seita & Irving L. Weissman

5. Department of Pathology, Stanford University School of Medicine, Stanford, CA, USA

Rahul Sinha, Stephanie D. Conley, Yasuo Mori, Jun Seita, Gerald J. Berry & Irving L. Weissman

6. Department of Cardiothoracic Surgery, Stanford University School of Medicine, Stanford, CA, USA

Joseph B. Shrager

7. Department of Pediatrics, Division of Cardiology, Stanford University School of Medicine, Stanford, CA, USA

Ross J. Metzger

8. Department of Pediatrics, Pulmonary Medicine, Stanford University School of Medicine, Stanford, CA, USA

Christin S. Kuo

9. Ludwig Center for Cancer Stem Cell Research and Medicine, Stanford University School of Medicine, Stanford, CA, USA

Irving L. Weissman

10. Stanford Cancer Institute, Stanford University School of Medicine, Stanford, CA, USA

Irving L. Weissman

11. Department of Bioengineering, Stanford University, Stanford, CA, USA

Stephen R. Quake

Authors

1. Kyle J. Travaglini

[View author publications](#)

You can also search for this author in [PubMed](#) [Google Scholar](#)

2. Ahmad N. Nabhan

[View author publications](#)

You can also search for this author in [PubMed](#) [Google Scholar](#)

3. Lolita Penland

[View author publications](#)

You can also search for this author in [PubMed](#) [Google Scholar](#)

4. Rahul Sinha

[View author publications](#)

You can also search for this author in [PubMed](#) [Google Scholar](#)

5. Astrid Gillich

[View author publications](#)

You can also search for this author in [PubMed](#) [Google Scholar](#)

6. Rene V. Sit

[View author publications](#)

You can also search for this author in [PubMed](#) [Google Scholar](#)

7. Stephen Chang

[View author publications](#)

You can also search for this author in [PubMed](#) [Google Scholar](#)

8. Stephanie D. Conley

[View author publications](#)

You can also search for this author in [PubMed](#) [Google Scholar](#)

9. Yasuo Mori

[View author publications](#)

You can also search for this author in [PubMed](#) [Google Scholar](#)

10. Jun Seita

[View author publications](#)

You can also search for this author in [PubMed](#) [Google Scholar](#)

11. Gerald J. Berry

[View author publications](#)

You can also search for this author in [PubMed](#) [Google Scholar](#)

12. Joseph B. Shrager

[View author publications](#)

You can also search for this author in [PubMed](#) [Google Scholar](#)

13. Ross J. Metzger

[View author publications](#)

You can also search for this author in [PubMed](#) [Google Scholar](#)

14. Christin S. Kuo

[View author publications](#)

You can also search for this author in [PubMed](#) [Google Scholar](#)

15. Norma Neff

[View author publications](#)

You can also search for this author in [PubMed](#) [Google Scholar](#)

16. Irving L. Weissman

[View author publications](#)

You can also search for this author in [PubMed](#) [Google Scholar](#)

17. Stephen R. Quake

[View author publications](#)

You can also search for this author in [PubMed](#) [Google Scholar](#)

18. Mark A. Krasnow

[View author publications](#)

You can also search for this author in [PubMed](#) [Google Scholar](#)

Contributions

K.J.T., A.N.N., L.P., R.S., A.G., C.S.K., R.J.M. and M.A.K. conceived the project and designed the lung and blood cell isolation strategy, J.B.S. and

C.S.K. designed clinical protocols, reviewed clinical histories and coordinated patient care teams to obtain profiled tissues, G.B. provided expert clinical evaluation and micrographs of donor tissue histology, K.J.T., A.N.N., R.S. and A.G. processed tissue to single-cell suspensions, K.J.T., A.N.N., L.P. A.G., R.S. and S.D.C. sorted cells for SS2, A.N.N., L.P., S.C. and R.V.S. prepared sequencing libraries, and K.J.T., R.V.S. and L.P. processed and aligned sequencing data. R.S., J.S. and Y.M. performed and supervised bulk mRNA sequencing on defined immune populations. K.J.T., A.N.N., R.S. A.G. and R.J.M. provided tissue expertise and annotated cell types. K.J.T., A.N.N. and M.A.K. designed and implemented bioinformatic methods and interpreted results. K.J.T., A.N.N. and A.G. performed follow up stains. M.A.K., S.R.Q., N.F.N., I.L.W., C.S.K. and R.J.M. supervised and supported the work. K.J.T., A.N.N. and M.A.K. wrote the manuscript, and all authors reviewed and edited the manuscript.

Corresponding authors

Correspondence to [Stephen R. Quake](#) or [Mark A. Krasnow](#).

Ethics declarations

Competing interests

The authors declare no competing interests.

Additional information

Peer review information *Nature* thanks Shalev Itzkovitz and the other, anonymous, reviewer(s) for their contribution to the peer review of this work.

Publisher's note Springer Nature remains neutral with regard to jurisdictional claims in published maps and institutional affiliations.

Extended data figures and tables

Extended Data Fig. 1 Strategy for scRNA-seq and annotation of human lung and blood cells.

a, Workflow for capture and mRNA sequencing of single cells from the healthy unaffected regions indicated (D, distal; M, medial; P, proximal lung tissue; see **d**) of fresh, surgically resected lungs with focal tumours from three participants (1, 2 and 3) and their matched peripheral blood. Cell representation was balanced among the major tissue compartments (endothelial, immune, epithelial and stroma) by magnetic and fluorescence activated cell sorting (MACS and FACS) using antibodies for the indicated surface markers (CD31, CD45, EPCAM). Cell capture and scRNA-seq was done using 10x droplet technology or SS2 analysis of plate-sorted cells. Number of profiled cells from each compartment are shown in parentheses. For blood, immune cells were isolated on a high density Ficoll gradient, and unsorted cells profiled by 10x and sorted cells (using canonical markers for the indicated immune populations) by SS2. Total cell number (all three participants) and median number of expressed genes per cell are indicated for each method. **b**, Cell clustering and annotation pipeline. Cell expression profiles were computationally clustered by nearest-neighbour relationships and clusters were then separated into tissue compartments based on expression of compartment-specific markers (*EPCAM* (blue), *CLDN5* (red), *COL1A2* (green), and *PTPRC* (purple)), as shown for *t*-distributed stochastic neighbour embedding (*t*-SNE) plot of lung and blood cell expression profiles obtained by 10x from participant 3. Cells from each tissue compartment were then iteratively re-clustered until differentially-expressed genes driving clustering were no longer biologically meaningful. Cell cluster annotation was based on expression of canonical marker genes from the literature, markers found through RNA sequencing of purified cell populations (bulk RNA markers), ascertained tissue location, and inferred molecular function from differentially-expressed genes. **c**, Heat map of pairwise Pearson correlations of the average expression profile of each cluster in the combined 10x dataset plus SS2 analysis of neutrophils. *n* values are in [Supplementary Table 2](#). Tissue compartment and identification number of each of the 58 clusters are indicated. For more details on statistics and reproducibility, see [Methods](#). **d**, Representative micrographs of donor lungs from formalin-fixed, paraffin-embedded sections stained with haematoxylin and eosin showing bronchi, bronchioles, submucosal

glands, arteries, veins and alveoli near regions used for scRNA-seq. Staining repeated on at least five sections (encompassing different anatomical regions) from each participant used for scRNA-seq. Scale bar, 100 μ m.

Extended Data Fig. 2 Selectively expressed RNA markers of human immune cell types from bulk mRNA sequencing of FACS-purified immune cells.

a, Heat map of RNA expression of the most selectively-expressed genes from bulk mRNA sequencing of the indicated FACS-sorted immune populations ([Supplementary Table 3](#)). This dataset provided RNA markers for human immune cell populations that have been classically defined by their cell surface markers. **b**, Heat map of pairwise Pearson correlation scores between the average expression profiles of the immune cell types indicated that were obtained from bulk mRNA sequencing (BulkSeq, **a**) to the average scRNA-seq profiles of human blood immune cells in the SS2 dataset annotated by canonical markers and enriched RNA markers from the bulk RNA-seq analysis. The highest correlation in overall gene expression (white dot) of each annotated immune cell cluster in the SS2 dataset (columns) was to the bulk RNA-seq of the same FACS-purified immune population (rows), supporting the scRNA-seq immune cluster annotations (red squares). Cell numbers are in [Supplementary Table 2](#). For more details on statistics and reproducibility, see [Methods](#).

Extended Data Fig. 3 Expression differences and localization of lung cell states and canonical epithelial and endothelial subtypes.

a, Proliferative signature score (based on expression of indicated genes in cells from 10x dataset; cell numbers are in [Supplementary Table 2](#)) of each cluster of basal cells, T and natural killer cells, and macrophages. Three clusters had high scores: proliferating basal cells (Bas-p), proliferating natural killer/T cells (NK/T-p), and proliferating macrophages. **b**, Dot plot of mean level of expression (dot intensity, grey scale) of indicated basal cell markers and percent of cells in population with detected expression (dot

size) for 10x dataset. Note partial overlap of markers among different basal populations. **c**, Immunostaining of adult human pseudostratified airway for differentiation marker HES1 (green) in basal cells (marked by KRT5, red) with DAPI (nuclear) counter stain (blue). Scale bars, 10 μ m. Note apical processes extending from HES1 $^+$ basal cells (arrowheads) indicating migration away from basal lamina as they differentiate. Other HES1 $^+$ cells have turned off basal marker KRT5. Dashed outlines, basal cell nuclei. Quantification shows fraction of basal cells (cuboidal KRT5 $^+$ cells on basement membrane) and differentiating basal (Bas-d) cells (KRT5 $^+$ cells with apical processes) that were HES1 $^+$. n denotes KRT5 $^+$ cells scored in sections of two human lungs with staining repeated on four participants. **d**, Immunostaining of adult human pseudostratified airway for proliferation marker MKI67 (green) in basal cells (marked by KRT5, red) with DAPI counter stain (blue). Scale bars, 5 μ m. Quantification shows abundance of proliferating (MKI67-expressing) basal cells in pseudostratified (pseudo) and simple epithelial airways; n denotes KRT5 $^+$ cells scored in sections of two human lungs with staining repeated on four participants. **e**, Relative abundance of epithelial and stromal cell types in scRNA-seq analysis of human lung samples obtained from proximal (blue; 10x cells from P3) and distal (red; 10x cells from D1a, D1b, D2, D3) lung sites. In addition to the expected proximal enrichment of some airway cell types (goblet cells, ionocytes, neuroendocrine cells) and distal enrichment of alveolar cell types (AT1, AT2, AT2-signalling, myofibroblasts), note three bracketed pairs of related cell types (ciliated and proximal ciliated; basal and proximal basal (Bas-px) cells; myofibroblasts and fibromyocytes) with one of them proximally enriched. Relative enrichment values are provisional because they can be influenced by efficiency of collection during cell dissociation and isolation. Cell number for proximal cells are (from left to right): 357, 275, 73, 175, 153, 191, 39, 145, 57, 24, 20, 10, 328, 1,505, 235, 25 and 70; and for distal cells are: 537, 806, 15, 197, 4, 58, 6, 14, 336, 0, 2, 1, 467, 2,095, 434, 198 and 28. **f**, RNAscope smFISH and quantification for general basal marker KRT5 (red) and proximal basal cell marker SERPINB3 (white) with DAPI counter stain (blue) and ECM autofluorescence (green) on proximal, pseudostratified bronchi and distal, simple bronchioles. Scale bars, 20 μ m (inset, 10 μ m). Note enrichment of proximal basal cells (KRT5 SERPINB3 double positive, yellow arrowhead and box) enrichment at base of pseudostratified airways. SERPINB3 was not detected in simple airways,

indicating that basal cells (but not proximal basal cells) are present there. Staining repeated on two participants. **g**, Dot plot of expression in ciliated and proximal ciliated cells of canonical (general) ciliated cell markers and specific proximal ciliated markers (in 10x dataset). **h**, smFISH and quantification of human pseudostratified epithelial (left) and simple epithelial (right) airways for general ciliated marker *C20orf85* (white) and proximal ciliated marker *DHRS9* (red) with DAPI counterstain (blue) and ECM autofluorescence (green). Note restriction of proximal ciliated cells to pseudostratified airways. Scale bars, 10 µm. Staining repeated on two participants. **i**, Heat map of expression of representative general AT2, AT2 selective, and AT2-signalling selective marker genes in AT2 and AT2-signalling human lung cells (SS2 data). AT2 selective markers include negative regulators of Hedgehog and Wnt signalling pathways (for example, *HHIP* and *WIF1*, highlighted red) and AT2-signalling selective markers include Wnt ligands, receptors and transcription factors (for example, *WNT5A*, *LRP5* and *TFC7L2* highlighted green). Values shown are $\ln(\text{CPM} + 1)$ for 50 randomly selected cells in each cluster (SS2 data). **j**, Dot plot of expression of endothelial markers (10x dataset). **k**, Micrograph (low magnification, left) of bronchial vessel (boxed region) showing vessel location near airway (dotted outline). smFISH for general endothelial marker *CLDN5* (red, centre), bronchial vessel-specific markers *MYC* (green) and Bro1-specific marker *ACKR1* (red, right) on serial sections of bronchial vessel cells (arrowheads), co-stained for DAPI (blue). Scale bar, 10 µm. Quantification shows relative abundance of Bro1 and Bro2 cells. Staining repeated on two participants. **l–n**, smFISH and quantification of vessel types indicated (dotted outlines) showing vein marker *ACKR1* (red; **l**), artery marker *GJA5* (red; **m**), lymphatic marker *CCL21* (red; **n**), and general endothelial marker *CLDN5* with DAPI counter stain (blue) and ECM autofluorescence (green). Scale bars, 50 µm (**l**), 30 µm (**m**) and 40 µm (**n**). Staining repeated on two participants. For more details on statistics and reproducibility, see [Methods](#). [Source data](#)

[Extended Data Fig. 4 Markers and lung localization of stromal and dendritic subtypes.](#)

a–d, smFISH for RNA of indicated marker genes of alveolar fibroblasts (**a**, **b**) and adventitial fibroblasts (**c**, **d**) in adult human (**a**, **c**) and mouse (**b**, **e**)

alveolar (**a**, **b**) and pulmonary artery (**c**, **d**) sections. ECM autofluorescence (green; **a**, **c**) to show blood vessels; Elastin (green, **b**, **d**); DAPI counterstain (blue, all panels). Staining repeated on two human participants or three mice. **a**, smFISH probes: general fibroblast marker *COL1A2* (white) and alveolar fibroblast-selective marker *GPC3* (red). Arrowheads denote alveolar fibroblasts. Inset, close-up of boxed region showing merged (top) and split channels of an alveolar fibroblast. Scale bars, 20 μm (inset 60 μm). **b**, smFISH probes: alveolar fibroblast-selective markers *Slc7a10* (white) and *Frfr4* (red). Elastin (green) shows alveolar entrance ring. Arrowheads denote alveolar fibroblasts. Scale bar, 5 μm . **c**, smFISH probes: general fibroblast marker *COL1A2* (white) and adventitial fibroblast -selective marker *SERPINF1* (red). Adventitial fibroblasts (some indicated by arrowheads) localize around blood vessels (ECM, green). Inset, close-up of boxed region showing merged (top) and split channels of an adventitial fibroblast. Dashed line denotes the artery boundary. Scale bars, 30 μm (inset 90 μm). **d**, smFISH probes: adventitial fibroblast-selective markers *Pi16* (white) and *Serpinf1* (red). Adventitial fibroblasts (arrowheads) surround artery (marked by elastin, green). Scale bar, 10 μm . **e**, Heat map of expression of representative general, adventitial-selective, and alveolar-selective fibroblast markers in 50 randomly selected cells from adventitial (left) and alveolar (right) fibroblast clusters (SS2 dataset). Note specialization (highlighted red) in growth factors (AdvF: *PDGFRL*, *IGFBP4*; AlvF: *FGFR4*, *VEGFD*) and morphogen (AdvF: *SFRP2*; AlvF: *NKD1*, *DKK3*) signalling or regulation. **f**, **g**, smFISH and quantification of cell abundance in human alveolar (**f**) and pseudostratified epithelial airway (**g**) sections probed for myofibroblast and fibromyocyte marker *ASPN* (red), and for fibromyocyte and airway smooth muscle markers *COX4I2* (white; **f**) and *ACTG2* (white; **g**). ECM autofluorescence, green; DAPI counterstain, blue. Inset (**f**), boxed region showing close-up of merged (top) and split channels of *ASPN*⁺ *COX4I2*⁻ myofibroblast. Myofibroblasts and fibromyocytes (see below) probably make up remaining cells in Fig. 1f quantification. Inset (**g**), boxed regions showing close-up of merged (top) and split channels of fibromyocyte (white box) and airway smooth muscle (yellow box) cells. Fibromyocytes (white arrowheads) and airway smooth muscle (yellow arrowheads) are intermingled in wall of pseudostratified airway (dotted outline). Staining repeated on two participants. **h**, **i**, smFISH of human alveolar sections probed for general stromal marker *COL1A2*

(white), pericyte marker *COX4I2* (red; **h**), lipofibroblast marker *APOE* (red; **i**). ECM autofluorescence, green; DAPI counterstain, blue. Inset (**h**), boxed region showing close-up of pericyte. Inset (**i**), boxed region showing close-up of *COL1A2 APOE* double-positive LipF. LipF cells are intermingled among other stromal cells (single-positive *COL1A2*) and macrophages (single-positive *APOE*). Quantification in Fig. [1f](#). Scale bars, 20 μm.

Staining repeated on two participants. **j**, Dot plot of *COX4I2* expression in alveolar stromal cell types (10x dataset). **k**, Heat map of expression of dendritic cell marker genes in 50 randomly selected cells from indicated dendritic cell clusters (human blood and lung 10x datasets). Cells in all clusters express general dendritic markers including antigen presenting genes but each cluster also has its own selective markers. Red highlighted markers distinguishing the newly identified dendritic cell clusters (*IGSF21⁺*, *EREG⁺*, *TREM2⁺*) suggest different roles in asthma (*IGSF21⁺*), growth factor regulation (*EREG⁺*), and lipid handling (*TREM2⁺*). **l–n**, smFISH of adult human lung proximal and alveolar (Alv) sections as indicated probed for *IGSF21⁺* dendritic cell markers *IGSF21* (red) and *GPR34* (white) (**l**), *EREG⁺* dendritic cell marker *EREG* (red) and general dendritic cell marker *GPR183* (white) (**m**), and *TREM2⁺* dendritic cell markers *TREM2* (red) and *CHI3L1* (white) (**n**). DAPI counterstain, blue. Non-punctate signal in red channel (**l**, **n**) is erythrocyte autofluorescence. Insets, boxed regions showing merged and split channels of close-up of single dendritic cell of indicated type. Scale bars, 20 μm. Arrowheads denote double-positive cells. Quantification shows distribution of each dendritic type; note *IGSF21⁺* and *EREG⁺* dendritic cells show strong proximal enrichment. Staining repeated on two participants. **o**, t-SNE of expression profile clusters of monocytes and B, T and natural killer cells (10x dataset, participant 1, 2,622 cells). Note separate cell clusters of each immune cell type isolated from lung (no outline) and blood (dashed outline). Asterisk denotes small number of B cells isolated from the lung that cluster next to blood B cells. For more details on statistics and reproducibility, see [Methods](#). [Source data](#)

[Extended Data Fig. 5 Markers and transcription factors that distinguish human lung cell types.](#)

a, Violin plots of expression levels ($\ln(\text{UP10K} + 1)$) of the most sensitive and specific markers (gene symbols) for each human lung cell type in its tissue compartment (10x dataset). Cell numbers given in [Supplementary Table 2](#). **b**, Scheme for selecting the most sensitive and specific marker genes for each cell type using Matthews correlation coefficient (MCC). Box-and-whisker plots below show MCCs, true positive rates (TPR), and false discovery rates (FDR) for each cell type ($n = 58$) using indicated number (nGene) of the most sensitive and specific markers (10x dataset). Note all measures saturate at approximately 2–4 genes, hence simultaneous *in situ* probing of a human lung for the approximately 100–200 optimal markers would assign identity to nearly every cell. **c**, Alveolar section of human lung probed by smFISH for AT1 marker *AGER* and transcription factor *MYRF*. *MYRF* is selectively expressed in AT1 cells (arrowheads; 97% of *MYRF*⁺ cells were *AGER*⁺, $n = 250$ scored cells). Inset, boxed region showing merged and split channels of AT1 cell. Scale bar, 10 μm . Staining repeated on two participants. **d**, Alveolar section of human lung probed by smFISH for pericyte marker *COX4I2* and transcription factor *TBX5*. *TBX5* is enriched in pericytes (arrowheads, 92% of *TBX5*⁺ cells were *COX4I2*⁺, $n = 250$). Inset, boxed region showing merged and split channels of pericyte. Scale bar, 5 μm . Staining repeated on two participants. **e**, Dot plot of expression of enriched transcription factors in each lung cell type (SS2 dataset). Red text, genes not previously associated with the cell type. Red shading, transcription factors including *MYRF* that are highly enriched in AT1 cells, and *TBX5* and others highly enriched in pericytes. For more details on statistics and reproducibility, see [Methods](#).

[Extended Data Fig. 6 Lung cell targets of circulating hormones and local signals.](#)

a, Dot plot of hormone receptor gene expression in lung cells (SS2 dataset). Type and name of cognate hormones for each receptor are shown at top. Teal, broadly-expressed receptors in lung; other colours, selectively-expressed receptors (<3 lung cell types). Small coloured dots next to cell type names show selectively targeted cell types. AA, amino acid; AM, adrenomedullin; CGRP, calcitonin gene-related peptide; EPO, erythropoietin; GCCT, glucocorticoid; GH, growth hormone; GIP, gastric inhibitory peptide; IGF, insulin-like growth factor; MCCT,

mineralocorticoid; RA, retinoic acid; SST, somatostatin. **b**, Schematic of inferred pericyte cell contractility pathway and its regulation by circulating hormones (AGT, PTH) and capillary expressed signals (EDN, NO). Dots show expression of indicated pathway genes: values at left (outlined red) in each pair of dots in capillary diagram (top) show expression in Cap-a cells (aerocytes) and at right (outlined blue) show expression in general Cap cells (SS2 dataset). Note most signal genes are preferentially expressed in Cap relative to Cap-a cells. **c**, Heat maps showing number of interactions predicted by CellPhoneDB software between human lung cell types located in proximal lung regions (left panel in each pair) and distal regions (right) based on expression patterns of ligand genes ('sending cell') and their cognate receptor genes ('receiving cell') (SS2 dataset). The pair of heat maps at the top left show values for all predicted signalling interactions ('all interactions'), and other pairs show values for the indicated types of signals (growth factors, cytokines, integrins, WNT, Notch, BMP, FGF and TFG β). Predicted interactions between cell types range from 0 (lymphocyte signalling to neutrophils) to 136 (AdvF signalling to Cap-i1). Note expected relationships, such as immune cells expressing integrins to interact with endothelial cells and having higher levels of cytokine signalling relative to their global signalling, and unexpected relationships, such as fibroblasts expressing most growth factors and lack of Notch signalling originating from immune cells. For more details on statistics and reproducibility, see [Methods](#).

Extended Data Fig. 7 Lung cell expression patterns of genes implicated in lung disease.

Dot plots of expression (in SS2 dataset) of 233 lung disease genes curated from genome-wide association studies (GWAS; genome-wide association genes $\geq 10^{-20}$ significance) and Online Mendelian Inheritance in Man (OMIM). For more details on statistics and reproducibility, see [Methods](#).

Extended Data Fig. 8 Mapping cellular origins of lung disease by cell-selective expression of disease genes.

a, Dot plots of expression of lung disease genes (numbered, associated disease shown above) enriched in specific lung cell types (SS2 datasets). Red, novel cell type association of gene or disease; grey, diseases with developmental phenotype. AWS, Alagille–Watson syndrome; BBS, Bardet–Biedl syndrome; CF, cystic fibrosis; Dys, dysplasia; EDS, Ehlers–Danlos syndrome; Fam Med, familial Mediterranean; IPF, idiopathic pulmonary fibrosis; PH, pulmonary hypertension; SGB, Simpson–Golabi–Behmel; SM, smooth muscle; SMD, surfactant metabolism dysfunction; TB, tuberculosis; VDES, Van den Ende–Gupta syndrome. **b**, Dot plot of expression (SS2 dataset) of all genes implicated in pulmonary hypertension, tuberculosis and COPD or emphysema (OMIM, Mendelian disease genes from OMIM database; GWAS, genome-wide association genes $\geq 10^{-20}$ significance). Note canonical AT2 cells (red shading) express all and AT2-signalling cells (blue shading) express most. **c**, smFISH of alveolar section of adult human lung probed for in pulmonary hypertension disease gene *KCNK3* (red) and pericyte marker *COX4I2* (white) with DAPI counterstain (blue) and ECM autofluorescence (green). Note pericyte-specific expression (arrowheads, 91% of *COX4I2*⁺ pericytes were *KCNK3*⁺, $n = 77$). Scale bar, 5 μm . Cell numbers for each type given in [Supplementary Table 2](#). **d**, smFISH of alveolar section of adult human lung probed for atrioventricular (AV) dysplasia gene *ACVRL1* (red), endothelial marker *CLDN5* (white) with DAPI counterstain. Note *ACVRL1* *CLDN5* double-positive capillaries (white arrowheads, 70% of *CLDN5*⁺ capillaries were *ACVRL1*⁺, $n = 102$) and some *CLDN5* single-positive capillaries (yellow arrowheads). Scale bar, 5 μm . **e**, smFISH of alveolar section of adult human lung probed for COPD or emphysema gene *SERPINA1* and AT2 marker *SFTPC*, and DAPI. Note AT2-specific expression (arrowheads; 93% of AT2 cells were *SERPINA1*⁺, $n = 176$). Scale bar, 5 μm . For more details on statistics and reproducibility, see [Methods](#).

[Extended Data Fig. 9 Lung cell expression patterns of respiratory virus receptors.](#)

a, Dot plot showing expression in human lung cell types of entry receptors (indicated at left) for respiratory viruses (indicated at right, numbers indicate viral families) (SS2 dataset). Red shading, cell types inhaled

viruses could directly access (epithelial cells and macrophages); darker red shading shows expression values for measles receptor *NECTIN4* and rhinovirus C receptor *CDHR3*. **b**, Violin plots (left) and dot plots (immediately above violin plots) showing expression of coronavirus receptors *ACE2*, *DPP4*, and *ANPEP* in lung cell types (10x dataset, cell numbers given in [Supplementary Table 2](#)). Grey shading, cell types inhaled viruses can directly access. Doughnut plots (right) showing relative number of receptor-expressing cells of cell types viruses can directly access (shaded grey in **a**), normalized by their abundance values from [Supplementary Table 1](#) (and refined by the relative abundance values in Fig. 1 and Extended Data Figs. 3 and 4). Note prevalence of AT2 alveolar cells for *ACE2*, receptor for SARS-CoV and SARS-CoV-2, and for *DPP4*, receptor for MERS-CoV, in contrast to prevalence of macrophages for *ANPEP*, receptor for common cold causing coronavirus 229E. For more details on statistics and reproducibility, see [Methods](#).

[Extended Data Fig. 10 Lung cell expression patterns of non-respiratory virus receptors.](#)

Dot plot of expression of entry receptors for non-respiratory viruses in human lung cell types (compare with Extended Data Fig. 9a showing expression of receptors for respiratory viruses). For more details on statistics and reproducibility, see [Methods](#).

[Extended Data Fig. 11 Comparison of mouse and human gene expression profiles in homologous lung cell types and across age.](#)

a, Scatter plots showing median expression levels ($\ln(\text{CPM} + 1)$) in indicated cell types of each expressed human gene and mouse orthologue (mouse and human SS2 datasets, human and mouse cell numbers given in Supplementary Tables 2 and 6, respectively). Note tens to hundreds of genes that show a 20-fold or greater expression difference (and $P < 0.05$, MAST) between species (red dots, gene names indicated for some and total number given above). Basophil/mast cell 1 (Bas/Ma 1) cells have the most differentially expressed genes (343), and CD4⁺ M/E T cells have the least

(79). Pearson correlation scores (R values) between the average mouse and human gene expression profiles for each cell type are indicated. ‘Mm()’ and ‘Hs()’ denotes genes in which duplications between mouse and human were collapsed to HomologyID. **b**, Heat map showing global transcriptome Pearson correlation between indicated human and mouse epithelial cells (SS2 dataset, human and mouse cell numbers given in Supplementary Tables 2 and 6, respectively). Red outline denotes homologous cell types based on classical markers described in [Supplementary Table 6](#). White dot denotes human-to-mouse correlation. **c**, Dot plot of expression of canonical goblet cell markers *MUC5B* and *MUC5AC* and transcription factor *SPDEF* in mouse (left) and human (right) goblet cells. **d**, Scatter plot showing average expression levels (dots) across all cells (‘pseudo-bulk’ lung expression) of each expressed human gene and mouse orthologue (mouse and human SS2 datasets). Scale, $\ln(\text{CPM} + 1)$. Pearson correlation (R values) between the average mouse and human gene expression profiles are indicated. **e**, Scatter plots comparing median expression levels ($\ln(\text{CPM} + 1)$) in indicated mouse lung cell types of each expressed gene at age 3 months (x axis) and 24 months (y axis) in SS2 datasets from Tabula Muris Senis⁴⁰ (cell numbers given in [Supplementary Table 6](#)). Pearson correlation scores between average gene expression profile for each cell type at each age are indicated (R values), along with number of genes (red dots) showing 20-fold or greater expression difference (and $P < 0.05$, MAST) between ages. Names of some genes are given next to the corresponding red dot. For more details on statistics and reproducibility, please see [Methods](#).

[Extended Data Fig. 12 Patterns of conserved and divergent gene expression across human and mouse lung cell types.](#)

a, Dot plots of *PTPRC* and *MYL6* expression in mouse and human lung cell types (SS2 datasets) showing two examples of conserved (type 0) expression pattern. Blue shading, homologous cell types with conserved expression. **b**, Dot plots showing gain of expression (type 1 change) in several human cell types of *RNASE1* (left) and all human cell types of *TRIM38* (right). Red shading, cell types with divergent (gained) expression. **c**, Alveolar section of adult mouse lung probed by smFISH for general alveolar epithelial marker *Nkx2-1*, AT2 marker *Sftpc*, and transcription

factor *Myrf*. Note *Myrf* is selectively expressed in mouse AT1 cells (*Nkx2-1⁺* *Sftpc⁻* cells), as it is in humans (Extended Data Fig. [6c](#)). Scale bar, 5 μm. Staining repeated on three mice. **d**, Dot plots of expression of CGRP and ADM hormone receptor genes showing expansion of expression (type 2 change) in human endothelial cells (10x data sets). **e**, Dot plots of expression of emphysema-associated gene *SERPINA1* showing switched expression (type 3 change) from mouse pericytes (top) to human AT2 cells (bottom) (SS2 datasets). **f**, Dot plots comparing expression and conservation of HHIP with those of other Hedgehog pathway genes including ligands (SHH, DHH, IHH), receptors (PTCH1, PTCH2, SMO), and transducers (GLI1, GLI2, GLI3) (SS2 datasets). **g**, Dot plots of expression of serous cell markers *LTF*, *LYZ*, *BPIFBP1* and *HP* showing switched expression (type 3 change) from mouse airway epithelial cells to human serous cells, which mice lack (asterisk). Dot plots of expression of lipid handling genes *APOE*, *PLIN2* and *FST* show switched expression (type 3 change) from mouse alveolar stromal cells to human lipofibroblasts, which mice lack (asterisks). ‘Mm()’ or ‘Hs()’, genes in which duplications between mouse and human were collapsed to HomologyIDs (10x and SS2 datasets). **h**, Pie chart of fraction of expressed genes in lung showing each of the four types of evolutionary changes in cellular expression patterns from mouse to human. Histogram below shows number of lung cell types that the 602 genes with perfectly conserved cellular expression patterns (type 0) are expressed in; note that almost all are expressed in either a single cell type (67%) or nearly all cell types (33%). For more details on statistics and reproducibility, see [Methods](#).

Supplementary information

Supplementary Data

Supplementary Figure 1. FACS gating strategies for human lung and peripheral blood cells. **a**, Sequential FACS data and sorting gates (red) for dissociated human lung cells from subject sample D1b (plate B001223) following MACS depletion of highly abundant immune (CD45+) and endothelial (CD31+) cells. The final sort (right) was of viable single cells from the lung epithelial (EPCAM+CD45-), immune (CD45+EPCAM-), and

stromal/endothelial (EPCAMCD45-) compartments into 384-well plates for SS2 scRNAseq. Plots are representative of FACS repeated on 3 subjects used for scRNAseq. **b**, Sequential FACS data and sorting gates (red) for white blood cells isolated on a Ficoll gradient of matched subject peripheral blood (subject 1, plate BP1). Viable, single CD235a- (non-RBC) cells were captured without additional gating (panel 4), or further sorted as CD8 T (CD8+; panel 8), CD4 T (CD4+; panel 7), B (CD19+CD3-; panel 6), NK (CD19-CD3-CD56+CD14-; panel 9), or CD14+ monocytes (CD19-CD3-CD56- CD14+; panel 9) for SS2 scRNAseq. Contours, 5% increments in cell density. Sorting on blood cells was done only for subject 1.

Reporting Summary

Supplementary Table

Supplementary Table 1. Canonical cell types (45) in the human lung and their abundances, markers, and available expression data. a, numbers of each type were calculated with their abundances and the total number of lung cells (estimated by comparing volume of lungs to the whole body). b, Canonical markers were obtained from referenced expression data or commonly used markers in the literature. c, Expression profiles captured immediately following tissue dissociation are considered primary. d, Alveoli were assumed to occupy ~90% of the total lung volume for all estimations. e, Inferred from mean relative abundance in proximal, medial and distal airway epithelium. f, Calculated by stereology g, Resin casts showed similar surface area of arteries and veins. h, Vascular smooth muscle is estimated to be slightly more abundant than airway smooth muscle. i, abundance of a more general cell type was split evenly. j, inferred from impression of light or electron microscopy. k, inferred from histological abundance in nonperfused healthy tissue. l, inferred from abundance among immune cells with FACS. m, Calculated using microfluidic capture.

Supplementary Table

Supplementary Table 2. Human lung cell cluster identities, abundances, and locations. Cell numbers are stratified by type, subject, and sequencing

technology. Cell abbreviations indicated are used throughout.

Supplementary Table

Supplementary Table 3. Surface markers used to isolate canonical immune cell types in bulk mRNA sequencing. See Methods for details on antibodies.

Supplementary Table

Supplementary Table 4. Enriched markers found in each cluster, with transcription factors, receptors/ligands, and disease associated genes annotated. Includes all enriched genes for each type ($p\text{-val} > 0.05$, MAST, downsampled cells per group to 100 for SS2 clusters or 500 for 10x clusters). Abbreviations: avg_logFC, the natural log of the average fold change between the cell type and other cell types in its tissue compartment; pct_in_cluster, percentage of cells within the cluster that express the gene; pct_out_cluster, percentage of cells outside cluster that express the gene; p_val_adj, p-value with Bonferroni correction applied; TF, transcription factor; OMIM, Online Mendelian Inheritance in Man; GWAS, genome wide association study.

Supplementary Table

Supplementary Table 5. P-value and scores of each CellPhoneDB Receptor-Ligand interaction from each cluster. Expression scores are given for significant ($p > 0.1$, CellPhoneDB statistical framework) pairwise interactions between all SS2 cells (cell numbers given in Supplementary Table 2). Table includes all 1,085 receptor-ligand pairs and all pairwise cell type combinations. Abbreviations: partner_a, cellphonedb ID for the first interaction partner protein; partner_b, cellphonedb ID for the second interaction partner protein; source, reference from cellphonedb; secreted, whether the ligand is secreted or membrane bound; is_integrin, whether the interaction includes an integrin complex.

Supplementary Table

Supplementary Table 6. Mouse lung cell cluster identities and their abundances in each dataset. Cell numbers are stratified by type, mouse, and sequencing technology. Mouse-specific molecular markers are indicated.

Supplementary Table

Supplementary Table 7. Genes specific to mouse and human in each cluster and lung wide. Includes all differentially expressed genes ($p\text{-val} > 0.05$, MAST) for all SS2 cells in indicated mouse and human clusters (human and mouse cell numbers given in Supplementary Tables 2 and 6, respectively). Abbreviations: avg_logFC, the natural log of the average fold change between the mouse and human cell type indicated; pct_mouse, percentage of mouse cells within the cluster that express the gene; pct_human, percentage of human cells within the cluster that express the gene; p_val_adj, p-value with Bonferroni correction applied; enriched, gene is enriched in cluster in mouse or human.

Supplementary Table

Supplementary Table 8. Evolutionary changes in cellular patterns of lung gene expression between mouse and human SS2 cells. Numbers of genes and percentages are mean ($\pm \text{SEM}$) from using a median expression cutoff minus 0 to 2 standard deviations (0.25 increments) and a median percent cutoff plus 0 to 2 standard deviations (0.25 increments). Human and mouse cell numbers given in Supplementary Tables 2 and 6, respectively.

Supplementary Table

Supplementary Table 9. Evolutionary and functional classes of genes. Includes genes conserved between mouse and human. Abbreviations: Evo type, evolutionary scenario gene falls into, with NA for genes not expressed; Gene class, type of gene (receptor, ligand, enzyme, transcription factor, etc); conserved clusters, number of homologous clusters gene where gene is expressed in both mouse and human; Human specific clusters, number of homologous clusters where the gene is only expressed in human; Mouse specific clusters, above for mouse.

Source data

[Source Data Fig. 1](#)

[Source Data Extended Data Fig. 3](#)

[Source Data Extended Data Fig. 4](#)

Rights and permissions

[Reprints and Permissions](#)

About this article



Check for
updates

Cite this article

Travaglini, K.J., Nabhan, A.N., Penland, L. *et al.* A molecular cell atlas of the human lung from single-cell RNA sequencing. *Nature* **587**, 619–625 (2020). <https://doi.org/10.1038/s41586-020-2922-4>

[Download citation](#)

- Received: 24 August 2019
- Accepted: 26 August 2020
- Published: 18 November 2020
- Issue Date: 26 November 2020
- DOI: <https://doi.org/10.1038/s41586-020-2922-4>

Comments

By submitting a comment you agree to abide by our [Terms](#) and [Community Guidelines](#). If you find something abusive or that does not comply with our terms or guidelines please flag it as inappropriate.

[Download PDF](#)

This article was downloaded by **calibre** from <https://www.nature.com/articles/s41586-020-2922-4>

| [Section menu](#) | [Main menu](#) |

- Article
- [Published: 28 October 2020](#)

Macrophage-derived glutamine boosts satellite cells and muscle regeneration

- [Min Shang](#) [ORCID: orcid.org/0000-0003-4511-4290^{1,2}](#),
- [Federica Cappellessa^{1,2}](#),
- [Ricardo Amorim^{1,2,3,4,5}](#),
- [Jens Serneels^{1,2}](#),
- [Federico Virga^{1,2,6,7}](#),
- [Guy Eelen](#) [ORCID: orcid.org/0000-0003-3354-5819^{8,9}](#),
- [Stefania Carobbio¹⁰](#),
- [Melvin Y. Rincon^{11,12,13}](#),
- [Pierre Maechler](#) [ORCID: orcid.org/0000-0002-2005-1433¹⁰](#),
- [Katrien De Bock](#) [ORCID: orcid.org/0000-0001-8232-4663¹⁴](#),
- [Ping-Chih Ho](#) [ORCID: orcid.org/0000-0003-3078-3774¹⁵](#),
- [Marco Sandri^{16,17,18}](#),
- [Bart Ghesquière^{19,20}](#),
- [Peter Carmeliet^{8,9}](#),
- [Mario Di Matteo](#) [ORCID: orcid.org/0000-0001-7811-7450^{1,2}](#),
- [Emanuele Berardi](#) ^{1,2 na1 nAff22} &
- [Massimiliano Mazzone](#) [ORCID: orcid.org/0000-0001-8824-4015^{1,2,21 na1}](#)

[Nature](#) volume 587, pages626–631(2020) [Cite this article](#)

- 6752 Accesses

- 77 Altmetric
- [Metrics details](#)

Subjects

- [Cell signalling](#)
- [Immunology](#)
- [Mechanisms of disease](#)

Abstract

Muscle regeneration is sustained by infiltrating macrophages and the consequent activation of satellite cells^{1,2,3,4}. Macrophages and satellite cells communicate in different ways^{1,2,3,4,5}, but their metabolic interplay has not been investigated. Here we show, in a mouse model, that muscle injuries and ageing are characterized by intra-tissue restrictions of glutamine. Low levels of glutamine endow macrophages with the metabolic ability to secrete glutamine via enhanced glutamine synthetase (GS) activity, at the expense of glutamine oxidation mediated by glutamate dehydrogenase 1 (GLUD1). *Glud1*-knockout macrophages display constitutively high GS activity, which prevents glutamine shortages. The uptake of macrophage-derived glutamine by satellite cells through the glutamine transporter SLC1A5 activates mTOR and promotes the proliferation and differentiation of satellite cells. Consequently, macrophage-specific deletion or pharmacological inhibition of GLUD1 improves muscle regeneration and functional recovery in response to acute injury, ischaemia or ageing. Conversely, SLC1A5 blockade in satellite cells or GS inactivation in macrophages negatively affects satellite cell functions and muscle regeneration. These results highlight the metabolic crosstalk between satellite cells and macrophages, in which macrophage-derived glutamine sustains the functions of satellite cells. Thus, the targeting of GLUD1 may offer therapeutic opportunities for the regeneration of injured or aged muscles.

[Access through your institution](#)

[Change institution](#)

[Buy or subscribe](#)

Access options

Subscription info for Chinese customers

We have a dedicated website for our Chinese customers. Please go to [naturechina.com](#) to subscribe to this journal.

[Go to naturechina.com](#)

Rent or Buy article

Get time limited or full article access on ReadCube.

from \$8.99

[Rent or Buy](#)

All prices are NET prices.

Additional access options:

- [Log in](#)
- [Access through your institution](#)
- [Learn about institutional subscriptions](#)

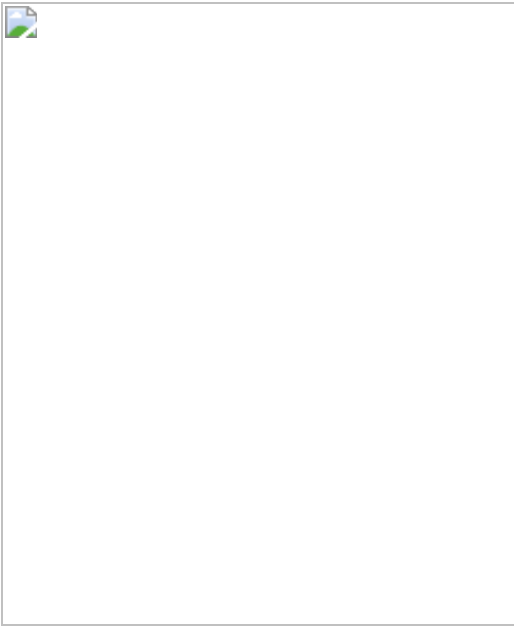
Fig. 1: GLUD1 loss in macrophages boosts the activation of satellite cells and muscle regeneration.



Fig. 2: Uptake of macrophage-derived glutamine by satellite cells boosts muscle regeneration.



Fig. 3: GLUD1 loss or inhibition in macrophages benefits damaged and aged muscles.



Data availability

RNA sequencing data have been deposited in the Gene Expression Omnibus (GEO) data repository, with accession number [GSE123825](#). Other data that support the findings of this study are available from the corresponding author (M.M.) upon reasonable request. [Source data](#) are provided with this paper.

References

1. 1.

Bentzinger, C. F., Wang, Y. X., Dumont, N. A. & Rudnicki, M. A. Cellular dynamics in the muscle satellite cell niche. *EMBO Rep.* **14**, 1062–1072 (2013).

[CAS Article](#) [Google Scholar](#)

2. 2.

Costamagna, D., Berardi, E., Ceccarelli, G. & Sampaoli, M. Adult stem cells and skeletal muscle regeneration. *Curr. Gene Ther.* **15**, 348–

363 (2015).

[CAS](#) [Article](#) [Google Scholar](#)

3. 3.

Saclier, M., Cuvellier, S., Magnan, M., Mounier, R. & Chazaud, B. Monocyte/macrophage interactions with myogenic precursor cells during skeletal muscle regeneration. *FEBS J.* **280**, 4118–4130 (2013).

[CAS](#) [Article](#) [Google Scholar](#)

4. 4.

Saclier, M. et al. Differentially activated macrophages orchestrate myogenic precursor cell fate during human skeletal muscle regeneration. *Stem Cells* **31**, 384–396 (2013).

[CAS](#) [Article](#) [Google Scholar](#)

5. 5.

Tidball, J. G. Regulation of muscle growth and regeneration by the immune system. *Nat. Rev. Immunol.* **17**, 165–178 (2017).

[CAS](#) [Article](#) [Google Scholar](#)

6. 6.

Perdiguero, E. et al. p38/MKP-1-regulated AKT coordinates macrophage transitions and resolution of inflammation during tissue repair. *J. Cell Biol.* **195**, 307–322 (2011).

[CAS](#) [Article](#) [Google Scholar](#)

7. 7.

Latroche, C. et al. Coupling between myogenesis and angiogenesis during skeletal muscle regeneration is stimulated by restorative

macrophages. *Stem Cell Reports* **9**, 2018–2033 (2017).

[CAS](#) [Article](#) [Google Scholar](#)

8. 8.

Summan, M. et al. Macrophages and skeletal muscle regeneration: a clodronate-containing liposome depletion study. *Am. J. Physiol. Regul. Integr. Comp. Physiol.* **290**, R1488–R1495 (2006).

[CAS](#) [Article](#) [Google Scholar](#)

9. 9.

Rennie, M. J. et al. Skeletal muscle glutamine transport, intramuscular glutamine concentration, and muscle–protein turnover. *Metabolism* **38** (Suppl 1), 47–51 (1989).

[CAS](#) [Article](#) [Google Scholar](#)

10. 10.

Biolo, G., Fleming, R. Y., Maggi, S. P. & Wolfe, R. R. Transmembrane transport and intracellular kinetics of amino acids in human skeletal muscle. *Am. J. Physiol.* **268**, E75–E84 (1995).

[CAS](#) [PubMed](#) [Google Scholar](#)

11. 11.

Nurjhan, N. et al. Glutamine: a major gluconeogenic precursor and vehicle for interorgan carbon transport in man. *J. Clin. Invest.* **95**, 272–277 (1995).

[CAS](#) [Article](#) [Google Scholar](#)

12. 12.

Palmieri, E. M. et al. Pharmacologic or genetic targeting of glutamine synthetase skews macrophages toward an M1-like phenotype and inhibits tumor metastasis. *Cell Rep.* **20**, 1654–1666 (2017).

[CAS](#) [Article](#) [Google Scholar](#)

13. 13.

St Pierre, B. A. & Tidball, J. G. Differential response of macrophage subpopulations to soleus muscle reloading after rat hindlimb suspension. *J. Appl. Physiol.* **77**, 290–297 (1994).

[Article](#) [Google Scholar](#)

14. 14.

Guardiola, O. et al. Induction of acute skeletal muscle regeneration by cardiotoxin injection. *J. Vis. Exp.* **119**, e54515 (2017).

[Google Scholar](#)

15. 15.

Takeda, Y. et al. Macrophage skewing by *Phd2* haplodeficiency prevents ischaemia by inducing arteriogenesis. *Nature* **479**, 122–126 (2011).

[ADS](#) [CAS](#) [Article](#) [Google Scholar](#)

16. 16.

von Maltzahn, J., Jones, A. E., Parks, R. J. & Rudnicki, M. A. Pax7 is critical for the normal function of satellite cells in adult skeletal muscle. *Proc. Natl Acad. Sci. USA* **110**, 16474–16479 (2013).

[ADS](#) [Article](#) [Google Scholar](#)

17. 17.

Zammit, P. S. Function of the myogenic regulatory factors Myf5, MyoD, myogenin and MRF4 in skeletal muscle, satellite cells and regenerative myogenesis. *Semin. Cell Dev. Biol.* **72**, 19–32 (2017).

[CAS](#) [Article](#) [Google Scholar](#)

18. 18.

Wenes, M. et al. Macrophage metabolism controls tumor blood vessel morphogenesis and metastasis. *Cell Metab.* **24**, 701–715 (2016).

[CAS](#) [Article](#) [Google Scholar](#)

19. 19.

Yang, C. et al. Glutamine oxidation maintains the TCA cycle and cell survival during impaired mitochondrial pyruvate transport. *Mol. Cell* **56**, 414–424 (2014).

[CAS](#) [Article](#) [Google Scholar](#)

20. 20.

Rodgers, J. T. et al. mTORC1 controls the adaptive transition of quiescent stem cells from G₀ to G_{Alert}. *Nature* **510**, 393–396 (2014).

[ADS](#) [CAS](#) [Article](#) [Google Scholar](#)

21. 21.

Zhang, P. et al. mTOR is necessary for proper satellite cell activity and skeletal muscle regeneration. *Biochem. Biophys. Res. Commun.* **463**, 102–108 (2015).

[CAS](#) [Article](#) [Google Scholar](#)

22. 22.

Jewell, J. L. et al. Differential regulation of mTORC1 by leucine and glutamine. *Science* **347**, 194–198 (2015).

[ADS](#) [CAS](#) [Article](#) [Google Scholar](#)

23. 23.

Rayagiri, S. S. et al. Basal lamina remodeling at the skeletal muscle stem cell niche mediates stem cell self-renewal. *Nat. Commun.* **9**, 1075 (2018).

[ADS](#) [Article](#) [Google Scholar](#)

24. 24.

Sousa-Victor, P. et al. Geriatric muscle stem cells switch reversible quiescence into senescence. *Nature* **506**, 316–321 (2014).

[ADS](#) [CAS](#) [Article](#) [Google Scholar](#)

25. 25.

Bernet, J. D. et al. p38 MAPK signaling underlies a cell-autonomous loss of stem cell self-renewal in skeletal muscle of aged mice. *Nat. Med.* **20**, 265–271 (2014).

[CAS](#) [Article](#) [Google Scholar](#)

26. 26.

Jin, L. et al. Glutamate dehydrogenase 1 signals through antioxidant glutathione peroxidase 1 to regulate redox homeostasis and tumor growth. *Cancer Cell* **27**, 257–270 (2015).

[CAS](#) [Article](#) [Google Scholar](#)

27. 27.

Liu, P. S. et al. α -Ketoglutarate orchestrates macrophage activation through metabolic and epigenetic reprogramming. *Nat. Immunol.* **18**, 985–994 (2017).

[CAS](#) [Article](#) [Google Scholar](#)

28. 28.

Obara, H., Matsubara, K. & Kitagawa, Y. Acute limb ischemia. *Ann. Vasc. Dis.* **11**, 443–448 (2018).

[Article](#) [Google Scholar](#)

29. 29.

Sayer, A. A. et al. New horizons in the pathogenesis, diagnosis and management of sarcopenia. *Age Ageing* **42**, 145–150 (2013).

[Article](#) [Google Scholar](#)

30. 30.

Vinciguerra, M., Musaro, A. & Rosenthal, N. Regulation of muscle atrophy in aging and disease. *Adv. Exp. Med. Biol.* **694**, 211–233 (2010).

[CAS](#) [Article](#) [Google Scholar](#)

31. 31.

Carobbio, S. et al. Deletion of glutamate dehydrogenase in β -cells abolishes part of the insulin secretory response not required for glucose homeostasis. *J. Biol. Chem.* **284**, 921–929 (2009).

[CAS](#) [Article](#) [Google Scholar](#)

32. 32.

He, Y. et al. Glutamine synthetase deficiency in murine astrocytes results in neonatal death. *Glia* **58**, 741–754 (2010).

[PubMed](#) [Google Scholar](#)

33. 33.

Mingote, S. et al. Genetic pharmacotherapy as an early CNS drug development strategy: testing glutaminase inhibition for schizophrenia treatment in adult mice. *Front. Syst. Neurosci.* **9**, 165 (2016).

[Article](#) [Google Scholar](#)

34. 34.

Guardiola, O. et al. Cripto regulates skeletal muscle regeneration and modulates satellite cell determination by antagonizing myostatin. *Proc. Natl Acad. Sci. USA* **109**, E3231–E3240 (2012).

[CAS](#) [Article](#) [Google Scholar](#)

35. 35.

LaFleur, M. W. et al. A CRISPR–Cas9 delivery system for in vivo screening of genes in the immune system. *Nat. Commun.* **10**, 1668 (2019).

[ADS](#) [Article](#) [Google Scholar](#)

36. 36.

Sanjana, N. E., Shalem, O. & Zhang, F. Improved vectors and genome-wide libraries for CRISPR screening. *Nat. Methods* **11**, 783–784 (2014).

[CAS](#) [Article](#) [Google Scholar](#)

37. 37.

Pasut, A., Jones, A. E. & Rudnicki, M. A. Isolation and culture of individual myofibers and their satellite cells from adult skeletal muscle. *J. Vis. Exp.* **73**, e50074 (2013).

[Google Scholar](#)

38. 38.

Casazza, A. et al. Impeding macrophage entry into hypoxic tumor areas by Sema3A/Nrp1 signaling blockade inhibits angiogenesis and restores antitumor immunity. *Cancer Cell* **24**, 695–709 (2013).

[CAS Article](#) [Google Scholar](#)

[Download references](#)

Acknowledgements

M.M. was supported by an ERC Consolidator grant (ImmunoFit), FWO-SBO (ZL3C3602), Horizon 2020 (research and innovation programme under the Marie Skłodowska-Curie grant agreement no. 766214). We thank V. van Hoef for bioinformatic analyses; S.-M. Fendt, C. Frezza, A. Musarò, G. Cossu and J.-C. Marine for advice; and S. Trusso Cafarello and S. Willox for technical support. P.C. and M.M. received long-term structural Methusalem funding by the Flemish Government; P.C. is supported by an ERC PoC (ERC-713758) and Advanced grant (EU-ERC743074). M. Shang received a grant from the China Scholarship Council (CSC); E.B. received a grant from the FWO (1525315N).

Author information

Author notes

1. Emanuele Berardi

Present address: Faculty of Rehabilitation Sciences, REVAL, Hasselt University (UHasselt), Diepenbeek, Belgium

2. These authors contributed equally: Emanuele Berardi, Massimiliano Mazzone

Affiliations

1. Laboratory of Tumor Inflammation and Angiogenesis, Center for Cancer Biology, VIB, Leuven, Belgium

Min Shang, Federica Cappellessos, Ricardo Amorim, Jens Serneels, Federico Virga, Mario Di Matteo, Emanuele Berardi & Massimiliano Mazzone

2. Laboratory of Tumor Inflammation and Angiogenesis, Center for Cancer Biology, Department of Oncology, KU Leuven, Leuven, Belgium

Min Shang, Federica Cappellessos, Ricardo Amorim, Jens Serneels, Federico Virga, Mario Di Matteo, Emanuele Berardi & Massimiliano Mazzone

3. Life and Health Sciences Research Institute, School of Medicine, University of Minho, Braga, Portugal

Ricardo Amorim

4. ICVS and 3B's PT Government Associate Laboratory, Braga, Portugal

Ricardo Amorim

5. ICVS and 3B's PT Government Associate Laboratory, Guimarães, Portugal

Ricardo Amorim

6. Molecular Biotechnology Center, University of Torino, Turin, Italy

Federico Virga

7. Department of Molecular Biotechnology and Health Sciences,
University of Torino, Turin, Italy

Federico Virga

8. Laboratory of Angiogenesis and Vascular Metabolism, Center for
Cancer Biology, VIB, Leuven, Belgium

Guy Eelen & Peter Carmeliet

9. Laboratory of Angiogenesis and Vascular Metabolism, Center for
Cancer Biology, Department of Oncology, KU Leuven, Leuven,
Belgium

Guy Eelen & Peter Carmeliet

10. Department of Cell Physiology and Metabolism, University of Geneva
Medical Center, Geneva, Switzerland

Stefania Carobbio & Pierre Maechler

11. VIB–KU Leuven Center for Brain and Disease Research, Leuven,
Belgium

Melvin Y. Rincon

12. Department of Neuroscience, KU Leuven, Leuven, Belgium

Melvin Y. Rincon

13. Centro de Investigaciones, Fundacion Cardiovascular de Colombia,
Floridablanca, Colombia

Melvin Y. Rincon

14. Department of Health Sciences and Technology, ETH, Zurich,
Switzerland

Katrien De Bock

15. Department of Oncology, Ludwig Cancer Research, University of Lausanne, Epalinges, Switzerland

Ping-Chih Ho

16. Venetian Institute of Molecular Medicine, Padua, Italy

Marco Sandri

17. Department of Biomedical Science, University of Padova, Padua, Italy

Marco Sandri

18. Department of Medicine, McGill University, Montreal, Quebec, Canada

Marco Sandri

19. Metabolomics Core Facility, Center for Cancer Biology, VIB, Leuven, Belgium

Bart Ghesquière

20. Metabolomics Core Facility, Center for Cancer Biology, Department of Oncology, KU Leuven, Leuven, Belgium

Bart Ghesquière

21. Department of Molecular Biotechnology and Health Science, Molecular Biotechnology Centre, University of Torino, Turin, Italy

Massimiliano Mazzone

Authors

1. Min Shang

[View author publications](#)

You can also search for this author in [PubMed](#) [Google Scholar](#)

2. Federica Cappellessو

[View author publications](#)

You can also search for this author in [PubMed](#) [Google Scholar](#)

3. Ricardo Amorim

[View author publications](#)

You can also search for this author in [PubMed](#) [Google Scholar](#)

4. Jens Serneels

[View author publications](#)

You can also search for this author in [PubMed](#) [Google Scholar](#)

5. Federico Virga

[View author publications](#)

You can also search for this author in [PubMed](#) [Google Scholar](#)

6. Guy Eelen

[View author publications](#)

You can also search for this author in [PubMed](#) [Google Scholar](#)

7. Stefania Carobbio

[View author publications](#)

You can also search for this author in [PubMed](#) [Google Scholar](#)

8. Melvin Y. Rincon

[View author publications](#)

You can also search for this author in [PubMed](#) [Google Scholar](#)

9. Pierre Maechler

[View author publications](#)

You can also search for this author in [PubMed](#) [Google Scholar](#)

10. Katrien De Bock

[View author publications](#)

You can also search for this author in [PubMed](#) [Google Scholar](#)

11. Ping-Chih Ho

[View author publications](#)

You can also search for this author in [PubMed](#) [Google Scholar](#)

12. Marco Sandri

[View author publications](#)

You can also search for this author in [PubMed](#) [Google Scholar](#)

13. Bart Ghesquière

[View author publications](#)

You can also search for this author in [PubMed](#) [Google Scholar](#)

14. Peter Carmeliet

[View author publications](#)

You can also search for this author in [PubMed](#) [Google Scholar](#)

15. Mario Di Matteo

[View author publications](#)

You can also search for this author in [PubMed](#) [Google Scholar](#)

16. Emanuele Berardi

[View author publications](#)

You can also search for this author in [PubMed](#) [Google Scholar](#)

17. Massimiliano Mazzone

[View author publications](#)

You can also search for this author in [PubMed](#) [Google Scholar](#)

Contributions

M. Shang performed experimental design, all experiments, data acquisition and interpretation, and wrote the manuscript. F.C. and R.A. performed in vitro assays and histology. J.S. performed all the ligations and histological staining. F.V. performed angiogenic and in vitro assays. M.Y.R. provided AAV vectors. G.E. performed Seahorse measurements. S.C. and P.M. generated GLUD1 conditional knockout mice and provided critical suggestions. K.D.B. provided the transgenic mice expressing Cre^{ERT} under the *Pax7* promoter, and provided critical edits to the text. M. Sandri provided critical edits to the text. P.-C.H. helped in the experiments with GLS-knockout macrophages and provided *Gls*^{ΔMo} mice. B.G. and P.C. supported with metabolic assays and critical suggestions in manuscript writing. M.D.M. designed and supervised all the in vitro and in vivo gene editing approaches, and provided critical edits to the text. E.B. and M.M. performed the experimental design and data analysis, conducted scientific direction and wrote the manuscript.

Corresponding authors

Correspondence to [Emanuele Berardi](#) or [Massimiliano Mazzone](#).

Ethics declarations

Competing interests

The authors declare no competing interests.

Additional information

Peer review information *Nature* thanks Terry Partridge and the other, anonymous, reviewer(s) for their contribution to the peer review of this work.

Publisher's note Springer Nature remains neutral with regard to jurisdictional claims in published maps and institutional affiliations.

Extended data figures and tables

Extended Data Fig. 1 Infiltrating GLUD1-deficient macrophages improve muscle repair.

a, Western blot for GLUD1 in BMDMs from control and *Glud1*^{ΔMo} mice. Vinculin was used as loading control. Representative image of three independent blots. **b, c**, RT-qPCR of *Glud1* in F4/80⁺ macrophages (**b**), and *Glud1* in Ly6G⁺ neutrophils (**c**), sorted from tibialis anterior muscles 1 day post-CTX ($n = 4$). **d**, Monocyte-derived macrophages (F4/80⁺GFP⁻) and tissue-resident macrophages (F4/80⁺GFP⁺) in tibialis anterior muscles 1 day post-CTX. Injured mice were CD68.eGFP transgenic mice reconstituted with wild-type (WT → CD68.eGFP) ($n = 3$) or *Glud1*^{ΔMo} bone marrow cells (Glud1 KO → CD68.eGFP) ($n = 4$). **e**, Necrotic area on H&E-stained sections from tibialis anterior muscles 6 days post-CTX. Injured mice were CD68.eGFP transgenic mice reconstituted with wild-type (WT → CD68.eGFP) or *Glud1*^{ΔMo} bone marrow cells (KO → CD68.eGFP) ($n = 6$). Baseline (B.): WT → CD68.eGFP ($n = 3$); KO → CD68.eGFP ($n = 4$). **f**, RT-qPCR of *Glud1* in F4/80⁺ macrophages, sorted from spleens upon tamoxifen-induced macrophage-specific *Glud1* deletion in *Glud1*^{L/L}; *Csf1r*^{creERT} mice (designated L/L in the figure); tamoxifen-injected littermates (*Glud1*^{L/L} and negative for *Csf1r*^{creERT}; designated WT in the figure) were used as controls ($n = 5$). **g–i**, Quantification of necrosis (**g**), apoptosis (**h**) and regenerating fibres (**i**), from tibialis anterior muscles 6 days post-CTX in tamoxifen-injected *Glud1*^{L/L}; *Csf1r*^{creERT} mice and littermate controls (*Glud1*^{L/L} and negative for *Csf1r*^{creERT}) ($n = 6$). **j–l**, Quantification of proliferating (Ki67-expressing) satellite cells in tibialis anterior muscles (**j**) 1 day post-CTX injury (control, $n = 4$; *Glud1*^{ΔMo} $n = 5$) with representative images (**k**), or in crural muscles (**l**) 3 days post-ligation ($n = 5$). The yellow arrows indicate PAX7⁺Ki67⁻ cells, and the white arrows indicate PAX7⁺Ki67⁺ cells. **m, n**, Western blot for PAX7 in tibialis anterior muscles lysates (**m**) from control or *Glud1*^{ΔMo} mice 1 day post-CTX ($n = 4$), and densitometric quantification (**n**). Vinculin was used as loading control. Numbers represent fold change versus vinculin. **o–u**, FACS quantification of total CD45⁺ leukocytes (**o**), F4/80⁺ macrophages (**p**),

Ly6G⁺ neutrophils (**q**), TCR β ⁺ total T cells (**r**), CD4⁺ T cells (**s**), CD8⁺ cytotoxic T cells (**t**) and CD45R⁺ B cells (**u**), in tibialis anterior muscles at baseline or 1 day post-CTX ($n = 3$). **v**, Laser Doppler analysis 1, 3, 6, 9 and 13 days post-ligation (control $n = 5$ for all the time points; $Glud1^{\Delta Mo}$, day 0, 1, 3 and 6, $n = 4$; day 9 and 13, $n = 3$). Toe perfusion of nonligated control was defined as 100%. **w**, Quantification of vessel density in crural muscles 14 days post-ligation (control, $n = 5$; $Glud1^{\Delta Mo}$, $n = 3$). A representative (**a–m**, **o–w**) or a pool (**n**) of at least two independent experiments is shown. Unpaired two-tailed *t*-test; NS, not significant ($P > 0.05$). Scale bars, 50 μ m. Graphs show mean \pm s.e.m. [Source data](#)

Extended Data Fig. 2 GLUD1 loss in macrophages does not alter either their recruitment or M1, M2 or wound-healing gene-expression patterns.

a, Crystal-violet-stained BMDMs, migrating towards CCL21, CCL2 or PBS (Uns) in glutamine (Q)-enriched or glutamine-reduced medium ($n = 3$). **b**, **c**, Quantification (**b**) and representative images (**c**) of F4/80 staining in ear sections with acetone (vehicle) or upon TPA-induced cutaneous rash, 3 days and 8 days after applying TPA (vehicle, $n = 4$; TPA day 3, $n = 6$ control and 5 $Glud1^{\Delta Mo}$; TPA day 8, $n = 4$). **d**, Heat map analysis of M1 and M2 macrophage gene expression in CD45⁺F4/80⁺ macrophages sorted from tibialis anterior muscles at baseline and 1 day post-CTX ($n = 4$). **e**, Heat map analysis of wound-healing gene expression in CD45⁺F4/80⁺ macrophages sorted from tibialis anterior muscles at baseline and 1 day post-CTX ($n = 4$). In **a–c**, experiments show representative values of two independent experiments; **d**, **e** show values from one single experiment. Unpaired two-tailed *t*-test; NS, not significant ($P > 0.05$). Scale bars, 50 μ m. Graphs show mean \pm s.e.m. [Source data](#)

Extended Data Fig. 3 GLUD1 loss in macrophages does not alter either M1 and M2 polarization or their related functions.

a–d, RT-qPCR of *Cxcl9* (**a**), *Tnfa* (**b**), *Arg1* (**c**) and *Il10* (**d**) in BMDMs isolated from control and $Glud1^{\Delta Mo}$ mice ($n = 3$). **e–h**, FACS analysis of different M1 (**e**, **f**) or M2 (**g**, **h**) polarization states in CD45⁺CD11b⁺F4/80⁺

macrophages isolated from tibialis anterior muscles at baseline ($n = 5$) or 1 day post-CTX ($n = 6$). **i**, Quantification of macrophage phagocytosis. BMDMs were treated with LPS or PBS (unstimulated) before the assay ($n = 3$). **j, k**, Quantification (**j**), and representative images (**k**), of total endothelial sprout length of spheroid containing HUVECs and wild-type or *Glud1^{ΔMo}* BMDMs. BMDMs were treated with IL-4 before the assay; unstimulated BMDMs were used as control (unstimulated $n = 7$; IL-4 $n = 8$). **l, m**, CD206⁺F4/80⁺ area in tibialis anterior muscles 1 day ($n = 5$) and 6 days ($n = 8$) post-CTX (**l**), or in crural muscles 3 days (control $n = 6$; *Glud1^{ΔMo}* $n = 5$), 7 days (control $n = 7$; *Glud1^{ΔMo}* $n = 5$) and 14 days (control $n = 6$; *Glud1^{ΔMo}* $n = 5$) post-ligation (**m**). All experiments show representative values of at least two independent experiments. Unpaired two-tailed *t*-test; NS, not significant ($P > 0.05$). Scale bars, 50 μ m. Graphs show mean \pm s.e.m. [Source data](#)

Extended Data Fig. 4 GLUD1 loss in macrophages enhances GS-mediated glutamine release.

a, Quantification (by gas chromatography–mass spectrometry) of intracellular 2-OG content in BMDMs cultured in glutamine-enriched or glutamine-reduced medium ($n = 3$). **b, c**, Liquid chromatography–mass spectrometry measurement of total cellular energy charge ([ATP + 1/2ADP]/[ATP + ADP + AMP]) (**b**) and ATP content (**c**) in BMDMs ($n = 3$). **d**, Oxygen consumption rate (OCR) in BMDMs ($n = 5$). **e, f**, Quantification of intracellular (**e**) and extracellular (**f**) glutamine content in BMDMs cultured in glutamine-enriched or glutamine-reduced medium ($n = 3$). **g**, [^{14}C]glutamine uptake in BMDMs cultured in glutamine-enriched ($n = 4$) or glutamine-reduced (wild type $n = 4$; *Glud1^{ΔMo}* $n = 3$) medium. **h**, Evaluation of [^{13}C]glutamine-derived carbon incorporation into glutamate in BMDMs ($n = 3$). **i, j**, Evaluation of [^{13}C]glucose-derived carbon incorporation levels into 2-OG (**i**) and glutamate (**j**) in BMDMs ($n = 3$). **k, l**, Quantification of intracellular (**k**) and extracellular (**l**) glutamine content in BMDMs upon silencing of BCAT1 or BCAT2 ($n = 3$). **m, n**, Quantification of intracellular (**m**) and extracellular (**n**) glutamine content in BMDMs upon silencing of GOT1 or GOT2 ($n = 3$). **o**, Quantification of satellite cells on tibialis anterior muscles 1 day post-CTX

injury, stained for pHH3 and PAX7. Control and *Glud1*^{ΔMo} mice were treated two times per day with the BCAT1 inhibitor gabapentin, or vehicle as control ($n = 6$). **p**, Fold change in glutamate-to-leucine ratio in the interstitial fluid of tibialis anterior muscles 1 day post-CTX, relative to PBS-injected control muscle (PBS $n = 6$; CTX $n = 9$). **q**, Fold change in glutamate-to-leucine ratio in the interstitial fluid of crural muscles 3 days post-ligation, relative to control baseline muscle (baseline $n = 7$, 8 control, *Glud1*^{ΔMo}, respectively; ligated $n = 11$, 12 control, *Glud1*^{ΔMo}, respectively). **r**, Evaluation of the conversion of glutamate to 2-OG by analysing [U-¹³C]glutamine (glutamine-enriched condition) or [U-¹³C]glutamate (glutamine-reduced condition) incorporation into 2-OG in wild-type BMDMs ($n = 3$). **s**, Evaluation of the conversion of 2-OG to glutamate by analysing ¹⁵NH₄⁺ incorporation into glutamate in wild-type BMDMs ($n = 3$). **t**, Evaluation of GS activity by analysing ¹⁵NH₄⁺ incorporation into glutamine in BMDMs ($n = 3$). **u**, **v**, Evaluation of the conversion of GLUD1 activity (**u**), and GS activity (**v**), in muscle-infiltrating macrophages, sorted 1 day post-CTX. One unit for the conversion of glutamate to 2-OG is the amount of enzyme that will generate 1 μmole of NADH per minute at pH 7.6 at 37 °C. One unit of GS activity is defined as the enzyme producing 1 nmole of γ-glutamyl hydroxamic acid per minute (control $n = 4$; *Glud1*^{ΔMo} $n = 3$). The control condition in **u**, **v** is the same one displayed in Fig. 2p at day 1. All experiments (except for **o**) show representative values of at least two independent experiments, **o** shows values from one single experiment. Unpaired two-tailed *t*-test; NS, not significant ($P > 0.05$); a.u., arbitrary unit. Graphs show mean ± s.e.m. [Source data](#)

Extended Data Fig. 5 Harnessing glutamine uptake in vitro.

a, b, Quantification (**a**) and representative images (**b**) of myotube diameter in C2C12 cells cultured in BMDM-conditioned medium ($n = 3$ except for glutamine-reduced C2C12, for which $n = 2$). **c**, RT-qPCR of *Slc1a5* knockdown efficiency in C2C12 cells. Cells were transduced with a lentivirus co-expressing Cas9 and a gRNA targeting the *Slc1a5* locus (SLC1A5-KD) ($n = 5$) or a nontargeting control gRNA ($n = 4$). **d**, [U-¹⁴C]glutamine uptake in SLC1A5-deficient C2C12 cells (SLC1A5 KD) generated by co-expressing Cas9 along with a gRNA targeting the *Slc1a5*

locus. Parental cells (control) and cells transduced with a nontargeting control gRNA were used as negative controls. C2C12 cells treated with SLC1A5 inhibitor GPNA were used as a positive control ($n = 3$). **e, f**, Quantification (**e**) and representative images (**f**) of myotube diameter in control or SLC1A5-KD C2C12 cells cocultured with BMDMs under glutamine deprivation ($n = 3$ except control C2C12 $n = 2$). **g**, RT-qPCR analysis of the proliferation marker *Pcna* in control or SLC1A5-KD C2C12 cells, or control C2C12 treated with the mTOR inhibitor Torin2, cultured for 18 h in BMDM-conditioned glutamine-reduced growth medium, in which the only glutamine present comes from wild-type or GLUD1-knockout BMDMs. A nontargeting control gRNA was used as control ($n = 3$). **h**, RT-qPCR analysis of the differentiation marker *Myog* in control or SLC1A5-KD C2C12 cells, or control C2C12 treated with the mTOR inhibitor Torin2, cultured for 72 h in BMDM-conditioned glutamine-reduced differentiation medium, in which the only glutamine present comes from wild-type or GLUD1-knockout BMDMs. A nontargeting control gRNA was used as control ($n = 3$). **i**, Representative images of an immunofluorescence for PAX7 on a pure satellite cell population, freshly isolated from hindlimb muscles of wild-type mice. **j**, RT-qPCR for *Slc1a5* in satellite cells, transduced with the same lentivirus as above. The graph shows values of three biological repetitions per condition. **k, l**, Quantification (**k**) and representative images (**l**) of EdU by immunofluorescence in control or SLC1A5-KD satellite cells. A nontargeting control gRNA was used as a control (control gRNA $n = 5$; SLC1A5-KD $n = 6$). **m–o**, Quantification (**m, n**) and representative images (**o**) of fusion index and myotube size in control or SLC1A5-KD satellite cells after 5 days of culture in differentiation medium. A nontargeting control gRNA was used as a control. The graph shows values of three biological repetitions per condition. All experiments show representative values of at least two independent experiments. Unpaired two-tailed *t*-test; NS, not significant ($P > 0.05$). Scale bars, 50 μm (**b, f, l**), 100 μm (**o**). Graphs show mean \pm s.e.m. [Source data](#)

[Extended Data Fig. 6 Selective and inducible knockdown of *Slc1a5* in satellite cells.](#)

a, Schematic of the AAV8 expression vector for in vivo targeting of satellite cells. U6, Pol III promoter driving the expression of the gRNA targeting the *Slc1a5* locus or a nontargeting control gRNA. Because the mice used in this experiment are *LSL-Cas9/Pax7^{creERT}* mice, Cas9 is exclusively activated in PAX7⁺ cells upon tamoxifen administration and genome editing of the *Slc1a5* locus will occur selectively in satellite cells. **b**, Schematic of an AAV8-based CRISPR–Cas9-mediated in vivo genome editing. **c**, **d**, Representative images (**c**) and quantification (**d**) for PAX7 and Cas9 staining on uninjured muscles before and after tamoxifen administration ($n = 4$). **e**, **f**, RT–qPCR for *Slc1a5* in freshly isolated satellite cells ($n = 4$) (**e**) and all other mononuclear cells (nonsatellite cells) ($n = 3$) (**f**) upon in vivo genome editing of the *Slc1a5* locus (SLC1A5-KD) specifically in satellite cells. Nontargeting control gRNA was used as a control. **g**, **h**, Quantification (**g**) and representative images (**h**) of SLC1A5 and PAX7 staining on freshly isolated satellite cells, upon in vivo genome editing of the *Slc1a5* locus (SLC1A5-KD) specifically in satellite cells ($n = 3$). All experiments show representative values of at least two independent experiments. Unpaired two-tailed *t*-test; NS, not significant ($P > 0.05$). Scale bars, 50 μm (**c**), 20 μm (**h**). Graphs show mean ± s.e.m. [Source data](#)

Extended Data Fig. 7 *Slc1a5* knockdown in satellite cells impairs the recovery of the muscle from CTX-induced damage.

a–d, Quantification of TUNEL⁺ cells (**a**), F4/80⁺ area (**c**) and representative images (**b**, **d**), in tibialis anterior muscle 6 days post-CTX obtained from *LSL-Cas9/Pax7^{creERT}* mice treated with an AAV8 vector encoding control gRNA or *Slc1a5* gRNA (SLC1A5-KD) ($n = 4$). **e**, **f**, Quantification (**e**) and representative images (**f**) of EdU⁺ myonuclei in tibialis anterior muscle 6 days post-CTX, upon in vivo genome editing of the *Slc1a5* locus (SLC1A5-KD) specifically in satellite cells. EdU was given by intraperitoneal injection at 24 h, 48 h and 72 h after CTX injection ($n = 6$). In **a–d**, representative values of two independent experiments are shown; **e**, **f** show values of one experiment. Unpaired two-tailed *t*-test; NS, not significant ($P > 0.05$). Scale bars, 20 μm. Graphs show mean ± s.e.m. [Source data](#)

Extended Data Fig. 8 Macrophage-specific genetic deletion or pharmacological inhibition of GLUD1 alters the basal inflammation and weight of muscle tissue only in aged mice.

a, Representative images of F4/80⁺ area in crural muscles of young and aged mice. **b–i**, Quantification and representative images of F4/80⁺ area in brain (**b**, **c**), liver (**d**, **e**), lung (**f**, **g**), and skin (**h**, **i**) of aged mice ($n = 5$ except in **b** for $Glud1^{\Delta Mo}$ $n = 4$). **j–n**, Body weight (**j**) and mass-to-body weight ratio of kidney (**k**), liver (**l**), spleen (**m**) and fat tissues (**n**) of aged mice upon R162 treatment (control $n = 5$; $Glud1^{\Delta Mo}$ $n = 6$). In **a–i**, representative values of at least two independent experiments are shown; **j–n** show values of one experiment. Unpaired two-tailed *t*-test; NS, not significant ($P > 0.05$). Scale bars, 50 μm (**a**, **i**); 20 μm (**c**, **e**, **g**). Graphs show mean \pm s.e.m. [Source data](#)

Extended Data Fig. 9 GLS loss in macrophages is not advantageous for muscle repair.

a, b, [U^{-14}C]glutamine uptake (**a**) and glutamine oxidation (**b**) in wild-type or GLS-knockout BMDMs cultured with glutamine-enriched or glutamine-reduced medium ($n = 3$). **c, d**, 2-OG-to-succinate ratio in wild-type or GLS-knockout BMDMs (**c**) and 2-OG-to-succinate ratio in wild-type or GLUD1-knockout BMDMs (**d**). BMDMs were treated with 50 ng/ml LPS or PBS (unstimulated) before the assay ($n = 3$). **e**, Evaluation of GS activity by analysing the percentage of the $^{15}\text{NH}_4^+$ -derived ammonia incorporation levels into glutamine in BMDMs isolated from control and $Gls^{\Delta Mo}$ mice ($n = 3$). **f**, Fold change in glutamine-to-glutamate ratio in the interstitial fluid of tibialis anterior muscle 1 day post-CTX, relative to PBS-injected control muscle ($n = 6$). **g, h**, Quantification of necrotic (right side of the graph) and regenerating (left side of the graph) areas on H&E-stained sections from tibialis anterior muscles 6 days post-CTX ($n = 6$) (**g**) and representative images (**h**). **i, j**, Quantification (**i**) and representative images (**j**) of TUNEL⁺ cells in tibialis anterior muscle 6 days post-CTX ($n = 6$). **k–m**, Representative images (**k**) and quantification of F4/80⁺ area (**l**), CD206[−]F4/80⁺ cells (M1) to CD206⁺F4/80⁺ cells (M2) ratio (**m**) in tibialis

anterior muscles 6 days post-CTX ($n = 6$). **n–q**, RT-qPCR of *Tnfa* (**n**), *Cxcl9* (**o**), *Mrc1* (**p**) and *Retnla* (**q**) in BMDMs isolated from control and *Gls^{ΔMo}* mice. BMDMs were treated with LPS or PBS (unstimulated) before the assay ($n = 3$). **r**, Scheme illustrating the physiological role of GLUD1 in macrophages in response to muscle damage. During muscle disruption, ischaemia or ageing, interstitial glutamine drops—probably because of the loss in myofibres (a major glutamine source) and poor blood supply. Infiltrating macrophages respond to glutamine starvation by reducing their oxidative GLUD1 activity in favour of GS activity. Macrophage-derived glutamine is released and progressively fills the muscle interstitium, where it is taken up by satellite cells, promoting their proliferation and differentiation into new fibres (two processes that are favoured by glutamine-dependent mTOR activation). Towards the end of this regenerative process, the newly generated fibres will undertake glutamine production and inflammation will be progressively resolved. GLUD1-deficient macrophages are metabolically pre-adapted towards glutamine synthesis and release, thus preventing this glutamine drop. It follows that—in the case of muscle damage—macrophage-specific knockout of *Glud1* or pharmacological GLUD1 blockade strengthens satellite cell activation, ultimately leading to therapeutic muscle regeneration. All experiments show representative values of at least two independent experiments. Unpaired two-tailed *t*-test; NS, not significant ($P > 0.05$). Scale bars, 20 μm (**h**), 10 μm (**j, k**). Graphs show mean \pm s.e.m. [Source data](#)

Extended Data Table 1 Blood count in control and *Glud1^{ΔMo}* mice
[Full size table](#)

Supplementary information

[Supplementary Figure](#)

Supplementary Figure 1 | Uncropped western blot scans. The figure shows the original, uncropped scans of the western blot images displayed in Fig. 1v-x, Fig. 2e, f, s, Extended Data Fig. 1a,m.

[Reporting Summary](#)

Source data

[Source Data Fig. 1](#)

[Source Data Fig. 2](#)

[Source Data Fig. 3](#)

[Source Data Extended Data Fig. 1](#)

[Source Data Extended Data Fig. 2](#)

[Source Data Extended Data Fig. 3](#)

[Source Data Extended Data Fig. 4](#)

[Source Data Extended Data Fig. 5](#)

[Source Data Extended Data Fig. 6](#)

[Source Data Extended Data Fig. 7](#)

[Source Data Extended Data Fig. 8](#)

[Source Data Extended Data Fig. 9](#)

[Source Data Extended Data Fig. 9](#)

Rights and permissions

[Reprints and Permissions](#)

About this article



Check for
updates

Cite this article

Shang, M., Cappellosso, F., Amorim, R. *et al.* Macrophage-derived glutamine boosts satellite cells and muscle regeneration. *Nature* **587**, 626–631 (2020). <https://doi.org/10.1038/s41586-020-2857-9>

[Download citation](#)

- Received: 01 February 2018
- Accepted: 05 August 2020
- Published: 28 October 2020
- Issue Date: 26 November 2020
- DOI: <https://doi.org/10.1038/s41586-020-2857-9>

Comments

By submitting a comment you agree to abide by our [Terms](#) and [Community Guidelines](#). If you find something abusive or that does not comply with our terms or guidelines please flag it as inappropriate.

[Access through your institution](#)

[Change institution](#)

[Buy or subscribe](#)

This article was downloaded by **calibre** from <https://www.nature.com/articles/s41586-020-2857-9>

- Article
- [Published: 30 July 2020](#)

DNA targeting and interference by a bacterial Argonaute nuclease

- [Anton Kuzmenko](#) ORCID: [orcid.org/0000-0001-7169-0561](#)^{1,2},
- [Anastasiya Ogienko](#) ORCID: [orcid.org/0000-0002-8473-6378](#)^{1 na1},
- [Daria Esyunina](#)^{1 na1},
- [Denis Yudin](#) ORCID: [orcid.org/0000-0002-4103-0543](#)^{1 na1 nAff4},
- [Mayya Petrova](#)¹,
- [Alina Kudinova](#)¹,
- [Olga Maslova](#)¹,
- [Maria Ninova](#) ORCID: [orcid.org/0000-0001-5051-5502](#)²,
- [Sergei Ryazansky](#) ORCID: [orcid.org/0000-0002-3171-2997](#)¹,
- [David Leach](#) ORCID: [orcid.org/0000-0003-4964-6913](#)³,
- [Alexei A. Aravin](#) ORCID: [orcid.org/0000-0002-6956-8257](#)^{1,2} &
- [Andrey Kulbachinskiy](#) ORCID: [orcid.org/0000-0002-2292-6424](#)¹

[Nature](#) volume 587, pages632–637(2020) [Cite this article](#)

- 9353 Accesses
- 3 Citations
- 84 Altmetric
- [Metrics details](#)

Subjects

- [Bacterial host response](#)

- [Phage biology](#)
- [RNAi](#)

Abstract

Members of the conserved Argonaute protein family use small RNA guides to locate their mRNA targets and regulate gene expression and suppress mobile genetic elements in eukaryotes^{1,2}. Argonautes are also present in many bacterial and archaeal species^{3,4,5}. Unlike eukaryotic proteins, several prokaryotic Argonaute proteins use small DNA guides to cleave DNA, a process known as DNA interference^{6,7,8,9,10}. However, the natural functions and targets of DNA interference are poorly understood, and the mechanisms of DNA guide generation and target discrimination remain unknown. Here we analyse the activity of a bacterial Argonaute nuclease from *Clostridium butyricum* (*CbAgo*) in vivo. We show that *CbAgo* targets multicopy genetic elements and suppresses the propagation of plasmids and infection by phages. *CbAgo* induces DNA interference between homologous sequences and triggers DNA degradation at double-strand breaks in the target DNA. The loading of *CbAgo* with locus-specific small DNA guides depends on both its intrinsic endonuclease activity and the cellular double-strand break repair machinery. A similar interaction was reported for the acquisition of new spacers during CRISPR adaptation, and prokaryotic genomes that encode Ago nucleases are enriched in CRISPR–Cas systems. These results identify molecular mechanisms that generate guides for DNA interference and suggest that the recognition of foreign nucleic acids by prokaryotic defence systems involves common principles.

[Access through your institution](#)

[Change institution](#)

[Buy or subscribe](#)

Access options

Subscription info for Chinese customers

We have a dedicated website for our Chinese customers. Please go to naturechina.com to subscribe to this journal.

[Go to naturechina.com](http://naturechina.com)

Rent or Buy article

Get time limited or full article access on ReadCube.

from \$8.99

[Rent or Buy](#)

All prices are NET prices.

Additional access options:

- [Log in](#)
- [Access through your institution](#)
- [Learn about institutional subscriptions](#)

Fig. 1: CbAgo targets specific genomic regions.

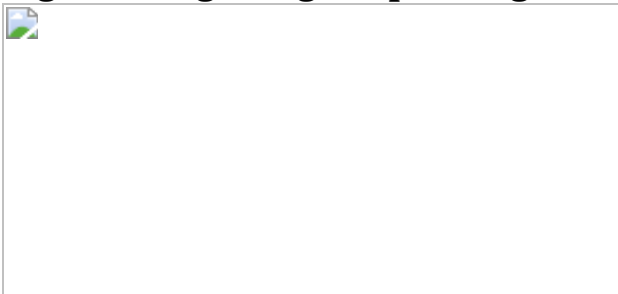


Fig. 2: CbAgo cooperates with RecBCD and targets DSBs.

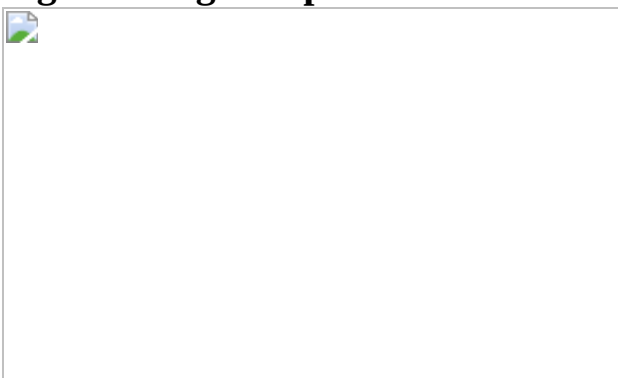


Fig. 3: CbAgo interferes with plasmids and phage infection.

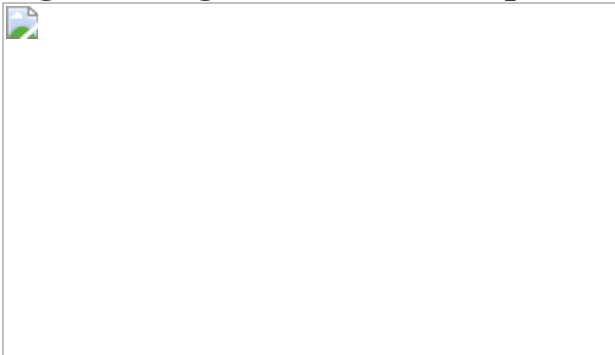
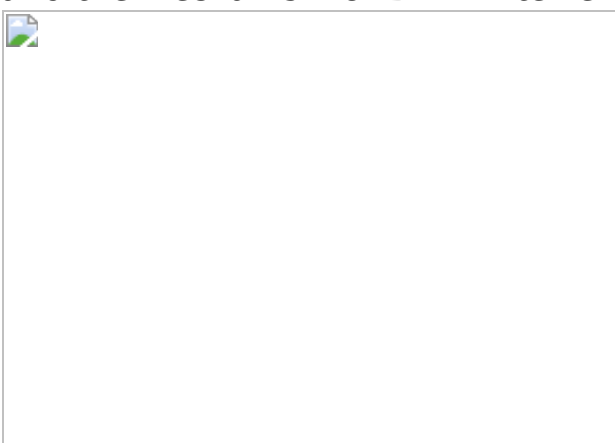


Fig. 4: Co-occurrence of pAgos, DSB repair systems and CRISPR–Cas, and the mechanism of DNA interference.



Data availability

All data generated during this study are included in the published Article and the Extended Data and are available from the Gene Expression Omnibus (GEO) database with the accession number [GSE148596](#).

Code availability

The code used for data analysis is available at the GitHub repository at https://github.com/AntKuzmenko/CbAgo_DNAi.git.

References

1. 1.

Gebert, D. & Rosenkranz, D. RNA-based regulation of transposon expression. *Wiley Interdiscip. Rev. RNA* **6**, 687–708 (2015).

[CAS](#) [PubMed](#) [Google Scholar](#)

2. 2.

Meister, G. Argonaute proteins: functional insights and emerging roles. *Nat. Rev. Genet.* **14**, 447–459 (2013).

[CAS](#) [PubMed](#) [Google Scholar](#)

3. 3.

Makarova, K. S., Wolf, Y. I., van der Oost, J. & Koonin, E. V. Prokaryotic homologs of Argonaute proteins are predicted to function as key components of a novel system of defense against mobile genetic elements. *Biol. Direct* **4**, 29 (2009).

[PubMed](#) [PubMed Central](#) [Google Scholar](#)

4. 4.

Ryazansky, S., Kulbachinskiy, A. & Aravin, A. A. The expanded universe of prokaryotic Argonaute proteins. *MBio* **9**, e01935–e01918 (2018).

[PubMed](#) [PubMed Central](#) [Google Scholar](#)

5. 5.

Swarts, D. C. et al. The evolutionary journey of Argonaute proteins. *Nat. Struct. Mol. Biol.* **21**, 743–753 (2014).

[CAS](#) [PubMed](#) [PubMed Central](#) [Google Scholar](#)

6. 6.

Hegge, J. W. et al. DNA-guided DNA cleavage at moderate temperatures by *Clostridium butyricum* Argonaute. *Nucleic Acids Res.* **47**, 5809–5821 (2019).

[CAS](#) [PubMed](#) [PubMed Central](#) [Google Scholar](#)

7. 7.

Kuzmenko, A., Yudin, D., Ryazansky, S., Kulbachinskiy, A. & Aravin, A. A. Programmable DNA cleavage by Ago nucleases from mesophilic bacteria *Clostridium butyricum* and *Limnothrix rosea*. *Nucleic Acids Res.* **47**, 5822–5836 (2019).

[CAS](#) [PubMed](#) [PubMed Central](#) [Google Scholar](#)

8. 8.

Swarts, D. C. et al. Argonaute of the archaeon *Pyrococcus furiosus* is a DNA-guided nuclease that targets cognate DNA. *Nucleic Acids Res.* **43**, 5120–5129 (2015).

[CAS](#) [PubMed](#) [PubMed Central](#) [Google Scholar](#)

9. 9.

Swarts, D. C. et al. DNA-guided DNA interference by a prokaryotic Argonaute. *Nature* **507**, 258–261 (2014).

[ADS](#) [CAS](#) [PubMed](#) [PubMed Central](#) [Google Scholar](#)

10. 10.

Zander, A. et al. Guide-independent DNA cleavage by archaeal Argonaute from *Methanocaldococcus jannaschii*. *Nat. Microbiol.* **2**, 17034 (2017).

[CAS](#) [PubMed](#) [Google Scholar](#)

11. 11.

Willkomm, S., Makarova, K. S. & Grohmann, D. DNA silencing by prokaryotic Argonaute proteins adds a new layer of defense against invading nucleic acids. *FEMS Microbiol. Rev.* **42**, 376–387 (2018).

[CAS](#) [PubMed](#) [PubMed Central](#) [Google Scholar](#)

12. 12.

Lisitskaya, L., Aravin, A. A. & Kulbachinskiy, A. DNA interference and beyond: structure and functions of prokaryotic Argonaute proteins. *Nat. Commun.* **9**, 5165 (2018).

[ADS](#) [PubMed](#) [PubMed Central](#) [Google Scholar](#)

13. 13.

Kaya, E. et al. A bacterial Argonaute with noncanonical guide RNA specificity. *Proc. Natl Acad. Sci. USA* **113**, 4057–4062 (2016).

[ADS](#) [CAS](#) [PubMed](#) [Google Scholar](#)

14. 14.

Sheng, G. et al. Structure-based cleavage mechanism of *Thermus thermophilus* Argonaute DNA guide strand-mediated DNA target cleavage. *Proc. Natl Acad. Sci. USA* **111**, 652–657 (2014).

[ADS](#) [CAS](#) [PubMed](#) [Google Scholar](#)

15. 15.

Willkomm, S. et al. Structural and mechanistic insights into an archaeal DNA-guided Argonaute protein. *Nat. Microbiol.* **2**, 17035 (2017).

[CAS](#) [PubMed](#) [Google Scholar](#)

16. 16.

Olina, A. et al. Genome-wide DNA sampling by Ago nuclease from the cyanobacterium *Synechococcus elongatus*. *RNA Biol.* **17**, 677–688 (2020).

[CAS](#) [PubMed](#) [Google Scholar](#)

17. 17.

Swarts, D. C. et al. Autonomous generation and loading of DNA guides by bacterial Argonaute. *Mol. Cell* **65**, 985–998.e6 (2017).

[CAS](#) [PubMed](#) [PubMed Central](#) [Google Scholar](#)

18. 18.

Olovnikov, I., Chan, K., Sachidanandam, R., Newman, D. K. & Aravin, A. A. Bacterial argonaute samples the transcriptome to identify foreign DNA. *Mol. Cell* **51**, 594–605 (2013).

[CAS](#) [PubMed](#) [Google Scholar](#)

19. 19.

Duggin, I. G. & Bell, S. D. Termination structures in the *Escherichia coli* chromosome replication fork trap. *J. Mol. Biol.* **387**, 532–539 (2009).

[CAS](#) [PubMed](#) [Google Scholar](#)

20. 20.

Dillingham, M. S. & Kowalczykowski, S. C. RecBCD enzyme and the repair of double-stranded DNA breaks. *Microbiol. Mol. Biol. Rev.* **72**, 642–671 (2008).

[CAS](#) [PubMed](#) [PubMed Central](#) [Google Scholar](#)

21. 21.

Smith, G. R. How RecBCD enzyme and Chi promote DNA break repair and recombination: a molecular biologist's view. *Microbiol. Mol. Biol. Rev.* **76**, 217–228 (2012).

[CAS](#) [PubMed](#) [PubMed Central](#) [Google Scholar](#)

22. 22.

Wigley, D. B. Bacterial DNA repair: recent insights into the mechanism of RecBCD, AddAB and AdnAB. *Nat. Rev. Microbiol.* **11**, 9–13 (2013).

[CAS](#) [PubMed](#) [Google Scholar](#)

23. 23.

Chaudhury, A. M. & Smith, G. R. *Escherichia coli* recBC deletion mutants. *J. Bacteriol.* **160**, 788–791 (1984).

[CAS](#) [PubMed](#) [PubMed Central](#) [Google Scholar](#)

24. 24.

Sinha, A. K. et al. Division-induced DNA double strand breaks in the chromosome terminus region of *Escherichia coli* lacking RecBCD DNA repair enzyme. *PLoS Genet.* **13**, e1006895 (2017).

[PubMed](#) [PubMed Central](#) [Google Scholar](#)

25. 25.

Sinha, A. K. et al. Broken replication forks trigger heritable DNA breaks in the terminus of a circular chromosome. *PLoS Genet.* **14**, e1007256 (2018).

[PubMed](#) [PubMed Central](#) [Google Scholar](#)

26. 26.

Capaldo, F. N. & Barbour, S. D. DNA content, synthesis and integrity in dividing and non-dividing cells of rec- strains of *Escherichia coli* K12. *J. Mol. Biol.* **91**, 53–66 (1975).

[CAS](#) [PubMed](#) [Google Scholar](#)

27. 27.

Marraffini, L. A. & Sontheimer, E. J. Self versus non-self discrimination during CRISPR RNA-directed immunity. *Nature* **463**, 568–571 (2010).

[ADS](#) [CAS](#) [PubMed](#) [PubMed Central](#) [Google Scholar](#)

28. 28.

Westra, E. R. et al. Type I-E CRISPR-cas systems discriminate target from non-target DNA through base pairing-independent PAM recognition. *PLoS Genet.* **9**, e1003742 (2013).

[CAS](#) [PubMed](#) [PubMed Central](#) [Google Scholar](#)

29. 29.

White, M. A., Azeroglu, B., Lopez-Vernaza, M. A., Hasan, A. M. M. & Leach, D. R. F. RecBCD coordinates repair of two ends at a DNA double-strand break, preventing aberrant chromosome amplification. *Nucleic Acids Res.* **46**, 6670–6682 (2018).

[CAS](#) [PubMed](#) [PubMed Central](#) [Google Scholar](#)

30. 30.

Eykelenboom, J. K., Blackwood, J. K., Okely, E. & Leach, D. R. SbcCD causes a double-strand break at a DNA palindrome in the *Escherichia coli* chromosome. *Mol. Cell* **29**, 644–651 (2008).

[CAS](#) [PubMed](#) [Google Scholar](#)

31. 31.

White, M. A., Darmon, E., Lopez-Vernaza, M. A. & Leach, D. R. F. DNA double strand break repair in *Escherichia coli* perturbs cell division and chromosome dynamics. *PLoS Genet.* **16**, e1008473 (2020).

[CAS](#) [PubMed](#) [PubMed Central](#) [Google Scholar](#)

32. 32.

Modell, J. W., Jiang, W. & Marraffini, L. A. CRISPR-Cas systems exploit viral DNA injection to establish and maintain adaptive immunity. *Nature* **544**, 101–104 (2017).

[ADS](#) [CAS](#) [PubMed](#) [PubMed Central](#) [Google Scholar](#)

33. 33.

Levy, A. et al. CRISPR adaptation biases explain preference for acquisition of foreign DNA. *Nature* **520**, 505–510 (2015).

[ADS](#) [CAS](#) [PubMed](#) [PubMed Central](#) [Google Scholar](#)

34. 34.

Ivančić-Baće, I., Cass, S. D., Wearne, S. J. & Bolt, E. L. Different genome stability proteins underpin primed and naïve adaptation in *E. coli* CRISPR-Cas immunity. *Nucleic Acids Res.* **43**, 10821–10830 (2015).

[PubMed](#) [PubMed Central](#) [Google Scholar](#)

35. 35.

Bobay, L. M., Touchon, M. & Rocha, E. P. Manipulating or superseding host recombination functions: a dilemma that shapes phage evolvability. *PLoS Genet.* **9**, e1003825 (2013).

[CAS](#) [PubMed](#) [PubMed Central](#) [Google Scholar](#)

36. 36.

Doron, S. et al. Systematic discovery of antiphage defense systems in the microbial pangenome. *Science* **359**, eaar4120 (2018).

[PubMed](#) [PubMed Central](#) [Google Scholar](#)

37. 37.

Ofir, G. et al. DISARM is a widespread bacterial defence system with broad anti-phage activities. *Nat. Microbiol.* **3**, 90–98 (2018).

[CAS](#) [PubMed](#) [Google Scholar](#)

38. 38.

Koonin, E. V. Evolution of RNA- and DNA-guided antivirus defense systems in prokaryotes and eukaryotes: common ancestry vs convergence. *Biol. Direct* **12**, 5 (2017).

[PubMed](#) [PubMed Central](#) [Google Scholar](#)

39. 39.

El Karoui, M., Biaudet, V., Schbath, S. & Gruss, A. Characteristics of Chi distribution on different bacterial genomes. *Res. Microbiol.* **150**, 579–587 (1999).

[CAS](#) [PubMed](#) [Google Scholar](#)

40. 40.

Jolly, S. M. et al. A DNA-guided Argonaute protein functions in DNA replication in *Thermus thermophilus*. *Cell* <https://doi.org/10.1016/j.cell.2020.07.036> (2020)

41. 41.

Datsenko, K. A. & Wanner, B. L. One-step inactivation of chromosomal genes in *Escherichia coli* K-12 using PCR products. *Proc. Natl Acad. Sci. USA* **97**, 6640–6645 (2000).

[ADS](#) [CAS](#) [PubMed](#) [Google Scholar](#)

42. 42.

Bohn, C., Collier, J. & Bouloc, P. Dispensable PDZ domain of *Escherichia coli* YaeL essential protease. *Mol. Microbiol.* **52**, 427–435 (2004).

[CAS](#) [PubMed](#) [Google Scholar](#)

43. 43.

He, F. *E. coli* genomic DNA extraction. *Bio-101* e97, <https://doi.org/10.21769/BioProtoc.97> (2011).

44. 44.

Thomason, L. C., Costantino, N. & Court, D. L. *E. coli* genome manipulation by P1 transduction. *Curr. Protocols Mol. Biol.* Ch. 1, Unit 1.17 (2007).

[Google Scholar](#)

45. 45.

Bernheim, A., Bikard, D., Touchon, M. & Rocha, E. P. C. A matter of background: DNA repair pathways as a possible cause for the sparse distribution of CRISPR-Cas systems in bacteria. *Phil. Trans. R. Soc. Lond. B* **374**, 20180088 (2019).

[CAS](#) [Google Scholar](#)

46. 46.

Couvin, D. et al. CRISPRCasFinder, an update of CRISRFinder, includes a portable version, enhanced performance and integrates search for Cas proteins. *Nucleic Acids Res.* **46** (W1), W246–W251 (2018).

[CAS](#) [PubMed](#) [PubMed Central](#) [Google Scholar](#)

[Download references](#)

Acknowledgements

We thank M. A. White for strains with engineered I-SceI sites, G. Smith for RecBCD antibodies, S. Lysenkov for the help with statistical analysis and A. Olina for the help with the phage experiments. D.Y. would like to thank M. Kolesnik for discussions. The project was in part supported by the Ministry of Science and Higher Education of the Russian Federation (14.W03.31.0007), Russian Science Foundation (19-14-00359, analysis of DSB formation), Russian Foundation for Basic Research (18-29-07086). A.A.A. is supported by an HHMI Faculty Scholar Award. D.L. is supported by grant MR/M019160/1 from the MRC (UK).

Author information

Author notes

1. Denis Yudin

Present address: Department of Biology, Institute of Molecular Biology and Biophysics, ETH Zurich, Zurich, Switzerland

2. These authors contributed equally: Anastasiya Oguienko, Daria Esyunina, Denis Yudin

Affiliations

1. Institute of Molecular Genetics, Russian Academy of Sciences, Moscow, Russia

Anton Kuzmenko, Anastasiya Ogienko, Daria Esyunina, Denis Yudin, Mayya Petrova, Alina Kudinova, Olga Maslova, Sergei Ryazansky, Alexei A. Aravin & Andrey Kulbachinskiy

2. Division of Biology and Biological Engineering, California Institute of Technology, Pasadena, CA, USA

Anton Kuzmenko, Maria Ninova & Alexei A. Aravin

3. Institute of Cell Biology, School of Biological Sciences, University of Edinburgh, Edinburgh, UK

David Leach

Authors

1. Anton Kuzmenko

[View author publications](#)

You can also search for this author in [PubMed](#) [Google Scholar](#)

2. Anastasiya Ogienko

[View author publications](#)

You can also search for this author in [PubMed](#) [Google Scholar](#)

3. Daria Esyunina

[View author publications](#)

You can also search for this author in [PubMed](#) [Google Scholar](#)

4. Denis Yudin

[View author publications](#)

You can also search for this author in [PubMed](#) [Google Scholar](#)

5. Mayya Petrova

[View author publications](#)

You can also search for this author in [PubMed](#) [Google Scholar](#)

6. Alina Kudinova

[View author publications](#)

You can also search for this author in [PubMed](#) [Google Scholar](#)

7. Olga Maslova

[View author publications](#)

You can also search for this author in [PubMed](#) [Google Scholar](#)

8. Maria Ninova

[View author publications](#)

You can also search for this author in [PubMed](#) [Google Scholar](#)

9. Sergei Ryazansky

[View author publications](#)

You can also search for this author in [PubMed](#) [Google Scholar](#)

10. David Leach

[View author publications](#)

You can also search for this author in [PubMed](#) [Google Scholar](#)

11. Alexei A. Aravin

[View author publications](#)

You can also search for this author in [PubMed](#) [Google Scholar](#)

12. Andrey Kulbachinskiy

[View author publications](#)

You can also search for this author in [PubMed](#) [Google Scholar](#)

Contributions

A. Kuzmenko, A.A.A. and A. Kulbachinskiy conceptualized the study. A. Kuzmenko, D.Y. and D.E. constructed strains. A. Kuzmenko, A.O., D.Y. and D.E. prepared smDNA libraries. A. Kuzmenko, A.O. and D.E. prepared genomic DNA libraries. A. Kuzmenko, A.O. and D.Y. analysed sequencing data, M.N. and S.R. helped with data analysis. S.R. performed phylogenetic analysis. D.L. conceptualized experiments with engineered DSBs. A. Kuzmenko, A. Kudinova, O.M., M.P., A.O. and D.E. performed experiments on plasmid elimination and phage infection. All authors interpreted the results. A. Kuzmenko and A.O. prepared the figures. A. Kulbachinskiy and A.A.A. wrote the manuscript with contribution from other authors.

Corresponding authors

Correspondence to [Anton Kuzmenko](#) or [Alexei A. Aravin](#) or [Andrey Kulbachinskiy](#).

Ethics declarations

Competing interests

The authors declare no competing interests.

Additional information

Publisher's note Springer Nature remains neutral with regard to jurisdictional claims in published maps and institutional affiliations.

Extended data figures and tables

[Extended Data Fig. 1 Small DNAs associated with CbAgo.](#)

a, Analysis of small nucleic acids isolated from wild-type *CbAgo* and *dCbAgo*. The samples were treated with alkaline phosphatase, ³²P-labelled with polynucleotide kinase and treated with DNase I (D), RNase A (R) or

left without further treatment (–). *CbAgo* is associated with small DNAs, as confirmed by their sensitivity to DNase treatment and resistance to RNase. The DNA marker (M) lengths are indicated. For gel source data, see Supplementary Fig. 1. **b**, Length distribution of smDNAs associated with *CbAgo* in the wild-type, *recBrecD*, *recC* and *recA* strains. For the *recC* strain, there is a small increase in the smDNA length, suggesting that their processing might be different in this strain. **c, d**, Analysis of nucleotide biases for chromosomal (wild-type *CbAgo* and *dCbAgo*), plasmid (pNonChi) and phage M13 smDNAs associated with *CbAgo*. **c**, Nucleotide frequencies at different guide positions. **d**, AT/GC-content along the guide length and in surrounding genomic sequences. Guide positions starting from the 5' end are indicated below the plots. For genomic DNA, the AT-bias around the first position is seen for both active *CbAgo* and *dCbAgo*. The AT-bias in the downstream region (positions 14–18) is seen for active *CbAgo* but not for *dCbAgo*. For each replicon, the average GC content of smDNAs corresponds to the GC content of this replicon (shown in percentage in each panel), indicating that the efficiency of smDNA processing does not strongly depend on the GC content. **e**, Model of processing of smDNAs by *CbAgo* from double-stranded DNA precursors. Binding of the guide 5' end in the MID-pocket of *CbAgo* may be facilitated by melting of the DNA duplex in the upstream guide region (left). Guide DNA loading is completed after *CbAgo*-dependent cleavage of the complementary DNA strand and its dissociation, depending on the AT content of the downstream guide-target duplex (right).

[Extended Data Fig. 2 Whole-genome mapping of smDNAs associated with *CbAgo* in strains with various genetic backgrounds.](#)

a–h, For each strain, the distribution of smDNAs along the chromosome is shown in RPKM. Left, total smDNA counts. Right, strand distribution of smDNAs for each strain (plus DNA strand, green; minus DNA strand, red). Positions of the *araC*, *lacI* and *ter* sites are shown above the plots. smDNA coverage is shown in RPKM. The identities of the strains and plasmids, with plasmid or chromosomal localizations of the *CbAgo* gene, are indicated (Supplementary Tables 2 and 3). **a**, Wild-type BL21(DE3) with plasmid-encoded *CbAgo* (pBAD containing the *araC* gene). **b**, As in **a**, in

BL21(DE3) with knockout of *Tus*. **c**, MG1655Z1 with genomic *CbAgo*. **d**, As in **a** with pET28b containing *lacI*. **e**, Plasmid-encoded catalytically dead d*CbAgo* in BL21(DE3). **f**, Knockout of RecB/RecD in BL21(DE3) with plasmid-encoded *CbAgo*. **g**, Knockout of RecC in BL21(DE3) with plasmid-encoded *CbAgo*. **h**, Knockout of RecA in BL21(DE3) with plasmid-encoded *CbAgo*. The observed enrichment of smDNAs around the *ori* region in the *recC* and *recA* strains may possibly reflect the higher DNA content and/or a higher likelihood of DSB formation in this region in these strains. **i**, Targeting of specific genomic regions depends on the catalytic activity of *CbAgo*. The ratio of smDNAs between wild-type *CbAgo* and d*CbAgo* (obtained for BL21(DE3) containing corresponding pBAD_CbAgo plasmids) is shown in the logarithmic scale. Normalized densities of smDNA reads (RPKM) were calculated for each *CbAgo* variant and plotted as a wild-type/d*Cb* ratio. The regions with the ratio of >1 correspond to the sites of active smDNA processing by *CbAgo*. *CbAgo* targets the *araC* locus, *ter* region and multicopy sequences: rDNA operons (indicated with arrows above the plot) and IS elements. Positions of IS1 (29 copies) and IS3 (12 copies) in the BL21(DE3) genome are shown with dotted lines below the plot.

Extended Data Fig. 3 Asymmetry in smDNA distribution at specific genomic loci.

a, Zoomed-in peaks of smDNAs around the *araC* and *lacI* genes in strains containing plasmids with corresponding genes. **b**, Examples of smDNA distributions around rRNA operons, *rrsD* and *rrsC*, in wild-type *E. coli* and strains with knockouts of *recB*/*recD* and *recC*. The reads from the plus and minus genomic strands are shown in green and red, respectively. Positions of Chi sites in surrounding genomic regions are indicated (forward for the plus strand and reverse for the minus strand); the closest Chi sites in the corresponding strands are shown with dotted lines. **c**, Metaplot of the number of smDNAs calculated in the 500-bp windows around Chi sites in each genomic strand (red, plus-strand smDNAs for plus-strand Chi sites; green, minus-strand smDNAs for minus-strand Chi sites) in the 2–3-Mb genomic region. Position around Chi is shown in kilobases. **d**, Strand-specific asymmetry in smDNA distribution for various strains (ratio of RPKM values for the plus and minus genomic strands). A similar bias is

observed for the wild-type and *recB**recD*, *recC* and *recA* mutant strains expressing *CbAgo* but not in wild-type cells expressing catalytically inactive d*CbAgo*.

Extended Data Fig. 4 Growth kinetics of *E. coli* strains depending on the expression of *CbAgo*.

a, b, Growth kinetics of *E. coli* BL21(DE3) and its mutant derivatives with or without *CbAgo* (containing pBAD_CbAgo or empty pBAD plasmids) at 30 °C in the rich LB (**a**) and minimal M9 (**b**) medium. Overnight cultures of cells were inoculated into fresh LB to OD₆₀₀ of 0.01 in the presence of the inducer (0.05% l-arabinose) and cell density was measured at 15 min intervals in a microplate reader.

Extended Data Fig. 5 Whole-genome analysis of DNA content in the wild-type and *tus*[−] *E. coli* strains depending on the expression of *CbAgo*.

a–d, The experiment was performed with wild-type (**a, b**) or *tus*[−] (**c, d**) BL21(DE3) containing or lacking the pBAD_CbAgo plasmid. The cells were collected at the exponential phase (OD₆₀₀ = 0.5) (**a, c**) or stationary phase (OD₆₀₀ = 6) (**b, d**), followed by isolation of total DNA and sequencing. For each condition, genomic DNA coverage is shown for strains without and with *CbAgo*, and the ratio for the +*CbAgo* and −*CbAgo* strains is shown in a separate panel (black). The enlarged *ter* region and the *araC* locus are shown separately. Genomic DNA coverage is shown in RPKM. At the stationary phase, a peak in genomic DNA coverage was detected in the strains containing *CbAgo*, which exactly corresponded to the DE3 prophage in BL21(DE3). This may indicate formation of DSBs in this region, possibly as a result of partial prophage excision, leading to DNA repair and replication.

Extended Data Fig. 6 Targeting of engineered DSBs by *CbAgo*.

a, Top, smDNA abundance in the chromosomal area spanning the engineered DSBs (palindrome or I-SceI-dependent; I-SceI^{mut}, the mutated cleavage site) and *ter* sites, for the wild-type *CbAgo* or *dCbAgo*. In each strain, the numbers of smDNAs mapping to the region of DSB are shown in percentage of total smDNAs. The presence of the DSB shifts the ratio between the *terA* and *terC* peaks in favour of *terA*, probably as a result of impediment of the clockwise replisome, moving towards *terC*, by the DSB formation. Bottom, strand-specific distribution of smDNAs around engineered DSBs for strains with *dCbAgo* (palindrome and I-SceI DSBs) or with wild-type *CbAgo* and the I-SceI^{mut} site. The reads from the plus and minus DNA strands are shown in green and red, respectively. Most smDNAs are produced from the 3' strand at each end of the DSB, and the boundaries of the smDNA peaks are defined by Chi sites. **b**, Genomic DNA coverage in the same region in palindrome-containing strains depending on the expression of active *CbAgo* or *dCbAgo*. **c**, The ratio of genomic DNA profiles for palindrome-containing strains with wild-type *CbAgo* and *dCbAgo* relative to the strain without *CbAgo*. Wild-type *CbAgo* but not *dCbAgo* triggers DNA loss around the DSB with overreplication of genomic DNA at the site of termination. **d**, Genomic DNA coverage at DSBs formed by the I-SceI meganuclease in *E. coli* strains with induced I-SceI but without expression of *CbAgo* (left) and with expression of both I-SceI and *CbAgo* (right). **e**, The ratio between genomic DNA profiles for the strains with and without expression of *CbAgo*. Genomic DNA coverage is shown in RPKM.

Extended Data Fig. 7 Targeting of plasmid and phage DNA by *CbAgo*.

a, smDNA coverage of plasmids (pNonChi, left; pBAD_CbAgo, right) in strains with plasmid-encoded *CbAgo*. The moving average of smDNA coverage in a 200-nucleotide window is shown for the plus and minus DNA strands (green and red, respectively). **b**, smDNA coverage of a pET28 plasmid in a strain with chromosomal *CbAgo*. **c**, Distribution of smDNAs along the M13 genome. smDNAs were isolated from *CbAgo* expressed in *E. coli* NEB Turbo strain during infection with M13. **d**, Coverage of plasmid DNA in whole-genome sequencing in the wild-type and *tus*⁻ strains, depending on the expression of *CbAgo*. The values represent the

moving average of genomic DNA coverage in a 200-nucleotide window (in RPM). **e–g**, Targeting of the F' plasmid by *CbAgo*. Total smDNA coverage (**e**), coverage of the plus and minus DNA strands (**f**) and the plus-to-minus strand ratio (**g**) are shown along the F' sequence. Positions of the three copies of IS3 element, the origin of replication (*oriS*), the core part of the F factor, and the chromosomal insertion ('chr') are indicated. For strand-specific smDNA distribution, positions of the nearest Chi sites in the corresponding strands are shown. Most reads map to the F episome core sequence lacking Chi sites, and the numbers of smDNAs drop considerably upon encountering the first Chi site. The distribution is also asymmetric relative to the origin of replication. Similarly to the chromosome (Extended Data Fig. 3d), the lagging DNA strand is targeted with a higher efficiency, which suggests a connection to replication.

Extended Data Fig. 8 Loss of plasmids after various number of passages in *E. coli* strains with or without *CbAgo*.

Cells expressing genome-encoded *CbAgo* (Cb), its catalytically dead mutant (dCb) or without Ago ('without') were transformed with one of the six different plasmids from different incompatibility groups. The percentage of plasmid-free cells was measured after indicated number of passages (mean and s.d. from 2–6 biological replicates). *CbAgo*, but not d*CbAgo*, facilitates plasmid elimination regardless of the plasmid type.

Extended Data Fig. 9 Effects of *CbAgo* and d*CbAgo* on P1 infection.

a, Bacterial culture growth during P1 infection with different MOI in strain with or without d*CbAgo*. Data are mean and s.d. from three independent experiments. **b**, Titres of P1 at MOI 1 and 5 at different times after infection in strains without *CbAgo* or with expression *CbAgo* or d*CbAgo*. Data are mean and s.d. from three–four independent measurements. * $P < 0.05$, ** $P < 0.01$, *** $P < 0.001$, Scheffe's test for multiple comparison of mean values after normalization of data by log-transformation.

Extended Data Fig. 10 Co-occurrence of pAgo proteins, DSB repair systems and CRISPR–Cas in prokaryotic genomes.

a, Circular phylogenetic tree of pAgos from prokaryotic strains with fully assembled genomes based on the multiple alignment of the MID-PIWI domains. Three major phylogenetic groups of pAgos are indicated⁴: long-A pAgos usually contain all characteristic domains of the Ago family (N, PAZ, MID and PIWI) and have a predicted nuclease site; long-B pAgos also contain all domains but are inactive; and short pAgos contain only MID and PIWI domains and are inactive. The pAgo proteins were annotated as follows, from the inner to the outer circles: the superkingdom to which the corresponding pAgo belongs; the type of the PIWI domain, depending on the presence of the catalytic tetrad DEDX; the type of the DSB repair system encoded in the corresponding genome; the class of CRISPR–Cas system; the type and subtype of CRISPR–Cas system. *CbAgo*, *T. thermophilus* Ago (*TtAgo*) and *Marinitoga piezophila* Ago (*MpAgo*) are highlighted in red. The scale bar represents the evolutionary rate calculated under the JTT+CAT evolutionary model. **b**, The distribution of various subtypes of type I and type III CRISPR–Cas system in the fully assembled genomes encoding pAgos. The number of genomes for each pAgo group is indicated.

Supplementary information

Supplementary Figure 1

The file contains raw images for all data obtained by gel electrophoresis in the indicated figures.

Reporting Summary

Supplementary Table

The file contains Supplementary Tables 1-5.

Peer Review File

Rights and permissions

[Reprints and Permissions](#)

About this article



Check for
updates

Cite this article

Kuzmenko, A., Ogienko, A., Esyunina, D. *et al.* DNA targeting and interference by a bacterial Argonaute nuclelease. *Nature* **587**, 632–637 (2020). <https://doi.org/10.1038/s41586-020-2605-1>

[Download citation](#)

- Received: 05 March 2020
- Accepted: 24 July 2020
- Published: 30 July 2020
- Issue Date: 26 November 2020
- DOI: <https://doi.org/10.1038/s41586-020-2605-1>

Further reading

- [Prokaryotic Argonautes Function beyond Immunity by Unlinking Replicating Chromosomes](#)
 - Daan C. Swarts

Cell (2020)

- **Thermus thermophilus Argonaute Functions in the Completion of DNA Replication**

- Samson M. Jolly
- , Ildar Gainetdinov
- , Karina Jouravleva
- , Han Zhang
- , Lara Strittmatter
- , Shannon M. Bailey
- , Gregory M. Hendricks
- , Avantika Dhabaria
- , Beatrix Ueberheide
- & Phillip D. Zamore

Cell (2020)

- **Recognition of double-stranded DNA by the Rhodobacter sphaeroides Argonaute protein**

- Lidia Lisitskaya
- , Ivan Petushkov
- , Daria Esyunina
- , Alexei Aravin
- & Andrey Kulbachinskiy

Biochemical and Biophysical Research Communications (2020)

Comments

By submitting a comment you agree to abide by our [Terms](#) and [Community Guidelines](#). If you find something abusive or that does not comply with our terms or guidelines please flag it as inappropriate.

[Access through your institution](#)

[Change institution](#)

[Buy or subscribe](#)

This article was downloaded by **calibre** from <https://www.nature.com/articles/s41586-020-2605-1>

| [Section menu](#) | [Main menu](#) |

Host ANP32A mediates the assembly of the influenza virus replicase
[Download PDF](#)

- Article
- [Published: 18 November 2020](#)

Host ANP32A mediates the assembly of the influenza virus replicase

- [Loïc Carrique](#) [ORCID: orcid.org/0000-0001-5332-8593](#)^{1 na1},
- [Haitian Fan](#)^{2 na1},
- [Alexander P. Walker](#) [ORCID: orcid.org/0000-0002-9650-382X](#)^{2 na1},
- [Jeremy R. Keown](#) [ORCID: orcid.org/0000-0003-0159-9257](#)^{1 na1},
- [Jane Sharps](#)²,
- [Ecco Staller](#)^{3 nAff5},
- [Wendy S. Barclay](#)³,
- [Ervin Fodor](#) [ORCID: orcid.org/0000-0003-3249-196X](#)^{2 na2} &
- [Jonathan M. Grimes](#) [ORCID: orcid.org/0000-0001-9698-0389](#)^{1,4 na2}

[Nature](#) volume 587, pages638–643(2020) [Cite this article](#)

- 3362 Accesses
- 47 Altmetric
- [Metrics details](#)

Subjects

- [Cryoelectron microscopy](#)
- [Influenza virus](#)

Abstract

Aquatic birds represent a vast reservoir from which new pandemic influenza A viruses can emerge¹. Influenza viruses contain a negative-sense segmented RNA genome that is transcribed and replicated by the viral heterotrimeric RNA

polymerase (FluPol) in the context of viral ribonucleoprotein complexes^{2,3}. RNA polymerases of avian influenza A viruses (FluPolA) replicate viral RNA inefficiently in human cells because of species-specific differences in acidic nuclear phosphoprotein 32 (ANP32), a family of essential host proteins for FluPol activity⁴. Host-adaptive mutations, particularly a glutamic-acid-to-lysine mutation at amino acid residue 627 (E627K) in the 627 domain of the PB2 subunit, enable avian FluPolA to overcome this restriction and efficiently replicate viral RNA in the presence of human ANP32 proteins. However, the molecular mechanisms of genome replication and the interplay with ANP32 proteins remain largely unknown. Here we report cryo-electron microscopy structures of influenza C virus polymerase (FluPolC) in complex with human and chicken ANP32A. In both structures, two FluPolC molecules form an asymmetric dimer bridged by the N-terminal leucine-rich repeat domain of ANP32A. The C-terminal low-complexity acidic region of ANP32A inserts between the two juxtaposed PB2 627 domains of the asymmetric FluPolA dimer, suggesting a mechanism for how the adaptive PB2(E627K) mutation enables the replication of viral RNA in mammalian hosts. We propose that this complex represents a replication platform for the viral RNA genome, in which one of the FluPol molecules acts as a replicase while the other initiates the assembly of the nascent replication product into a viral ribonucleoprotein complex.

[Download PDF](#)

Main

The influenza virus genome is composed of negative-sense single-stranded RNA segments, which are assembled into separate viral ribonucleoprotein (vRNP) complexes with FluPol, a heterotrimeric complex of PB1, PB2 and PA (P3 in influenza C virus) proteins, and the viral nucleoprotein (NP)^{2,3}. Following virus entry, vRNPs are trafficked to the cell nucleus where FluPol, in complex with various host factors, directs the transcription and replication of the viral genome⁵. For replication, FluPol first generates complementary RNA (cRNA), which then serves as template for viral RNA (vRNA) synthesis. The molecular details of the replicase complex and, in particular, the role of the ANP32 family of host proteins, known to be essential for genome replication⁶, remain unknown. Here we investigate the role of ANP32A in promoting FluPol function and uncover a complex of ANP32A with a FluPol dimer, which we propose acts as a replication platform for the viral genome.

ANP32A forms a complex with a FluPol dimer

Host ANP32 proteins are essential for the activity of FluPol of both influenza A and influenza B viruses^{7,8}. To address whether FluPol from influenza C virus also requires ANP32 proteins, we performed minigenome assays in human cells lacking ANP32A and ANP32B (Extended Data Fig. 1). No detectable FluPol activity was observed in the double-knockout cells, but expression of human ANP32A (huANP32A), human ANP32B (huANP32B) or chicken ANP32A (chANP32A) restored FluPolC activity. We then used cryo-electron microscopy (cryo-EM) to solve the structures of FluPolC in complex with huANP32A and chANP32A at a resolution ranging from 3.0 Å to 3.6 Å (Fig. 1a, b, Extended Data Figs. 2, 3, Extended Data Table 1, Supplementary Video 1). In these structures, two heterotrimeric FluPolC molecules assemble into an asymmetric dimer with the N-terminal leucine-rich repeat domain of ANP32A (ANP32A^{LRR})⁹ bridging the two FluPolC molecules. The C-terminal low-complexity acidic region of ANP32A (ANP32A^{LCAR}) could not be fully resolved in the structures. The structures of FluPolC dimers with huANP32A and chANP32A are largely identical, exhibiting the same FluPolC–FluPolC and FluPolC–ANP32A^{LRR} interaction interfaces. About 22% of particles in the FluPolC–chANP32A dataset lack density for ANP32A and were used to reconstruct a 3.4 Å resolution polymerase-only structure, which shows the same arrangement of FluPolC dimer as the ANP32A-containing complexes (Fig. 1c, Extended Data Figs. 2 and 3, Extended Data Table 1).

Fig. 1: Structures of dimers of FluPolC heterotrimers with or without bound ANP32A.



a–c, Cryo-EM structures of dimers of FluPolC heterotrimers with huANP32A (a) or chANP32A (b), and without ANP32A (c).

[Full size image](#)

FluPol forms an asymmetric dimer

The first FluPol molecule (hereafter designated as the FluPol replicase, FluPol_R) is fully resolved in the density map and shows a configuration of the peripheral flexible domains that is distinct from the one in the cap-snatching competent transcriptase, but similar to the configuration previously observed for RNA-free FluPol and FluPol bound to cRNA^{10,11} (Fig. 1, Extended Data Fig. 4, Supplementary Video 1). Specifically, the cap-binding domain of PB2 (PB2^{cap}) is immobilized through extensive contacts with the palm subdomain of PB1, while the nuclear localization signal domain of PB2 (PB2^{NLS}) intimately associates with the N-terminal endonuclease domain of P3 (P3^{endo}). The 627 domain of PB2 (PB2⁶²⁷), named after the host-specific amino acid residue 627, makes relatively few contacts with the rest of FluPol_R. FluPol_R is bound to a 47-nucleotide long vRNA, whose 5' terminus is clearly resolved and shows the typical hook structure bound in a pocket formed by P3 and PB1, as observed previously^{12,13} (Fig. 1, Extended Data Fig. 5). In the majority of particles, the 3' vRNA terminus cannot be resolved, but the density observed around the template entry channel suggests that it has entered the active site. In about 10% of FluPolC–chANP32A and about 7% of FluPolC–huANP32A particles, the 3' vRNA terminus is bound at the interface of the C-terminal domain of P3, the thumb subdomain of PB1 and the N1 subdomain of PB2, as recently described for FluPolA and influenza D FluPol^{12,14,15}. The second FluPol molecule (hereafter designated as the encapsidating FluPol, FluPol_E) shows a markedly different configuration of the flexible domains. The C-terminal flexible domains of PB2 (PB2^{cap}, PB2 mid-link domain (PB2^{mid-link}), PB2⁶²⁷ and PB2^{NLS}) flip over to pack against the C-terminal domain of the P3 subunit (P3^{CTD}) (Extended Data Fig. 4, Supplementary Video 1). P3^{endo}, several N-terminal domains of PB2 and the C-terminal 18 amino acid residues of PB2^{NLS} are disordered in FluPol_E. Furthermore, approximately 52% of FluPolC–chANP32A and all FluPolC–huANP32A particles lack density for PB2^{cap} and PB2^{mid-link} in FluPol_E, suggesting that these domains are flexible. No RNA was found associated with FluPol_E. The two FluPolC molecules make extensive interactions, mainly between their respective PB2 and P3 subunits, to form a large polymerase dimer interface burying a total of ~1,500 Å² (Fig. 2a). The PB2⁶²⁷ domain of FluPol_R interacts with the P3^{CTD}, PB2⁶²⁷ and PB2^{NLS} domains of FluPol_E (Fig. 2b), and the P3^{CTD} domain of FluPol_E stacks against the PB2 N2 (PB2^{N2}) and PB2^{mid-link} domains of FluPol_R (Fig. 2c). In addition, the P3 arch and PB1 β-hairpin of FluPol_E contact the P3^{CTD} and PB2^{N2} domains of FluPol_R (Fig. 2d). This dimer interface is distinct from the one

observed previously in FluPolA, which promotes template realignment and is required for replication initiation on a cRNA^{12,16}. To address the functional relevance of this dimer interface in influenza A virus, we introduced alanine mutations to several clusters of amino acid residues in FluPolA located at or close to the dimer interface on the basis of the structure of the FluPolC heterotrimeric dimer. These include the residues PA K324/H326/E327, PA K339/Q340 and PB2 P132, which are structurally equivalent to P3 R299/K301/D302, P3 N318/Q319 and PB2 E139 in FluPolC, respectively (Supplementary Fig. 1). All of these mutations resulted in a reduction of viral RNA levels in a minigenome assay analysing FluPol function (Extended Data Fig. 6a). These data indicate that amino acid residues at the asymmetric FluPol dimer interface we have identified in the FluPolC–ANP32A complexes are important for FluPol activity.

Fig. 2: FluPolC–FluPolC and ANP32A–FluPolC interaction interfaces.



a, The FluPolC–FluPolC dimer interface with interacting regions in FluPol_R and FluPol_E highlighted on the molecular surface; the two molecules are shown peeled apart by 30° to highlight the surface. Letters denote the close-up views shown in **b–d**. **b–d**, Close-up views of the FluPolC–FluPolC-interaction interface indicated in **a**. Dashed lines indicate hydrogen bonds. **e**, ANP32A–FluPolC interface with interacting regions in FluPolC highlighted. Letters denote the close-up views shown in **f–h**. **f–h**, Close-up views of the ANP32A–FluPolC-interaction interface indicated in **e**. Dashed lines indicate hydrogen bonds.

[Full size image](#)

ANP32A^{LRR} bridges the asymmetric FluPol dimer

In both the FluPolC–huANP32A and FluPolC–chANP32A structures, the ANP32A^{LRR} domain binds in a depression formed by the FluPolC dimer interface (Figs. 1a, b, 2e, Supplementary Video 1). The N-terminal region of ANP32A^{LRR} interacts with FluPol_R, involving multiple regions of PB2, including the lid domain (PB2^{lid}), PB2⁶²⁷ and PB2^{NLS} (Fig. 2e,f). These interactions bury a total of about 600 Å² at the interface between ANP32A and FluPol_R. The C-terminal region of ANP32A^{LRR} interacts with the P3^{CTD} domain and the N terminus of PB1 of FluPol_E, and buries a total of about 490 Å² at the interface (Fig. 2e,g,h). ANP32A N129 and D130, previously identified as important for FluPolA binding and activity^{8,17}, are directly involved in the interaction with FluPol_E. Specifically, N129 is sandwiched between M387 and K391 of P3 and interacts with K391 directly through hydrogen bonding, whereas D130 interacts with K608 of P3 (Fig. 2g). To address the functional relevance of this interaction, we mutated PA K413 in FluPolA—equivalent to P3 K391 in FluPolC (Fig. 2g, Supplementary Fig. 1)—to alanine. This mutant FluPolA showed reduced binding to huANP32A and loss of activity in a minigenome assay (Extended Data Fig. 7). Further mutations in FluPolA at PA D529 and PB2 T609, corresponding to P3 E513 and PB2 H631 in FluPolC (Fig. 2f, g, Supplementary Fig. 1), had similar inhibitory effects on both ANP32A binding and FluPol activity. Together, these data confirm the functional relevance of the identified ANP32A–FluPol interaction and provide an explanation for why chicken ANP32B (chANP32B) with I129 and N130 is unable to support FluPol activity^{8,17}.

ANP32A^{LCAR} interacts with PB2⁶²⁷

Species-specific differences in ANP32 proteins underpin the low activity of avian FluPolA in mammalian cells⁴. Amino acid differences important for FluPol activity have been identified in both ANP32A^{LRR} and ANP32A^{LCAR}, but a 33-amino-acid insertion in the avian ANP32A^{LCAR} relative to mammalian ANP32A^{LCAR} was found to be the most critical for the ability of avian ANP32A to support the activity of avian FluPolA^{4,18,19} (Fig. 3a). Although the ANP32A^{LCAR} could not be assigned unambiguously in the map, continuous density shows that it contacts PB2⁶²⁷ of FluPol_R (Fig. 3b,c, Supplementary Video 2). These data are in agreement with previous reports of a direct interaction between ANP32A and the PB2⁶²⁷ domain using biochemical methods and NMR^{20,21,22}. In the FluPolC–chANP32A structure, the negatively charged chANP32A^{LCAR} binds in a basic groove formed by the PB2⁶²⁷ domains of FluPol_R and FluPol_E, with the avian-specific 33-amino-acid insertion directly contacting the PB2⁶²⁷ domain of FluPol_R. This interaction

positions a previously identified hydrophobic SUMO interaction motif-like sequence²³ (Extended Data Fig. 1c) on top of PB2⁶²⁷, as well as a downstream region of the ANP32^{LCAR} which contains a mixture of basic and acidic amino acid residues (176-VLSLVKDR-183) (Fig. 3a–c). Specifically, this motif is located next to PB2 K649 (equivalent to E627 in the PB2 of avian FluPolA) and V614. PB2 V614 is equivalent to K591 in the 2009 H1N1 pandemic influenza A virus, which was of swine origin, and retained E627 in its avian PB2 but used a Q591K adaptation to increase polymerase activity^{24,25} (Extended Data Fig. 8, Supplementary Fig. 1). Interaction of this region of ANP32A with PB2⁶²⁷ could be critical for stabilization of the interaction between ANP32A and FluPol and, consequently, for the ability of ANP32A to support FluPol activity. The presence of a mixture of basic and acidic amino acid residues in this region could explain why avian ANP32A is able to support FluPol with either avian-specific 627E or mammalian-specific 627K in PB2. The corresponding region in huANP32A (176-EEEYDEDA-183), as well as in the huANP32B isoform (176-DEEDEDDE-183), is entirely acidic (Fig. 3a), potentially explaining the need to eliminate the acidic residue 627 in avian FluPolA upon viral transmission to a mammalian host. To test this hypothesis, we replaced the acidic 176–183 region of huANP32A with the corresponding region from chANP32A and found that this mutant form of huANP32A was able to fully support the activity of FluPolA with 627E in mammalian cells (Fig. 3d). These data are also in agreement with a previous study reporting that FluPolA can tolerate a range of non-acidic amino acid residues at position 627 and activity is positively correlated with the pI value of the amino acid²⁶. Thus, our data provide an explanation for adaptive mutations observed in FluPolA upon transmission of influenza A virus from an avian to a human host.

Fig. 3: Interaction of ANP32^{LCAR} with FluPolC and the effect of ANP32A on FluPolA activity.

 **figure3**

a, Schematic of huANP32A and chANP32A, highlighting the 33-amino-acid insertion (33 aa) (yellow) in chANP32A and sequence differences. huANP32A(ch176–183) is a huANP32A construct in which residues 176–183 are replaced by those from chANP32A. Acidic and basic amino acid residues are highlighted in red and blue, respectively. **b**, Close-up view of the cryo-EM density attributed to chANP32A (grey, threshold 0.934) with the chANP32A^{LRR} domain represented in cartoon (orange) and the positions of PB2⁶²⁷ of FluPol_R (blue) and FluPol_E (green). Regions potentially corresponding to the N-terminal part of ANP32A^{LCAR} and part of the avian 33-amino-acid insertion are highlighted in cyan and yellow, respectively. V614 and K649 in FluPolC correspond to K591 (Q) and K627 (E) in FluPolA (residues in parentheses are avian species-specific), respectively. **c**, Same view as shown in **b**, with PB2⁶²⁷ of FluPol_R and FluPol_E shown in surface representation. **d**, Effect of wild-type chANP32A and huANP32A, and huANP32A(ch176–183) on the activity of FluPolA with mammalian-adapted PB2^{K627} or avian-signature PB2^{E627} in a vRNP-reconstitution assay in mammalian HEK 293T cells. Top, primer-extension analysis of viral RNA levels with quantification. Bottom, western blot analysis of ANP32A levels with molecular weight markers. Data are mean \pm s.e.m., $n = 3$ biologically independent samples from 3 independent experiments. Ordinary one-way ANOVA with Dunnett's post hoc test for multiple comparisons. $P < 0.05$ is considered significant to reject the null hypothesis. Gel source data are presented in Supplementary Fig. 2.

[Full size image](#)

Implications for genome replication

The product exit channel of vRNA-bound FluPol_R, located along the PB1 finger domains and PB2^{cap}, points towards the 5'-cRNA binding site of FluPol_E, which is located next to the PA arch (residues 343–376) and the PB1 β-hairpin (residues 353–370)^{13,15}. A path lined with basic amino acid residues connects this exit channel with the 5'-cRNA binding site of FluPol_E (Fig. 4a, Supplementary Video 3) and FluPol_E is thus ideally positioned to capture the 5' end of a nascent cRNA product emerging from the active site of FluPol_R. This suggests that in the FluPolC–ANP32A complex, FluPol_R functions as the replicase, whereas FluPol_E acts as an ‘encapsidating’ polymerase, initiating the co-replicative assembly of the nascent cRNA with NP into a complementary ribonucleoprotein (cRNP) complex. To test this hypothesis, we performed a cRNA-stabilization assay²⁷ to examine the ability of FluPol to encapsidate nascent cRNA product. Mutations in FluPol_E at PA K324/H326/E327 and PA K339/Q340 caused a substantial reduction in cRNA accumulation. Note that PB2 P132 is located on the FluPol_R side of the interface and therefore this mutation could not be tested using this assay. These data confirm that the FluPol_R–FluPol_E interface is important for encapsidation of a nascent cRNA product (Extended Data Fig. 6b). The PB2⁶²⁷ domain of FluPol_E has been implicated in cRNA encapsidation using this assay, which is consistent with our model²⁸. We propose that a similar mechanism is likely to apply for cRNA-bound FluPol_R, owing to intrinsic similarities between cRNA synthesis and vRNA synthesis, which both require co-replicative encapsidation of nascent RNA.

Fig. 4: Functional implications of the FluPolC–ANP32A complex.

 **figure4**

a, Relative positions of the RNA-product exit channel in FluPol_R and the 5'-RNA binding site in FluPol_E in the chANP32A–FluPolC complex. The positions of the RNA-product exit channel in FluPol_R and the 5'-RNA binding site in FluPol_E were determined by superposing FluPol_R and FluPol_E with the structure of FluPolA bound to capped RNA and vRNA template (Protein Data Bank (PDB): 6RR7). **b**, Model for the role of FluPol–ANP32A complex in the replication of the influenza virus RNA genome and its assembly into vRNPs. FluPol in the context of vRNP or cRNP is flexible (1) but is stabilized in a replicase FluPol_R conformation upon binding of a newly synthesized FluPol in the presence of ANP32A (2). FluPol_R

initiates replication in a primer-independent manner (3), with a *trans*-activating FluPol involved in cRNA to vRNA replication by promoting cRNA template realignment (3'). As the 5' end of the nascent replication product is released from the polymerization active site of FluPol_R, it is captured in the 5'-RNA binding pocket of the encapsidating FluPol_E bound to FluPol_R (4), initiating the encapsidation of the nascent RNA with NP (5). Nascent vRNA or cRNA assemble into vRNPs or cRNPs, respectively (6), and are released upon FluPol_R termination. FluPol_E becomes the resident polymerase of the newly produced vRNP or cRNP.

[Full size image](#)

Such a role for the FluPol–ANP32A complex in viral genome replication is consistent with previous observations; in particular, ANP32A and the adaptive PB2 E627K mutation have been specifically linked to viral genome replication rather than transcription^{7,29,30} providing strong support for a role of the FluPol–ANP32A complex in replication. We were unable to fully resolve ANP32A^{LCAR} in our structures, indicating that this part of ANP32A is highly dynamic. Replication involves viral NP, which co-replicatively coats viral RNA along its length, but it is currently unknown how NP is recruited onto the growing nascent chain of RNA. Non-segmented negative-strand RNA viruses encode an acidic phosphoprotein (P) that is an essential component of their RNA polymerase complex and is involved in recruiting NP to nascent replication product³¹. Segmented negative-strand RNA viruses do not encode an equivalent protein and it is tempting to speculate that its function is performed by a cellular protein such as ANP32A. Specifically, the unstructured region of ANP32A^{LCAR}, downstream of the region interacting with FluPol_R, could act as a molecular whip recruiting NP in a manner analogous to that proposed for the P phosphoprotein.

Understanding the structural basis for why ANP32A is fundamental to influenza virus replication opens a new perspective on the role of ANP32A and host-adaptive mutations in FluPol function. Specifically, our data suggest that the FluPol–ANP32A complex represents a replication platform for the influenza virus RNA genome. The mechanistic insights gained from this study have enabled us to build a more complete picture of the structural basis for the viral replication cycle. During infection, incoming vRNPs bind to the C-terminal domain of host RNA polymerase II through interactions primarily mediated by the C-terminal domain of FluPol PA^{32,33}. This interaction stabilizes FluPol in a cap-snatching-competent conformation, enabling the cleavage of host capped RNAs that serve as primers for the initiation of viral mRNA synthesis³³. Accumulation of newly synthesized FluPol favours genome replication over transcription, consistent with a transition from

transcription to replication as infection proceeds, through forming an asymmetric dimer with the vRNP-associated resident FluPol and stabilizing it in a replication-competent conformation, enabling primer-independent initiation of replication (Fig. 4). ANP32A contributes to the stabilization of this dimer by bridging the two FluPol molecules. Several lines of evidence suggest that ANP32A is involved in cRNA-to-vRNA replication, although there is also evidence in favour of a role during vRNA-to-cRNA replication^{7,18,29,30}. In particular, avian polymerase in human cells is incapable of generating replication-competent cRNPs, suggesting that cRNA encapsidation—and hence the correct assembly of cRNPs—might be affected²⁹; this is fully consistent with our data showing that mutations at the FluPol_R–FluPol_E dimer interface interfere with cRNA encapsidation. ANP32A may have a particularly important role in stabilizing the interaction of a free FluPol with a cRNP-associated FluPol, as cRNPs need to make at least two different interactions with free FluPol molecules using two different interaction interfaces, to promote template realignment and nascent-product encapsidation. These interactions need to be fine-tuned in a host-dependent manner, in agreement with the observation of adaptive mutations at the dimer interfaces^{12,34}. Dependence on free FluPol to ensure template realignment during replication initiation on a cRNA template¹² and co-replicative genome assembly into a vRNP both provide the virus with a safety mechanism to avoid the generation of naked viral RNA in the absence of viral protein synthesis, which could otherwise be a trigger for activating innate immune responses³⁵. The identification of amino acid residues involved in mediating ANP32A–FluPol interactions will facilitate both the development of novel small-molecule inhibitors that disrupt the interaction interface and the design of genetically engineered animals resilient to influenza virus.

Methods

No statistical methods were used to predetermine sample size. The experiments were not randomized and investigators were not blinded to allocation during experiments and outcome assessment.

Cells

Human embryonic kidney 293T (HEK 293T) and Sf9 insect cells were sourced from the Cell Bank of the Sir William Dunn School of Pathology, University of Oxford. HEK 293T cells were maintained in Dulbecco's Modified Eagle Medium (DMEM) and Sf9 cells were maintained in Sf-900 II serum free medium (Gibco). Human eHAP cells (Horizon Discovery), control or lacking ANP32A and ANP32B proteins (dKO), were cultured in Iscove's modified Dulbecco's medium (IMDM; Sigma)

supplemented with 10% fetal bovine serum (FBS; Sigma), 1% nonessential amino acids (NEAA; Gibco), and 1% penicillin/streptomycin (Gibco) and have been described⁷. Cell lines have not been authenticated but tested negative for mycoplasma contamination.

Protein expression and purification

The three subunits of influenza C/Johannesburg/1/1966 virus polymerase, together with human or chicken ANP32A, were co-expressed in Sf9 cells from codon-optimized genes (GeneArt) cloned into a single baculovirus using the MultiBac system³⁶. Expression and purification of the co-expressed complex were performed as previously described^{10,12} with minor modifications: the salt concentration in all buffers was set to 150 mM to maintain FluPolC–ANP32A complex formation. Size-exclusion chromatography was performed using 25 mM HEPES–NaOH, pH 7.5, 150 mM NaCl and 5% (v/v) glycerol on a Superdex 200 Increase 10/300 GL column (GE Healthcare).

Cryo-EM sample preparation

Protein surface charges of the purified complex were neutralized by adding 0.001% glutaraldehyde for 20 min on ice to minimize preferential orientation of particles. After quenching the reaction by adding Tris-HCl, pH 8.0 to a final concentration of 100 mM, the sample was injected onto a Superdex 200 Increase 10/300 GL column (GE Healthcare) together with a 47 nt vRNA (5'-AGUAGAAACAAGGGUAUUUUUCUUUACUAGCUACCCUGCUUUUGCU-3') using 25 mM HEPES–NaOH, pH 7.5, 150 mM NaCl as the running buffer. This 47-nucleotide (nt) vRNA contains the 5' and 3' promoter elements recognized and bound by FluPol. The fractions of interest were concentrated to 0.23–0.28 mg ml⁻¹ and RNA binding was confirmed by measuring the A₂₆₀/A₂₈₀ ratio. A final concentration of 0.005% (v/v) Tween 20 was added before grid preparation. A volume of 3–4 µl of sample was placed on glow-discharged Quantifoil Holey Carbon grids (R 2/1, with 2 µm holes and 1 µm spacing and applied on biocompatible 200 gold mesh), before blotting for 3.0–3.5 s and flash-freezing in liquid ethane. All grids were prepared using a Vitrobot mark IV (FEI) at 95–100% humidity.

Cryo-EM image collection and processing

Cryo-EM data for the FluPolC–chANP32A sample were collected on a 300 kV Titan Krios microscope (Thermo Fisher Scientific) at the Division of Structural Biology (Strubi). Automated data collection was setup in EPU 2.1 using a K2 Summit (Gatan) direct electron detector at 1.37 Å per pixel operating in counting mode and a GIF Quantum energy filter (Gatan) with 20 eV slit. Sample was collected with a tilt angle of 30° at a dose of ~38.8 e⁻ Å⁻² across 44 frames for a dose rate of ~3.527 e⁻ Å⁻² s⁻¹, using a defocus range of -2 μm to -3.5 μm. Cryo-EM data for the FluPolC–huANP32A sample were collected on a 300 kV Titan Krios microscope (Thermo Fisher Scientific) at Electron Bio-Imaging Centre (eBIC). Automated data collection was setup in SerialEM 3.7 using a K3 (Gatan) direct electron detector operating in super-resolution mode at 0.5425 Å per pixel and a GIF Quantum energy filter (Gatan) with 20 eV slit. Sample was collected with a tilt angle of 20° at a dose of ~32.1 e⁻ Å⁻² across 34 frames for a dose rate of ~16 e⁻ Å⁻² s⁻¹, using a defocus range of -2 μm to -3.5 μm. Sample-specific data collection parameters are summarized in Extended Data Table 1. Data processing pipelines are shown in Extended Data Fig. 1. In brief, raw movies were processed using MotionCor2-1.1.0³⁷, with a five-by-five patch-based alignment, keeping all of the frames and dose-weighting up to the total exposure. For the K3 super-resolution, the data have been binned 2 times at the motion correction step, giving a final pixel size of 1.085 Å per pixel. The contrast transfer function (CTF) of full-dose, non-weighted micrographs was initially estimated using Gctf-v.1.06³⁸ or cryoSPARC v.2.12.0³⁹ Patch-CTF. Poor-quality images were discarded after manual inspection. Particles were blob picked in cryoSPARC v.2.12.0³⁹ and the 2D classes were inspected and classes of interest were selected to generate templates for complete particle picking. For the FluPolC–chANP32A dataset, a total number of 2,534,332 particles were picked and a final number of 772,989 particles were exported to RELION 3.1⁴⁰ after 2D and 3D class selection. The consensus map was refined to 3.50 Å. Bayesian polishing and per particle CTF refinement and B-factor estimation with beam tilt correction were performed in RELION 3.1 which improved map resolution to 3.2 Å. High order aberration and magnification

anisotropy refinement improved map resolution to 3.1 Å. Global and focus 3D classification were performed within RELION (Extended Data Fig. 2a). For the 3D variability analysis, polished particles and model were imported into cryoSPARC v.2.12.0 and refined using the non-uniform refinement job. A mask was then designed around the density corresponding to the PB2⁶²⁷ domains of both polymerases and chANP32A. The 3D variability analysis was then performed using this mask, asking for solving the three main modes on a structure low pass filtered to 6 Å. The results of this principal component analysis were clustered in twenty sub-populations and models were reconstructed for each of the individual clusters. One cluster was showing a clear density for the chANP32A^{LCAR} region and was refined using the non-uniform refinement job to 3.6 Å (Subclass 2). In parallel, all of the particles having a strong density for chANP32A were selected and refined using the non-uniform refinement job to 3.1 Å. The same 3D variability analysis was performed, asking for solving the three main modes on a structure low pass filtered to 6 Å. Mode 3 is displayed as Supplementary Video 2. For the FluPolC–huANP32A dataset, a total number of 2,312,045 particles were picked and a final number of 835,198 particles were exported to RELION 3.1 after 2D and 3D class selection. The consensus map was refined to 3.2 Å. Bayesian polishing and per particle CTF refinement and B-factor estimation with beam tilt correction were performed in RELION 3.1 which improved map resolution to 2.8 Å. Global and focus 3D classification were performed within RELION (Extended Data Fig. 2b). CryoEF⁴¹ and 3D Fourier shell correlation (FSC)⁴² sphericity scores were used to confirm that the final maps were not suffering from distortion bias due to preferred specimen orientation. The structures were modelled by first fitting ANP32A^{LRR} (PDB ID: 4XOS), FluPolC (PDB ID: 5D98) and 5' and 3' vRNA termini (PDB ID: 6RR7) using UCSF Chimera⁴³. One cycle of rigid body real space refinement followed by manual adjustment in Coot⁴⁴ was performed to correctly position the Cα chain into the density. Locally sharpened maps were generated using LocScale⁴⁵ in the CCP-EM⁴⁶ package. Finally, cycles of PHENIX⁴⁷ real space refinement and manual building in Coot⁴⁴ were used to improve model geometry. Map-to-model comparison in PHENIX mtriage validated that no over-fitting was present in the structures. Model geometry was validated for all models using MolProbity⁴⁸. All map and model

statistics are detailed in Extended Data Table 1. A homology model of FluPolA–ANP32A complex structure was generated using SWISS-MODEL⁴⁹.

Plasmids

Plasmids pHMG-PB1, pHMG-PB2, pHMG-P3 and pHMG-NP expressing the subunits of FluPolC and NP of influenza C/Johannesburg/1/66 virus and pPolI-Luci-CP3-RT expressing a luciferase reporter have been described^{50,51}. pcDNA-PB1, pcDNA-PB1a (catalytically inactive; D445A/D446A), pcDNA-PB2, pcDNA-PB2 K627E, pcDNA-PA, pcDNA-NP and pPOLI-NA, which encodes an NA vRNA segment, are derived from influenza A/WSN/33 virus and have been described previously^{27,52,53,54}. pCAGGS-chANP32A has been described previously⁴. pcDNA-huANP32A and pCAGGS-huANP32A-Strep were produced from pCAGGS-huANP32A⁴ by restriction-ligation cloning. pcDNA-huANP32A(ch176-183), pcDNA-PB2 T609A, pcDNA-PB2 P132A, pcDNA-PA D529A/R531A/E533A, pcDNA-PA K413A, pcDNA-PA K324A/H326A/E327A and pcDNA-PA K339A/Q340A were generated from pcDNA-huANP32A, pcDNA-PB2 and pcDNA-PA by site-directed PCR mutagenesis and validated by Sanger sequencing.

Influenza C virus vRNP-reconstitution and luciferase-reporter assays

Approximately 0.2×10^6 eHAP cells, control or dKO, were transfected with plasmids pHMG-PB1, pHMG-PB2, pHMG-P3, pHMG-NP, pPolI-Luci-CP3-RT and pcDNA-Renilla using Lipofectamine 2000 according to the manufacturer's instructions. Where indicated, plasmids pCAGGS-huANP32A, pCAGGS-huANP32B or pCAGGS-chANP32A were included. Cells were lysed 24 h after transfection using Passive lysis buffer (Promega). Firefly and Renilla luciferase activities were measured using a Promega dual luciferase kit and firefly activity levels were normalized to the Renilla control.

Influenza A virus vRNP-reconstitution assay and primer extension analysis

Approximately 0.2×10^6 HEK 293T cells were transfected with plasmids pcDNA-PB1, pcDNA-PB2, pcDNA-PA, pcDNA-NP and pPOLI-NA using Lipofectamine 2000 according to the manufacturer's instructions. Where indicated, plasmids encoding ANP32A proteins or mutant polymerase subunits were included. Total cellular RNA was extracted 20 h after transfection using TRI reagent (Sigma) according to the manufacturer's instructions. NA segment RNA levels were assessed using primer extension⁵⁵. In brief, primers complementary to the positive (5'-TGGACTAGTGGGAGCATC-3') and negative (5'-TCCAGTATGGTTTGATTCCG-3') sense NA segment viral RNA species were labelled with ^{32}P and total cellular RNA was reverse transcribed. A primer complementary to 5S rRNA (5'-TCCCAGGCCTCTCCATCC-3') was included as a loading control. Products were resolved by 6% denaturing PAGE and visualized by phosphorimaging. Product bands were identified by comparison with previously published data^{56,57}. Analysis was carried out using ImageJ⁵⁸ and Prism 8 (GraphPad), and viral RNA signals were normalized to the 5S rRNA loading control.

Western blotting

Western blotting of all proteins was carried out using specific rabbit polyclonal antibodies. PB1 and PB2 were blotted using commercially available antibodies (Genetex), while PA was blotted using a custom-made antibody⁵⁹. ANP32A and actin were blotted using commercially available antibodies (Sigma). In all cases the secondary antibody used was goat anti-rabbit conjugated to HRP, and Amersham ECL Western Blotting Detection Reagents (GE Healthcare) were used for detection.

Affinity purification assays

Approximately 2×10^6 HEK 293T cells were transfected with pcDNA-PB1, pcDNA-PB2, pcDNA-PA and pCAGGS-huANP32A-Strep. 48 h after

transfection, cells were lysed in 500 µl of lysis buffer (50 mM Tris-HCl pH 8.0, 200 mM NaCl, 25% glycerol, 0.5% Igepal CA-630, 1 mM DTT, 1 mM PMSF, 1 × complete EDTA-free protease inhibitor cocktail tablet (Roche)) for 1 h at 4 °C and cellular debris was cleared by centrifugation for 5 min at 17,000*g*. The supernatant was diluted in 2 ml 150 mM NaCl and incubated with Strep-Tactin beads (IBA) for 2 h at 4 °C. Beads were washed three times in wash buffer (10 mM Tris-HCl pH 8.0, 150 mM NaCl, 10% glycerol, 0.1% Igepal CA-630, 1 mM PMSF) and complexes were eluted in 1× buffer E (IBA) for 16 h at 4 °C. Eluted complexes were analysed by 12% SDS PAGE and western blotting.

cRNA-encapsulation assays

cRNA-encapsulation assays were performed as described previously²⁷. In brief, approximately 1×10^6 HEK 293T cells were transfected with pcDNA-PB1a, pcDNA-PB2, pcDNA-PA and pcDNA-NP using Lipofectamine 2000 according to the manufacturer's instructions. Forty-eight hours after transfection, culture medium was replaced with DMEM containing 0.5% FBS and 5 µg ml⁻¹ actinomycin D and influenza A/WSN/33 virus at multiplicity of infection 5.0. Total cellular RNA was extracted 6 h after infection using Trizol (Sigma) according to the manufacturer's instructions, and viral RNA levels were determined by primer extension analysis as described above.

Reporting summary

Further information on research design is available in the [Nature Research Reporting Summary](#) linked to this paper.

Data availability

All data are available from the corresponding authors and/or included in the manuscript or [Supplementary Information](#). Cryo-EM density maps with the corresponding atomic coordinates have been deposited in the Electron Microscopy Data Bank with accession codes [EMD-10665](#) (FluPolC–huANP32A subclass 1), [EMD-10667](#) (FluPolC–huANP32A subclass 2),

[EMD-10666](#) (FluPolC–chANP32A subclass 1), [EMD-10659](#) (FluPolC–chANP32A subclass 2), [EMD-10662](#) (FluPolC–chANP32A subclass 3) and [EMD-10664](#) (FluPolC–chANP32A subclass 4), and the Protein Data Bank with accession codes [6XZQ](#) (FluPolC–huANP32A subclass 1), [6Y0C](#) (FluPolC–huANP32A subclass 2), [6XZR](#) (FluPolC–chANP32A subclass 1), [6XZD](#) (FluPolC–chANP32A subclass 2), [6XZG](#) (FluPolC–chANP32A subclass 3) and [6XZP](#) (FluPolC–chANP32A subclass 4).

References

1. 1.

Krammer, F. et al. Influenza. *Nat. Rev. Dis. Primers* **4**, 3 (2018).

[PubMed](#) [PubMed Central](#) [Google Scholar](#)

2. 2.

Fodor, E. & Te Velthuis, A. J. W. Structure and function of the influenza virus transcription and replication machinery. *Cold Spring Harb. Perspect. Med.* **10**, a038398 (2019).

[Google Scholar](#)

3. 3.

Wandzik, J. M., Kouba, T. & Cusack, S. Structure and function of influenza polymerase. *Cold Spring Harb. Perspect. Med.* **10**, a038372 (2020).

[Google Scholar](#)

4. 4.

Long, J. S. et al. Species difference in ANP32A underlies influenza A virus polymerase host restriction. *Nature* **529**, 101–104 (2016).

[ADS](#) [CAS](#) [PubMed](#) [PubMed Central](#) [Google Scholar](#)

5. 5.

Walker, A. P. & Fodor, E. Interplay between influenza virus and the host RNA polymerase II transcriptional machinery. *Trends Microbiol.* **27**, 398–407 (2019).

[CAS](#) [PubMed](#) [PubMed Central](#) [Google Scholar](#)

6. 6.

Peacock, T. P., Sheppard, C. M., Staller, E. & Barclay, W. S. Host determinants of influenza RNA synthesis. *Annu. Rev. Virol.* **6**, 215–233 (2019).

[CAS](#) [PubMed](#) [Google Scholar](#)

7. 7.

Staller, E. et al. ANP32 proteins are essential for influenza virus replication in human cells. *J. Virol.* **93**, e00217-19 (2019).

[CAS](#) [PubMed](#) [PubMed Central](#) [Google Scholar](#)

8. 8.

Zhang, H. et al. Fundamental contribution and host range determination of ANP32A and ANP32B in influenza A virus polymerase activity. *J. Virol.* **93**, e00174-19 (2019).

[CAS](#) [PubMed](#) [PubMed Central](#) [Google Scholar](#)

9. 9.

Huyton, T. & Wolberger, C. The crystal structure of the tumor suppressor protein pp32 (Anp32a): structural insights into Anp32 family of proteins. *Protein Sci.* **16**, 1308–1315 (2007).

[CAS](#) [PubMed](#) [PubMed Central](#) [Google Scholar](#)

10. 10.

Hengrung, N. et al. Crystal structure of the RNA-dependent RNA polymerase from influenza C virus. *Nature* **527**, 114–117 (2015).

[ADS](#) [CAS](#) [PubMed](#) [PubMed Central](#) [Google Scholar](#)

11. 11.

Thierry, E. et al. Influenza polymerase can adopt an alternative configuration involving a radical repacking of PB2 domains. *Mol. Cell* **61**, 125–137 (2016).

[CAS](#) [PubMed](#) [PubMed Central](#) [Google Scholar](#)

12. 12.

Fan, H. et al. Structures of influenza A virus RNA polymerase offer insight into viral genome replication. *Nature* **573**, 287–290 (2019).

[ADS](#) [CAS](#) [PubMed](#) [PubMed Central](#) [Google Scholar](#)

13. 13.

Pflug, A., Guilligay, D., Reich, S. & Cusack, S. Structure of influenza A polymerase bound to the viral RNA promoter. *Nature* **516**, 355–360 (2014).

[ADS](#) [CAS](#) [PubMed](#) [Google Scholar](#)

14. 14.

Peng, Q. et al. Structural insight into RNA synthesis by influenza D polymerase. *Nat. Microbiol.* **4**, 1750–1759 (2019).

[CAS](#) [PubMed](#) [Google Scholar](#)

15. 15.

Wandzik, J.M. et al. A structure-based model for the complete transcription cycle of influenza polymerase. *Cell* **181**, 877–893 (2020).

[CAS](#) [PubMed](#) [Google Scholar](#)

16. 16.

Chang, S. et al. Cryo-EM structure of influenza virus RNA polymerase complex at 4.3 Å resolution. *Mol. Cell* **57**, 925–935 (2015).

[CAS](#) [PubMed](#) [Google Scholar](#)

17. 17.

Long, J. S. et al. Species specific differences in use of ANP32 proteins by influenza A virus. *eLife* **8**, e45066 (2019).

[CAS](#) [PubMed](#) [PubMed Central](#) [Google Scholar](#)

18. 18.

Bi, Z. et al. Insights into species-specific regulation of ANP32A on the mammalian-restricted influenza virus polymerase activity. *Emerg. Microbes Infect.* **8**, 1465–1478 (2019).

[PubMed](#) [PubMed Central](#) [Google Scholar](#)

19. 19.

Zhang, H. et al. A unique feature of swine ANP32A provides susceptibility to avian influenza virus infection in pigs. *PLoS Pathog.* **16**, e1008330 (2020).

[CAS](#) [PubMed](#) [PubMed Central](#) [Google Scholar](#)

20. 20.

Baker, S.F., Ledwith, M.P. & Mehle, A. Differential splicing of ANP32A in birds alters its ability to stimulate rna synthesis by

restricted influenza polymerase. *Cell Rep.* **24**, 2581–2588 (2018).

[CAS](#) [PubMed](#) [PubMed Central](#) [Google Scholar](#)

21. 21.

Camacho-Zarco, A. R. et al. Molecular basis of host-adaptation interactions between influenza virus polymerase PB2 subunit and ANP32A. *Nat. Commun.* **11**, 3656 (2020).

[ADS](#) [CAS](#) [PubMed](#) [PubMed Central](#) [Google Scholar](#)

22. 22.

Mistry, B. et al. Elucidating the interactions between influenza virus polymerase and host factor ANP32A. *J. Virol.* **94**, e01353-19 (2020).

[CAS](#) [PubMed](#) [PubMed Central](#) [Google Scholar](#)

23. 23.

Domingues, P. & Hale, B. G. Functional insights into ANP32A-dependent influenza A virus polymerase host restriction. *Cell Rep.* **20**, 2538–2546 (2017).

[CAS](#) [PubMed](#) [PubMed Central](#) [Google Scholar](#)

24. 24.

Mehle, A. & Doudna, J. A. Adaptive strategies of the influenza virus polymerase for replication in humans. *Proc. Natl Acad. Sci. USA* **106**, 21312–21316 (2009).

[ADS](#) [CAS](#) [PubMed](#) [Google Scholar](#)

25. 25.

Yamada, S. et al. Biological and structural characterization of a host-adapting amino acid in influenza virus. *PLoS Pathog.* **6**, e1001034

(2010).

[PubMed](#) [PubMed Central](#) [Google Scholar](#)

26. 26.

Chin, A. W. H. et al. Influenza A viruses with different amino acid residues at PB2-627 display distinct replication properties in vitro and in vivo: revealing the sequence plasticity of PB2-627 position. *Virology* **468–470**, 545–555 (2014).

[PubMed](#) [Google Scholar](#)

27. 27.

Vreede, F. T., Jung, T. E. & Brownlee, G. G. Model suggesting that replication of influenza virus is regulated by stabilization of replicative intermediates. *J. Virol.* **78**, 9568–9572 (2004).

[CAS](#) [PubMed](#) [PubMed Central](#) [Google Scholar](#)

28. 28.

Nilsson, B. E., Te Velthuis, A. J. W. & Fodor, E. Role of the PB2 627 domain in influenza A virus polymerase function. *J. Virol.* **91**, e02467-16 (2017).

[PubMed](#) [PubMed Central](#) [Google Scholar](#)

29. 29.

Mänz, B., Brunotte, L., Reuther, P. & Schwemmle, M. Adaptive mutations in NEP compensate for defective H5N1 RNA replication in cultured human cells. *Nat. Commun.* **3**, 802 (2012).

[ADS](#) [PubMed](#) [Google Scholar](#)

30. 30.

Sugiyama, K., Kawaguchi, A., Okuwaki, M. & Nagata, K. pp32 and APRIL are host cell-derived regulators of influenza virus RNA synthesis from cRNA. *eLife* **4**, e08939 (2015).

[PubMed](#) [PubMed Central](#) [Google Scholar](#)

31. 31.

Pan, J. et al. Structure of the human metapneumovirus polymerase phosphoprotein complex. *Nature* **577**, 275–279 (2020).

[ADS](#) [CAS](#) [PubMed](#) [Google Scholar](#)

32. 32.

Lukarska, M. et al. Structural basis of an essential interaction between influenza polymerase and Pol II CTD. *Nature* **541**, 117–121 (2017).

[ADS](#) [CAS](#) [PubMed](#) [Google Scholar](#)

33. 33.

Serna Martin, I. et al. A mechanism for the activation of the influenza virus transcriptase. *Mol. Cell* **70**, 1101–1110 (2018).

[CAS](#) [PubMed](#) [PubMed Central](#) [Google Scholar](#)

34. 34.

Chen, K. Y., Santos Afonso, E. D., Enouf, V., Isel, C. & Naffakh, N. Influenza virus polymerase subunits co-evolve to ensure proper levels of dimerization of the heterotrimer. *PLoS Pathog.* **15**, e1008034 (2019).

[CAS](#) [PubMed](#) [PubMed Central](#) [Google Scholar](#)

35. 35.

Killip, M. J., Fodor, E. & Randall, R. E. Influenza virus activation of the interferon system. *Virus Res.* **209**, 11–22 (2015).

[CAS](#) [PubMed](#) [PubMed Central](#) [Google Scholar](#)

36. 36.

Bieniossek, C., Imasaki, T., Takagi, Y. & Berger, I. MultiBac: expanding the research toolbox for multiprotein complexes. *Trends Biochem. Sci.* **37**, 49–57 (2012).

[CAS](#) [PubMed](#) [Google Scholar](#)

37. 37.

Zheng, S. Q. et al. MotionCor2: anisotropic correction of beam-induced motion for improved cryo-electron microscopy. *Nat. Methods* **14**, 331–332 (2017).

[CAS](#) [PubMed](#) [PubMed Central](#) [Google Scholar](#)

38. 38.

Zhang, K. Gctf: Real-time CTF determination and correction. *J. Struct. Biol.* **193**, 1–12 (2016).

[ADS](#) [CAS](#) [PubMed](#) [PubMed Central](#) [Google Scholar](#)

39. 39.

Punjani, A., Rubinstein, J. L., Fleet, D. J. & Brubaker, M. A. cryoSPARC: algorithms for rapid unsupervised cryo-EM structure determination. *Nat. Methods* **14**, 290–296 (2017).

[CAS](#) [Google Scholar](#)

40. 40.

Scheres, S. H. RELION: implementation of a Bayesian approach to cryo-EM structure determination. *J. Struct. Biol.* **180**, 519–530 (2012).

[CAS](#) [PubMed](#) [PubMed Central](#) [Google Scholar](#)

41. 41.

Naydenova, K. & Russo, C. J. Measuring the effects of particle orientation to improve the efficiency of electron cryomicroscopy. *Nat. Commun.* **8**, 629 (2017).

[ADS](#) [PubMed](#) [PubMed Central](#) [Google Scholar](#)

42. 42.

Tan, Y. Z. et al. Addressing preferred specimen orientation in single-particle cryo-EM through tilting. *Nat. Methods* **14**, 793–796 (2017).

[CAS](#) [PubMed](#) [PubMed Central](#) [Google Scholar](#)

43. 43.

Pettersen, E. F. et al. UCSF Chimera—a visualization system for exploratory research and analysis. *J. Comput. Chem.* **25**, 1605–1612 (2004).

[CAS](#) [PubMed](#) [PubMed Central](#) [Google Scholar](#)

44. 44.

Emsley, P., Lohkamp, B., Scott, W. G. & Cowtan, K. Features and development of Coot. *Acta Crystallogr. D* **66**, 486–501 (2010).

[CAS](#) [Google Scholar](#)

45. 45.

Jakobi, A. J., Wilmanns, M. & Sachse, C. Model-based local density sharpening of cryo-EM maps. *eLife* **6**, e27131 (2017).

[PubMed](#) [PubMed Central](#) [Google Scholar](#)

46. 46.

Burnley, T. Introducing the Proceedings of the CCP-EM Spring Symposium. *Acta Crystallogr. D* **73**, 467–468 (2017).

[Google Scholar](#)

47. 47.

Adams, P. D. et al. PHENIX: a comprehensive Python-based system for macromolecular structure solution. *Acta Crystallogr. D* **66**, 213–221 (2010).

[CAS](#) [Google Scholar](#)

48. 48.

Davis, I. W. et al. MolProbity: all-atom contacts and structure validation for proteins and nucleic acids. *Nucleic Acids Res.* **35**, W375–W383 (2007).

[ADS](#) [PubMed](#) [PubMed Central](#) [Google Scholar](#)

49. 49.

Waterhouse, A. et al. SWISS-MODEL: homology modelling of protein structures and complexes. *Nucleic Acids Res.* **46** (W1), W296–W303 (2018).

[CAS](#) [PubMed](#) [PubMed Central](#) [Google Scholar](#)

50. 50.

Crescenzo-Chaigne, B., Naffakh, N. & van der Werf, S. Comparative analysis of the ability of the polymerase complexes of influenza viruses type A, B and C to assemble into functional RNP s that allow

expression and replication of heterotypic model RNA templates in vivo. *Virology* **265**, 342–353 (1999).

[CAS](#) [PubMed](#) [Google Scholar](#)

51. 51.

Tang, Y. S., Lo, C. Y., Mok, C. K., Chan, P. K. & Shaw, P. C. The extended C-terminal region of influenza C virus nucleoprotein is important for nuclear import and ribonucleoprotein activity. *J. Virol.* **93**, e02048-18 (2019).

[CAS](#) [PubMed](#) [PubMed Central](#) [Google Scholar](#)

52. 52.

Fodor, E. et al. A single amino acid mutation in the PA subunit of the influenza virus RNA polymerase inhibits endonucleolytic cleavage of capped RNAs. *J. Virol.* **76**, 8989–9001 (2002).

[CAS](#) [PubMed](#) [PubMed Central](#) [Google Scholar](#)

53. 53.

Fodor, E. et al. Rescue of influenza A virus from recombinant DNA. *J. Virol.* **73**, 9679–9682 (1999).

[CAS](#) [PubMed](#) [PubMed Central](#) [Google Scholar](#)

54. 54.

Paterson, D., te Velthuis, A. J., Vreede, F. T. & Fodor, E. Host restriction of influenza virus polymerase activity by PB2 627E is diminished on short viral templates in a nucleoprotein-independent manner. *J. Virol.* **88**, 339–344 (2014).

[PubMed](#) [PubMed Central](#) [Google Scholar](#)

55. 55.

Robb, N. C., Smith, M., Vreede, F. T. & Fodor, E. NS2/NEP protein regulates transcription and replication of the influenza virus RNA genome. *J. Gen. Virol.* **90**, 1398–1407 (2009).

[CAS](#) [PubMed](#) [Google Scholar](#)

56. 56.

Deng, T. et al. Role of ran binding protein 5 in nuclear import and assembly of the influenza virus RNA polymerase complex. *J. Virol.* **80**, 11911–11919 (2006).

[CAS](#) [PubMed](#) [PubMed Central](#) [Google Scholar](#)

57. 57.

Vreede, F. T. & Brownlee, G. G. Influenza virion-derived viral ribonucleoproteins synthesize both mRNA and cRNA in vitro. *J. Virol.* **81**, 2196–2204 (2007).

[CAS](#) [PubMed](#) [Google Scholar](#)

58. 58.

Schneider, C. A., Rasband, W. S. & Eliceiri, K. W. NIH Image to ImageJ: 25 years of image analysis. *Nat. Methods* **9**, 671–675 (2012).

[CAS](#) [PubMed](#) [PubMed Central](#) [Google Scholar](#)

59. 59.

Engelhardt, O. G., Smith, M. & Fodor, E. Association of the influenza A virus RNA-dependent RNA polymerase with cellular RNA polymerase II. *J. Virol.* **79**, 5812–5818 (2005).

[CAS](#) [PubMed](#) [PubMed Central](#) [Google Scholar](#)

60. 60.

Robert, X. & Gouet, P. Deciphering key features in protein structures with the new ENDscript server. *Nucleic Acids Res.* **42**, W320–W324 (2014).

[CAS](#) [PubMed](#) [PubMed Central](#) [Google Scholar](#)

[Download references](#)

Acknowledgements

We thank N. Naffakh, P.-C. Shaw, G. G. Brownlee and F. Vreede for plasmids; I. Berger for the MultiBac system; D. Karia, A. Howe and D. Clare for assistance with cryo-EM; and G. G. Brownlee and members of the Fodor and Grimes laboratories for helpful comments and discussions. This work was supported by Medical Research Council (MRC) programme grant MR/R009945/1 (to E.F.), Wellcome Investigator Awards 200835/Z/16/Z (to J.M.G.) and 205100/Z/16/Z (to W.S.B.), MRC Studentship (to A.P.W.) and Imperial College President's PhD Scholarship (to E.S.). We thank Diamond Light source for access and support of the cryo-EM facilities at the UK national Electron Bio-Imaging Centre (eBIC) (proposal EM20223), funded by the Wellcome, MRC and BBSRC. Further electron microscopy provision was provided through the OPIC electron microscopy facility, which was founded by a Wellcome JIF award (060208/Z/00/Z) and is supported by a Wellcome equipment grant (093305/Z/10/Z). Computation was performed at the Oxford Biomedical Research Computing (BMRC) facility, a joint development between the Wellcome Centre for Human Genetics and the Big Data Institute supported by Health Data Research UK and the NIHR Oxford Biomedical Research Centre. The views expressed are those of the author(s) and not necessarily those of the NHS, the NIHR or the Department of Health. Part of this work was supported by Wellcome administrative support grant (203141/Z/16/Z).

Author information

Author notes

1. Ecco Staller

Present address: Sir William Dunn School of Pathology, University of Oxford, Oxford, UK

2. These authors contributed equally: Loïc Carrique, Haitian Fan, Alexander P. Walker, Jeremy R. Keown

3. These authors jointly supervised this work: Jonathan M. Grimes, Ervin Fodor

Affiliations

1. Division of Structural Biology, University of Oxford, Oxford, UK

Loïc Carrique, Jeremy R. Keown & Jonathan M. Grimes

2. Sir William Dunn School of Pathology, University of Oxford, Oxford, UK

Haitian Fan, Alexander P. Walker, Jane Sharps & Ervin Fodor

3. Section of Molecular Virology, Imperial College London, London, UK

Ecco Staller & Wendy S. Barclay

4. Diamond Light Source Ltd, Harwell Science and Innovation Campus, Didcot, UK

Jonathan M. Grimes

Authors

1. Loïc Carrique

[View author publications](#)

You can also search for this author in [PubMed](#) [Google Scholar](#)

2. Haitian Fan

[View author publications](#)

You can also search for this author in [PubMed](#) [Google Scholar](#)

3. Alexander P. Walker

[View author publications](#)

You can also search for this author in [PubMed](#) [Google Scholar](#)

4. Jeremy R. Keown

[View author publications](#)

You can also search for this author in [PubMed](#) [Google Scholar](#)

5. Jane Sharps

[View author publications](#)

You can also search for this author in [PubMed](#) [Google Scholar](#)

6. Ecco Staller

[View author publications](#)

You can also search for this author in [PubMed](#) [Google Scholar](#)

7. Wendy S. Barclay

[View author publications](#)

You can also search for this author in [PubMed](#) [Google Scholar](#)

8. Ervin Fodor

[View author publications](#)

You can also search for this author in [PubMed](#) [Google Scholar](#)

9. Jonathan M. Grimes

[View author publications](#)

You can also search for this author in [PubMed](#) [Google Scholar](#)

Contributions

L.C., H.F., A.P.W., J.R.K., E.F. and J.M.G. conceived and designed the study. H.F., L.C. and J.R.K. carried out cloning of recombinant baculoviruses and protein purification, collected and processed electron microscopy data and built and refined models. A.P.W. and J.S. performed functional assays and analysed data. E.S. and W.S.B. provided plasmids and cell lines. J.M.G. and E.F. supervised the structural and functional studies, respectively. L.C., H.F., A.P.W., J.R.K., E.F. and J.M.G. wrote the manuscript with input from all co-authors.

Corresponding authors

Correspondence to [Ervin Fodor](#) or [Jonathan M. Grimes](#).

Ethics declarations

Competing interests

The authors declare no competing interests.

Additional information

Peer review information *Nature* thanks Julien Lescar, Yi Shi, Xiu-Feng Wan and the other, anonymous, reviewer(s) for their contribution to the peer review of this work. Peer reviewer reports are available.

Publisher's note Springer Nature remains neutral with regard to jurisdictional claims in published maps and institutional affiliations.

Extended data figures and tables

[Extended Data Fig. 1 FluPolC activity depends on ANP32A and alignment of ANP32 proteins.](#)

a, b, Luciferase reporter gene activities reflecting FluPolC activity in control (**a**) and dKO (**b**) eHAP cells in the presence or absence of overexpressed huANP32A, huANP32B or chANP32A. Data are presented as mean values \pm s.e.m. $n = 3$ biologically independent samples from $n = 3$ independent experiments. Ordinary one-way ANOVA with Dunnett's post hoc test for multiple comparisons. $P < 0.05$ is considered significant to reject the null hypothesis. **c**, Sequence alignment of huANP32A, huANP32B, chANP32A, chANP32B. Residues involved in hydrogen bonding interactions with FluPolC are indicated in orange. The chANP32A avian-specific 33 amino acid insertion is highlighted in cyan. The SUMO interaction motif (SIM) sequence is indicated by black triangles. The figure was prepared with Esprit 3.0⁶⁰.

Extended Data Fig. 2 Data collection, processing and analysis scheme.

a, b, Flowchart for the processing and the classification of the FluPolC-huANP32A complex (**a**) and FluPolC-chANP32A complex (**b**).

Extended Data Fig. 3 Single-particle cryo-EM analysis of FluPolC-huANP32A and FluPolC-chANP32A complexes.

a, e, Representative micrograph of FluPolC-huANP32A (**a**) and FluPolC-chANP32A (**e**) embedded in vitreous ice. Scale bar, 200 Å. **b, f**, Representative 2D class averages of FluPolC-huANP32A (**b**) and FluPolC-chANP32A (**f**). **c, d**, Data analysis for FluPolC-huANP32A Subclass1 (**c**) and Subclass2 (**d**). 3D reconstruction locally filtered and coloured according to RELION local resolution (left panel). FSC curve indicating overall map resolution and model-to-map FSC (middle panel). Curves are shown for phase randomization, unmasked, masked and phase-randomization-corrected masked maps. Angular distribution of particle projections with the cryo-EM map shown in grey (right panel). **g–j**, Data analysis for FluPolC-chANP32A Subclass1 (**g**), Subclass2 (**h**), Subclass3 (**i**) and Subclass4 (**j**). 3D reconstruction locally filtered and coloured according to RELION local resolution (top panel). FSC curve indicating overall map resolution and the model-to-map FSC (middle panel). Curves

are shown for phase randomization, unmasked, masked and phase-randomization-corrected masked maps. Angular distribution of particle projections with the cryo-EM map shown in grey (bottom panel).

Extended Data Fig. 4 Comparison of FluPol_R and FluPol_E structures with the transcriptase and apo conformations of FluPol.

a–d, Comparison of structures of human influenza A/NT/60/68 (H3N2) bound to vRNA and capped RNA in the transcriptase conformation (PDB: 6RR7) (**a**) and human influenza C/Johannesburg/1/66 in the apo conformation (PDB: 5D98) (**b**) with structures of FluPol_R (**c**) and FluPol_E (**d**) in the FluPolC-chANP32A complex. **e–h**, Comparison of the PB2 domain arrangements in the complexes shown in **a–d**.

Extended Data Fig. 5 Close-up view of the interaction of 5' and 3' vRNA termini with FluPol_R.

a, c, Close-up view of the 3' vRNA pointing towards the active site in the FluPolC-huANP32A (**a**) and FluPolC-chANP32A (**c**) structures. **b, d**, Close-up view of the 3' vRNA binding in a groove located between P3^{CTD} and the PB1^{thumb} and PB2^{N1} subdomains in the FluPolC-huANP32A (**b**) and FluPolC-chANP32A (**d**) structures.

Extended Data Fig. 6 Effect of FluPol_R-FluPol_E dimer interface mutations on FluPolA activity.

a, b, Effect of mutations at the FluPol_R-FluPol_E dimer interface on FluPolA activity in viral minigenome assays (**a**) and cRNA encapsidation by FluPolA (**b**). Data are presented as mean values \pm s.e.m. $n = 3$ biologically independent samples from $n = 3$ independent experiments. Ordinary one-way ANOVA with Dunnett's post hoc test for multiple comparisons. $P < 0.05$ is considered significant to reject the null hypothesis. Western blot analyses were repeated from $n = 3$ independent experiments with similar results. For gel source data, see Supplementary Fig. 2.

Extended Data Fig. 7 Effect of FluPolA mutations at the FluPolA-ANP32A interface on FluPolA activity and interaction with huANP32A.

a, b, Effect of FluPolA mutations at the FluPolA-ANP32A interface on FluPolA activity in viral minigenome assays on (**a**) and FluPolA-ANP32A interaction (**b**). Data are presented as mean values \pm s.e.m. $n = 3$ biologically independent samples from $n = 3$ independent experiments. Ordinary one-way ANOVA with Dunnett's post hoc test for multiple comparisons. $P < 0.05$ is considered significant to reject the null hypothesis. Western blot analyses were repeated from $n = 3$ independent experiments with similar results. For gel source data, see Supplementary Fig. 2.

Extended Data Fig. 8 Structural comparison of PB2⁶²⁷ domains of FluPolA and FluPolC.

Structures of the PB2⁶²⁷ domains from crystal structures of FluPol from influenza C/Johannesburg/1/1966 (**a**, PDB ID: 5D98) and A/NT/60/1968 (H3N2) (**b**, PDB ID: 6QNW) viruses are aligned and shown in cartoon mode. Residues discussed in this study are highlighted in stick mode and coloured in orange.

Extended Data Table 1 Cryo-EM data collection, refinement and validation statistics

[Full size table](#)

Supplementary information

Supplementary Figure

Supplementary Fig. 1 Sequence alignment of FluPolA and FluPolC. **a - c**, Sequence alignment of FluPol subunits (**a**, PA/P3; **b**, PB1; **c**, PB2) from influenza A/WSN/33 (H1N1) and C/Johannesburg/1/1966 viruses. Residues involved in forming the asymmetric FluPol dimer interface are highlighted

in cyan, and residues involved in ANP32A binding are highlighted in orange. The figure was prepared with Esprift 3.0⁶⁰.

Reporting Summary

Supplementary Figure

Supplementary Fig. 2 Source data (gels).

Peer Review File

Video 1

Overview of the FluPolC-chANP32A structure. The movie shows how vRNA-bound FluPolC (FluPol_R) assembles with an apo FluPolC (FluPol_E) to form an asymmetric dimer stabilized by ANP32A.

Video 2

Cryo-EM map of the FluPolC-chANP32A complex. The movie shows the repositioning of the reconstructed densities, corresponding to the PB2⁶²⁷ domains of both polymerases and chANP32A, along the third eigenvector.

Video 3

Cryo-EM map of the FluPolC-chANP32A complex. The movie shows the cryo-EM density of the FluPolC-chANP32A complex, highlighting the proximity of the product exit channel of FluPol_R to the 5' RNA binding site of FluPol_E.

Rights and permissions

Reprints and Permissions

About this article



Check for
updates

Cite this article

Carrique, L., Fan, H., Walker, A.P. *et al.* Host ANP32A mediates the assembly of the influenza virus replicase. *Nature* **587**, 638–643 (2020). <https://doi.org/10.1038/s41586-020-2927-z>

[Download citation](#)

- Received: 07 February 2020
- Accepted: 01 September 2020
- Published: 18 November 2020
- Issue Date: 26 November 2020
- DOI: <https://doi.org/10.1038/s41586-020-2927-z>

Comments

By submitting a comment you agree to abide by our [Terms](#) and [Community Guidelines](#). If you find something abusive or that does not comply with our terms or guidelines please flag it as inappropriate.

[Download PDF](#)

This article was downloaded by **calibre** from <https://www.nature.com/articles/s41586-020-2927-z>

- Article
- [Published: 14 October 2020](#)

Cell-type-specific 3D epigenomes in the developing human cortex

- [Michael Song](#) ORCID: [orcid.org/0000-0002-3355-4806^{1,2 na1}](https://orcid.org/0000-0002-3355-4806),
 - [Mark-Phillip Pebworth](#) ORCID: [orcid.org/0000-0001-8224-9480^{3,4 na1}](https://orcid.org/0000-0001-8224-9480),
 - [Xiaoyu Yang^{1 na1}](#),
 - [Armen Abnousi](#) ORCID: [orcid.org/0000-0003-1822-0928⁵](https://orcid.org/0000-0003-1822-0928),
 - [Changxu Fan^{6,7}](#),
 - [Jia Wen](#) ORCID: [orcid.org/0000-0003-3273-7704⁸](https://orcid.org/0000-0003-3273-7704),
 - [Jonathan D. Rosen](#) ORCID: [orcid.org/0000-0001-6396-4219⁹](https://orcid.org/0000-0001-6396-4219),
 - [Mayank N. K. Choudhary](#) ORCID: [orcid.org/0000-0002-9824-7217^{6,7}](https://orcid.org/0000-0002-9824-7217),
 - [Xiekui Cui¹](#),
 - [Ian R. Jones¹](#),
 - [Seth Bergenholz¹](#),
 - [Ugomma C. Eze](#) ORCID: [orcid.org/0000-0001-8142-6318^{4,10}](https://orcid.org/0000-0001-8142-6318),
 - [Ivan Juric⁵](#),
 - [Bingkun Li](#) ORCID: [orcid.org/0000-0001-6822-9440¹](https://orcid.org/0000-0001-6822-9440),
 - [Lenka Maliskova](#) ORCID: [orcid.org/0000-0001-7677-3833¹](https://orcid.org/0000-0001-7677-3833),
 - [Jerry Lee¹](#),
 - [Weifang Liu⁹](#),
 - [Alex A. Pollen^{4,11}](#),
 - [Yun Li](#) ORCID: [orcid.org/0000-0002-9275-4189^{8,9,12}](https://orcid.org/0000-0002-9275-4189),
 - [Ting Wang](#) ORCID: [orcid.org/0000-0002-6800-242X^{6,7,13}](https://orcid.org/0000-0002-6800-242X),
 - [Ming Hu](#) ORCID: [orcid.org/0000-0003-0987-2916^{5 na1}](https://orcid.org/0000-0003-0987-2916),
 - [Arnold R. Kriegstein](#) ORCID: [orcid.org/0000-0001-5742-2990^{4,11}](https://orcid.org/0000-0001-5742-2990)
- &

- [Yin Shen](#) [ORCID: orcid.org/0000-0001-9901-5613^{1,11,14}](#)

[Nature](#) **volume 587**, pages644–649(2020)[Cite this article](#)

- 9741 Accesses
- 2 Citations
- 114 Altmetric
- [Metrics details](#)

Subjects

- [Cell fate and cell lineage](#)
- [Epigenomics](#)

Abstract

Lineage-specific epigenomic changes during human corticogenesis have been difficult to study owing to challenges with sample availability and tissue heterogeneity. For example, previous studies using single-cell RNA sequencing identified at least 9 major cell types and up to 26 distinct subtypes in the dorsal cortex alone^{1,2}. Here we characterize cell-type-specific *cis*-regulatory chromatin interactions, open chromatin peaks, and transcriptomes for radial glia, intermediate progenitor cells, excitatory neurons, and interneurons isolated from mid-gestational samples of the human cortex. We show that chromatin interactions underlie several aspects of gene regulation, with transposable elements and disease-associated variants enriched at distal interacting regions in a cell-type-specific manner. In addition, promoters with increased levels of chromatin interactivity—termed super-interactive promoters—are enriched for lineage-specific genes, suggesting that interactions at these loci contribute to the fine-tuning of transcription. Finally, we develop CRISPRview, a technique that integrates immunostaining, CRISPR interference, RNAscope, and image analysis to validate cell-type-specific *cis*-regulatory elements in heterogeneous populations of primary cells. Our findings provide insights

into cell-type-specific gene expression patterns in the developing human cortex and advance our understanding of gene regulation and lineage specification during this crucial developmental window.

[Access through your institution](#)

[Change institution](#)

[Buy or subscribe](#)

Access options

Subscription info for Chinese customers

We have a dedicated website for our Chinese customers. Please go to [naturechina.com](#) to subscribe to this journal.

[Go to naturechina.com](#)

Rent or Buy article

Get time limited or full article access on ReadCube.

from \$8.99

[Rent or Buy](#)

All prices are NET prices.

Additional access options:

- [Log in](#)
- [Access through your institution](#)
- [Learn about institutional subscriptions](#)

Fig. 1: Experimental design and features of 3D epigenomes during human corticogenesis.



Fig. 2: H3K4me3-mediated chromatin interactions influence cell-type-specific transcription.



Fig. 3: SIPs are enriched for lineage-specific genes.



Fig. 4: Features of cortical development and partitioning SNP heritability for complex disorders and traits.

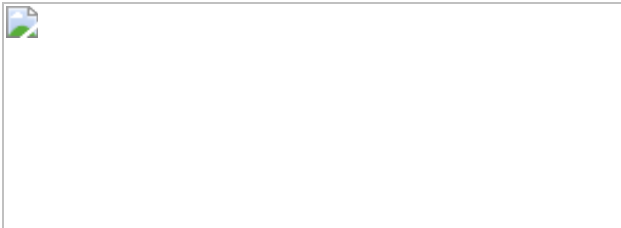
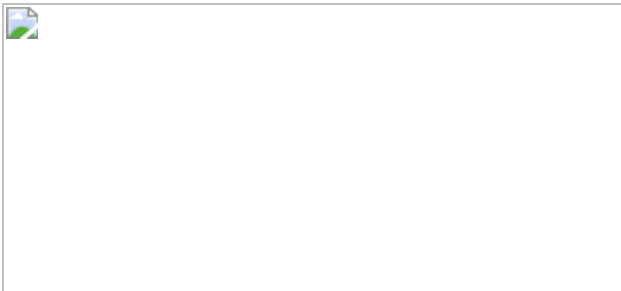


Fig. 5: Validation of cell-type-specific distal regulatory elements using CRISPRview.



Data availability

All datasets used in this study (PLAC-seq, ATAC-seq, RNA-seq) are available at the Neuroscience Multi-Omic Archive (NeMO Archive) under controlled access. Chromatin interactions, open chromatin peaks, and gene expression profiles for each cell type can be downloaded from the NeMO Archive using the following link: <https://assets.nemoarchive.org/datuioqy8b>. Cell-type-specific 3D epigenomes can be visualized on the WashU Epigenome Browser using the datahub at the following link: http://epigenomegateway.wustl.edu/browser/?genome=hg38&position=chr17:72918238-73349675&hub=https://shen-msong.s3-us-west-1.amazonaws.com/hfb_submission/hfb_datahub.json.

Code availability

All of the software used in this study are listed in the Reporting Summary along with their versions.

References

1. 1.

Nowakowski, T. J. et al. Spatiotemporal gene expression trajectories reveal developmental hierarchies of the human cortex. *Science* **358**, 1318–1323 (2017).

[CAS](#) [PubMed](#) [PubMed Central](#) [ADS](#) [Google Scholar](#)

2. 2.

Zhong, S. et al. A single-cell RNA-seq survey of the developmental landscape of the human prefrontal cortex. *Nature* **555**, 524–528 (2018).

[CAS](#) [PubMed](#) [PubMed Central](#) [ADS](#) [Google Scholar](#)

3. 3.

Hansen, D. V., Lui, J. H., Parker, P. R. & Kriegstein, A. R. Neurogenic radial glia in the outer subventricular zone of human neocortex. *Nature* **464**, 554–561 (2010).

[CAS](#) [PubMed](#) [ADS](#) [Google Scholar](#)

4. 4.

Pontious, A., Kowalczyk, T., Englund, C. & Hevner, R. F. Role of intermediate progenitor cells in cerebral cortex development. *Dev. Neurosci.* **30**, 24–32 (2008).

[CAS](#) [PubMed](#) [Google Scholar](#)

5. 5.

Anderson, S., Mione, M., Yun, K. & Rubenstein, J. L. Differential origins of neocortical projection and local circuit neurons: role of Dlx genes in neocortical interneuronogenesis. *Cereb. Cortex* **9**, 646–654 (1999).

[CAS](#) [PubMed](#) [Google Scholar](#)

6. 6.

Zheng, H. & Xie, W. The role of 3D genome organization in development and cell differentiation. *Nat. Rev. Mol. Cell Biol.* **20**, 535–550 (2019).

[CAS](#) [PubMed](#) [Google Scholar](#)

7. 7.

Li, Y., Hu, M. & Shen, Y. Gene regulation in the 3D genome. *Hum. Mol. Genet.* **27** (R2), R228–R233 (2018).

[CAS](#) [PubMed](#) [PubMed Central](#) [Google Scholar](#)

8. 8.

Schoenfelder, S. & Fraser, P. Long-range enhancer-promoter contacts in gene expression control. *Nat. Rev. Genet.* **20**, 437–455 (2019).

[CAS](#) [Google Scholar](#)

9. 9.

Won, H. et al. Chromosome conformation elucidates regulatory relationships in developing human brain. *Nature* **538**, 523–527 (2016).

[PubMed](#) [PubMed Central](#) [ADS](#) [Google Scholar](#)

10. 10.

Thomsen, E. R. et al. Fixed single-cell transcriptomic characterization of human radial glial diversity. *Nat. Methods* **13**, 87–93 (2016).

[CAS](#) [PubMed](#) [Google Scholar](#)

11. 11.

Fang, R. et al. Mapping of long-range chromatin interactions by proximity ligation-assisted ChIP-seq. *Cell Res.* **26**, 1345–1348 (2016).

[CAS](#) [PubMed](#) [PubMed Central](#) [Google Scholar](#)

12. 12.

Juric, I. et al. MAPS: Model-based analysis of long-range chromatin interactions from PLAC-seq and HiChIP experiments. *PLoS Comput. Biol.* **15**, e1006982 (2019).

[PubMed](#) [PubMed Central](#) [Google Scholar](#)

13. 13.

Heinz, S. et al. Simple combinations of lineage-determining transcription factors prime *cis*-regulatory elements required for macrophage and B cell identities. *Mol. Cell* **38**, 576–589 (2010).

[CAS](#) [PubMed](#) [PubMed Central](#) [Google Scholar](#)

14. 14.

Englund, C. et al. Pax6, Tbr2, and Tbr1 are expressed sequentially by radial glia, intermediate progenitor cells, and postmitotic neurons in developing neocortex. *J. Neurosci.* **25**, 247–251 (2005).

[CAS](#) [PubMed](#) [PubMed Central](#) [Google Scholar](#)

15. 15.

Lim, L., Mi, D., Llorca, A. & Marín, O. Development and functional diversification of cortical interneurons. *Neuron* **100**, 294–313 (2018).

[CAS](#) [PubMed](#) [PubMed Central](#) [Google Scholar](#)

16. 16.

Liu, S. J. et al. Single-cell analysis of long non-coding RNAs in the developing human neocortex. *Genome Biol.* **17**, 67 (2016).

[PubMed](#) [PubMed Central](#) [Google Scholar](#)

17. 17.

Luo, C. et al. Cerebral organoids recapitulate epigenomic signatures of the human fetal brain. *Cell Rep.* **17**, 3369–3384 (2016).

[CAS](#) [PubMed](#) [PubMed Central](#) [Google Scholar](#)

18. 18.

Javierre, B. M. et al. Lineage-specific genome architecture links enhancers and non-coding disease variants to target gene promoters. *Cell* **167**, 1369–1384 (2016).

[CAS](#) [PubMed](#) [PubMed Central](#) [Google Scholar](#)

19. 19.

Choudhary, M. N. et al. Co-opted transposons help perpetuate conserved higher-order chromosomal structures. *Genome Biol.* **21**, 16 (2020).

[CAS](#) [PubMed](#) [PubMed Central](#) [Google Scholar](#)

20. 20.

Feschotte, C. Transposable elements and the evolution of regulatory networks. *Nat. Rev. Genet.* **9**, 397–405 (2008).

[CAS](#) [PubMed](#) [PubMed Central](#) [Google Scholar](#)

21. 21.

Zhang, Y. et al. Transcriptionally active HERV-H retrotransposons demarcate topologically associating domains in human pluripotent

stem cells. *Nat. Genet.* **51**, 1380–1388 (2019).

[CAS](#) [PubMed](#) [PubMed Central](#) [Google Scholar](#)

22. 22.

Bailey, S. D. et al. ZNF143 provides sequence specificity to secure chromatin interactions at gene promoters. *Nat. Commun.* **2**, 6186 (2015).

[PubMed](#) [ADS](#) [Google Scholar](#)

23. 23.

Ngondo-Mbongo, R. P., Myslinski, E., Aster, J. C. & Carbon, P. Modulation of gene expression via overlapping binding sites exerted by ZNF143, Notch1 and THAP11. *Nucleic Acids Res.* **41**, 4000–4014 (2013).

[CAS](#) [PubMed](#) [PubMed Central](#) [Google Scholar](#)

24. 24.

Sundaram, V. & Wang, T. Transposable element mediated innovation in gene regulatory landscapes of cells: re-visiting the “gene-battery” model. *BioEssays* **40**, (2018).

25. 25.

Davis, C. A. et al. The Encyclopedia of DNA elements (ENCODE): data portal update. *Nucleic Acids Res.* **46** (D1), D794–D801 (2018).

[CAS](#) [PubMed](#) [Google Scholar](#)

26. 26.

Miller, D. J., Bhaduri, A., Sestan, N. & Kriegstein, A. Shared and derived features of cellular diversity in the human cerebral cortex. *Curr. Opin. Neurobiol.* **56**, 117–124 (2019).

[CAS](#) [PubMed](#) [PubMed Central](#) [Google Scholar](#)

27. 27.

Suzuki, I. K. et al. Human-specific NOTCH2NL genes expand cortical neurogenesis through Delta/Notch regulation. *Cell* **173**, 1370–1384 (2018).

[CAS](#) [PubMed](#) [PubMed Central](#) [Google Scholar](#)

28. 28.

Rani, N. et al. A Primate lncRNA mediates Notch signaling during neuronal development by sequestering miRNA. *Neuron* **90**, 1174–1188 (2016).

[CAS](#) [PubMed](#) [PubMed Central](#) [Google Scholar](#)

29. 29.

Carbon, S. et al. AmiGO: online access to ontology and annotation data. *Bioinformatics* **25**, 288–289 (2009).

[CAS](#) [PubMed](#) [Google Scholar](#)

30. 30.

Reilly, S. K. et al. Evolutionary genomics. Evolutionary changes in promoter and enhancer activity during human corticogenesis. *Science* **347**, 1155–1159 (2015).

[CAS](#) [PubMed](#) [PubMed Central](#) [ADS](#) [Google Scholar](#)

31. 31.

Visel, A., Minovitsky, S., Dubchak, I. & Pennacchio, L. A. VISTA Enhancer Browser—a database of tissue-specific human enhancers. *Nucleic Acids Res.* **35**, D88–D92 (2007).

[CAS](#) [PubMed](#) [Google Scholar](#)

32. 32.

Walker, R. L. et al. Genetic control of expression and splicing in developing human brain informs disease mechanisms. *Cell* **179**, 750–771 (2019).

[CAS](#) [PubMed](#) [Google Scholar](#)

33. 33.

Hoffman, G. E. et al. CommonMind Consortium provides transcriptomic and epigenomic data for schizophrenia and bipolar disorder. *Sci. Data* **6**, 180 (2019).

[PubMed](#) [PubMed Central](#) [Google Scholar](#)

34. 34.

Bulik-Sullivan, B. K. et al. LD score regression distinguishes confounding from polygenicity in genome-wide association studies. *Nat. Genet.* **47**, 291–295 (2015).

[CAS](#) [PubMed](#) [PubMed Central](#) [Google Scholar](#)

35. 35.

Finucane, H. K. et al. Partitioning heritability by functional annotation using genome-wide association summary statistics. *Nat. Genet.* **47**, 1228–1235 (2015).

[CAS](#) [PubMed](#) [PubMed Central](#) [Google Scholar](#)

36. 36.

Jansen, I. E. et al. Genome-wide meta-analysis identifies new loci and functional pathways influencing Alzheimer’s disease risk. *Nat. Genet.* **51**, 404–413 (2019).

[CAS](#) [PubMed](#) [PubMed Central](#) [Google Scholar](#)

37. 37.

Demontis, D. et al. Discovery of the first genome-wide significant risk loci for attention deficit/hyperactivity disorder. *Nat. Genet.* **51**, 63–75 (2019).

[CAS](#) [PubMed](#) [Google Scholar](#)

38. 38.

Grove, J. et al. Identification of common genetic risk variants for autism spectrum disorder. *Nat. Genet.* **51**, 431–444 (2019).

[CAS](#) [PubMed](#) [PubMed Central](#) [Google Scholar](#)

39. 39.

Stahl, E. A. et al. Genome-wide association study identifies 30 loci associated with bipolar disorder. *Nat. Genet.* **51**, 793–803 (2019).

[CAS](#) [PubMed](#) [PubMed Central](#) [Google Scholar](#)

40. 40.

Savage, J. E. et al. Genome-wide association meta-analysis in 269,867 individuals identifies new genetic and functional links to intelligence. *Nat. Genet.* **50**, 912–919 (2018).

[CAS](#) [PubMed](#) [PubMed Central](#) [Google Scholar](#)

41. 41.

Howard, D. M. et al. Genome-wide meta-analysis of depression identifies 102 independent variants and highlights the importance of the prefrontal brain regions. *Nat. Neurosci.* **22**, 343–352 (2019).

[CAS](#) [PubMed](#) [PubMed Central](#) [Google Scholar](#)

42. 42.

Pardiñas, A. F. et al. Common schizophrenia alleles are enriched in mutation-intolerant genes and in regions under strong background selection. *Nat. Genet.* **50**, 381–389 (2018).

[PubMed](#) [PubMed Central](#) [Google Scholar](#)

43. 43.

Gazal, S. et al. Linkage disequilibrium-dependent architecture of human complex traits shows action of negative selection. *Nat. Genet.* **49**, 1421–1427 (2017).

[CAS](#) [PubMed](#) [PubMed Central](#) [Google Scholar](#)

44. 44.

Sey, N. Y. A. et al. A computational tool (H-MAGMA) for improved prediction of brain-disorder risk genes by incorporating brain chromatin interaction profiles. *Nat. Neurosci.* **23**, 583–593 (2020).

[CAS](#) [PubMed](#) [PubMed Central](#) [Google Scholar](#)

45. 45.

Andersen, O. M. & Willnow, T. E. Lipoprotein receptors in Alzheimer's disease. *Trends Neurosci.* **29**, 687–694 (2006).

[CAS](#) [PubMed](#) [Google Scholar](#)

46. 46.

Akbarian, S. Epigenetic mechanisms in schizophrenia. *Dialogues Clin. Neurosci.* **16**, 405–417 (2014).

[PubMed](#) [PubMed Central](#) [Google Scholar](#)

47. 47.

Yang, X. et al. SMART-Q: an integrative pipeline quantifying cell-type-specific RNA transcription. *PLoS One* **15**, e0228760 (2020).

[CAS](#) [PubMed](#) [PubMed Central](#) [Google Scholar](#)

48. 48.

Lieberman-Aiden, E. et al. Comprehensive mapping of long-range interactions reveals folding principles of the human genome. *Science* **326**, 289–293 (2009).

[CAS](#) [PubMed](#) [PubMed Central](#) [ADS](#) [Google Scholar](#)

49. 49.

Dixon, J. R. et al. Topological domains in mammalian genomes identified by analysis of chromatin interactions. *Nature* **485**, 376–380 (2012).

[CAS](#) [PubMed](#) [PubMed Central](#) [ADS](#) [Google Scholar](#)

50. 50.

Schmitt, A. D. et al. A compendium of chromatin contact maps reveals spatially active regions in the human genome. *Cell Rep.* **17**, 2042–2059 (2016).

[CAS](#) [PubMed](#) [PubMed Central](#) [Google Scholar](#)

51. 51.

Sobhy, H., Kumar, R., Lewerentz, J., Lizana, L. & Stenberg, P. Highly interacting regions of the human genome are enriched with enhancers and bound by DNA repair proteins. *Sci. Rep.* **9**, 4577 (2019).

[PubMed](#) [PubMed Central](#) [ADS](#) [Google Scholar](#)

52. 52.

Corces, M. R. et al. An improved ATAC-seq protocol reduces background and enables interrogation of frozen tissues. *Nat. Methods* **14**, 959–962 (2017).

[CAS](#) [PubMed](#) [PubMed Central](#) [Google Scholar](#)

53. 53.

Reimand, J., Kull, M., Peterson, H., Hansen, J. & Vilo, J. g:Profiler—a web-based toolset for functional profiling of gene lists from large-scale experiments. *Nucleic Acids Res.* **35**, W193–W200(2007).

[PubMed](#) [PubMed Central](#) [Google Scholar](#)

54. 54.

Hnisz, D. et al. Super-enhancers in the control of cell identity and disease. *Cell* **155**, 934–947 (2013).

[CAS](#) [PubMed](#) [Google Scholar](#)

55. 55.

Grant, C. E., Bailey, T. L. & Noble, W. S. FIMO: scanning for occurrences of a given motif. *Bioinformatics* **27**, 1017–1018 (2011).

[CAS](#) [PubMed](#) [PubMed Central](#) [Google Scholar](#)

56. 56.

Diao, Y. et al. A tiling-deletion-based genetic screen for cis-regulatory element identification in mammalian cells. *Nat. Methods* **14**, 629–635 (2017).

[CAS](#) [PubMed](#) [PubMed Central](#) [Google Scholar](#)

57. 57.

Xie, S., Duan, J., Li, B., Zhou, P. & Hon, G. C. Multiplexed engineering and analysis of combinatorial enhancer activity in single cells. *Mol Cell* **66**, 285–299 (2017).

[CAS](#) [PubMed](#) [Google Scholar](#)

58. 58.

Datlinger, P. et al. Pooled CRISPR screening with single-cell transcriptome readout. *Nat. Methods* **14**, 297–301 (2017).

[CAS](#) [PubMed](#) [PubMed Central](#) [Google Scholar](#)

59. 59.

Labun, K. et al. CHOPCHOP v3: expanding the CRISPR web toolbox beyond genome editing. *Nucleic Acids Res.* **47**, W171–W174 (2019).

[CAS](#) [PubMed](#) [PubMed Central](#) [Google Scholar](#)

[Download references](#)

Acknowledgements

This work was supported by the UCSF Weill Institute for Neuroscience Innovation Award (to Y.S. and A.R.K.), the National Institutes of Health (NIH) grants R01AG057497, R01EY027789, and UM1HG009402 (to Y.S.) and R35NS097305 (to A.R.K.), the Hillblom Foundation, and the American Federation for Aging Research New Investigator Award in Alzheimer's Disease (to Y.S.). This work was also supported by the NIH grants R01HL129132, U544HD079124, and R01MH106611 (to Y.L.), R01HG007175, U24ES026699, and U01HG009391 (to T.W.), and the American Cancer Society grant RSG-14-049-01-DMC (to T.W.). M.S. is supported by T32GM007175. M.P. is supported by the National Science Foundation Graduate Research Fellowship Program grant 1650113. U.C.E. is supported by 5T32GM007618-42. This work was made possible in part by the NIH grants P30EY002162 to the UCSF Core Grant for Vision

Research, P30DK063720, and S101S10OD021822-01 to the UCSF Parnassus Flow Cytometry Core.

Author information

Author notes

1. These authors contributed equally: Michael Song, Mark-Phillip Pebworth, Xiaoyu Yang, Ming Hu

Affiliations

1. Institute for Human Genetics, University of California, San Francisco, San Francisco, CA, USA

Michael Song, Xiaoyu Yang, Xiekui Cui, Ian R. Jones, Seth Bergenholz, Bingkun Li, Lenka Maliskova, Jerry Lee & Yin Shen

2. Pharmaceutical Sciences and Pharmacogenomics Graduate Program, University of California, San Francisco, San Francisco, CA, USA

Michael Song

3. Biomedical Sciences Graduate Program, University of California, San Francisco, San Francisco, CA, USA

Mark-Phillip Pebworth

4. The Eli and Edythe Broad Center of Regeneration Medicine and Stem Cell Research, University of California, San Francisco, San Francisco, CA, USA

Mark-Phillip Pebworth, Ugomma C. Eze, Alex A. Pollen & Arnold R. Kriegstein

5. Department of Quantitative Health Sciences, Lerner Research Institute, Cleveland Clinic Foundation, Cleveland, OH, USA

Armen Abnousi, Ivan Juric & Ming Hu

6. Department of Genetics, Washington University School of Medicine,
St Louis, MO, USA

Changxu Fan, Mayank N. K. Choudhary & Ting Wang

7. The Edison Family Center for Genome Sciences and Systems Biology,
Washington University School of Medicine, St Louis, MO, USA

Changxu Fan, Mayank N. K. Choudhary & Ting Wang

8. Department of Genetics, University of North Carolina, Chapel Hill,
NC, USA

Jia Wen & Yun Li

9. Department of Biostatistics, University of North Carolina, Chapel Hill,
NC, USA

Jonathan D. Rosen, Weifang Liu & Yun Li

10. Medical Scientist Training Program, University of California, San
Francisco, San Francisco, CA, USA

Ugomma C. Eze

11. Department of Neurology, University of California, San Francisco, San
Francisco, CA, USA

Alex A. Pollen, Arnold R. Kriegstein & Yin Shen

12. Department of Computer Science, University of North Carolina,
Chapel Hill, NC, USA

Yun Li

13. McDonnell Genome Institute, Washington University School of
Medicine, St Louis, MO, USA

Ting Wang

14. Weill Institute for Neurosciences, University of California, San Francisco, San Francisco, CA, USA

Yin Shen

Authors

1. Michael Song

[View author publications](#)

You can also search for this author in [PubMed](#) [Google Scholar](#)

2. Mark-Phillip Pebworth

[View author publications](#)

You can also search for this author in [PubMed](#) [Google Scholar](#)

3. Xiaoyu Yang

[View author publications](#)

You can also search for this author in [PubMed](#) [Google Scholar](#)

4. Armen Abnousi

[View author publications](#)

You can also search for this author in [PubMed](#) [Google Scholar](#)

5. Changxu Fan

[View author publications](#)

You can also search for this author in [PubMed](#) [Google Scholar](#)

6. Jia Wen

[View author publications](#)

You can also search for this author in [PubMed](#) [Google Scholar](#)

7. Jonathan D. Rosen

[View author publications](#)

You can also search for this author in [PubMed](#) [Google Scholar](#)

8. Mayank N. K. Choudhary

[View author publications](#)

You can also search for this author in [PubMed](#) [Google Scholar](#)

9. Xiekui Cui

[View author publications](#)

You can also search for this author in [PubMed](#) [Google Scholar](#)

10. Ian R. Jones

[View author publications](#)

You can also search for this author in [PubMed](#) [Google Scholar](#)

11. Seth Bergenholz

[View author publications](#)

You can also search for this author in [PubMed](#) [Google Scholar](#)

12. Ugomma C. Eze

[View author publications](#)

You can also search for this author in [PubMed](#) [Google Scholar](#)

13. Ivan Juric

[View author publications](#)

You can also search for this author in [PubMed](#) [Google Scholar](#)

14. Bingkun Li

[View author publications](#)

You can also search for this author in [PubMed](#) [Google Scholar](#)

15. Lenka Maliskova

[View author publications](#)

You can also search for this author in [PubMed](#) [Google Scholar](#)

16. Jerry Lee

[View author publications](#)

You can also search for this author in [PubMed](#) [Google Scholar](#)

17. Weifang Liu

[View author publications](#)

You can also search for this author in [PubMed](#) [Google Scholar](#)

18. Alex A. Pollen

[View author publications](#)

You can also search for this author in [PubMed](#) [Google Scholar](#)

19. Yun Li

[View author publications](#)

You can also search for this author in [PubMed](#) [Google Scholar](#)

20. Ting Wang

[View author publications](#)

You can also search for this author in [PubMed](#) [Google Scholar](#)

21. Ming Hu

[View author publications](#)

You can also search for this author in [PubMed](#) [Google Scholar](#)

22. Arnold R. Kriegstein

[View author publications](#)

You can also search for this author in [PubMed](#) [Google Scholar](#)

23. Yin Shen

[View author publications](#)

You can also search for this author in [PubMed](#) [Google Scholar](#)

Contributions

Y.S., A.A.P., and A.R.K. conceived the study. Y.S., M.H., A.A.P., and A.R.K. supervised the study. M.S., M.-P.P., X.Y., I.R.J., X.C., U.C.E., L.M., and J.L. performed experiments. M.S., A.A., S.B., J.D.R., B.L., I.R.J., and M.H. performed computational analysis. C.F. and M.N.K.C. performed TE analysis under the supervision of T.W. J.W., and W.L. performed SNP heritability enrichment analysis under the supervision of Y.L. M.S., M.-P.P., X.Y., and Y.S. analysed and interpreted the data. M.S., M.-P.P., X.Y., M.H., and Y.S. prepared the manuscript with input from all other authors.

Corresponding authors

Correspondence to [Ming Hu](#) or [Arnold R. Kriegstein](#) or [Yin Shen](#).

Ethics declarations

Competing interests

The authors declare no competing interests.

Additional information

Peer review information *Nature* thanks Andrew Adey, Chongyuan Luo and Barbara Treutlein for their contribution to the peer review of this work.

Publisher's note Springer Nature remains neutral with regard to jurisdictional claims in published maps and institutional affiliations.

Extended data figures and tables

Extended Data Fig. 1 Representative contour plots depicting FACS gating strategy.

a, Cells were separated from debris of various sizes based on the forward scatter area (FSC-A) and side scatter area (SSC-A). **b, c**, Specifically, they were passed through two singlet gates using the width and height metrics of the side scatter (SSC-H versus SSC-W) (**b**) and forward scatter (FSC-H versus FSC-W) (**c**). **d**, SOX2⁺ and SOX2⁻ and IPC populations were isolated by gating on EOMES-PE-Cy7 and SOX2-PerCP-Cy5.5 staining. **e**, RG and interneurons were isolated based on high PAX6/high SOX2 and medium SOX2/low PAX6 staining, respectively. **f**, excitatory neurons were isolated from the SOX2- population by gating on SATB2-Alexa Fluor 647 staining.

Extended Data Fig. 2 Reproducibility between RNA-seq, ATAC-seq and PLAC-seq replicates.

a, RNA-seq replicates were hierarchically clustered according to gene expression sample distances using DESeq2. **b**, Heat map showing correlations between gene expression profiles for the sorted cell populations and single-cell RNA sequencing (scRNA-seq) data in the developing human cortex. The sorted cell populations exhibit the highest correlation with their corresponding subtypes while exhibiting reduced correlation with the endothelial, mural, microglial, and choroid plexus lineages. **c**, Heat map showing correlations and hierarchical clustering for read densities at open chromatin peaks across all ATAC-seq replicates. **d**, Principal component analysis (PCA) was performed based on normalized contact frequencies across all PLAC-seq replicates (Methods). PCA was performed using interacting 5-kb bins in both 300- and 600-kb windows.

Extended Data Fig. 3 Identification of significant H3K4me3-mediated chromatin interactions.

a, Illustration of XOR and AND interactions in a representative PLAC-seq contact matrix. The blue tracks represent H3K4me3 peaks at anchor bins. Purple cells represent AND interactions where both of the interacting bins

are anchor bins. Orange cells represent XOR interactions where only one of the interacting bins is an anchor bin. Grey cells represent NOT interactions where neither of the interacting bins are anchor bins. **b**, Venn diagram displaying cell-type-specificity for interactions in each cell type. **c**, Proportions of interactions occurring within and across topologically associated domains in the germinal zones and cortical plate for matching cell types.

Extended Data Fig. 4 Chromatin interactions influence cell-type-specific transcription.

a, GO enrichment analysis for genes participating in cell-type-specific interactions. The top annotation clusters from DAVID are reported along with their group enrichment scores for each cell type ([Methods](#)). **b**, Scatter plots showing the correlation between the difference in the number of interactions for each promoter and the difference in the expression of the corresponding genes across all cell types (Pearson product-moment correlation coefficient, two-tailed, $n = 13,996$ anchor bins with promoters). The trend line from linear regression is shown. **c**, Fold enrichment of open chromatin peaks over distance-matched background regions in 1-Mb windows around distal interacting regions in IPCs, excitatory neurons and interneurons.

Extended Data Fig. 5 SIPs are enriched for lineage-specific genes.

a, Scatter plots showing the correlation between interaction counts and gene expression at promoters for each cell type (Pearson product-moment correlation coefficient, two-tailed, $n = 13,996$ anchor bins with promoters). **b**, CDF plots of the numbers of interactions for shared versus cell-type-specific genes for each cell type. P values determined by two-tailed two-sample t -test, two-tailed. **c**, Anchor bins were ranked according to their cumulative interaction scores in RG, IPCs and interneurons. SIPs are located past the point in each curve where the slope is equal to 1. **d**, Venn diagram displaying cell-type-specificity for SIPs in each cell type. **e, f**, Enrichment of super-enhancers and DNA methylation valleys at SIPs

versus non-SIPs (left) and distal interacting regions for SIPs versus non-SIPs (right), *P* values determined by two-tailed Fisher's exact test. Super-enhancers were based on data in the fetal brain and adult cortex, and DNA methylation valleys were based on data in 40- and 60-day cerebral organoids with closely matched gene expression profiles to mid-fetal cortex samples. **g**, Forrest plot showing that SIPs identified in haematopoietic cells are analogously enriched for cell-type-specific over shared genes. Odds ratios and 95% confidence intervals are shown. We identified 554, 709, 460, 712 and 401 SIPs in neutrophils, naive CD4⁺ T cells, monocytes, megakaryocytes, and erythroblasts, respectively.

Extended Data Fig. 6 Transposable elements in SIP formation.

a–c, Enrichment of TEs at the class (**a**), family (**b**), and subfamily (**c**) levels in SIPGs for each cell type. Only TE families occupying more than 1% of the genome are shown in **b**. Only TE subfamilies from the MIR and ERVL-MaLR TE families occupying more than 0.1% of the genome are shown in **c**. **d**, Both ERVL-MaLR TEs (left, 32% versus 19% of sequences, $P < 2.2 \times 10^{-16}$, binomial test, two-tailed) and THE1C TEs (right, 73% versus 19% of sequences, $P < 2.2 \times 10^{-16}$, binomial test, two-tailed) are enriched over background sequences for ZNF143 motifs in excitatory neurons. **e**, ZNF143 motifs are enriched at SIPGs in excitatory neurons (left, $P = 5.39 \times 10^{-82}$, two-sample *t*-test, two-tailed, $n = 8,894$ distal interacting regions). Data are mean and s.e.m. Distributions comparing the number of ZNF143 motifs per bin for actual versus shuffled SIPGs are shown (right, $P < 2.2 \times 10^{-16}$, Kolmogorov–Smirnov test, two-tailed, $n = 638$ SIPGs). **f**, ERVL-MaLR TEs in SIPGs are enriched over background sequences for ZNF143 motifs in excitatory neurons (31% versus 17% of sequences, $P = 4.3 \times 10^{-98}$, binomial test, two-tailed). **g**, Box plots showing elevated *ADRA2A* gene expression in excitatory neurons. The median, upper and lower quartiles, minimum and maximum are indicated. **h**, Illustration of the 12 distal interacting regions containing ERVL-MaLR TE-localized ZNF143 motifs in the *ADRA2A* SIPG. ZNF143 motifs are coloured by strand. The bin numbers correspond to Fig. [3g](#). **i**, Conservation of ERVL-MaLR TEs in the *ADRA2A* SIPG. Blue bars indicate consensus sequences, yellow bars indicate ERVL-MaLR TEs, and red bars indicate

ZNF143 motifs. **j**, Alignment of THE1C TEs in the human genome to their consensus sequence. The THE1C subfamily contains two ZNF143 motifs, one at positions 47–61 (P1), and another at positions 96–110 (P2).

Extended Data Fig. 7 Developmental trajectories and mapping complex disorder- and trait-associated variants to their target genes.

a, Box plots showing the distributions of gene expression and cumulative interaction scores for the groups identified in Fig. [4a](#). The median, upper and lower quartiles, minimum, and maximum are indicated. **b**, Groups 4 and 5 are enriched for interactions with transcription factors containing domains associated with transcriptional repression. **c, d**, Counts of the numbers of GWAS SNPs ($P < 10^{-8}$) interacting with their nearest gene only, with both their nearest and more distal genes, and with more distal genes only across all diseases (**c**) and specific disorders and traits (**d**).

Extended Data Fig. 8 Partitioning SNP heritability for complex disorders and traits using alternative epigenomic annotations.

a, Forrest plot showing the enrichment of fetal and adult brain eQTL–TSS pairs in our interactions compared to $n = 50$ sets of distance-matched control interactions. P values determined by two-tailed Fisher’s exact test. Odds ratios and 95% confidence intervals are shown. The increased significance of adult brain eQTLs can be attributed to the larger sample size of the CommonMind Consortium (CMC) study ($n = 1,332,863$), while larger odds ratios were observed for the more closely matched fetal brain eQTLs ($n = 6,446$). **b, c**, Histograms displaying the numbers of adult and fetal brain eQTL–TSS pairs recapitulated by $n = 50$ sets of distance-matched control interactions in each cell type. The numbers of eQTL–TSS pairs recapitulated by our interactions are indicated by red lines. P values determined by two-tailed Fisher’s exact test. **d**, LDSC enrichment scores for each disease and cell type, conditioned on the baseline model previously described^{[43](#)} and stratified by PLAC-seq anchor and target bins. Non-significant enrichment scores are shown as striped bars. **e, f**, LDSC enrichment scores for each disease and cell type, conditioned on the

baseline model previously described⁴² and using either distal open chromatin peaks (**e**) or cell-type-specific genes (**f**). Non-significant enrichment scores are shown as striped bars.

Extended Data Fig. 9 Enriched biological processes for genes interacting with non-coding variants for each disease and cell type.

Gene Ontology enrichment analysis for genes interacting with non-coding variants for each disease and cell type using H-MAGMA and gProfileR. *P* values determined by two-tailed Fisher's exact test, BH method. The full results can be found in Supplementary Table [12](#).

Extended Data Fig. 10 Characterization of RG- and excitatory neuron-specific loci using CRISPRview.

a, b, Validation of distal interacting regions at the *IDH1* locus in RG and excitatory neurons. Silencing region 1, which interacts with the *IDH1* promoter only in excitatory neurons, results in the significant downregulation of *IDH1* expression in excitatory neurons but not in RG. Silencing region 2, which interacts with the *IDH1* promoter only in RG, results in the significant downregulation of *IDH1* expression in RG but not in excitatory neurons. Silencing region 3, which interacts with the *IDH1* promoter in both RG and excitatory neurons, results in the significant downregulation of *IDH1* expression in both cell types. Interactions between the promoter of *IDH1* and distal interacting regions containing open chromatin peaks that were targeted for silencing are highlighted. Box plots show results for experimental (red) and control (green) sgRNA-treated cells for each region. *P* values determined by two-tailed two-sample *t*-test. The median, upper and lower quartiles and 10% to 90% range are indicated. Open circles represent single cells. Sample sizes are indicated above each box plot. **c–h,** Validation of distal interacting regions at the *TNC* and *HES1* loci in RG. Interactions between the promoters of *TNC* and *HES1* and distal interacting regions containing open chromatin peaks that were targeted for silencing are highlighted. Representative images show staining for intronic

RNAscope probes (white), DAPI (blue), GFAP (light blue), GFP (green), and mCherry (red). Scale bar, 50 µm.

Supplementary information

Supplementary Information

This file contains a guide to Supplementary Tables 1-13.

Reporting Summary

Supplementary Tables

This zipped file contains Supplementary Tables 1-13.

Rights and permissions

Reprints and Permissions

About this article



Check for
updates

Cite this article

Song, M., Pebworth, MP., Yang, X. *et al.* Cell-type-specific 3D epigenomes in the developing human cortex. *Nature* **587**, 644–649 (2020).
<https://doi.org/10.1038/s41586-020-2825-4>

Download citation

- Received: 01 September 2019

- Accepted: 23 July 2020
- Published: 14 October 2020
- Issue Date: 26 November 2020
- DOI: <https://doi.org/10.1038/s41586-020-2825-4>

Comments

By submitting a comment you agree to abide by our [Terms](#) and [Community Guidelines](#). If you find something abusive or that does not comply with our terms or guidelines please flag it as inappropriate.

[Access through your institution](#)

[Change institution](#)

[Buy or subscribe](#)

This article was downloaded by **calibre** from <https://www.nature.com/articles/s41586-020-2825-4>

| [Section menu](#) | [Main menu](#) |

- Article
- [Published: 04 November 2020](#)

Combinatorial expression of GPCR isoforms affects signalling and drug responses

- [Maria Marti-Solano](#) [ORCID: orcid.org/0000-0003-0373-8927¹](#),
- [Stephanie E. Crilly²](#),
- [Duccio Malinverni^{1,3}](#),
- [Christian Munk⁴](#),
- [Matthew Harris⁵](#),
- [Abigail Pearce](#) [ORCID: orcid.org/0000-0001-9845-0541⁵](#),
- [Tezz Quon⁶](#),
- [Amanda E. Mackenzie⁶](#),
- [Xusheng Wang^{7,8}](#),
- [Junmin Peng](#) [ORCID: orcid.org/0000-0003-0472-7648^{7,9}](#),
- [Andrew B. Tobin](#) [ORCID: orcid.org/0000-0002-1807-3123⁶](#),
- [Graham Ladds](#) [ORCID: orcid.org/0000-0001-7320-9612⁵](#),
- [Graeme Milligan](#) [ORCID: orcid.org/0000-0002-6946-3519⁶](#),
- [David E. Gloriam](#) [ORCID: orcid.org/0000-0002-4299-7561⁴](#),
- [Manojkumar A. Puthenveedu](#) [ORCID: orcid.org/0000-0002-3177-4231^{2,10}](#) &
- [M. Madan Babu](#) [ORCID: orcid.org/0000-0003-0556-6196^{1,3}](#)

[Nature](#) volume 587, pages650–656(2020) [Cite this article](#)

- 6816 Accesses
- 90 Altmetric

- [Metrics details](#)

Subjects

- [Computational biology and bioinformatics](#)
- [Systems biology](#)

An [Author Correction](#) to this article was published on 25 November 2020

This article has been [updated](#)

Abstract

G-protein-coupled receptors (GPCRs) are membrane proteins that modulate physiology across human tissues in response to extracellular signals. GPCR-mediated signalling can differ because of changes in the sequence^{1,2} or expression³ of the receptors, leading to signalling bias when comparing diverse physiological systems⁴. An underexplored source of such bias is the generation of functionally diverse GPCR isoforms with different patterns of expression across different tissues. Here we integrate data from human tissue-level transcriptomes, GPCR sequences and structures, proteomics, single-cell transcriptomics, population-wide genetic association studies and pharmacological experiments. We show how a single GPCR gene can diversify into several isoforms with distinct signalling properties, and how unique isoform combinations expressed in different tissues can generate distinct signalling states. Depending on their structural changes and expression patterns, some of the detected isoforms may influence cellular responses to drugs and represent new targets for developing drugs with improved tissue selectivity. Our findings highlight the need to move from a canonical to a context-specific view of GPCR signalling that considers how combinatorial expression of isoforms in a particular cell type, tissue or organism collectively influences receptor signalling and drug responses.

[Access through your institution](#)

[Change institution](#)

[Buy or subscribe](#)

Access options

Subscription info for Chinese customers

We have a dedicated website for our Chinese customers. Please go to [naturechina.com](#) to subscribe to this journal.

[Go to naturechina.com](#)

Rent or Buy article

Get time limited or full article access on ReadCube.

from \$8.99

[Rent or Buy](#)

All prices are NET prices.

Additional access options:

- [Log in](#)
- [Access through your institution](#)
- [Learn about institutional subscriptions](#)

Fig. 1: Structural diversity and functional impact of receptor isoforms.



Fig. 2: Tissue distribution of GPCR isoforms.



Fig. 3: Combinatorial isoform expression influences pharmacological responses.



Fig. 4: GPCR isoforms as potential drug targets.



Fig. 5: From a canonical to a context-specific view of GPCR signalling.



Data availability

All data accessed from public repositories—namely the GTEx database (www.gtexportal.org, version 7), GPCRdb (<https://gpcrdb.org>), Ensembl (www.ensembl.org, GRCh37 assembly), Uniprot (www.uniprot.org), Protein DataBank (PDB; www.rcsb.org), PRIDE (www.ebi.ac.uk/pride), accession numbers PXD0079985 and PXD010154), ProteomicsDB (www.proteomicsdb.org), Guide to Pharmacology (www.guidetopharmacology.org), GeneAtlas (geneatlas.roslin.ed.ac.uk) and BioProject (www.ncbi.nlm.nih.gov/bioproject), accession numbers PRJNA183192 and PRJNA322355)—are detailed in the Methods. We declare that all data supporting the findings of this study are available within the paper, via the GPCRdb (<https://gpcrdb.org/protein/isoforms>) and in the Supplementary Information files.

Change history

- **25 November 2020**

An amendment to this paper has been published and can be accessed via a link at the top of the paper.

References

1. 1.

Hauser, A. S. et al. Pharmacogenomics of GPCR drug targets. *Cell* **172**, 41–54 (2018).

[CAS](#) [PubMed](#) [PubMed Central](#) [Google Scholar](#)

2. 2.

Thompson, M. D. et al. Pharmacogenetics of the G protein-coupled receptors. *Methods Mol. Biol.* **1175**, 189–242 (2014).

[PubMed](#) [Google Scholar](#)

3. 3.

Kenakin, T. Biased receptor signaling in drug discovery. *Pharmacol. Rev.* **71**, 267–315 (2019).

[CAS](#) [PubMed](#) [Google Scholar](#)

4. 4.

Smith, J. S., Lefkowitz, R. J. & Rajagopal, S. Biased signalling: from simple switches to allosteric microprocessors. *Nat. Rev. Drug Discov.* **17**, 243–260 (2018).

[CAS](#) [PubMed](#) [PubMed Central](#) [Google Scholar](#)

5. 5.

Urban, J. D. et al. Functional selectivity and classical concepts of quantitative pharmacology. *J. Pharmacol. Exp. Ther.* **320**, 1–13 (2007).

[CAS](#) [PubMed](#) [Google Scholar](#)

6. 6.

Stallaert, W., Christopoulos, A. & Bouvier, M. Ligand functional selectivity and quantitative pharmacology at G protein-coupled receptors. *Expert Opin. Drug Discov.* **6**, 811–825 (2011).

[CAS](#) [PubMed](#) [Google Scholar](#)

7. 7.

Kenakin, T. & Christopoulos, A. Signalling bias in new drug discovery: detection, quantification and therapeutic impact. *Nat. Rev. Drug Discov.* **12**, 205–216 (2013).

[CAS](#) [PubMed](#) [Google Scholar](#)

8. 8.

Buljan, M. et al. Alternative splicing of intrinsically disordered regions and rewiring of protein interactions. *Curr. Opin. Struct. Biol.* **23**, 443–450 (2013).

[CAS](#) [PubMed](#) [Google Scholar](#)

9. 9.

Kilpatrick, G. J., Dautzenberg, F. M., Martin, G. R. & Eglen, R. M. 7TM receptors: the splicing on the cake. *Trends Pharmacol. Sci.* **20**, 294–301 (1999).

[CAS](#) [PubMed](#) [Google Scholar](#)

10. 10.

Markovic, D. & Challiss, R. A. J. Alternative splicing of G protein-coupled receptors: physiology and pathophysiology. *Cell. Mol. Life Sci.* **66**, 3337–3352 (2009).

[CAS](#) [PubMed](#) [Google Scholar](#)

11. 11.

Zhou, J., Zhao, S. & Dunker, A. K. Intrinsically disordered proteins link alternative splicing and post-translational modifications to complex cell signaling and regulation. *J. Mol. Biol.* **430**, 2342–2359 (2018).

[CAS](#) [PubMed](#) [Google Scholar](#)

12. 12.

Sriram, K. & Insel, P. A. G protein-coupled receptors as targets for approved drugs: how many targets and how many drugs? *Mol. Pharmacol.* **93**, 251–258 (2018).

[CAS](#) [PubMed](#) [PubMed Central](#) [Google Scholar](#)

13. 13.

Hauser, A. S., Attwood, M. M., Rask-Andersen, M., Schiöth, H. B. & Gloriam, D. E. Trends in GPCR drug discovery: new agents, targets and indications. *Nat. Rev. Drug Discov.* **16**, 829–842 (2017).

[CAS](#) [PubMed](#) [PubMed Central](#) [Google Scholar](#)

14. 14.

Melé, M. et al. The human transcriptome across tissues and individuals. *Science* **348**, 660–665 (2015).

[ADS](#) [PubMed](#) [PubMed Central](#) [Google Scholar](#)

15. 15.

Kooistra, A. J., Mordalski, S., Pándy-Szekeres, G., Esguerra, M., Mamyrbekov, A., Munk, C., Keserű, G. M. & Gloriam, D. E. GPCRdb in 2021: integrating GPCR sequence, structure and function. *Nucleic Acids Res.* (in the press).

16. 16.

Langenhan, T. Adhesion G protein-coupled receptors—candidate metabotropic mechanosensors and novel drug targets. *Basic Clin. Pharmacol. Toxicol.* **126** (Suppl. 6), 5–16 (2019).

[PubMed](#) [Google Scholar](#)

17. 17.

Knierim, A. B. et al. Genetic basis of functional variability in adhesion G protein-coupled receptors. *Sci. Rep.* **9**, 11036 (2019).

[ADS](#) [PubMed](#) [PubMed Central](#) [Google Scholar](#)

18. 18.

Milligan, G. A day in the life of a G protein-coupled receptor: the contribution to function of G protein-coupled receptor dimerization. *Br. J. Pharmacol.* **153** (Suppl 1), S216–S229 (2008).

[CAS](#) [PubMed](#) [Google Scholar](#)

19. 19.

Berchiche, Y. A. & Sakmar, T. P. CXC chemokine receptor 3 alternative splice variants selectively activate different signaling pathways. *Mol. Pharmacol.* **90**, 483–495 (2016).

[CAS](#) [PubMed](#) [Google Scholar](#)

20. 20.

Hirata, T., Ushikubi, F., Kakizuka, A., Okuma, M. & Narumiya, S. Two thromboxane A₂ receptor isoforms in human platelets. Opposite coupling to adenylyl cyclase with different sensitivity to Arg60 to Leu mutation. *J. Clin. Invest.* **97**, 949–956 (1996).

[CAS](#) [PubMed](#) [PubMed Central](#) [Google Scholar](#)

21. 21.

Venkatakrishnan, A. J. et al. Structured and disordered facets of the GPCR fold. *Curr. Opin. Struct. Biol.* **27**, 129–137 (2014).

[CAS](#) [PubMed](#) [Google Scholar](#)

22. 22.

Martin, C. B. P. et al. RNA splicing and editing modulation of 5-HT_{2C} receptor function: relevance to anxiety and aggression in VGV mice. *Mol. Psychiatry* **18**, 656–665 (2013).

[CAS](#) [PubMed](#) [Google Scholar](#)

23. 23.

Grosse, R., Schöneberg, T., Schultz, G. & Gudermann, T. Inhibition of gonadotropin-releasing hormone receptor signaling by expression of a splice variant of the human receptor. *Mol. Endocrinol.* **11**, 1305–1318 (1997).

[CAS](#) [PubMed](#) [Google Scholar](#)

24. 24.

Marrone, G. F. et al. Truncated mu opioid GPCR variant involvement in opioid-dependent and opioid-independent pain modulatory systems within the CNS. *Proc. Natl Acad. Sci. USA* **113**, 3663–3668 (2016).

[ADS](#) [CAS](#) [PubMed](#) [Google Scholar](#)

25. 25.

Howlett, A. C. et al. Endocannabinoid tone versus constitutive activity of cannabinoid receptors. *Br. J. Pharmacol.* **163**, 1329–1343 (2011).

[CAS](#) [PubMed](#) [PubMed Central](#) [Google Scholar](#)

26. 26.

Finan, B. et al. Reappraisal of GIP pharmacology for metabolic diseases. *Trends Mol. Med.* **22**, 359–376 (2016).

[CAS](#) [PubMed](#) [Google Scholar](#)

27. 27.

Schwarzchild, M. A., Agnati, L., Fuxe, K., Chen, J. F. & Morelli, M. Targeting adenosine A_{2A} receptors in Parkinson's disease. *Trends Neurosci.* **29**, 647–654 (2006).

[CAS](#) [PubMed](#) [Google Scholar](#)

28. 28.

Canela-Xandri, O., Rawlik, K. & Tenesa, A. An atlas of genetic associations in UK Biobank. *Nat. Genet.* **50**, 1593–1599 (2018).

[CAS](#) [PubMed](#) [PubMed Central](#) [Google Scholar](#)

29. 29.

MacKenzie, A. E. et al. The antiallergic mast cell stabilizers lodoxamide and bufrolin as the first high and equipotent agonists of human and rat GPR35. *Mol. Pharmacol.* **85**, 91–104 (2014).

[PubMed](#) [PubMed Central](#) [Google Scholar](#)

30. 30.

Zhao, P. et al. Targeting of the orphan receptor GPR35 by pamoic acid: a potent activator of extracellular signal-regulated kinase and β-arrestin2 with antinociceptive activity. *Mol. Pharmacol.* **78**, 560–568 (2010).

[CAS](#) [PubMed](#) [PubMed Central](#) [Google Scholar](#)

31. 31.

Thal, D. M., Glukhova, A., Sexton, P. M. & Christopoulos, A. Structural insights into G-protein-coupled receptor allostery. *Nature* **559**, 45–53 (2018).

[ADS](#) [CAS](#) [PubMed](#) [Google Scholar](#)

32. 32.

Shin, H. et al. Recent advances in RNA therapeutics and RNA delivery systems based on nanoparticles. *Adv. Ther.* **1**, 1800065 (2018).

[Google Scholar](#)

33. 33.

Adhikari, S., Sharma, S., Ahn, S. B. & Baker, M. S. In silico peptide repertoire of human olfactory receptor proteome on high-stringency mass spectrometry. *J. Proteome Res.* **18**, 4117–4123 (2019).

[PubMed](#) [Google Scholar](#)

34. 34.

Insel, P. A. et al. G protein-coupled Receptor (GPCR) expression in native cells: “novel” endoGPCRs as physiologic regulators and therapeutic targets. *Mol. Pharmacol.* **88**, 181–187 (2015).

[CAS](#) [PubMed](#) [PubMed Central](#) [Google Scholar](#)

35. 35.

Wang, D. et al. A deep proteome and transcriptome abundance atlas of 29 healthy human tissues. *Mol. Syst. Biol.* **15**, e8503 (2019).

[PubMed](#) [PubMed Central](#) [Google Scholar](#)

36. 36.

Enge, M. et al. Single-cell analysis of human pancreas reveals transcriptional signatures of aging and somatic mutation patterns. *Cell* **171**, 321–330 (2017).

[CAS](#) [PubMed](#) [PubMed Central](#) [Google Scholar](#)

37. 37.

De Mei, C., Ramos, M., Iitaka, C. & Borrelli, E. Getting specialized: presynaptic and postsynaptic dopamine D2 receptors. *Curr. Opin. Pharmacol.* **9**, 53–58 (2009).

[PubMed](#) [PubMed Central](#) [Google Scholar](#)

38. 38.

Kopelman, N. M., Lancet, D. & Yanai, I. Alternative splicing and gene duplication are inversely correlated evolutionary mechanisms. *Nat. Genet.* **37**, 588–589 (2005).

[CAS](#) [PubMed](#) [Google Scholar](#)

39. 39.

Zerbino, D. R. et al. Ensembl 2018. *Nucleic Acids Res.* **46** (D1), D754–D761 (2018).

[CAS](#) [Google Scholar](#)

40. 40.

Durinck, S., Spellman, P. T., Birney, E. & Huber, W. Mapping identifiers for the integration of genomic datasets with the R/Bioconductor package biomaRt. *Nat. Protoc.* **4**, 1184–1191 (2009).

[CAS](#) [PubMed](#) [PubMed Central](#) [Google Scholar](#)

41. 41.

The GTEx Consortium. The Genotype-tissue expression (GTEx) pilot analysis: multitissue gene regulation in humans. *Science* **348**, 648–660 (2015).

[Google Scholar](#)

42. 42.

Saha, A. et al. Co-expression networks reveal the tissue-specific regulation of transcription and splicing. *Genome Res.* **27**, 1843–1858 (2017).

[CAS](#) [PubMed](#) [PubMed Central](#) [Google Scholar](#)

43. 43.

Harding, S. D. et al. The IUPHAR/BPS Guide to PHARMACOLOGY in 2018: updates and expansion to encompass the new guide to IMMUNOPHARMACOLOGY. *Nucleic Acids Res.* **46** (D1), D1091–D1106 (2018).

[CAS](#) [PubMed](#) [Google Scholar](#)

44. 44.

Edgar, R. C. MUSCLE: multiple sequence alignment with high accuracy and high throughput. *Nucleic Acids Res.* **32**, 1792–1797 (2004).

[CAS](#) [PubMed](#) [PubMed Central](#) [Google Scholar](#)

45. 45.

Isberg, V. et al. Generic GPCR residue numbers—aligning topology maps while minding the gaps. *Trends Pharmacol. Sci.* **36**, 22–31 (2015).

[CAS](#) [PubMed](#) [Google Scholar](#)

46. 46.

DiPilato, L. M. & Zhang, J. The role of membrane microdomains in shaping β_2 -adrenergic receptor-mediated cAMP dynamics. *Mol. Biosyst.* **5**, 832–837 (2009).

[CAS](#) [PubMed](#) [Google Scholar](#)

47. 47.

Weinberg, Z. Y., Zajac, A. S., Phan, T., Shiwartska, D. J. & Puthenveedu, M. A. Sequence-specific regulation of endocytic lifetimes modulates arrestin-mediated signaling at the μ opioid receptor. *Mol. Pharmacol.* **91**, 416–427 (2017).

[PubMed](#) [PubMed Central](#) [Google Scholar](#)

48. 48.

Bailey, S. et al. Interactions between RAMP2 and CRF receptors: the effect of receptor subtypes, splice variants and cell context. *Biochim. Biophys. Acta Biomembr.* **1861**, 997–1003 (2019).

[CAS](#) [PubMed](#) [Google Scholar](#)

49. 49.

Weston, C. et al. Receptor activity-modifying protein-directed G protein signaling specificity for the calcitonin gene-related peptide family of receptors. *J. Biol. Chem.* **291**, 21925–21944 (2016).

[CAS](#) [PubMed](#) [PubMed Central](#) [Google Scholar](#)

50. 50.

Knight, A. et al. Discovery of novel adenosine receptor agonists that exhibit subtype selectivity. *J. Med. Chem.* **59**, 947–964 (2016).

[CAS](#) [PubMed](#) [Google Scholar](#)

51. 51.

Griffin, M. T., Figueroa, K. W., Liller, S. & Ehlert, F. J. Estimation of agonist activity at G protein-coupled receptors: analysis of M₂ muscarinic receptor signaling through G_{i/o}, G_s, and G₁₅. *J. Pharmacol. Exp. Ther.* **321**, 1193–1207 (2007).

[CAS](#) [PubMed](#) [Google Scholar](#)

52. 52.

Mackenzie, A. E. et al. Receptor selectivity between the G proteins G α_{12} and G α_{13} is defined by a single leucine-to-isoleucine variation. *FASEB J.* **33**, 5005–5017 (2019).

[CAS](#) [PubMed](#) [PubMed Central](#) [Google Scholar](#)

53. 53.

Milligan, G. Orthologue selectivity and ligand bias: translating the pharmacology of GPR35. *Trends Pharmacol. Sci.* **32**, 317–325 (2011).

[CAS](#) [PubMed](#) [Google Scholar](#)

54. 54.

Jenkins, L. et al. Agonist activation of the G protein-coupled receptor GPR35 involves transmembrane domain III and is transduced via G α_{13} and β -arrestin-2. *Br. J. Pharmacol.* **162**, 733–748 (2011).

[CAS](#) [PubMed](#) [PubMed Central](#) [Google Scholar](#)

55. 55.

Hornbeck, P. V. et al. PhosphoSitePlus, 2014: mutations, PTMs and recalibrations. *Nucleic Acids Res.* **43**, D512–D520 (2015).

[CAS](#) [PubMed](#) [Google Scholar](#)

56. 56.

Bai, B. et al. Deep multilayer brain proteomics identifies molecular networks in Alzheimer's disease progression. *Neuron* **105**, 975–991 (2020).

[CAS](#) [PubMed](#) [Google Scholar](#)

57. 57.

Peng, J., Elias, J. E., Thoreen, C. C., Licklider, L. J. & Gygi, S. P. Evaluation of multidimensional chromatography coupled with tandem mass spectrometry (LC/LC-MS/MS) for large-scale protein analysis: the yeast proteome. *J. Proteome Res.* **2**, 43–50 (2003).

[CAS](#) [PubMed](#) [Google Scholar](#)

58. 58.

Wang, X. et al. JUMP: a tag-based database search tool for peptide identification with high sensitivity and accuracy. *Mol. Cell. Proteomics* **13**, 3663–3673 (2014).

[CAS](#) [PubMed](#) [PubMed Central](#) [Google Scholar](#)

59. 59.

Eng, J. K., Jahan, T. A. & Hoopmann, M. R. Comet: an open-source MS/MS sequence database search tool. *Proteomics* **13**, 22–24 (2013).

[CAS](#) [PubMed](#) [Google Scholar](#)

60. 60.

Samaras, P. et al. ProteomicsDB: a multi-omics and multi-organism resource for life science research. *Nucleic Acids Res.* **48** (D1), D1153–D1163 (2020).

[CAS](#) [PubMed](#) [Google Scholar](#)

61. 61.

Barrett, T. et al. BioProject and BioSample databases at NCBI: facilitating capture and organization of metadata. *Nucleic Acids Res.* **40**, D57–D63 (2012).

[CAS](#) [PubMed](#) [Google Scholar](#)

62. 62.

Li, B. & Dewey, C. N. RSEM: accurate transcript quantification from RNA-Seq data with or without a reference genome. *BMC Bioinformatics* **12**, 323 (2011).

[CAS](#) [PubMed](#) [PubMed Central](#) [Google Scholar](#)

[Download references](#)

Acknowledgements

We thank A. Hummer, R. Henderson, F. Heidenreich, W. R. Orchard and E. Villanueva for reading the manuscript. M.M.-S. and M.M.B. acknowledge the UK Medical Research Council (MRC; grant number MC_U105185859) for support. M.M.-S. is a Wolfson College Junior Research Fellow and has been supported by a Federation of European Biochemical Societies Long-Term Fellowship and a Marie Skłodowska-Curie Individual Fellowship from the European Union’s Horizon 2020 research and innovation programme under grant agreement 832620. D.M. acknowledges the support of the Swiss National Science foundation (SNF) under grant P2ELP3_18910. J.P. is partially supported by National Institutes of Health (NIH) grant R01AG053987. X.W. is partially supported by a pilot grant from the NIH Center of Biomedical Research Excellence (COBRE) for epigenomics of development and disease, and a pilot grant from the Core National Institute on Drug Abuse (NIDA) Center of Excellence in Omics, Systems Genetics, and the Addictome. M.A.P. was supported by NIH grant GM117425 and National Science Foundation (NSF) grant 1935926. M.H. and G.L. were supported by an MRC confidence in concept award

(MC_PC_17156). A.P. was supported by a UK Biotechnology and Biological Sciences Research Council (BBSRC)-iCase studentship (BB/JO14540/1), co-funded with AstraZeneca. D.E.G. acknowledges the Lundbeck Foundation (R313-2019-526) and Novo Nordisk Foundation (NNF17OC0031226) for financial support. C.M. acknowledges the Lundbeck Foundation (R218-2016-1266). S.E.C. was supported by an NSF Graduate Research Fellowship under grant DGE 1256260. G.M. and A.B.T. were supported by BBSRC grants BB/P000649/1 and BB/P00069X/1, respectively. M.M.B. is a Lister Institute Fellow and is also supported by the European Research Council (ERC; ERC-COG-2015-682414), the Novo Nordisk Foundation Challenge Grant (ADIPOSIGN) and the American Lebanese Syrian Associated Charities (ALSAC).

Author information

Affiliations

1. MRC Laboratory of Molecular Biology, Cambridge, UK

Maria Marti-Solano, Duccio Malinverni & M. Madan Babu

2. Cellular and Molecular Biology Program, University of Michigan, Ann Arbor, MI, USA

Stephanie E. Crilly & Manojkumar A. Puthenveedu

3. Department of Structural Biology and Center for Data Driven Discovery, St Jude Children's Research Hospital, Memphis, TN, USA

Duccio Malinverni & M. Madan Babu

4. Department of Drug Design and Pharmacology, University of Copenhagen, Copenhagen, Denmark

Christian Munk & David E. Gloriam

5. Department of Pharmacology, University of Cambridge, Cambridge, UK

Matthew Harris, Abigail Pearce & Graham Ladds

6. Centre for Translational Pharmacology, Institute of Molecular, Cell and Systems Biology, College of Medical, Veterinary and Life Sciences, University of Glasgow, Glasgow, UK

Tezz Quon, Amanda E. Mackenzie, Andrew B. Tobin & Graeme Milligan

7. Center for Proteomics and Metabolomics, St Jude Children's Research Hospital, Memphis, TN, USA

Xusheng Wang & Junmin Peng

8. Department of Biology, University of North Dakota, Grand Forks, ND, USA

Xusheng Wang

9. Departments of Structural Biology and Developmental Neurobiology, St Jude Children's Research Hospital, Memphis, TN, USA

Junmin Peng

10. Department of Pharmacology, University of Michigan Medical School, Ann Arbor, MI, USA

Manojkumar A. Puthenveedu

Authors

1. Maria Marti-Solano

[View author publications](#)

You can also search for this author in [PubMed](#) [Google Scholar](#)

2. Stephanie E. Crilly

[View author publications](#)

You can also search for this author in [PubMed](#) [Google Scholar](#)

3. Duccio Malinvernini

[View author publications](#)

You can also search for this author in [PubMed](#) [Google Scholar](#)

4. Christian Munk

[View author publications](#)

You can also search for this author in [PubMed](#) [Google Scholar](#)

5. Matthew Harris

[View author publications](#)

You can also search for this author in [PubMed](#) [Google Scholar](#)

6. Abigail Pearce

[View author publications](#)

You can also search for this author in [PubMed](#) [Google Scholar](#)

7. Tezz Quon

[View author publications](#)

You can also search for this author in [PubMed](#) [Google Scholar](#)

8. Amanda E. Mackenzie

[View author publications](#)

You can also search for this author in [PubMed](#) [Google Scholar](#)

9. Xusheng Wang

[View author publications](#)

You can also search for this author in [PubMed](#) [Google Scholar](#)

10. Junmin Peng

[View author publications](#)

You can also search for this author in [PubMed](#) [Google Scholar](#)

11. Andrew B. Tobin

[View author publications](#)

You can also search for this author in [PubMed](#) [Google Scholar](#)

12. Graham Ladds

[View author publications](#)

You can also search for this author in [PubMed](#) [Google Scholar](#)

13. Graeme Milligan

[View author publications](#)

You can also search for this author in [PubMed](#) [Google Scholar](#)

14. David E. Gloriam

[View author publications](#)

You can also search for this author in [PubMed](#) [Google Scholar](#)

15. Manojkumar A. Puthenveedu

[View author publications](#)

You can also search for this author in [PubMed](#) [Google Scholar](#)

16. M. Madan Babu

[View author publications](#)

You can also search for this author in [PubMed](#) [Google Scholar](#)

Contributions

M.M.-S. collected data, wrote scripts and performed all of the computational analyses. S.E.C. and M.A.P. experimentally characterized the

pharmacology of CNR1 isoforms. M.H., A.P. and G.L. experimentally characterized the pharmacology of GIPR isoforms. T.Q., A.E.M., G.M. and A.B.T. experimentally characterized the pharmacology of GPR35 isoforms. D.M. collected data and carried out genomics analyses. C.M. and D.E.G. designed and implemented the GPCRdb receptor-isoform browser. X.W. and J.P. collected data and analysed MS data. D.E.G. helped with aspects of data interpretation. M.M.-S. and M.M.B. designed the project, analysed and interpreted the results, and wrote the manuscript. All authors read, and provided comments on, the draft. M.M.-S. led the project. M.M.B. initiated, managed and set the direction of research.

Corresponding authors

Correspondence to [Maria Marti-Solano](#) or [M. Madan Babu](#).

Ethics declarations

Competing interests

The authors declare no competing interests.

Additional information

Peer review information *Nature* thanks Sudarshan Rajagopal, Roser Vento and the other, anonymous, reviewer(s) for their contribution to the peer review of this work.

Publisher's note Springer Nature remains neutral with regard to jurisdictional claims in published maps and institutional affiliations.

Extended data figures and tables

[**Extended Data Fig. 1 Isoform diversity in GPCRs.**](#)

a, Alternative transcriptional start or termination sites, together with alternative splicing, can generate non-reference receptor isoforms (that is, isoforms with sequences that are different to those of the GPCRdb-annotated receptor), with altered structural and signalling properties. **b**, Analysis pipeline combining GTEx isoform-level data with GPCRdb, Ensembl and UniProt annotations to filter for highly expressed, protein-coding isoforms. Isoforms with truncated signal peptides, or those without at least one conserved transmembrane helix compared with the reference isoform, are not considered (see [Methods](#)). **c**, Number of isoforms in different receptor classes (left) and grouped by the type of natural ligand of each receptor (right). **d**, Number of isoforms per receptor, grouped by each receptor's coupling partners (G-protein subunits), as annotated in the IUPHAR/BPS Guide To Pharmacology database (www.guidetopharmacology.org). Box plots in **c**, **d** show medians and 25th and 75th percentiles; whiskers represent 1.5 times the interquartile range from the 25th to the 75th quartiles.

[Extended Data Fig. 2 Classification of receptor isoforms according to topology.](#)

Structural classification of non-reference isoforms. Isoforms are considered topologically preserved if all transmembrane (TM) segments are conserved in sequence with respect to the reference isoform; this includes receptor isoforms with changes (including deletions and unique isoform sequences) in the receptor N- and C termini, as well as in intracellular and extracellular loops (ECLs) and the helix 8 (H8) segment. Isoforms are classified as topologically truncated if at least one TM segment is altered (that is, is partially or totally missing or has a different sequence to the reference isoform). Both topologically preserved and truncated isoforms can either have an alternative sequence in the segments that differ from the reference (unique sequence, represented as solid coloured lines) or lack parts of those segments altogether, thus representing a shorter version of the reference sequence (non-unique, represented as dotted coloured lines).

[Extended Data Fig. 3 Non-reference isoforms with missing phosphorylation motifs.](#)

a, Analysis of PhosphoSitePlus (<https://www.phosphosite.org/>) phosphorylation motifs with annotated regulatory function in non-reference receptor isoforms. Left, frequency of phosphosites related to regulatory effects (for example, receptor trafficking and interaction) that are found to be missing in non-reference isoforms. Right, examples of the potential consequences of this lack of regulation on receptor function for somatostatin receptor type 2 (SSR2), thromboxane A2 receptor (TA2R) and adenosine receptor A2A (AA2AR). **b**, Table showing all detected non-reference receptor isoforms in which a phosphorylation motif can be lost, together with details about the function of that particular phosphosite in the reference isoform and its associated literature evidence (with the examples in **a** highlighted in grey in the table).

Extended Data Fig. 4 Tissue distribution of different isoforms.

a, Binary representation of the presence or absence of particular receptor isoforms in the 30 different GTEx tissues according to their classification as reference isoform (grey), topologically preserved isoform (dark blue) or topologically truncated isoform (light blue). This figure shows that every tissue expresses all these types of isoforms, and that non-reference isoforms can be consistently found in multiple tissues. **b**, Heatmap showing whether the most prevalent isoform for a receptor in a particular tissue is a reference (grey), topologically preserved (dark blue) or topologically truncated (light blue) receptor isoform. The most prevalent isoform in a particular tissue is considered to be the one with the highest median expression (in TPM). Only tissues in which more than one isoform was expressed have been retained and represented. **c**, Mean number of isoforms expressed per receptor for every GTEx donor-tissue combination. All available combinations of donor-tissue expression had a mean number of isoforms per receptor of more than one (that is, reference and non-reference isoforms are coexpressed in each GTEx donor-tissue combination). Empty cells (white) represent donor-tissue combinations with no expression data. For the underlying data in **a–c**, see Supplementary Table 2. **d**, For receptors with multiple isoforms, two scenarios are possible. In one scenario, all receptor isoforms could be consistently expressed in human tissues, resulting in a uniform expression pattern. In a second scenario, different isoform combinations may be expressed in different tissues, resulting in a

complex expression pattern. In order to assess this, we calculated the number of tissue-expression signatures per receptor (see Fig. 2).

Extended Data Fig. 5 Characterization of the pharmacological and signalling effects of the coexpression of different isoforms of CNR1 and GIPR.

a, Alignment of the N-terminal segments of the reference and non-reference CNR1 isoforms. Regions that are missing or vary in isoforms 1 and 2 are highlighted in blue. **b**, Left, change in mean CFP/FRET ratios induced by 5 μ M forskolin (Fsk) in HEK293 cells. Data from cells from the same coverslip expressing (grey line) and not expressing (black line) the CNR1 reference isoform are shown. Cells expressing CNR1 show a lower Fsk response, as expected for G_i signalling. CFP/FRET ratios were obtained in HEK293 cells expressing the CNR1 reference isoform (+CNR1, $n = 30$ cells) or not (−CNR1 $n = 40$ cells). Right, the baseline ratios are not significantly different ($P = 0.527$ by unpaired, two-sided t -test). Boxplot whiskers show minima and maxima; centres indicate medians; and box boundaries indicate the 25th and 75th percentiles. **c**, The increased response to Fsk in CNR1-expressing cells treated with Rimonabant (SR) is consistent with the superactivation of adenylyl cyclase, as found in cell lines stably expressing G_i -coupled receptors such as CNR1. **d**, Total cAMP response induced by Fsk in CNR1-expressing cells. The response is decreased in CNR1-expressing cells compared with non-expressing cells. Pretreatment with 10 μ M Rimonabant reversed the CNR1-dependent decrease. **e**, The endpoint cAMP response (R_{Endpoint}), expressed as fold change over baseline cAMP (R_{Baseline}), induced by Fsk in CNR1-expressing cells is significantly decreased in CNR1-expressing cells compared with non-expressing cells. Pretreatment with 10 μ M Rimonabant reverses the CNR1-dependent decrease (−CNR1 −Rimonabant, $n = 24$ cells; +CNR1 −Rimonabant, $n = 19$ cells; −CNR1 +Rimonabant, $n = 27$ cells; +CNR1 +Rimonabant, $n = 17$ cells, from 3 independent experiments). **f**, Pretreatment with 5 μ M of the neutral antagonist AM4113 significantly increased the Fsk-stimulated total cAMP levels in CNR1-expressing relative to non-expressing cells. **g**, Pretreatment with AM4113 significantly increased the Fsk-stimulated endpoint cAMP levels in CNR1-expressing cells relative to non-expressing

cells (−CNR1 −AM4113, $n = 55$ cells; +CNR1 −AM4113, $n = 50$ cells; −CNR1 +AM4113, $n = 44$ cells; +CNR1 +AM4113, $n = 48$ cells, from 3 independent experiments). In **d–g**, P -values were obtained by one-way ANOVA with Sidak's multiple comparisons tests; boxplot whiskers show 10th and 90th percentiles; centre lines indicate medians; box bounds indicate the 25th and 75th percentile; + indicates means. **h**, Expression ratios of SNAP-tagged CNR1 isoforms to the Flag-tagged reference isoform are not significantly different across the combinatorial expression conditions (one-way ANOVA with Dunnett's multiple comparisons test). In all cases, boxplot whiskers show 10th and 90th percentiles; centre lines indicate medians; box bounds indicate the 25th and 75th percentiles; + indicates mean. Individual data points are overlaid on the boxplot. **i**, The total cAMP response, normalized to cells expressing the reference isoform, is increased in cells coexpressing the reference isoform and non-reference isoform 2 compared with control cells (ref + ref ('ref'), $n = 23$ cells; ref + iso1, $n = 18$ cells; ref + iso2, $n = 27$ cells from 3 independent experiments; one-way ANOVA with Dunnett's multiple comparisons test). **j**, Endpoint cAMP levels are significantly decreased in cells coexpressing the reference isoform and non-reference isoform 1 compared with cells expressing only the reference isoform (one-way ANOVA with Dunnett's multiple comparisons test). For box plots in **i, j**, whiskers show 10th and 90th percentiles; centre lines indicate medians; box bounds indicate 25th and 75th percentiles; + indicates mean. Individual data points are overlaid on the boxplot. **k**, Heatmap representation of cAMP levels after treatment with Fsk and Rimonabant over time in individual HEK293 cells expressing a Flag-tagged reference isoform and different SNAP-tagged isoforms. CFP/FRET ratios were normalized using the baseline ratio as 0 and the maximum ratio after Fsk, but before Rimonabant, treatment as 1. **l**, Alignment of the C-terminal segment of the reference and non-reference GIPR isoforms. Varying regions in isoform 1 are highlighted in blue. **m**, Concentration–response curves for cAMP accumulation, intracellular calcium ($(\text{Ca}^{2+})_i$) mobilization and β -arrestin-1/2 recruitment in response to GIP(1–42) stimulation, in HEK293T cells expressing GIPR–Nluc reference alone (dark grey, $n = 4$ independent experiments performed in duplicate), GIPR–Nluc isoform 1 alone (pink, $n = 4$ independent experiments performed in duplicate) or GIPR–Nluc reference and GIPR–Nluc isoform 1 combined (magenta, $n = 4$ independent experiments performed in

duplicate). Data normalized to GIPR–Nluc reference alone and expressed as mean \pm s.e.m. **n**, Cell-surface expression of Nluc–GIPR reference ($n = 7$ independent experiments performed in duplicate) or Nluc–GIPR isoform 1 ($n = 7$ independent experiments performed in duplicate). Data normalized to Nluc–GIPR reference, with significance determined by Mann–Whitney test. **o**, Left part of graph, cell-surface expression of Nluc–GIPR reference alone (dark grey, $n = 4$ independent experiments performed in duplicate) versus Nluc–GIPR reference and Nluc–GIPR isoform 1 combined (magenta, $n = 4$ independent experiments performed in duplicate). Middle, cell-surface expression of Flag–GIPR reference in the absence (dark grey, $n = 5$ independent experiments performed in duplicate) versus presence (light grey, $n = 4$ independent experiments performed in duplicate) of Nluc–GIPR isoform 1. Right, cell-surface expression of Nluc–GIPR isoform 1 in the absence (pink, $n = 5$ independent experiments performed in duplicate) versus presence (light pink, $n = 5$ independent experiments performed in duplicate) of Flag–GIPR reference. Data normalized to Nluc–GIPR reference alone (left), Flag–GIPR reference alone (middle), or Nluc–GIPR isoform 1 alone (right). Significance in **n**, **o** was determined by a two-tailed Mann–Whitney test. Box plots in **n**, **o** show the maximum and minimum (whiskers), as well as medians, 25th and 75th percentiles and means (+).**p**, GIP(1–42)-stimulated β -arrestin-1 and β -arrestin-2 recruitment to GIPR–Nluc reference in the absence (dark grey) or presence (light grey) of Nluc–GIPR isoform 1, or to GIPR–Nluc isoform 1 in the absence (pink) or presence (light pink) of Nluc–GIPR reference. Data are means \pm s.e.m. of $n = 4$ experiments performed in triplicate, normalized to GIPR–Nluc reference alone.

Extended Data Fig. 6 Receptor isoforms and drug targets.

a, Number of receptors categorized by the number of tissue-expression signatures for all GPCRs (grey) and for those belonging to the 111 targets of 474 FDA-approved drugs (in green). **b**, The number of approved drugs varies greatly for receptors with the same number of tissue-expression signatures. Count plot of the 111 GPCRs that are targeted by 474 FDA-approved drugs. The radius of each circle indicates the number of GPCR targets for each combination of ‘number of tissue-expression signatures’ (x-axis) versus ‘number of approved drugs’ (y-axis). **c**, Disease-related

phenotypes that can be exclusively linked to non-reference receptor isoforms were extracted from Gene ATLAS (see [Methods](#) and Supplementary Table 3). Non-reference isoform sequences for the N-terminal segment of the chemokine receptor CXCR3 and C-terminal segment of the metabotropic glutamate receptor 8 (GRM8) are represented in blue; the reference isoform is in grey. Polymorphisms are indicated in bold, together with their associated phenotypes in light grey boxes. **d**, Filtering based on structural and expression considerations identifies non-reference isoforms with changes in extracellular structure and tissue distribution with respect to the reference isoform, potentially allowing the development of ligands that specifically target them. **e**, Alignment of the N-terminal segment of the reference and non-reference GPR35 isoforms. Varying regions in isoform 1 are highlighted in blue. **f**, pEC_{50} and E_{max} values for the coupling of $G\alpha_{13}$ and β -arrestin-2 to the reference GPR35 isoform and isoform 1 in response to lodoxamide, pamoic acid and zaprinast. ($n = 3$ biologically independent samples; error values correspond to s.e.m.) **g**, BRET signals were monitored after treatment of HEK293T cells with varying concentrations of pamoic acid and zaprinast using a GPR35– $G\alpha_{13}$ SPASM sensor (left panel; $n = 3$ biologically independent samples) or eYFP-tagged GPR35 isoforms and β -arrestin-2 tagged with nanoluciferase (right panel; $n = 3$ biologically independent samples; Methods). Error values correspond to s.e.m.

[Extended Data Fig. 7 GPCRdb receptor-isoform browser.](#)

Screenshot of the isoform browser as implemented in GPCRdb. The classification tree (left) depicts the number of unique isoforms for each receptor, receptor family and GPCR class. In the structural annotation table (right), conserved, partially conserved and non-conserved structural segments are coloured in green, orange and red. Purple triangles indicate insertions. Each entry includes the receptor name, isoform number (assigned according to sequence length, with the longest non-reference isoform considered to be isoform 1), topological preservation or truncation status, the number of tissues in which it has been found to be expressed, an average value of segment completeness with respect to the reference receptor sequence (Ref(%)), its functional annotation (either inferred

through structural fingerprint identity with other characterized isoforms, or derived from the literature for isoforms with an associated PubMed reference), and a link to its isoform-level proteomics evidence in ProteomicsDB.

Extended Data Fig. 8 Analysis of MS-based proteomics data for receptor isoforms.

a, Analysis pipeline for investigating proteomics data to detect GPCR isoforms that had been identified using transcriptomics data at an isoform level. All transcripts from GPCRs with two or more isoforms that were detected in brain tissue through our GTEx analysis were filtered to identify those with unique peptide sequences. These transcripts were then matched with brain proteomics hits to discover how many receptor isoforms with unique protein sequences detected by transcriptomics could be identified by proteomics. **b**, Analysis of the number of matching peptides found in all receptor isoforms, considering receptor segments. Non-reference isoforms are highlighted in blue shaded boxes. Consistent with previous studies, non-transmembrane receptor regions are the ones that are often detected by MS. **c**, Proteomic detection of isoforms using MS data from a study of 29 healthy human tissues and 50 MS runs (see [Methods](#)). Searching for GPCRs detected in GTEx in this data set identified a number of receptors with more than one isoform. Of these, we filtered isoforms that had peptides matching one isoform only. **d**, Analysis of the number of matching peptides found in all receptor isoforms in **c**, considering receptor segments. Non-reference isoforms are highlighted in violet. As seen in **b**, non-transmembrane receptor regions are the ones that are more often detected by MS. Isoforms with an asterisk are found in both data sets. For all data, see Supplementary Table [5](#).

Extended Data Fig. 9 Receptor-centric isoform distribution in cell lines and single cells.

a, Analysis pipeline combining isoform-level data extracted from transcriptomics experiments of 11 human cell lines deposited in BioProject, with GPCRdb, Ensembl and Uniprot annotations to filter for highly

expressed, protein-coding isoforms. Isoforms with truncated signal peptides or those without at least one conserved transmembrane helix as compared with their GPCRdb reference are not considered (see [Methods](#)). **b**, Relationship between the number of GPCRs expressed in the 11 different cell lines (left axis, grey line) and the mean number of isoforms per receptor found in each tissue (right axis; means are shown as black dots and standard errors are grey lines). **c**, Relationship between the total number of isoforms per receptor and its number of cell-line expression signatures in the analysed cell lines. The dark grey regression line was obtained using a linear model; the light grey confidence interval represents the standard error. **d**, Mean number of isoforms per receptor expressed in single pancreatic cells as measured by single-cell RNA-seq, with each point representing the mean number of isoforms per receptor in a single cell whose transcriptome was sequenced. This analysis shows that, for every inferred cell type, there are several cells that express more than one isoform per receptor. See underlying data for **a–d** in Supplementary Table [6](#). Boxplots show median and 25th and 75th percentiles; whiskers represent 1.5 times the interquartile range from the 25th and 75th quartiles.

[**Extended Data Fig. 10 Integration of several data sets provides an isoform-centric view of GPCR signalling.**](#)

For receptors with multiple isoforms, combining tissue-specific and cell-specific transcriptomics information, sequence and structural data, functional annotations, population-wide genetic-association studies, proteomics evidence and details on receptor pharmacology allows us to obtain a GPCR diversity map with which to assess the possible contribution of GPCR isoform diversity to physiological signalling bias and system-specific drug responses.

Supplementary information

[**Reporting Summary**](#)

[**Supplementary Table 1**](#)

Functional changes reported in the literature for GPCR isoforms with particular structural fingerprints.

Supplementary Table 2

Tissue expression distribution of the analysed GPCR isoforms.

Supplementary Table 3

Statistically significant associations between disease-related phenotypes and single nucleotide polymorphisms available via Gene ATLAS that map to non-reference GPCR isoforms.

Supplementary Table 4

Tissue distribution of non-reference GPCR isoforms with extracellular structural variation and different tissue distribution compared to the reference isoform.

Supplementary Table 5

Evidence from mass spectrometry experiments for reference and non-reference GPCR isoforms.

Supplementary Table 6

Cancer cell line and human pancreatic single cell RNA sequencing evidence for GPCR isoforms.

Rights and permissions

[Reprints and Permissions](#)

About this article



Check for
updates

Cite this article

Marti-Solano, M., Crilly, S.E., Malinvern, D. *et al.* Combinatorial expression of GPCR isoforms affects signalling and drug responses. *Nature* **587**, 650–656 (2020). <https://doi.org/10.1038/s41586-020-2888-2>

[Download citation](#)

- Received: 09 October 2019
- Accepted: 24 September 2020
- Published: 04 November 2020
- Issue Date: 26 November 2020
- DOI: <https://doi.org/10.1038/s41586-020-2888-2>

Comments

By submitting a comment you agree to abide by our [Terms](#) and [Community Guidelines](#). If you find something abusive or that does not comply with our terms or guidelines please flag it as inappropriate.

[Access through your institution](#)

[Change institution](#)

[Buy or subscribe](#)

Associated Content

Nature | News & Views

Isoforms of GPCR proteins combine for diverse signalling

- Joshua C. Snyder
- & Sudarshan Rajagopal

This article was downloaded by **calibre** from <https://www.nature.com/articles/s41586-020-2888-2>

| [Section menu](#) | [Main menu](#) |

Papain-like protease regulates SARS-CoV-2 viral spread and innate immunity
[Download PDF](#)

- Article
- [Published: 29 July 2020](#)

Papain-like protease regulates SARS-CoV-2 viral spread and innate immunity

- [Donghyuk Shin](#) ORCID: [orcid.org/0000-0002-8272-6133](#)^{1,2,3},
- [Rukmini Mukherjee](#) ORCID: [orcid.org/0000-0001-7955-6324](#)^{1,2},
- [Diana Grewé](#) ORCID: [orcid.org/0000-0002-4685-1383](#)²,
- [Denisa Bojkova](#)⁴,
- [Kheewoong Baek](#) ORCID: [orcid.org/0000-0002-6853-4936](#)⁵,
- [Anshu Bhattacharya](#) ORCID: [orcid.org/0000-0002-7383-3594](#)^{1,2},
- [Laura Schulz](#) ORCID: [orcid.org/0000-0002-2403-7129](#)⁶,
- [Marek Widera](#) ORCID: [orcid.org/0000-0001-5417-9307](#)⁴,
- [Ahmad Reza Mehdipour](#) ORCID: [orcid.org/0000-0002-0193-3334](#)⁶,
- [Georg Tascher](#) ORCID: [orcid.org/0000-0002-5907-3947](#)¹,
- [Paul P. Geurink](#) ORCID: [orcid.org/0000-0003-1849-1111](#)⁷,
- [Alexander Wilhelm](#)^{4,8},
- [Gerbrand J. van der Heden van Noort](#) ORCID: [orcid.org/0000-0001-5955-6431](#)⁷,
- [Huib Ovaa](#) ORCID: [orcid.org/0000-0002-0068-054X](#)^{7 na1},
- [Stefan Müller](#) ORCID: [orcid.org/0000-0002-8792-7700](#)¹,
- [Klaus-Peter Knobeloch](#) ORCID: [orcid.org/0000-0003-1587-1944](#)⁹,
- [Krishnaraj Rajalingam](#) ORCID: [orcid.org/0000-0002-4175-9633](#)¹⁰,
- [Brenda A. Schulman](#) ORCID: [orcid.org/0000-0002-3083-1126](#)⁵,
- [Jindrich Cinatl](#) ORCID: [orcid.org/0000-0002-6744-2087](#)⁴,
- [Gerhard Hummer](#) ORCID: [orcid.org/0000-0001-7768-746X](#)^{6,11},
- [Sandra Ciesek](#) ORCID: [orcid.org/0000-0002-1802-7565](#)^{4,8,12} &
- [Ivan Dikic](#) ORCID: [orcid.org/0000-0001-8156-9511](#)^{1,2,3,12}

- 65k Accesses
- 12 Citations
- 475 Altmetric
- [Metrics details](#)

Subjects

- [SARS-CoV-2](#)
- [Ubiquitylated proteins](#)
- [X-ray crystallography](#)

Abstract

The papain-like protease PLpro is an essential coronavirus enzyme that is required for processing viral polyproteins to generate a functional replicase complex and enable viral spread^{1,2}. PLpro is also implicated in cleaving proteinaceous post-translational modifications on host proteins as an evasion mechanism against host antiviral immune responses^{3,4,5}. Here we perform biochemical, structural and functional characterization of the severe acute respiratory syndrome coronavirus 2 (SARS-CoV-2) PLpro (SCoV2-PLpro) and outline differences with SARS-CoV PLpro (SCoV-PLpro) in regulation of host interferon and NF-κB pathways. SCoV2-PLpro and SCoV-PLpro share 83% sequence identity but exhibit different host substrate preferences; SCoV2-PLpro preferentially cleaves the ubiquitin-like interferon-stimulated gene 15 protein (ISG15), whereas SCoV-PLpro predominantly targets ubiquitin chains. The crystal structure of SCoV2-PLpro in complex with ISG15 reveals distinctive interactions with the amino-terminal ubiquitin-like domain of ISG15, highlighting the high affinity and specificity of these interactions. Furthermore, upon infection, SCoV2-PLpro contributes to the cleavage of ISG15 from interferon responsive factor 3 (IRF3) and attenuates type I interferon responses. Notably, inhibition of SCoV2-PLpro with GRL-0617 impairs the virus-induced cytopathogenic effect, maintains the antiviral interferon pathway and reduces viral replication in infected cells. These results highlight a potential dual therapeutic strategy in which targeting of SCoV2-PLpro can suppress SARS-CoV-2 infection and promote antiviral immunity.

[Download PDF](#)

Main

The novel coronavirus SARS-CoV-2 is the cause of the current worldwide outbreak of the respiratory disease coronavirus disease 2019 (COVID-19)⁶. COVID-19 generally has less severe symptoms and a lower case-fatality rate but is transmitted more rapidly compared with the related SARS-CoV, which caused the SARS outbreak in 2003. The SARS-CoV-2 genome shares high sequence identity with SARS-CoV^{7,8}. Both viruses critically rely on the activity of viral proteases: the main protease (Mpro, also known as 3CLpro or non-structural protein 5 (nsp5)) and the papain-like protease (PLpro, the protease domain of nsp3) to generate a functional replicase complex and enable viral spread^{1,2}. SCoV-PLpro cleaves ubiquitin and ISG15, known regulators of host innate immune pathways, and inhibition of SCoV-PLpro has been shown to block SARS-CoV replication^{3,4,5}.

SARS-CoV-2 PLpro preferentially cleaves ISG15

SCoV-PLpro and SCoV2-PLpro are closely related and diverge from Middle East respiratory syndrome (MERS) coronavirus PLpro (MERS-PLpro) (Extended Data Fig. 1a). Purified SCoV-PLpro and SCoV2-PLpro exhibit differences in their substrate preferences, as revealed by their cleavage of ubiquitin or ISG15 from substrates in HeLa cells treated with interferon- α (IFN- α) (Extended Data Fig. 1b). SCoV-PLpro strongly reduced the appearance of ubiquitinated substrates, with a lesser effect on ISGylated substrates, whereas SCoV2-PLpro preferentially reduced appearance of ISG15-conjugated (ISGylated) protein substrates (Extended Data Fig. 1b).

We next used activity-based probes, namely a highly reactive propargylamide (Prg) ‘warhead’, which forms a covalent bond with catalytic cysteines, and a 7-amido-4-methylcoumarine (AMC) probe, which emits fluorescence upon cleavage, enabling the monitoring of the kinetics of the protease activity^{9,10,11,12,13}. SCoV2-PLpro preferentially reacted with the ISG15–Prg probe, but showed weak activity towards K48-linked di-ubiquitin (K48-Ub₂) and Nedd8, and no activity towards SUMO-based Prg probes (Fig. 1a, Extended Data Fig. 1c). SCoV-PLpro showed highest reactivity with K48-Ub₂ Prg probes, and less reactivity towards the ISG15–Prg probe (Fig. 1a, Extended Data Fig. 1c). This substrate preference was further confirmed using competition assays with increasing doses of K48-Ub₂ (Extended Data Fig. 1d,e). In the reaction with SCoV-PLpro, K48-Ub₂ effectively competed with both ISG15–Prg and ISG15–AMC, whereas competitive displacement was much less effective with SCoV2-PLpro. We also examined the catalytic efficiency

(turnover number (k_{cat})/Michaelis constant (K_m)) of both PLpro proteins (Fig. 1b, Extended Data Table 2), which indicated that SCoV2-PLpro cleaved AMC from ISG15–AMC more efficiently than from K48-Ub₂–AMC, whereas SCoV-PLpro cleaved AMC from K48-Ub₂ more efficiently. Of note, the apparent catalytic efficiencies (k_{cat}/K_m) of the two PLpro enzymes towards ISG15 were similar, but SCoV2-PLpro showed slightly higher specificity towards ISG15 (indicated by lower K_m) (Fig. 1b, Extended Data Table 2). Consistently, SCoV2-PLpro bound ISG15 with a 20-fold higher affinity compared with K48-Ub₂, whereas SCoV-PLpro bound K48-Ub₂ with a 10-fold higher affinity compared with both mouse and human ISG15¹⁴ (Fig. 1c, [Extended Data Table 3](#)). Indeed, the deISGylase activity of SCoV2-PLpro towards Prg- or AMC-based substrates, was similar to or higher than that of mouse USP18, a specific deISGylase^{12,15} (Extended Data Fig. 1f,g). Both PLpro enzymes also displayed weak deneddylase activity towards hyperneddylated CUL1, a common feature of deneddylases such as DEN1 (Extended Data Fig. 1c,h,i). Together, these results indicate that SCoV2-PLpro preferentially cleaves ISG15 from substrates over ubiquitin chains and Nedd8 in vitro, whereas SCoV-PLpro targets ubiquitin chains and, to a lesser extent, ISG15 and Nedd8 (Fig. 1d).

Fig. 1: DeISGylating and deubiquitylating activities of SCoV-PLpro and SCoV2-PLpro.

 **figure1**

a, SCoV-PLpro (left) or SCoV2-PLpro (right) were incubated with indicated Prg probes. Experiments were repeated three times independently with similar results. **b**, Catalytic efficiency (k_{cat}/K_m) of SCoV2-PLpro and SCoV-PLpro cleavage of K48-Ub₂-AMC or ISG15-AMC. **c**, Dissociation constant (K_d) of SCoV2-PLpro and SCoV-PLpro. Data in **c**, **d**, are mean \pm s.d. or mean \pm s.e.m. ($n = 3$ independent experiments). * $P < 0.05$, ** $P < 0.01$, **** $P < 0.0001$; two-tailed paired *t*-test. **d**, Schematic representation of substrate specificity of SCoV2-PLpro (red) and SCoV-PLpro (blue). The preferred substrate is shown on the left.

[Source data](#)

[Full size image](#)

Structural analysis of SCoV2-PLpro-ISG15

To gain insight into the molecular basis underlying specificity of SCoV2-PLpro–ISG15, we determined the crystal structure of a complex comprising SCoV2-PLpro(C111S) and mouse ISG15 (Fig. 2a, Extended Data Fig. 2a). Notably, ISG15 displays two tandem ubiquitin-like folds. The overall assembly of SCoV2-PLpro and the two ISG15 domains was similar to the complex of MERS-PLpro with human ISG15 complex¹⁶ (Protein Data Bank (PDB) ID: 6BI8; Extended Data Fig. 2a). The catalytic cysteine residue is also conserved in SARS (Extended Data Fig. 2b). Compared with the crystal structure of ISG15 in isolation (PDB ID: 5TLA)¹⁷, the N-terminal half of ISG15 is rotated by almost 90° and rests on the S2 helix of SCoV2-PLpro (Fig. 2b). The structure of SCoV-PLpro in complex with the C terminus of mouse ISG15 (PDB ID: 5TL7)¹⁷ showed that SCoV-PLpro and SCoV2-PLpro share the same binding mode to the C-lobe of mouse ISG15 (Extended Data Fig. 2c). We next compared the structure of the SCoV2-PLpro–ISG15 complex to that of SCoV-PLpro bound to K48-Ub₂, in which the proximal ubiquitin is linked to the catalytic site. The main difference between these complexes is an interaction remote from the catalytic site, in which a protease S2 site binds the distal ubiquitin in the K48-linked chain, or the N-terminal ubiquitin-like fold in ISG15. Whereas SCoV-PLpro Leu76 mediates a hydrophobic interaction with Ile44 on ubiquitin, the corresponding residue on SCoV2-PLpro is Thr75 (Fig. 2c). To mimic the hydrophobic interaction observed in SCoV-PLpro, we generated two variants of SCoV2-PLpro (T75A and T75L). The T75L mutant, but not T75A, resulted in a K48-Ub₂–AMC cleavage (Fig. 2d). This indicates that the presence and size of the hydrophobic residue at this site are critical determinants for ubiquitin binding. We also compared papain-like proteases from other coronaviruses, including the common human coronaviruses OC43, 229E and NL63 (Extended Data Fig. 3). The S2 binding site in papain-like proteases is poorly conserved across coronaviruses and exhibits variable hydrophobicity at the position corresponding to Thr75 of SCoV2-PLpro, which might influence substrate specificity.

Fig. 2: Structural analysis of SARS-CoV-2 PLpro in complex with full length ISG15.

 figure2

a, Crystal structure of SARS-CoV-2 PLpro(C111S) in complex with mouse ISG15. The C-terminal glycine of ISG15 and catalytic triad of SCoV2-PLpro are highlighted as stick model. The ubiquitin like domain (Ubl) is coloured orange. **b**,

Comparison of unbound form of ISG15 with ISG15 in complex with SCoV2-PLpro. **c**, Comparison of N-terminal half of K48-linked di-ubiquitin (K48 Ub₂-N)–SCoV-PLpro complex structure (PDB ID: 5E6J) with ISG15–SCoV2-PLpro. Residues forming hydrophobic interactions are highlighted as stick model. **d**, Initial velocity (V_i) of AMC release from AMC probes (K48-Ub₂-AMC and ISG15-AMC) with the indicated wild-type (WT) and mutant PLpro. Data are mean ± s.d. ($n = 3$ independent experiments). ** $P < 0.01$; two-tailed paired t -test. **e**, Comparison of N-terminal half of mouse ISG15 (ISG15-N) and SCoV2-PLpro and SCoV-PLpro (PDB ID: 5E6J). Residues forming hydrophobic interactions are highlighted as stick model. **f**, ISG15-Prg was incubated with wild type and mutant SCoV2-PLpro. Experiments were repeated three times independently with similar results.

[Source data](#)

[Full size image](#)

Next, we examined whether other residues in SCoV2-PLpro contribute to its enhanced affinity for ISG15. SCoV2-PLpro Val66 faces the hydrophobic patch (Ala2, Thr20 and Met23) on the N-terminal ubiquitin fold domain of ISG15 (Fig. [2e](#)). Both PLpro enzymes share Phe (SCoV2-PLpro Phe69 and SCoV-PLpro Phe70) as the core residue mediating hydrophobic interactions with either ubiquitin or ISG15. Mutating Phe69 (F69A) or Val66 (V66A) on SCoV2-PLpro decreased its enzymatic activity and showed slower reaction with ISG15-Prg compared to the wild type (Fig. [2f](#)).

The interaction between SCoV2-PLpro and K48-Ub₂ and mouse ISG15 was also examined using molecular dynamics simulations (Extended Data Fig. [2d,e](#)). Multi-microsecond molecular dynamics simulations confirmed that SCoV2-PLpro interacts more tightly with ISG15 compared with K48-Ub₂ (reconfirming K_d values measured in Fig. [1e](#)). In three independent runs of 3.2 μ s, ISG15 remained bound as in the SCoV2-PLpro–ISG15 X-ray structure. By contrast, the distal ubiquitin of K48-Ub₂ separated from SCoV2-PLpro in four out of six runs on a microsecond time scale. We identified L75T to be the differentiator between K48-Ub₂ and SCoV-PLpro, as it weakens the hydrophobic cluster within the binding interface. We observed that water transiently enters between K48-Ub₂ Ile44 and SCoV2-PLpro Thr75 before dissociation. Indeed, in simulations of the SCoV-PLpro double mutant (S67V/L76T) with K48-Ub₂, a similar water-mediated dissociation mechanism was observed (Extended Data Fig. [2f,g](#)). Together, these results suggest that the S2 region determines substrate specificity and that SCoV2-PLpro shows a relative preference towards ISG15.

GRL-0617 is an inhibitor of SCoV2-PLpro

Given the urgency to identify novel therapeutic strategies against COVID-19, we tested the effect of GRL-0617, a non-covalent inhibitor of SCoV-PLpro¹⁸, on SCoV2-PLpro (Fig. 3a). GRL-0617 was developed as an inhibitor of SCoV-PLpro and does not inhibit other host proteases^{18,19}. On the basis of the binding mode of GRL-0617 and other naphthalene-based inhibitors to SCoV-PLpro^{18,19,20,21}, we postulated that the conserved Tyr268 of SCoV2-PLpro could also bind GRL-0617 and block the entry of the ISG15 C terminus towards the catalytic cleft of the protease (Fig. 3b, Extended Data Fig. 4a–c). Indeed, the half maximal inhibitory concentration (IC_{50}) of GRL-0617 for SCoV2-PLpro was similar to the one for SCoV-PLpro (Fig. 3c, Extended Data Fig. 4d,e). GRL-0617 is ineffective against MERS-PLpro²²; we hypothesized that this could be due to the presence of Thr instead of Tyr at this conserved position (Tyr268 in SCoV2-PLpro) (Extended Data Fig. 3a). Accordingly, the mutation of Tyr268 to either Thr (Y269T) or Gly (Y268G) in SCoV2-PLpro strongly reduced the inhibitory effect of GRL-0617 (Fig. 3c, Extended Data Fig. 4d,e), indicating the critical role of Tyr268 in this process. Molecular dynamics simulations of GRL-0617 with SCoV-PLpro and SCoV2-PLpro further confirmed a common binding mode between GRL-0617 and Tyr268 (Tyr269 in SCoV-PLpro) (Extended Data Fig. 4b,c).

Fig. 3: Effect of GRL-0617 on SCoV2-PLpro.



a, Structure of GRL-0617. **b**, Comparison of ISG15-bound (left) and GRL-0617 bound (right) structure. Blocking loop 2 (BL2 loop) of SCoV2-PLpro is modelled on the basis of GRL-0617 bound SCoV-PLpro and SCoV2-PLpro structures (PDB ID: 3E9S¹⁸ and 6W9C). GRL-0617-interacting Tyr268 and catalytic Cys. His residues are highlighted as stick model. **c**, Cleavage of ISG15–AMC was measured and normalized to DMSO control. IC_{50} value of GRL-0617 in relation to SCoV2-PLpro activity is presented. Data are mean \pm s.d. $n = 3$ independent experiments.

[Source data](#)

[Full size image](#)

To assess the potential therapeutic value of GRL-0617 against COVID-19, we tested the effect of GRL-0617 on the deISGylase or deubiquitinase activities of SCoV2-PLpro on host proteins. GRL-0617 effectively blocked SCoV2-PLpro activity, leading to increased levels of ISGylated proteins in lysates of IFN- α -treated cells (Extended Data Fig. 4f). GRL-0617 also blocked the deubiquitination activity of SCoV-PLpro (Extended Data Fig. 4f). Of note, the effects of GRL-0617 on the reaction between Prg probes with SCoV2-PLpro were more prominent with ISG15_{C-term}-Prg than ISG15_{FL}-Prg or ubiquitin versus K48-Ub₂ to SCoV-PLpro (Extended Data Fig. 4g, h), which is consistent with the structural data indicating that the ISG15 N-terminal ubiquitin-fold domain potentiates the interaction with SCoV2-PLpro. These results showed that GRL-0617 inhibits both SCoV2-PLpro and SCoV-PLpro.

PLpro regulates IFN and NF- κ B pathways

To understand the differences in the pathophysiological roles of SCoV2-PLpro and SCoV-PLpro, and to expand our knowledge of the SARS-CoV-2 protein interaction map²³, we analysed the cellular interactome of both proteins. ISG15 was significantly enriched in complexes with a catalytically inactive version of SCoV2-PLpro (C111S), whereas a SCoV-PLpro mutant (C111S) predominantly associated with ubiquitin (Fig. 4a, b). In mammalian cells treated with type I IFNs (IFN- α), unconjugated ISG15 and ISG15-positive smears (probably representing ISGylated substrates) on western blots were more pronounced in immunoprecipitates of GFP-SCoV2-PLpro(C111S) than those of GFP-SCoV-PLpro(C111S) (Fig. 4c). GRL-0617 treatment blocked this association (Fig. 4c). Moreover, these closely related PLpro enzymes associate with distinct and specific sets of host proteins (Fig. 4a). For SCoV2-PLpro, these interactions include PRKDC (associated with induction by type I interferons²⁴), heterogenous nuclear ribonucleoprotein K (HNRNPK; involved in host RNA splicing, a process essential for SARS-CoV-2 replication in cells²⁵) and galectin1, which can induce viral fusion with target cells during HIV infection²⁶ (Fig. 4a). By contrast SCoV-PLpro strongly associates with several serine protease inhibitors (serpins), including serpin B3, which has been proposed to inhibit papain proteases^{27,28}. Co-expression of serpin B3 with PLpro enzymes partially restored NF- κ B signalling in cells expressing SCoV-PLpro, but had no effect on SCoV2-PLpro regulation of the IFN pathway (Extended Data Fig. 5a, b).

Fig. 4: Effect on PLpros on IFN and NF- κ B pathways.

 **figure4**

a, Interactome analysis comparing SCoV2-PLpro(C111S) and SCoV-PLpro(C111S). Statistically significant and immunity-related proteins are highlighted. **b**, \log_2 (fold change) of ubiquitin and ISG15 proteins enriched by SCoV2-PLpro or SCoV-PLpro immunoprecipitates versus empty vector. Data are mean \pm s.d. ($n = 3$, independent experiments). **c**, ISGylated proteins were enriched from A549 cells treated with IFN- α (200 U ml $^{-1}$) by immunoprecipitation of the indicated C111S mutant PLPro. **d**, ISGylation level of Myc–IRF3 in A549 cells expressing the indicated GFP–PLpro. Experiments in **c**, **d**, were repeated three times independently with similar results.

[Source data](#)

[Full size image](#)

Consistently, expression of SCoV2-PLpro and SCoV-PLpro in mammalian cells decreased ISGylation of cellular proteins following IFN- α stimulation (Extended Data Fig. 5c), including ISGylation of interferon regulatory factor 3 (IRF3), a critical component in the type 1 interferon pathway²⁹. Both SCoV2-PLpro and SCoV-PLpro reduced IRF3 ISGylation, with SCoV2-PLpro having a more potent effect (Fig. 4d). Decreases in phosphorylation of TBK1 and IRF3, and nuclear translocation of IRF3 were detected upon expression of SCoV-PLpro or SCoV2-PLpro (Extended Data Fig. 5d,e). SCoV2-PLpro(C111S) showed stronger dominant negative effects on IRF3 phosphorylation compared with SCoV-PLpro(C111S) (Extended Data Fig. 5d,e). TBK1 phosphorylation also activates the NF- κ B pathway, causing upregulation of inflammatory signalling³⁰. Although expression of SCoV-PLpro had less effect on IRF3 ISGylation (Fig. 4d), it strongly attenuated degradation of I κ B- α (Extended Data Fig. 5f,g). SCoV-PLpro also caused a severe reduction in nuclear translocation of p65 in cells treated with TNF (Extended Data Fig. 5h).

Sensing of viral nucleic acids is mimicked by poly(I:C) treatment, which induces IFN- β expression³¹. Expression of SCoV2-PLpro more effectively decreased the activation of the *IFNB1* promoter compared with SCoV-PLpro following poly(I:C) treatment. This inhibitory effect of both PLpro enzymes was neutralized by GRL-0617 treatment (Extended Data Fig. 6a,c). By contrast, expression of SCoV-PLpro predominantly blocked TNF-induced NF- κ B p65 expression, also in a GRL-0617-dependent manner (Extended Data Fig. 6b,d). Together, we show how two closely related coronaviruses (SARS and SARS-CoV-2) differentially counteract the host immune system using their PLpro enzymes.

Role of PLpro in viral spread and IFN responses

GRL-0617 has been shown to inhibit viral replication of SARS-CoV¹⁸. Thus, to determine whether inhibiting SCoV2-PLpro can also block SARS-CoV-2 replication, we infected CaCo-2 cells with SARS-CoV-2 and treated them with GRL-0617 (Fig. 5a). The effect of GRL-0617 was measured by inhibition of cytopathogenic effect (CPE). We observed a gradual dose-dependent inhibition of SARS-CoV-2-induced CPE in the presence of GRL-0617, with 100 μ M GRL-0617 almost completely inhibiting CPE (Fig. 5b). In addition, GRL-0617 treatment reduced active viral replication (SARS-CoV-2 subgenomic RNA4-encoding E gene), as measured by genetic monitoring of the intracellular production of viral RNA (Fig. 5c). Consequently, a decrease in the release of viral particles from infected cells into the supernatant was also observed upon GRL-0617 treatment (Fig. 5d, Extended Data Fig. 7a). This suggests that inhibition of SCoV2-PLpro by

GRL-0617 impedes viral replication, thereby attenuating the ongoing viral RNA synthesis.

Fig. 5: Inhibitory effects of GRL-0617 on SARS-CoV2.

 figure5

a, Schematic representation of the SARS-CoV-2 (strain FFM1) growth inhibition test with GRL-0617. MOI, multiplicity of infection. **b**, CPE inhibition rate of GRL-0617 on CaCo-2 cells infected with SARS-CoV2. **c**, Intracellular active virus replication was analysed by measuring SARS-CoV-2 subgenomic RNA (subgRNA E) level and normalized to the cellular *ACTB* gene. **d**, Release of viral particles in culture medium was analysed by PCR targeting the open reading frame of the RNA-dependent RNA polymerase (*RdRP*) gene of SARS-CoV-2. **e, f**, The effect of GRL-0617 on the type I IFN pathway. CaCo-2 cells were infected with SARS-CoV-2 or SARS-CoV with or without GRL-0617 (50 µM). pTBK1, phosphorylated TBK1; pIRF3, phosphorylated IRF3; pNF-κB p65, phosphorylated pNF-κB p65. **e**, Endogenous IRF3 was immunoprecipitated and analysed by immunoblotting. **f**, Phosphorylation of TBK1 was analysed by immunoblotting. **g**, Relative mRNA levels of indicated genes from infected cells with or without GRL-0617 (25 µM)

treatment were analysed and normalized to 18S RNA. *P* values in parentheses. Data in **c**, **d**, **g**, are mean \pm s.d.; *n* = 3 independent experiments. **P* < 0.05, ***P* < 0.01, ****P* < 0.001, *****P* < 0.0001; two-tailed paired *t*-test. Experiments in **e**, **f**, were repeated three times independently with similar results.

[Source data](#)

[Full size image](#)

Having demonstrated a role for expression of SCoV2-PLpro and SCoV-PLpro in attenuating host antiviral IFN pathways, we anticipated that inhibition by GRL-0617 would reverse this process. Indeed, GRL-0617 treatment of SARS-CoV-2-infected cells led to a marked increase in IRF3 ISGylation (Fig. 5e), which has previously been shown to regulate antiviral immune response³². Moreover, phosphorylation of IRF3 and TBK1, markers for IFN pathway activation, and p65 phosphorylation, used to monitor NF- κ B pathway activation, were increased in SARS-CoV-2-infected cells upon GRL-0617 treatment (Fig. 5f). Notably, GRL-0617 treatment significantly rescued the expression of IFN-responsive genes (*ISG15*, *OAS1*, *PKR* (also known as *EIF2AK2*) and *MX1*) in SARS-CoV-2-infected cells (Fig. 5g, Extended Data Fig. 7b). These findings provide evidence that inhibition of SCoV2-PLpro, in addition to blocking viral RNA synthesis, can also increase antiviral signalling via TBK1 and IRF3 (Extended Data Fig. 7c). Although experiments conducted with GRL-0617 provide evidence supporting the therapeutic value of pharmacologically targeting SCoV2-Plpro in patients, the low potency of GRL-0617 suggests that additional studies are needed to develop more potent and selective PLpro inhibitors.

Finally, we tested changes in CaCo-2 cells upon infection with SARS-CoV and SARS-CoV-2. GRL-0617 treatment of infected cells showed an overall similar pattern in biochemical and transcriptional parameters of the type I IFN and NF- κ B pathways (Fig. 5e–g). However, we found that GRL-0617 was consistently more effective in restoring ISGylation and phosphorylation level of IRF3 and expression of IFN-responsive genes upon infection with SARS-CoV-2 compared with SARS-CoV (Fig. 5e–g). By contrast, transcription levels of the proinflammatory cytokines IL-6 and IL-8 appeared similar between SARS-CoV and SARS-CoV-2 in this epithelial cell culture model (Fig. 5g). Consistent with these observations, a recent study has shown that SARS-CoV-2 infection in animal models and in human patients with COVID-19 is correlated with low IFN type I and type III responses³³. Although preferential deISGylation activity of SCoV2-PLpro may contribute to decreased type I IFN signalling, more detailed studies are needed to understand the

key regulatory factors contributing to innate and adaptive immunity that control the distinct pathologic outcomes of SARS-CoV and SARS-CoV-2 infections³⁴.

In summary, this study provides mechanistic understanding of the functions of SCoV2-PLpro during SARS-CoV-2 infection and establishes SCoV2-PLpro as a promising target for therapeutic intervention against COVID-19. Recent reports of newly identified inhibitors of SCoV2-PLpro^{35,36,37} could lead to the rapid development of novel anti-COVID-19 therapeutics with dual effects—blocking SARS-CoV-2 spread and promoting antiviral immunity in the host. Furthermore, the main protease of SARS-CoV-2 has been in focus as a potential drug target against COVID-19 and several novel inhibitors have already been described^{38,39,40}. Combining drugs targeting essential SARS-CoV-2 proteases (PLpro and/or main protease) with drugs targeting SARS-CoV-2 RNA-dependent polymerase may offer successful therapeutic options in future⁴¹.

Methods

No statistical methods were used to predetermine sample size. The experiments were not randomized. The investigators were not blinded to allocation during experiments and outcome assessment.

Plasmids construction

The papain-like protease domain sequence was obtained from the SARS-CoV-2 complete genome (NCBI genome databank, Severe acute respiratory syndrome coronavirus 2 isolate Wuhan-Hu-1, complete genome; NC_045512). Protein sequence for CoV2 PLpro Ubl domain (amino acids, 746–1060) of Nsp3 protein from SARS-CoV-2 (Nsp3; YP_009725299.1) was codon optimized, synthesized and cloned into pET28b with NcoI and XhoI to have C-terminal His-tag (Genescrypt). Protein sequences of the PLpro-Ubl domain of SARS and MERS (PDB ID: 3MJ5 and 5W8U, respectively^{20,42}) were also codon optimized, synthesized and cloned into pET28b with NcoI and XhoI to add C-terminal His tags (Genescrypt). Mutants were generated by PCR and verified by sequencing. For mammalian expression, PLpros were cloned into pEGFP-C1 (clontech). To produce the vector pACE-ISG15, a synthetic cDNA was used for murine ISG15 (residues 1–155) with an added N-terminal His₆ tag and the recognition site for the HRV-3C protease (Mr. Gene).

Protein purification

BL21(DE3) *Escherichia coli* competent cells (NEB) were transformed with plasmids and grown in LB medium to an OD₆₀₀ of 0.6–0.8 at 37 °C. Protein production was induced by addition of 0.5 mM isopropyl-d-thiogalactopyranoside (IPTG) and 1 mM zinc chloride ($ZnCl_2$). The cells were further grown overnight at 18 °C and collected. The cell pellet was resuspended in lysis buffer (50 mM Tris-HCl, 150 mM NaCl, 10 mM Imidazole, 2 mM DTT, pH 8.5) and lysed by sonication and centrifuged at 13,000 rpm to clarify the supernatant. The supernatant was incubated 2 h with TALON beads (Takara) pre-equilibrated with lysis buffer and non-specific proteins were cleared with washing. Proteins were eluted with elution buffer (50 mM Tris-HCl, 150 mM NaCl, 250 mM imidazole, 2 mM DTT, pH 8.5). Eluted proteins were buffer exchanged to storage buffer (20 mM Tris-HCl, 100 mM NaCl, 2 mM DTT, pH 8.5) and stored for biochemical analysis. For crystallization of SCov2-PLpro(C111S), the cell pellet was resuspended in lysis buffer (50 mM Tris-HCl, 150 mM NaCl, 10 mM imidazole, 1 mM TCEP, pH 7.4) and lysed by sonication and centrifuged at 13,000 rpm to clarify the supernatant. The supernatant was incubated 2 h with TALON beads (Takara) pre-equilibrated with lysis buffer and non-specific proteins were cleared with washing. Proteins were eluted with elution buffer (50 mM Tris-HCl, 150 mM NaCl, 250 mM imidazole, 1 mM TCEP, pH 7.4) and further purified on size-exclusion column (Superdex 75 16/60, GE Healthcare) pre-equilibrated with 20 mM Tris-HCl, 100 mM NaCl, 1 mM TCEP, pH 7.4. Proteins were concentrated to 20 mg ml⁻¹ and stored for crystallization. For the expression of mouse ISG15, BL21(DE3) *E. coli* competent cells (NEB) were transformed with pACE-ISG15. A single bacterial colony was picked and transferred in 5 ml DYT medium with 0.2% (w/v) glucose and 100 µg ml⁻¹ ampicillin and grown overnight at 37 °C. The preculture was centrifuged for 3 min at 3,000g centrifuged and resuspended in 5 ml of fresh medium. Two litres of DYT medium was mixed with 5 ml of the pre-culture and grown at 37 °C until it reached an OD₆₀₀ of 0.6. Protein expression was induced by adding IPTG (final concentration 1 mM). The cells were grown for 20 h at 28 °C and collected by centrifugation (10 min, 5,000g, 4 °C). Five grams of *E. coli* pellet (ISG15 or ISG15(C76S)) were thawed on ice and resuspended in 30 ml of buffer A-ISG15 (50 mM Na₂HPO₄, 500 mM NaCl pH 7.0, 1 protease inhibitor tablet (Roche)). The cells were disrupted using a French press and the lysate was centrifuged for 1 h 40,000g and 4 °C. All cleaning steps were carried out with an ÄkTA chromatography system (GE Healthcare) at 4 °C. The supernatant was applied to a 15 ml Ni-FF Sepharose column (GE Healthcare). The column was filled with 4 column volumes of 50 mM Na₂HPO₄, 500 mM NaCl, 15 mM imidazole pH 7.0, washed and the protein was eluted with a linear imidazole gradient over 20 column volumes and final imidazole concentration of 500 mM (buffer B-ISG15). About 30 mg of the eluted protein was treated with 1 mg His₆-HRV-3C and dialysed against buffer A-ISG15 at 16 °C for

16 h. The protein was then applied to the same column containing the protein, concentrated to about 6 mg ml⁻¹ and further purified with a size-exclusion column (Superdex 75 16/60, GE Healthcare) pre-equilibrated with 20 mM Tris-HCl, 100 mM NaCl, 1 mM TCEP, pH7.4.

Ubiquitin, NEDD8, SUMO and ISG15 activity-based probe assay

PLpro proteins were diluted (2 μ M final concentration) with activation buffer (25 mM Tris-HCl pH 7.5, 150 mM NaCl, 10 mM DTT) and incubated for 10 min at 25 °C. and the activity-based probes were diluted (0.2 mg ml⁻¹ final concentration) in dilution buffer (50 mM Tris-HCl 7.5, 150 mM NaCl). The reaction mixture was prepared by mixing equal volume of activated PLpro proteins (2 μ M) and activity-based probes (0.2 mg ml⁻¹). Reactions were conducted at indicated temperature (on ice (0 °C) or 37 °C) and samples were taken at the indicated time points and the reactions were quenched by the addition of SDS sample buffer. Samples were further analysed by SDS-PAGE and stained with a silver staining kit (Thermo Fisher).

AMC probe-based kinetic assay

For determination of enzyme kinetics (k_{cat} and K_m), ubiquitin-AMC or ISG15-AMC was used as substrate of PLpro or mouse USP18 and the release of AMC was measured by increase of fluorescence (excitation/emission, 360/487 nm) on a 384-well microplate reader (PHERAstar FSX, BMG Labtech). Five microlitres of solution containing different concentration of K48-Ub₂-AMC (76–0 μ M) or ISG15-AMC (40–0 μ M) were aliquoted into 384 well plate and reaction was initiated by addition of 5 μ l of PLpro or mouse USP18 (20 nM) to the well. Initial velocities of AMC release were normalized to a standard curve and the velocity versus substrate concentration plot were further analysed by Michaelis–Menten enzymatic kinetics, using the k_{cat} function with fixed value of total enzyme concentration as provided above. The experiment was repeated at least three times.

Bio-layer interferometry

Binding kinetics were determined with the OctetRed system (ForteBio). Either SCoV2-PLpro(C111S) or SCoV-PLpro(C111S) at 1 μ M were loaded onto an Ni-NTA biosensor and equilibrated with binding buffer for the baseline. To examine the association rate, equilibrated sensors were transferred into solutions containing various concentration of K48-Ub₂ (90–0 μ M), human ISG15 (3–0 μ M) or mouse ISG15 (90–0 μ M). Dissociation of PLpro was initiated by placing the sensor into

reaction buffer. Values of association rate constant (k_{on}), dissociation rate constant (k_{off}) and dissociation constant (K_d) values were calculated by Octet Data analysis software (ForteBio).

Crystallization

Equal amounts of SCoV2-PLpro(C111S) and full-length murine ISG15 were mixed, giving a final concentration of 250 μM . Protein mixtures were screened with sitting-drop matrix screens in a 96-well plate with 100 nl of protein and 100 nl of precipitant solution at 293 K. Initial crystals appeared from solution containing 20% PEG 3350, 200 mM potassium thiocyanate with 125 μM protein. To optimize the crystallization condition, we diluted the protein to vary the concentration, and the diffraction-quality crystals were grown in optimized solution containing 18% PEG 3350, 100 mM bis-tris propane pH 6.5, 200 mM potassium thiocyanate with 100 μM protein.

Data collection, processing and structure determination

Crystals were cryo-protected using mother liquor solution supplemented with 25% (v/v) ethylene glycerol. Diffraction data were collected on single frozen crystal in a nitrogen stream at 100 K at 1.00001 Å in the X06SA beamline at the Swiss Light Source, Villigen. Initial data sets were processed using XDS⁴³, and phases were determined by Phaser molecular replacement in ccp4 module with SCoV2-PLpro and mouse ISG15 as the template model⁴⁴; PDB IDs: 6W9C and 5TLA). Structure refinement and manual model building were performed with Coot and Phenix.Refine^{45,46} (Extended Data Table 1). There were 93.26% and 6.74% of the residues in the favoured and allowed regions of the Ramachandran plot respectively, and no residues were found in disallowed regions.

Cell lysates, deubiquitination and deISGylation assay

HeLa or A549 cells were treated with IFN- α (200 U ml⁻¹) for 48 h to induce ISGylation. Cells were lysed with lysis buffer (50 mM Tris-HCl (pH 8.0), 150 mM NaCl, 1% (v/v) NP-40) and concentration was measured with the BCA assay (Thermo Fisher). Ten micrograms of lysates were incubated with 100 nM of PLpro for indicated time points at 37 °C and analysed by immunoblotting with indicated antibodies. To test the inhibitory effect of GRL-0617, 40 μM of GRL-0617 was included during the reaction. Images were obtained using Image lab software (Bio-Rad).

Deneddylation and I κ B α deubiquitination assay

All proteins described are of human origin. CUL1–RBX1, SKP1– β -TRCP2, UBE2M, UBE2D3, NEDD8, UB, APPBP1–UBA3 and UBA1 were purified as previously described⁴⁷. Neddylated CUL1–RBX1 was generated as previously described⁴⁷. The reaction for generating hyperneddylated CUL1–RBX1 was driven at pH 8.8 at 37 °C for 30 min and purified by size exclusion chromatography. The USP2 catalytic core was purified with nickel affinity chromatography, liberated of the His tag by overnight thrombin cleavage, followed by ion exchange and size-exclusion chromatography. Den1 was purified by GST affinity chromatography, liberated of the GST tag by overnight TEV cleavage, followed by ion exchange and size-exclusion chromatography. The Cop9 signalosome (CSN) was purified as previously described⁴⁸. Deneddylation assays were performed with 1 μ M hyperneddylated CUL1–RBX1, and 5 μ M protease (SCoV-PLpro, SCoV2-PLpro, DEN1 and USP2) or 20 nM CSN. The reaction was performed at 37 °C in 2.5 mM Tris 100 mM NaCl, 5 mM DTT pH 8.5, and in the case of CSN, with additional 10 mM MgCl₂. Samples were taken at each indicated time point and quenched with 2 \times SDS–PAGE sample buffer. Gels were stained by Coomassie blue and scanned on an Amersham imager 600. I κ B α deubiquitylation assays were performed by first generating a ubiquitylated I κ B α , with 200 nM UBA1, 1 μ M UBE2D3, 20 μ M UB, 500 nM neddylated CRL1– β -TRCP, and 5 μ M fluorescently labelled I κ B α at 37 °C in 50 mM Tris, 50 mM NaCl, 10 mM MgCl₂, 5 mM DTT pH 7.5 for 30 min. Reaction was quenched by adding 80 mM EDTA for 5 min. The deubiquitylation reaction was started by mixing 3 μ M of protease (SCoV-PLpro, SCoV2-PLpro or USP2) with the ubiquitylation reaction, and samples were taken at each time point and quenched with 2 \times SDS–PAGE sample buffer. Gels were scanned on an Amersham Typhoon (GE) detecting the fluorescently labelled I κ B α .

Molecular dynamics simulations

SCoV-PLpro (wild type and double mutant) and SCoV2-PLpro with K48-Ub₂

The coordinates of SCoV-PLpro with bound K48-Ub₂ were taken from PDB ID: 5E6J⁴⁹. For the double mutant setup, the mutations S67V and L76T were introduced using MODELLER⁵⁰. For SCoV2-PLpro with bound K48-Ub₂, we set up two models. We combined the substrate coordinates taken from PDB ID: 5E6J with (1) the X-ray crystal structure of the unbound form (PDB ID: 6W9C, re-refined by T. Croll (University of Cambridge, UK) (<https://drive.google.com/drive/folders/1JBo50CdkBU7K1pFThuqrzhQ-NcsIAWyG>) and (2) with the X-ray crystal structure of the SCoV2-PLpro–mouse ISG15 complex (PDB ID: 6YVA) after PLpro alignment using PyMol⁵¹. In all di-ubiquitin systems, the triazole linker was replaced with Lys using MODELLER. To mimic the linker, a harmonic-distance restraint potential was applied between the backbone carbonyl carbon atoms of Lys48 and Gly75 with a target distance of 9.5 Å and a force constant of 502,080 kJ mol⁻¹ nm⁻². The covalent propargylamide linker was removed.

SCoV-PLpro and SCoV2-PLpro in complex with inhibitor GRL-0617

The coordinates of the SCoV-PLpro–GRL-0617 complex were taken from PDB ID: 3E9S¹⁸. The oxidized Cys112 was changed to the reduced form (SH) using MODELLER. The simulation model of the SCoV2-PLpro–GRL-0617 complex was built according to the X-ray structure of the unbound form of SCoV2-PLpro (PDB ID: 6W9C, re-refined by T. Croll). The coordinates of the compound GRL-0617 were modelled according to PDB ID: 3E9S after PLpro alignment using PyMol. The blocking loop 2 (BL2 loop, GNYQCGH) capping the GRL-0617 binding site was remodelled according to the SCoV-PLpro X-ray crystal structure of the complex (PDB ID: 3E9S)¹⁸ using MODELLER. The GRL-0617 ligand was parameterized with the general amber force field (GAFF)⁵².

SCoV2-PLpro with mouse ISG15

The X-ray crystal structure of the SCoV2-PLpro–mouse ISG15 complex (PDB ID: 6YVA) served as starting point. Missing residues of SCoV2-PLpro and one Zn ion were modelled according to the X-ray crystal structure (PDB ID: 6W9C, re-refined by T. Croll).

Missing side chains in all setups were modelled using MODELLER. All crystallographic water molecules and ions were retained, except a nickel ion in PDB ID: 5E6J. According to pK_a calculations using Prop K_a and additional visual inspections, in all setups His17 of SCoV2-PLpro (His18 of SCoV-PLpro) and His272 of SCoV2-PLpro (His273 of SCoV-PLpro) were charged. We cannot exclude that the protonation state of the catalytic His272 of SCoV2-PLpro (His273 of SCoV-PLpro) is in equilibrium between charged and neutral forms. All other residues were simulated in their physiological protonation state. The proteins were solvated in TIP4P-D water⁵³ with 150 mM NaCl. Molecular dynamics simulations were carried out using Gromacs 2018⁵⁴ and the AMBER99SB*-ILDN-q force field^{55,56,57,58}. Each system was energy minimized, followed by five equilibration steps, in which we gradually weakened the position restraints on heavy atoms, first in an NVT ensemble (0.25 ns) and then in an NPT ensemble (4×0.5 ns) using a Berendsen thermostat and barostat⁵⁹. Production simulations were run at a temperature of 310 K and a pressure of 1 bar in an NPT ensemble using a Nosé–Hoover thermostat^{60,61} and a Parrinello-Rahman barostat⁶². We set up three independent runs of the SCoV2-PLpro systems with bound substrates, starting from different MODELLER results for the apo-like model of SCoV2-PLpro:K48-Ub₂ and for the SCoV2-PLpro–mouse ISG15 complex. For simulations with bound substrates and with bound inhibitor, we monitored the root-mean-square deviation (r.m.s.d.) of each backbone substrate (distal ubiquitin in K48-Ub₂ and N-terminal domain of mouse ISG15) and of GRL-0617 (heavy atoms) to the respective equilibrated structure after alignment on the helix backbone of PLpro (without the flexible UBL domain). From simulations of SCoV-PLpro–K48-Ub₂, we extracted the minimum heavy-atom distance between F70 of SARS and I44 of ubiquitin.

Inhibitor IC₅₀ determination

For IC₅₀ value for inhibitors, ubiquitin–AMC or ISG15–AMC was used as substrate of PLpro and the release of AMC was measured by increase of fluorescence (excitation/emission, 360/487 nm) on a 384-well microplate reader (PHERAstar FSX, BMG Labtech). Five microlitres of solution containing different concentrations of GRL-0617 (200–0 µM) and 10 µM of ubiquitin–AMC or ISG15–AMC were aliquoted into 384 well plate and reaction was initiated by addition of 5 µl of PLpro (30 nM) to the well. Initial velocities of AMC release were normalized against DMSO control. The IC₅₀ value was calculated by the dose–response–inhibition function in Graphpad Prism with [inhibitor] vs normalized response equation. The experiment was repeated three times.

Mass-spectrometry

For interactome analysis, A549 cells were transfected with wild-type or mutant (C111S) SCoV-PLpro or SCoV2-PLpro, and for comparison between SARS-CoV and SARS-CoV-2, PLpro(C111S) versions of both proteins were transfected. Cells were stimulated with IFN-α (200 U ml⁻¹) for 36 h to mimic an infection scenario. Cells were lysed in ice cold lysis buffer (50 mM Tris-Cl, pH 7.5; 150 mM NaCl; 1% Triton X-100) and equal amounts of lysates were incubated with GFP nanotrap beads in IP buffer (Lysis buffer without detergent). After incubation, immunoprecipitates were washed three times with wash buffer (50 mM Tris-HCl, pH7.5; 400 mM NaCl; 0.5 mM EDTA) and two times with IP buffer. Then, beads were incubated with 25 µl of 50 mM Tris-HCl (pH 8.5) containing 4 M urea, 1 mM TCEP, 4 mM chloroacetamide for 1 h in the dark at 37 °C. Afterwards, samples were diluted with 50 mM Tris-HCl pH 8.5 to a final urea concentration <2 M and digested with 0.5 µg trypsin (Promega) at 37 °C overnight. Digests were acidified using trifluoroacetic acid to a pH of 2–3 and peptides were desalted using C18-stage tips⁶³. Peptides were labelled with tandem mass tag (TMT) reagents (Thermo fisher) as described previously⁶⁴. In brief, peptides were resuspended in TMT labelling buffer (0.2 M EPPS pH 8.2, 20% acetonitrile) and were mixed with TMT reagents in a 2:1 TMT: peptide ratio. Reaction was performed for one hour at room

temperature and subsequently quenched by addition of hydroxylamine to a final concentration of 0.5% at room temperature for 15 min. Samples were pooled in equimolar ratio, acidified and again cleaned-up using C18-stage tips. After drying, peptides were resuspended in 0.1% formic acid for liquid chromatography–mass spectrometry. All mass spectrometry data was acquired in centroid mode on an Orbitrap Fusion Lumos mass spectrometer hyphenated to an easy-nLC 1200 nano HPLC system with a nanoFlex ion source (ThermoFisher Scientific). A spray voltage of 2.6 kV was applied with the transfer tube heated to 300 °C and funnel RF set to 30%. Internal mass calibration was enabled (lock mass 445.12003 *m/z*). Peptides were separated on a self-made 32 cm long, 75 µm internal diameter fused-silica column, packed in house with 1.9 µm C18 particles (ReproSil-Pur, Dr. Maisch) and heated to 50 °C using an integrated column oven (Sonation). HPLC solvents consisted of 0.1% formic acid in water (buffer A) and 0.1% formic acid, 80% acetonitrile in water (buffer B). Peptides were eluted by a nonlinear gradient from 7 to 40% buffer B over 90 min followed by a step-wise increase to 95% buffer B in 6 min which was held for another 9 min. Full scan mass spectra (350–1400 *m/z*) were acquired with a resolution of 120,000 at *m/z* 200, maximum injection time of 100 ms and AGC target value of 4×10^5 . The 20 most intense precursors per full scan with a charge state between 2 and 5 were selected for fragmentation ('Top 20'), isolated with a quadrupole isolation window of 0.7 Th and fragmented via higher-energy collisional dissociation applying a normalized collision energy of 38%. MS2 scans were performed in the Orbitrap using a resolution of 50,000 at *m/z* 200, maximum injection time of 86 ms and automatic gain control target value of 1×10^5 . Repeated sequencing of already acquired precursors was limited by setting a dynamic exclusion of 60 s and 7 ppm and advanced peak determination was deactivated. Raw mass spectrometry data were analysed with Proteome Discoverer (v.2.4, ThermoFisher Scientific) using Sequest HT as a search engine and performing re-calibration of precursor masses by the Spectrum RC-node. Fragment spectra were searched against the human reference proteome ('one sequence per gene', 20,531 sequences, version March 2020) and protein sequences for SARS (15 sequences, version March 2020) and CoV2 (14 sequences, version February 2020) downloaded from Uniprot in March 2020, as well as common contaminants as included in 'contaminants.fasta' provided with the MaxQuant software. Static modifications were TMT at

the peptide N terminus and lysines as well as carbamidomethyl at cysteine residues, dynamic modifications were set as oxidation of methionine and acetylation at the protein N-terminus. Matched spectra were filtered with Percolator, applying a false discovery rate of 1% on peptide spectrum match and protein level. Reporter intensities were normalized to the total protein intensities in Proteome Discoverer, assuming equal sample loading and additionally by median normalization using the NormalizerDE package⁶⁵. Statistically significant changes between samples were determined in Perseus (v.1.6.6.0) and significant candidates were chosen having *p*-value ≤ 0.01 and \log_2 (fold change) value minimum of ± 0.5 (ref. ⁶⁶).

Cell culture

Human CaCo-2 cells were obtained from the Deutsche Sammlung von Mikroorganismen und Zellkulturen. Cells were grown at 37 °C in Minimal Essential Medium (MEM) supplemented with 10% fetal bovine serum (FBS) and containing 100 IU ml⁻¹ penicillin and 100 µg ml⁻¹ streptomycin. A549 and HeLa cells were obtained from ATCC (ATCC CCL-185 and ATCC CCL-2, respectively). All cell lines used tested negative for mycoplasma.

Antibodies

We used the following antibodies and dilutions for this study: ubiquitin (catalogue (cat.) no. 3936S, Cell Signaling Technology; 1:20:00), ISG15 (cat. no. HPA004627, Sigma Aldrich/Merck; 1:1,000), GAPDH (cat. no. 2118, Cell Signaling Technology; 1:2,000), GFP trap beads (cat no. gta-100, ChromoTek), GFP (cat. no. sc-9996, Santa Cruz Biotechnology; 1:2,000), IRF3 (cat. no. 4302, Cell Signaling Technology; 1:2,000), phospho-IRF3(Ser396) (cat. no. 4947, Cell Signaling Technology; 1:1,000), IκBα (cat. no. 4812, Cell Signaling Technology; 1:2,000), phospho-IκBα(Ser32/36) (cat. no. 9246, Cell Signaling Technology; 1:1,000), TBK1 (cat. no. 3013, Cell Signaling Technology; 1:2,000), pTBK1 (cat. no. 3300-1 Epitomics; 1:1,000), NF-κB p65 (cat. no. 8008, Santa Cruz Biotechnology; 1:2,000), lamin B1 (cat. no. sc-373918, Santa Cruz Biotechnology; 1:2,000).

Virus preparation

SARS-CoV-2 strain FFM1 (accession no. MT358638)⁶⁷ was isolated from travellers returning from Wuhan (China) to Frankfurt (Germany) using CaCo-2 cells. SARS-CoV-2 FFM1 stocks used in the experiments had undergone one passage on CaCo-2 cells, as described previously²⁵. Virus titres were determined as TCID₅₀ per ml in confluent cells in 96-well microtitre plates.

Antiviral and cytotoxicity assays

Confluent layers of CaCo-2 cells in 96-well plates were infected with SARS-CoV-2 FFM1 at a MOI of 0.01. Virus was added simultaneously with GRL-0617 and incubated in MEM supplemented with 1% FBS with different drug dilutions. CPE was assessed visually 48 h after infection. To assess effects of GRL-0617 on CaCo-2 cell viability, confluent cell layers were treated with different drug concentration. Cell viability was determined by MTT assay, modified after Mosman⁶⁸, as previously described⁶⁹. Data for each condition were collected for at least three biological replicates.

Luciferase activity assay

To analyse the induction of IFN- β induced genes, a luciferase reporter assay was used in A549 cells. In brief, an expression construct containing the luciferase ORF and the IFN- β promoter (IFN- β -luciferase) was co-transfected with either a GFP control plasmid or the designated PLpro plasmid. For all transfections, 100 ng of luciferase plasmid, 400 ng of PLpro or GFP vector was used in each well of a 12-well plate All transfections were performed in triplicate and the average of three experiments is shown in figures. Twenty-four hours after transfection, cells were treated with 500 ng poly(I:C) for 18 h or 50 ng ml⁻¹ of TNF for 30 min. Luciferase expression was measured using the Luciferase Reporter Assay System (Promega). Fold change was calculated by taking vector treated with poly(I:C) or TNF as 1.

Immunofluorescence and confocal imaging

HeLa cells expressing GFP-tagged PLpro was treated with TNF (50 ng ml^{-1}) for 45 min. Cells were fixed with paraformaldehyde, blocked in 5% serum and immunostained overnight at 4°C with antibody against p65. Confocal imaging was performed using the Zeiss LSM780 microscope system. An Ar ion laser (for excitation of GFP at 488 nm), a He-Ne laser (for excitation of Alexa Fluor 546 nm) were used with a $63\times 1.4 \text{ NA}$ oil-immersion objective. Images were analysed in FIJI to determine colocalization between DAPI and immunostained p65. Results are indicative of 50 cells taken from 3 independent experiments; error bars indicate standard deviation.

Nuclear fractionation

A549 cells from a confluent 60-mm dish were transiently transfected with GFP-tagged PLPro followed by treatment with IFN- α (200 ml^{-1} , 36 h). Cells were lysed in hypotonic buffer (10 mM HEPES (pH 7.4), 2 mM MgCl₂, 25 mM KCl, 1 mM DTT, 1 mM PMSF, and protease inhibitor cocktail), kept on ice for 30 min followed by syringe lysis, and 2 M sucrose solution was added dropwise, followed by centrifugation at 1,000*g* for 15 min. The supernatant was saved as the cytosolic fraction. The pellet was washed twice in wash buffer (10 mM HEPES (pH 7.4), 2 mM MgCl₂, 25 mM KCl, 250 mM sucrose, 1 mM DTT, 1 mM PMSF, and protease inhibitor cocktail) and saved as the nuclear fraction.

Quantification of viral and cellular RNA

SARS-CoV-2 RNA from cell culture supernatant samples was isolated using ACL buffer and the QIAamp 96 Virus kit (Qiagen) according to the manufacturer's instructions. RNA was subjected to OneStep quantitative PCR with reverse transcription (RT-qPCR) analysis using the LightCycler Multiplex RNA Virus Master kit (Roche). Intracellular RNA was isolated using RLT buffer and the RNeasy 96 HT Kit according to the manufacturer's instructions. PCR was performed on a CFX96 Real-Time System, C1000 Touch Thermal Cycler. Primers and probe were adapted

from the WHO protocol⁷⁰ targeting the open reading frame of RNA-dependent RNA polymerase (*RdRP*) of both SARS-CoV-2: RdRP_SARSr-F2 (GTGARATGGTCATGTGTGGCGG) and RdRP_SARSr-R1 (CARATGTTAAASACACTATTAGCATA) primers were used at a final concentration of 0.4 μM and RdRP_SARSr_P2 probe (6-Fam CAGGTGGAACCTCATCAGGAGATGC BBQ1) was used at 0.2 μM. Primers for *ACTB* (fwd: CATCGAGCACGGCATCGTCA; rev: TAGCACAGCCTGGATAGCAAC)⁷¹, *ISG15* (fwd: GAGAGGCAGCGAACTCATCT; rev: AGGGACACCTGGAATTGTT)⁷² *IL6* (fwd: GCAGAAAAAAGGCAAAGAAC; rev: CTACATTGCCGAAGAGC), *IL8* (fwd: GTTTTGAAAGAGGGCTGAG; rev: TTTGCTTGAAGTTCACTGG) and 18S rRNA (fwd: AGAAACGGCTACCACATCCA ; rev: CACCAGACTTGCCTCCA) were used for SYBR green-based detection of cellular genes in a final concentration of 0.4 μM per reaction. For each condition, three biological replicates were used. Mean and s.d. were calculated for each group. For interferon-responsive genes, the following primers were used. *MX1* (fwd: TTTCAAGAAGGAGGCCAGCAA; rev: TCAGGAACCTCCGCTTGTG), *OAS1* (fwd: TGGCCTTCTATGCCCTCTATCC; rev: TCCCATCAGGTGCACAGAAGA) and *PKR* (fwd: GGAACTTGCGATACATGAGCC; rev: CGTCCCGTAGGTCAGTGAAAAA). SARS-CoV-2 subgenomic RNA4 encoding E gene, which is processed during discontinuous transcription in productively infected cells⁷³, was quantified using primer pairs (fwd: AACGTACCTGTCTCTCCGA; rev: CCAACCAACTTCGATCTCTTGT) spanning a junction of the SARS-CoV-2 subgenomic RNAs and used as a measure of viral activity.

Reporting summary

Further information on research design is available in the [Nature Research Reporting Summary](#) linked to this paper.

Data availability

The atomic coordinates of PLpro–mouse ISG15 have been deposited in the PDB with accession code [6YVA](#). The mass spectrometry data have been deposited to the ProteomeXchange Consortium⁷⁴ via the PRIDE partner repository⁷⁵ with the data set identifier [PXD018983](#). The papain-like protease domain sequence was obtained from the SARS-CoV-2 complete genome (NCBI nucleotide, severe acute respiratory syndrome coronavirus 2 isolate Wuhan-Hu-1, complete genome; [NC_045512](#)). Protein sequence for SCoV2-PLpro Ubl domain (amino acids, 746–1060) of Nsp3 protein from SARS-CoV-2 (Nsp3; YP_009725299.1). Full gel images are shown in Supplementary Fig. 1. Any other relevant data are available from the corresponding authors upon reasonable request. [Source data](#) are provided with this paper.

References

1. 1.

Harcourt, B. H. et al. Identification of severe acute respiratory syndrome coronavirus replicase products and characterization of papain-like protease activity. *J. Virol.* **78**, 13600–13612 (2004).

[CAS](#) [PubMed](#) [PubMed Central](#) [Google Scholar](#)

2. 2.

Lim, K. P., Ng, L. F. P. & Liu, D. X. Identification of a novel cleavage activity of the first papain-like proteinase domain encoded by open reading frame 1a of the coronavirus Avian infectious bronchitis virus and characterization of the cleavage products. *J. Virol.* **74**, 1674–1685 (2000).

[CAS](#) [PubMed](#) [PubMed Central](#) [Google Scholar](#)

3. 3.

Frieman, M., Ratia, K., Johnston, R. E., Mesecar, A. D. & Baric, R. S. Severe acute respiratory syndrome coronavirus papain-like protease

ubiquitin-like domain and catalytic domain regulate antagonism of IRF3 and NF-κB signaling. *J. Virol.* **83**, 6689–6705 (2009).

[CAS](#) [PubMed](#) [PubMed Central](#) [Google Scholar](#)

4. 4.

Devaraj, S. G. et al. Regulation of IRF-3-dependent innate immunity by the papain-like protease domain of the severe acute respiratory syndrome coronavirus. *J. Biol. Chem.* **282**, 32208–32221 (2007).

[CAS](#) [PubMed](#) [PubMed Central](#) [Google Scholar](#)

5. 5.

Bailey-Elkin, B. A. et al. Crystal structure of the Middle East respiratory syndrome coronavirus (MERS-CoV) papain-like protease bound to ubiquitin facilitates targeted disruption of deubiquitinating activity to demonstrate its role in innate immune suppression. *J. Biol. Chem.* **289**, 34667–34682 (2014).

[PubMed](#) [PubMed Central](#) [Google Scholar](#)

6. 6.

Huang, C. et al. Clinical features of patients infected with 2019 novel coronavirus in Wuhan, China. *Lancet* **395**, 497–506 (2020).

[CAS](#) [PubMed](#) [PubMed Central](#) [Google Scholar](#)

7. 7.

Lu, R. et al. Genomic characterisation and epidemiology of 2019 novel coronavirus: implications for virus origins and receptor binding. *Lancet* **395**, 565–574 (2020).

[CAS](#) [PubMed](#) [PubMed Central](#) [Google Scholar](#)

8. 8.

Zhou, P. et al. A pneumonia outbreak associated with a new coronavirus of probable bat origin. *Nature* **579**, 270–273 (2020).

[ADS](#) [CAS](#) [PubMed](#) [PubMed Central](#) [Google Scholar](#)

9. 9.

Sommer, S., Weikart, N. D., Linne, U. & Mootz, H. D. Covalent inhibition of SUMO and ubiquitin-specific cysteine proteases by an in situ thiol-alkyne addition. *Bioorg. Med. Chem.* **21**, 2511–2517 (2013).

[CAS](#) [PubMed](#) [Google Scholar](#)

10. 10.

Ekkebus, R. et al. On terminal alkynes that can react with active-site cysteine nucleophiles in proteases. *J. Am. Chem. Soc.* **135**, 2867–2870 (2013).

[CAS](#) [PubMed](#) [PubMed Central](#) [Google Scholar](#)

11. 11.

Flierman, D. et al. Non-hydrolyzable diubiquitin probes reveal linkage-specific reactivity of deubiquitylating enzymes mediated by S2 pockets. *Cell Chem. Biol.* **23**, 472–482 (2016).

[CAS](#) [Google Scholar](#)

12. 12.

Basters, A. et al. Structural basis of the specificity of USP18 toward ISG15. *Nat. Struct. Mol. Biol.* **24**, 270–278 (2017).

[CAS](#) [PubMed](#) [PubMed Central](#) [Google Scholar](#)

13. 13.

Geurink, P. P. et al. Profiling DUBs and Ubl-specific proteases with activity-based probes. *Methods Enzymol.* **618**, 357–387 (2019).

[CAS](#) [PubMed](#) [PubMed Central](#) [Google Scholar](#)

14. 14.

Freitas, B. T. et al. Characterization and noncovalent inhibition of the deubiquitinase and deISGylase activity of SARS-CoV-2 papain-like protease. *ACS Infect. Dis.* **6**, 2009–2109 (2020).

[Google Scholar](#)

15. 15.

Basters, A. et al. Molecular characterization of ubiquitin-specific protease 18 reveals substrate specificity for interferon-stimulated gene 15. *FEBS J.* **281**, 1918–1928 (2014).

[CAS](#) [PubMed](#) [Google Scholar](#)

16. 16.

Clasman, J. R., Everett, R. K., Srinivasan, K. & Mesecar, A. D. Decoupling deISGylating and deubiquitinating activities of the MERS virus papain-like protease. *Antiviral Res.* **174**, 104661 (2020).

[CAS](#) [PubMed](#) [Google Scholar](#)

17. 17.

Daczkowski, C. M. et al. Structural insights into the interaction of coronavirus papain-like proteases and interferon-stimulated gene product 15 from different species. *J. Mol. Biol.* **429**, 1661–1683 (2017).

[CAS](#) [PubMed](#) [PubMed Central](#) [Google Scholar](#)

18. 18.

Ratia, K. et al. A noncovalent class of papain-like protease/deubiquitinase inhibitors blocks SARS virus replication. *Proc. Natl Acad. Sci. USA* **105**, 16119–16124 (2008).

[ADS](#) [CAS](#) [PubMed](#) [Google Scholar](#)

19. 19.

Báez-Santos, Y. M. et al. X-ray structural and biological evaluation of a series of potent and highly selective inhibitors of human coronavirus papain-like proteases. *J. Med. Chem.* **57**, 2393–2412 (2014).

[PubMed](#) [PubMed Central](#) [Google Scholar](#)

20. 20.

Ghosh, A. K. et al. Severe acute respiratory syndrome coronavirus papain-like novel protease inhibitors: design, synthesis, protein-ligand X-ray structure and biological evaluation. *J. Med. Chem.* **53**, 4968–4979 (2010).

[CAS](#) [PubMed](#) [PubMed Central](#) [Google Scholar](#)

21. 21.

Ghosh, A. K. et al. Structure-based design, synthesis, and biological evaluation of a series of novel and reversible inhibitors for the severe acute respiratory syndrome-coronavirus papain-like protease. *J. Med. Chem.* **52**, 5228–5240 (2009).

[CAS](#) [PubMed](#) [PubMed Central](#) [Google Scholar](#)

22. 22.

Kilianski, A. & Baker, S. C. Cell-based antiviral screening against coronaviruses: developing virus-specific and broad-spectrum inhibitors. *Antiviral Res.* **101**, 105–112 (2014).

[CAS](#) [PubMed](#) [Google Scholar](#)

23. 23.

Gordon, D. E. et al. A SARS-CoV-2 protein interaction map reveals targets for drug repurposing. *Nature* **583**, 459–468 (2020).

[ADS](#) [CAS](#) [PubMed](#) [PubMed Central](#) [Google Scholar](#)

24. 24.

Ferguson, B. J., Mansur, D. S., Peters, N. E., Ren, H. & Smith, G. L. DNA-PK is a DNA sensor for IRF-3-dependent innate immunity. *eLife* **1**, e00047 (2012).

[PubMed](#) [PubMed Central](#) [Google Scholar](#)

25. 25.

Bojkova, D. et al. Proteomics of SARS-CoV-2-infected host cells reveals therapy targets. *Nature* **583**, 469–472 (2020).

[ADS](#) [CAS](#) [PubMed](#) [Google Scholar](#)

26. 26.

Ouellet, M. et al. Galectin-1 acts as a soluble host factor that promotes HIV-1 infectivity through stabilization of virus attachment to host cells. *J. Immunol.* **174**, 4120–4126 (2005).

[CAS](#) [PubMed](#) [Google Scholar](#)

27. 27.

Schick, C. et al. Cross-class inhibition of the cysteine proteinases cathepsins K, L, and S by the serpin squamous cell carcinoma antigen 1: a kinetic analysis. *Biochemistry* **37**, 5258–5266 (1998).

[CAS](#) [PubMed](#) [Google Scholar](#)

28. 28.

Takeda, A., Yamamoto, T., Nakamura, Y., Takahashi, T. & Hibino, T. Squamous cell carcinoma antigen is a potent inhibitor of cysteine proteinase cathepsin L. *FEBS Lett.* **359**, 78–80 (1995).

[CAS](#) [PubMed](#) [Google Scholar](#)

29. 29.

Stetson, D. B. & Medzhitov, R. Type I interferons in host defense. *Immunity* **25**, 373–381 (2006).

[CAS](#) [PubMed](#) [Google Scholar](#)

30. 30.

Liu, T., Zhang, L., Joo, D. & Sun, S.-C. NF-κB signaling in inflammation. *Signal Transduct. Target. Ther.* **2**, 17023 (2017).

[PubMed](#) [PubMed Central](#) [Google Scholar](#)

31. 31.

Sheikh, F., Dickensheets, H., Gamero, A. M., Vogel, S. N. & Donnelly, R. P. An essential role for IFN- β in the induction of IFN-stimulated gene expression by LPS in macrophages. *J. Leukoc. Biol.* **96**, 591–600 (2014).

[PubMed](#) [PubMed Central](#) [Google Scholar](#)

32. 32.

Shi, H.-X. et al. Positive regulation of interferon regulatory factor 3 activation by Herc5 via ISG15 modification. *Mol. Cell. Biol.* **30**, 2424–2436 (2010).

[CAS](#) [PubMed](#) [PubMed Central](#) [Google Scholar](#)

33. 33.

Blanco-Melo, D. et al. Imbalanced host response to SARS-CoV-2 drives development of COVID-19. *Cell* **181**, 1036–1045 (2020).

[CAS](#) [PubMed](#) [PubMed Central](#) [Google Scholar](#)

34. 34.

Niemeyer, D. et al. The papain-like protease determines a virulence trait that varies among members of the SARS-coronavirus species. *PLoS Pathog.* **14**, e1007296 (2018).

[PubMed](#) [PubMed Central](#) [Google Scholar](#)

35. 35.

Anson, B. J. et al. Broad-spectrum inhibition of coronavirus main and papain-like 2 proteases by HCV drugs. Preprint at <https://doi.org/10.21203/rs.3.rs-26344/v1> (2020).

36. 36.

Shanker, A. K., Bhanu, D., Alluri, A. & Gupta, S. Whole-genome sequence analysis and homology modelling of the main protease and non-structural protein 3 of SARS-CoV-2 reveal an aza-peptide and a lead inhibitor with possible antiviral properties. *New J. Chem.* **44**, 9202–9212 (2020).

[CAS](#) [Google Scholar](#)

37. 37.

Rut, W. et al. Activity profiling and structures of inhibitor-bound SARS-CoV-2-PLpro protease provides a framework for anti-COVID-19 drug design. Preprint at *bioRxiv* <https://doi.org/10.1101/2020.04.29.068890> (2020).

38. 38.

Zhang, L. et al. Crystal structure of SARS-CoV-2 main protease provides a basis for design of improved α -ketoamide inhibitors. *Science* **368**, 409–412 (2020).

[ADS](#) [CAS](#) [PubMed](#) [PubMed Central](#) [Google Scholar](#)

39. 39.

Jin, Z. et al. Structure of Mpro from COVID-19 virus and discovery of its inhibitors. *Nature* **582**, 289–293 (2020).

[ADS](#) [CAS](#) [PubMed](#) [Google Scholar](#)

40. 40.

Dai, W. et al. Structure-based design of antiviral drug candidates targeting the SARS-CoV-2 main protease. *Science* **368**, 1331–1335 (2020).

[ADS](#) [CAS](#) [PubMed](#) [Google Scholar](#)

41. 41.

Lo, H. S. et al. Simeprevir suppresses SARS-CoV-2 replication and synergizes with remdesivir. Preprint at *bioRxiv* <https://doi.org/10.1101/2020.05.26.116020> (2020).

42. 42.

Daczkowski, C. M., Goodwin, O. Y., Dzimianski, J. V., Farhat, J. J. & Pegan, S. D. Structurally guided removal of DeISGylase biochemical activity from papain-like protease originating from Middle East respiratory syndrome coronavirus. *J. Virol.* **91**, e01067-17 (2017).

[CAS](#) [PubMed](#) [PubMed Central](#) [Google Scholar](#)

43. 43.

Kabsch, W. XDS. *Acta Crystallogr. D* **66**, 125–132 (2010).

[CAS](#) [PubMed](#) [Google Scholar](#)

44. 44.

McCoy, A. J. et al. Phaser crystallographic software. *J. Appl. Cryst.* **40**, 658–674 (2007).

[CAS](#) [Google Scholar](#)

45. 45.

Afonine, P. V. et al. Towards automated crystallographic structure refinement with phenix.refine. *Acta Crystallogr. D* **68**, 352–367 (2012).

[CAS](#) [PubMed](#) [Google Scholar](#)

46. 46.

Emsley, P., Lohkamp, B., Scott, W. G. & Cowtan, K. Features and development of Coot. *Acta Crystallogr. D* **66**, 486–501 (2010).

[CAS](#) [Google Scholar](#)

47. 47.

Baek, K. et al. NEDD8 nucleates a multivalent cullin-RING–UBE2D ubiquitin ligation assembly. *Nature* **578**, 461–466 (2020).

[ADS](#) [CAS](#) [PubMed](#) [PubMed Central](#) [Google Scholar](#)

48. 48.

Enchev, R. I. et al. Structural basis for a reciprocal regulation between SCF and CSN. *Cell Rep.* **2**, 616–627 (2012).

[CAS](#) [PubMed](#) [PubMed Central](#) [Google Scholar](#)

49. 49.

Békés, M. et al. Recognition of Lys48-linked di-ubiquitin and deubiquitinating activities of the SARS coronavirus papain-like protease. *Mol. Cell* **62**, 572–585 (2016).

[PubMed](#) [PubMed Central](#) [Google Scholar](#)

50. 50.

Šali, A. & Blundell, T. L. Comparative protein modelling by satisfaction of spatial restraints. *J. Mol. Biol.* **234**, 779–815 (1993).

[PubMed](#) [Google Scholar](#)

51. 51.

Schrödinger, L. *The PyMol Molecular Graphics System*, version 1.8. (2015)

52. 52.

Wang, J., Wolf, R. M., Caldwell, J. W., Kollman, P. A. & Case, D. A. Development and testing of a general amber force field. *J. Comput. Chem.* **25**, 1157–1174 (2004).

[CAS](#) [PubMed](#) [Google Scholar](#)

53. 53.

Piana, S., Donchev, A. G., Robustelli, P. & Shaw, D. E. Water dispersion interactions strongly influence simulated structural properties of disordered protein states. *J. Phys. Chem. B* **119**, 5113–5123 (2015).

[CAS](#) [PubMed](#) [Google Scholar](#)

54. 54.

Abraham, M. J. et al. GROMACS: High performance molecular simulations through multi-level parallelism from laptops to

supercomputers. *SoftwareX* **1–2**, 19–25 (2015).

[ADS](#) [Google Scholar](#)

55. 55.

Hornak, V. et al. Comparison of multiple Amber force fields and development of improved protein backbone parameters. *Proteins* **65**, 712–725 (2006).

[CAS](#) [PubMed](#) [PubMed Central](#) [Google Scholar](#)

56. 56.

Best, R. B., de Sancho, D. & Mittal, J. Residue-specific α -helix propensities from molecular simulation. *Biophys. J.* **102**, 1462–1467 (2012).

[ADS](#) [CAS](#) [PubMed](#) [PubMed Central](#) [Google Scholar](#)

57. 57.

Best, R. B. & Hummer, G. Optimized molecular dynamics force fields applied to the helix-coil transition of polypeptides. *J. Phys. Chem. B* **113**, 9004–9015 (2009).

[CAS](#) [PubMed](#) [PubMed Central](#) [Google Scholar](#)

58. 58.

Lindorff-Larsen, K. et al. Improved side-chain torsion potentials for the Amber ff99SB protein force field. *Proteins* **78**, 1950–1958 (2010).

[CAS](#) [PubMed](#) [PubMed Central](#) [Google Scholar](#)

59. 59.

Berendsen, H. J. C., Postma, J. P. M., van Gunsteren, W. F., DiNola, A. & Haak, J. R. Molecular dynamics with coupling to an external bath. *J.*

Chem. Phys. **81**, 3684–3690 (1984).

[ADS](#) [CAS](#) [Google Scholar](#)

60. 60.

Evans, D. J. & Holian, B. L. The Nose–Hoover thermostat. *J. Chem. Phys.* **83**, 4069–4074 (1985).

[ADS](#) [CAS](#) [Google Scholar](#)

61. 61.

Nosé, S. A unified formulation of the constant temperature molecular dynamics methods. *J. Chem. Phys.* **81**, 511–519 (1984).

[ADS](#) [Google Scholar](#)

62. 62.

Parrinello, M. & Rahman, A. Polymorphic transitions in single crystals: a new molecular dynamics method. *J. Appl. Phys.* **52**, 7182–7190 (1981).

[ADS](#) [CAS](#) [Google Scholar](#)

63. 63.

Rappaport, J., Ishihama, Y. & Mann, M. Stop and go extraction tips for matrix-assisted laser desorption/ionization, nanoelectrospray, and LC/MS sample pretreatment in proteomics. *Anal. Chem.* **75**, 663–670 (2003).

[CAS](#) [PubMed](#) [Google Scholar](#)

64. 64.

Klann, K., Tascher, G. & Münch, C. Functional translatome proteomics reveal converging and dose-dependent regulation by

mTORC1 and eIF2 α . *Mol. Cell* **77**, 913–925 (2020).

[CAS](#) [PubMed](#) [PubMed Central](#) [Google Scholar](#)

65. 65.

Willforss, J., Chawade, A. & Levander, F. NormalizerDE: online tool for improved normalization of omics expression data and high-sensitivity differential expression analysis. *J. Proteome Res.* **18**, 732–740 (2019).

[CAS](#) [PubMed](#) [Google Scholar](#)

66. 66.

Tyanova, S. et al. The Perseus computational platform for comprehensive analysis of (prote)omics data. *Nat. Methods* **13**, 731–740 (2016).

[CAS](#) [PubMed](#) [Google Scholar](#)

67. 67.

Toptan, T. et al. Optimized qRT-PCR approach for the detection of intra- and extracellular SARS-CoV-2 RNAs. *Int. J. Mol. Sci.* **21**, 4396 (2020).

[CAS](#) [PubMed Central](#) [Google Scholar](#)

68. 68.

Mosmann, T. Rapid colorimetric assay for cellular growth and survival: application to proliferation and cytotoxicity assays. *J. Immunol. Methods* **65**, 55–63 (1983).

[CAS](#) [PubMed](#) [Google Scholar](#)

69. 69.

Onafuye, H. et al. Doxorubicin-loaded human serum albumin nanoparticles overcome transporter-mediated drug resistance in drug-adapted cancer cells. *Beilstein J. Nanotechnol.* **10**, 1707–1715 (2019).

[CAS](#) [PubMed](#) [PubMed Central](#) [Google Scholar](#)

70. 70.

Corman, V. M. et al. Detection of 2019 novel coronavirus (2019-nCoV) by real-time RT-PCR. *Euro Surveill.* **25**, 2000045 (2020).

[PubMed Central](#) [Google Scholar](#)

71. 71.

Zhang, X., Ding, L. & Sandford, A. J. Selection of reference genes for gene expression studies in human neutrophils by real-time PCR. *BMC Mol. Biol.* **6**, 4 (2005).

[PubMed](#) [PubMed Central](#) [Google Scholar](#)

72. 72.

Moll, H. P., Maier, T., Zommer, A., Lavoie, T. & Brostjan, C. The differential activity of interferon- α subtypes is consistent among distinct target genes and cell types. *Cytokine* **53**, 52–59 (2011).

[CAS](#) [PubMed](#) [PubMed Central](#) [Google Scholar](#)

73. 73.

Kim, D. et al. The architecture of SARS-CoV-2 transcriptome. *Cell* **181**, 914–921 (2020).

[CAS](#) [PubMed](#) [PubMed Central](#) [Google Scholar](#)

74. 74.

Vizcaíno, J. A. et al. ProteomeXchange provides globally coordinated proteomics data submission and dissemination. *Nat. Biotechnol.* **32**, 223–226 (2014).

[PubMed](#) [PubMed Central](#) [Google Scholar](#)

75. 75.

Vizcaíno, J. A. et al. 2016 update of the PRIDE database and its related tools. *Nucleic Acids Res.* **44** (D1), D447–D456 (2016).

[PubMed](#) [Google Scholar](#)

[Download references](#)

Acknowledgements

We thank A. Gubas, C. Joazeiro, D. Hoeller and K. Koch for critical comments on the manuscript. We also thank Swiss Light Source (SLS) for providing special beam time for this project during the peak of the COVID-19 pandemic in Switzerland and W. Meitian and O. Vincent for providing on-site support during the data collection. We thank the Quantitative Proteomics Unit (IBCII, Goethe University Frankfurt) for support and expertise in sample preparation, LC–MS instrumentation and data analysis. This work was supported by the DFG-funded Collaborative Research Centre on Selective Autophagy (SFB 1177), by the Max Planck Society, by NWO (H.O. and G.J.v.d.H.v.N.) by the European Research Council (ERC) under the European Union’s Horizon 2020 research and innovation programme (grant agreement no. 789016) to B.A.S., LYSFOR2625 (DFG) to A.B. and (grant agreement no. 742720) to I.D., by the grants from Else Kroener Fresenius Stiftung, Dr. Rolf M. Schwiete Stiftung, and by internal IBC2 funds to I.D.

Author information

Author notes

1. Deceased: Huib Ovaa

Affiliations

1. Institute of Biochemistry II, Faculty of Medicine, Goethe University, Frankfurt, Germany

Donghyuk Shin, Rukmini Mukherjee, Anshu Bhattacharya, Georg Tascher, Stefan Müller & Ivan Dikic

2. Buchmann Institute for Molecular Life Sciences, Goethe University, Frankfurt, Germany

Donghyuk Shin, Rukmini Mukherjee, Diana Grewe, Anshu Bhattacharya & Ivan Dikic

3. Max Planck Institute of Biophysics, Frankfurt, Germany

Donghyuk Shin & Ivan Dikic

4. Institute of Medical Virology, University Hospital Frankfurt, Frankfurt, Germany

Denisa Bojkova, Marek Widera, Alexander Wilhelm, Jindrich Cinatl & Sandra Ciesek

5. Department of Molecular Machines and Signaling, Max Planck Institute of Biochemistry, Martinsried, Germany

Kheewoong Baek & Brenda A. Schulman

6. Department of Theoretical Biophysics, Max Planck Institute of Biophysics, Frankfurt, Germany

Laura Schulz, Ahmad Reza Mehdipour & Gerhard Hummer

7. Oncode Institute and Department of Chemical Immunology, Leiden University Medical Centre, Leiden, The Netherlands

Paul P. Geurink, Gerbrand J. van der Heden van Noort & Huib Ovaar

8. Institute of Pharmaceutical Biology, Goethe-University, Frankfurt, Germany

Alexander Wilhelm & Sandra Ciesek

9. Institute of Neuropathology, Faculty of Medicine, University of Freiburg, Freiburg, Germany

Klaus-Peter Knobeloch

10. Cell Biology Unit, University Medical Center of the Johannes Gutenberg University Mainz, Mainz, Germany

Krishnaraj Rajalingam

11. Institute of Biophysics, Goethe University Frankfurt, Frankfurt, Germany

Gerhard Hummer

12. Fraunhofer Institute for Molecular Biology and Applied Ecology (IME), Branch Translational Medicine and Pharmacology, Frankfurt, Germany

Sandra Ciesek & Ivan Dikic

Authors

1. Donghyuk Shin

[View author publications](#)

You can also search for this author in [PubMed](#) [Google Scholar](#)

2. Rukmini Mukherjee

[View author publications](#)

You can also search for this author in [PubMed](#) [Google Scholar](#)

3. Diana Grawe

[View author publications](#)

You can also search for this author in [PubMed](#) [Google Scholar](#)

4. Denisa Bojkova

[View author publications](#)

You can also search for this author in [PubMed](#) [Google Scholar](#)

5. Kheewoong Baek

[View author publications](#)

You can also search for this author in [PubMed](#) [Google Scholar](#)

6. Anshu Bhattacharya

[View author publications](#)

You can also search for this author in [PubMed](#) [Google Scholar](#)

7. Laura Schulz

[View author publications](#)

You can also search for this author in [PubMed](#) [Google Scholar](#)

8. Marek Widera

[View author publications](#)

You can also search for this author in [PubMed](#) [Google Scholar](#)

9. Ahmad Reza Mehdipour

[View author publications](#)

You can also search for this author in [PubMed](#) [Google Scholar](#)

10. Georg Tascher

[View author publications](#)

You can also search for this author in [PubMed](#) [Google Scholar](#)

11. Paul P. Geurink

[View author publications](#)

You can also search for this author in [PubMed](#) [Google Scholar](#)

12. Alexander Wilhelm

[View author publications](#)

You can also search for this author in [PubMed](#) [Google Scholar](#)

13. Gerbrand J. van der Heden van Noort

[View author publications](#)

You can also search for this author in [PubMed](#) [Google Scholar](#)

14. Huib Ovaa

[View author publications](#)

You can also search for this author in [PubMed](#) [Google Scholar](#)

15. Stefan Müller

[View author publications](#)

You can also search for this author in [PubMed](#) [Google Scholar](#)

16. Klaus-Peter Knobeloch

[View author publications](#)

You can also search for this author in [PubMed](#) [Google Scholar](#)

17. Krishnaraj Rajalingam

[View author publications](#)

You can also search for this author in [PubMed](#) [Google Scholar](#)

18. Brenda A. Schulman

[View author publications](#)

You can also search for this author in [PubMed](#) [Google Scholar](#)

19. Jindrich Cinatl

[View author publications](#)

You can also search for this author in [PubMed](#) [Google Scholar](#)

20. Gerhard Hummer

[View author publications](#)

You can also search for this author in [PubMed](#) [Google Scholar](#)

21. Sandra Ciesek

[View author publications](#)

You can also search for this author in [PubMed](#) [Google Scholar](#)

22. Ivan Dikic

[View author publications](#)

You can also search for this author in [PubMed](#) [Google Scholar](#)

Contributions

D.S. and I.D. conceived the project. D.S. contributed protein purification, biochemical and biophysical activity assay and structure determination. R.M. performed cell biology experiments. D.G. contributed protein purification. D.B. contributed virus infection experiments, M.W. and A.W. performed RT–qPCR measurements, K.B. performed the deneddylation assay. A.B. and G.T. designed and performed mass spectrometry experiments and analysed data. L.S. and A.R.M. performed molecular dynamics simulations. K.R. contributed to RT–qPCR materials and critical advice. P.P.G. and G.J.v.d.H.v.N. synthesized Ub(l) probes and reagents in the laboratory of H.O. S.M. and K.-P.K. provided Ubl probes and reagents. B.A.S., G.H., J.C., S.C. and I.D. supervised the project. D.S. and I.D. analysed the data and wrote the manuscript with input from all co-authors.

Corresponding author

Correspondence to [Ivan Dikic](#).

Ethics declarations

Competing interests

The authors declare no competing interests.

Additional information

Peer review information *Nature* thanks Rolf Hilgenfeld, Ingrid Wertz and the other, anonymous, reviewer(s) for their contribution to the peer review of this work.

Publisher's note Springer Nature remains neutral with regard to jurisdictional claims in published maps and institutional affiliations.

Extended data figures and tables

Extended Data Fig. 1 Biochemical properties of SCoV2-PLpro.

a, Sequence similarity of PLpro from SARS, MERS and SARS-CoV-2. **b**, IFN- α -treated HeLa cell lysates were incubated with PLpro for indicated time points and analysed by immunoblot **c**, Propargylamide-activity based probes of ubiquitin like modifiers were reacted with (left) SCoV-PLpro (right) PLpro^{CoV2}. **d**, ISG15-Prg were incubated with SCoV-PLpro (left) or SCoV2-PLpro (right) with increasing amount of non-hydrolysable K48-Ub₂. **e**, Initial AMC release rate from ISG15-AMC. Purified SCoV-PLpro and SCoV2-PLpro were incubated with ISG15-AMC and indicated amounts of K48-Ub₂. The release of AMC was measured by increase of fluorescence at (Ex./Em. 360/487 nm). **f**, Purified mUSP18 (left) and SCoV2-PLpro (right) were incubated with ISG15-propargylamide activity-based probes for indicated time points. **g**, Catalytic efficiency (k_{cat}/K_m) of mUSP18 and SCoV2-PLpro on ISG15-AMC cleavage. **h**, Sequence alignment of PLpro cleavage site of Nsp1/2, Nsp2/3, Nsp3/4 from SARS-CoV2 and human ubiquitin like modifiers. **i**, Hyper-NEDDylated CUL1-RBX1 was incubated with purified PLpro proteins for indicated time points

at 37 °C. Reactions were performed side-by-side by with well-characterized deneddylating enzymes (DEN1 with broad specificity or COP9 Signalosome CSN specific for NEDD8 linked directly to a cullin), or the broad specificity deubiquitinating enzyme USP2 as controls. Data in **e, g** are presented as mean ± s.d. ($n = 3$, independent experiments). ** $P < 0.01$, *** $P < 0.001$, **** $P < 0.0001$; two-tailed paired *t*-tests. Experiments in **b–d, f, i** were repeated three times independently with similar results. [Source data](#)

Extended Data Fig. 2 Complex structure of SCoV2-PLpro with mouseISG15.

a, Structural comparison of mouseISG15:SCoV2-PLpro with humanISG15:MERS-PLpro (PDB: 6BI8¹⁶) and sequence alignment of human and mouse ISG15. **b**, Activity test of wild type or catalytically inactive mutant (C111S) of SCoV-PLpro and SCoV2-PLpro. ISG15 Propargyl-activity based probes were mixed with indicated PLpro proteins. Experiments were repeated three times independently with similar results. **c**, Structural comparison of C-terminal domain of ISG15 in complex with SCoV2-PLpro and SCoV-PLpro (PDB: 5TL7¹⁷). **d**, Snapshots from molecular dynamics simulations of SCoV2-PLpro (light pink cartoon) with (left) K48-Ub₂ at 340 ns and (right) mISG15 at 3.2 μs. Key residues in the interface are highlighted. **e**, Backbone r.m.s.d. of the N-terminal domain of mISG15 (green) and of the distal ubiquitin in K48-Ub₂ in an apo-like model (orange, model 1, SCoV2-PLpro coordinates from substrate unbound form, PDB: 6W9C) and in an mISG15-like model (yellow, model 2, SCoV2-PLpro coordinates from substrate bound form, PDB: 6YVA) from their respective SCoV2-PLpro-bound starting structures as function of time. The r.m.s.d. was calculated after superimposing the helix backbone atoms of SCoV2-PLpro. Time points for structural snapshots in **e**) are marked with a cross. **f**, Minimum heavy atom distance between F70 (SARS) and I44(Ub) in wild type and double mutant (S67V/L76T) of SCoV-PLpro:K48-Ub₂ as function of time. **g**, Water mediated dissociation pathway. Left, initial hydrophobic interactions between F69(CoV2), T75(CoV2) and I44(Ub). Middle, water wedges in between T75(CoV2) and I44(Ub). Right, water

penetration between T75(CoV2)/F69 (CoV2) and I44(Ub) leads to dissociation.

Extended Data Fig. 3 Sequence alignment of papain like protease domain from corona viruses.

The amino acid sequences of papain-like protease domain from eight different coronaviruses (SARS-CoV-2, SARS, MERS, humanCoV-OC43, humanCoV-229E, humanCoV-NL63, murine HepatitisV, bovine CoV) were aligned with Clustal Omega. Accession numbers: SARS-CoV-2 (NC_045512), SARS (PDB: 3MJ5), MERS (PDB: 5W8U), hCoV-OC43 (AY585228), hCoV-229E (X69721), hCoV-NL63 (NC_005831), murine HepatitisV (NC_001846), bCoV (NC_003045).

Extended Data Fig. 4 Structural analysis of GRL-0167, SCoV2-PLpro complex.

a, Structural model of GRL-0617 bound SCoV2-PLpro. The conformation of Tyr268 on SCoV2-PLpro and the coordinates of GRL-0617 is obtained from the SCoV-PLpro:GRL-0617 structure (PDB: 3E9S¹⁸) **b**, Snapshots of SCoV-PLpro (light cyan) and SCoV2-PLpro (light pink) with bound GRL-0617 (dark colours) after 1 μs of molecular dynamics simulation. The protein backbones are shown in cartoon representation, and the ligand with contacting residues as sticks. **c**, r.m.s.d. of the GRL-0617 bound to SCoV-PLpro (light blue) and SCoV2-PLpro (light pink) as a function of time. The r.m.s.d. was calculated for non-hydrogen atoms of GRL-0617 with respect to the starting structures in the MD simulations after superimposing the helix backbone atoms of PLpro. **d**, In vitro PLpro inhibition assay. Initial velocity of AMC release from ubiquitin-AMC in different concentration of GRL-0617 was measured and normalized to DMSO control. IC₅₀ value of GRL-0617 to SCoV-PLpro and SCoV2-PLpro were presented. Data are presented as mean ± s.d. (*n* = 3, independent experiments). **e**, In vitro PLpro inhibition assay. Initial velocity of AMC release from ISG15-AMC in different concentration of GRL-0617 was measured and normalized to DMSO control. IC₅₀ value of GRL-0617 to SCoV-PLpro were presented. Data are presented as mean ± s.d. (*n* = 3, independent experiments). **f**,

Effects of GRL-0617 on (left) deISGylase or (right) deubiquitinase activity of PLpro of SARS and SARS-CoV-2. **g**, Effects of GRL-0617 on SCoV-PLpro activity to (left) ubiquitin or (right) K48-Ub₂ propargyl activity-based probes. Inhibitory effect of GRL-0617 on ubiquitin species was tested with various concentration of GRL-0617 (0-400 μM). **h**, Effects of GRL-0617 on SCoV2-PLpro activity to (left) ISG15-C_{term} or (right) ISG15 propargylamide activity-based probes. Inhibitory effect of GRL-0617 on ISG15 was tested with various concentration of GRL-0617 (0-400 μM). Experiments in **f–h** were repeated three times independently with similar results. [Source data](#)

Extended Data Fig. 5 Physiological roles of PLpro in cells.

a, b, Effect of SERPIN B3 on PLpro mediated IFN-β (**a**) or NF-κB p65 (**b**) expression level. A549 Cells were co-transfected with indicated GFP-PLpro and Myc-SERPINs and treated with either poly(I:C) or TNF-α to induce IFN-β and NF-κB p65 expression, respectively. Fold changes of luciferase level are presented. **c**, Effect of PLpro on IFN-induced cellular ISGylation. A549 cells were transfected with indicated PLpro plasmids and treated with IFN-α. Lysates were analysed by immune-blotting with indicated antibodies. **d, e**, Effect of PLpro on IFN-signalling pathway. **d**, A549 cells were transfected with indicated PLpro plasmids and treated with IFN-α. Lysates were analysed by immune-blotting with indicated antibodies. **e**, Effect of PLpro on cellular localization of IRF3. Cells from **d** were fractionated into cytosol and nucleus and the level of IRF3 was analysed. Lamin B1 was used for nuclear fraction control. **f**, Effect of PLpro on the NF-κB pathway. IκB-α phosphorylation and degradation were examined from A549 cells expressing indicated GFP-PLpro under treatment of TNF-α. **g**, in vitro IκBα deubiquitylation assay. Ubiquitinated IκBα were incubated with SCoV-PLpro or SCoV2-PLpro. USP2 were used as positive control. **h**, Effect of PLpro on NF-κB p65 cellular localization. Scale bar, 10 μm. Data in **a, b, h** are presented as mean ± s.d. ($n = 3$, independent experiments). * $P < 0.05$, ** $P < 0.01$; two-tailed paired *t*-tests. Experiments in **c–h** were repeated three times independently with similar results. **e**, Effect of PLpro on the NF-κB pathway. IκB-α phosphorylation and degradation were examined from A549 cells expressing indicated GFP-PLpro under treatment of TNF-α. [Source data](#)

Extended Data Fig. 6 Effect of PLpro on IFN- β or NF- κ B p65 expression level.

a, b, Effect of PLpro on IFN- β (**a**) or NF- κ B p65 (**b**) expression level. A549 Cells were transfected with indicated GFP-PLpro and treated with either poly(I:C) or TNF- α to induce IFN- β and NF- κ B p65 expression, respectively. **c, d**, Effect of GRL-0617 on PLpro mediated IFN- β (**c**) or NF- κ B p65 (**d**) expression level. A549 Cells were transfected with indicated GFP-PLpro and treated with either poly (I:C) or TNF- α to induce IFN- β and NF- κ B p65 expression, respectively. GRL-0617 is treated as indicated. All data are presented as mean \pm s.d. ($n = 3$, independent experiments).

* $P < 0.05$, ** $P < 0.01$, *** $P < 0.001$; two-tailed paired *t*-tests. [Source data](#)

Extended Data Fig. 7 Inhibitory effects of GRL-0617 on SARS-CoV2 infection.

a, Intracellular virus production was analysed by PCR targeting SARS-CoV-2 RdRP mRNA. Relative expression level of SARS-CoV2-2 genomic RNA was normalized to cellular GAPDH level. **b**, Intracellular RNA was isolated from cells without infection or cells infected with SARS-CoV-2 with or without treatment of GRL-0617. Relative mRNA-level fold change of indicated genes were analysed in a qRT-PCR analysis and normalized to ACTB levels. Data in **a, b** are presented as mean \pm s.d. ($n = 3$, independent experiments). * $P < 0.05$, ** $P < 0.01$; two-tailed paired *t*-tests. **c**, Schematic representation of the role of SARS-CoV-2 PLpro in the viral life cycle. The physiological role of SCoV2-PLpro in both host-immune response and polypeptide processing is shown. Inhibition of PLpro by GRL-0617 is also presented. [Source data](#)

Extended Data Table 1 Data collection and refinement statistics (molecular replacement)

[Full size table](#)

Extended Data Table 2 Kinetic parameters on AMC substrates

[Full size table](#)

Extended Data Table 3 Binding kinetics of PLpro to K48-Ub₂ or ISG15

[Full size table](#)

Supplementary information

Supplementary Figure 1

This file contains uncropped full-size gel images used in the mansucrtipt.

Reporting Summary

Peer Review File

Source data

Source Data Fig. 1

Source Data Fig. 2

Source Data Fig. 3

Source Data Fig. 4

Source Data Fig. 5

Source Data Extended Data Fig. 1

Source Data Extended Data Fig. 4

Source Data Extended Data Fig. 5

Source Data Extended Data Fig. 6

Source Data Extended Data Fig. 7

Rights and permissions

[Reprints and Permissions](#)

About this article



Check for
updates

Cite this article

Shin, D., Mukherjee, R., Grewe, D. *et al.* Papain-like protease regulates SARS-CoV-2 viral spread and innate immunity. *Nature* **587**, 657–662 (2020). <https://doi.org/10.1038/s41586-020-2601-5>

[Download citation](#)

- Received: 30 April 2020
- Accepted: 23 July 2020
- Published: 29 July 2020
- Issue Date: 26 November 2020
- DOI: <https://doi.org/10.1038/s41586-020-2601-5>

Further reading

- [**Host-pathogen interaction in COVID-19: Pathogenesis, potential therapeutics and vaccination strategies**](#)
 - Praveen Mathews Varghese
 - , Anthony G. Tsolaki
 - , Hadida Yasmin
 - , Abhishek Shastri
 - , Janez Ferluga

- , Manu Vatish
- , Taruna Madan
- & Uday Kishore

Immunobiology (2020)

- **Mesenchymal Stem Cells and Their Extracellular Vesicles: A Potential Game Changer for the COVID-19 Crisis**

- Dina H. Kassem
- & Mohamed M. Kamal

Frontiers in Cell and Developmental Biology (2020)

- **The role of death domain proteins in host response upon SARS-CoV-2 infection: modulation of programmed cell death and translational applications**

- Nikita V. Ivanisenko
- , Kamil Seyrek
- , Nikolay A. Kolchanov
- , Vladimir A. Ivanisenko
- & Inna N. Lavrik

Cell Death Discovery (2020)

- **Synthesis, spectroscopy, crystal structure, TGA/DTA study, DFT and molecular docking investigations of (E)-4-(4-methylbenzyl)-6-styrylpyridazin-3(2H)-one**

- Fouad El Kalai
- , Emine Berrin Çınar
- , Chin-Hung Lai
- , Said Daoui
- , Tarik Chelfi
- , Mustapha Allali

- , Necmi Dege
- , Khalid Karrouchi
- & Noureddine Benchat

Journal of Molecular Structure (2020)

- **Papain-Like Proteases as Coronaviral Drug Targets: Current Inhibitors, Opportunities, and Limitations**

- Anastasiia I. Petushkova
- & Andrey A. Zamyatnin

Pharmaceuticals (2020)

Comments

By submitting a comment you agree to abide by our [Terms](#) and [Community Guidelines](#). If you find something abusive or that does not comply with our terms or guidelines please flag it as inappropriate.

[Download PDF](#)

This article was downloaded by **calibre** from <https://www.nature.com/articles/s41586-020-2601-5>

- Article
- [Published: 28 October 2020](#)

Site-specific RNA methylation by a methyltransferase ribozyme

- [Carolin P. M. Scheitl¹](#),
- [Mohammad Ghaem Maghami¹](#),
- [Ann-Kathrin Lenz¹](#) &
- [Claudia Höbartner](#) ORCID: [orcid.org/0000-0002-4548-2299¹](https://orcid.org/0000-0002-4548-2299)

[Nature](#) volume 587, pages663–667(2020) [Cite this article](#)

- 7787 Accesses
- 252 Altmetric
- [Metrics details](#)

Subjects

- [Chemical modification](#)
- [Nucleic acids](#)
- [Chemical origin of life](#)
- [RNA](#)

Abstract

Nearly all classes of coding and non-coding RNA undergo post-transcriptional modification, including RNA methylation. Methylated nucleotides are among the evolutionarily most-conserved features of transfer (t)RNA and ribosomal (r)RNA^{1,2}. Many contemporary

methyltransferases use the universal cofactor S-adenosylmethionine (SAM) as a methyl-group donor. SAM and other nucleotide-derived cofactors are considered to be evolutionary leftovers from an RNA world, in which ribozymes may have catalysed essential metabolic reactions beyond self-replication³. Chemically diverse ribozymes seem to have been lost in nature, but may be reconstructed in the laboratory by in vitro selection. Here we report a methyltransferase ribozyme that catalyses the site-specific installation of 1-methyladenosine in a substrate RNA, using *O*⁶-methylguanine as a small-molecule cofactor. The ribozyme shows a broad RNA-sequence scope, as exemplified by site-specific adenosine methylation in various RNAs. This finding provides fundamental insights into the catalytic abilities of RNA, serves a synthetic tool to install 1-methyladenosine in RNA and may pave the way to in vitro evolution of other methyltransferase and demethylase ribozymes.

[Access through your institution](#)

[Change institution](#)

[Buy or subscribe](#)

Access options

Subscription info for Chinese customers

We have a dedicated website for our Chinese customers. Please go to [naturechina.com](#) to subscribe to this journal.

[Go to naturechina.com](#)

Rent or Buy article

Get time limited or full article access on ReadCube.

from \$8.99

[Rent or Buy](#)

All prices are NET prices.

Additional access options:

- [Log in](#)
- [Access through your institution](#)
- [Learn about institutional subscriptions](#)

Fig. 1: Methyltransferase ribozyme-catalysed synthesis of m¹A in RNA using m⁶G as methyl-group donor.



Fig. 2: Characterization of reaction products.

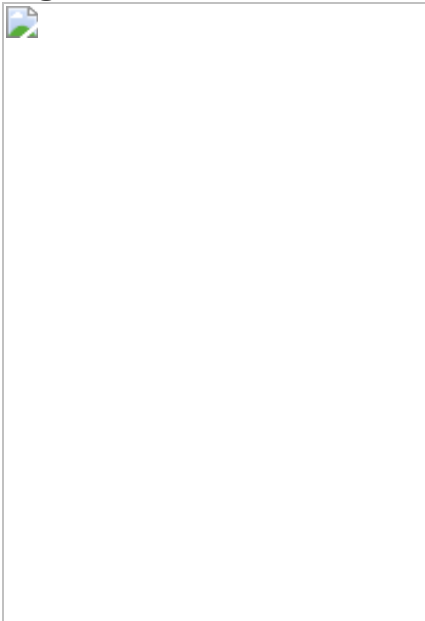


Fig. 3: MTR1-catalysed methylation of tRNA.

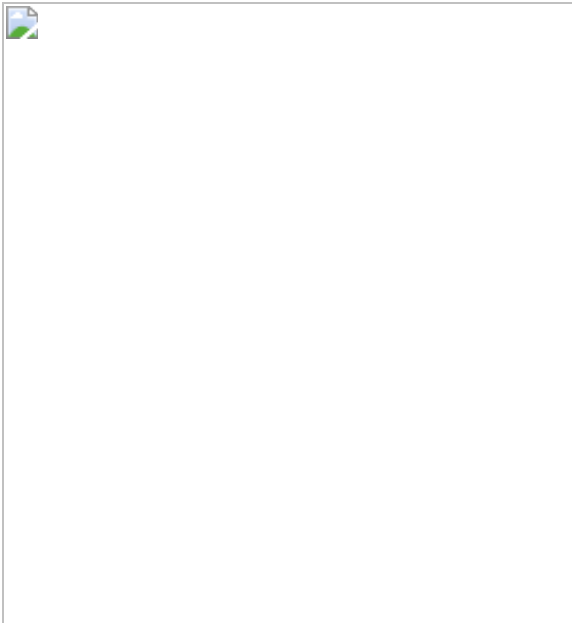
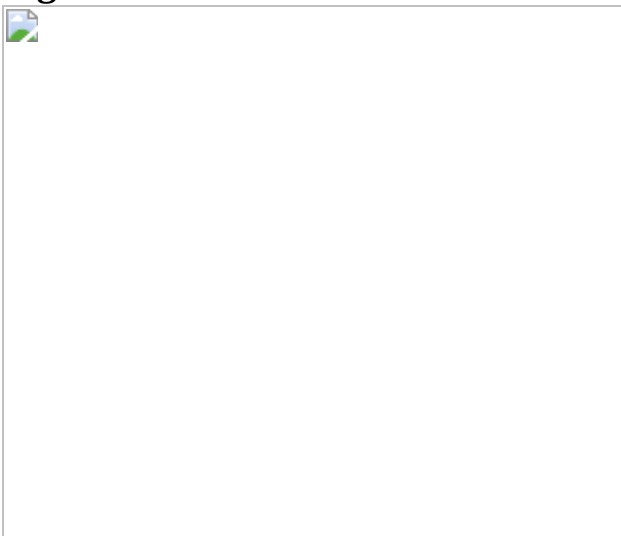


Fig. 4: Plasmid-encoded *cis*- and *trans*-active MTR1.



Data availability

All data generated and analysed during this study are included in this published Article and its Supplementary Information. [Source data](#) are provided with this paper.

References

1. 1.

Motorin, Y. & Helm, M. RNA nucleotide methylation. *Wiley Interdiscip. Rev. RNA* **2**, 611–631 (2011).

[CAS](#) [PubMed](#) [Google Scholar](#)

2. 2.

Waddell, T. G., Eilders, L. L., Patel, B. P. & Sims, M. Prebiotic methylation and the evolution of methyl transfer reactions in living cells. *Orig. Life Evol. Biosph.* **30**, 539–548 (2000).

[CAS](#) [PubMed](#) [ADS](#) [Google Scholar](#)

3. 3.

Jadhav, V. R. & Yarus, M. Coenzymes as coribozymes. *Biochimie* **84**, 877–888 (2002).

[CAS](#) [PubMed](#) [Google Scholar](#)

4. 4.

Frye, M., Jaffrey, S. R., Pan, T., Rechavi, G. & Suzuki, T. RNA modifications: what have we learned and where are we headed? *Nat. Rev. Genet.* **17**, 365–372 (2016).

[CAS](#) [PubMed](#) [Google Scholar](#)

5. 5.

Traube, F. R. & Carell, T. The chemistries and consequences of DNA and RNA methylation and demethylation. *RNA Biol.* **14**, 1099–1107 (2017).

[PubMed](#) [PubMed Central](#) [Google Scholar](#)

6. 6.

Zaccara, S., Ries, R. J. & Jaffrey, S. R. Reading, writing and erasing mRNA methylation. *Nat. Rev. Mol. Cell Biol.* **20**, 608–624 (2019).

[CAS](#) [PubMed](#) [Google Scholar](#)

7. 7.

Frye, M., Harada, B. T., Behm, M. & He, C. RNA modifications modulate gene expression during development. *Science* **361**, 1346–1349 (2018).

[CAS](#) [PubMed](#) [PubMed Central](#) [ADS](#) [Google Scholar](#)

8. 8.

Bohnsack, K. E., Höbartner, C. & Bohnsack, M. T. Eukaryotic 5-methylcytosine (m^5C) RNA methyltransferases: mechanisms, cellular functions, and links to disease. *Genes (Basel)* **10**, 102 (2019).

[CAS](#) [Google Scholar](#)

9. 9.

Becker, S., Schneider, C., Crisp, A. & Carell, T. Non-canonical nucleosides and chemistry of the emergence of life. *Nat. Commun.* **9**, 5174 (2018).

[CAS](#) [PubMed](#) [PubMed Central](#) [ADS](#) [Google Scholar](#)

10. 10.

Schneider, C. et al. Noncanonical RNA nucleosides as molecular fossils of an early Earth-generation by prebiotic methylations and carbamoylations. *Angew. Chem. Int. Ed.* **57**, 5943–5946 (2018).

[CAS](#) [Google Scholar](#)

11. 11.

Higgs, P. G. & Lehman, N. The RNA world: molecular cooperation at the origins of life. *Nat. Rev. Genet.* **16**, 7–17 (2015).

[CAS](#) [PubMed](#) [Google Scholar](#)

12. 12.

Doudna, J. A. & Cech, T. R. The chemical repertoire of natural ribozymes. *Nature* **418**, 222–228 (2002).

[CAS](#) [PubMed](#) [ADS](#) [Google Scholar](#)

13. 13.

Pyle, A. M. Group II intron self-splicing. *Annu. Rev. Biophys.* **45**, 183–205 (2016).

[CAS](#) [PubMed](#) [Google Scholar](#)

14. 14.

Ren, A., Micura, R. & Patel, D. J. Structure-based mechanistic insights into catalysis by small self-cleaving ribozymes. *Curr. Opin. Chem. Biol.* **41**, 71–83 (2017).

[CAS](#) [PubMed](#) [Google Scholar](#)

15. 15.

Attwater, J., Raguram, A., Morgunov, A. S., Gianni, E. & Holliger, P. Ribozyme-catalysed RNA synthesis using triplet building blocks. *eLife* **7**, e35255 (2018).

[PubMed](#) [PubMed Central](#) [Google Scholar](#)

16. 16.

Wachowius, F., Attwater, J. & Holliger, P. Nucleic acids: function and potential for abiogenesis. *Q. Rev. Biophys.* **50**, e4 (2017).

[PubMed](#) [Google Scholar](#)

17. 17.

Tjhung, K. F., Shokhirev, M. N., Horning, D. P. & Joyce, G. F. An RNA polymerase ribozyme that synthesizes its own ancestor. *Proc. Natl Acad. Sci. USA* **117**, 2906–2913 (2020).

[CAS](#) [PubMed](#) [Google Scholar](#)

18. 18.

Wilson, C. & Szostak, J. W. In vitro evolution of a self-alkylating ribozyme. *Nature* **374**, 777–782 (1995).

[CAS](#) [PubMed](#) [ADS](#) [Google Scholar](#)

19. 19.

Sharma, A. K. et al. Fluorescent RNA labeling using self-alkylating ribozymes. *ACS Chem. Biol.* **9**, 1680–1684 (2014).

[CAS](#) [PubMed](#) [Google Scholar](#)

20. 20.

Ameta, S. & Jäschke, A. An RNA catalyst that reacts with a mechanistic inhibitor of serine proteases. *Chem. Sci. (Camb.)* **4**, 957–964 (2013).

[CAS](#) [Google Scholar](#)

21. 21.

McDonald, R. I. et al. Electrophilic activity-based RNA probes reveal a self-alkylating RNA for RNA labeling. *Nat. Chem. Biol.* **10**, 1049–1054 (2014).

[CAS](#) [PubMed](#) [PubMed Central](#) [Google Scholar](#)

22. 22.

Peselis, A. & Serganov, A. Themes and variations in riboswitch structure and function. *Biochim. Biophys. Acta* **1839**, 908–918 (2014).

[CAS](#) [PubMed](#) [PubMed Central](#) [Google Scholar](#)

23. 23.

McCown, P. J., Corbino, K. A., Stav, S., Sherlock, M. E. & Breaker, R. R. Riboswitch diversity and distribution. *RNA* **23**, 995–1011 (2017).

[CAS](#) [PubMed](#) [PubMed Central](#) [Google Scholar](#)

24. 24.

Breaker, R. R. Riboswitches and translation control. *Cold Spring Harb. Perspect. Biol.* **10**, a032797 (2018).

[CAS](#) [PubMed](#) [PubMed Central](#) [ADS](#) [Google Scholar](#)

25. 25.

Batey, R. T. Recognition of S-adenosylmethionine by riboswitches. *Wiley Interdiscip. Rev. RNA* **2**, 299–311 (2011).

[CAS](#) [PubMed](#) [PubMed Central](#) [Google Scholar](#)

26. 26.

Sun, A. et al. SAM-VI riboswitch structure and signature for ligand discrimination. *Nat. Commun.* **10**, 5728 (2019).

[CAS](#) [PubMed](#) [PubMed Central](#) [ADS](#) [Google Scholar](#)

27. 27.

Burke, D. H. & Gold, L. RNA aptamers to the adenosine moiety of S-adenosyl methionine: structural inferences from variations on a theme

and the reproducibility of SELEX. *Nucleic Acids Res.* **25**, 2020–2024 (1997).

[CAS](#) [PubMed](#) [PubMed Central](#) [Google Scholar](#)

28. 28.

Lindahl, T., Demple, B. & Robins, P. Suicide inactivation of the *E. coli* O⁶-methylguanine-DNA methyltransferase. *EMBO J.* **1**, 1359–1363 (1982).

[CAS](#) [PubMed](#) [PubMed Central](#) [Google Scholar](#)

29. 29.

Ghaem Maghami, M., Scheitl, C. P. M. & Höbartner, C. Direct *in vitro* selection of *trans*-acting ribozymes for posttranscriptional, site-specific, and covalent fluorescent labeling of RNA. *J. Am. Chem. Soc.* **141**, 19546–19549 (2019).

[CAS](#) [PubMed](#) [Google Scholar](#)

30. 30.

Ghaem Maghami, M., Dey, S., Lenz, A. K. & Höbartner, C. Repurposing antiviral drugs for orthogonal RNA-catalyzed labeling of RNA. *Angew. Chem. Int. Ed.* **59**, 9335–9339 (2020).

[CAS](#) [Google Scholar](#)

31. 31.

Keppler, A. et al. A general method for the covalent labeling of fusion proteins with small molecules *in vivo*. *Nat. Biotechnol.* **21**, 86–89 (2003).

[CAS](#) [PubMed](#) [Google Scholar](#)

32. 32.

Dalhoff, C., Lukinavicius, G., Klimasauskas, S. & Weinhold, E. Direct transfer of extended groups from synthetic cofactors by DNA methyltransferases. *Nat. Chem. Biol.* **2**, 31–32 (2006).

[CAS](#) [PubMed](#) [Google Scholar](#)

33. 33.

Oerum, S., Dégué, C., Barraud, P. & Tisné, C. m¹A post-transcriptional modification in tRNAs. *Biomolecules* **7**, 20 (2017).

[PubMed Central](#) [Google Scholar](#)

34. 34.

Chujo, T. & Suzuki, T. Trmt61B is a methyltransferase responsible for 1-methyladenosine at position 58 of human mitochondrial tRNAs. *RNA* **18**, 2269–2276 (2012).

[CAS](#) [PubMed](#) [PubMed Central](#) [Google Scholar](#)

35. 35.

Reichle, V. F., Weber, V. & Kellner, S. NAIL-MS in *E. coli* determines the source and fate of methylation in tRNA. *ChemBioChem* **19**, 2575–2583 (2018).

[CAS](#) [PubMed](#) [PubMed Central](#) [Google Scholar](#)

36. 36.

Filonov, G. S., Kam, C. W., Song, W. & Jaffrey, S. R. In-gel imaging of RNA processing using broccoli reveals optimal aptamer expression strategies. *Chem. Biol.* **22**, 649–660 (2015).

[CAS](#) [PubMed](#) [PubMed Central](#) [Google Scholar](#)

37. 37.

Xiong, X., Li, X. & Yi, C. N^1 -methyladenosine methylome in messenger RNA and non-coding RNA. *Curr. Opin. Chem. Biol.* **45**, 179–186 (2018).

[CAS](#) [PubMed](#) [Google Scholar](#)

38. 38.

Grozhik, A. V. et al. Antibody cross-reactivity accounts for widespread appearance of m¹A in 5'UTRs. *Nat. Commun.* **10**, 5126 (2019).

[PubMed](#) [PubMed Central](#) [ADS](#) [Google Scholar](#)

39. 39.

Safra, M. et al. The m¹A landscape on cytosolic and mitochondrial mRNA at single-base resolution. *Nature* **551**, 251–255 (2017).

[CAS](#) [PubMed](#) [ADS](#) [Google Scholar](#)

40. 40.

Zhou, H. et al. Evolution of a reverse transcriptase to map N^1 -methyladenosine in human messenger RNA. *Nat. Methods* **16**, 1281–1288 (2019).

[CAS](#) [PubMed](#) [PubMed Central](#) [Google Scholar](#)

41. 41.

Terns, M. P. & Terns, R. M. Small nucleolar RNAs: versatile *trans*-acting molecules of ancient evolutionary origin. *Gene Expr.* **10**, 17–39 (2002).

[CAS](#) [PubMed](#) [Google Scholar](#)

42. 42.

Serganov, A. et al. Structural basis for discriminative regulation of gene expression by adenine- and guanine-sensing mRNAs. *Chem. Biol.* **11**, 1729–1741 (2004).

[CAS](#) [PubMed](#) [PubMed Central](#) [Google Scholar](#)

43. 43.

Gilbert, S. D., Reyes, F. E., Edwards, A. L. & Batey, R. T. Adaptive ligand binding by the purine riboswitch in the recognition of guanine and adenine analogs. *Structure* **17**, 857–868 (2009).

[CAS](#) [PubMed](#) [PubMed Central](#) [Google Scholar](#)

44. 44.

Pitsch, S., Weiss, P. A., Jenny, L., Stutz, A. & Wu, X. Reliable chemical synthesis of oligoribonucleotides (RNA) with 2'-O-[(triisopropylsilyl)oxy]methyl(2'-O-tom)-protected phosphoramidites. *Helv. Chim. Acta* **84**, 3773–3795 (2001).

[CAS](#) [Google Scholar](#)

45. 45.

Wachowius, F. & Höbartner, C. Probing essential nucleobase functional groups in aptamers and deoxyribozymes by nucleotide analogue interference mapping of DNA. *J. Am. Chem. Soc.* **133**, 14888–14891 (2011).

[CAS](#) [PubMed](#) [Google Scholar](#)

46. 46.

Košutić, M. et al. A mini-twister variant and impact of residues/cations on the phosphodiester cleavage of this ribozyme class. *Angew. Chem. Int. Ed.* **54**, 15128–15133 (2015).

[Google Scholar](#)

47. 47.

Höbartner, C. et al. The synthesis of 2'-O-[(triisopropylsilyl)oxy] methyl (TOM) phosphoramidites of methylated ribonucleosides (m^1G , m^2G , m^2_2G , m^1I , m^3U , m^4C , m^6A , m^6_2A) for use in automated RNA solid-phase synthesis. *Monatshefte Chemie* **134**, 851–873 (2003).

[Google Scholar](#)

48. 48.

Rio, D. C. Expression and purification of active recombinant T7 RNA polymerase from *E. coli*. *Cold Spring Harb. Protoc.* **2013**, pdb.prot078527 (2013).

[PubMed](#) [Google Scholar](#)

49. 49.

Mortimer, S. A. & Weeks, K. M. A fast-acting reagent for accurate analysis of RNA secondary and tertiary structure by SHAPE chemistry. *J. Am. Chem. Soc.* **129**, 4144–4145 (2007).

[CAS](#) [PubMed](#) [Google Scholar](#)

50. 50.

Fujii, T., Itaya, T. & Saito, T. Purines. 18. Kinetic studies of base-catalysed conversion of 1-alkyladenosines into *N*-alkyladenosines – effect of substituents on rearrangement rate. *Chem. Pharm. Bull. (Tokyo)* **23**, 54–61 (1975).

[CAS](#) [Google Scholar](#)

[Download references](#)

Acknowledgements

This work was supported by the European Research Council (ERC-CoG 682586) and by the Deutsche Forschungsgemeinschaft (DFG) (SPP1784 Chemical Biology of native nucleic acid modifications). We thank J. Adelmann and S. Mayer for help with mass spectrometric analyses, C. Steinmetzger for synthesis of 1M7 and S. Dey for providing m⁶dG.

Author information

Affiliations

1. Institut für Organische Chemie, Julius-Maximilians-Universität Würzburg, Würzburg, Germany

Carolin P. M. Scheitl, Mohammad Ghaem Maghami, Ann-Kathrin Lenz & Claudia Höbartner

Authors

1. Carolin P. M. Scheitl

[View author publications](#)

You can also search for this author in [PubMed](#) [Google Scholar](#)

2. Mohammad Ghaem Maghami

[View author publications](#)

You can also search for this author in [PubMed](#) [Google Scholar](#)

3. Ann-Kathrin Lenz

[View author publications](#)

You can also search for this author in [PubMed](#) [Google Scholar](#)

4. Claudia Höbartner

[View author publications](#)

You can also search for this author in [PubMed](#) [Google Scholar](#)

Contributions

In vitro selection was carried out by C.P.M.S. RNA solid-phase synthesis was performed by A.-K.L. and C.H. Ribozymes were characterized by C.P.M.S., M.G.M. and A.-K.L. Plasmids were constructed by M.G.M., A.-K.L. and C.P.M.S. RNA structure probing and detection of RNA methylation by primer extension was performed by C.P.M.S. LC–MS analyses were run by C.P.M.S. and C.H. C.P.M.S., M.G.M. and C.H. designed experiments. C.P.M.S. and C.H. wrote the paper. All authors analysed data and commented on the manuscript.

Corresponding author

Correspondence to [Claudia Höbartner](#).

Ethics declarations

Competing interests

The authors declare no competing interests.

Additional information

Peer review information *Nature* thanks Pål Falnes and the other, anonymous, reviewer(s) for their contribution to the peer review of this work. Peer reviewer reports are available.

Publisher's note Springer Nature remains neutral with regard to jurisdictional claims in published maps and institutional affiliations.

Extended data figures and tables

[**Extended Data Fig. 1 In vitro selection of methyltransferase ribozymes.**](#)

a, In vitro selection scheme consisting of incubation, capture, wash, elution, amplification and transcription steps. The RNA substrate (blue) contains an unpaired adenosine (red, A) and is connected to the RNA library via the single-stranded loop (black). The library contains 40 random nucleotides (green) and 2 constant binding arms (cyan) complementary to the RNA substrate upstream and downstream of the bulged A. Incubation was 50 μ M RNA, 100 μ M BG–biotin, 50 mM HEPES, pH 7.5, 120 mM KCl, 5 mM NaCl and 40 mM MgCl₂, at 37 °C (round 1–8: 16 h; round 9–11: 4 h; and round 11: 50 μ M BG–biotin). For capture, beads were blocked with *E. coli* tRNA; streptavidin and neutravidin beads were switched every other round. Denaturing wash buffer was 8 M urea, 10 mM Tris-HCl, pH 7.5, 1 mM EDTA, 0.01% Tween-20. Elution used 95% formamide, 1 mM EDTA, at 95 °C for 5 min. **b**, For RT–PCR, the following conditions were used: 42 °C, 30 min, 10 cycles of PCR with 1 μ M primer D4 and 0.5 μ M primer D5. For the following PCR, we used: 25 cycles, 5% (v/v) RT–PCR product as template, 1 μ M D4 and 0.5 μ M D3, 10% (v/v) DMSO, and an annealing temperature of 65 °C. For in vitro transcription, we used a dsDNA template from a 200 μ l PCR reaction, 100 μ l reaction volume with 4 mM each NTP, followed by PAGE purification.

Extended Data Fig. 2 Activity of methyltransferase ribozymes.

Examination of mutations in the stem-loop. **a**, 3'-Fluorescein-labelled R10a tested with 100 μ M m⁶G. **b**, 5'-Fluorescein-labelled R1 tested with 100 μ M BG-NH₂. ON, overnight (23 h). **c**, Kinetics of CA13 (Rz1/Rz1s)-catalysed alkylation of R1 using BG-NH₂ cofactor. Fraction modified is shown as mean \pm s.d. ($n = 3$), and fit to a mono-exponential model ($Y = Y_{\max}(1 - e^{-kt})$) (blue) or a bi-exponential model ($Y = Y_{\max}(a(1 - e^{-k_1 t}) + (1 - a)(1 - e^{-k_2 t}))$) (black). **d**, Dependence of MTR1 methylation yield on Mg²⁺ concentration; reactions were performed with 100 μ M m⁶G (on R2 with Rz3) at 37 °C. Individual data points are shown as empty symbols ($n = 2$ for 5 h and 23 h, $n = 3$ for 7 h time points), and mean is depicted as a filled symbol. [Source data](#)

Extended Data Fig. 3 RNA structure probing by DMS and SHAPE.

MTR1 (Rz3) was annealed with 17-nt RNA (R6), treated with DMS or 1M7, in presence (+) or absence (−) of m⁶G, and the modification pattern was analysed by primer extension (5'-³²P-labelled D4) with Superscript III. DMS probes the accessibility of the Watson–Crick face of A and C, and SHAPE with 1M7 probes the flexibility of the backbone. Both probing methods confirm the central base-paired stem and reveal the protection of several additional nucleotides (bold). The experiment was repeated three times with similar results.

Extended Data Fig. 4 Mutagenesis of target RNA.

Representative gel images of RNA-catalysed alkylation reactions of RNA-substrate mutants by their corresponding ribozymes, with complementary binding arms as listed in Supplementary Table 1. **a**, Adenosine point mutations. **b**, Atomic mutagenesis of backbone. **c**, **d**, Atomic mutagenesis of adenosine. **e**, Reaction sites blocked by methylation. **f**, Binding-arm mutations outside of GAG. **g**, Point mutations next to the target nucleoside A. Reactions were performed with 100 μM BG-NH₂ (**a–e**) or BG-biotin (**f**, **g**) at pH 7.5, 40 mM MgCl₂ and 37 °C, and repeated two times for each substrate. The parent reaction with adenosine was performed with fluorescently labelled and radioactively labelled RNA independently six times.

Extended Data Fig. 5 RNA-catalysed methylation of tRNAs.

a, tRNA sequences studied. **b**, Synthetic fragments and corresponding ribozymes. **c**, Exemplary gel images for kinetic analysis of MTR1-catalysed fragment methylation showing quantitative formation of m¹A. **d**, Exemplary HR-ESI-MS of isolated methylated *R. norvegicus* RNA fragment. **e**, Full gel images of primer extension analyses shown in Fig. 3. Representative gel images of three independent experiments with similar results.

Extended Data Fig. 6 Specificity of ribozyme for the target tRNA.

a, Secondary structure schemes of six *E. coli* tRNAs, with very similar TΨC-stem-loop sequences (drawn without natural modifications). Target tRNA^{Asp} in top left corner, with A58 indicated in blue. The nucleotides complementary to the binding arms of MTR1–tRNA^{Asp}(A58) (Rz23) are shown in bold. The purple nucleotides indicate mismatched positions with the binding arms. **b**, Full gel image of primer extension analysis on total *E. coli* tRNA with six primers, shown in Fig. 3c. Primer extension analyses were repeated twice.

Extended Data Fig. 7 Plasmid-encoded cis-active ribozyme.

a, Schematic of FBC–MTR1 construct. **b**, Dot plot for FBC–MTR1 generated by Vienna RNAfold (<http://rna.tbi.univie.ac.at/>), indicating a high probability of folding into the designed structure. **c**, LC–MS analysis of the in vitro transcript FBC–MTR1 digested by snake venom phosphodiesterase and bacterial alkaline phosphatase, after reaction with m⁶G. EIC for detection of MH⁺ 282.11 ± 0.05 (methylated adenosines) shows production of m¹A, and m⁶A to a small extent (due to partial Dimroth rearrangement during digestion). The bottom trace for the synthetic references m¹A and m⁶A (50 nM each) is the same as shown in Fig. 3d. **d**, Primer extension stop assays also confirm activity of FBC–MTR1 transcribed in vitro and in vivo, in the presence of total *E. coli* RNA. Left, full gel image shown in Fig. 4a for in vitro-transcribed FBC–MTR1. Right, primer extension on total *E. coli* RNA, isolated 1 h after IPTG induction and incubated with the indicated m⁶G or BG concentration in vitro. These experiments were independently repeated two times with similar results.

Extended Data Fig. 8 Plasmid-encoded trans-active ribozyme.

a, Schematic of FBT–MTR1 with specific binding arms for *E. coli* tRNA^{Asp} (A58). **b**, Primer extension stop assays confirm the activity and specificity of the FBT–MTR1 in vitro transcript. Left, full gel image shown in Fig. 4b for FBT–MTR1 reacted with m⁶G and BG on total *E. coli* tRNA. Right,

primer extension on BG-treated sample with six different *E. coli* tRNA-specific primers (P4–P9), repeated twice. **c**, LC–MS analysis after digestion of total *E. coli* tRNA treated with FBT–MTR1 and BG (same sample as for the right gel image). EIC for MH^+ 282.11 (methylated adenosines) and 298.11 (methylated guanosines) demonstrate the presence of natural tRNA modifications. EIC 358.11 in comparison to reference nucleosides bn^1A and bn^6A shows bn-modified adenosines produced by FBT–MTR1.

Supplementary information

Supplementary Figure 7

-page pdf file showing uncropped images (full scans) of gels used in Figures 1b-d, 2e, and ED Fig 2a-c, 4a-g, 5c. The regions used are indicated by red boxes and labeled with the used RNA substrate and ribozyme, according to the numbers in Supplementary Table 1.

Reporting Summary

Supplementary Table

This file contains Supplementary Tables 1-3.

Peer Review File

Source data

Source Data Fig. 1

Source Data Fig. 2

Source Data Extended Data Fig. 2

Rights and permissions

[Reprints and Permissions](#)

About this article



Check for
updates

Cite this article

Scheitl, C.P.M., Ghaem Maghami, M., Lenz, AK. *et al.* Site-specific RNA methylation by a methyltransferase ribozyme. *Nature* **587**, 663–667 (2020). <https://doi.org/10.1038/s41586-020-2854-z>

[Download citation](#)

- Received: 29 March 2020
- Accepted: 27 July 2020
- Published: 28 October 2020
- Issue Date: 26 November 2020
- DOI: <https://doi.org/10.1038/s41586-020-2854-z>

Comments

By submitting a comment you agree to abide by our [Terms](#) and [Community Guidelines](#). If you find something abusive or that does not comply with our terms or guidelines please flag it as inappropriate.

[Access through your institution](#)

[Change institution](#)

[Buy or subscribe](#)

This article was downloaded by **calibre** from <https://www.nature.com/articles/s41586-020-2854-z>

| [Section menu](#) | [Main menu](#) |

- Article
- [Published: 10 September 2020](#)

Structural mechanism of cGAS inhibition by the nucleosome

- [Ganesh R. Pathare](#)^{1,2} na1,
- [Alexiane Decout](#) [ORCID: orcid.org/0000-0001-7761-6434](#)³ na1,
- [Selene Glück](#)³,
- [Simone Cavadini](#)^{1,2},
- [Kristina Makasheva](#) [ORCID: orcid.org/0000-0002-0645-6848](#)⁴,
- [Ruud Hovius](#) [ORCID: orcid.org/0000-0001-9258-6587](#)⁴,
- [Georg Kempf](#)^{1,2},
- [Joscha Weiss](#) [ORCID: orcid.org/0000-0002-4149-0478](#)^{1,2},
- [Zuzanna Kozicka](#)^{1,2},
- [Baptiste Guey](#) [ORCID: orcid.org/0000-0002-7750-9214](#)³,
- [Pauline Melenec](#) [ORCID: orcid.org/0000-0001-6486-2003](#)³,
- [Beat Fierz](#) [ORCID: orcid.org/0000-0002-2991-3044](#)⁴,
- [Nicolas H. Thomä](#) [ORCID: orcid.org/0000-0003-2685-906X](#)^{1,2} &
- [Andrea Ablasser](#) [ORCID: orcid.org/0000-0002-8475-8999](#)³

[Nature](#) volume 587, pages668–672(2020) [Cite this article](#)

- 10k Accesses
- 2 Citations
- 202 Altmetric
- [Metrics details](#)

Subjects

- [Pattern recognition receptors](#)
- [Signal transduction](#)

Abstract

The DNA sensor cyclic GMP–AMP synthase (cGAS) initiates innate immune responses following microbial infection, cellular stress and cancer¹. Upon activation by double-stranded DNA, cytosolic cGAS produces 2'3' cGMP–AMP, which triggers the induction of inflammatory cytokines and type I interferons ^{2,3,4,5,6,7}. cGAS is also present inside the cell nucleus, which is replete with genomic DNA⁸, where chromatin has been implicated in restricting its enzymatic activity⁹. However, the structural basis for inhibition of cGAS by chromatin remains unknown. Here we present the cryo-electron microscopy structure of human cGAS bound to nucleosomes. cGAS makes extensive contacts with both the acidic patch of the histone H2A–H2B heterodimer and nucleosomal DNA. The structural and complementary biochemical analysis also find cGAS engaged to a second nucleosome in *trans*. Mechanistically, binding of the nucleosome locks cGAS into a monomeric state, in which steric hindrance suppresses spurious activation by genomic DNA. We find that mutations to the cGAS–acidic patch interface are sufficient to abolish the inhibitory effect of nucleosomes in vitro and to unleash the activity of cGAS on genomic DNA in living cells. Our work uncovers the structural basis of the interaction between cGAS and chromatin and details a mechanism that permits self–non-self discrimination of genomic DNA by cGAS.

[Access through your institution](#)

[Change institution](#)

[Buy or subscribe](#)

Access options

Subscription info for Chinese customers

We have a dedicated website for our Chinese customers. Please go to naturechina.com to subscribe to this journal.

[Go to naturechina.com](#)

Rent or Buy article

Get time limited or full article access on ReadCube.

from \$8.99

[Rent or Buy](#)

All prices are NET prices.

Additional access options:

- [Log in](#)
- [Access through your institution](#)
- [Learn about institutional subscriptions](#)

Fig. 1: Cryo-electron microscopy structure of cGAS bound to nucleosomes.

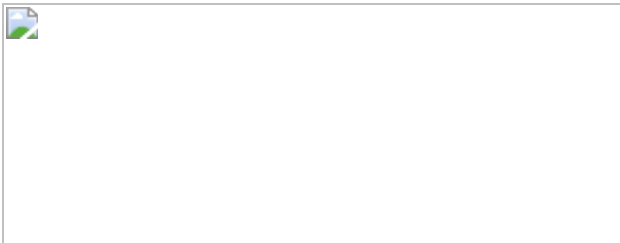


Fig. 2: The cGAS1–NCP1 complex and structural mechanism of inhibition.



Fig. 3: cGAS interactions with the second nucleosome in *trans*.



Fig. 4: Effect of structure-based mutations on cellular cGAS activity.



Data availability

The electron density reconstructions and corresponding final models for NCP1–cGAS1–cGAS2–NCP2 and NCP1–cGAS1 were deposited in the Electron Microscopy Data Bank (accession codes: EMDB-10694 and EMDB-10695) and in the PDB (accession codes: 6Y5D and 6Y5E). The electron density reconstructions for NCP1–WT cGAS1–WT cGAS2–NCP2 and NCP1–WT cGAS1 were deposited in the Electron Microscopy Data Bank (accession codes: EMDB-11006 and EMDB-11005).

References

1. 1.

Ablässer, A. & Chen, Z. J. cGAS in action: expanding roles in immunity and inflammation. *Science* **363**, eaat8657 (2019).

[CAS](#) [PubMed](#) [Google Scholar](#)

2. 2.

Sun, L., Wu, J., Du, F., Chen, X. & Chen, Z. J. Cyclic GMP–AMP synthase is a cytosolic DNA sensor that activates the type I interferon pathway. *Science* **339**, 786–791 (2013).

[ADS](#) [CAS](#) [PubMed](#) [Google Scholar](#)

3. 3.

Wu, J. et al. Cyclic GMP–AMP is an endogenous second messenger in innate immune signaling by cytosolic DNA. *Science* **339**, 826–830 (2013).

[ADS](#) [CAS](#) [PubMed](#) [Google Scholar](#)

4. 4.

Ablasser, A. et al. cGAS produces a 2'-5'-linked cyclic dinucleotide second messenger that activates STING. *Nature* **498**, 380–384 (2013).

[ADS](#) [CAS](#) [PubMed](#) [PubMed Central](#) [Google Scholar](#)

5. 5.

Gao, P. et al. Cyclic [G(2',5')pA(3',5')p] is the metazoan second messenger produced by DNA-activated cyclic GMP–AMP synthase. *Cell* **153**, 1094–1107 (2013).

[CAS](#) [PubMed](#) [PubMed Central](#) [Google Scholar](#)

6. 6.

Diner, E. J. et al. The innate immune DNA sensor cGAS produces a noncanonical cyclic dinucleotide that activates human STING. *Cell Rep.* **3**, 1355–1361 (2013).

[CAS](#) [PubMed](#) [PubMed Central](#) [Google Scholar](#)

7. 7.

Zhang, X. et al. Cyclic GMP–AMP containing mixed phosphodiester linkages is an endogenous high-affinity ligand for STING. *Mol. Cell* **51**, 226–235 (2013).

[CAS](#) [PubMed](#) [Google Scholar](#)

8. 8.

Gentili, M. et al. The N-terminal domain of cGAS determines preferential association with centromeric DNA and innate immune activation in the nucleus. *Cell Rep.* **26**, 2377–2393.e13 (2019).

[CAS](#) [PubMed](#) [PubMed Central](#) [Google Scholar](#)

9. 9.

Volkman, H. E., Cambier, S., Gray, E. E. & Stetson, D. B. Tight nuclear tethering of cGAS is essential for preventing autoreactivity. *eLife* **8**, e47491 (2019).

[CAS](#) [PubMed](#) [PubMed Central](#) [Google Scholar](#)

10. 10.

Barber, G. N. STING: infection, inflammation and cancer. *Nat. Rev. Immunol.* **15**, 760–770 (2015).

[CAS](#) [PubMed](#) [PubMed Central](#) [Google Scholar](#)

11. 11.

Orzalli, M. H. et al. cGAS-mediated stabilization of IFI16 promotes innate signaling during herpes simplex virus infection. *Proc. Natl Acad. Sci. USA* **112**, E1773–E1781 (2015).

[CAS](#) [PubMed](#) [Google Scholar](#)

12. 12.

Lahaye, X. et al. NONO detects the nuclear HIV capsid to promote cGAS-mediated innate immune activation. *Cell* **175**, 488–501.e22 (2018).

[CAS](#) [PubMed](#) [Google Scholar](#)

13. 13.

Zierhut, C. et al. The cytoplasmic DNA sensor cGAS promotes mitotic cell death. *Cell* **178**, 302–315.e23 (2019).

[CAS](#) [PubMed](#) [PubMed Central](#) [Google Scholar](#)

14. 14.

Pang, B. et al. Drug-induced histone eviction from open chromatin contributes to the chemotherapeutic effects of doxorubicin. *Nat. Commun.* **4**, 1908 (2013).

[ADS](#) [PubMed](#) [PubMed Central](#) [Google Scholar](#)

15. 15.

Stark, H. GraFix: stabilization of fragile macromolecular complexes for single particle cryo-EM. *Methods Enzymol.* **481**, 109–126 (2010).

[CAS](#) [PubMed](#) [Google Scholar](#)

16. 16.

Li, X. et al. Cyclic GMP–AMP synthase is activated by double-stranded DNA-induced oligomerization. *Immunity* **39**, 1019–1031 (2013).

[CAS](#) [PubMed](#) [Google Scholar](#)

17. 17.

McGinty, R. K. & Tan, S. Nucleosome structure and function. *Chem. Rev.* **115**, 2255–2273 (2015).

[CAS](#) [PubMed](#) [Google Scholar](#)

18. 18.

Civril, F. et al. Structural mechanism of cytosolic DNA sensing by cGAS. *Nature* **498**, 332–337 (2013).

[ADS](#) [CAS](#) [PubMed](#) [PubMed Central](#) [Google Scholar](#)

19. 19.

Barbera, A. J. et al. The nucleosomal surface as a docking station for Kaposi's sarcoma herpesvirus LANA. *Science* **311**, 856–861 (2006).

[ADS](#) [CAS](#) [PubMed](#) [Google Scholar](#)

20. 20.

Abe, T. & Barber, G. N. Cytosolic-DNA-mediated, STING-dependent proinflammatory gene induction necessitates canonical NF-κB activation through TBK1. *J. Virol.* **88**, 5328–5341 (2014).

[PubMed](#) [PubMed Central](#) [Google Scholar](#)

21. 21.

Zhang, X. et al. The cytosolic DNA sensor cGAS forms an oligomeric complex with DNA and undergoes switch-like conformational changes in the activation loop. *Cell Rep.* **6**, 421–430 (2014).

[CAS](#) [PubMed](#) [PubMed Central](#) [Google Scholar](#)

22. 22.

Andreeva, L. et al. cGAS senses long and HMGB/TFAM-bound U-turn DNA by forming protein–DNA ladders. *Nature* **549**, 394–398

(2017).

[ADS](#) [CAS](#) [PubMed](#) [Google Scholar](#)

23. 23.

Zhou, W. et al. Structure of the human cGAS–DNA complex reveals enhanced control of immune surveillance. *Cell* **174**, 300–311.e11 (2018).

[CAS](#) [PubMed](#) [PubMed Central](#) [Google Scholar](#)

24. 24.

Xie, W. et al. Human cGAS catalytic domain has an additional DNA-binding interface that enhances enzymatic activity and liquid-phase condensation. *Proc. Natl Acad. Sci. USA* **116**, 11946–11955 (2019).

[CAS](#) [PubMed](#) [Google Scholar](#)

25. 25.

Ablasser, A. et al. Cell intrinsic immunity spreads to bystander cells via the intercellular transfer of cGAMP. *Nature* **503**, 530–534 (2013).

[ADS](#) [CAS](#) [PubMed](#) [PubMed Central](#) [Google Scholar](#)

26. 26.

Dobbs, N. et al. STING activation by translocation from the ER is associated with infection and autoinflammatory disease. *Cell Host Microbe* **18**, 157–168 (2015).

[MathSciNet](#) [CAS](#) [PubMed](#) [PubMed Central](#) [Google Scholar](#)

27. 27.

Konno, H., Konno, K. & Barber, G. N. Cyclic dinucleotides trigger ULK1 (ATG1) phosphorylation of STING to prevent sustained innate

immune signaling. *Cell* **155**, 688–698 (2013).

[CAS](#) [PubMed](#) [Google Scholar](#)

28. 28.

Janeway, C. A. Jr. Approaching the asymptote? Evolution and revolution in immunology. *Cold Spring Harb. Symp. Quant. Biol.* **54**, 1–13 (1989).

[CAS](#) [PubMed](#) [Google Scholar](#)

29. 29.

Ablasser, A. & Hur, S. Regulation of cGAS- and RLR-mediated immunity to nucleic acids. *Nat. Immunol.* **21**, 17–29 (2020).

[CAS](#) [PubMed](#) [Google Scholar](#)

30. 30.

Guey, B. et al. BAF restricts cGAS on nuclear DNA to prevent innate immune activation. *Science* **369**, 823–828 (2020).

31. 31.

Dolinsky, T.J. et al. PDB2PQR: an automated pipeline for the setup of Poisson–Boltzmann electrostatics calculations. *Nucleic Acids Res.* **32**, W665–W667 (2004).

[CAS](#) [PubMed](#) [PubMed Central](#) [Google Scholar](#)

32. 32.

Ran, F. A. et al. Genome engineering using the CRISPR–Cas9 system. *Nat. Protocols* **8**, 2281–2308 (2013).

[CAS](#) [PubMed](#) [Google Scholar](#)

33. 33.

Haag, S. M. et al. Targeting STING with covalent small-molecule inhibitors. *Nature* **559**, 269–273 (2018).

[ADS](#) [CAS](#) [PubMed](#) [Google Scholar](#)

34. 34.

Marks, B. D. et al. Multiparameter analysis of a screen for progesterone receptor ligands: comparing fluorescence lifetime and fluorescence polarization measurements. *Assay Drug Dev. Technol.* **3**, 613–622 (2005).

[CAS](#) [PubMed](#) [Google Scholar](#)

35. 35.

Hanson, B. L., Alexander, C., Harp, J. M. & Bunick, G. J. Preparation and crystallization of nucleosome core particle. *Methods Enzymol.* **375**, 44–62 (2004).

[CAS](#) [PubMed](#) [Google Scholar](#)

36. 36.

Luger, K., Rechsteiner, T. J. & Richmond, T. J. Preparation of nucleosome core particle from recombinant histones. *Methods Enzymol.* **304**, 3–19 (1999).

[CAS](#) [PubMed](#) [Google Scholar](#)

37. 37.

Schenk, A. D., Cavardini, S., Thomä, N. H. & Genoud, C. Live analysis and reconstruction of single-particle cryo-electron microscopy data with CryoFLARE. *J. Chem. Inf. Model.* **60**, 2561–2569 (2020).

[CAS](#) [PubMed](#) [Google Scholar](#)

38. 38.

Zhang, K. Gctf: real-time CTF determination and correction. *J. Struct. Biol.* **193**, 1–12 (2016).

[ADS](#) [CAS](#) [PubMed](#) [PubMed Central](#) [Google Scholar](#)

39. 39.

Wagner, T. et al. SPHIRE-crYOLO is a fast and accurate fully automated particle picker for cryo-EM. *Commun. Biol.* **2**, 218 (2019).

[Google Scholar](#)

40. 40.

Punjani, A., Rubinstein, J. L., Fleet, D. J. & Brubaker, M. A. cryoSPARC: algorithms for rapid unsupervised cryo-EM structure determination. *Nat. Methods* **14**, 290–296 (2017).

[CAS](#) [Google Scholar](#)

41. 41.

Zivanov, J. et al. New tools for automated high-resolution cryo-EM structure determination in RELION-3. *eLife* **7**, e42166 (2018).

[PubMed](#) [PubMed Central](#) [Google Scholar](#)

42. 42.

Scheres, S. H. RELION: implementation of a Bayesian approach to cryo-EM structure determination. *J. Struct. Biol.* **180**, 519–530 (2012).

[CAS](#) [PubMed](#) [PubMed Central](#) [Google Scholar](#)

43. 43.

de la Rosa-Trevín, J. M. et al. Xmipp 3.0: an improved software suite for image processing in electron microscopy. *J. Struct. Biol.* **184**, 321–328 (2013).

[PubMed](#) [Google Scholar](#)

44. 44.

Matsumoto, S. et al. DNA damage detection in nucleosomes involves DNA register shifting. *Nature* **571**, 79–84 (2019).

[CAS](#) [PubMed](#) [PubMed Central](#) [Google Scholar](#)

45. 45.

Pettersen, E. F. et al. UCSF Chimera—a visualization system for exploratory research and analysis. *J. Comput. Chem.* **25**, 1605–1612 (2004).

[CAS](#) [PubMed](#) [PubMed Central](#) [Google Scholar](#)

46. 46.

Emsley, P. & Cowtan, K. Coot: model-building tools for molecular graphics. *Acta Crystallogr. D Biol. Crystallogr.* **60**, 2126–2132 (2004).

[Google Scholar](#)

47. 47.

Lowary, P. T. & Widom, J. New DNA sequence rules for high affinity binding to histone octamer and sequence-directed nucleosome positioning. *J. Mol. Biol.* **276**, 19–42 (1998).

[CAS](#) [PubMed](#) [Google Scholar](#)

48. 48.

Adams, P. D. et al. PHENIX: a comprehensive Python-based system for macromolecular structure solution. *Acta Crystallogr. D Biol. Crystallogr.* **66**, 213–221 (2010).

[CAS](#) [PubMed](#) [PubMed Central](#) [Google Scholar](#)

49. 49.

Terwilliger, T. C. et al. phenix.mr_rosetta: molecular replacement and model rebuilding with Phenix and Rosetta. *J. Struct. Funct. Genomics* **13**, 81–90 (2012).

[CAS](#) [PubMed](#) [PubMed Central](#) [Google Scholar](#)

50. 50.

Lebedev, A. A. et al. JLigand: a graphical tool for the CCP4 template-restraint library. *Acta Crystallogr. D Biol. Crystallogr.* **68**, 431–440 (2012).

[CAS](#) [PubMed](#) [PubMed Central](#) [Google Scholar](#)

51. 51.

Davis, I. W. et al. MolProbity: all-atom contacts and structure validation for proteins and nucleic acids. *Nucleic Acids Res.* **35**, W375–W383 (2007).

[ADS](#) [PubMed](#) [PubMed Central](#) [Google Scholar](#)

52. 52.

Waterhouse, A. M., Procter, J. B., Martin, D. M., Clamp, M. & Barton, G. J. Jalview version 2—a multiple sequence alignment editor and analysis workbench. *Bioinformatics* **25**, 1189–1191 (2009).

[CAS](#) [PubMed](#) [PubMed Central](#) [Google Scholar](#)

[Download references](#)

Acknowledgements

We thank N. Jordan and J. Ricci for technical assistance. A.A. received grants from the SNF (BSSGI0-155984 and 31003A_159836), NCCR in Chemical Biology, and was supported by the European Union's Horizon 2020 Research and Innovation program grant agreement (grant no: 804933, ImAgine). N.H.T. was supported by the European Research Council (ERC) under the European Union's Horizon 2020 Research and Innovation program grant agreement (grant no. 666068), the Novartis Research Foundation and by the SNF (31003A_179541). B.F. is supported by the European Union's Horizon 2020 Research and Innovation program grant agreement (grant no: 724022, chromo-SUMMIT) and the NCCR in Chemical Biology. Z.K. was supported by the European Union's Horizon 2020 Research and Innovation program under the Marie Skłodowska-Curie grant agreement no. 765445.

Author information

Author notes

1. These authors contributed equally: Ganesh R. Pathare, Alexiane Decout

Affiliations

1. Friedrich Miescher Institute for Biomedical Research, Basel, Switzerland

Ganesh R. Pathare, Simone Cavadini, Georg Kempf, Joscha Weiss, Zuzanna Kozicka & Nicolas H. Thomä

2. University of Basel, Basel, Switzerland

Ganesh R. Pathare, Simone Cavadini, Georg Kempf, Joscha Weiss, Zuzanna Kozicka & Nicolas H. Thomä

3. Global Health Institute, Swiss Federal Institute of Technology Lausanne (EPFL), Lausanne, Switzerland

Alexiane Decout, Selene Glück, Baptiste Guey, Pauline Melenec & Andrea Ablasser

4. Institute of Chemical Sciences and Engineering, Swiss Federal Institute of Technology Lausanne (EPFL), Lausanne, Switzerland

Kristina Makasheva, Ruud Hovius & Beat Fierz

Authors

1. Ganesh R. Pathare

[View author publications](#)

You can also search for this author in [PubMed](#) [Google Scholar](#)

2. Alexiane Decout

[View author publications](#)

You can also search for this author in [PubMed](#) [Google Scholar](#)

3. Selene Glück

[View author publications](#)

You can also search for this author in [PubMed](#) [Google Scholar](#)

4. Simone Cavadini

[View author publications](#)

You can also search for this author in [PubMed](#) [Google Scholar](#)

5. Kristina Makasheva

[View author publications](#)

You can also search for this author in [PubMed](#) [Google Scholar](#)

6. Ruud Hovius

[View author publications](#)

You can also search for this author in [PubMed](#) [Google Scholar](#)

7. Georg Kempf

[View author publications](#)

You can also search for this author in [PubMed](#) [Google Scholar](#)

8. Joscha Weiss

[View author publications](#)

You can also search for this author in [PubMed](#) [Google Scholar](#)

9. Zuzanna Kozicka

[View author publications](#)

You can also search for this author in [PubMed](#) [Google Scholar](#)

10. Baptiste Guey

[View author publications](#)

You can also search for this author in [PubMed](#) [Google Scholar](#)

11. Pauline Melenec

[View author publications](#)

You can also search for this author in [PubMed](#) [Google Scholar](#)

12. Beat Fierz

[View author publications](#)

You can also search for this author in [PubMed](#) [Google Scholar](#)

13. Nicolas H. Thomä

[View author publications](#)

You can also search for this author in [PubMed](#) [Google Scholar](#)

14. Andrea Ablasser

[View author publications](#)

You can also search for this author in [PubMed](#) [Google Scholar](#)

Contributions

G.R.P. conducted the cryo-electron microscopy experiments and data processing with help from S.C. and G.K. for the model building. A.D. performed the in vitro assays and purified recombinant cGAS. S.G., P.M. and A.A. performed the cellular experiments. K.M. and R.H. purified recombinant histone proteins and assembled the recombinant nucleosomes and chromatin fibres. Electron microscopy samples were prepared by G.R.P. with help from J.W. Z.K. and J.W. performed the fluorescence polarization assays. B.G. performed the FRAP experiments. B.F. supervised experiments related to the in vitro reconstitution of nucleosomes/chromatin and provided valuable discussion. N.H.T. supervised the structural work and the biophysical assays. A.A. supervised the in vitro assays and cellular studies. N.H.T. and A.A. wrote the manuscript with input from all authors.

Corresponding authors

Correspondence to [Nicolas H. Thomä](#) or [Andrea Ablasser](#).

Ethics declarations

Competing interests

A.A. is a member of the scientific advisory board of IFM Therapeutics and scientific co-founder of IFM-Due.

Additional information

Peer review information *Nature* thanks Osamu Nureki and the other, anonymous, reviewer(s) for their contribution to the peer review of this work.

Publisher's note Springer Nature remains neutral with regard to jurisdictional claims in published maps and institutional affiliations.

Extended data figures and tables

Extended Data Fig. 1 H2A-H2B dimers bind to and inhibit cGAS.

a, Confocal microscopy images of human BJ fibroblasts stained with primary antibodies against cGAS (green) and H2B (red). DNA was stained with DAPI (blue). Scale bar, 25 μ m. **b**, Human BJ fibroblasts were treated with aclarubicin (20 μ M) as indicated. Differential nuclear salt fractions were obtained, and the presence of the indicated proteins within each fraction was monitored by immunoblot. In **a** and **b**, the experiments were independently repeated at least three times. **c**, Human BJ fibroblasts were treated with DMSO (control) or aclarubicin (20 μ M) for 2 h. After fixation, cells were subjected to PLA with anti-cGAS, anti-H2B, and anti-H4, respectively. PLA signals were quantified from at least 50 individual cells. Representative images are displayed (left) and data (right) are mean \pm s.d. of one representative experiment out of $n = 3$ independent experiments. Two-tailed student's *t*-test. Scale bar, 20 μ m. **d**, Specificity control for PLA with human BJ fibroblasts using single antibody staining for cGAS, H2B, and H4, respectively. Scale bar, 20 μ m. The experiment was repeated three times with similar results. **e**, Relative levels of in vitro cGAMP synthesis in the presence or absence of a concentration gradient of nucleosomes (from 75 nM to 1 nM) and chromatin fibres (from 6 nM to 0.1 nM). **f**, **g**, Relative levels of in vitro cGAMP synthesis in the presence or absence of a concentration gradient of histone H2A, H2B or H2A-H2B dimers (from 5 μ M to 0.3125 μ M; 1:2 step dilutions) (**f**) or H3 and H4 (from 5 μ M to 0.3125 μ M) (**g**). cGAS (catalytic domain; aa 155-522; hcGAS) activation was induced by HT DNA and data are mean \pm s.d. of $n = 3$ independent experiments. One-way ANOVA with post hoc Dunnett multiple comparison test (**e–g**). **h**, Calculated IC₅₀ values without (IC₅₀) or with (cor. IC₅₀) correction for the number of cGAS binding sites per molecule (nucleosome or fibre). Data points are from experimentally independent experiments. For gel source data, see Supplementary Fig. 1.

Extended Data Fig. 2 Cryo-EM analysis of cGAS bound to nucleosomes.

a, Cryo-EM micrograph of the non-crosslinked sample containing wild-type cGAS(WT) bound to NCP. Scale bar, 20 nm (Micrograph is representative of 20 images taken). **b**, Cryo-EM micrograph of the non-crosslinked sample containing dimerization mutant cGAS(K392E) bound to NCP. Scale bar, 20 nm (Micrograph is representative of 20 images taken). The cGAS-NCP complexes were directly concentrated and frozen on grids after gel filtration chromatography. Chromatin fibres induced by cGAS binding are highlighted by white rectangles (**a**, **b**). **c**, **d**, Magnified view of oligomeric assemblies extracted from **a** and **b** (starred rectangles), respectively.

Extended Data Fig. 3 Schematics of cGAS-NCP structure determination, classification and refinements.

a, Representative denoised cryo-EM micrograph of cGAS-NCP complex derived using JANNI ($n = 2,890$ micrographs). Scale bar, 20 nm. **b**, Reference-free 2D class averages of the particles picked using crYOLO. **c**, Data processing scheme starting with an ab initio model derived from 2D classes (**b**) for 34,000 particles. The scheme is divided into two separate data sets. On the right, data processing for the a 4.1 Å dimeric structure of 2NCP-2cGAS. 103,688 particles were subjected to 3D classification using RELION 3.0⁴² leading to four classes. The best class containing dimeric particles with 2NCP-2cGAS was further subjected to a second round of 3D classification producing two classes. The class containing 13,943 dimeric particles was further polished, 3D refined using RELION 3.0 and later CTF refined using cryoSPARC⁴⁰, generating a 4.1 Å map. The left side of the scheme shows the data processing for the 3.1 Å structure of 1NCP-1cGAS. 289,518 particles were subjected to 3D classification using RELION 3.0⁴² resulting in four classes. The best class containing 87,323 dimeric particles with 2NCP-2cGAS was further polished and merged with the 13,943 particles used for 4.1 Å map. The merged particles were subjected to CTF refinement and signal subtraction for the density accounting for 1cGAS-1NCP. 3D classification followed by non-uniform refinement in cryoSPARC led to a 3.1 Å map. **d**, Gold-standard Fourier

shell correlation curves are shown for the 3.1 Å monomer map (blue) and the 4.1 Å dimer map (orange). **e, f**, Local resolution filtered maps (MonoRes) for the 4.1 Å dimer map and 3.1 Å monomer map, respectively. **g, h**, Angular distribution plots shown for the 3.1 Å monomer map and 4.1 Å dimer map respectively.

Extended Data Fig. 4 Cryo-EM structure of wild-type cGAS bound to nucleosomes.

a, A 5.1 Å 3D reconstruction of the complex containing two wild-type cGAS protomers, cGAS₁ (red) and cGAS₂ (orange), and two nucleosomal core particles, NCP1 and NCP2, respectively. **b**, Ribbon diagram of the dimerization mutant (K394E) NCP1-cGAS1-cGAS2-NCP2 model rigid-body fit into wild type NCP1-cGAS1-cGAS2-NCP2 electron-density maps. **c**, 3D focused classification map of NCP1-cGAS1 shown at low contour levels. **d**, Magnified view of cGAS1 and NCP1 DNA interactions. The zinc ion (cyan sphere) is coordinated by residues H390, C396, C397 and C404 forming the zinc finger motif. Residue K394 (sapphire blue sphere), is part of loop coordinating the zinc ion and is positioned close to the DNA of NCP1. Electron density connecting the NCP1 DNA and the cGAS1 zinc ion coordinating loop is shown in the background. **e**, A 4.1 Å EM map of the dimerization mutant cGAS(K394E)-NCP complex. **f**, A 5.1 Å EM map of the wild-type cGAS-NCP complex. **g**, EM maps from the mutant cGAS-NCP complex (grey) (**e**) superposed onto the wild-type cGAS-NCP complex map (blue) (**f**). The map-to-map fit gives a correlation value of 0.87 (Extended Data Table [1\(b\)](#)).

Extended Data Fig. 5 Schematics of wild-type cGAS-NCP structure determination, classification and refinements.

a, Representative denoised cryo-EM micrograph of cGAS-NCP complex derived using JANNI ($n = 5,007$ micrographs). Scale bar, 25 nm. **b**, Reference-free 2D class averages of the particles picked using crYOLO. **c**, Data processing scheme starting with an ab initio model derived from 2Ds (**b**) is shown using 16,000 particles. The scheme is divided into two sub-schemes. The left side shows the processing of data for a 5.1 Å dimeric

structure of NCP1-WTcGAS1-WTcGAS1-NCP1. 142,743 particles were subjected to 3D hetero refinement classification using cryoSPARC leading to two classes. The best class containing dimeric particles with WTcGAS2-NCP2 was further subjected to local refinement and later CTF refined using cryoSPARC generating a 5.1 Å map. For the scheme on the right, 56,747 particles were subjected to particle subtraction. The class containing 56,747 dimeric particles with WTcGAS1-NCP1 was locally refined and later CTF refined using cryoSPARC generating a 4.7 Å map. **d**, Gold-standard Fourier shell correlation curves are shown for the reconstructions, 5.1 Å (blue) and 4.7 Å (red). **e**, Local resolution filtered maps (MonoRes) for the 5.1 Å dimer map. **f**, Local resolution filtered maps (MonoRes) for the 4.7 Å monomer map. **g**, Angular distribution for the dimer 5.1 Å map. **h**, Angular distribution for the 4.7 Å monomer map.

Extended Data Fig. 6 Interaction of cGAS1 with NCP1 and mechanism of inhibition.

a, Ribbon diagram and a 3D reconstruction of the complex containing cGAS1 (red) and NCP1 (grey, blue). **b–f**, EM densities (shown as mesh at 4.5σ) for the residues interacting with the nucleosome in *cis*. Shown are cGAS Loop1, Loop2 and Loop3 interactions in *cis* with H2A-H2B dimer respectively (**b–d**) and the interactions of cGAS helix α5 residues with the DNA backbone from NCP1 (**e, f**). **g**, Overview of the hcGAS-DNA 2:2 minimal cGAS-DNA active dimer complex to highlight the two distinct DNA-binding surfaces (A-site and B-site) as previously defined¹⁶ (PDB: 4LEY). **h**, Superposition of the hcGAS-DNA complex (**g**) onto the cGAS-NCP complex as defined in this work (Fig. 2g). **i**, Magnified view of the common binding site (B-site) showing the clash of the two DNA strands with the nucleosomal DNA (orange, ligand DNA and grey, nucleosomal DNA).

Extended Data Fig. 7 Interaction of cGAS with nucleosomes in vitro.

a, EMSA gel showing the interaction of nucleosomes (40 ng μl^{-1}) with WT cGAS (40 pmol) in presence of increasing concentrations of LANA peptide

WT or AA mutant (from 0.6 mg ml⁻¹ to 78 µg ml⁻¹; 1:2 step dilution). Dark grey arrowhead: nucleosomes complexed with cGAS, light grey arrowhead: free nucleosomes. Data are representative for three independent experiments. **b**, In vitro cGAMP synthesis of WT hcGAS (50 nM) with chromatin (5 nM) in presence of a gradient concentration of LANA peptide WT or AA mutated (from 0.5 mg ml⁻¹ to 0.125 mg ml⁻¹; 1:2 step dilution) normalized by cGAMP levels in absence of chromatin. Mean ± s.d. of $n = 3$ independent experiments is shown. One-way ANOVA with post hoc Dunnett multiple comparison test. Data points are from independent experiments. **c**, In vitro cGAMP synthesis of WT, R255A and R236A hcGAS (all 200 nM) with a concentration gradient of 147bp dsDNA or nucleosome (no DNA overhang) (left) or 227bp dsDNA or nucleosomes (80bp dsDNA overhang) (right) (from 200 nM to 50 nM; 1:2 step dilutions) normalized to cGAMP levels for 200 nM dsDNA for each individual mutant. Mean ± s.d. of $n = 3$ independent experiments is shown. **d**, Fluorescein (Flc) labelled 21 bp dsDNA tracer (10 nM) were mixed with cGAS protein (300 nM) and counter-titrated with unlabelled DNA (left) or nucleosomes (right) (see [Methods](#)). **e**, Forward titration experiments using 10 nM Flc-labelled probe in the presence of increasing amounts of either WT cGAS or cGAS pre-treated with 0.1-5 mM EDTA as indicated. **f**, Forward titration as in **a** but with cGAS K394E, either pre-treated with 0.1 mM EDTA or not. **g**, As in **(d)** but the cGAS protein was pre-treated with EDTA as indicated. For **d** and **g**, all data include two technical replicates and all data points are explicitly shown. Affinities are indicated as IC₅₀ values. For **e** and **f**, all data include three technical replicates and are shown as mean ± s.d. Affinities are indicated as apparent K_d (K_{app}) values. For gel source data, see Supplementary Fig. 1.

Extended Data Fig. 8 cGAS interactions with the second nucleosome in trans.

a, EM envelope of the dimeric complex containing NCP1-cGAS1-cGAS2-NCP2. **b**, A magnified view of an additional density accounting for N-terminal tail of histone H4. **c**, A 3D class showing the additional EM density found (dotted circles) near the outward facing acidic patch. The dimeric structure of NCP1-cGAS1-cGAS2-NCP2 is modelled into the

major density. **d**, Modelling of cGAS molecules on the outer sides of the two NCP molecules in the map (**c**) resulting in a complex of cGAS1'-NCP1-cGAS1-cGAS2-NCP2-cGAS2'. **e**, A representative micrograph containing a cGAS (WT)-NCP multimeric complex ($n = 20$ micrographs). **f**, Magnified view on oligomeric assemblies extracted from (**e**) (left), Scale bar, 10 nm, and a modelled arrangement of cGAS-NCP in cartoon representation (right). **g**, Differential nuclear salt fractions probed for cGAS and H2B by immunoblot from HeLa cGAS KO cells reconstituted with doxycycline-inducible WT cGAS or cGAS K285A/R300A/K427A after 2 days of doxycycline treatment. One representative experiment of $n = 3$ independent experiments is shown. For gel source data, see Supplementary Fig. 1.

Extended Data Fig. 9 Effect of structure-guided mutations in cells.

a, Lines show FRAP recovery curves obtained after photo-bleaching WT cGAS-GFP or cGAS-GFP mutants inside the nucleus of cGAS KO HeLa cells. Data show mean \pm SEM from 20-25 measurements. Graph is representative of $n = 3$ (left panel) or 4 (right panel) independent experiments. **b-d**, HeLa cGAS KO cells reconstituted with doxycycline-inducible WT cGAS or cGAS mutants were treated with doxycycline (1 μ g/ml) for 16h and 40h (**b**, **c**) or 40h (**d**), respectively. In **b**, cells were lysed and mRNA levels of *IFI44*, *IFIT2* and *CGAS* were assessed. Data are presented as fold induction relative to non-treated WT cGAS and are mean \pm s.d. of $n = 5$ independent experiments. Two-way ANOVA with post hoc Tukey multiple comparison test. In **c**, cells were lysed and STING and GAPDH levels were assessed by immunoblot. One representative experiment for $n = 3$ (16h) and $n = 3$ (40h) experiments with similar results is shown. In **d**, cells were stimulated with dsDNA (90mer) for 4h or left untreated (Ctrl.) and mRNA levels of *IFI44* and *IFIT2* were measured. Data show mean \pm s.d. of $n = 2$ independent experiments. Individual data points represent biological replicates. For gel source data, see Supplementary Fig. 1. **e**, cGAS multiple sequence alignments showing the sequence conservation of residues involved in interactions with the acidic patch, nucleosome binding in *cis*, and nucleosome binding in *trans*. cGAS sequences from human, monkey, bovine, pig, mouse and rat corresponding

to UniProt ID's Q8N884, F7B8L6, E1BGN7, I3LM39, Q8C6L5 and A0A0G2JVC4 have been used in the alignment. The key residues involved in the interactions are highlighted in cyan. The consensus sequence and logo representation of the residues is shown below the sequence alignment. The alignment figure was created using Jalview⁵².

Extended Data Table 1 Cryo-EM data statistics and comparison of WT cGAS and cGAS (K394) structures

[Full size table](#)

Supplementary information

[**Supplementary Figure**](#)

This file contains the uncropped blots.

[**Reporting Summary**](#)

[**Supplementary Video1**](#)

NCP1-cGAS1-cGAS2-NCP2 sandwich arrangement This file contains Supplementary Video1 which shows the surface and cartoon representation of the sandwich arrangement of NCP1-cGAS1-cGAS2-NCP2.

[**Supplementary Video2**](#)

NCP1-cGAS1 monomeric arrangement This file contains Supplementary Video2 which shows the surface and cartoon representation of monomeric arrangement of cGAS1 bound to NCP1.

[**Supplementary Video3**](#)

Structural insights into the cGAS1-NCP1 complex This file contains Supplementary Video3 which highlights the bipartite interactions of cGAS1 bound to NCP1 via Loop1, Loop2, Loo3 and the cGAS-DNA.

Supplementary Video4

Mechanism of cGAS inhibition by NCP1 This file contains Supplementary Video4 which shows how the cGAS activation is prevented by H2A-H2B dimer and also by nucleosome. Additionally, it highlights the steric clashes that occurs when a second cGAS1' molecule would try to dimerize with cGAS1.

Rights and permissions

Reprints and Permissions

About this article



Check for
updates

Cite this article

Pathare, G.R., Decout, A., Glück, S. *et al.* Structural mechanism of cGAS inhibition by the nucleosome. *Nature* **587**, 668–672 (2020).
<https://doi.org/10.1038/s41586-020-2750-6>

Download citation

- Received: 25 February 2020
- Accepted: 22 July 2020
- Published: 10 September 2020
- Issue Date: 26 November 2020
- DOI: <https://doi.org/10.1038/s41586-020-2750-6>

Further reading

- [Keeping innate immune response in check: when cGAS meets the nucleosome](#)

- Wei Xie
- & Dinshaw J. Patel

Cell Research (2020)

- [Structural basis for nucleosome-mediated inhibition of cGAS activity](#)

- Duanfang Cao
- , Xiaonan Han
- , Xiaoyi Fan
- , Rui-Ming Xu
- & Xinzheng Zhang

Cell Research (2020)

Comments

By submitting a comment you agree to abide by our [Terms](#) and [Community Guidelines](#). If you find something abusive or that does not comply with our terms or guidelines please flag it as inappropriate.

[Access through your institution](#)

[Change institution](#)

[Buy or subscribe](#)

This article was downloaded by **calibre** from <https://www.nature.com/articles/s41586-020-2750-6>

- Article
- [Published: 10 September 2020](#)

The molecular basis of tight nuclear tethering and inactivation of cGAS

- [Baoyu Zhao^{1 na1}](#),
- [Pengbiao Xu ORCID: orcid.org/0000-0003-0098-8875^{1 na1}](#),
- [Chesley M. Rowlett ORCID: orcid.org/0000-0003-1678-2206²](#),
- [Tao Jing¹](#),
- [Omkar Shinde ORCID: orcid.org/0000-0002-4219-5876¹](#),
- [Yuanjiu Lei ORCID: orcid.org/0000-0002-7486-4261³](#),
- [A. Phillip West ORCID: orcid.org/0000-0003-2884-6895³](#),
- [Wenshe Ray Liu ORCID: orcid.org/0000-0002-7078-6534^{1,2}](#) &
- [Pingwei Li ORCID: orcid.org/0000-0002-1815-3107¹](#)

[Nature](#) volume 587, pages673–677(2020)[Cite this article](#)

- 9700 Accesses
- 2 Citations
- 158 Altmetric
- [Metrics details](#)

Subjects

- [Electron microscopy](#)
- [Innate immunity](#)

Abstract

Nucleic acids derived from pathogens induce potent innate immune responses^{1,2,3,4,5,6}. Cyclic GMP–AMP synthase (cGAS) is a double-stranded DNA sensor that catalyses the synthesis of the cyclic dinucleotide cyclic GMP–AMP, which mediates the induction of type I interferons through the STING–TBK1–IRF3 signalling axis^{7,8,9,10,11}. cGAS was previously thought to not react with self DNA owing to its cytosolic localization^{2,12,13}; however, recent studies have shown that cGAS is localized mostly in the nucleus and has low activity as a result of tight nuclear tethering^{14,15,16,17,18}. Here we show that cGAS binds to nucleosomes with nanomolar affinity and that nucleosome binding potently inhibits its catalytic activity. To elucidate the molecular basis of cGAS inactivation by nuclear tethering, we determined the structure of mouse cGAS bound to human nucleosome by cryo-electron microscopy. The structure shows that cGAS binds to a negatively charged acidic patch formed by histones H2A and H2B via its second DNA-binding site¹⁹. High-affinity nucleosome binding blocks double-stranded DNA binding and maintains cGAS in an inactive conformation. Mutations of cGAS that disrupt nucleosome binding alter cGAS-mediated signalling in cells.

[Access through your institution](#)

[Change institution](#)

[Buy or subscribe](#)

Access options

Subscription info for Chinese customers

We have a dedicated website for our Chinese customers. Please go to naturechina.com to subscribe to this journal.

[Go to naturechina.com](#)

Rent or Buy article

Get time limited or full article access on ReadCube.

from \$8.99

[Rent or Buy](#)

All prices are NET prices.

Additional access options:

- [Log in](#)
- [Access through your institution](#)
- [Learn about institutional subscriptions](#)

Fig. 1: Tight nucleosome binding inactivates cGAS.



Fig. 2: Cryo-EM structure of mouse cGAS catalytic domain bound to human nucleosome.

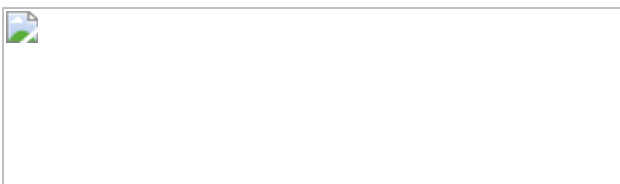


Fig. 3: Interactions between cGAS and the nucleosome.



Fig. 4: Mutations at the cGAS–nucleosome interface affect nucleosome binding, dsDNA binding, cGAS activity and cGAS-mediated signalling.



Data availability

The three-dimensional cryo-EM density maps are deposited into the Electron Microscopy Data Bank (EMDB) under accession numbers [EMD-22046](#), [EMD-22206](#) and [EMD-22047](#). The coordinates were deposited in the Protein Data Bank (PDB) with accession numbers [6X59](#), [6XJD](#) and [6X5A](#). [Source data](#) are provided with this paper.

References

1. 1.

Wu, J. & Chen, Z. J. Innate immune sensing and signaling of cytosolic nucleic acids. *Annu. Rev. Immunol.* **32**, 461–488 (2014).

[CAS](#) [Article](#) [Google Scholar](#)

2. 2.

Hopfner, K. P. & Hornung, V. Molecular mechanisms and cellular functions of cGAS–STING signalling. *Nat. Rev. Mol. Cell Biol.* **21**, 501–521 (2020).

[CAS](#) [Article](#) [Google Scholar](#)

3. 3.

Roers, A., Hiller, B. & Hornung, V. Recognition of endogenous nucleic acids by the innate immune system. *Immunity* **44**, 739–754 (2016).

[CAS](#) [Article](#) [Google Scholar](#)

4. 4.

Kato, H., Takahasi, K. & Fujita, T. RIG-I-like receptors: cytoplasmic sensors for non-self RNA. *Immunol. Rev.* **243**, 91–98 (2011).

[Article](#) [Google Scholar](#)

5. 5.

Paludan, S. R. & Bowie, A. G. Immune sensing of DNA. *Immunity* **38**, 870–880 (2013).

[CAS](#) [Article](#) [Google Scholar](#)

6. 6.

Ablasser, A. & Chen, Z. J. cGAS in action: Expanding roles in immunity and inflammation. *Science* **363**, eaat8657 (2019).

[CAS](#) [Article](#) [Google Scholar](#)

7. 7.

Burdette, D. L. & Vance, R. E. STING and the innate immune response to nucleic acids in the cytosol. *Nat. Immunol.* **14**, 19–26 (2013).

[CAS](#) [Article](#) [Google Scholar](#)

8. 8.

Barber, G. N. Innate immune DNA sensing pathways: STING, AIMII and the regulation of interferon production and inflammatory responses. *Curr. Opin. Immunol.* **23**, 10–20 (2011).

[CAS](#) [Article](#) [Google Scholar](#)

9. 9.

Ablasser, A. et al. cGAS produces a 2'-5'-linked cyclic dinucleotide second messenger that activates STING. *Nature* **498**, 380–384 (2013).

[ADS](#) [CAS](#) [Article](#) [Google Scholar](#)

10. 10.

Gao, P. et al. Cyclic [G(2',5')pA(3',5')p] is the metazoan second messenger produced by DNA-activated cyclic GMP-AMP synthase. *Cell* **153**, 1094–1107 (2013).

[CAS](#) [Article](#) [Google Scholar](#)

11. 11.

Zhao, B. et al. A conserved PLPLRT/SD motif of STING mediates the recruitment and activation of TBK1. *Nature* **569**, 718–722 (2019).

[ADS](#) [CAS](#) [Article](#) [Google Scholar](#)

12. 12.

Stetson, D. B. & Medzhitov, R. Recognition of cytosolic DNA activates an IRF3-dependent innate immune response. *Immunity* **24**, 93–103 (2006).

[CAS](#) [Article](#) [Google Scholar](#)

13. 13.

Sun, L., Wu, J., Du, F., Chen, X. & Chen, Z. J. Cyclic GMP-AMP synthase is a cytosolic DNA sensor that activates the type I interferon pathway. *Science* **339**, 786–791 (2013).

[ADS](#) [CAS](#) [Article](#) [Google Scholar](#)

14. 14.

Volkman, H. E., Cambier, S., Gray, E. E. & Stetson, D. B. Tight nuclear tethering of cGAS is essential for preventing autoreactivity. *eLife* **8**, e47491 (2019).

[CAS](#) [Article](#) [Google Scholar](#)

15. 15.

Zierhut, C. et al. The cytoplasmic DNA sensor cGAS promotes mitotic cell death. *Cell* **178**, 302–315 (2019).

[CAS](#) [Article](#) [Google Scholar](#)

16. 16.

Jiang, H. et al. Chromatin-bound cGAS is an inhibitor of DNA repair and hence accelerates genome destabilization and cell death. *EMBO J.* **38**, e102718 (2019).

[CAS](#) [Article](#) [Google Scholar](#)

17. 17.

Gentili, M. et al. The N-terminal domain of cGAS determines preferential association with centromeric DNA and innate immune activation in the nucleus. *Cell Rep.* **26**, 2377–2393 (2019).

[CAS](#) [Article](#) [Google Scholar](#)

18. 18.

Liu, H. et al. Nuclear cGAS suppresses DNA repair and promotes tumorigenesis. *Nature* **563**, 131–136 (2018).

[ADS](#) [CAS](#) [Article](#) [Google Scholar](#)

19. 19.

Li, X. et al. Cyclic GMP-AMP synthase is activated by double-stranded DNA-induced oligomerization. *Immunity* **39**, 1019–1031 (2013).

[CAS](#) [Article](#) [Google Scholar](#)

20. 20.

Wang, W. W., Zeng, Y., Wu, B., Deiters, A. & Liu, W. R. A chemical biology approach to reveal Sirt6-targeted histone H3 sites in nucleosomes. *ACS Chem. Biol.* **11**, 1973–1981 (2016).

[CAS](#) [Article](#) [Google Scholar](#)

21. 21.

Tachiwana, H. et al. Structural basis of instability of the nucleosome containing a testis-specific histone variant, human H3T. *Proc. Natl Acad. Sci. USA* **107**, 10454–10459 (2010).

[ADS](#) [CAS](#) [Article](#) [Google Scholar](#)

22. 22.

Liebschner, D. et al. Macromolecular structure determination using X-rays, neutrons and electrons: recent developments in Phenix. *Acta Crystallogr. D* **75**, 861–877 (2019).

[CAS](#) [Article](#) [Google Scholar](#)

23. 23.

Emsley, P., Lohkamp, B., Scott, W. G. & Cowtan, K. Features and development of Coot. *Acta Crystallogr. D* **66**, 486–501 (2010).

[CAS](#) [Article](#) [Google Scholar](#)

[Download references](#)

Acknowledgements

We acknowledge University of Texas, McGovern Medical School in Houston for providing access to their cryo-EM facility for data collection. We thank V. Mallampalli, G. Fan and I. Serysheva for assistance with cryo-EM data collection and Z. Cui at Texas A&M University for assistance with cryo-EM data processing. This research was supported in part by the Welch Foundation (Grants A-1931-20170325 to P.L. and A-1715 to W.R.L.) and National Institutes of Health (Grants R01 AI145287 to P.L., R01 GM121584 and R01 GM127575 to W.R.L.). A.P.W. and Y.L. were supported by NIH grant R01 HL148153 and award W81XWH-17-1-0052 through the Office of the Assistant Secretary of Defense for Health Affairs, Peer Reviewed Medical Research Programs.

Author information

Author notes

1. These authors contributed equally: Baoyu Zhao, Pengbiao Xu

Affiliations

1. Department of Biochemistry and Biophysics, Texas A&M University, College Station, TX, USA

Baoyu Zhao, Pengbiao Xu, Tao Jing, Omkar Shinde, Wenshe Ray Liu & Pingwei Li

2. Department of Chemistry, Texas A&M University, College Station, TX, USA

Chesley M. Rowlett & Wenshe Ray Liu

3. Department of Microbial Pathogenesis and Immunology, Texas A&M University Health Science Center, College Station, TX, USA

Yuanjiu Lei & A. Phillip West

Authors

1. Baoyu Zhao

[View author publications](#)

You can also search for this author in [PubMed](#) [Google Scholar](#)

2. Pengbiao Xu

[View author publications](#)

You can also search for this author in [PubMed](#) [Google Scholar](#)

3. Chesley M. Rowlett

[View author publications](#)

You can also search for this author in [PubMed](#) [Google Scholar](#)

4. Tao Jing

[View author publications](#)

You can also search for this author in [PubMed](#) [Google Scholar](#)

5. Omkar Shinde

[View author publications](#)

You can also search for this author in [PubMed](#) [Google Scholar](#)

6. Yuanjiu Lei

[View author publications](#)

You can also search for this author in [PubMed](#) [Google Scholar](#)

7. A. Phillip West

[View author publications](#)

You can also search for this author in [PubMed](#) [Google Scholar](#)

8. Wenshe Ray Liu

[View author publications](#)

You can also search for this author in [PubMed](#) [Google Scholar](#)

9. Pingwei Li

[View author publications](#)

You can also search for this author in [PubMed](#) [Google Scholar](#)

Contributions

P.L. conceived the study. B.Z. and P.X. expressed proteins, conducted binding studies and determined the structures. C.M.R. prepared the reconstituted nucleosome. T.J. conducted the binding studies and generated and purified the cGAS mutants. O.S. purified the cGAS mutants. Y.L. and

A.P.W. studied the nuclear localization of cGAS. B.Z., P.X., W.R.L. and P.L. wrote the paper.

Corresponding authors

Correspondence to [Wenshe Ray Liu](#) or [Pingwei Li](#).

Ethics declarations

Competing interests

The authors declare no competing interests.

Additional information

Peer review information *Nature* thanks Yuan He, Jae U Jung and the other, anonymous, reviewer(s) for their contribution to the peer review of this work. Peer reviewer reports are available.

Publisher's note Springer Nature remains neutral with regard to jurisdictional claims in published maps and institutional affiliations.

Extended data figures and tables

[Extended Data Fig. 1 cGAS binds tightly with nucleosome.](#)

a, Gel-filtration chromatography and SDS–PAGE analyses of nucleosomes purified from HEK293T cells. **b**, Gel-filtration chromatography and SDS–PAGE analyses of the in vitro reconstituted nucleosomes. **c**, Gel-filtration chromatography showing that mouse cGAS catalytic domain binds to nucleosomes. **d**, SDS–PAGE analysis of nucleosome and mouse cGAS catalytic domain complex purified by gel-filtration chromatography. **e**, Polyacrylamide gel EMSA showing the interactions between mouse cGAS catalytic domain with reconstituted nucleosomes and nucleosomes purified from HEK293T cells. cGAS is mixed with nucleosomes at a molar ratio of

6:1. **f**, Agarose gel electrophoresis of the dsDNA from purified mononucleosomes and oligonucleosomes. The histones have been digested with proteinase K. **g**, SDS-PAGE analyses of purified mononucleosomes and oligonucleosomes. **h**, Polyacrylamide gel EMSA showing that mouse cGAS catalytic domain binds to mononucleosomes and oligonucleosomes (left panel). In the mixtures, the molar ratio of cGAS/mononucleosome is 3:1 and cGAS/oligonucleosome is 6:1. SDS-PAGE analyses of the input samples for EMSA were shown in the right panel. **i**, SDS-PAGE analyses of biotin-Avi-His₆-SUMO fusion of human and mouse cGAS full length and catalytic domain proteins used for nucleosome binding studies. [Source data](#)

Extended Data Fig. 2 cGAS-nucleosome binding studies and activity assays of cGAS-nucleosome complex.

a, SPR binding studies show that full-length human cGAS binds to nucleosomes purified from HEK293T cells with nanomolar affinity. **b**, SPR binding studies show that human cGAS catalytic domain binds to reconstituted nucleosomes with nanomolar affinity. **c**, **d**, Bio-layer interferometry binding studies of full-length human cGAS and its catalytic domain with nucleosomes (HEK293T). **e**, **f**, SPR binding studies show that full-length mouse cGAS and its catalytic domain bind nucleosomes (HEK293T) with nanomolar affinities. **g**, **h**, Bio-layer interferometry binding studies of full-length mouse cGAS and its catalytic domain with nucleosomes (HEK293T). **i**, Gel-filtration chromatography (top) and SDS-PAGE (bottom) analyses of 45-bp ISD dsDNA, nucleosome and cGAS mixture show that the nucleosome efficiently competes with dsDNA to bind cGAS. **j**, Agarose gel electrophoresis of the salmon sperm DNA used in cGAS activity assays. **k**, cGAS activity assays by ion exchange chromatography show that oligonucleosome binding potently inhibits the activity of cGAS and ligand-free cGAS can be activated by the cGAS-oligonucleosome complex. [Source data](#)

Extended Data Fig. 3 Cryo-EM analysis of mouse cGAS catalytic domain in complex with the reconstituted nucleosome.

a, Purification and SDS–PAGE analysis of nucleosomes from HEK293T cells in complex with mouse cGAS catalytic domain. **b**, Purification and SDS–PAGE analysis of reconstituted nucleosomes in complex with mouse cGAS catalytic domain. **c**, Representative micrograph of mouse cGAS - nucleosome complex in vitrified ice. Scale bar, 50 nm. **d**, 2D class averages of mouse cGAS-nucleosome complex particles. Scale bar, 10 nm. **e**, Flowchart of data processing; see [Methods](#) for details. **f**, Angular distribution of the mouse cGAS-nucleosome (1:1) particles included in the final reconstruction. **g**, Angular distribution of the mouse cGAS-nucleosome (2:1) particles included in the final reconstruction. **h**, Final 3D reconstruction of the mouse cGAS-nucleosome (1:1) complex, coloured according to the local resolution. **i**, Final 3D reconstruction of the mouse cGAS-nucleosome (2:1) complex, coloured according to the local resolution. **j**, Corrected Gold-standard Fourier shell correlation curves of the mouse cGAS-nucleosome (1:1) complex for the 3D electron microscopy reconstruction. **k**, Corrected Gold-standard Fourier shell correlation curves of the mouse cGAS-nucleosome (2:1) complex for the 3D electron microscopy reconstruction. **l**, Polyacrylamide gel shift assay (left) showing that one nucleosome can bind to two molecules of mouse cGAS catalytic domain. Nucleosome is mixed with mouse cGAS at molar ratio of 1:1, 1:2 and 1:3. SDS–PAGE analysis of the samples used for the gel shift assays was shown on right panel. **m**, Density map (contoured at 3σ) and structural model of mouse cGAS-nucleosome (2:1) complex at 6.8 Å resolution.

[Source data](#)

[Extended Data Fig. 4 Density maps and structural models of cGAS-nucleosome \(reconstituted, 1:1\) complex.](#)

a–f, The density maps (grey mesh) of histones H2A, H2B, H3, H4, part of mouse cGAS catalytic domain, and the Widom 601 nucleosome positioning sequence DNA contoured at 3σ . The protein and DNA structures fitted into the density map are shown by the stick models.

[Extended Data Fig. 5 Cryo-EM analysis of mouse cGAS domain in complex with nucleosome purified from HEK293T cells.](#)

a, Representative micrograph of mouse cGAS-nucleosome complex in vitrified ice. Scale bar, 50 nm. **b**, 2D class averages of mouse cGAS-nucleosome complex particles. Scale bar, 10 nm. **c**, Flowchart of data processing; see [Methods](#) for details. **d**, Angular distribution of particles included in the final reconstruction. **e**, Final 3D reconstruction, coloured according to the local resolution. **f**, Corrected Gold-standard Fourier shell correlation curves for the 3D electron microscopy reconstruction. **g**, Density map (contoured at 3σ) and structural model of cGAS-nucleosome (1:1) complex.

Extended Data Fig. 6 Mutations in the acidic patch of the nucleosome abolished cGAS binding.

a, Superposition of structures of ligand-free mouse cGAS (PDB, 4K8V), mouse cGAS in complex with dsDNA (PDB, 4LEY), and mouse cGAS bound to the nucleosome. **b**, Sequence alignment of human and mouse cGAS around the nucleosome binding site. The conserved basic residues around the nucleosome binding site are coloured red. Residues that abolish nucleosome binding when mutated are highlighted yellow. **c**, Superposition for the structures of ligand-free human cGAS (PDB, 4LEV), ligand-free mouse cGAS (PDB, 4K8V) and mouse cGAS bound to the nucleosome. **d**, Ni-NTA agarose pull-down assays of mouse cGAS catalytic domain by His-tagged H2A-H2B dimer. The 6A dimer contains mutations E61A, E64A, D90A, E91A, E92A of H2A and D51A of H2B. The 6K dimer contains mutations E61K, E64K, D90K, E91K, E92K of H2A and D51K of H2B. **e**, Sequence alignment of wild-type (WT) human H2A and human H2A.Bbd. The acidic patch residues of WT H2A are coloured red. **f**, Polyacrylamide gel shift assay (left) showing that the recombinant nucleosome variant (H2A.Bbd) does not bind to mouse cGAS catalytic domain. In this assay, mouse cGAS was mixed with nucleosomes at a molar ratio of 3:1. SDS-PAGE analysis of the samples for gel shift assay were shown on the right panel.

Extended Data Fig. 7 Characterization of mouse cGAS catalytic domain mutants and oligonucleosome binding studies.

a, SDS-PAGE analysis of mouse cGAS catalytic domain mutants used for the gel shift assays and enzyme activity assays. **b**, SDS-PAGE analysis of mouse cGAS and nucleosome mixture samples used for the gel shift assay. **c**, Polyacrylamide gel EMSA shows that mutations at the cGAS-nucleosome interface affect oligonucleosome binding by cGAS. In these samples, mouse cGAS was mixed with oligonucleosomes at a molar ratio of 6:1. The samples used for the binding studies were analysed by SDS-PAGE (right panel). **d**, Circular dichroism of mouse cGAS catalytic domain and its mutants used for gel shift assays and enzyme activity assays. cGAS mutants that have strong binding to nucleosomes are shown by the spectra on the left. cGAS mutants that have weak or no binding to nucleosomes are shown by the spectra on the right. [Source data](#)

Extended Data Fig. 8 Mutations at the cGAS-nucleosome interface affect nucleosome binding by human cGAS.

a, SDS-PAGE analysis of biotin-labelled full-length human cGAS mutants used for the SPR binding studies. **b–n**, SPR binding studies of full-length human cGAS mutants with reconstituted nucleosomes. [Source data](#)

Extended Data Fig. 9 Mutations at the cGAS-nucleosome interface affect dsDNA binding, cGAS activity and cGAS-mediated signalling.

a, Agarose gel shift assay shows that mutations at the nucleosome binding surface of human cGAS affect the binding of a 45-bp dsDNA. **b**, Enzyme activity assays of mouse cGAS catalytic domain mutants by ion exchange chromatography. In this assay, 2.5 µM mouse cGAS was incubated with 0.2 mg ml⁻¹ salmon sperm DNA. Wild-type mouse cGAS and negative control without DNA are coloured in green and blue. Mutations that abolish nucleosome binding are coloured red. The negative control mutation K382E is coloured orange. **c**, Enzyme activity assays of full-length human cGAS mutants by ion exchange chromatography. In this assay, 2.5 µM human cGAS was incubated with 0.2 mg ml⁻¹ salmon sperm DNA. WT human cGAS and negative control without DNA are coloured in green and blue. Mutations that abolish nucleosome binding are coloured red. The negative

control mutation K394E is coloured orange. **d**, IFN- β luciferase reporter assays show that mutations of human cGAS affect signalling in HEK293T cells. Luciferase reporter signals from the cells transfected with 0.025 ng cGAS and 0.4 ng STING are indicated by the orange bars, from cells transfected with 0.00625 ng cGAS and 0.4 ng STING by the cyan bars, from cells transfected with 0.025 ng cGAS, 0.4 ng STING, or the vector control by the green, brown and purple bars, respectively. The data (mean \pm s.e.m.) are representative of three independent experiments. Each dot represents a biological replicate ($n = 3$). Two-tailed Student's *t*-test: * $P < 0.05$, ** $P < 0.01$, *** $P < 0.001$; NS, not significant. **e**, Western blot shows that WT mouse cGAS and its mutants have similar expression level in the transfected HEK293T cells. **f**, Western blot shows WT human cGAS and its mutants have similar expression level in the transfected HEK293T cells. [Source data](#)

Extended Data Table 1 Cryo-EM data collection, refinement and validation statistics

[Full size table](#)

Supplementary information

[Supplementary Figure 1](#)

This file contains uncropped images with molecular mass markers.

[Reporting Summary](#)

[Peer Review File](#)

Source data

[Source Data Fig. 1](#)

[Source Data Fig. 4](#)

[Source Data Extended Data Fig. 1](#)

[Source Data Extended Data Fig. 2](#)

[Source Data Extended Data Fig. 3](#)

[Source Data Extended Data Fig. 7](#)

[Source Data Extended Data Fig. 8](#)

[Source Data Extended Data Fig. 9](#)

Rights and permissions

[Reprints and Permissions](#)

About this article



Check for
updates

Cite this article

Zhao, B., Xu, P., Rowlett, C.M. *et al.* The molecular basis of tight nuclear tethering and inactivation of cGAS. *Nature* **587**, 673–677 (2020).
<https://doi.org/10.1038/s41586-020-2749-z>

[Download citation](#)

- Received: 26 May 2020
- Accepted: 12 August 2020
- Published: 10 September 2020

- Issue Date: 26 November 2020
- DOI: <https://doi.org/10.1038/s41586-020-2749-z>

Further reading

- [**Keeping innate immune response in check: when cGAS meets the nucleosome**](#)

- Wei Xie
- & Dinshaw J. Patel

Cell Research (2020)

- [**Structural basis for nucleosome-mediated inhibition of cGAS activity**](#)

- Duanfang Cao
- , Xiaonan Han
- , Xiaoyi Fan
- , Rui-Ming Xu
- & Xinzheng Zhang

Cell Research (2020)

Comments

By submitting a comment you agree to abide by our [Terms](#) and [Community Guidelines](#). If you find something abusive or that does not comply with our terms or guidelines please flag it as inappropriate.

[Access through your institution](#)

[Change institution](#)

[Buy or subscribe](#)

| [Section menu](#) | [Main menu](#) |

- Article
- [Published: 10 September 2020](#)

Structural basis for sequestration and autoinhibition of cGAS by chromatin

- [Sebastian Michalski](#) [ORCID: orcid.org/0000-0002-8190-3855](#)^{1,2 na1},
- [Carina C. de Oliveira Mann](#)^{1,2 na1},
- [Che A. Stafford](#)^{1,2},
- [Gregor Witte](#) [ORCID: orcid.org/0000-0003-0313-0962](#)^{1,2},
- [Joseph Bartho](#) [ORCID: orcid.org/0000-0003-3853-2347](#)^{1,2},
- [Katja Lammens](#)^{1,2},
- [Veit Hornung](#) [ORCID: orcid.org/0000-0002-4150-194X](#)^{1,2} &
- [Karl-Peter Hopfner](#) [ORCID: orcid.org/0000-0002-4528-8357](#)^{1,2}

[Nature](#) volume 587, pages678–682(2020) [Cite this article](#)

- 9567 Accesses
- 4 Citations
- 247 Altmetric
- [Metrics details](#)

Subjects

- [Cryoelectron microscopy](#)
- [Pattern recognition receptors](#)

Abstract

Cyclic GMP–AMP synthase (cGAS) is an innate immune sensor for cytosolic microbial DNA¹. After binding DNA, cGAS synthesizes the messenger 2'3'-cyclic GMP–AMP (cGAMP)^{2,3,4}, which triggers cell-autonomous defence and the production of type I interferons and pro-inflammatory cytokines via the activation of STING⁵. In addition to responding to cytosolic microbial DNA, cGAS also recognizes mislocalized cytosolic self-DNA and has been implicated in autoimmunity and sterile inflammation^{6,7}. Specificity towards pathogen- or damage-associated DNA was thought to be caused by cytosolic confinement. However, recent findings place cGAS robustly in the nucleus^{8,9,10}, where tight tethering of chromatin is important to prevent autoreactivity to self-DNA⁸. Here we show how cGAS is sequestered and inhibited by chromatin. We provide a cryo-electron microscopy structure of the cGAS catalytic domain bound to a nucleosome, which shows that cGAS does not interact with the nucleosomal DNA, but instead interacts with histone 2A–histone 2B, and is tightly anchored to the ‘acidic patch’. The interaction buries the cGAS DNA-binding site B, and blocks the formation of active cGAS dimers. The acidic patch robustly outcompetes agonistic DNA for binding to cGAS, which suggests that nucleosome sequestration can efficiently inhibit cGAS, even when accessible DNA is nearby, such as in actively transcribed genomic regions. Our results show how nuclear cGAS is sequestered by chromatin and provides a mechanism for preventing autoreactivity to nuclear self-DNA.

[Access through your institution](#)

[Change institution](#)

[Buy or subscribe](#)

Access options

Subscription info for Chinese customers

We have a dedicated website for our Chinese customers. Please go to naturechina.com to subscribe to this journal.

[Go to naturechina.com](#)

Rent or Buy article

Get time limited or full article access on ReadCube.

from \$8.99

[Rent or Buy](#)

All prices are NET prices.

Additional access options:

- [Log in](#)
- [Access through your institution](#)
- [Learn about institutional subscriptions](#)

Fig. 1: Nucleosomes inhibit cGAS activity in the presence of DNA.



Fig. 2: Structure of the cGAS catalytic domain–nucleosome complex.



Fig. 3: cGAS is sequestered by the acidic patch of the nucleosome.



Fig. 4: Nucleosome sequestration sterically blocks cGAS activation.



Data availability

The electron density reconstruction and final model were deposited at the Electron Microscopy Data Bank (EMDB) with accession code [EMD-11601](#), and the Protein Data Bank (PDB) with accession code [7A08](#). [Source data](#) are provided with this paper.

References

1. 1.

Sun, L., Wu, J., Du, F., Chen, X. & Chen, Z. J. Cyclic GMP-AMP synthase is a cytosolic DNA sensor that activates the type I interferon pathway. *Science* **339**, 786–791 (2013).

[ADS](#) [CAS](#) [PubMed](#) [Google Scholar](#)

2. 2.

Ablasser, A. et al. cGAS produces a 2'-5'-linked cyclic dinucleotide second messenger that activates STING. *Nature* **498**, 380–384 (2013).

[ADS](#) [CAS](#) [PubMed](#) [PubMed Central](#) [Google Scholar](#)

3. 3.

Gao, P. et al. Cyclic [G(2',5')pA(3',5')p] is the metazoan second messenger produced by DNA-activated cyclic GMP-AMP synthase. *Cell* **153**, 1094–1107 (2013).

[CAS](#) [PubMed](#) [PubMed Central](#) [Google Scholar](#)

4. 4.

Zhang, X. et al. Cyclic GMP-AMP containing mixed phosphodiester linkages is an endogenous high-affinity ligand for STING. *Mol. Cell* **51**, 226–235 (2013).

[CAS](#) [PubMed](#) [Google Scholar](#)

5. 5.

Hopfner, K. P. & Hornung, V. Molecular mechanisms and cellular functions of cGAS-STING signalling. *Nat. Rev. Mol. Cell Biol.* **21**, 501–521 (2020).

[CAS](#) [PubMed](#) [Google Scholar](#)

6. 6.

Ablasser, A. & Chen, Z. J. cGAS in action: Expanding roles in immunity and inflammation. *Science* **363**, eaat8657 (2019).

[CAS](#) [PubMed](#) [Google Scholar](#)

7. 7.

Motwani, M., Pesiridis, S. & Fitzgerald, K. A. DNA sensing by the cGAS-STING pathway in health and disease. *Nat. Rev. Genet.* **20**, 657–674 (2019).

[CAS](#) [PubMed](#) [Google Scholar](#)

8. 8.

Volkman, H. E., Cambier, S., Gray, E. E. & Stetson, D. B. Tight nuclear tethering of cGAS is essential for preventing autoreactivity. *eLife* **8**, e47491 (2019).

[CAS](#) [PubMed](#) [PubMed Central](#) [Google Scholar](#)

9. 9.

Jiang, H. et al. Chromatin-bound cGAS is an inhibitor of DNA repair and hence accelerates genome destabilization and cell death. *EMBO J.* **38**, e102718 (2019).

[CAS](#) [PubMed](#) [PubMed Central](#) [Google Scholar](#)

10. 10.

Gentili, M. et al. The N-terminal domain of cGAS determines preferential association with centromeric dna and innate immune activation in the nucleus. *Cell Rep.* **26**, 2377–2393 (2019).

[CAS](#) [PubMed](#) [PubMed Central](#) [Google Scholar](#)

11. 11.

Kranzusch, P. J. cGAS and CD-NTase enzymes: structure, mechanism, and evolution. *Curr. Opin. Struct. Biol.* **59**, 178–187 (2019).

[CAS](#) [PubMed](#) [PubMed Central](#) [Google Scholar](#)

12. 12.

Civril, F. et al. Structural mechanism of cytosolic DNA sensing by cGAS. *Nature* **498**, 332–337 (2013).

[ADS](#) [CAS](#) [PubMed](#) [PubMed Central](#) [Google Scholar](#)

13. 13.

Li, X. et al. Cyclic GMP-AMP synthase is activated by double-stranded DNA-induced oligomerization. *Immunity* **39**, 1019–1031 (2013).

[CAS](#) [PubMed](#) [Google Scholar](#)

14. 14.

Zhang, X. et al. The cytosolic DNA sensor cGAS forms an oligomeric complex with DNA and undergoes switch-like conformational changes in the activation loop. *Cell Rep.* **6**, 421–430 (2014).

[CAS](#) [PubMed](#) [PubMed Central](#) [Google Scholar](#)

15. 15.

Andreeva, L. et al. cGAS senses long and HMGB/TFAM-bound U-turn DNA by forming protein-DNA ladders. *Nature* **549**, 394–398 (2017).

[ADS](#) [CAS](#) [PubMed](#) [Google Scholar](#)

16. 16.

Du, M. & Chen, Z. J. DNA-induced liquid phase condensation of cGAS activates innate immune signaling. *Science* **361**, 704–709 (2018).

[ADS](#) [CAS](#) [PubMed](#) [Google Scholar](#)

17. 17.

Xie, W. et al. Human cGAS catalytic domain has an additional DNA-binding interface that enhances enzymatic activity and liquid-phase condensation. *Proc. Natl Acad. Sci. USA* **116**, 11946–11955 (2019).

[CAS](#) [PubMed](#) [Google Scholar](#)

18. 18.

Hooy, R. M. & Sohn, J. The allosteric activation of cGAS underpins its dynamic signaling landscape. *eLife* **7**, e39984 (2018).

[PubMed](#) [PubMed Central](#) [Google Scholar](#)

19. 19.

Herzner, A. M. et al. Sequence-specific activation of the DNA sensor cGAS by Y-form DNA structures as found in primary HIV-1 cDNA. *Nat. Immunol.* **16**, 1025–1033 (2015).

[CAS](#) [PubMed](#) [PubMed Central](#) [Google Scholar](#)

20. 20.

Mackenzie, K. J. et al. cGAS surveillance of micronuclei links genome instability to innate immunity. *Nature* **548**, 461–465 (2017).

[ADS](#) [CAS](#) [PubMed](#) [PubMed Central](#) [Google Scholar](#)

21. 21.

Liu, H. et al. Nuclear cGAS suppresses DNA repair and promotes tumorigenesis. *Nature* **563**, 131–136 (2018).

[ADS](#) [CAS](#) [PubMed](#) [Google Scholar](#)

22. 22.

Zierhut, C. et al. The cytoplasmic DNA sensor cGAS promotes mitotic cell death. *Cell* **178**, 302–315 (2019).

[CAS](#) [PubMed](#) [PubMed Central](#) [Google Scholar](#)

23. 23.

McGinty, R. K. & Tan, S. Recognition of the nucleosome by chromatin factors and enzymes. *Curr. Opin. Struct. Biol.* **37**, 54–61 (2016).

[CAS](#) [PubMed](#) [PubMed Central](#) [Google Scholar](#)

24. 24.

Arya, G. & Schlick, T. A tale of tails: how histone tails mediate chromatin compaction in different salt and linker histone environments. *J. Phys. Chem. A* **113**, 4045–4059 (2009).

[CAS](#) [PubMed](#) [PubMed Central](#) [Google Scholar](#)

25. 25.

Kalia, R. et al. Structural basis of mitochondrial receptor binding and constriction by DRP1. *Nature* **558**, 401–405 (2018).

[ADS](#) [CAS](#) [PubMed](#) [PubMed Central](#) [Google Scholar](#)

26. 26.

Harding, S. M. et al. Mitotic progression following DNA damage enables pattern recognition within micronuclei. *Nature* **548**, 466–470 (2017).

[ADS](#) [CAS](#) [PubMed](#) [PubMed Central](#) [Google Scholar](#)

27. 27.

Dou, Z. et al. Cytoplasmic chromatin triggers inflammation in senescence and cancer. *Nature* **550**, 402–406 (2017).

[ADS](#) [CAS](#) [PubMed](#) [PubMed Central](#) [Google Scholar](#)

28. 28.

Seo, G. J. et al. TRIM56-mediated monoubiquitination of cGAS for cytosolic DNA sensing. *Nat. Commun.* **9**, 613 (2018).

[ADS](#) [PubMed](#) [PubMed Central](#) [Google Scholar](#)

29. 29.

Klinker, H., Haas, C., Harrer, N., Becker, P. B. & Mueller-Planitz, F. Rapid purification of recombinant histones. *PLoS One* **9**, e104029 (2014).

[ADS](#) [PubMed](#) [PubMed Central](#) [Google Scholar](#)

30. 30.

Huynh, V. A., Robinson, P. J. & Rhodes, D. A method for the in vitro reconstitution of a defined “30 nm” chromatin fibre containing stoichiometric amounts of the linker histone. *J. Mol. Biol.* **345**, 957–968 (2005).

[CAS](#) [PubMed](#) [Google Scholar](#)

31. 31.

Rogge, R. A. et al. Assembly of nucleosomal arrays from recombinant core histones and nucleosome positioning DNA. *J. Vis. Exp.* **79**, e50354 (2013).

[Google Scholar](#)

32. 32.

Rueden, C. T. et al. ImageJ2: ImageJ for the next generation of scientific image data. *BMC Bioinformatics* **18**, 529 (2017).

[PubMed](#) [PubMed Central](#) [Google Scholar](#)

33. 33.

Zheng, S. Q. et al. MotionCor2: anisotropic correction of beam-induced motion for improved cryo-electron microscopy. *Nat. Methods* **14**, 331–332 (2017).

[CAS](#) [PubMed](#) [PubMed Central](#) [Google Scholar](#)

34. 34.

Rohou, A. & Grigorieff, N. CTFFIND4: fast and accurate defocus estimation from electron micrographs. *J. Struct. Biol.* **192**, 216–221 (2015).

[PubMed](#) [PubMed Central](#) [Google Scholar](#)

35. 35.

Scheres, S. H. RELION: implementation of a Bayesian approach to cryo-EM structure determination. *J. Struct. Biol.* **180**, 519–530 (2012).

[CAS](#) [PubMed](#) [PubMed Central](#) [Google Scholar](#)

36. 36.

Punjani, A., Rubinstein, J. L., Fleet, D. J. & Brubaker, M. A. cryoSPARC: algorithms for rapid unsupervised cryo-EM structure determination. *Nat. Methods* **14**, 290–296 (2017).

[CAS](#) [Google Scholar](#)

37. 37.

Tan, Y. Z. et al. Addressing preferred specimen orientation in single-particle cryo-EM through tilting. *Nat. Methods* **14**, 793–796 (2017).

[CAS](#) [PubMed](#) [PubMed Central](#) [Google Scholar](#)

38. 38.

Pettersen, E. F. et al. UCSF Chimera—a visualization system for exploratory research and analysis. *J. Comput. Chem.* **25**, 1605–1612 (2004).

[CAS](#) [PubMed](#) [PubMed Central](#) [Google Scholar](#)

39. 39.

Emsley, P. & Cowtan, K. Coot: model-building tools for molecular graphics. *Acta Crystallogr. D* **60**, 2126–2132 (2004).

[PubMed](#) [PubMed Central](#) [Google Scholar](#)

40. 40.

Goddard, T. D. et al. UCSF ChimeraX: meeting modern challenges in visualization and analysis. *Protein Sci.* **27**, 14–25 (2018).

[CAS](#) [PubMed](#) [Google Scholar](#)

41. 41.

Schmid-Burgk, J. L. et al. OutKnocker: a web tool for rapid and simple genotyping of designer nuclease edited cell lines. *Genome Res.* **24**, 1719–1723 (2014).

[CAS](#) [PubMed](#) [PubMed Central](#) [Google Scholar](#)

[Download references](#)

Acknowledgements

We thank K. Schall and V. Niebauer for guidance with nucleosome preparation and A. Drescher for discussions of SPR data. C.C.O.M. is supported as a Cancer Research Institute/Eugene V. Weissman Fellow. This work was supported by the German Research Council (grants CRC/TRR237 and the Gottfried Wilhelm Leibniz-Prize to K.-P.H. and V.H.; RTG1721 to K.-P.H. and G.W.; HO2489/8 to K.-P.H.; WI3717/3-1 to G.W.; and CRC1054 to K.L.).

Author information

Author notes

1. These authors contributed equally: Sebastian Michalski, Carina C. de Oliveira Mann

Affiliations

1. Gene Center, Ludwig-Maximilians-Universität, Munich, Germany

Sebastian Michalski, Carina C. de Oliveira Mann, Che A. Stafford, Gregor Witte, Joseph Bartho, Katja Lammens, Veit Hornung & Karl-Peter Hopfner

2. Department of Biochemistry, Ludwig-Maximilians-Universität, Munich, Germany

Sebastian Michalski, Carina C. de Oliveira Mann, Che A. Stafford, Gregor Witte, Joseph Bartho, Katja Lammens, Veit Hornung & Karl-Peter Hopfner

Authors

1. Sebastian Michalski

[View author publications](#)

You can also search for this author in [PubMed](#) [Google Scholar](#)

2. Carina C. de Oliveira Mann

[View author publications](#)

You can also search for this author in [PubMed](#) [Google Scholar](#)

3. Che A. Stafford

[View author publications](#)

You can also search for this author in [PubMed](#) [Google Scholar](#)

4. Gregor Witte

[View author publications](#)

You can also search for this author in [PubMed](#) [Google Scholar](#)

5. Joseph Bartho

[View author publications](#)

You can also search for this author in [PubMed](#) [Google Scholar](#)

6. Katja Lammens

[View author publications](#)

You can also search for this author in [PubMed](#) [Google Scholar](#)

7. Veit Hornung

[View author publications](#)

You can also search for this author in [PubMed](#) [Google Scholar](#)

8. Karl-Peter Hopfner

[View author publications](#)

You can also search for this author in [PubMed](#) [Google Scholar](#)

Contributions

C.C.O.M. and S.M. prepared cryo-EM samples and performed biochemical analysis. C.C.O.M., S.M. and J.B. optimized and screened cryo-EM grids. K.L. collected cryo-EM data. C.C.O.M. performed structure determination and model building with assistance from J.B. and K.L. SPR experiments were performed by G.W. C.S. performed cell-based assays and V.H. supervised cell-based experiments and interpreted data. C.C.O.M. and K.-P.H. designed the overall study, analysed the results and wrote the paper with contributions from all other authors.

Corresponding author

Correspondence to [Karl-Peter Hopfner](#).

Ethics declarations

Competing interests

The authors declare no competing interests.

Additional information

Peer review information *Nature* thanks Yuan He and the other, anonymous, reviewer(s) for their contribution to the peer review of this work. Peer reviewer reports are available.

Publisher's note Springer Nature remains neutral with regard to jurisdictional claims in published maps and institutional affiliations.

Extended data figures and tables

[Extended Data Fig. 1 cGAS binds nucleosomes even in the presence of free DNA.](#)

a, Gel-mobility shift binding analysis of purified cGAS and nucleosomes. Nucleosomes without linker DNA (0N0) were tested for binding to purified human (h) and mouse (m) full-length cGAS and cGAS^{cat}. Data are representative of two biological replicates. **b**, Human cGAS activity assay preincubated with dsDNA followed by titration of 0N0 nucleosomes. Data are representative of two biological replicates. [Source data](#)

[Extended Data Fig. 2 Cryo-EM data processing for cGAS–nucleosome structure.](#)

a, Representative micrograph of the dataset used to determine the cGAS–nucleosome complex structure. **b**, Left, final reconstruction of the cGAS–nucleosome complex coloured by local resolution. Right, representation of angular distribution of particles contributing to the final map. **c**, Histogram and directional Fourier shell correlation (FSC) plot for the final 3D reconstitution of the cGAS–nucleosome complex (3.11 Å). A sphericity of 0.9 was determined indicating very isotropic angular distribution (a value of

1 stands for completely isotropic angular distribution). The global resolution was determined to 3.11 Å (0.143 criterion). Directional FSC determination was performed with the 3DFSC software. **d**, Flow chart for image processing using RELION and cryoSPARC.

Extended Data Fig. 3 Sample density maps for cGAS-nucleosome structure.

a, Representative examples of cryo-EM map areas of cGAS, nucleosomal DNA and histones used for model building. **b**, Electron density for cGAS (blue) and H2A–H2B (yellow, red) interacting residues in interface I and interface II. cGAS tethering loops 1 and 2 with key interacting residues R222 and R241 are depicted as well as DNA-binding site B residues. Dashed lines represent hydrogen bonds.

Extended Data Fig. 4 Mutational analysis of binding interface between cGAS and the nucleosome.

a, Protein–protein residue interactions across the interface of cGAS with histone H2A and cGAS with histone H2B. Interacting amino acids are joined by coloured lines, each representing a different type of interaction, as per the key below. Interaction maps for the cGAS–nucleosome complex were generated using PDBsum. **b**, Thermal shift assay derivative melt curve plots of human cGAS^{cat} mutants. Respective inflection temperatures are: cGAS^{cat} 61.8 °C; cGAS^{cat}(K407E/K411E) 61.3 °C; cGAS^{cat}(C396A/C397A) (55.5 °C; cGAS^{cat}(R236E) 61.9 °C, cGAS^{cat}(R300E/K301E) 62.5 °C. Data are representative of two biological replicates. **c**, Coomassie stained SDS-PAGE gels of purified recombinant human and mouse cGAS (7 µg each) constructs used in this study. Gels are representative of one replicate. **d**, Representative EMSAs for mouse cGAS–nucleosome interface I and interface II mutants binding to fluorescently labelled nucleosomes. Data are representative of three biological replicates. **e**, EMSAs for mouse cGAS mutants in tethering loops 1 and 2 (R222E, R241E) and DNA-binding site B (R337E, R341E) binding to fluorescently labelled nucleosomal DNA. Data are representative of two biological replicates. **f**, EMSAs for human cGAS full-length and catalytic domain, DNA-binding site A

(K407E/K411E), Zn-thumb (C396A/C397A), site B (R236E) and site C (R300E/K301E) mutants binding to fluorescently labelled nucleosomes. Data are representative of two biological replicates. **g**, Representative EMSAs for mouse cGAS full-length binding to fluorescently labelled acidic patch mutant nucleosomes apI (H2A(E61A/E64A/D90A)) and apII (H2A(R71A), H2B(H49A/D51A)) and apI + apII (H2A(E61A/E64A/R71A/D90A/E92A), H2B(H49A/D51A)). Data are representative of three biological replicates. [Source data](#)

Extended Data Fig. 5 cGAS DNA-binding site B is required for cGAS tethering by the nucleosome.

a, SPR analysis of single-cycle-kinetics experiment with immobilized nucleosomes via biotinylated DNA and mouse cGAS^{cat} and cGAS^{cat}(R241E) mutant as analytes. Shown are injections of 1.1, 3.3, 9, 10, 30 and 90 nM mouse cGAS^{cat} and cGAS^{cat}(R241E). Data are representative of two biological replicates. **b**, SPR analysis with acidic patch mutant nucleosomes (H2A(E61A/E64A/D90A)) immobilized via biotinylated DNA and cGAS^{cat} as analyte. Shown are buffer injections, injections of 1.1, 3.3, 9, 10, 30 and 90 nM mouse cGAS^{cat} and the cGAS^{cat} background-corrected data. Mouse cGAS^{cat} has orders of magnitude lower affinity to acidic patch mutant nucleosomes than wild-type nucleosomes. Data are representative of two biological replicates. **c**, Human cGAS(R236E) mutant activity assay preincubated with dsDNA followed by titration of ON0 nucleosome. Data are representative of two biological replicates. **d**, Human cGAS(R236E) mutant activity assay pre-incubated with ON0 nucleosome followed by titration of dsDNA. Data are representative of two biological replicates. **e**, Mouse cGAS mutations tested affecting cGAS–nucleosome interactions were tested for DNA-dependent activation with plasmid DNA in the presence of ON0 nucleosomes. cGAMP production was assayed by thin-layer chromatography. Data are representative of two biological replicates. **f**, Mouse cGAS mutations affecting cGAS–nucleosome interactions were tested for DNA-dependent activation with 147-bp nucleosomal DNA in the presence of ON0 nucleosomes. Data are representative of two biological replicates. **g**, Mouse cGAS single and double mutations of tethering loop and DNA-binding site B were tested for

cGAMP production in the presence of plasmid DNA alone or plasmid DNA and ON0 nucleosome. Data are representative of two biological replicates. **h**, Mouse cGAS mutants R222E, K240E and R241E require plasmid DNA for activation. Data are representative of two biological replicates. **i**, Mouse cGAS mutants R222E, K240E and R241E were tested for DNA-dependent activation with plasmid DNA in the presence of ON0 nucleosomes. Mutation of DNA-binding site A abolishes activation by plasmid DNA. Data are representative of two biological replicates. **j**, Human cGAS activity assay in the presence of dsDNA, followed by titration of ON0 and ON0 acidic patch mutant I (apI; H2A(E61A/E64A/D90A)). Data are representative of two biological replicates. **k**, Wild-type and R236E mutant cGAS activity assays with 40N40 nucleosomes (40-bp linker DNA on each side). Data are representative of two biological replicates. **l**, Fluorescence anisotropy analysis of human cGAS^{cat} human cGAS^{cat} site A mutant (K407E/K411E) binding to fluorescently labelled 20-bp dsDNA and in the presence of ON0 nucleosomes. Data are representative of two biological replicates. **m**, Agarose gel of micrococcal nuclease (MNase)-digested synthetic 601 chromatin indicating a regular nucleosomal structure. Data are representative of two biological replicates. [Source data](#)

Extended Data Fig. 6 IP-10 cytokine and ISG production upon self and non-self DNA recognition.

a, PMA-differentiated wild-type or knockout human *CGAS*^{-/-} THP-1 cells were treated with doxycycline ($1 \mu\text{g ml}^{-1}$) overnight and either left untreated or treated with HT-DNA (975 ng per 550 μl) for 8 h. Cell lysates were separated on SDS-PAGE gels, western blotted and probed with the indicated antibodies. Data are representative of three biological replicates. **b**, PMA-differentiated THP-1 cells were left untreated or treated with doxycycline overnight to express the indicated human cGAS mutants, followed by stimulation using HT-DNA (200 ng per well) for 8 h. Supernatant was collected and IP-10 cytokines were measured from supernatant using ELISA. Data are mean and s.e.m. of four biological replicates. *** $P < 0.001$, ** $P < 0.01$, two-way ANOVA. ns, not significant. Doxycycline R236E $P < 0.001$; doxycycline R255E $P < 0.001$; doxycycline + HT-DNA R236E $P = 0.002$; doxycycline + HT-DNA R255E $P < 0.001$.

[Source data](#)

Extended Data Fig. 7 Structurally conserved loop for protein–protein interactions in MAB21 family nucleotidyltransferases.

Structures of cGAS–nucleosome (blue) and MID49–DRP1 (red, PDB code 5WP9). The structurally conserved loop is depicted in green, showing interacting residues. Dashed lines represent hydrogen bonds. Positively charged, basic amino acids on the nucleotidyltransferase loop interact with the acidic patch of the nucleosome or with the protein DRP1, respectively.

Extended Data Table 1 Cryo-EM data collection, refinement and validation statistics

[Full size table](#)

Supplementary information

[**Reporting Summary**](#)

[**Peer Review File**](#)

Source data

[**Source Data Fig. 1**](#)

[**Source Data Fig. 3**](#)

[**Source Data Extended Data Fig. 1**](#)

[**Source Data Extended Data Fig. 4**](#)

[**Source Data Extended Data Fig. 5**](#)

[**Source Data Extended Data Fig. 6**](#)

Rights and permissions

Reprints and Permissions

About this article



Check for
updates

Cite this article

Michalski, S., de Oliveira Mann, C.C., Stafford, C. *et al.* Structural basis for sequestration and autoinhibition of cGAS by chromatin. *Nature* **587**, 678–682 (2020). <https://doi.org/10.1038/s41586-020-2748-0>

Download citation

- Received: 13 May 2020
- Accepted: 24 August 2020
- Published: 10 September 2020
- Issue Date: 26 November 2020
- DOI: <https://doi.org/10.1038/s41586-020-2748-0>

Further reading

- **Regulation and inhibition of the DNA sensor cGAS**

- Jonny Hertzog
 - & Jan Rehwinkel

EMBO reports (2020)

- **Structural basis for nucleosome-mediated inhibition of cGAS activity**

- Duanfang Cao
- , Xiaonan Han
- , Xiaoyi Fan
- , Rui-Ming Xu
- & Xinzheng Zhang

Cell Research (2020)

- **Interrogating Host Antiviral Environments Driven by Nuclear DNA Sensing: A Multiomic Perspective**

- Timothy R. Howard
- & Ileana M. Cristea

Biomolecules (2020)

- **Keeping innate immune response in check: when cGAS meets the nucleosome**

- Wei Xie
- & Dinshaw J. Patel

Cell Research (2020)

Comments

By submitting a comment you agree to abide by our [Terms](#) and [Community Guidelines](#). If you find something abusive or that does not comply with our terms or guidelines please flag it as inappropriate.

[Access through your institution](#)

[Change institution](#)

[Buy or subscribe](#)

This article was downloaded by **calibre** from <https://www.nature.com/articles/s41586-020-2748-0>

| [Section menu](#) | [Main menu](#) |

- Article
- [Published: 18 November 2020](#)

Structural basis for the final steps of human 40S ribosome maturation

- [Michael Ameismeier](#) ORCID: [orcid.org/0000-0002-1194-3448¹](https://orcid.org/0000-0002-1194-3448),
- [Ivo Zemp²](#),
- [Jasmin van den Heuvel^{2,3}](#),
- [Matthias Thoms¹](#),
- [Otto Berninghausen](#) ORCID: [orcid.org/0000-0002-9255-0522¹](https://orcid.org/0000-0002-9255-0522),
- [Ulrike Kutay²](#) &
- [Roland Beckmann](#) ORCID: [orcid.org/0000-0003-4291-3898¹](https://orcid.org/0000-0003-4291-3898)

[Nature](#) volume 587, pages683–687(2020)[Cite this article](#)

- 1373 Accesses
- 106 Altmetric
- [Metrics details](#)

Subjects

- [Cryoelectron microscopy](#)
- [Molecular biology](#)
- [Ribosome](#)
- [RNA](#)

Abstract

Eukaryotic ribosomes consist of a small 40S and a large 60S subunit that are assembled in a highly coordinated manner. More than 200 factors ensure correct modification, processing and folding of ribosomal RNA and the timely incorporation of ribosomal proteins^{1,2}. Small subunit maturation ends in the cytosol, when the final rRNA precursor, 18S-E, is cleaved at site 3 by the endonuclease NOB1³. Previous structures of human 40S precursors have shown that NOB1 is kept in an inactive state by its partner PNO1⁴. The final maturation events, including the activation of NOB1 for the decisive rRNA-cleavage step and the mechanisms driving the dissociation of the last biogenesis factors have, however, remained unresolved. Here we report five cryo-electron microscopy structures of human 40S subunit precursors, which describe the compositional and conformational progression during the final steps of 40S assembly. Our structures explain the central role of RIOK1 in the displacement and dissociation of PNO1, which in turn allows conformational changes and activation of the endonuclease NOB1. In addition, we observe two factors, eukaryotic translation initiation factor 1A domain-containing protein (EIF1AD) and leucine-rich repeat-containing protein 47 (LRRC47), which bind to late pre-40S particles near RIOK1 and the central rRNA helix 44. Finally, functional data shows that EIF1AD is required for efficient assembly factor recycling and 18S-E processing. Our results thus enable a detailed understanding of the last steps in 40S formation in human cells and, in addition, provide evidence for principal differences in small ribosomal subunit formation between humans and the model organism *Saccharomyces cerevisiae*.

[Access through your institution](#)

[Change institution](#)

[Buy or subscribe](#)

Access options

Subscription info for Chinese customers

We have a dedicated website for our Chinese customers. Please go to naturechina.com to subscribe to this journal.

[Go to naturechina.com](http://naturechina.com)

Rent or Buy article

Get time limited or full article access on ReadCube.

from \$8.99

[Rent or Buy](#)

All prices are NET prices.

Additional access options:

- [Log in](#)
- [Access through your institution](#)
- [Learn about institutional subscriptions](#)

Fig. 1: Structures of human pre-40S ribosomal intermediates during final processing steps.

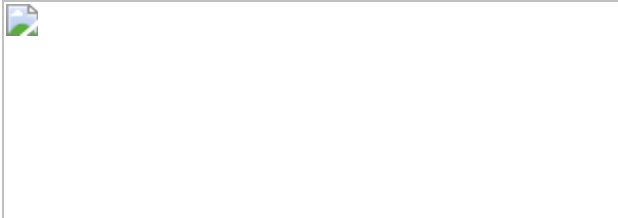


Fig. 2: Conformational rearrangements of RIOK1 coordinate late steps in 40S maturation.

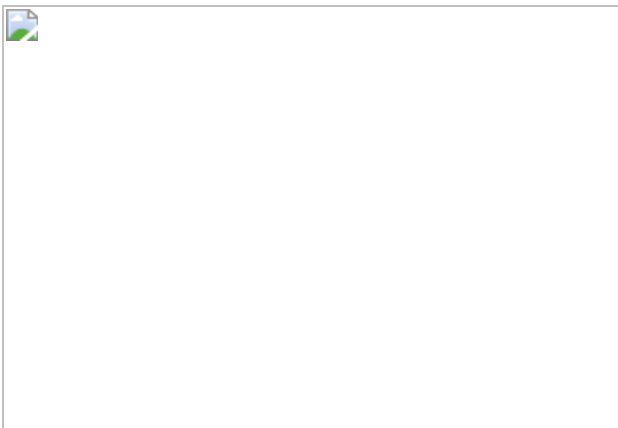


Fig. 3: Association of LRRC47 and EIF1AD with 40S subunit precursors.



Fig. 4: EIF1AD depletion leads to late cytoplasmic 40S maturation defects.



Fig. 5: Active conformation of NOB1 for site 3 cleavage.



Data availability

Cryo-EM density maps have been deposited in the Electron Microscopy Data Bank under the accession codes [EMD-11517](#), [EMD-11518](#), [EMD-11519](#), [EMD-11520](#) and [EMD-11521](#). The atomic models have been deposited in the Protein Data Bank under accession codes [6ZXD](#), [6ZXE](#), [6ZXF](#), [6ZXG](#) and [6ZXH](#).

References

1. 1.

Woolford, J. L. Jr & Baserga, S. J. Ribosome biogenesis in the yeast *Saccharomyces cerevisiae*. *Genetics* **195**, 643–681 (2013).

[CAS](#) [PubMed](#) [PubMed Central](#) [Google Scholar](#)

2. 2.

Bohnsack, K. E. & Bohnsack, M. T. Uncovering the assembly pathway of human ribosomes and its emerging links to disease. *EMBO J.* **38**, e100278 (2019).

[PubMed](#) [PubMed Central](#) [Google Scholar](#)

3. 3.

Henras, A. K., Plisson-Chastang, C., O'Donohue, M.-F., Chakraborty, A. & Gleizes, P.-E. An overview of pre-ribosomal RNA processing in eukaryotes. *Wiley Interdiscip. Rev. RNA* **6**, 225–242 (2015).

[CAS](#) [PubMed](#) [Google Scholar](#)

4. 4.

Ameismeier, M., Cheng, J., Berninghausen, O. & Beckmann, R. Visualizing late states of human 40S ribosomal subunit maturation. *Nature* **558**, 249–253 (2018).

[ADS](#) [CAS](#) [PubMed](#) [Google Scholar](#)

5. 5.

Cerezo, E. et al. Maturation of pre-40S particles in yeast and humans. *Wiley Interdiscip. Rev. RNA* **10**, e1516 (2019).

[PubMed](#) [Google Scholar](#)

6. 6.

Strunk, B. S., Novak, M. N., Young, C. L. & Karbstein, K. A translation-like cycle is a quality control checkpoint for maturing 40S ribosome subunits. *Cell* **150**, 111–121 (2012).

[CAS](#) [PubMed](#) [PubMed Central](#) [Google Scholar](#)

7. 7.

Lebaron, S. et al. Proofreading of pre-40S ribosome maturation by a translation initiation factor and 60S subunits. *Nat. Struct. Mol. Biol.* **19**, 744–753 (2012).

[CAS](#) [PubMed](#) [PubMed Central](#) [Google Scholar](#)

8. 8.

Turowski, T. W. et al. Rio1 mediates ATP-dependent final maturation of 40S ribosomal subunits. *Nucleic Acids Res.* **42**, 12189–12199 (2014).

[CAS](#) [PubMed](#) [PubMed Central](#) [Google Scholar](#)

9. 9.

Widmann, B. et al. The kinase activity of human Rio1 is required for final steps of cytoplasmic maturation of 40S subunits. *Mol. Biol. Cell* **23**, 22–35 (2012).

[CAS](#) [PubMed](#) [PubMed Central](#) [Google Scholar](#)

10. 10.

Angermayr, M., Roidl, A. & Bandlow, W. Yeast Rio1p is the founding member of a novel subfamily of protein serine kinases involved in the control of cell cycle progression. *Mol. Microbiol.* **44**, 309–324 (2002).

[CAS](#) [PubMed](#) [Google Scholar](#)

11. 11.

Ferreira-Cerca, S., Kiburu, I., Thomson, E., LaRonde, N. & Hurt, E. Dominant Rio1 kinase/ATPase catalytic mutant induces trapping of late pre-40S biogenesis factors in 80S-like ribosomes. *Nucleic Acids Res.* **42**, 8635–8647 (2014).

[CAS](#) [PubMed](#) [PubMed Central](#) [Google Scholar](#)

12. 12.

Laronde-LeBlanc, N., Guszczynski, T., Copeland, T. & Wlodawer, A. Structure and activity of the atypical serine kinase Rio1. *FEBS J.* **272**, 3698–3713 (2005).

[CAS](#) [PubMed](#) [Google Scholar](#)

13. 13.

Meyer, B. et al. Ribosome biogenesis factor Tsr3 is the aminocarboxypropyl transferase responsible for 18S rRNA hypermodification in yeast and humans. *Nucleic Acids Res.* **44**, 4304–4316 (2016).

[CAS](#) [PubMed](#) [PubMed Central](#) [Google Scholar](#)

14. 14.

Babaian, A. et al. Loss of m¹acp³Ψ ribosomal RNA modification is a major feature of cancer. *Cell Rep.* **31**, 107611 (2020).

[CAS](#) [PubMed](#) [Google Scholar](#)

15. 15.

Hector, R. D. et al. Snapshots of pre-rRNA structural flexibility reveal eukaryotic 40S assembly dynamics at nucleotide resolution. *Nucleic Acids Res.* **42**, 12138–12154 (2014).

[CAS](#) [PubMed](#) [PubMed Central](#) [Google Scholar](#)

16. 16.

Heuer, A. et al. Cryo-EM structure of a late pre-40S ribosomal subunit from *Saccharomyces cerevisiae*. *eLife* **6**, e30189 (2017).

[PubMed](#) [PubMed Central](#) [Google Scholar](#)

17. 17.

Scaiola, A. et al. Structure of a eukaryotic cytoplasmic pre-40S ribosomal subunit. *EMBO J.* **37**, e98499 (2018).

[PubMed](#) [PubMed Central](#) [Google Scholar](#)

18. 18.

O'Donohue, M. F., Choesmel, V., Faubladier, M., Fichant, G. & Gleizes, P. E. Functional dichotomy of ribosomal proteins during the synthesis of mammalian 40S ribosomal subunits. *J. Cell Biol.* **190**, 853–866 (2010).

[PubMed](#) [PubMed Central](#) [Google Scholar](#)

19. 19.

Montellese, C. et al. USP16 counteracts mono-ubiquitination of RPS27a and promotes maturation of the 40S ribosomal subunit. *eLife* **9**, e54435 (2020).

[CAS](#) [PubMed](#) [PubMed Central](#) [Google Scholar](#)

20. 20.

Badertscher, L. et al. Genome-wide RNAi screening identifies protein modules required for 40S subunit synthesis in human cells. *Cell Rep.* **13**, 2879–2891 (2015).

[CAS](#) [PubMed](#) [Google Scholar](#)

21. 21.

Farley-Barnes, K. I. et al. Diverse regulators of human ribosome biogenesis discovered by changes in nucleolar number. *Cell Rep.* **22**, 1923–1934 (2018).

[CAS](#) [PubMed](#) [PubMed Central](#) [Google Scholar](#)

22. 22.

Yu, J. & Marintchev, A. Comparative sequence and structure analysis of eIF1A and eIF1AD. *BMC Struct. Biol.* **18**, 11 (2018).

[PubMed](#) [PubMed Central](#) [Google Scholar](#)

23. 23.

Bertomeu, T. et al. A high-resolution genome-wide CRISPR/Cas9 viability screen reveals structural features and contextual diversity of the human cell-essential proteome. *Mol. Cell. Biol.* **38**, e00302-17 (2018).

[CAS](#) [PubMed](#) [Google Scholar](#)

24. 24.

Acker, M. G., Shin, B. S., Dever, T. E. & Lorsch, J. R. Interaction between eukaryotic initiation factors 1A and 5B is required for

efficient ribosomal subunit joining. *J. Biol. Chem.* **281**, 8469–8475 (2006).

[CAS](#) [PubMed](#) [Google Scholar](#)

25. 25.

Zemp, I. et al. Distinct cytoplasmic maturation steps of 40S ribosomal subunit precursors require hRio2. *J. Cell Biol.* **185**, 1167–1180 (2009).

[CAS](#) [PubMed](#) [PubMed Central](#) [Google Scholar](#)

26. 26.

Pertschy, B. et al. RNA helicase Prp43 and its co-factor Pfa1 promote 20 to 18 S rRNA processing catalyzed by the endonuclease Nob1. *J. Biol. Chem.* **284**, 35079–35091 (2009).

[CAS](#) [PubMed](#) [PubMed Central](#) [Google Scholar](#)

27. 27.

Sloan, K. E., Knox, A. A., Wells, G. R., Schneider, C. & Watkins, N. J. Interactions and activities of factors involved in the late stages of human 18S rRNA maturation. *RNA Biol.* **16**, 196–210 (2019).

[PubMed](#) [PubMed Central](#) [Google Scholar](#)

28. 28.

Lamanna, A. C. & Karbstein, K. Nob1 binds the single-stranded cleavage site D at the 3'-end of 18S rRNA with its PIN domain. *Proc. Natl Acad. Sci. USA* **106**, 14259–14264 (2009).

[ADS](#) [CAS](#) [PubMed](#) [Google Scholar](#)

29. 29.

Espinar-Marchena, F. J., Babiano, R. & Cruz, J. Placeholder factors in ribosome biogenesis: please, pave my way. *Microb. Cell* **4**, 144–168 (2017).

[CAS](#) [PubMed](#) [PubMed Central](#) [Google Scholar](#)

30. 30.

Wyler, E. et al. Tandem affinity purification combined with inducible shRNA expression as a tool to study the maturation of macromolecular assemblies. *RNA* **17**, 189–200 (2011).

[CAS](#) [PubMed](#) [PubMed Central](#) [Google Scholar](#)

31. 31.

Zheng, S. Q. et al. MotionCor2: anisotropic correction of beam-induced motion for improved cryo-electron microscopy. *Nat. Methods* **14**, 331–332 (2017).

[CAS](#) [PubMed](#) [PubMed Central](#) [Google Scholar](#)

32. 32.

Zhang, K. Gctf: Real-time CTF determination and correction. *J. Struct. Biol.* **193**, 1–12 (2016).

[CAS](#) [PubMed](#) [PubMed Central](#) [Google Scholar](#)

33. 33.

Scheres, S. H. RELION: implementation of a Bayesian approach to cryo-EM structure determination. *J. Struct. Biol.* **180**, 519–530 (2012).

[CAS](#) [PubMed](#) [PubMed Central](#) [Google Scholar](#)

34. 34.

Zivanov, J. et al. New tools for automated high-resolution cryo-EM structure determination in RELION-3. *eLife* **7**, e42166 (2018).

[PubMed](#) [PubMed Central](#) [Google Scholar](#)

35. 35.

Punjani, A., Rubinstein, J. L., Fleet, D. J. & Brubaker, M. A. cryoSPARC: algorithms for rapid unsupervised cryo-EM structure determination. *Nat. Methods* **14**, 290–296 (2017).

[CAS](#) [Google Scholar](#)

36. 36.

Emsley, P. & Cowtan, K. Coot: model-building tools for molecular graphics. *Acta Crystallogr. D* **60**, 2126–2132 (2004).

[PubMed](#) [PubMed Central](#) [Google Scholar](#)

37. 37.

Brown, A. et al. Tools for macromolecular model building and refinement into electron cryo-microscopy reconstructions. *Acta Crystallogr. D* **71**, 136–153 (2015).

[CAS](#) [PubMed](#) [Google Scholar](#)

38. 38.

Taoka, M. et al. Landscape of the complete RNA chemical modifications in the human 80S ribosome. *Nucleic Acids Res.* **46**, 9289–9298 (2018).

[CAS](#) [PubMed](#) [PubMed Central](#) [Google Scholar](#)

39. 39.

Kelley, L. A., Mezulis, S., Yates, C. M., Wass, M. N. & Sternberg, M. J. The Phyre2 web portal for protein modeling, prediction and analysis. *Nat. Protoc.* **10**, 845–858 (2015).

[CAS](#) [PubMed](#) [PubMed Central](#) [Google Scholar](#)

40. 40.

Adams, P. D. et al. PHENIX: a comprehensive Python-based system for macromolecular structure solution. *Acta Crystallogr. D* **66**, 213–221 (2010).

[Google Scholar](#)

41. 41.

Goddard, T. D. et al. UCSF ChimeraX: meeting modern challenges in visualization and analysis. *Protein Sci.* **27**, 14–25 (2018).

[CAS](#) [PubMed](#) [Google Scholar](#)

42. 42.

Zemp, I. et al. CK1 δ and CK1 ϵ are components of human 40S subunit precursors required for cytoplasmic 40S maturation. *J. Cell Sci.* **127**, 1242–1253 (2014).

[CAS](#) [PubMed](#) [Google Scholar](#)

43. 43.

van Tran, N. et al. The human 18S rRNA m6A methyltransferase METTL5 is stabilized by TRMT112. *Nucleic Acids Res.* **47**, 7719–7733 (2019).

[PubMed](#) [PubMed Central](#) [Google Scholar](#)

[Download references](#)

Acknowledgements

We thank S. Rieder, C. Ungewickell, H. Sieber and A. Gilmozzi for technical assistance, T. Fröhlich for mass-spectrometry analysis and L. Kater, J. Cheng and T. Becker for discussions and critical comments on the manuscript. This project has received funding from the Deutsche Forschungsgemeinschaft (DFG) through the GRK1721 to R.B., a DFG fellowship through the QBM (Quantitative Biosciences Munich) graduate school to M.A., from the European Research Council (ERC) under the European Union’s Horizon 2020 research and innovation programme (Grant agreement No. 885711—Human-Ribogenesis) to R.B., and the Swiss National Science Foundation (the NCCR ‘RNA and disease’ and grant 31003A_166565) to U.K.

Author information

Affiliations

1. Gene Center Munich, Department of Biochemistry, University of Munich, Munich, Germany

Michael Ameismeier, Matthias Thoms, Otto Berninghausen & Roland Beckmann

2. Institute of Biochemistry, Department of Biology, ETH Zurich, Zurich, Switzerland

Ivo Zemp, Jasmin van den Heuvel & Ulrike Kutay

3. Molecular Life Sciences Ph.D. Program, Zurich, Switzerland

Jasmin van den Heuvel

Authors

1. Michael Ameismeier

[View author publications](#)

You can also search for this author in [PubMed](#) [Google Scholar](#)

2. Ivo Zemp

[View author publications](#)

You can also search for this author in [PubMed](#) [Google Scholar](#)

3. Jasmin van den Heuvel

[View author publications](#)

You can also search for this author in [PubMed](#) [Google Scholar](#)

4. Matthias Thoms

[View author publications](#)

You can also search for this author in [PubMed](#) [Google Scholar](#)

5. Otto Berninghausen

[View author publications](#)

You can also search for this author in [PubMed](#) [Google Scholar](#)

6. Ulrike Kutay

[View author publications](#)

You can also search for this author in [PubMed](#) [Google Scholar](#)

7. Roland Beckmann

[View author publications](#)

You can also search for this author in [PubMed](#) [Google Scholar](#)

Contributions

M.A., R.B., I.Z., J.v.d.H. and U.K designed the study. M.A. and M.T. generated stable cell lines and purified native complexes. M.A. and M.T. prepared the cryo-EM samples and O.B. collected cryo-EM data. M.A. processed the cryo-EM data and built the molecular models. For the functional analysis of novel RBFs, I.Z. and J.v.d.H. performed cellular

analyses. I.Z., J.v.d.H. and U.K. analysed the data and interpreted results. All authors interpreted the combined results and wrote the manuscript.

Corresponding author

Correspondence to [Roland Beckmann](#).

Ethics declarations

Competing interests

The authors declare no competing interests.

Additional information

Peer review information *Nature* thanks Sebastian Klinge, David Tollervey and the other, anonymous, reviewer(s) for their contribution to the peer review of this work.

Publisher's note Springer Nature remains neutral with regard to jurisdictional claims in published maps and institutional affiliations.

Extended data figures and tables

[Extended Data Fig. 1 Sample preparation and cryo-EM data analysis.](#)

a, SDS-PAGE analysis of native pre-40S complexes purified with RIOK1(D324) and NOB1(D10N). Identified protein bands are labelled. For gel source data, see Supplementary Fig. 1. **b**, Representative micrographs from the three data sets. Scale bar 50 nm **c**, Subset of 2D averages of extracted particles after initial 2D classification. **d, e**, Summarized classification scheme of RIOK1(D324A) (**d**) and NOB1(D10N) (**e**). Particles of final states, marked in orange, were subjected to CTF parameter refinement and Bayesian polishing before the last 3D refinement. **f**,

Particles of state G from both NOB1(D10N) data sets were combined and classified. Final volume is marked in orange. **g**, Summarized classification scheme of LRRC47.

Extended Data Fig. 2 Local resolution, refinement and model statistics.

a, Local resolution distribution of states F1 – H2 with their respective colour grading scheme as estimated by Relion. **b**, Fourier shell correlation (FSC) curve for all states. Average resolution values as stated in Fig. 1 are calculated according to the ‘gold standard’ at FSC = 0.143. **c**, FSC plot of the models against their volume as provided by Phenix. **d**, Local resolution estimation of the ‘head’ region of state F2 after focused refinement. **e, f**, Model and cryo-EM density of state H1 around the post-transcriptionally modified rRNA residues C1337, G1490 (**e**), and A1832 (see ref. 43.) (**f**).

Extended Data Fig. 3 Details on RIOK1 binding to the pre-40S particle.

a, Superposition of models of RIOK1 and RIOK2 after alignment of state D (PDB-6G51) and H1 highlight the overlapping binding site at the decoding centre and the rotation of their central RIO domain by approximately 15°. **b**, Cartoon representation of eL41 (PDB-6G5H), as well as the C terminus of LTV1 (PDB-6G51) and RIOK1 relative to the top of the matured h44 in state H1. Overlaps in binding sites highlight mutually exclusive binding. **c**, Models of state F1, F2 and H1 with focus on RIOK1 position. Unaccounted density within the mRNA entry tunnel in states F1 and F2 (yellow) is likely the flexible N terminus of RIOK1, which overlaps with the two helices of factor X present in state E (marked with a red cross, see ref. 4.). **d**, Surface representation of state D (PDB-6G51) with RBF TSR1 in cartoon representation. Models of RIOK1 (left) and LRRC47 (right) of state F1 after alignment of the particles emphasize the overlaps in binding sites around h44. **e**, Post-transcriptional modification of U1248 leads to formation of 1-methyl-3- α -amino- α -carboxypropyl pseudouridine ($m^1acp^3\Psi$). Modifying enzymes and their contribution to the structure are

indicated by colours. **f**, Cartoon representation showing the coordination of $m^1\text{acp}^3\Psi 1248$ by RIOK1.

Extended Data Fig. 4 Structural details of novel factors LRRC47 and EIF1AD.

a, Overall structure of the two domains of LRRC47. Leucine residues, secondary structure elements and position of h44 are highlighted. **b**, Low-resolution cryo-EM reconstruction of a sample using N-terminally tagged LRRC47 (left) and state H1 filtered at 7 Å (right). The leucine-rich domain of LRRC47 (blue) binds simultaneously with TSR1, while the C-terminal domain remains delocalized and is therefore not visible. **c**, Models of LRRC47, h44 and parts of TSR1 show the conformational changes in h44 that accompany the transition between the states. A central part of h44 moves after release of TSR1, enabled by the lack of its N-terminal helix (left). The B3/4 domain of LRRC47 would clash with both displayed helices of TSR1. LRRC47 continues to bind in an almost unchanged position after maturation of h44 (right). **d**, Structure of EIF1AD with its N-terminal helix and residues N36, R58, K59 and W62 labelled. **e**, Cartoon representation of rRNA segments and ribosomal proteins surrounding EIF1AD in state H1. Model of yeast eIF1A (PDB-6GSN) after alignment of a pre-48S translation initiation complex to the pre-40S particle shows a shifted binding location. **f**, Sequence alignment of human EIF1AD and eIF1A. Conserved residues that bind to rRNA are coloured blue and the IDDI motif of eIF1A in red. The conserved C-terminal stretch that binds to uS13 and uS19 is marked with a blue box. **g**, Model of state H1 with cryo-EM volume of EIF1AD and eS25 Gaussian filtered at 1.5 standard deviations. Additional density extends from well resolved parts of the C terminus of EIF1AD. Detailed views on eS25 N terminus and EIF1AD C terminus are shown in boxes A and B.

Extended Data Fig. 5 EIF1AD but not LRRC47 depletion affects late 40S subunit maturation.

a, Western blot analysis of the experiment shown in Fig. 4 confirming the effectiveness of siRNA treatments for EIF1AD and RIOK2. **b**, Western blot

analysis for the experiment in **c** confirming the depletion of LRRC47 or RIOK2 upon siRNA treatment. For gel source data of **a** and **b**, see Supplementary Fig. 1. **c**, Immunofluorescence analysis of HeLa cells treated with siRNAs against LRRC47 or RIOK2 using antibodies against the indicated RBFs. For immunofluorescence analysis of NOB1, cells were treated with 20 nM leptomycin B (LMB) for 90 min. Note that only RIOK2 but not LRRC47 depletion leads to cytoplasmic recycling defects of the tested RBFs. Scale bar, 20 μ m. **d**, FISH analysis of experiment in **b**, revealing cytoplasmic accumulation of 18S-E pre-rRNA upon RIOK2 but not LRRC47 depletion. FISH pictures were processed in parallel, using a gamma correction of 1.5. All experiments were done in triplicates ($n = 3$).

[Extended Data Fig. 6 Structural details of rRNA 3'end maturation.](#)

a, Cartoon representation of the 3' end of 18S-E rRNA with PNO1, NOB1 and eS26 throughout the maturation process in states F2, G and H1. Panel of eS26 with 18S rRNA in state H1 has been shifted slightly upwards as indicated by the line to the right. **b**, Detailed view of NOB1(D10N) active site with its substrate. Dashed circle marks site 3 cleavage site. Electron density around ITS1 and the 3'end shown in blue. **c**, Stick representation of NOB1 residues that interact with the ITS1 and 3' end with electron density shown in blue.

Extended Data Table 1 Data collection and refinement statistics [Full size table](#)

Supplementary information

[Supplementary Figure](#)

Supplementary Figure 1 This file contains a figure with the uncropped SDS-PAGE and western blot images. Related to Extended Data Figs. 1 and 5.

[Reporting Summary](#)

Rights and permissions

[Reprints and Permissions](#)

About this article



Check for
updates

Cite this article

Ameismeier, M., Zemp, I., van den Heuvel, J. *et al.* Structural basis for the final steps of human 40S ribosome maturation. *Nature* **587**, 683–687 (2020). <https://doi.org/10.1038/s41586-020-2929-x>

[Download citation](#)

- Received: 14 October 2019
- Accepted: 28 August 2020
- Published: 18 November 2020
- Issue Date: 26 November 2020
- DOI: <https://doi.org/10.1038/s41586-020-2929-x>

Comments

By submitting a comment you agree to abide by our [Terms](#) and [Community Guidelines](#). If you find something abusive or that does not comply with our terms or guidelines please flag it as inappropriate.

[Access through your institution](#)

[Change institution](#)

Buy or subscribe

This article was downloaded by **calibre** from <https://www.nature.com/articles/s41586-020-2929-x>

| [Section menu](#) | [Main menu](#) |

Collections